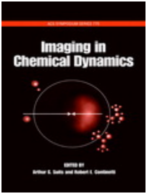

ACS SYMPOSIUM SERIES 770

# Imaging in Chemical Dynamics

EDITED BY

Arthur G. Suits and Robert E. Continetti

# Imaging in Chemical Dynamics

Downloaded by 89.163.34.136 on September 17, 2012 | http://pubs.acs.org
Publication Date: October 18, 2000 | doi: 10.1021/bk-2001-0770.fw001

Downloaded by 89.163.34.136 on September 17, 2012 | http://pubs.acs.org
Publication Date: October 18, 2000 | doi: 10.1021/bk-2001-0770.fw001

Downloaded by 89.163.34.136 on September 17, 2012 | http://pubs.acs.org
Publication Date: October 18, 2000 | doi: 10.1021/bk-2001-0770.fw001

ACS SYMPOSIUM SERIES **770**

# Imaging in Chemical Dynamics

**Arthur G. Suits,** EDITOR
*Berkeley Laboratory*

**Robert E. Continetti,** EDITOR
*University of California*

American Chemical Society, Washington, DC

Downloaded by 89.163.34.136 on September 17, 2012 | http://pubs.acs.org
Publication Date: October 18, 2000 | doi: 10.1021/bk-2001-0770.fw001

**Library of Congress Cataloging-in-Publication Data**

Imaging in Chemical Dynamics / Arthur G. Suits, editor, Robert E. Continetti, editor.

p. cm.—(ACS symposium series ; 770)

Includes bibliographical references and index.

ISBN 0-8412-3690-9

1. Molecular dynamics—Congresses. 2. Imaging systems in Chemistry—Congresses.

I. Suits, Arthur G., 1954- . II. Continetti, Robert E., 1962- . III. Series.

QD461..I53 2000
541.3'94'0284—dc21 00-44188

The paper used in this publication meets the minimum requirements of American National Standard for Information Sciences—Permanence of Paper for Printed Library Materials, ANSI Z39.48-1984.

Copyright © 2001 American Chemical Society

Distributed by Oxford University Press

All Rights Reserved. Reprographic copying beyond that permitted by Sections 107 or 108 of the U.S. Copyright Act is allowed for internal use only, provided that a per-chapter fee of $20.00 plus $0.50 per page is paid to the Copyright Clearance Center, Inc., 222 Rosewood Drive, Danvers, MA 01923, USA. Republication or reproduction for sale of pages in this book is permitted only under license from ACS. Direct these and other permission requests to ACS Copyright Office, Publications Division, 1155 16th St., N.W., Washington, DC 20036.

The citation of trade names and/or names of manufacturers in this publication is not to be construed as an endorsement or as approval by ACS of the commercial products or services referenced herein; nor should the mere reference herein to any drawing, specification, chemical process, or other data be regarded as a license or as a conveyance of any right or permission to the holder, reader, or any other person or corporation, to manufacture, reproduce, use, or sell any patented invention or copyrighted work that may in any way be related thereto. Registered names, trademarks, etc., used in this publication, even without specific indication thereof, are not to be considered unprotected by law.

PRINTED IN THE UNITED STATES OF AMERICA

American Chemical Society
Library
1155 16th St., N.W.
Washington, D.C. 20036

# Foreword

THE ACS SYMPOSIUM SERIES was first published in 1974 to provide a mechanism for publishing symposia quickly in book form. The purpose of the series is to publish timely, comprehensive books developed from ACS sponsored symposia based on current scientific research. Occasionally, books are developed from symposia sponsored by other organizations when the topic is of keen interest to the chemistry audience.

Before agreeing to publish a book, the proposed table of contents is reviewed for appropriate and comprehensive coverage and for interest to the audience. Some papers may be excluded in order to better focus the book; others may be added to provide comprehensiveness. When appropriate, overview or introductory chapters are added. Drafts of chapters are peer-reviewed prior to final acceptance or rejection, and manuscripts are prepared in camera-ready format.

As a rule, only original research papers and original review papers are included in the volumes. Verbatim reproductions of previously published papers are not accepted.

ACS BOOKS DEPARTMENT

Downloaded by 89.163.34.136 on September 17, 2012 | http://pubs.acs.org
Publication Date: October 18, 2000 | doi: 10.1021/bk-2001-0770.fw001

Downloaded by 89.163.34.136 on September 17, 2012 | http://pubs.acs.org
Publication Date: October 18, 2000 | doi: 10.1021/bk-2001-0770.pr001

# Preface

Chemical dynamics is a field poised at the intersection between chemistry and physics, relying on sophisticated experimental and theoretical techniques to answer, in rich quantum mechanical detail, the most basic questions one can ask about the dynamics of fundamental chemical reactions, questions such as: What are the products in a given reaction or photochemical process? Which part of a molecule is most reactive? What approach geometries are important? Where does the energy go in a reaction? How is the angular momentum distributed in the products?. The importance of questions such as these lies in their general nature and the deep understanding that the answers can provide. Practical chemical systems, from planetary atmospheres to automobile engines, all feature a vast array of elementary reactions involving large and complex molecules, and these systems are far too numerous to be modeled in detailed from first principles. A predictive understanding of macroscopic chemical systems thus can only be built upon a foundation of knowledge of the general trends and underlying principles governing these phenomena. Chemical dynamics is the field that builds this foundation. As mentioned above, it is an effort largely driven by technological advances: as new experimental and theoretical methods emerge, advances in understanding inevitably follow. Molecular beam methods and universal mass spectrometric detection represent the initial advance that defined the pioneering efforts in the 1960s and 1970s; laser methods have played a crucial role since the early 1970s, culminating with the 1999 Nobel Prize for femtochemistry; and imaging methods are now driving new advances in the field in several key areas.

The symposium on Imaging in Chemical Dynamics at the 212th National American Chemical Society (ACS) Meeting in New Orleans, Louisiana, brought together researchers from around the world to discuss current state-of-the-art applications of imaging techniques in chemical dynamics. As the presentations at the symposium and the 21 chapters in this volume indicate, imaging methods have provided important insights into diverse phenomena in chemical reaction dynamics. Although a large number of the experimental studies presented here are based on CCD-camera ion-imaging methods, a number of contributions use event-wise three-dimensional methods appropriate for coincidence measurements. A driving force behind the organization of this symposium was a desire to bring the scientists using these distinct approaches together for an exchange of ideas and problems. In that regard, this symposium follows the 1993 "Workshop on Imaging Methods" held at Neve Ilan, Israel, organized by George McBane and Daniel Zajfman, and attended by some 44 researchers from around the world. This symposium at the 212th ACS National Meeting in New Orleans, Louisiana, was the next international meeting specifically intended to bring together researchers using imaging methods for the study of chemical dynamics. The purpose of this volume is to showcase these advances, provide a useful reference for those entering the field, and foster new developments and new directions. We believe that the book provides a timely snapshot of the development of this important tool in modern chemical dynamics.

## Acknowledgments

We thank Professor G. C. Schatz for the invitation to organize an ACS Symposium on this topic, and the Petroleum Research Fund of the ACS for grant-in-aid number 33793-SE in support of this symposium. We also thank Anne Wilson and Kelly Dennis of the ACS Editorial Staff for their help in producing this volume. Finally, we wish to thank all of the authors for their stimulating contributions.

ARTHUR G. SUITS
Chemical Sciences Division, MS 6–2100
Ernest Orlando Lawrence Berkeley National Laboratory
Berkeley, CA 94720

ROBERT E. CONTINETTI
Department of Chemistry and Biochemistry, 0314
University of California at San Diego
9500 Gilman Drive
La Jolla, CA 92093–0314

Downloaded by 89.163.34.136 on September 17, 2012 | http://pubs.acs.org
Publication Date: October 18, 2000 | doi: 10.1021/bk-2001-0770.pr001

Downloaded by 89.163.34.136 on September 17, 2012 | http://pubs.acs.org
Publication Date: October 18, 2000 | doi: 10.1021/bk-2001-0770.ch001

## Chapter 1

# Imaging in Chemical Dynamics: The State of the Art

**Arthur G. Suits[1] and Robert E. Continetti[2]**

[1]**Chemical Sciences Division, Ernest Orlando Lawrence Berkeley National Laboratory, Berkeley, CA 94720**
[2]**Department of Chemistry and Biochemistry, University of California at San Diego, 9500 Gilman Drive, La Jolla, CA 92093–0314**

We present a snapshot of the rapidly growing field of imaging-based probes of chemical dynamics. This chapter is broadly divided into two sections corresponding to the two fundamentally distinct experimental approaches. The first concerns 'ion imaging' and the more recent variant 'velocity map imaging', characterized by the use of phosphor screens viewed by CCD cameras. The second approach may be considered event-wise data acquisition, in which a variety of techniques are used to obtain both time and position data for each event, often in coincidence applications. We provide a brief historical overview and highlight significant current advances showcasing the broad range of applicability of these powerful techniques. We conclude with some thoughts on the future promise of imaging methods in chemical dynamics.

## Introduction

Chemical dynamics is a thriving enterprise, a field continually spurred to new frontiers by technological advances. Molecular beams and lasers have each played key roles in stimulating such advances at various times in the history of the field. Beginning in the late 1980s, ion imaging emerged as a uniquely powerful combination of these experimental tools. With the advent of the velocity map imaging method ten years later, the applications of imaging to chemical dynamics experienced a renewed explosion of interest, and much of this recent work is illustrated in this volume.

---

[1]*Permanent address:* **Department of Chemistry, State University of New York, Stony Brook, New York, 11794, and Department of Chemistry, Brookhaven National Laboratory, Upton NY, 11973**

Although the use of ion imaging methods in chemical dynamics is often dated to work by Chandler and Houston(*1*), application of position sensitive detection to problems in physics has a long history, shown for example in the 1992 Nobel prize awarded to Georges Charpak for the development of the multiwire proportional counter. These techniques have typically been employed in an event-wise approach that is not so well suited to the low repetition-rate nanosecond lasers that have been the workhorses of the chemical dynamics field. These methods are ideal, however, for application in quasi-continuous modes at accelerators and synchrotrons, with high-repetition rate lasers, and particularly for coincidence applications. The lines between the ion imaging and event-wise approaches, at least with regard to the systems of study, have begun to blur in recent years, and there is no question that a great deal is to be gained from effective communication between these two constituencies in the imaging community. Nevertheless, these two approaches are quite distinct, and provide a convenient means of separating the broader field into identifiable camps. We have thus chosen to subdivide this overview into two sections, the first dealing with the ion imaging technique and its later variant Velocity Map Imaging (which we will abbreviate VELMI), the second dealing with event-wise detection schemes and their applications.

Downloaded by 89.163.34.136 on September 17, 2012 | http://pubs.acs.org
Publication Date: October 18, 2000 | doi: 10.1021/bk-2001-0770.ch001

## Ion Imaging and Velocity Map Imaging

The birth of the imaging technique in application to chemical dynamics problems is generally considered to be the 1987 paper by David Chandler and Paul Houston on the photodissociation of methyl iodide, (*1*) in which the original ion imaging technique was described. It is interesting to note, however, that Solomon and coworkers(*2,3*), as early as 1967 used a coated reaction vessel to demonstrate that photolysis of molecules by polarized lasers can give rise to anisotropic distributions of products. Although this approach was clearly limited in scope, it provided a dramatic mapping of the phenomenon under study. It is precisely this compelling "analog" aspect of imaging that is both its power and its joy. Since 1987, the ion imaging technique has been applied, with surprisingly little modification, to a vast number of problems in chemistry and physics, and we will present many examples below. We will not here attempt a review of the field of ion imaging or the recent introduction of the higher-resolution VELMI technique; this has been accomplished in a number of other recent reviews(*4-8*). Instead, we will highlight examples of current work, some of which is documented in detail elsewhere in this volume, that affords a measure of the breadth of the studies and the excitement associated with it. We divide what follows roughly according to the subject of study, providing only enough of the history to place the current work in context.

## Photodissociation dynamics

The original ion imaging paper of Chandler and Houston set the stage for much of what followed by employing tunable probe lasers to record images of state-selected photofragments. This same fundamental approach has been used with little modification by many others to study a wide range of photochemical problems, and this work has largely been the subject of a number of earlier reviews mentioned above. The next substantial advance came in 1997 with the technique of 'velocity map imaging' of Eppink and Parker. In the velocity map imaging method, electrostatic ion lenses are employed rather than grids to achieve momentum focusing. Under these conditions, all particles with the same initial velocity vector are mapped onto the same point on a 2D detector, irrespective of their position of creation in the ionization volume. This led to a dramatic increase in image resolution (both speed and angle) and a burst in interest in the technique. In the following section we illustrate the technique with a few examples of photodissociation studies that have appeared since the advent of the VELMI method.

In the original reports on the VELMI technique, the authors measured both the oxygen atoms and corresponding photoelectrons formed in the state-selected photodissociation/ionization of $O_2$. They found that excited atom production and subsequent photoionization accounts for half of the $O^+$ formation on excitation from the chosen Rydberg state. Autoionization gives rise to a complete range of vibrational excitation (v= 2-23), much more than previously expected, and dissociation of levels v>4 leads to the other half of the measured $O^+$ production. (*9*)

Velocity map imaging has also been used to measure $O(^3P_j)$, j=0, 1, 2 atom angular distributions arising from the photodissociation of molecular oxygen at several wavelengths across the Herzberg continuum. The high image quality afforded by the method has allowed the determination of anisotropy parameters, even for such extremely weak transitions as those involved in the Herzberg systems. (*10*)

Bakker *et al* performed a two-photon dissociation study of NO near 275 nm using velocity map imaging. They observed two channels: $O(^3P_2) + N(^4S)$ and $O(^3P_2) + N(^2D)$; $N(^4S)$ had a $\beta = 0.4$, while the channel leading to the formation $N(^2D)$ produced unaligned products. The authors were interested in exploiting two-photon dissocation processes as a strategy to form monoenergetic O and N atoms with known angular distributions for their use in measurements of the stereodynamics of their chemical reactions. (*11*) (*12*)

Ashfold and co-workers studied the photodissociation dynamics of BrCl at 26 excitation wavelengths between 235 and 540 nm; they detected both ground and spin-orbit excited Cl and Br. Anisotropy parameters for the various Cl and Br spin-orbit components showed extensive variation with wavelength which could be understood

Downloaded by 89.163.34.136 on September 17, 2012 | http://pubs.acs.org
Publication Date: October 18, 2000 | doi: 10.1021/bk-2001-0770.ch001

in terms of excitation to different states. (*13*). Similar studies were also performed on $Br_2$. (*14*)

In a study of the photoinitiated unimolecular decomposition of jet cooled $NO_2$, it was shown that the recoil anisotropy parameter of the photofragments, $\beta$, depended strongly on the rotational angular momentum of the photoproduct. (*15*) The experimental observations were rationalized with a classical model that takes into account the transverse recoil component mandated by angular momentum conservation.

$O_3$ photodissociation has long been of interest to the practitioners of ion imaging owing to its importance in atmospheric chemistry, and the fact that $O_3$ photodissociation in the UV is a good source for $O(^1D)$ atoms for use in bimolecular reaction dynamics studies. Houston's group has extended earlier studies by performing photodissociation studies of ozone at 226, 230, 240 and 266 nm. (*16*). For dissociation at 226 and 230 nm, the probed oxygen atoms exhibit bimodal velocity distributions; the bimodality becomes less pronounced for photolysis at the longer wavelengths. The anisotropy parameter showed a marked dependence on the translational energy release; this dependence reflecting a strong correlation between the average ozone bond angle prior to dissociation and the partitioning of available energy between the translational and internal energies of the photofragments.

Photodissociation of $O_3$ was performed near 305 nm, and the resulting $O(^1D)$ fragment was measured using a new ion-counting method (*17*) in conjunction with velocity map imaging. (*18*) The kinetic energy distribution obtained from the image showed rotational structure due to the $O_2$ (a $^1\Delta_g$, v" = 0) fragment. The bond energy into $O(^1D)$ + $O_2$ (a $^1\Delta_g$) was obtained from rotational assignment of these kinetic energy distributions. From this the authors could determine the heat of formation of $O_3$, the results were consistent with those determined using laser-induced fluorescence spectroscopy in the same study.

Tanaka *et al* imaged the recoil velocity and angular distributions of ground and spin-orbit excited chlorine formed in the photodissociation of $Cl_2O$ and HOCl at 235nm. (*19*) In the case of $Cl_2O$, both Cl spin-orbit products had the same angular distribution, but the recoil velocity distribution was markedly different. The ground state atoms are partnered by ClO fragments carrying significantly higher average levels of internal excitation. The slowest Cl atoms were formed n a three body fragmentation of $Cl_2O$. These findings were rationalized in terms of a model potential energy surface for the 1 $^1B_2$ state, which correlates diabatically with ClO(X) radicals together with a spin-orbit excited Cl atom, with efficient radiationless transfer to one or more lower energy surfaces at extended Cl-O bond lengths accounting for the dominance of ground state Cl fragments. In the case of HOCl, the image of the ground state Cl atom was consistent with parent excitation via a transition for which the dipole moment was closely aligned with the Cl-O bond, followed by prompt dissociation with the bulk of the excess energy partitioned into product recoil.

Samartzis and Kitsopoulos performed a one-color two-photon dissociation study of $CS_2$ using ion imaging. From the S atom photofragment translational energy distribution they surmised that CS was produced in both the X $^1\Sigma^+$ and $a^3\Pi$ electronic states and that half of the available energy was taken up by the CS internal degrees of

Downloaded by 89.163.34.136 on September 17, 2012 | http://pubs.acs.org
Publication Date: October 18, 2000 | doi: 10.1021/bk-2001-0770.ch001

freedom. By analysing the angular distributions, the authors concluded that the excited electronic states involved in the photodissociation process were Rydberg states with predissociation lifetimes estimated at ~ 1 ps. (*20*)

Kim *et al* studied the photodissociation dynamics of IBr near 267nm using a "center-stripe analysis" of a 2-D ion image. (*21*)The center-stripe intensity profile is equivalent to the 1D projection of a center cross section of the 3D spatial distribution. This technique is similar in spirit to that proposed by Tonokura and Suzuki (*22*) where a slice of the 3D distribution is obtained directly by ion imaging in conjunction with laser sheet ionization. The results for IBr photodissocation showed fragmentation into three channels: $I(^2P_{3/2}) + Br(^2P_{3/2})$, $I(^2P_{3/2}) + Br(^2P_{1/2})$ and $I(^2P_{1/2}) + Br(^2P_{3/2})$, and all three channels, judging from their anisotropy parameters showed mixed character of parallel and perpendicular transtions. The nonadiabatic couplings and the order of the vertical energy levels between the excited states were discussed in terms of difference of the relative quantum yield at different excitation energies. This approach has also been used to study the photodissociation of bromine molecules at 265 nm. (*23*); dissociation was predominantly to the $Br(^2P_{1/2}) + Br(^2P_{3/2})$ channel.

The study of radical photodissociation represents an important emerging area for imaging studies, as it has the potential to provide useful thermochemical and dynamical insight into these important species. Neumark and coworkers have made many contributions using their fast beam technique; their work is described in the following section and an example is shown in Chapter 17. Using VELMI, Ahmed and coworkers have studied the photodissociation of the vinyl radical in a one-color experiment at 243nm. Their results provide insight into the dissociation dynamics, and suggest the occurrence of a channel yielding triplet acetylene.

Downloaded by 89.163.34.136 on September 17, 2012 | http://pubs.acs.org
Publication Date: October 18, 2000 | doi: 10.1021/bk-2001-0770.ch001

## Orientation and alignment studies

Ion imaging in conjunction with polarized laser light can provide information on the angular distribution of angular momentum polarization, which in turn affords insight into the dynamics of a photochemical event in the frame of the molecule. This can be used to reveal the symmetries of the excited states involved, to probe nonadiabatic processes in the photodissociation dynamics and to reveal coherence effects. Houston and coworkers reported strong alignment of the $O_2$ rotational angular momentum in ozone dissociation at 248nm(*24*). Recently, Nesterov and Cline have reported on rotational orientation effects in the NO products from the 355 nm photodissociation of $NO_2$ (*25*). Most imaging vector correlation studies since have focused on angular momentum polarization in atoms, as this represents a relatively undeveloped area.

The first published imaging study of atomic alignment was a report from Suzuki's group on the $S(^1D)$ from OCS photodissociation(*26*). Bracker *et al.* recently developed the theoretical machinery making the connection between ion imaging experiments and anisotropy parameters developed by Vasyutinskii *et al.*(*27*) that characterize the electronic angular momentum polarization in a rigorous quantum mechanical framework(*28*). This approach is described in detail in chapter 15. These tools allowed them to show the contribution of nonadiabatic processes in $Cl_2$ dissociation at 355 nm. (*29*), and have subsequently been applied to a number of polyatomic systems. (*30,31*). The photodissociation of $Cl_2$ has been recently examined between 310 and 470 nm using velocity map imaging. These studies extend earlier work performed using ion imaging by the same investigators. (*32*) The authors were able to determine the $Cl^*$ /Cl branching ratio as a function of photolysis wavelength and they found the ratio increased with wavelength increase, reaching a maximum around 430 nm. The $Cl(^2P_{3/2})$ photofragment was shown to be aligned and the magnitude of the alignment was quantitatively determined.(*33*).

Neyer *et al.* have recently performed an extensive study on the ultraviolet photodissociation of $N_2O$. (*34*) Around ~200 nm, the authors showed that images of $O(^1D_2)$ revealed a speed-dependent angular distribution resulting from both variation in the spatial anisotropy of the recoil and alignment of the electronic angular momentum of the $O(^1D_2)$ fragment. Velocity map imaging experiments for the matching co-fragment $N_2$ were also performed (*35*), revealing a J-dependent anistropy. Velocity mapping was essential to provide the detail in which these systems could be studied.

More recently, Parker and co-workers found that two-step photodissociation of $O_2$ with a total excitation energy of 7.7 eV yielded $O(^1D)$ atoms with their angular momentum strongly aligned perpendicular to the fragment recoil axis. This result is surprising given the numerous manifold of states leading to the lower $O(^3P) + O(^3P)$ dissociation limit that had to be crossed and the many possibilities of curve-crossing within the $O(^3P) + O(^1D)$ manifold. The dissociation of $O_2$ is apparently very adiabatic, leading to a large preference for the lowest O-atom fine structure state and near-complete conservation of atomic alignment during dissociation. (*36*)

Rakitzis *et al* have recently observed symmetry breaking in the angular distributions of oriented photofragments in the first imaging study of atomic orientation. They measured this phenomenon in $S(^1D_2)$ photofragments formed in the photodissociation of OCS.(*37*).

A fascinating and distinct approach to these problems has been employed by Janssen and coworkers, using hexapole focusing first to orient the molecule, then imaging to detect the angular distributions of the photofragments(*38,39*). Their results beautifully demonstrate the ability of the hexapole state selection to produce effectively single, fully oriented quantum states for photodissociation.

## Scattering studies

Crossed-beam scattering has long been one of the natural applications of the imaging method, where the detailed differential cross sections may be directly revealed in the center-of-mass frame. Crossed-beam imaging was first reported by Houston and coworkers for Ar-NO inelastic scattering(*40,41*). The first reactive scattering study, on the fundamental hydrogen exchange reaction by Chandler and coworkers (*42*), followed soon after. Since the early studies, most of the scattering work has been on a variety of inelastic processes; and there are several excellent

Downloaded by 89.163.34.136 on September 17, 2012 | http://pubs.acs.org
Publication Date: October 18, 2000 | doi: 10.1021/bk-2001-0770.ch001

examples discussed in this volume (see Chapter 12 and 13) Reactive scattering has been reported recently by Suits and coworkers for $O(^1D)+D_2$, and more recently for the Cl+ROH systems using single-photon vacuum ultraviolet photoionization, with the latter described in Chapter XX. One novel approach to "imaging" scattering is embodied in the work of Kopin Liu, who has used a Doppler-selected time-of-flight method to explore the reaction dynamics for a number of important systems(*43*). In this method, a laser beam is directed along the relative velocity vector for the reaction to select one "slice" of the recoiling product sphere. A subset of this sphere is then core-sample into an ion flight region to obtain the product distributions in a velocity-flux grid, effectively yielding an "image" of the cartesian contour map directly. The results have shown clear vibrational structure in the recoil distributions for the $O(^1D) + H_2$ reaction. Crossed-beam studies can lead to significant issues with regard to detection inhomogeneity; this topic is considered in detail by McBane in Chapter 13. One other novel application of imaging to scattering is shown by the work of Jacobs and coworkers on surface scattering described in Chapter 9.

Downloaded by 89.163.34.136 on September 17, 2012 | http://pubs.acs.org
Publication Date: October 18, 2000 | doi: 10.1021/bk-2001-0770.ch001

### Imaging photoelectron spectroscopy

The power of imaging to reveal simultaneous energy and angular distributions for photoelectrons has been exploited extensively by Helm and coworkers(*44,45*). This approach has the advantage over conventional time-of-flight and electrostatic electron energy analyzers in that: 1) the energy and angular distributions are obtained simultaneously, and 2) *all* electrons are collected, leading to vast improvements in sensitivity. Helm and coworkers have used the approach extensively to study multiphoton ionization processes in high laser fields(*46,47*). The 'photodetachment microscope,' introduced in 1996, effectively employs momentum focusing of the electrons as in the VELMI approach(*48*). The goal of these studies is not to record electron kinetic energy distributions, however. Instead, the intent is to observe interference patters in the electrons photodetached from atoms very near threshold. These interference patterns are said to manifest directly the wave function of the atom itself.

Since the advent of the VELMI approach, and the widespread adoption of the method, many groups are employing imaging techniques to record photoelectron spectra. Some of these are employed in a coincidence approach, discussed below, while others have used photoelectron imaging as an additional diagnostic to gain additional insight into a particular problem. Examples of this may be found in the work of Parker et al. on $O_2$ mentioned above (*9*); another is the work of Peterka et al. on $O_4^*$ discussed in Chapter 11. An example of recent efforts to use femtosecond time-resolved photoelectron studies to study neutral dissociation dynamics is found in the work by Suzuki discussed in Chapter 16.

## Coincidence Studies using Three-Dimensional Time- and Position-Sensitive Detection Techniques

The current applications of three-dimensional imaging techniques involving the implementation of time- and position-sensitive detectors to problems in chemical dynamics represents an influence that can be traced directly to applications in nuclear physics. A brief review of some of the important steps along this pathway will be reviewed here, along with some of the important applications of these approaches represented in this symposium and the current literature.

## Experimental Techniques

The three-dimensional or event-wise techniques differ from the currently more popular imaging experiments discussed above in that they seek to determine by direct measurement the three-dimensional velocity distributions of the atomic or molecular fragments or photoelectrons produced in a dissociation process. One could think of almost any angle-resolved time-of-flight experiment in this manner, but for the purposes of this overview, we will restrict our comments to large-solid angle, multiplexed measurements using time and position-sensitive detectors for chemical dynamics studies. This distinction means that experimental approaches involving detection of small product solid-angles including most photoelectron-photoion coincidence spectroscopies used in synchrotron experiments, (*49*) and (e,2e) experiments on molecular electronic structure, (*50*) among others, will not be discussed here.

One of the key technical developments that have made the three-dimensional spectroscopies and the more conventional imaging techniques discussed above feasible is the availability of large-area microchannel-plate electron multipliers (MCPs).(*51*) These only became widely available in the late 1970's, and shortly thereafter a number of applications to problems in chemical physics were made. MCP's were essential to the application of imaging methods in chemical dynamics due to the fact that they provided a means of amplifying single electrons, ions and neutral atoms and molecules into measurable (pC) charges over large solid angles. This allows some of the powerful detection techniques used so successfully in nuclear physics studies to be applied to chemical problems. An important difference, however, is that compared to high energy particles that can pass through a number of momentum and energy analyzing detectors, in chemistry one only gets one chance to measure the momentum vector of the particle – upon impact on the face of the MCP.

One of the first disciplines to make wide use of microchannel plate image intensifiers was the experimental astrophysics community. Interest in measurements of astrophysical emission spectra using satellite-based instruments drove the development of multiplexed spectrometers that could provide wide spectral coverage by dispersing the output of a grating spectrometer over a large detector area. Astrophysical applications continue to be an important driving force in the further development of these technologies. A variety of readout methods have been employed to convert the charge cloud generated from a set of microchannel plates into

Downloaded by 89.163.34.136 on September 17, 2012 | http://pubs.acs.org
Publication Date: October 18, 2000 | doi: 10.1021/bk-2001-0770.ch001

position information, including crossed-grids (either individually instrumented or connected to delay lines), (*52*) resistive anodes (*53*) and patterned conducting anodes such as the wedge-and-strip anode and other designs. (*54*) Many of these techniques had a long history in nuclear physics and X-ray imaging applications, but had to be adapted to small-area detectors (several cm in diameter, typically) and reliable, unattended operation for space-flight applications. While the astrophysical applications typically do not focus on the recording of particle times-of-flight (a parameter of central interest in a number of chemical physics applications), MCP-based detectors can be conveniently adapted to provide such information. An important aspect of MCP-based detectors is that they can conveniently be used to detect not only electrons and ions, but also neutral molecules as long as the laboratory kinetic energy is sufficiently large. This has driven the application of fast ionic and neutral beams for the study of chemical dynamics as discussed further below.

As mentioned in the introduction, a new generation of coincidence measurements has become feasible using event-wise three-dimensional imaging techniques. This has been enabled by developments in both detection technology and the increased availability of new light sources including synchrotrons and kHz repetition-rate laboratory laser systems. In two-body dissociation processes, coincidence measurements allow for convenient removal of experimental averaging including finite collision volumes. More fundamentally, however, coincidence measurements allow for the determination of correlated product state distributions. This was shown, for example, by Neumark and co-worker's study of the correlated product state distributions of the $O(^3P_J)$ distributions from the photodissociation of $O_2$. (*55*) In the case of dissociative photoionization or dissociative photodetachment experiments, coincidence detection methods can provide a further level of detail by allowing determination of molecular-frame photoelectron angular distributions in the case of rapid dissociation processes. Examples of these experiments include studies of the multiple ionization of $D_2$, (*56*) recent time-resolved dissociative multiphoton studies of $NO_2$ (*57*) and the dissociative photodetachment of $O_4^-$.(*58*) In addition, determination of the correlations between photoelectron and photofragment kinetic energies measurable in these coincidence measurements often provides important insights into the dissociation dynamics. In studies of three-body dissociation dynamics of heavy particles, determination of the product angular correlations reveals the partitioning of momenta in the dissociation and can even yield structural insights, as shown in the study by Luong *et al.* on the dissociative photodetachment of $O_6^-$ in Chapter 18 of this volume.

## Applications to Reaction Dynamics

For the purposes of this brief overview, we will chiefly limit our consideration to applications of three-dimensional imaging techniques to problems in chemical reaction dynamics. This means that we will not further discuss the many beautiful applications of 'display-type' electron and ion detection schemes in surface science applications. (*59*) We will also not discuss in detail techniques focusing on the determination of molecular structure, including the Coulomb explosion technique used

Downloaded by 89.163.34.136 on September 17, 2012 | http://pubs.acs.org
Publication Date: October 18, 2000 | doi: 10.1021/bk-2001-0770.ch001

Downloaded by 89.163.34.136 on September 17, 2012 | http://pubs.acs.org
Publication Date: October 18, 2000 | doi: 10.1021/bk-2001-0770.ch001

to determine the structure of small molecular ions (*60*),(*61*) and X-ray diffraction experiments on the determination of macromolecular structure. (*62*) We will focus instead on two areas: (1) fast beam methods for studying dissociative charge exchange, dissociative recombination, dissociative photodetachment and photodissociation reactions and (2) energy and angle-resolved photoelectron-photoion coincidence experiments. Many of these approaches were represented among the papers presented at this symposium and among the papers presented in this volume. The examples addressed in this volume include the studies by Neumark and co-workers of the photodissociation dynamics of NCN and HNCN in Chapter 17 and the charge-exchange experiments on $Na_n^+$ + He collisions by Aguillon and coworkers in Chapter19. Multi-particle coincidence experiments are also represented by the work by Luong *et al.* in Chapter 18 on the three-body dissociative photodetachment dynamics of $O_6^-$ and by the cold-target recoil-ion momentum spectroscopy (COLTRIMS) experiments on the dissociative multiple photoionization of diatomic molecules discussed by Dörner *et al.* in Chapter 20.

## Fast Beam Experiments

Fast-beam experiments are in many ways ideal for the application of MCP-based imaging detectors since the kinematics of the dissociative or collisional processes under study often dictate that all of the products scatter into a relatively small angular range in the laboratory centered on the primary beam velocity. Furthermore, in these studies neutral atoms and molecules can also be detected as long as the laboratory velocity of the fragments is sufficiently high to eject secondary electrons upon impact with the MCP detector. The high-sensitivity of this experimental arrangement has led to a number of applications of imaging techniques to study collisional and photo-induced reaction dynamics over the last two decades.

## Dissociative Charge Exchange and Recombination

Applications of the fast-beam method coupled with imaging detection for unimolecular processes was pioneered by Los and co-workers in their seminal studies of the dissociative charge exchange of diatomic molecules. In these experiments, a positive ion beam is resonantly neutralized by passage through a collision cell containing a low ionization potential alkali metal. Variation of the alkali metal can be used to alter the level of excitation in the nascent neutral produced by the large-cross-section resonant-charge-exchange process. A coincidence imaging approach applicable to dissociative charge exchange using continuous mass-selected positive ion beams was described by DeBruijn and Los in 1982. (*63*) As they showed, measurement of the time and position of particle arrival, coupled with the knowledge of the parent mass and velocity allows determination of the product mass ratio, scattering angles and kinetic energy release. It should be noted, however, that the product mass ratio is determined by momentum conservation. The finite size of the parent beam typically limits the mass resolution to $m/\Delta m < 15$. The low mass-resolution is a challenge when the branching ratio between several open channels must be determined in the dissociation of a polyatomic molecule. Examples of the application of this technique to the elucidation of the highly excited states of a number of diatomic molecules (*64*) and the photodissociation of cations have been presented. (*65*) Studies of larger polyatomic systems using this technique have also been carried out by Los and co-workers. (*66*) and by the study of the neutralization of $O_4^+$ by Helm and Walter. (*65*) One aspect of resonant charge exchange is that a relatively wide range of neutral internal states are produced. In the case of studies of diatomic molecules this can often be an important advantage, allowing characterization of a wide range of optically forbidden excited states. For polyatomic systems, with more degrees of freedom available, there is seldom the product state resolution required to assign the neutral excited states accessed in resonant charge exchange leading to some ambiguity.

Helm and co-workers have recently extended the charge-exchange technique to study the three-body breakup of triatomic hydrogen. (*67*) In this study single rovibronic states of $H_3$ were prepared by laser excitation owing to the fact that only a single long-lived rotational state of neutral $H_3$ is prepared by charge-exchange of a 3 keV $H_3^+$ beam with Cs. Using time- and position-sensitive multiparticle detection techniques, they were able to show that the three-body dissociation dynamics shows a strong dependence on the initially excited Rydberg states of $H_3$. Further examples of three-body dissociation dynamics will be discussed below.

Imaging studies of fast neutrals produced by charge-exchange of mass and energy-selected ion beams has also been applied to investigation of ion-surface interactions by a number of investigators as well, including Los and co-workers (*68*) and Snowdon *et al.* (*69*). Use of several keV ion beams at extreme grazing-incidence angles allows relatively low perpendicular collision energies to be probed in these studies, providing important insights into the dynamics of ionic neutralization in the several eV collision energy range. Once again, the low-momentum transfer and high laboratory kinetic energy of the neutral products constrains them to a small solid angle and provides the high efficiency detection required for carrying out coincidence measurements.

With the recent development of ion storage rings at a number of locations in Europe and Japan, high-resolution studies of dissociative recombination (DR) cross-sections and dynamics have become possible. The merging of cooled, low-energy electron beams with cooled MeV ion beams allows examination of fundamental DR reactions at relative collision energies approaching zero. Characterization of DR is extremely important for an understanding of the chemistry of plasmas and astrophysical processes, and most of the studies to date have focused on the determination of cross-sections and excitation functions for these reactions. Recently, the application of time- and position-sensitive detection schemes to characterize the dynamics of the DR processes have also been pursued in some laboratories, including by Rosen *et al.* (*70*)and Amitay *et al.* (*71*)

Studies of collision dynamics in fast beams using imaging techniques has focused on both charge-exchange processes and collisional detachment reactions. The contribution in this volume by Aguillon and co-workers (Chapter 19) is an example of the application of multicoincidence techniques to interpreting the dynamics of metal

Downloaded by 89.163.34.136 on September 17, 2012 | http://pubs.acs.org
Publication Date: October 18, 2000 | doi: 10.1021/bk-2001-0770.ch001

cluster cation - rare gas collisions. There have also been a number of studies of collisional detachment processes of negative ions with a variety of reactive and non-reactive partners that have employed multiparticle coincidence imaging techniques as discussed in the review by Brenot and Durup-Ferguson. (*72*) Reference (*72*) also covers in some detail the various experimental techniques for multiparticle time- and position-sensitive detection available in 1992.

## Photodissociation Dynamics

Photodetachment of a fast negative ion beam is another approach that can be taken to produce either stable or dissociative states of neutral molecules in a fast beam. An additional advantage of photodetachment over charge exchange is that the use of tunable lasers allows one to control the energy available to the neutral species under study. Alternatively, carrying out a photoelectron coincidence measurement is another approach to preparing energy-selected neutral molecules. Both of these approaches have been adopted in recent years and are represented by contributions in this volume.

Neumark and co-workers adopted the coincidence imaging approach of DeBruijn and Los for use in the study of the photodissociation dynamics of neutral free radicals. In these experiments, a cold negative ion beam is photodetached near threshold with a tunable dye laser to produce a cold neutral free radical. After separation of the neutral radicals from residual negative ions, a second tunable laser is used to photodissociate the radical. The energy and angular distributions of the photofragments can then be recorded using the coincidence imaging technique, as first reported in a study of the $N_3$ free radical in 1993. (*73*) Among other experiments, this approach was also used to record the correlated $O(^3P_J)$ distribution discussed above. (*55*) An example of the application of this technique to the study of other reactive free radicals appears in this volume, in Chapter 17 on the photodissociation of the NCN, CNN and HNCN free radicals.

## Dissociative Photodetachment Dynamics

A number of interesting neutral systems may not be bound at the geometry of the corresponding stable anions. Thus, photodetachment of these anions will lead to dissociation of the neutral in a dissociative photodetachment event. In such cases the dissociation dynamics of the system can still be studied by carrying out a photoelectron-photofragment coincidence experiment as shown by Continetti and co-workers. In these experiments, complete kinematic characterization of two- and three-body dissociative photodetachment processes is achieved by detection of the photoelectron in coincidence with the two or three heavy atomic or molecular products. (*74*),(*75*) Large-solid-angle time- and position-sensitive detectors provide the sensitivity required to carry out successful coincidence experiments of this type. Determination of the energies and recoil angles of all the products allows determination of the correlated photoelectron-photofragment kinetic energy release

Downloaded by 89.163.34.136 on September 17, 2012 | http://pubs.acs.org
Publication Date: October 18, 2000 | doi: 10.1021/bk-2001-0770.ch001

and molecular frame photoelectron angular distributions for photodetachment as shown in studies of $O_4^-$. (*76*)

An example of the photoelectron-photofragment coincidence technique applied to the study of the three-body dissociation dynamics of an important neutral system is given in the contribution by Luong, et al. to this volume in Chapter 18. In this study, they applied new multi-hit time- and position-sensitive particle detectors to record the photoelectron and three photofragments produced in the dissociative photodetachment of $O_6^-$ clusters. Among other results, the observed partitioning of the momentum in the dissociative photodetachment of this cluster reveals a striking anisotropic distribution in which two of the $O_2$ products carry away the majority of the momentum, with the third $O_2$ playing the role of a spectator. These dynamics are consistent with an $O_4^-$ core weakly interacting with the third $O_2$.

Downloaded by 89.163.34.136 on September 17, 2012 | http://pubs.acs.org
Publication Date: October 18, 2000 | doi: 10.1021/bk-2001-0770.ch001

## Photoelectron-Photoion and Photoion-Photoion Coincidence Experiments

Photoionization processes always yield at least two charged products, the photoelectron and a photoion. Extending the capabilities from the traditional resonance lamps, the advent of broadly tunable synchrotron light sources and high intensity UV and VUV laser systems has enabled a large number of detailed studies of the energetics and dynamics of photoionization processes. If the nascent photoion is unstable, or the process under study is the photoionization of a cation, subsequent dissociation of the ion or a Coulomb explosion of the doubly charged cation product can occur leading to a number of charged products. The high detection efficiency for charged particles and the ability to determine product mass-to-charge ratios directly by time-of-flight means that such systems are amenable to coincidence experiments using three-dimensional imaging techniques as briefly reviewed here.

Coulomb explosions induced by multiple ionization of simple molecules has been investigated by a number of workers using three-dimensional imaging techniques. In the experiments by Hsieh and Eland (*77*) and Lavollee *et al.* (*78*), for example, the three-body dissociation dynamics of species like $OCS^{++}$ and $SO_2^{3+}$, respectively, have been studied. After photoionization, the subsequent Coulomb explosion of these species produce two charged particles which can be detected using an MCP-based time- and position-sensitive detector. Neglecting the momenta carried away by the photoelectrons, then, a complete picture of the three-body dissociation dynamics can be acquired by measuring the momenta of the two charged particles in coincidence. The development of detection schemes for these experiments is continuing, with a recent report from Lavollee describing a new multiparticle detector. (*79*) Another way to produce a Coulomb explosion is by impact of a neutral molecule with a high energy $\alpha$ particle. This approach has been used by Lutz and co-workers to study the $\alpha$-particle-induced Coulomb explosion of highly ionized water molecules. (*80*),(*81*) Using a multi-particle detector based on a crossed-wire-grid anode in these experiments, up to three charged fragments are recorded in coincidence, once again providing a kinematic characterization of the heavy particle dissociation dynamics, and potential insights into molecular structure. In all of these experiments, however, one or more photo- or collision-induced electrons are not recorded, and thus the internal energy of the system under study is not well characterized.

In dissociative photoionization processes yielding a free electron and two heavy particles, kinematically complete measurements can be straightforwardly carried out by detection of the photoelectron and the photoion. Photoelectron-photoion coincidence experiments of this type employing imaging detectors have been used to provide detailed insights into fixed-molecular or molecular-frame photoelectron angular distributions (MF-PADs). In studies of the dissociative Auger ionization of $O_2$, Golovin *et al.* used a fixed electron recoil direction and a photoion imaging detector to observe the anisotropic ion-recoil distribution relative to the electron recoil direction. (*82*) In more recent experiments, Downie and Powis have combined time- and position-sensitive detectors for photoelectron and photoions to yield the MF-PADs for the valence photoionization of a polyatomic molecule, $CF_3I$. (*83*) In the atomic and molecular physics community, kinematically complete experiments on a number of collisional and photo-induced processes have been carried out using the cold target recoil ion momentum spectroscopy (COLTRIMS) technique. (*84*) An example of this type of study is seen in the contribution by Dörner *et al.* in Chapter 20 of this volume, focusing on multiple dissociative photoionization of spatially aligned $D_2$. (*56*) In these experiments the momenta of both deuterons and one of the two photoelectrons are measured, yielding kinematically complete data on the dynamics of this dissociative photoionization process. The velocity map imaging technique discussed in the first section of this overview has also been previously used in the COLTRIMS community for improving resolution as well, and was introduced in reference (*85*).

Finally, the advances in detection techniques and advances in ultrafast laser technology have made time-resolved photoelectron-photoion coincidence measurements possible. Hayden and co-workers have studied the dissociative multiphoton ionization of $NO_2$ at wavelengths near 375 nm, and shown unambiguously that dissociative multiphoton ionization with 150 fs laser pulses at this wavelength occurs via three-photon excitation to a state of $NO_2$ correlating to the NO(C) + O dissociation limit.(*86*) The photoelectron-photoion kinetic energy correlations can be used to examine the breaking of the O-NO bond over a timescale of a few hundred fs. More recent work by Davies *et al.* (*57*) has shown that the evolution of the molecular-frame photoelectron angular distribution of the dissociating $NO_2$ molecule can also be recorded in a coincidence measurement. It is expected that these results will provide a sensitive test of electronic structure and dynamics calculations, and should motivate a new interest in understanding the time-resolved reaction dynamics of $NO_2$.

## Prospects for the Future

Continued advances in particle detection techniques will lead further advances in imaging studies of chemical reaction dynamics. Improvements in temporal and spatial resolution using crossed-delay-line detectors are currently being made and implemented in a number of laboratories. In the near future, pixellated detectors

Downloaded by 89.163.34.136 on September 17, 2012 | http://pubs.acs.org
Publication Date: October 18, 2000 | doi: 10.1021/bk-2001-0770.ch001

composed of many individual detectors will become available, as a spin-off of application-specific-integrated-circuit technology originally developed for particle physics experiments and currently being driven by the need for real-time high-throughput X-ray crystallography applications in biophysics. (*62*) These devices will share many of the characteristics of the current charge-coupled and charge-injection devices used in some of the imaging experiments described above, but will have the added benefit of full three-dimensional information: x,y position and particle time-of-flight. Of course the application of detection schemes like this will need to be coupled with improved, higher-speed data acquisition interfaces, but it is likely that this will occur. There is also increasing use of hybrid techniques involving CCD based detectors for imaging coupled with less-dense discrete-anode photomultiplier tubes for acquiring timing information. This type of detector has been used by Zajfman and co-workers (*87*) in dissociative recombination studies and will likely see further application in coincidence experiments, in particular as the readout rate for CCD cameras continues to increase.

Downloaded by 89.163.34.136 on September 17, 2012 | http://pubs.acs.org
Publication Date: October 18, 2000 | doi: 10.1021/bk-2001-0770.ch001

In conclusion, in this overview we have discussed some of the current applications of imaging techniques in chemical dynamics. The impact of this experimental technique has been large, as evidenced by the large body of current work and shown in the breadth of problems represented by the chapters in this volume. We anticipate that the continued development and application of imaging techniques will provide a powerful tool for understanding diverse phenomena in chemical dynamics.

## Acknowledgement

AGS was supported by the Director, Office of Energy Research, Office of Basic Energy Sciences, Chemical Sciences Division of the U.S. Department of Energy under contract No. DE-AC03-76SF00098. REC acknowledges the support of the Air Force Office of Scientific Research and the National Science Foundation.

## Literature Cited

1. Chandler, D. W.; Houston, P. L. *J. Chem. Phys.* **1987**, *87*, 1445.
2. Solomon, J. *J. Chem. Phys.* **1967**, *47*, 889.
3. Solomon, J.; Jonah, C.; Chandra, P.; Bersohn, R. *J. Chem. Phys.* **1971**, *55*, 1908.
4. Whitaker, B. J. In *Research in Chemical Kinetics Vol. I*; Compton, R. G., Hancock, G., Eds.; Elsevier: Amsterdam, 1993.
5. Heck, A. J. R.; Chandler, D. W. *Ann. Rev. Phys. Chem.* **1995**, *46*, 335.
6. Houston, P. L. *Acc. Chem. Res* **1995**, *28*, 453.
7. Houston, P. L. *J. Phys. Chem.* **1996**, *100*, 12757.
8. Heck, A. J. R. *Eur. Mass Spectrom* **1997**, *3*, 171.
9. Parker, D. H.; Eppink, A. *J. Chem. Phys.* **1997**, *107*, 2357.
10. Buijsse, B.; vanderZande, W. J.; Eppink, A.; Parker, D. H.; Lewis, B. R.; Gibson, S. T. *J. Chem. Phys.* **1998**, *108*, 7229.

11. Bakker, B. L. G.; Eppink, A.; Parker, D. H.; Costen, M. L.; Hancock, G.; Ritchie, G. A. D. *Chem. Phys. Lett.* **1998**, *283*, 319.
12. Bakker, B. L. G.; Parker, D. H.; Hancock, G.; Ritchie, G. A. D. *Chem. Phys. Lett.* **1998**, *294*, 565.
13. Cooper, M. J.; Jackson, P. J.; Rogers, L. J.; Orr-Ewing, A. J.; Ashfold, M. N. R. *J. Chem. Phys.* **1998**, *109*, 4367.
14. Cooper, M. J.; Wrede, E.; Orr-Ewing, A. J.; Ashfold, M. N. R. *J. Chem. Soc. Faraday Trans.* **1998**, *94*, 2901.
15. Demyanenko, A. V.; Dribinski, V.; Reisler, H.; Meyer, H.; Qian, C. X. W. *J. Chem. Phys.* **1999**, *111*, 7383.
16. Wilson, R. J.; Mueller, J. A.; Houston, P. L. *J. Phys. Chem. A* **1997**, *101*, 7593.
17. Chang, B.-Y.; Hoetzein, R. C.; Mueller, J. A.; Geiser, J. D.; Houston, P. L. *Rev. Sci. Instrum.* **1998**, *69*, 1665.
18. Taniguchi, N.; Takahashi, K.; Matsumi, Y.; Dylewski, S. M.; Geiser, J. D.; Houston, P. *J. Chem. Phys.* **1999**, *111*, 6350.
19. Tanaka, Y.; Kawasaki, M.; Matsumi, Y.; Fujiwara, H.; Ishiwata, T.; Rogers, L. J.; Dixon, R. N.; Ashfold, M. N. R. *J. Chem. Phys.* **1998**, *109*, 1315.
20. Samartzis, P. C.; Kitsopoulos, T. N. *J. Phys. Chem. A* **1997**, *101*, 5620.
21. Kim, Y. S.; Jung, Y.-J.; Jung, K.-H. *J. Chem. Phys.* **1997**, *107*, 3805.
22. Tonokura, K.; Suzuki, T. *Chem. Phys. Lett.* **1994**, *224*, 1.
23. Jee, Y. J.; Park, M. S.; Kim, Y. S.; Jung, Y. J.; H., J. K. *Chem. Phys. Lett.* **1998**, *287*, 701.
24. Suits, A. G.; Miller, R. L.; Bontuyan, L. S.; Houston, P. L. *Journal of the Chemical Society-Faraday Transactions* **1993**, *89*, 1443.
25. Nestorov, V. K.; Cline, J. I. *J. Chem. Phys.* **1999**, *111*, 5287.
26. Suzuki, T.; Katayanagi, H.; Nanbu, S.; Aoyagi, M. *J. Chem. Phys.* **1998**, *109*, 5778.
27. Picheyev, B. V.; Smolin, A. G.; Vasyutinskii, O. S. *J. Phys. Chem. A* **1997**, *101*, 7614.
28. Bracker, A. S.; Wouters, E. R.; Suits, A. G.; Vasyutinskii, O. S. *J. Chem. Phys.* **1999**, *110*, 6749.
29. Bracker, A. S.; Wouters, E. R.; Suits, A. G.; Lee, Y. T.; Vasyutinskii, O. S. *Phys. Rev. Lett.* **1998**, *80*, 1626.
30. Ahmed, M.; Peterka, D. S.; Bracker, A. S.; Vasyutinskii, O. S.; Suits, A. G. *J. Chem. Phys.* **1999**, *110*, 4115.
31. Ahmed, M.; Wouters, E. R.; Peterka, D. S.; Vasyutinskii, O. S.; Suits, A. G. *Faraday Discuss.* **1999**, *113*, 425.
32. Samartzis, P. C.; Sakellariou, I.; Gougousi, T.; Kitsopoulos, T. N. *J. Chem. Phys.* **1997**, *107*, 43.
33. Samartzis, P. C.; Bakker, B. L. G.; Rakitzis, T. P.; Parker, D. H.; Kitsopoulos, T. N. *J. Chem. Phys.* **1999**, *110*, 5201.
34. Neyer, D. W.; Heck, A. J. R.; Chandler, D. W.; Teule, J. M.; Janssen, H. M. *J. Phys. Chem. A* **1999**, *103*, 10388.
35. Neyer, D. W.; Heck, A. J. R.; Chandler, D. W. *J. Chem. Phys.* **1999**, *110*, 3411.

Downloaded by 89.163.34.136 on September 17, 2012 | http://pubs.acs.org
Publication Date: October 18, 2000 | doi: 10.1021/bk-2001-0770.ch001

36. Eppink, A.; Parker, D. H.; Janssen, M. H. M.; Buijsse, B.; vanderZande, W. J. *J. Chem. Phys.* **1998**, *108*, 1305.
37. Rakitzis, T. P.; Samartzis, P. C.; Kitsopoulos, T. N. *J. Chem. Phys.* **1999**, *111*, 10415.
38. Mastenbroek, J. W. G.; Taatjes, C. A.; Nauta, K.; Janssen, M. H. M.; Stolte, S. *J. Phys. Chem.* **1995**, *99*, 4360.
39. Janssen, M. H. M.; Mastenbroek, J. W. G.; Stolte, S. *J. Phys. Chem. A* **1997**, *101*, 7605.
40. Suits, A. G.; Bontuyan, L. S.; Houston, P. L.; Whitaker, B. J. *J. Chem. Phys.* **1992**, *96*, 8618.
41. Bontuyan, L. S.; Suits, A. G.; Houston, P. L.; Whitaker, B. J. *J. Phys. Chem.* **1993**, *97*, 6342.
42. Kitsopoulos, T. N.; Buntine, M. A.; Baldwin, D. P.; Zare, R. N.; Chandler, D. W. *Science* **1993**, *260*, 1605.
43. Hsu, Y. T.; Liu, K. P. *J. Chem. Phys.* **1997**, *107*, 1664.
44. Helm, H.; Bjerre, N.; Dyer, M. J.; Huestis, D. L.; Saeed, M. *Phys. Rev. Lett.* **1993**, *70*, 3221.
45. Bordas, C.; Paulig, F.; Helm, H.; Huestis, D. L. *Rev. Sci. Instrum.* **1996**, *67*, 2257.
46. Bordas, C.; Dyer, M. J.; Fairfield, T.; Helm, H.; Kulander, K. C. *Phys. Rev. A* **1995**, *51*, 3726.
47. Bordas, C.; Dyer, M. J.; Fairfield, T. A.; Saeed, M.; Helm, H. *Journal De Physique Iv* **1994**, *4*, 647.
48. Blondel, C.; Delsart, C.; Dulieu, F. *Phys. Rev. Lett.* **1996**, *77*, 3755.
49. Baer, T. *Ann. Rev. Phys. Chem.* **1989**, *40*, 637.
50. El-Marji, B.; Doering, J. P.; Moore, J. H.; Coplan, M. A. *Phys. Rev. Lett.* **1999**, *93*, 1574.
51. Wiza, J. L. *Nucl. Instr. Meth.* **1979**, *162*, 587.
52. Knapp, G. *Rev. Sci. Instrum.* **1978**, *49*, 982.
53. Lampton, M.; Paresce, F. *Rev. Sci. Instrum.* **1974**, *45*, 1098.
54. Martin, C.; Jelinsky, P.; Lampton, M.; Malina, R. F.; Anger, H. O. *Rev. Sci. Instrum.* **1981**, *52*, 1067.
55. Leahy, D. J.; Osborn, D. L.; Cyr, D. R.; Neumark, D. M. *J. Chem. Phys.* **1995**, *103*, 2495.
56. Doerner, R.; Brauning, H.; Jagutzki, O.; Mergel, V.; Achler, M.; Moshammer, R.; Feagin, J. F.; Osipov, T.; Brauening-Demian, A.; Spielberger, L.; McGuire, J. H.; Prior, M. H.; Berrah, N.; Bozek, J. D.; Cocke, C. L.; Schmidt-Bocking, H. *Phys. Rev. Lett.* **1998**, *81*, 5776.
57. Davies, J. A.; Continetti, R. E.; Chandler, D. W.; Hayden, C. C. *Phys. Rev. Lett.* **2000**.
58. Hanold, K. A.; Garner, M. C.; Continetti, R. E. *Phys. Rev. Lett.* **1996**, *77*, 3335.
59. Richter, L. J.; Mieher, W. D.; Whitman, L. J.; Noonan, W. A.; Ho, W. *Rev. Sci. Instrum.* **1989**, *60*, 12.
60. Belkacem, A.; Faibis, A.; Kanter, E. P.; Koenig, W.; Mitchell, R. E.; Vager, Z.; Zabransky, B. J. *Rev. Sci. Instrum.* **1990**, *61*, 945.

Downloaded by 89.163.34.136 on September 17, 2012 | http://pubs.acs.org
Publication Date: October 18, 2000 | doi: 10.1021/bk-2001-0770.ch001

61. Levin, J.; Feldman, H.; Baer, A.; Ben-Hamu, D.; Heber, O.; Zajfman, D.; Vager, Z. *Phys. Rev. Lett.* **1998**, *81*, 3347.
62. Datte, P.; Beuville, E.; Beche, J. F.; Cork, C.; Earnest, T.; Millaud, J.; Nygren, D.; Padmore, H.; Turko, B.; Xuong, N. H. *Nucl. Inst. and Meth. A* **1997**, *391*, 471.
63. DeBruijn, D. P.; Los, J. *Rev. Sci. Instrum.* **1982**, *53*, 1020.
64. van der Zande, W. J.; Koot, W.; Los, J. *J. Chem. Phys.* **1989**, *91*, 4597.
65. Helm, H.; Walter, C. W. *J. Chem. Phys.* **1993**, *98*, 5444.
66. Beijersbergen, J. H. M.; van der Zande, W. J.; Kistemaker, P. G.; Los, J.; Drewello, T.; Nibbering, N. M. M. *J. Phys. Chem.* **1992**, *96*, 9288.
67. Mueller, U.; Eckert, T.; Braun, M.; Helm, H. *Phys. Rev. Lett.* **1999**, *83*, 2718.
68. Schins, J. M.; Vrijen, R. B.; van der Zande, W. J.; Los, J. *Surf. Sci.* **1993**, *280*, 145.
69. Snowdon, K. J.; Harder, R.; Nesbitt, A. *Surf. Sci.* **1996**, *363*, 42.
70. Rosen, S.; Peverall, R.; Larsson, M.; Le Padellec, A.; Semaniak, J.; Larson, A.; Stroemholm, C.; van der Zande, W. J.; Danared, H.; Dunn, G. H. *Phys. Rev. A* **1998**, *57*, 4462.
71. Amitay, Z.; Baer, A.; Dahan, M.; Levin, J.; Vager, Z.; Zajfman, D.; Knoll, L.; Lange, M.; Schwalm, D.; Wester, R.; Wolf, A.; Schneider, I. F.; Suzor-Weiner, A. *Phys. Rev. A* **1999**, *60*, 3769.
72. Brenot, J.-C.; Durup-Ferguson, M. *Adv. Chem. Phys.* **1992**, *82*, 3769.
73. Continetti, R. E.; Cyr, D. R.; Osborn, D. L.; Leahy, D. J.; Neumark, D. M. *J. Chem. Phys.* **1993**, *99*, 2616.
74. Hanold, K. A.; Sherwood, C. R.; Garner, M. C.; Continetti, R. E. *Rev. Sci. Instrum.* **1995**, *66*, 5507.
75. Hanold, K. A.; Luong, A. K.; Clements, T. G.; Continetti, R. E. *Rev. Sci. Instrum.* **1999**, *70*, 2268.
76. Hanold, K. A.; Continetti, R. E. *Chem. Phys.* **1998**, *239*, 493.
77. Hsieh, S.; Eland, J. H. D. *J. Phys.B* **1997**, *30*, 4515.
78. Lavollee, M.; Brems, V. *J. Chem. Phys.* **1999**, *110*, 918.
79. Lavollee, M. *Rev. Sci. Instrum.* **1999**, *70*, 2968.
80. Werner, U.; Beckord, K.; Becker, J.; Lutz, H. O. *Phys. Rev. Lett.* **1995**, *74*, 1962.
81. Becker, J.; Beckord, K.; Werner, U.; Lutz, H. O. *Nucl. Instr. Meth. A* **1994**, *337*, 409.
82. Golovin, A. V.; Heiser, F.; Quayle, C. J. K.; Morin, P.; Simon, M.; Gessner, O.; Guyon, P.-M.; Becker, U. *Phys. Rev. Lett.* **1997**, *79*, 4554.
83. Downie, P.; Powis, I. *Phys. Rev. Lett.* **1999**, *82*, 2864.
84. Doerner, R.; Mergel, V.; Spielberger, L.; Achler, M.; Khayyat, K.; Vogt, T.; Brauening, H.; Jagutzki, O.; Weber, T.; Ulrich, J.; Moshammer, R.; Unverzagt, M.; W., S.; Khemliche, H.; Prior, M. H.; Cocke, C. L.; Feagin, J.; Olson, R. E.; Schmidt-Bocking, H. *Nuclear Instruments and Methods in Physics Research. B* **1997**, *124*, 225.
85. Frohne, V. Ph. D., Kansas State University, 1994.
86. Davies, J. A.; LeClaire, J. E.; Continetti, R. E.; Hayden, C. C. *J. Chem. Phys.* **1999**, *111*, 1.
87. Amitay, Z.; Zajfman, D. *Rev. Sci. Instrum.* **1997**, *68*, 1387.

Downloaded by 89.163.34.136 on September 17, 2012 | http://pubs.acs.org
Publication Date: October 18, 2000 | doi: 10.1021/bk-2001-0770.ch001

## Chapter 2

# What Have We Learned from β?

**Richard Bersohn**

**Columbia University, MC 3104 Havemeyer, New York, NY 10027**

Downloaded by STANFORD UNIV GREEN LIBR on September 21, 2012 | http://pubs.acs.org
Publication Date: October 18, 2000 | doi: 10.1021/bk-2001-0770.ch002

The values of β have helped us understand continuum spectroscopy on a deeper level than was previously thought possible. However, the angular distribution of the fragments has turned out to be just one of several distribution functions which stem from the alignment of the dissociating molecules. Because both the axis of dissociation and the angular momentum direction are fixed in the molecule as is the transition moment, there are correlations between all of them. These correlations become observable because the dissociating molecules unlike the original gas are aligned with respect tothe space fixed axis of the optical electric field. The core advantage of imaging is its multiplex nature, i.e. energy and angular distribution are simultaneously measured. As more experiments are carried out, the subpicosecond world will become ever more familiar.

Molecular spectroscopy for the past century was devoted to the study of transitions between bound states. Continuous spectra were mostly ignored because there were no observables other than the usually featureless spectrum. The intensity of the spectrum provides a clue as to the nature of the transition, i.e. whether it is allowed or partly forbidden. In special, simple cases the spectrum can be inverted to derive a repulsive upper state potential but that is not typical.

A spectrum is continuous because one of the two states involved is not bound. In the last few decades a new spectroscopy has arisen which might be called continuum spectroscopy. It is based on our present ability to measure a rich array of observables characterizing the continuum state. These include the translational energy distribution of the fragments (or equivalently their internal state distribution) together with their angular distribution. When a molecule is dissociated by polarized light using a single photon transition, the angular distribution *(1,2)* has the form:

$$f(\theta) = (1/4\pi)\{1 + \beta P_2(\cos\theta)\} \quad (1)$$

where θ is the angle between the axis of polarization of the light and the velocity of either of the two fragments. The parameter β which defines the angular distribution can be expressed as an average over the distribution of angles $\chi$ between the axis of the transition dipole and a fragment velocity vector:

$$\beta = 2\langle P_2(\cos\chi)\rangle \qquad (2)$$

As $\chi$ decreases from $\pi/2$ to zero, $\beta$ increases from -1 to 2. Many examples have bee found in which the measured $\beta$ is close to one of the extreme values,typically -0.8 or +1.8. The difference can be explained by the fact that the molecule rotates a little during the dissociation so that the tangential velocity of the fragment is not infinitesimally small compared to the velocity that it gains from the repulsion on the upper state.*(1,3)*.

Continuum spectroscopy or more generally photodissociation dynamics has been studied by three basically different methods. The original experiments of K.R.Wilson *(4)* and R.Bersohn (*5*) later greatly extended by Y.T.Lee and collaborators (*6*) measure the fragment flux as a function of polarization angle. These experiments measure a $\beta$ which is an average over all kinetic energies of the fragments. More recently $\beta$ has been measured for individual quantum states of a fragment or even at particular velocity components with the use of Doppler spectroscopy.*(7)* The culmination of this progress is the development of an imaging method by Chandler and Houston,(*8*) recently improved by Parker.(*9*) The imaging method uses the technique of Resonance Enhanced Multi Photon Ionization (REMPI) to ionize a fragment in a particular quantum state and to measure an "image" of its velocity as a function of polarization angle. The atoms H, Cl and I have been studied in this way as well as the molecules CO, HCl and $CH_3$.

This chapter makes no attempt to survey all the systems for which $\beta$ has been measured. (The interested reader will find an extensive bibliography of experiments on photodissociation in the book by Sato and its supplements.*(10)*) Instead, by citing case examples we will review the *types* of information obtained from measured $\beta$ values. Five topics will be discussed: 1) the symmetry of the upper state, 2) potential surface crossing, 3) slow anisotropic dissociation, 4) J-v correlation, 5) the femtosecond time scale.

## Symmetry of the Upper State

We begin with some simple examples in which beta has a value close to the ideal value for a perpendicular ($\beta$ =-1) or a parallel ($\beta$=+2) transition. These straightforward cases serve to confirm definitively and pictorially what spectroscopists had already deduced from other evidence. After that, more complex examples will be described.

$CH_3 + h\nu \dashrightarrow H + CH_2$

Electronic absorption spectroscopy and spin resonance show that the methyl radical is planar in its ground state. The rather small hyperfine interaction proves that the unpaired electron is in a 2p state whose axis is perpendicular to the molecular plane. The first absorption band has been demonstrated to be a transition to a 3s state both

Downloaded by STANFORD UNIV GREEN LIBR on September 21, 2012 | http://pubs.acs.org
Publication Date: October 18, 2000 | doi: 10.1021/bk-2001-0770.ch002

theoretically and experimentally because a series of transitions starting with the lowest energy one can be fitted to a Rydberg formula.*(11,12)* Because the initial state is odd and the final state is even with respect to reflection in the molecular plane, the transition dipole must be perpendicular to the plane. In turn this means that the transition dipole must be perpendicular to the H atom and $CH_2$ carbene velocities. This is an ideal perpendicular transition. While the measurement of a value of -0.9 for the β parameter (*13*) associated with the first transition of the methyl radical adds nothing new to our understanding, it is vital to establish that in well known cases, the value of this new observable is consistent with what was known before.

Downloaded by STANFORD UNIV GREEN LIBR on September 21, 2012 | http://pubs.acs.org
Publication Date: October 18, 2000 | doi: 10.1021/bk-2001-0770.ch002

$H_2O + h\nu \rightarrow H + OH$

The first electronic transition in the water molecule ($A^1B_1 \leftarrow X^1A_1$) extends from 54600 to 71400 $cm^{-1}$. Again, theoretical calculations show that the highest occupied molecular orbital is the lone pair $1b_1$ 2p state whose axis is perpendicular to the molecular plane and the lowest unoccupied state is an antibonding $4a_1$* state. Again this means that the transition dipole will be normal to the molecular plane and therefore to the velocities of the dissociating fragments. This was demonstrated in an appealing way by the orbital alignment of the OH product.*(14,15)* If the E vector of the polarized 157 nm light promotes one of the lone pair 2p electrons to an antibonding state, then the remaining electron carries the angular momentum of the OH. This angular momentum was aligned relative to the E vector of the light as shown in Figure1. The first transitions in $H_2S$, $CH_3OH$ and $CH_3SH$ are similarly continuous and the fragments have β values of -0.84, -0.60 and -1.0 respectively.*(16-18)*

The next few examples of observed anisotropies are less obvious than the preceding ones and the β values strengthen inferences from electronic spectroscopy.

$(CH_3)_3COCl + h\nu \rightarrow (CH_3)_3CO + Cl$

At first sight the spectroscopy of t-butyl hypochlorite appears formidable. Coming closer one sees that it is an example of the general bent molecule ROCl whose chromophore is just the O and Cl atoms. Indeed HOCl and t-butylOCl have very similar spectra. *Ab initio* calculations on HOCl show that the lowest energy transition is very weak and the next, stronger transition further in the uv is an in plane, lone pair to antibonding ($\sigma^*_{OCl} \leftarrow n_{Cl}$) transition.*(19)* The beta observed for t-butyl hypochlorite at 248 nm is 1.9±0.1.*(20)* Thus one can generate from a complex molecule a set of Cl atoms with a highly parallel velocity distribution and an average energy of 1.1 eV.

$HONO + h\nu \rightarrow HO + NO$

HONO is isoelectronic with an 18 valence electron triatomic which is predicted by Walsh's rules to be bent and planar as indeed it is. (*21*) Spectroscopists have concluded that the first transition is AA"<--XA', i.e. a transition between states even and odd with respect to reflection in the plane, a lone pair to an antibonding π* state. The transition dipole must be perpendicular to the plane and, in agreement, β was

Downloaded by STANFORD UNIV GREEN LIBR on September 21, 2012 | http://pubs.acs.org
Publication Date: October 18, 2000 | doi: 10.1021/bk-2001-0770.ch002

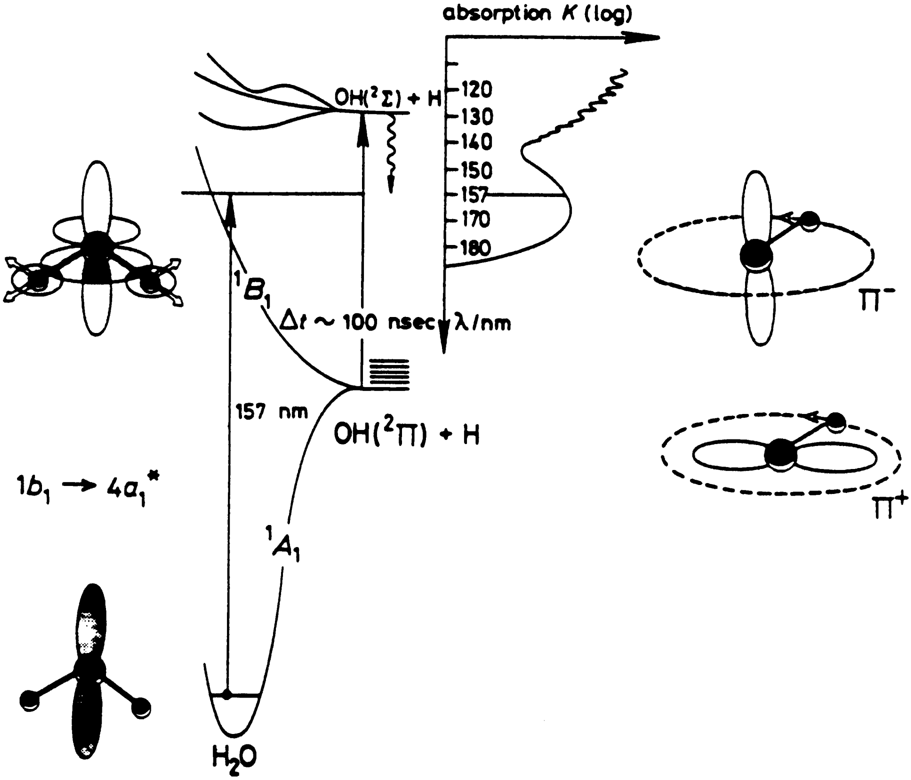
absorption K (log)
OH(²Σ) + H
120
130
140
150
157
170
180
¹B₁
Δt ~ 100 nsec
λ/nm
157 nm
OH(²Π) + H
¹A₁
H₂O
1b₁ → 4a₁*
Π⁻
Π⁺

*Figure1 The electronic ground state $X^1A_1$, the repulsive first electronically excited state $A^1B_1$ and a few other higher states are shown. The electronic structure of water in the ground and first excited states are sketched in the left side. The two possible orientations of the unpaired electron relative to the OH rotation plane are shown on the right side. The absorption spectrum of water is shown at the top. From Ref. 14 with permission.*

found to be -0.9±0.1. .(*22*) The absorption spectrum exhibits structure associated with an N-terminal O vibration. The most revealing aspect of the experiment is that scanning the photon energy through these peaks has no influence on the OH state distribution. There is an N-central O repulsion turned on in the upper state which is unlinked to the vibrational energy in the other N-O bond. A similar phenomenon was observed with 4,4'-diodobiphenyl. In that case increasing the energy of the dissociating photon by 2400 $cm^{-1}$ caused no change in the kinetic energy of the I atom released. (*23*) In both molecules the added energy went into coordinates orthogonal to the reaction coordinate.

Downloaded by STANFORD UNIV GREEN LIBR on September 21, 2012 | http://pubs.acs.org
Publication Date: October 18, 2000 | doi: 10.1021/bk-2001-0770.ch002

$(CO)_5M\text{-}M(CO)_5 + h\nu \text{ --> } 2\ M(CO)_5 \quad M = Mn, Re$

Possibly the simplest transition one could think of is a transition in a two electron system from a σ to a σ* state as, for example, in the hydrogen molecule. However, to satisfy the Pauli principle, the upper state has to be a triplet so the transition is nominally forbidden. If the atoms involved are heavy enough, the spin-orbit coupling will cause singlet states to be mixed with the upper state making the transition possible. The β value for the above dimetal decacarbonyls when dissociated in the first band around 300 nm is 1.9. (*24*) The transition is believed to be of dσ*<--dσ type. (*25*) This is an example in which the excitation energy of a complex molecule with twenty one bonds is largely confined to a single one of them. The dissociation is much faster than internal vibrational redistribution.

## Potential Surface Crossing

$C_{10}H_7I + h\nu \text{ --> } C_{10}H_7 + I$

When 1-iodonaphthalene is excited near 280 nm, it releases iodine atoms with a β = 1.18. (*5*) This means that the separation is complete in a time of the order of a picosecond. What is the pathway for dissociation? Is it direct, i.e. on one repulsive potential surface or is it indirect, passing from the initially excited state to another? We know enough from RRKM and related theories that the dissociation does not proceed through the ground state. It would take microseconds for the hot molecule to dissociate in this way. Both of the above questions are answered by the fact that the β parameter for 2-iodonaphthalene is close to zero.

The π*<--π transitions of naphthalene, as in all such planar systems, are polarized in plane. Symmetry demands that they be polarized either along the short or the long twofold axis. The first transition, $S_1$<--$S_0$ is polarized along the short axis. The C-I bond at the 2 position makes a roughly 60° angle with respect to the short axis (connecting carbons 9 and 10). The "magic angle", 54.7° substituted in Eq.(2) yields β = 0. 60° is close enough to the magic angle that β is still rather small. In 1-iodonaphthalene the C-I bond is parallel to the short axis, χ in Eq.(2) is zero and β is large. The initially excited π state is delocalized but the final state, repulsive in the C-I coordinate must be localized. This surface crossing takes place on a subpicosecond time scale. Such a time scale is no longer beyond reach of experiment and the measurement of level crossing rates is a rich field for fs experiments.

RI + hν --> R + I

Electron states in molecules are, roughly, of four types-core, bonding, nonbonding and antibonding. In a typical stable molecule the core, bonding and nonbonding states are filled and the antibonding states are empty. The lone pair, nonbonding electrons are usually in p states aligned perpendicular to the bond axis. The lowest energy transition, usually σ*<--n, will have a dipole oriented perpendicular to the bond causing β to be negative.

Strong spin-orbit coupling will change this simple picture particularly with halogen atoms. Let us take HI as a paradigm following Mulliken. (26) Among the set of valence states based on the 1s state of the H atom and the various 5p states of the I atom the most conspicuous are the $^1\Sigma$ ground state and two excited states, $^1\Pi_1$ and $^3\Pi_0$. Because the 2p states of H are so high in energy the $^1\Pi_1$ state is largely a 5pπ I atom function. This state can have no dipole moment matrix element with the 5pσ function. The strength of the transition is derived only from the small degree of s hybridization in the ground state wave function and the H atom 1s function. The transition is therefore weak. As the molecule in the $^3\Pi_0$ state dissociates, it forms a H atom which has an angular momentum quantum number of ½ and an I atom which must also have an angular momentum of ½ in order that the total angular momentum around the molecular axis be zero. This property of the $^3\Pi_0$ state would normally be irrelevant because singlet to triplet transitions are forbidden. However this triplet state having zero angular momentum around the axis is mixed by the very strong spin-orbit coupling of the I atom with $^1\Sigma$ states making the transition partially allowed. Similar arguments with a slightly different notation apply to polyatomics with a threefold or higher symmetry axis such as $CH_3I$.

If no potential surface crossing occurred, $I(5^2P_{1/2})$ atoms (hereafter called I) would be derived exclusively from excitation to a state with zero angular momentum around the symmetry axis. Similarly, $I(5^2P_{3/2})$ atoms (hereafter called I*) would be derived exclusively from excitation to states with unit angular momentum around the symmetry axis. It follows that ground state, J=3/2 iodine atoms should be formed in a perpendicular transition with negative β whereas excited, J=1/2 atoms should be formed in a parallel transition with positive β. When $CH_3I$ is excited in the middle of its A band near 250 nm, I atoms in *both* states are formed with a parallel distribution. Thus β supplies the vital clue that the J=3/2 ground state I atoms are formed by surface crossing. There is a huge literature on the continuum spectroscopy of $CH_3I$, HI and ICN in which β values play a key role. The interested reader might start with Ref. 9 and the references therein.

## $CH_4$ + hν --> H + $CH_3$ or $CH_2$ or CH + $H_2$

The generation of an anisotropic fragment velocity distribution in an isotropic

Downloaded by STANFORD UNIV GREEN LIBR on September 21, 2012 | http://pubs.acs.org
Publication Date: October 18, 2000 | doi: 10.1021/bk-2001-0770.ch002

gas depends on the irradiation of molecules which have anisotropic absorption coefficients by an anisotropic dissociating light source. At first sight, molecules with tetrahedral or octahedral symmetry which have isotropic absorption coefficients should exhibit a β which is zero. The first such symmetrical molecule whose fragment angular distribution was measured is methane.*(27)* As shown in Figure3 a rich variation of β with fragment speed was found contrary to expectations. It is precisely the highly symmetrical molecules which will have degenerate upper states which can not be potential minima according to the Jahn-Teller principle. This means that the upper state structure will have a lower symmetry than that of the ground state which will produce anisotropy in the fragmentation. The ground state of methane in the tetrahedral structure has a configuration $1a_1^2 2a_1^2 1t_2^6$. Observation of non zero β values at a certain energy is a proof that some of the transition is to a degenerate level. If not, tetrahedral geometry would have been preserved and β would have been zero. The usual interpretation of methane absorption is that it involves a $3s \leftarrow 1t_2$ excitation; the β measurement confirms this.

An extensive calculation of the ground $^1A_1$, first triplet $T_1$ and first excited singlet $S_1$ surfaces by Mebel *et al.* established that there are two potential minima on the upper surface. *(28)* The geometry of one with nearly $C_{3v}$ symmetry strongly resembles a methyl radical with a fourth extended bond to a H atom. The geometry of the other is $C_{2v}$ with a methylene with two extended bonds to a pair of H atoms which have approached to within 1 Å of each other. The fact that these minima exist does not mean that they are easily accessible. Their energies, 9.2 and 8.5 eV respectively are far above the energies needed for dissociation and with a very high density of states. They readily dissociate. The minima do affect the Franck-Condon factors. The transition dipole to a region near the $C_{3v}$ minimum is polarized along a C-H bond. The transition dipole to a region near the $C_{2v}$ minimum is polarized between two C-H bonds. The translational energy distributions of Figure. 3 all consist of a slow peak and a fast peak. The slow H atoms were thought to originate from three particle dissociations in which the H atom was produced by a secondary dissociation of an energized $CH_2$ or $CH_3$. On the other hand the $\beta(E_T)$ curves change sign in the energy region where the only partner of the H atom must be a $CH_3$. Two transitions are envisioned, one to the $C_{2v}$ minimum with a negative β, the other to the $C_{3v}$ with a positive but energy dependent β. Surprisingly fast internal conversion and intersystem crossing lead to H atoms on the excited and ground singlet surfaces as well as on the triplet surface. The rotation period for a $CH_4$ molecule in its ground state is 10/J ps. In a cooled beam, J values are low. Therefore reduced values of β may be a result not of rotation but of internal motions which increase the angle χ between the dissociation direction and the transition dipole.

## Slow anisotropic dissociation

The classical picture which leads to Eq.(1) envisions a gas of initially unoriented molecules which, upon excitation, dissociate in a time short compared to a rotation period. The quantum mechanical model which leads to the same equation assumes a coherent excitation of P, Q and R transitions.*(1)* The upper state lifetime is

Downloaded by STANFORD UNIV GREEN LIBR on September 21, 2012 | http://pubs.acs.org
Publication Date: October 18, 2000 | doi: 10.1021/bk-2001-0770.ch002

so short that the rotational lines can no longer be resolved. A molecule in a state with a definite J has a rather diffuse angular distribution of its axes. To achieve a narrower angular distribution, states of different angular momentum have to be mixed. Suppose that the lifetime is long enough that rotational lines can be resolved albeit broadened by the finite lifetime of the upper state in accordance with the uncertainty principle. What is the effect of this "predissociation" on $\beta$? This question has been answered in considerable detail by R.N.Dixon using both quantum mechanical and classical limits.

Let us consider a hypothetical, possibly fictitious but instructive example. A set of molecules $CH_3X$ with transition dipole moment along the threefold axis are excited with polarized photons having enough energy to break the C-X bond. Supposing that the molecule is a symmetric top, it will have a small moment of inertia about the threefold axis and two large moments of inertia corresponding to end over end rotation. In a typical case the first moment of inertia is an order of magnitude smaller than the others. This means that rotation around the symmetry axis will be fast but end over end rotation will be slow. Suppose further that the dissociation lifetime is intermediate between the slow and the fast rotation periods. In this case rotation will have little effect on $\beta$. Suppose instead that the dissociation rate is slower than either rate of rotation. A molecule in a state with $J \gg K$ will have a greatly reduced $\beta$ but if $J \approx K$, $\beta$ will be only slightly reduced by rotation.

The model above was a high symmetry special case. In the general case, suppose we have a distribution of dissociation axes with respect to the E vector of the dissociating light given by Eq.(1) but the molecule rotates about a certain axis before dissociating. Let that axis make an angle $\alpha$ with respect to the transition dipole axis. Rotating the distribution around that axis with the help of the addition theorem for Legendre polynomials yields

$$\beta = \beta_o P_2(\cos \alpha) \tag{3}$$

where $\beta_o$ is the value of $\beta$ in the absence of this rotation.

The molecules HCO(DCO), $ND_3$ and $HN_3$ to be discussed below are examples of predissociating molecules whose $\beta$ values have been determined as a function of the initial and final rovibrational quantum numbers.

HCO(DCO) + hν --> H(D) + CO

HCO is bent in both its ground $X^1A'$ and first excited $A^1A''$ state. However, the two states are degenerate in the linear configuration. Because the two states are even and odd respectively with respect to reflection in the molecular plane, the transition dipole must be perpendicular to that plane leading to the expectation that $\beta$ will be close to -1. In fact the $\beta$ values are generally small and positive.*(30)*

The dissociation is delayed because the upper state has a potential minimum but crosses to the ground state near to the linear configuration. HCO is a nearly symmetric spherical top with two large and nearly equal moments of inertia and one small moment of inertia for rotation of the H atom around the C-O axis. Some of the rotational lines are resolved but the fluorescence yield in the upper state is only about

Downloaded by STANFORD UNIV GREEN LIBR on September 21, 2012 | http://pubs.acs.org
Publication Date: October 18, 2000 | doi: 10.1021/bk-2001-0770.ch002

$10^{-4}$ corresponding to a lifetime of the order of ps. Assuming that the lifetime is much longer than the rotation period around the CO axis, we can substitute $\alpha = \pi/2$ in Eq.(3) and obtain $\beta = -\beta_0/2$. This only roughly agrees with the observations which are sensitive to the initial and final rotational states; however, the essential point is that rotation during the predissociation can reduce the magnitude and even change the sign of $\beta$.

$ND_3 + h\nu \dashrightarrow ND_2 + D$

The first A<--X transition in ammonia is a Rydberg transition of one of the lone pair electrons to a 3s state. As the lone pair hybrid is directed along the threefold axis, the transition dipole moment must also lie along the threefold axis. The first excited state of ammonia, the A state is planar. Because the ground state structure is pyramidal, it follows that the absorption spectrum consists of a long progression in the symmetrical bending frequency of the upper state. However, there is predissociation in the upper state taking place at the conical intersection of the ground and excited state surfaces. *(30,31)* Use of $ND_3$ allows resolution of rotational structure in the first two peaks in the vibrational progression. This is a rare example in which the quantum states of both the precursor molecule and a dissociated molecular fragment, in this case, $ND_2$ can be measured. In turn, $\beta$ can be measured as a function of all these quantum numbers. Figure2 shows, for the $R_0(0)$ line of the (0,0) band the variation of $\beta$ as a function of the rotational angular momentum, N of the $ND_2$ fragment. The rotation of the radical is derived from the erstwhile bending vibration and is about an axis perpendicular to the threefold axis. The values of $\beta$ are close to -1 for low N because the dissociation is perpendicular to the threefold axis. At high N $\beta$ rises rapidly becoming large and positive. This means that because of the strong rotation the D atoms tend to be ejected along the threefold axis rather than perpendicular to it. released along the threefold axis.

$HN_3 + h\nu \dashrightarrow NH + N_2$

$HN_3$ was excited by a two photon process to states with six or seven quanta of N-H vibration and with known rotational quantum numbers. The predissociation which followed resulted in vibrationally cold NH and $N_2$; the NH was also rotationally cold but the $N_2$ was rotationally hot. These results were interpreted in terms of an excitation from a quasi linear ground state to a bent upper state; in the transition state the main force is the repulsion between the internal N atoms.*(32)* The lifetime of the upper state was clearly longer than a rotation period as evidenced by the rotational line widths. Under these conditions the angular distribution of molecular axes is given by the square of the rotational wave function.*(33)* If one knows the orientation of the transition dipole moment and the dissociation direction in the molecular axis system, the fragment angular distribution can be calculated and it is not isotropic. For this experiment $\beta$ values varied with the rotational state but were positive.

Downloaded by STANFORD UNIV GREEN LIBR on September 21, 2012 | http://pubs.acs.org
Publication Date: October 18, 2000 | doi: 10.1021/bk-2001-0770.ch002

Downloaded by STANFORD UNIV GREEN LIBR on September 21, 2012 | http://pubs.acs.org
Publication Date: October 18, 2000 | doi: 10.1021/bk-2001-0770.ch002

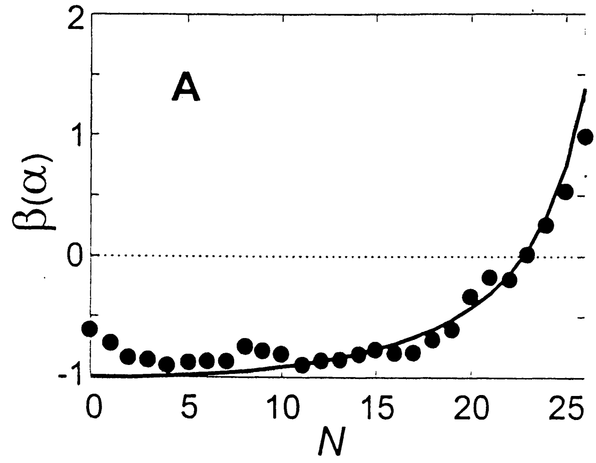

*Figure2 Experimentally resolved (•) and theoretically predicted(-) anisotropy parameter for photodissociation of $ND_3$ $(A)_{v=0}$ following preparation via the $(A)R_0(0)$ transition From Ref. 30 with permission.*

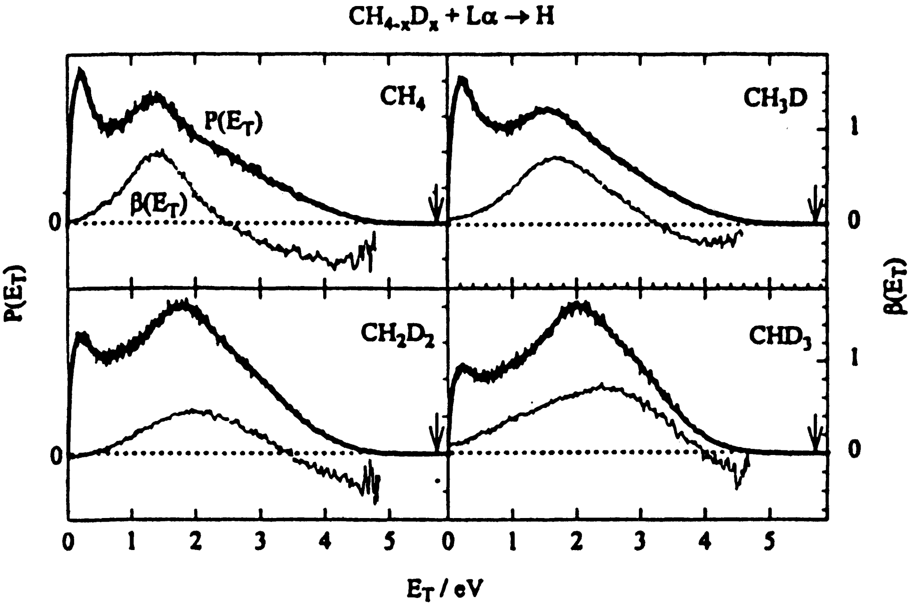

*Figure3 Photofragment cm translational energy distribution $P(E_T)$ of H atoms (heavy line) and the anisotropy parameter distribution $\beta(E_T)$ (light line). The arrow marks the maximum kinetic energy possible for a H atom at the dissociating wavelength 121.6 nm. From Ref. 28 with permission.*

## V-J correlation effects; beyond β

Another way of stating that the distribution of fragments from a dissociation by polarized light is anisotropic is that there is a correlation between the velocity vectors and the electric vector, **E** of the light wave. Dixon and Hall et al. observed that there are other vector correlations involved in photodissociation. *(34,35)* There is a larger set of tools to study photodissociation. If a fragment has an angular momentum, the angular momentum can be aligned or oriented with respect to the E vector. If the angular momentum and the velocity are both correlated with the E vector, then they must be correlated with each other. Moreover, as Dixon showed, this correlation must persist even after many rotations.

The **v-J** correlation is conveniently determined by Doppler spectroscopy of a fragment in which the laser line width is much less than the Doppler line broadening. Although this review is mainly devoted to β, we give below a nice examples of the information that can be obtained from **v-J** correlation measurements.

$H_2O_2 + h\nu \rightarrow 2OH$

Hydrogen peroxide is a nonplanar molecule with HOO angles of 95° and a dihedral angle of 112°. If we think of the O atoms as independent chromophores, each similar to that of water, there will be two transition dipoles each normal to an HOO plane. The resultant will be along the bisector of the dihedral angle and perpendicular to the O-O axis. The angular distribution of OH radicals at 266 nm has a β of -0.71.*(36)* Most of the excess energy is released as translational energy. The transition is perpendicular and therefore the velocity distribution is peaked along the O-O axis. In the excited state evidently a repulsive force is switched on which rapidly separates the two OH radicals. However, there is also a positive **v-J** correlation which means that in addition to the repulsion which is along the O-O bond there is also a strong torque in the excited state which causes the OH radicals to rotate. To conserve momentum the two OH radicals have equal and opposite momenta; to conserve angular momentum, their angular momenta must also be equal and opposite. These OH radicals share one property with newly generated muons. Their angular momentum is parallel to their velocity.

Generalized angular distributions

The original quantum mechanical treaqtment of photodissociation by Zare treated the basic separation process without considering the internal states of the fragments. Balint-Kurti and Shapiro extended this theory to the case of a triatomic ABC which was dissociated into an atom A and a diatomic BC. *(37,38)* The molecule ABC had initial rotational quantum numbers $J_i$,M, parity $p_i$ and the diatomic fragment had quantum numbers v,j,m. The differential photodissociation cross section has the form

$$\sigma(kEvjm|E_iJMp) = \sum_{J\lambda} \sum_{J'\lambda'} f(EJ_ivj\lambda p_iE_iJJ'\lambda'p'\} F(M)D^{j}_{\lambda M}(\Omega)D^{J'*}_{\lambda' M}(\Omega)D^{j}_{-\lambda\text{-}m}(\Omega)D^{j8}_{-\lambda' m}(\Omega) \qquad (4)$$

Downloaded by STANFORD UNIV GREEN LIBR on September 21, 2012 | http://pubs.acs.org
Publication Date: October 18, 2000 | doi: 10.1021/bk-2001-0770.ch002

Downloaded by STANFORD UNIV GREEN LIBR on September 21, 2012 | http://pubs.acs.org
Publication Date: October 18, 2000 | doi: 10.1021/bk-2001-0770.ch002

In this equation J,J' are final angular momentum quantum numbers of the system after absorption. The parity of the final wave functions are $(-1)^J p$ and $(-1)^{J'} p'$. $\Omega$ is a symbol for $\phi,\theta,0$ which define the orientation of the fragment velocity with respect to the E vector of the dissociating light. $E_i$ is the initial total energy of the system and E is the relative translational energy of the fragments. The D factors are the unitary matrix elements of representations of the rotation group. $\lambda$ and $\lambda'$ are helicity quantum numbers, the component of the vector **j** along the vector joining the centers of mass of atom A and the molecule BC.

The above cross section refers to a parent molecule in a specific state M dissociating to form a diatomic in a specific state m. This ideal situation is rarely achieved. In the usual case the initial set of molecules are isotropically distributed and no attempt is made to measure the flux of an individual m state. In other words, one must, generally, average Eq.(4) over M and m at which point Eq.(1) is obtained. If the distribution over initial M states is not uniform, the angular distribution will be altered. As an example, suppose that the weighting factor for a state M is proportional to $M^2$. The sum

$$(4\pi/(2J+1)) \sum_M \{M^2/J(J+1)\} \; |Y_{JM}(\theta,\phi)|^2 = \cos^2\theta \, . \qquad (5)$$

A parallel transition occurring in a gas aligned as in Eq.(5) would have a $\cos^4\theta$ fragment distribution, certainly not represented by Eq.(1). If one sums Eq.(4) over M one obtains an angular distribution which depends on m; in other words each m state will in general have a different angular distribution, not describable by Eq.(1). If there is interference between states of different helicity, $\lambda$, the angular distribution will contain Legendre polynomials of both even and odd L leading to a breaking of forward and backward symmetry. If the dissociation is accomplished simultaneously by one photon at frequency $2\omega$ and two photons at frequency $\omega$ there will also be a breaking of forward-backward symmetry. (*39*) Actually Zare pointed out that two photon transitions produce fragment distributions containiug $P_L(\cos\theta)$ with L=0, 2 and 4 so that again Eq.(1) is not complete.(*1*)

## The Femtosecond Time Scale

The parameter $\beta$ is an asymptotic quantity. It is a measure of the angular distribution of the flux of fragments long after the fragmentation or, equivcalently when the fragments are so far from each other that they no longer interact. The symmetry of the transition and time delays during the fragmentation do, of course, leave their imprint on $\beta$ but the quantity which has been measured is an average over the time of dissociation. The use of a fs laser allows, in favorable cases, a mesasurement of the process in real time. The caveat is that direct dissociations producing fast light particles are still too fast to measure. However, many interesting processes involve delays due to curve crossing or to separation of slow heavy fragments.

Downloaded by STANFORD UNIV GREEN LIBR on September 21, 2012 | http://pubs.acs.org
Publication Date: October 18, 2000 | doi: 10.1021/bk-2001-0770.ch002

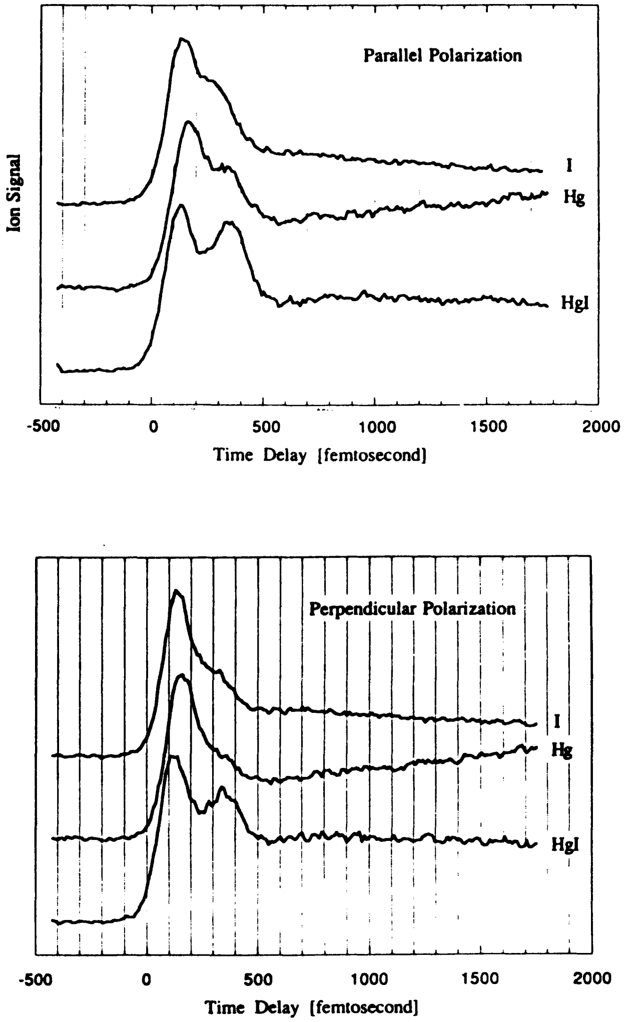

*Figure4 Fs transients of different masses for parallel (left) and perpendicular (right) polarization of the probe E vector relative to the E vector which dissociates $HgI_2$. From Ref. 40 with permision.*

$HgI_2 + h\nu \rightarrow HgI + I$ or $I^*$

The process above, studied by Zewail shows the potential of fs measurements (*40)* A beam of $HgI_2$ molecules was dissociated by a fs pulse of 311 nm light. The precursor and products were subsequently ionized by a 622 nm fs pulse and then mass analyzed in a time-of-flight (TOF) mass spectrometer. The latter wavelength was chosen because it is in resonance with the $B^1\Sigma$<--$X^A\Sigma$ transition of HgI. This is the initial, controlling absorption on the way to ionization. The E vector of the dissociating light $E_d$ was fixed parallel to the axis of the TOF tube. Figure4 shows the rise time of the various ions. On the left the E vector of the probing laser $E_{pr}$ is parallel to $E_d$; on the right it is perpendicular. The transitions which lead to I and I* are polarized, respectively, perpendicular and parallel to the molecular axis of the linear molecule. The proof is that when $E_{pr}$ is parallel to $E_d$ for the I* channel the REMPI signal of HgI+ is increased. Conversely for the I channel, when $E_{pr}$ is parallel to $E_d$ the REMPI signal is decreased. The rise of the HgI+ signal has two peaks. The earlier peak is due to the HgI whose partner fragments are I atoms and the later peak is due to those HgI whose partners are I* atoms.

## Acknowledgment

The writing of this review was supported by the U.S. National Science Foundation.

## References

1. Zare,R.N., *Mol.Photochem.* **1972**,*4*,1
2. Jonah,C., *J.Chem.Phys.* **1971**,*55*,1515
3. Yang,S.C. and Bersohn,R., *J.Chem.Phys.* **1974**,*61*,4400
4. Busch,G.E. and Wilson,K.R., *J.Chem.Phys.* **1972**,*56*,3638
5. .Dzvonik,M.;Yang,S.C.;,Bersohn,R., *J.Chem.Phys.* **1974**,*61*,4408
6. Lin,J.J.;Hwang,D.W.;Harlich,S;,Lee,Y.T;,Yang,X.; *Rev.Sci.Instrum.* **1998**,*69*,1692
7. .Houston,P. *J.Phys.Chem.* **1987**,*91*,5388
8. Chandler,D.W. and Houston,P. *J.Chem.Phys.* **1987**,*87*,1445
9. Eppink,A.T.;Andre,T.J.;Parker,D.H. *J.Chem.Phys.* **1998**,*109*,4758
10. Sato,H.,*Photodissociation of Simple Molecules in the Gas Phase,* Bunshin Publishing, Tokyo,1992
11. .Lengsfield,B.H.; Siegbahn,P.E.M.;.Liu,B. *J.Chem.Phys.* **1984**,*81*,710
12. .Wendt,H.R.; Hunziker,H.E. *J.Chem.Phys.* **1984**,*81*,717
13. North,S.W.;.Blank,D.A.; Chu,P.M.; .Lee,Y.T. *J.Chem.Phys.* **1995**,*102*,792
14. .Andresen,P.;.Ondrey,G.S.;.Titze,B.; Rothe,E.W. *J.Chem.Phys.* **1984**,*80*,2598
15. .Andresen,P. and Schink,R.e in *Molecular Photodissociation Dynamics*,.Ashfold,M.N.R. and.Baggott,J.E. eds. Royal Society of Chemistry, London, 1987
16. Van Veen,G.N.A.; Mohammed,K.A.;.Baller,T.; de Vries,A.E *Chem.Phys.* **1983**,*74*,261.

Downloaded by STANFORD UNIV GREEN LIBR on September 21, 2012 | http://pubs.acs.org
Publication Date: October 18, 2000 | doi: 10.1021/bk-2001-0770.ch002

17..Satyapal,S.;.Park,J.; Bersohn,R.; Katz,B. *J.Chem.Phys.* **1989**,*91*,6873

18. Jensen,E.;.Keller,J.L.;.Waschewsky,G.C.G.; Stevens,J.E.; .Graham,R.L. Freed,K.F.;.Butler,L.J. *J.Chem.Phys.* **1993**,*98*,2882

19. Nanbu,S.; Iwata,S. *J.Phys.Chem.* **1992**,*96*,2103

20. Thelen,M.A.; Felder,P.; Frey,J.G.;.Huber,J.R. *J.Phys.Chem.* **1993**,*97*,6220

21..Walsh,A.D. *J.Chem.Soc.* **1953**,23266

22. Vasudev,R.; ZareR.N;, Dixon,R.N *J.Chem.Phys.* **1984**,*80*,4863

23..Kawasaki,M;.LeeS.J.;,.Bersohn, R. *J.Chem.phys.* **1977**,*66*,2647

24. Freedman,A. and Bersohn,R. *J.Am.Chem.Soc.* **1978**,*100*,4116

25..Levenson,R.A. and.Gray,H.B. *J.Am.Chem.Soc.* **1975**,*97*,6042

26..Mulliken,R.S. *Phys.Rev.* **1936**,*50*,1017

27. Mebel,A.M. ;Lin,S-H.;Chang, C-H. *J.Chem.Phys.* **1997**,*106*,2612

28. Wang,J-H.; Liu,K. *J.Chem.Phys.* **1998**,*109*, 7105

29. Kable,S.H.; Loison,J-C..Neyer,D.W.; Houston,P.L.;.Burak,I.; Dixon,R.N. *B* *J.Phys.Chem.* **1991**,*95*,8013

30..Mordaunt, D.H.;Ashfold,M.N.R.; Dixon,R.N. *J.Chem.Phys.* **1998**,*109*,7659

31. Dixon,R.N.;.Hancock,T. *J.Phys.Chem.* **1997**,***101***,7567

32..Cassassa,M.P.;.Foy,R.R.;.Stephenson,J.C.; King,D.R. *J.Chem.Phys.* **1991**,*94,250*

33. Zare,R.N. *Ber.Bunsenges.Phys.Chem.* **1982**,*86*,422

34. R.N.Dixon, R.N. *J.Chem.Phys.* **1986**,*85*,1866

35..Hall,G.E.;.Sivakumar,N.;.Chawla,D.;.Houston,P.L.;.Burak,I. *J.Chem.Phys.* **1988**,*88*,3682

36. GerickeK-H.;.Klee,S..Comes,F.J.;.Dixon,R.N. *J.Chem.Phys.* **1096**,*85*,4463

37..Balint-Kurti, G.G.;;Shapiro,M. *Chem.Phys.* **1981**,*61,137*

38...Pe'er,A.;Shapiro,M.;.Balint-Kurti,G.G. *J.Chem.Phys.* **1999**,*110*,11928

39..Kim,H.L.; R.Bersohn,R. *J.Chem.Phys.* **1997**,*107*,4546

40. Baumert,T.;.Pedersen,S.;.Zewail,A.H *J.Phys.Chem.* **1993**,*97*,12947

Downloaded by STANFORD UNIV GREEN LIBR on September 21, 2012 | http://pubs.acs.org
Publication Date: October 18, 2000 | doi: 10.1021/bk-2001-0770.ch002

## Chapter 3

# Improvements in the Product Imaging Technique and Their Application to Ozone Photodissociation

**Joseph D. Geiser[1], Scott M. Dylewski[2], Julie A. Mueller[1], Ruth J. Wilson[1], B.-Y. Chang[1], R. C. Hoetzlein[1], and Paul L. Houston[1]**

**[1]Department of Chemistry and Chemical Biology and [2]School of Applied and Engineering Physics, Cornell University, Ithaca, NY 14853**

Ion counting and velocity mapping have been used to increase the speed and angular resolution of product imaging. Applications to the photodissociation of ozone will be discussed. The channel giving $O(^1D)$ and $O_2(^1\Delta)$ has been examined at a wide range of wavelengths. Results include the variation in vibrational distribution at these wavelengths, the orbital alignment of the $O(^1D)$, the observation that vibrationally excited ozone absorbs much more strongly than ground state ozone, and the observation of rotational resolution in the recoil velocity, leading to an improved dissociation energy for ozone. The channel giving $O(^3P)$ and $O_2(^3\Sigma)$ has also been examined at a variety of wavelengths from 226 to 266 nm. The vibrational distributions obtained for the various $^3P_J$ products, when combined with measurements of the yields of these channels, allow us to calculate how much $O_2(v\geq26)$ is produced as a function of wavelength.

In Imaging in Chemical Dynamics; Suits, A., et al.;
ACS Symposium Series; American Chemical Society: Washington, DC, 2000.

## Introduction: Evolution of the Technique

As the work in this symposium demonstrates, product imaging techniques have transformed the field of molecular dynamics. In this paper, we review the application of product imaging to the photodissociation of ozone. In particular, we will see that imaging of the oxygen atoms in either the $O_3 \rightarrow O_2(^3\Sigma_g^-) + O(^3P_J)$ or $O_3 \rightarrow O_2(^1\Delta_g) + O(^1D_2)$ channel provides a wealth of detail about this photolytic process of importance to atmospheric chemistry.

The principle of the product imaging technique is nicely illustrated by an etching by M. C. Esher called "Three spheres I," which shows a sphere being deformed from three dimensions to two dimensions (all illustrated on a two dimensional surface!).[1] Imagine the center of mass of a chemical reaction as the center of the sphere. A certain time after the reaction, the products of a particular speed will be located on the surface of the sphere, and their distribution on the surface of that sphere will indicate the angular dependence of the scattering. The projection of the sphere carries information about both the speed and angular distributions and can be used to determine both.

In practice we accomplish product imaging as shown in **Figure 1**. Although it is illustrated here for a photodissociation reaction, the same ideas apply to crossed beam reactions. A pulsed molecular beam carrying, for example, ozone is crossed with a dissociation laser of known polarization. Products then fly out from the center-of-mass point with velocity distributions that we would like to measure. Shortly after the photolysis pulse, another laser pulse ionizes a particular electronic, vibrational, and rotational state of one of the products. Knocking an electron off the product does not change the product velocity, because the electron carries away so little momentum. The resulting ions are then accelerated into a pair of microchannel plates. Roughly $10^7$ electrons come out the back side of these plates for each ion that produces a pulse, about 50-80% of the ions that strike the front of the plate. The electrons are accelerated into a fluorescent screen. Finally, a digital camera takes a picture of the screen and sends it to a computer. The experiment is repeated at 10 Hz. The experiment may be performed in the configuration shown or with the detection apparatus rotated 90° and pointed toward the pulsed nozzle.

Excited molecules are aligned in space due to the molecular absorption. $CH_3I$, which has its transition dipole moment along the C-I bond, absorbs more strongly if the C-I bond is parallel to the electric vector of the polarized dissociation light than if it is perpendicular. If the molecules dissociate rapidly compared to their rotation time, then we would expect the I and $CH_3$ fragments to be flying predominantly toward the top or bottom of the image. In terms of spheres around the center of mass, there would be more fragments at the north and south pole than at the equator. The very first image obtained with this

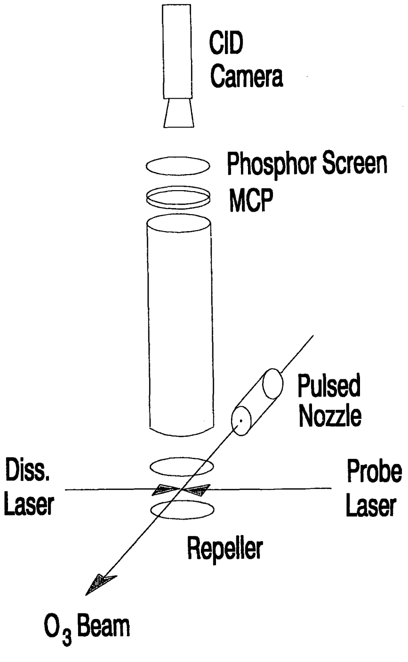
CID
Camera
Phosphor Screen
MCP
Pulsed
Nozzle
Diss.
Laser
Probe
Laser
Repeller
$O_3$ Beam

Figure 1 Experimental apparatus for product imaging

technique[2] is shown in **Figure 2**, which depicts the $CH_3$ fragment velocity distribution following photodissociation of methyl iodide. It is evident that there are more fragments at the north and south poles of the projected sphere than around the equator.

A mathematical technique called the inverse Abel transform allows us to recover the complete three dimensional information from the projection as long as there is an axis of cylindrical symmetry. In the case of dissociation with linearly polarized light, this polarization vector is the symmetry axis.

A problem in the resolution of the technique is that there is a finite overlap volume between the molecular beam and the laser beams. This overlap causes a blurring of the resulting image. For example, if the overlap dimension is say, 1 mm, then the resolution of the image taken with a normal Wiley-McLaren time-of-flight mass spectrometer cannot be better than 1 mm. Fortunately, Eppink and Parker discovered that the use of an einzel lens can almost completely correct for this blurring.[3] Images collected using such a lens are called velocity mapped images.

Another improvement in the resolutions is accomplished by an ion counting technique.[4] Ions hitting the screen are first discriminate from noise using a threshold function. On every shot of the laser, a computer program then locates the center of each cluster of ion pixels and replaces the cluster with a single count. The counts are then accumulated to produce an image.

**Figure 3** shows an example of the increase in resolution obtained by the ion counting technique. Consider ionization of the $N_2(v{=}0,J)$ product of the photodissociation of $N_2O$ at a fixed wavelength. Because the sibling $O(^1D_2)$ product is in a specific electronic state, the fixed wavelength and the dissociation energy can be used to calculate that dissociation of ground-state $N_2O$ should produce $N_2(v{=}0,\mathrm{J})$ with a delta-function speed distribution. The top row shows the raw data, the inverse Abel transform, and an expanded view of one eighth of the transform, all obtained by using velocity mapped imaging but not ion counting. The lower panel shows the additional effect of ion counting. One sees that the ring of the transform can actually now be resolved into two rings. The two rings occur because there is some vibrationally excited $N_2O$ in the beam that absorbs light and dissociates with appropriately higher recoil. The main point, however, is that the ion counting improves the resolution. From such images, we can count the number of pixels (1-2) for the width of a resolvable ring and estimate that the velocity resolution is better than 1% for our apparatus when the ring is near the edge of our image (about 256 pixels wide). Of course, for smaller rings, the resolution is correspondingly worse, but we can always adjust the acceleration voltages to produce an expanded image at the detector. Also, it should be noted that because the energy is a non-linear function of the velocity, equal energy spacings will be more closely spaced at

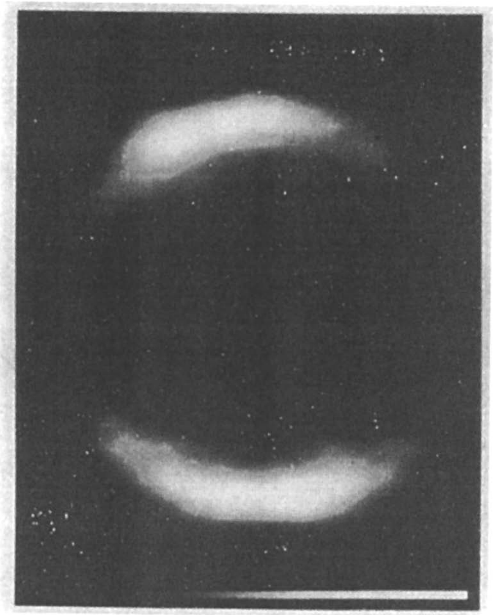

Figure 2 First image of methyl radicals from the photodissociation of methyl iodide.

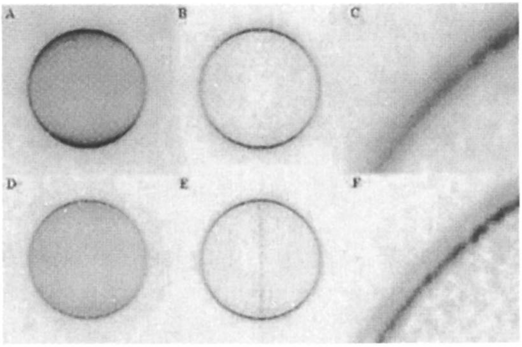

Figure 3

Panels A and D show images collected using velocity mapped imaging and using the ion-counting method, respectively, for the $N_2(v''=0,\ J''\approx 74)$ product of $N_2O$ photodissociation at 203.2 nm. Panels B and E show the Abel inverse-transformed images of A and D, respectively. Panels 3C and 3F show 8x enlargements of B and E, respectively.

high velocity than at low velocity, so that the center of the image provides the most discrimination between closely spaced energy levels.

A comparison of the raw data between that in **Figure 2** for methyl iodide and that in **Figure 3** for $N_2O$ indicates the improvement in the product imaging technique in the 12 years since its first use.

## The Application of Product Imaging to the Photodissociation of Ozone

The photodissociation of ozone in the Hartley band predominantly occurs by two channels:

$$\begin{array}{lllll} O_3 & \rightarrow & O_2(^1\Delta_g) & + \; O(^1D_2) & 90\% \\ & \rightarrow & O_2(^3\Sigma_g^-) & + \; O(^3P_J) & 10\% \end{array}$$

We have used product imaging to examine each of these two channels.

### The Singlet Channel

Consider first the channel producing singlet products, $O_2(^1\Delta_g) + O(^1D_2)$. For a dissociation wavelength of 265 nm, enough energy is available to populate these electronic states of the O and $O_2$ products as well as to excite the $O_2(^1\Delta_g)$ product to $v = 3$. **Figure 4** shows the inverse-Abel-transformed image we obtain. Four rings clearly correspond to the population of $v = 0,1,2,3$ of the $O_2(^1\Delta_g)$. An analysis of the image provides the vibrational distribution shown in **Figure 5**.

When the dissociation wavelength is varied, one obtains the variety of images shown in **Figure 6**. The 265-nm image is in the top row, fourth from the left. As one goes to shorter wavelengths (higher energy), more and more rings are visible because more and more vibrational levels of $O_2(^1\Delta_g)$ are energetically accessible. As one goes to longer wavelengths (lower energy), the rings disappear one by one until a single ring remains. Interestingly, at 305.7456 nm as the last ring disappears near the threshold for production of $O_2(^1\Delta_g)$, the inverse-Abel transform still shows structure, as shown in **Figure 7**. The structure is due to *rotational* resolution of the $O_2(^1\Delta_g, v{=}0)$. An analysis of the speed distribution of this image is shown in **Figure 8**.

Because the energy of the dissociation laser is known to high accuracy, and because the product states can be assigned completely, it is possible to deduce from **Figure 8** the dissociation energy of ozone to a high degree of accuracy. We obtain from this measurement a new value for the heat of formation of ozone of -144.31 ± 0.14 kJ/mol.[5]

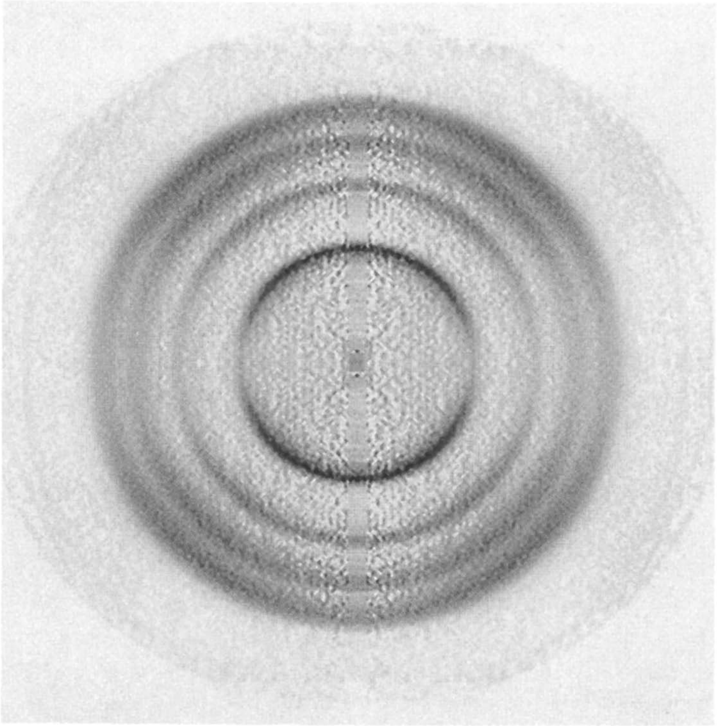

Figure 4
Inverse-Abel-transformed image of $O(^1D_2)$ velocity following 265-nm photodissociation of ozone.

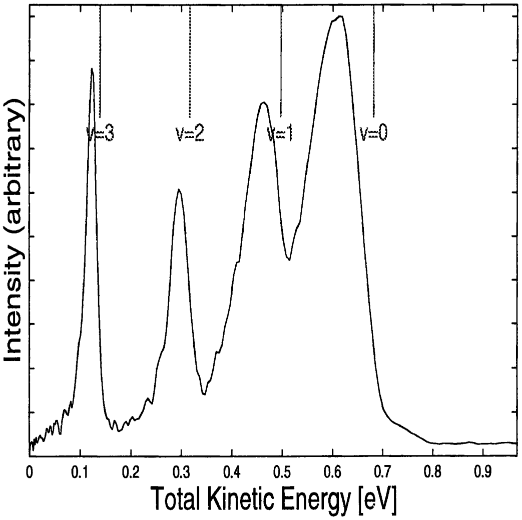

Figure 5

An analysis of the data in **Figure 4** shows the vibrational distribution of $O_2(^1\Delta_g)$ from the 265-nm photodissociation of ozone.

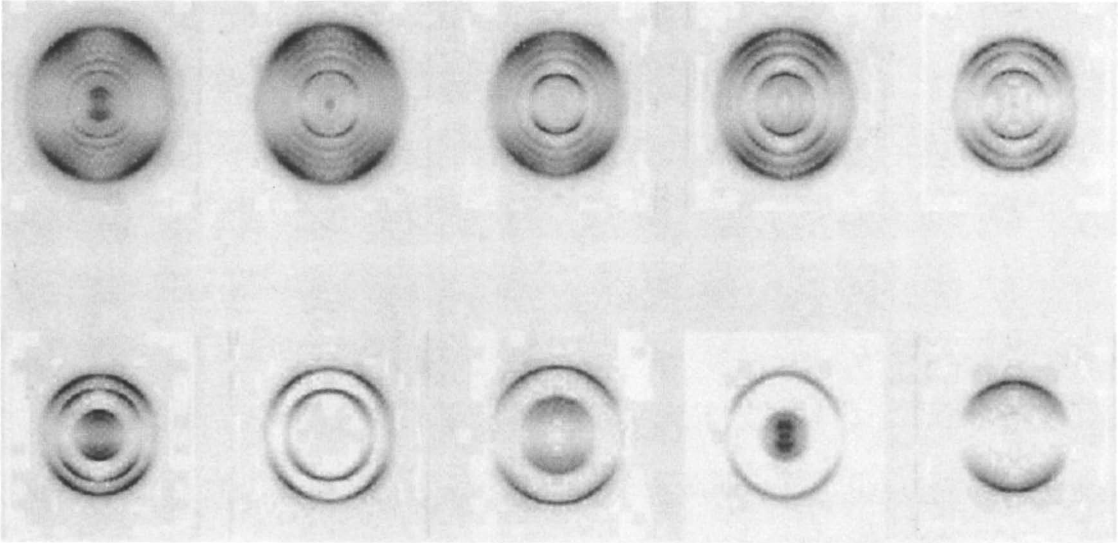

Figure 6 Inverse-Abel-transformed images of the O($^1D_2$) velocity following photodissociation of ozone at (from upper left to lower right) 235, 245, 255, 265, 275, 280, 285, 290, 294, and 300 nm.

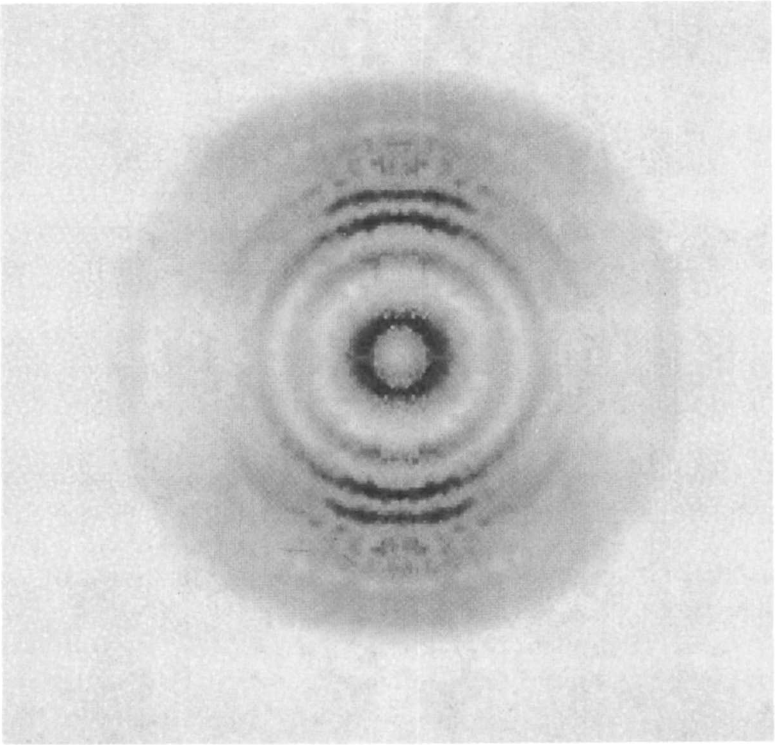

Figure 7
O($^1D_2$) inverse-Abel-transformed image following ozone photodissociation at 305.7456 nm.

At higher total kinetic energies than those shown in **Figure 8** we should no longer see production of O($^1$D), but, as shown in **Figure 9**, we still observe its formation with kinetic energies of 0.15-0.25 eV. The reason is that the small amount of vibrationally excited ozone in the molecular beam can absorb at longer wavelengths than the threshold for the vibrationless ground state. The assignments in the figure show that all vibrational levels of ozone contribute to some extent. Hot band absorption may be of some importance in the modeling of the stratospheric ozone concentration, because the hot band absorption occurs at wavelengths where the solar flux is higher than for absorption by ground-state ozone.

A further interesting feature of the O($^1D_2$) images is that the angular distribution is not peaked along the (vertical) direction of the photodissociation electric vector but rather at about 45° from that axis. The explanation for this phenomenon comes from the further observation that the image depends on the polarization of the ionization laser as well as on the polarization of the photodissociation laser, as shown in **Figure 10**. The notation above the images corresponds to the polarization direction of the dissociation and probe lasers. Vertical (V) indicates that the polarization is parallel to the front surface of the channel plate detector, while horizontal (H) means that it is perpendicular to that surface. This dependence on the polarization direction of the ionization laser indicates that the O($^1D_2$) fragment has an aligned angular momentum distribution.

Using the analysis developed by Mo and Suzuki,[6] we calculated the angular dependence for different values of $m_J$ and for ionization on the O($^1$P) ← O($^1$D) vs. O($^1$F) ← O($^1$D) transition, as shown in **Figure 11** and **Figure 12**, respectively. The value of $m_J$ gives the projection of the O($^1D_2$) angular momentum on the recoil velocity axis.

The fits to the angular distributions of the O($^1D_2$) in $v$ = 0, 1, and 3 are shown in **Figure 13**, **Figure 14**, and **Figure 15**, respectively, while the overall $m_J$ distribution is shown in **Figure 16**. In this analysis we use images from both ionization transitions and fit all the data towith the same $m_J$ populations and anisotropy parameter, β. The $m_J$ distribution suggests that the angular momentum of the O($^1$D) is aligned predominantly perpendicular to the recoil velocity vector.

## The Triplet Channel

The Hartley band of ozone is a broad absorption feature from about 200 to 310 nm consisting of a continuum with some structure superimposed on it. Although the singlet channel is the dominant of the two channels and has 85 to

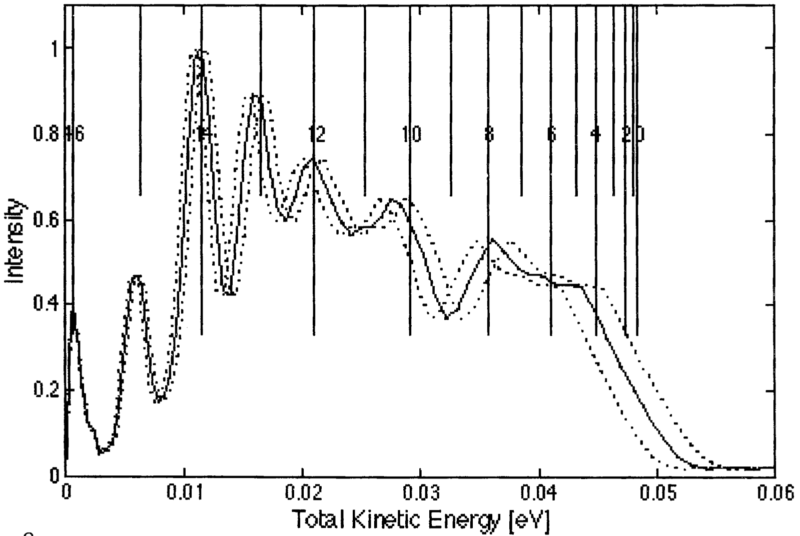

Figure 8
Rotational distribution of $O_2(^1\Delta_g)$ following dissociation of ozone at 305.7456 nm.

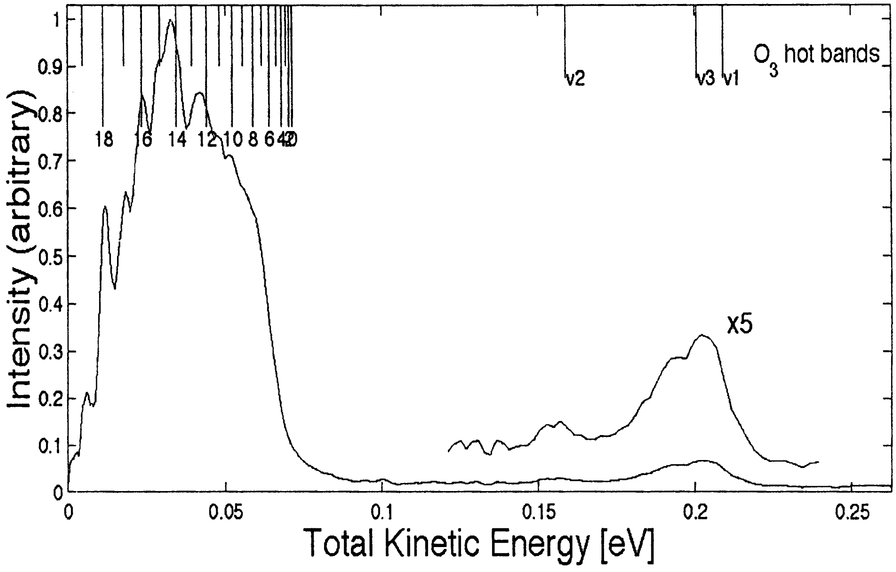

Figure 9

A lower-resolution view of the analyzed data from the 305-nm photodissociation of ozone showing both the rotationally resolved $O_2(^1\Delta, \nu=0)$ band (left) and the hot band production of $O(^1D_2)$ (right)

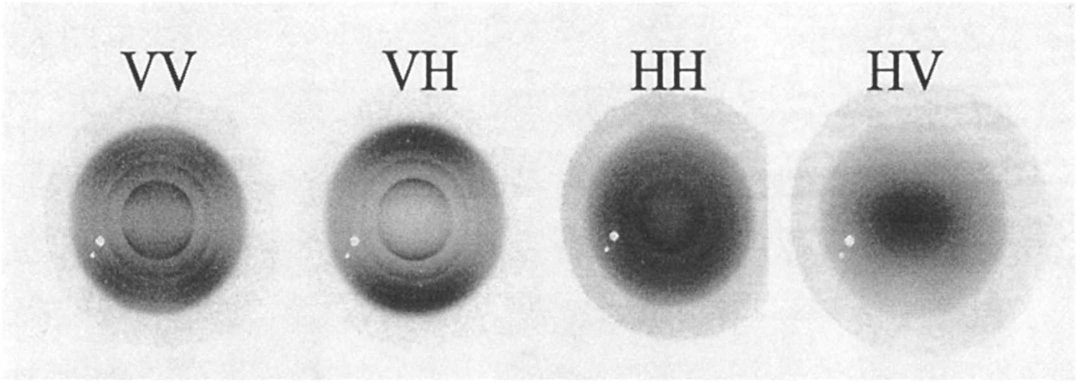

Figure 10 Images for different combinations of the photodissociation and ionization polarization for dissociation of ozone at 255 nm and ionization at 203 nm.

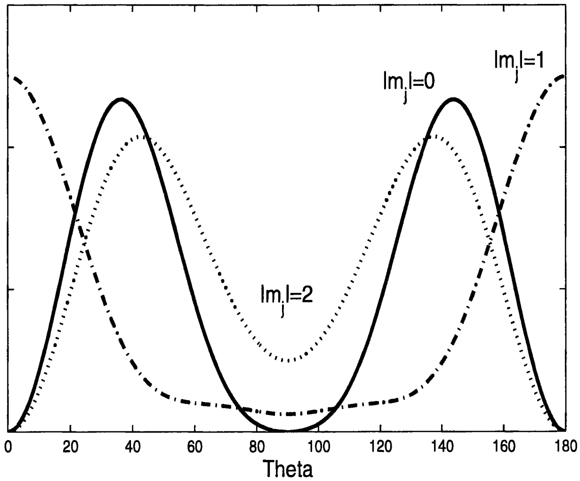

Figure 11

Detection sensitivity to various $m_J$ levels for $\beta=1.5$ and detection on the $O(^1P) \leftarrow O(^1D)$ transition.

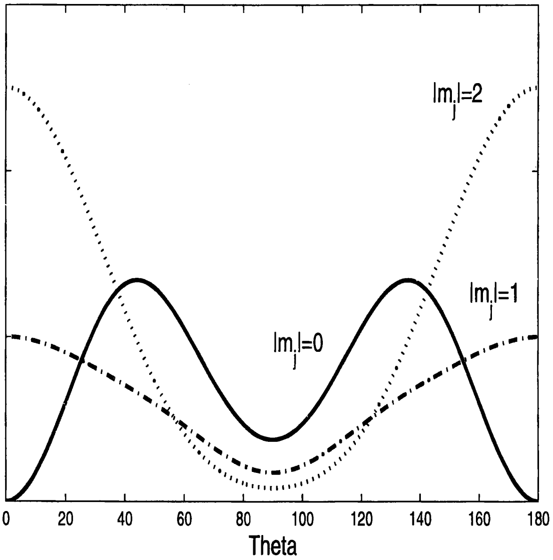

Figure 12

Detection sensitivity to various $m_J$ levels for $\beta=1.5$ and detection on the $O(^1F) \leftarrow O(^1D)$ transition.

American Chemical Society
Library
1155 16th St., N.W.
Washington, D.C. 20036

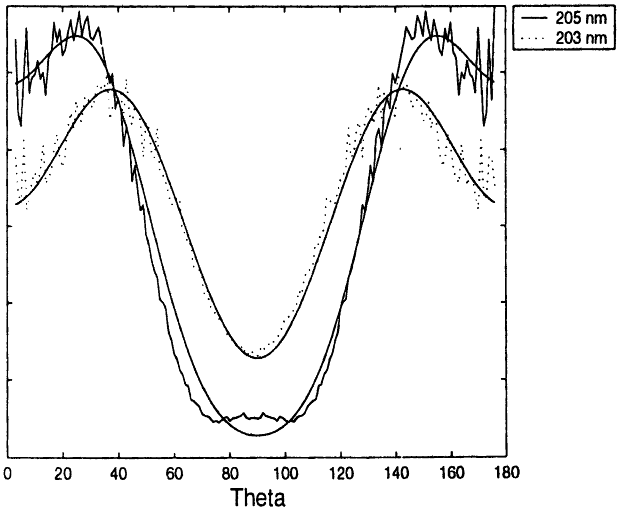

Figure 13
Fit to angular distribution for O($^1D_2$, $v$=0) produced in 265 nm dissociation of ozone.

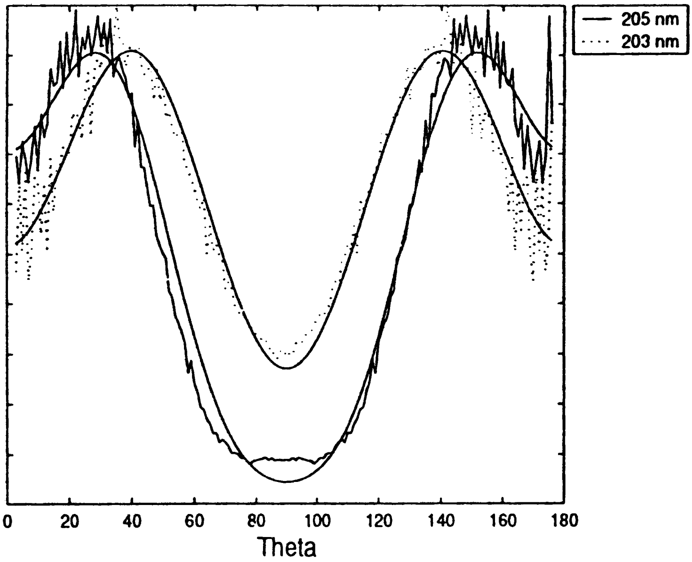

Figure 14
Fit to angular distribution for O($^1D_2$, $v$=1) produced in 265 nm dissociation of ozone.

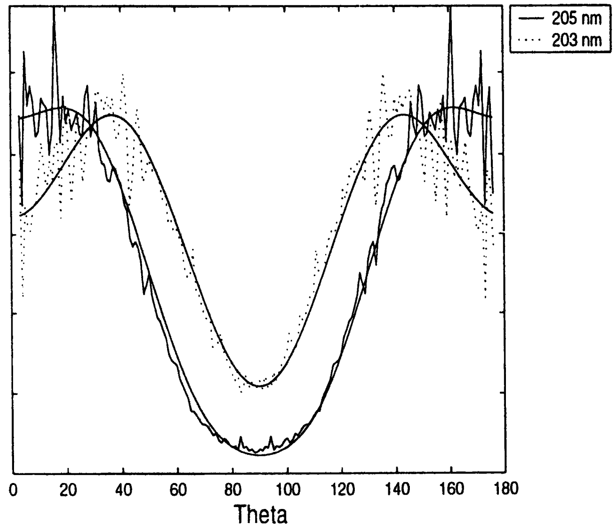

Figure 15
Fit to angular distribution for O($^1D_2$, $v$=3) produced in 265 nm dissociation of ozone.

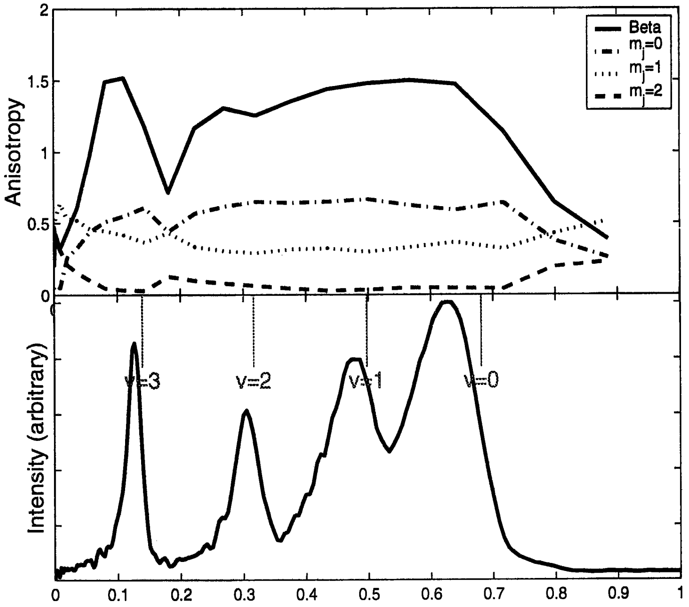

Figure 16
The $m_J$ distribution for dissociation of ozone at 265 nm (top) and the vibrational distribution (bottom)

90% of yield, the minor triplet channel is both interesting and important because it yields oxygen molecules with a bimodal energy distribution with a significant fraction of the molecules formed in very high vibrational states.[7] It is important to determine the quantity and fate of these energetic molecules generated in the stratosphere. Even though only 10 to 15% of the photodissociation events follow this minor channel, a relatively large amount of vibrationally excited $O_2$ might be generated because the cycle of $O + O_2$ recombination and ozone dissociation occurs more than 50 times, depending on altitude, for every ozone formed by photodissociation of $O_2$ or lost by catalytic decomposition. One possible influence these high-energy $O_2$ molecules might have is on the ozone deficit problem, *i.e.* the possible mismatch between modeled ozone concentrations and measured concentrations as a function of altitude.[8-17] If there is an ozone deficit, and if $O_2(^3\Sigma_g^-, v \geq 26)$ participates in the production of ozone, the yield of $O_2(^3\Sigma_g^-, v \geq 26)$ may play an important role in understanding the possible mismatch. A mechanism in which the vibrationally excited oxygen produced in the ozone photodissociation reacts to produce $O + O_3$ can account for the ozone deficit at about 40 km,[7] but cannot account completely for the deficit at higher altitudes. We have recently examined the vibrational distributions of this triplet channel by imaging the $O(^3P_J)$ product as a function of ozone dissociation wavelength.

**Figure 17** shows the $O(^3P_J)$ images obtained for dissociation of ozone at a variety of wavelengths. For the most part, the images are characterized by a bimodal speed distribution. Of course, from conservation of momentum and energy, this bimodal speed distribution implies that the internal energy distribution of the sibling $O_2(^3\Sigma_g^-)$ is also bimodal. In many images it is possible to discern individual rings in the center of the image corresponding to $O_2(^3\Sigma_g^-)$ with $v = 27$ and 28.

Vibrational distributions derived from the images of **Figure 17** are shown in **Figure 18**. Perhaps the most interesting aspect of this study is that the very vibrationally excited part of the distribution disappears when the ozone photolysis energy falls below the threshold for production of $O_2(^3\Sigma_g^-)$ $v = 27$. Apparently, the channel producing very highly vibrationally excited $O_2(^3\Sigma_g^-)$ from ozone depends strongly on dissociation wavelength.

It is interesting to ascertain the wavelength dependence of the yield of $O_2(^3\Sigma_g^-, v \geq 26)$ produced in the photodissociation of ozone, since Miller *et al.*[7] have suggested that vibrationally excited oxygen might explain the "ozone deficit" problem. **Figure 19** shows the dependence found in this study, along with a point at 193 found in the study by Stranges *et al.*[18] We find that at 226, 230, 233, 234, and 240 nm, the yield is 11.6±1.9%, 11.4±2.1%, 8.7±3.0, 4.2±1.5, and 0.6±0.1%, respectively.

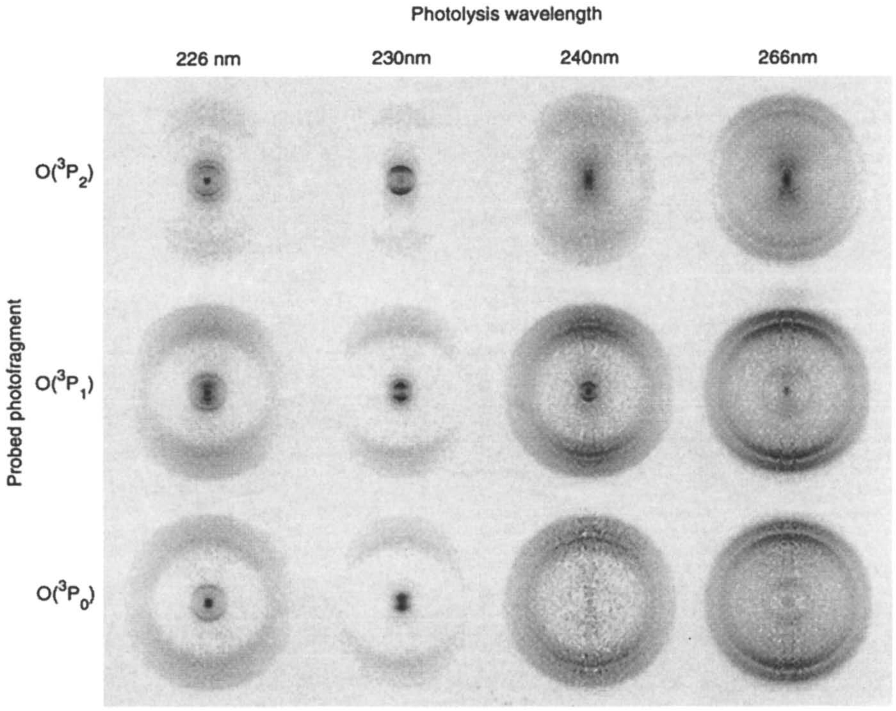

Figure 17 O($^3P_J$) inverse-Abel-transformed images for dissociation of ozone at a variety of wavelengths.

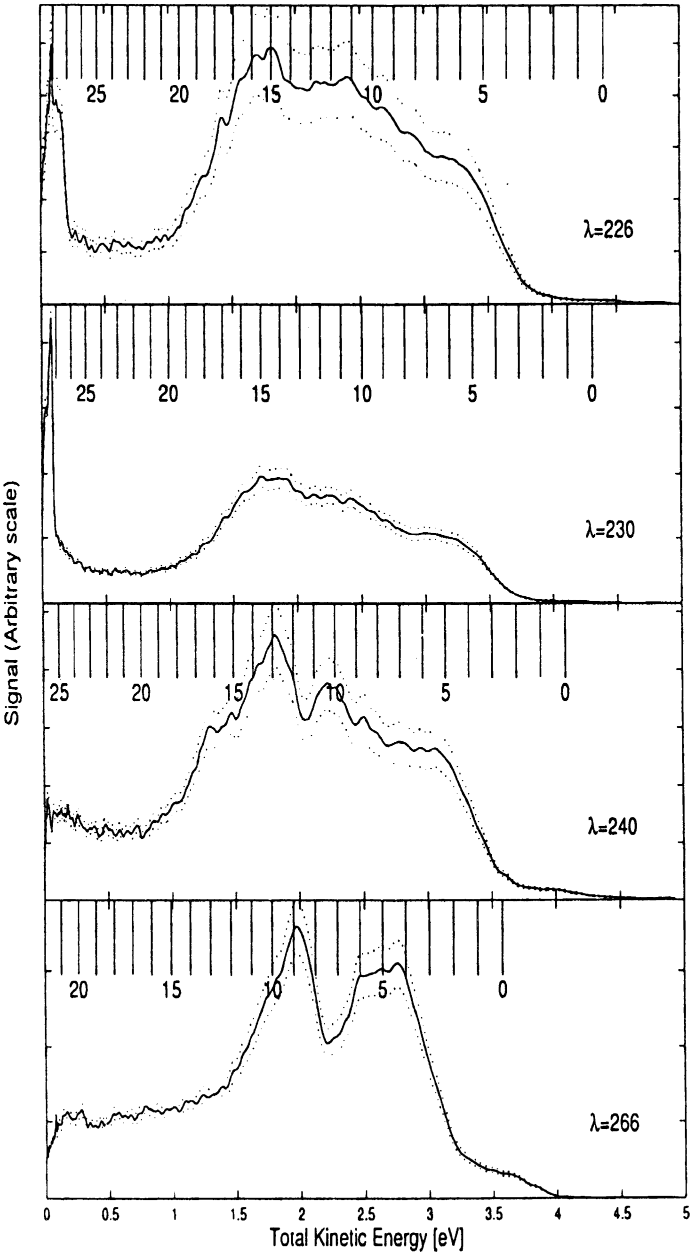

Figure 18
Translational energy distributions for O($^3$P) from the photodissociation of ozone at wavelengths indicated and averaged over the O($^3$P$_J$) distribution. Lines at the top of each figure indicate the energies corresponding to specific $O_2$ vibrational levels.

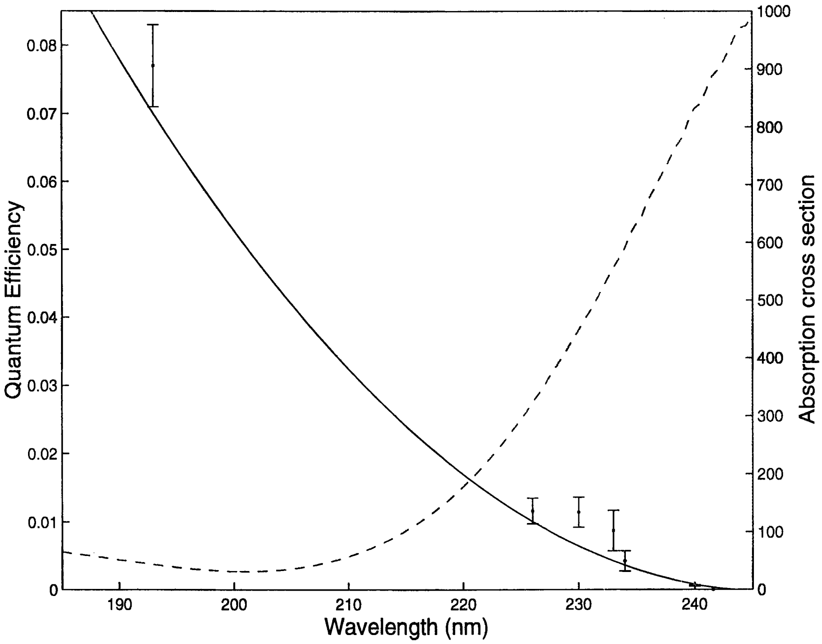

Figure 19 Wavelength dependence of the yield of $O_2(^3\Sigma_g^-, v \geq 26)$.

## Conclusion

The results of this study show that the dissociation of ozone is much more complicated than previously thought. Although the general features of the ozone formation and destruction in the stratospheric are now determined, it is likely that the more detailed features, such as the internal energy distributions of the photoproducts, are also significant in determining the stratospheric ozone budget. Many minor channels participate in the dissociation. Because even a one percent change in the ozone concentration can cause significant health changes due to, for example, skin cancer and cataract formation, a better understanding of the ozone photodissociation is needed.

The new improvements of ion counting and velocity mapping have been used to increase the speed and angular resolution of product imaging. Applications to the photodissociation of ozone show several new features of the dissociation.

The channel giving $O(^1D)$ and $O_2(^1\Delta)$ has been examined at a wide range of wavelengths. Results include the variation in vibrational distribution at these wavelengths, the orbital alignment of the $O(^1D)$, the observation that vibrationally excited ozone absorbs much more strongly than ground state ozone, and the observation of rotational resolution in the recoil velocity, leading to an improved dissociation energy for ozone. The bond dissociation energy into $O(^1D) + O_2(^1\Delta_g)$ is found to be 386.59 ± 0.04 kJ/mol.

The triplet channel producing $O(^3P_j)$ and $O_2(X\,^3\Sigma_g^-)$ was studied at photolysis wavelengths of 226, 230, 233, 234, 240, and 266 nm. These imaging experiments, together with a measurement of the branching ratio into the different spin orbit states of the O atom, allowed the determination of the yields of the $O_2$ product in vibrational states greater than or equal to 26 as a function of wavelength. It was found that at 226, 230, 233, 234, and 240 nm, the yield was 11.6 ± 1.9%, 11.4 ± 2.1%, 8.7 ± 3.0, 4.2 ± 1.5, and 0.6 ± 0.1%, respectively. This yield may play an important role in analyzing the ozone deficit, the mismatch between measured ozone concentrations as a function of altitude and those predicted by modeling calculations. A mechanism in which the vibrationally excited oxygen produced in the ozone photodissociation reacts to produce $O + O_3$ can account for the ozone deficit at about 40 km, but cannot account completely for the deficit at higher altitudes.

## Acknowledgments

This work was supported by the National Science Foundation under Grant ATM-9528086 and by the Research Institute of Innovative Technology for the

Earth administered by the New Energy and Industrial Technology Development Organization of Japan.

## References

1. "Three spheres I," plate 68 in *The Graphic Work of M. C. Escher,* (Ballantine Books, New York, 1960).
2. Chandler, D. W.; Houston, P. L. *J. Chem. Phys.* **1987**, *87*, 1445-1447.
3. Eppink, A. T. J. B.; Parker, D. H. *Rev. Sci. Instrum.* **1997**, *68*, 3477-3484.
4. Chang, B.-Y.; Hoetzlein, R. C.; Mueller, J. A.; Geiser, J. D.; Houston, P. L. *Rev. Sci. Instrum.* **1998**, *69*, 1665-1670.
5. Taniguchi, N.; Takahashi, K.; Matsumi, Y.; Dylewski, S.; Geiser, J.; Houston, P. L. "Determination of the heat of formation of $O_3$ using vacuum ultraviolet laser-induced fluorescence spectroscopy and two-dimensional product imaging techniques," *J. Chem. Phys.,* accepted.
6. Mo, Y.; Katayanagi, H.; Heaven, M. C.; Suzuki, T. *Phys. Rev. Lett.* **1996**, *77*, 830-833.
7. Miller, R. L.; Suits, A. G.; Houston, P. L.; Toumi, R.; Mack, J. A.; Wodtke, A. M. *Science* **1994**, *265*, 1831-1838.
8. Toumi, R.; Kerridge, B. J.; Pyle, J. A. *Nature* **1991**, *351*, 217-219.
9. Eluszkiewicz, J.; Allen, M. *J. Geophys. Res.* **1993**, *98*, 1069-1082.
10. Siskind, D. E.; Connor, B. J.; Eckman, R. S.; Remsberg, E. E.; Tsou, J. J.; Parrish, A. *J. Geophys. Res.* **1995**, *100*, 11191-11201.
11. Slanger, T. G. *Science* **1994**, *265*, 1817-1818.
12. Dessler, A. E.; Kawa, S. R.; Considine, D. B.; Waters, J. W.; Froidevaux, L.; Kumer, J. B. *Geophys. Res. Lett.* **1996**, *23*, 339-342.
13. Jucks, K. W.; Johnson, D. G.; Chance, K. V.; Traub, W. A.; Salawitch, R. J.; Stachnik, R. A. *J. Geophys. Res.* **1996**, *101*, 28785-28792.
14. Crutzen, P. *Science* **1997**, *277*, 1951-1952.
15. McElroy, M. B.; Salawitch, R. J. *Planet. Space Sci.* **1989**, *37*, 1653.
16. Natarajan, M.; Callis, L. B. *Geophys. Res. Lett.* **1989**, *16*, 473-476.
17. Crutzen, P. J.; Grooß, J.-U.; Brühl, C.; Müller, R.; Russell III, J. M. *Science* **1995**, *268*, 705-708.
18. Stranges, D.; Yang, X.; Chesko, J. D.; Suits, A. G. *J. Chem. Phys.* **1995**, *102*, 6067-6077.

Downloaded by STANFORD UNIV GREEN LIBR on September 21, 2012 | http://pubs.acs.org
Publication Date: October 18, 2000 | doi: 10.1021/bk-2001-0770.ch004

## Chapter 4

# Velocity Map Imaging: Technique and Applications to $O_2$ Photodissociation

**D. H. Parker[1], B. L. G. Bakker[1], R. Delmdahl[1], T. Berg[2], and A. T. J. B. Eppink[3]**

**[1]Department of Molecular and Laser Physics, University of Nijmegen, Toernooiveld 1, 6525 ED, Nijmegen, The Netherlands**
**[2]LaVision GmbH, Göttingen, Gerhard-Gerder Strasse 3, D–37079 Göttingen, Germany**
**[3]Faculty of Physics, University of Bielefeld, Universitätsstrasse 25, D–33615 Bielefeld, Germany**

Velocity mapping was introduced in Nijmegen in 1997 as an improvement of ion imaging, a two-dimensional product imaging technique. The method has increased the velocity resolution of imaging dramatically, to the point that product vibrational energy disposal can be directly characterized for most molecules. A further improvement of the method involves the well-known event-centroiding method, which compensates for spatial blurring by the multi-channel plate / phosphor screen detector. The basics of velocity mapping and current developments are illustrated in studies of the photo-dissociation / ionization dynamics of $O_2$.

## Introduction

Velocity mapping (*1*,*2*) is an improvement of the ion imaging technique (*3*) introduced by Chandler and Houston in 1987. As the present authors showed in 1997, an electrostatic immersion lens when used in the ion imaging setup has the wonderful property of mapping each different product velocity to the same point on the imaging detector, independent of the initial position of the particle. Furthermore, this is possible without the use of fine-wire grids that tend to block and distort the ion trajectories. This advance led to a very substantial improvement in the velocity resolution of ion imaging, so substantial that the introduction of a new name for the technique, velocity mapping, seemed justified. The mapping

In Imaging in Chemical Dynamics; Suits, A., et al.;
ACS Symposium Series; American Chemical Society: Washington, DC, 2000.

technique is leading to new progress in several fields of molecular dynamics research reported in this symposium issue. Whereas the obtainable resolution was limited by the imaging detection system, this bottleneck is removed by application of event counting, based on thresholding techniques and event centroiding. As a result, high-resolution kinetic energy distributions are obtained, with the apparatus function limited by the velocity spread intrinsic in the experiment, and to a lesser extent the remaining aberrations of the relatively simple three-plate ion lens assembly employed in the experiment. In this paper the velocity mapping technique is described and applications are illustrated in studies of the photodissociation / ionization dynamics of molecular oxygen. Emphasis will be given to the utility of the product angular distributions for the deconvolution of overlapped continua in direct dissociation and the analysis of rotational effects in predissociation. The advantages of velocity map imaging of photoelectrons is also illustrated in analysis of resonance enhanced multiphoton ionization (REMPI) processes in $O_2$.

Downloaded by STANFORD UNIV GREEN LIBR on September 21, 2012 | http://pubs.acs.org
Publication Date: October 18, 2000 | doi: 10.1021/bk-2001-0770.ch004

## Experimental: Velocity Mapping and Event Counting

### Ion imaging and velocity mapping

Figure 1 illustrates the basic principles of ion imaging, velocity mapping, and event counting. An on-axis molecular beam geometry is used so that the projection of the velocity spread of the parent molecule beam onto the plane of the imaging detector is minimized. The beam of oxygen molecules is skimmed and then passes through a small hole in a repeller plate disc to enter the ionization region. A laser beam crosses the molecular beam, causing dissociation and ionization of the O atom photofragments. These $O^+$ ions are accelerated along the time-of-flight axis towards the two-dimensional multi-channel plate (MCP) / phosphor screen detector, which is monitored by a CCD camera.

In the ion imaging configuration the center holes in the two downstream electrode discs shown in cross section in Fig. 1 are covered with a fine-wire mesh in order to create a uniform electric field gradient in the time-of-flight direction. The holes are left open in velocity mapping, causing the field lines to penetrate into the repeller and ground (time-of-flight) regions and form an electrostatic immersion lens. With the proper ratio of repeller / extractor voltages for a given flight length the electrostatic lens will project each velocity to a unique point on the detector plane, regardless of the initial position of ionization (*1*). This is important because the ionization region is always a finite volume. With a crossed laser beam - molecular beam configuration this may extend along the laser propagation direction as far as 2000 microns (μm). In ion imaging the mapping of velocity on the detector then carries this 2000 μm spread onto the final image. For crossed molecular beam scattering the ionization volume can be even larger. In velocity mapping, however, the spread in mapping is reduced to ~10 μ

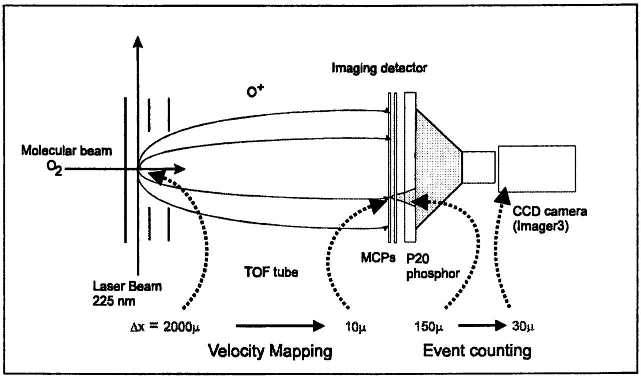

*Figure 1. Schematic diagram of the velocity mapping apparatus.*

perpendicular to and ~50 μm along the laser beam propagation. 10 μ is coincidentally a typical channel spacing in an MCP detector. All ions of a particular mass arrive at the MCP front surface within a time window of few nanoseconds with their arrival time ∝ $\text{mass}^{1/2}$. Mass selective detection is achieved by gating on the gain of the MCP or phosphor at the proper arrival time. An Abel inversion routine[3] recovers the full three-dimensional Newton sphere from the two-dimensional projection of the Newton sphere of ions. recorded by the CCD camera.

The advantages of velocity mapping are illustrated in Figure 2, which shows an image of $O^+$ atoms from the photodissociation / ionization of $O_2$ at 225 nm (*4*). The left side of the figure shows the ion image while the right side shows the velocity map image taken under otherwise identical conditions. The improvement in resolution is obvious. At least 20 different rings (two-dimensional projections of Newton spheres) are resolved in the velocity map image. In the middle image of Fig. 2 the velocity map image is copied 20 times with each successive copy displaced by 100 μm. The set of shifted images is then added together in order to simulate the effect of an origin line of ions 2000 μm long. As seen in this simulation, the ion image is still lower in resolution. This is the effect of the grids themselves. Grids not only decrease the total transmission of the lens to below 60%, they also deflect many of the ion trajectories that do reach the detector. Origin spreading is thus not the only problem in conventional ion imaging using grids.

Downloaded by STANFORD UNIV GREEN LIBR on September 21, 2012 | http://pubs.acs.org
Publication Date: October 18, 2000 | doi: 10.1021/bk-2001-0770.ch004

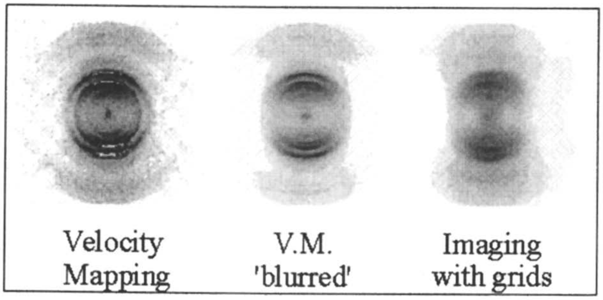

*Figure 2. A comparison of velocity mapping and ion imaging under identical conditions.*

Downloaded by STANFORD UNIV GREEN LIBR on September 21, 2012 | http://pubs.acs.org
Publication Date: October 18, 2000 | doi: 10.1021/bk-2001-0770.ch004

## EVENT COUNTING

Each ion event appears as a localized light flash on the (P-20) phosphor screen of the two-dimensional detector. For each laser shot an image of the phosphor screen is taken by the CCD camera, which can either be summed directly, or event-counted before summation. Event counting provides an additional increase in the kinetic energy resolution, enables background free detection, and compensates for any inhomogeneity of the imaging detector. Since all signals below a preset threshold value are rejected, the resulting image is free from dark current and read out noise. For a laser produced event, the signal will exceed this threshold and the location of the event is determined at sub-pixel accuracy. In this way, the smear-out of each event to a spot size of typically 150 μm is compensated by this center-of-gravity position localization easily down to 30 μm. In Figure 3 an example of a single shot image a), and corresponding the event counted image b) is shown.

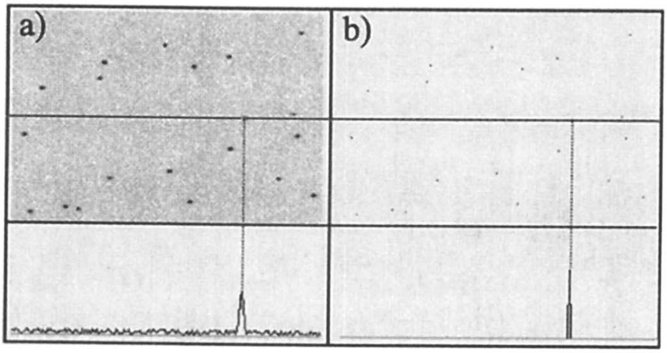

*Figure 3. a) Image from a single laser shot showing typical spot sizes of single ion events and read-out background. b) Same image after event counting.*

Downloaded by STANFORD UNIV GREEN LIBR on September 21, 2012 | http://pubs.acs.org
Publication Date: October 18, 2000 | doi: 10.1021/bk-2001-0770.ch004

In Figure 4 a velocity map image using event counting is shown for the same process described in Fig. 2. The normally averaged image is the direct summation of signal (6000 shots) which appears on the CCD, while the event counted image is a summation of 50,000 individual event counted laser shots. The enhancement of resolution is clear on inspection by eye and from the radial distributions shown on the right side of Fig. 4. Ring spacings down to 80 μm are resolved, which is about a factor 4 better than without event counting. Not shown here, but very clearly observed, is that event counting compensates for the inhomogeneous gain of the detector. The intensity between upper and lower half of the strongest ring differed by ~20 % without event counting, while the event counts yielded equal signals. With current computer processors (Pentium III, 450 MHz) as many as 200 events per laser shot can be processed at a 20Hz repetition rate. Events that fall too close to each other are under-counted however, thus for a single channel product signal a much lower number of events per laser shot is required. Space charge problems are also avoided with a low number of ions formed per laser shot.

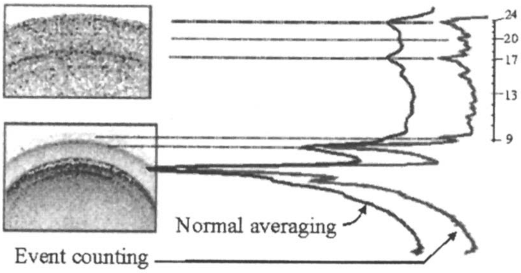

*Figure 4. Image using event counting for the same signal shown in Fig. 2. A vertical profile through the normal and event counted images are compared on the right side of the figure. The individual peaks arise from dissociation of* $O_2^+(v^+)$ *with the* $v^+$ *values indicated on the right-hand side of the figure.*

In summary, event counting recovers most of the resolution of velocity mapping lost in the two-dimensional detector. Removal of background counts and detector inhomogenity is an added plus. All of the needed equipment for real-time analysis is readily available, the only drawback is the requirement of low count rates. In the following section applications of velocity map imaging are illustrated in studies of the photodissociation / ionization dynamics of molecular oxygen. Applications making use of the product angular distribution will be given for the deconvolution of overlapped continua in direct dissociation (*5,6,7*) and for the analysis of rotational effects in predissociation (*8*). The advantages of velocity map imaging of photoelectrons (*4,9,10*) is also illustrated in analysis of resonance enhanced multiphoton ionization (REMPI) processes in $O_2$ (*4,11*).

## Velocity Mapping of $O_2$ Photophysics

Molecular oxygen plays a central role in many research fields including atmospheric physics, combustion analysis, and in fundamental studies of advanced small-molecule quantum mechanics. Over the past few years our group has developed and applied velocity map imaging to investigate several aspects of molecular oxygen photophysics. These include deconvolution of the Herzberg continuum *(5)* (260-180 nm), predissociation *(8)* and direct dissociation *(12)* via the Schumann-Runge bands, and analysis of the processes forming $O^+$ during REMPI through $O_2$ molecular Rydberg states. Figure 5 is a schematic potential energy diagram for the electronic states of $O_2$ relevant to these studies.

In photodissociation studies the two main questions posed are which state(s) are excited at the dissociation wavelength, and which final product states result from this photodissociation. From the potential energy diagrams it can then be ascertained if the dissociation process remains on the initially excited potential energy curve or if curve crossing takes place. Final products are identified by their kinetic energy release and initial states by the product angular distribution under the assumption that optical excitation to mixed states is incoherent and much faster than any nuclear motion. For one-photon dissociation on a repulsive curve the product angular distributions $I(\theta)$ is given by the expression[13]

$$I(\theta) \propto 1+\beta P_2(\cos\theta) \qquad (1)$$

where $\theta$ is the angle between the laser polarization and the velocity vector of the particles and $P_2$ is the second-order Legendre polynomial. The anisotropy parameter $\beta$ ranges from limiting values -1 to 2, corresponding to a perpendicular ($\Pi \leftarrow \Sigma$) and parallel ($\Sigma \leftarrow \Sigma$) transition, respectively. For predissociation when the lifetime $\tau$ of the excited state is similar to the parent molecule rotational period T and the according rotational frequency $\nu=1/T$ of that state; the anisotropy parameter is given by:

$$\beta_{\xi\xi}(\tau) = 2(\nu^2\tau^2+1)/(4\nu^2\tau^2+1) \qquad (2)$$

for a parallel transition, and

$$\beta_{\perp}(\tau) = -(\nu^2\tau^2+1)/(4\nu^2\tau^2+1) \qquad (3)$$

for a perpendicular transition. The limiting values for these anisotropy parameters are $\beta_{\parallel} = 0.5$ and $\beta_{\perp} = -0.25$. Measurement of $\beta$ for each final product channel thus provides information on the symmetry of the electronic states involved in the absorption process and their lifetimes with respect to rotation.

Downloaded by STANFORD UNIV GREEN LIBR on September 21, 2012 | http://pubs.acs.org
Publication Date: October 18, 2000 | doi: 10.1021/bk-2001-0770.ch004

Downloaded by STANFORD UNIV GREEN LIBR on September 21, 2012 | http://pubs.acs.org
Publication Date: October 18, 2000 | doi: 10.1021/bk-2001-0770.ch004

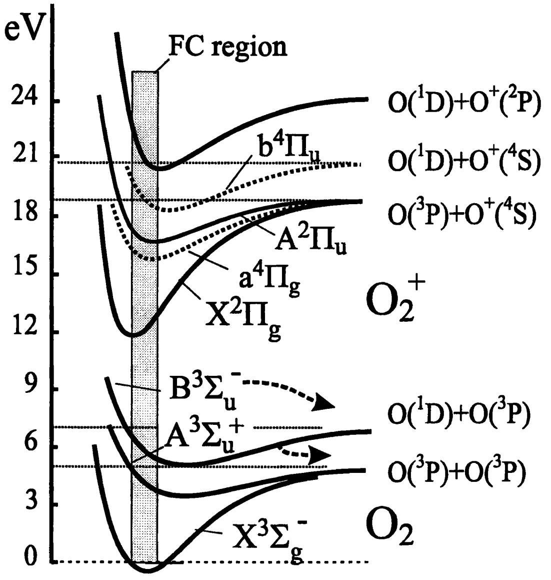

*Figure 5. Schematic potential energy diagram of selected electronic states of $O_2$ and $O_2^+$. Horizontal lines at 5.1, 7.1, 18.7 and 20.7 eV indicates the first and second dissociation limits of $O_2$ and $O_2^+$ respectively.*

## Deconvolution of the Herzberg continuum

Although the absorption cross section of $O_2$ between 240 and 200 nm is extremely small ($< 10^{-23}$ $cm^2$), photodissociation in this region, producing two $O(^3P)$ atoms, is the main source of ozone in the stratosphere. In the past few years much effort has been made to better characterize this absorption process in order to improve the accuracy of atmospheric models. Three optically forbidden electronic states, $A^3\Sigma_u^+$, $A'^3\Delta_u$, and $c^1\Sigma_u^-$, all converging on the first dissociation limit of $O_2$ at 5.1145 eV are responsible for this very weak absorption. The dominant state, $A^3\Sigma_u^-$, is shown in Fig. 5. For wavelengths shorter than 240 nm direct dissociation takes place and the angular distribution of the O atom products is an average of the relative contribution of the three different states at each dissociation wavelength. Because each state is optically forbidden from the $O_2$ $^3\Sigma_g^-$ ground state by the selection rules ($- \rightarrow -$, $\Delta S=0$, $\Delta\Lambda=0,1$) the complicated mixing due to spin-orbit and spin-rotation coupling for each component state with other optically allowed states must first be evaluated theoretically. The relative strength of each J state in the $O(^3P_J)$ manifold is first measured at each dissociation wavelength in order to find the weighted average for the angular distributions. Comparing this result with calculation for the known rotational population distribution in the molecular beam, it is then possible to estimate the relative contributions the Herzberg continuum states for any rotational distribution, thus any height in the atmosphere. Figure 6 shows the results for the deconvolution (*5*).

Downloaded by STANFORD UNIV GREEN LIBR on September 21, 2012 | http://pubs.acs.org
Publication Date: October 18, 2000 | doi: 10.1021/bk-2001-0770.ch004

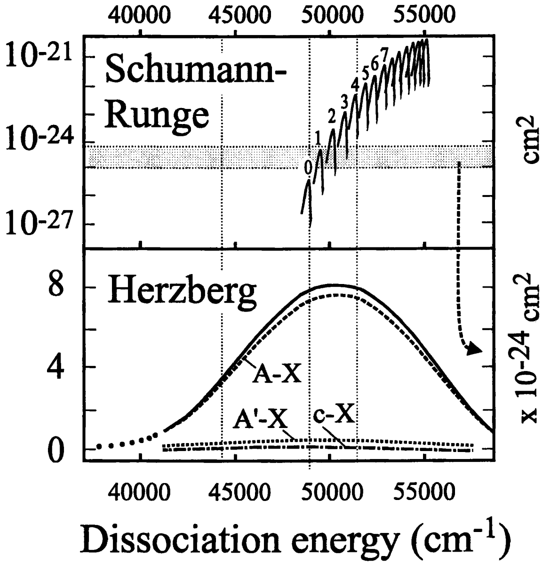

*Figure 6. Absorption spectrum and deconvolution of the Herzberg continuum (5) of $O_2$. The upper panel shows the vibrational components of the Schumann-Runge bands, which begin around 200 nm. In the lower panel the total absorption and separate components of the three Herzberg states are shown. Note the difference in scales for the two panels.*

## Predissociation in the Schumann-Runge bands

Deeper into the UV region, the strong but pre-dissociated bands of the Schumann-Runge system (205 -130 nm) arise from the optically allowed $X^3\Sigma^-_g$ → $B^3\Sigma^-_u$ transition. The Schumann-Runge bands are the dominant photoabsorption system in the Earth's atmosphere. They change over to a continuum below 175 nm, corresponding to the second dissociation limit, $O(^3P)+O(^1D)$, at 7.08 eV. Predissociation of bound levels of the $B^3\Sigma^-_u$ state takes place, resulting in the production of two $O(^3P)$ atoms. Predissoci-ation lifetimes of the $B^3\Sigma_u^-$ excited electronic state can be determined from the angular distribution anisotropy (*8*), these values are compared with previously measured rates from spectroscopic linewidths (*14*). In this study a tunable ArF laser was used to selectively excite a single rotational level in the $B^3\Sigma_u^-$ (v=4) manifold. A velocity map image obtained with the 193 nm dissociation and $O(^3P_2)$ atom product detection is shown in Figure 7a.

The image (7a) shows a series of sharp concentric rings whose velocity are directly calibrated using the known $O(^3P_2)$ atom signals from the detection laser alone, which also produces $O(^3P_2)$ atoms from the photodissociation of $O_2$ via one- and two-photon absorption (*5*). The total kinetic energy release distribution (i.e., twice the atom kinetic energy) extracted from the raw image is shown in Fig. 7b. This is obtained from the Abel inverted raw image by integrating over the full angular distribution. Finally, Figure 7c shows the angular distributions for the one-photon dissociation signal at 1.29 eV when resonant with a Schumann-Runge band, in this case the P(17) band at 51,736 $cm^{-1}$. Fitting to eq. 1 yields $\beta$=0.68 ± 0.05. Correction for a broad-band frequency component present in the laser output yields the experimental $\beta$=0.82±0.05. Previous studies have determined the lifetime-broadened linewidth and rotational constants of the same upper state (*14*). These values when converted to state lifetime $\tau$ and rotational frequency $\nu$ yield from Eq. 2 a value of $\beta$=0.78±0.02 which is in good agreement with the corrected experimental value. Similar agreement is found for the other rotational states of the $B^3\Sigma^-_u$ (v=4) manifold that lie with the tuning curve of the ArF laser. This and other studies have helped to build confidence in extracting quantitative information from velocity mapping angular distributions.

Downloaded by STANFORD UNIV GREEN LIBR on September 21, 2012 | http://pubs.acs.org
Publication Date: October 18, 2000 | doi: 10.1021/bk-2001-0770.ch004

## REMPI / dissociation of $O_2$

Inspection of Fig. 7b shows that $O^+$ production is possible when using the 193 nm excitation laser only. This is the case for $O_2$ throughout the 300-190 nm region when the laser is tuned to two-photon resonances with molecular Rydberg states[11]. One more photon ionizes the molecule to form $O_2^+$ along with a photoelectron in a so-called (2+1) resonance enhanced multi-photon ionization (REMPI) process. REMPI is a standard means for detection $O_2$ molecules, therefore it is important to understand how and why $O^+$ is created. Velocity mapping is very useful in sorting out the $O^+$ production methods in that both the $O^+$ and photoelectron angle-velocity distributions can be measured with equal sensitivity and resolution. Figure 8 illustrates this capability for (2+1) REMPI of $O_2$ at 225 nm, which is in same wavelength region used in the images shown in Figs. 2, 4, and 5.

Inspection of Fig. 5 shows that at least four 225 nm photons are needed to reach the first ionic dissociation limit at 18.733 eV. Analysis of the photoelectron kinetic energy distributions shown in Fig. 8 indicates that the photoionization process yields a very wide range of vibrationally excited X $^2\Pi_g$ $O_2^+$ ions. One-photon dissociation of $O_2^+(v^+)$ occurs for all $v^+$ levels with $v^+>6$, yielding the range of $O^+$ kinetic energies also seen in Fig. 7. Another important processes taking place after three-photon absorption is dissociation to $O(^3P)+O^{**}$, where $O^{**}$ is a highly electronically excited O atom. One more photon immediately ionizes $O^{**}$, producing equal amounts of $O^+$ and photoelectrons (*4*). Data peaks from this process are used to directly scale the photoelectron and $O^+$ curves. From energy balance the sum of the photoelectron and $O^+$ kinetic energy is a constant. The two curves can thus be plotted in reverse, as shown in Fig. 8, so that the signals from each vibrational state underlie each other. Because the curves are already scaled it can also be concluded from the relative heights of the individual $v^+$ peaks that dissociation of each $O_2^+(v^+)$ state is complete.

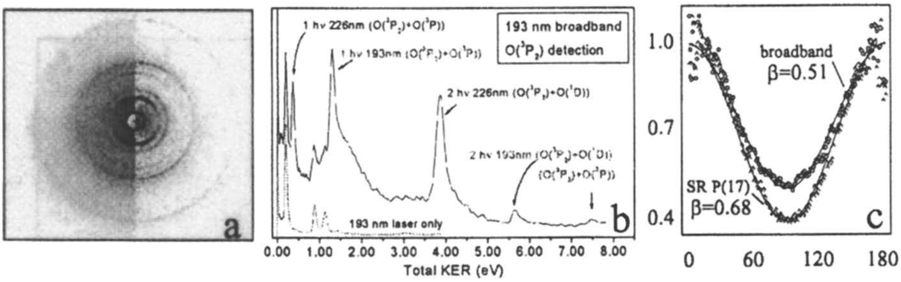

*Figure 7. Predissociation of $O_2$ after excitation of the P(17) line of the (v=4) manifold. Panel a) shows the raw image (left side) and Abel-inverted image (right side) for excitation at 193 nm and detection of $O(^3P_2)$ atoms. Panel b) is a kinetic energy distribution extracted from image. Panel c) shows the angular distributions for both broad-band and narrow-band 193nm light resonant with the P(17) line.*

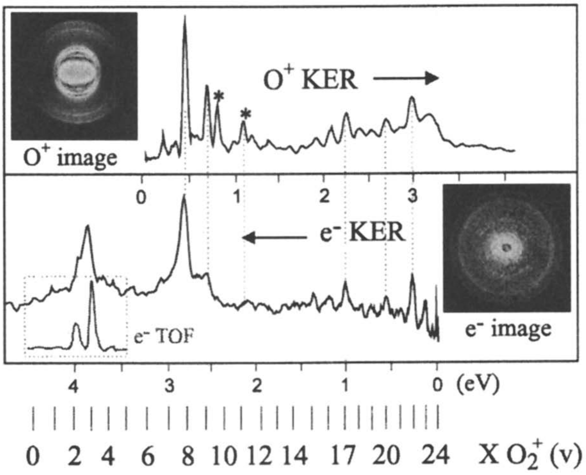

*Figure 8. Kinetic energy distributions of $O^+$ and photoelectrons produced by (2+1) REMPI of $O_2$ at 225 nm. Raw images are shown as inserts. Data from a time-of-flight study for the same processes reported by Park et al (15) is shown below the photoelectron curve.*

Downloaded by STANFORD UNIV GREEN LIBR on September 21, 2012 | http://pubs.acs.org
Publication Date: October 18, 2000 | doi: 10.1021/bk-2001-0770.ch004

Two peaks at 0.75 and 1.1 eV are marked with a (*) in Fig. 8. These arise from formation of $O_2^+(v^+)$ in the electronically excited a $^4\Pi_g$ state. Dissociation of these levels occurs to the second dissociation limit of the ion (see Fig. 5), presumably to the repulsive wall of the bound $b^4\Pi_u$ state via the optically allowed $a^4\Pi_g \rightarrow b^4\Pi_u$ transition. The kinetic energy release for this dissociation is shifted 1.967 eV lower in energy, which is the difference in energy between the first and second dissociation limits.

The data shown in Fig. 8 illustrates the very reasonable kinetic energy resolution of velocity mapping of photoelectrons. Resolution scales with $(KE)^{1/2}$ and at 1 eV the apparatus resolution for this data is ~35 meV. At 4 eV kinetic energy release this becomes 70 meV (560 $cm^{-1}$) which is not sufficient to fully resolve the energy splitting of ~1500 $cm^{-1}$ between the $O_2^+$ $v^+$ =2 and 3 states. Magnetic bottle photoelectron time-of-flight spectrometers offer better resolution at this high kinetic energy release. Plotted below the photoelectron kinetic energy distribution is a time-of-flight (TOF) spectrum for the same process measured by Park et al *(15)*. As seen the TOF resolution in this region is better than velocity mapping, but no data could be presented for lower kinetic energy releases. Velocity mapping measures distance-of-flight instead of time-of-flight and thus velocity instead of reciprocal velocity. Velocity mapping is equally sensitive to all velocities, even the very slowest, and in addition provides the full angular distribution information. With larger detectors and further improvements in the electrostatic lens it can be expected that velocity mapping will also make a major impact in the field of photoelectron spectroscopy.

pacs{82.40.Py, 52.70.Kz, 81.15.Gh}

## Acknowledgements

Financial support from the EU-TMR network program "IMAGINE" - ERB 4061 (PL 97-0264) is gratefully acknowledged. The work in Nijmegen is also supported by the NWO-FOM.

## References

---

[1] Eppink, A. T. J. B.; Parker, D. H. *Rev. Sci. Instr.* **1997,** *68,* 3477.

[2] Eppink, A. T. J. B.; Bakker, B. L. G.; Parker, D. H. *SPIE* **1998,** *Vol. 3271,* 177; Chandler, D. W.; Parker, D. H. In *Advances in Photochemistry* **1999,** *25,* 59

Downloaded by STANFORD UNIV GREEN LIBR on September 21, 2012 | http://pubs.acs.org
Publication Date: October 18, 2000 | doi: 10.1021/bk-2001-0770.ch004

Wiley, New York,; D. H. Parker, In *Photoionization and Photodetachment, Advanced Series in Physical Chemistry,* Vol 10A and 10B. Ng, C., Ed., World Scientific Publishing Co. Ltd. Singapore, 2000.

[3] Chandler, D. W.; Houston, P. L. *J. Chem. Phys.* **1987**, *87*, 1445; Heck, A. J. R.; Chandler, D. W., *Annu. Rev. Phys. Chem.* **1995,** *46*, 335.

[4] Parker, D. H.; Eppink, A. T. J. B. *J. Chem. Phys.* **1997,** *107*, 2357.

[5] Buijsse, B.; van der Zande, W. J.; Eppink, A. T. J. B.; Parker, D. H.; Lewis, B. R.; Gibson, S. T. *J. Chem. Phys.* **1998,** *108,* 7229.

[6] Eppink, A. T. J. B.; Parker, D. H. *J. Chem. Phys.* **1998,** *109*, 4758.

[7] Samartzis, P. C.; Bakker, B. L. G.; Parker, D. H.; Rakitzis, T. P.; Kitsopoulos, T. N. *J. Chem. Phys.* **1999,** *110*, 5201.

[8] Bakker, B.; Parker, D. H. *J. Chem. Phys.* **2000,** *111,* in press

[9] Samartzis, P. C.; Bakker, B. L. G.; Parker, D. H.; Kitsopoulos, T. N. *J. Phys. Chem.* **1999,** *A103*, 6106.

[10] Parker, D. H.; Kitsopolous, T. N. *J. Chin. Chem. Soc.* **1999,** *46*, 513.

[11] Parker, D. H. submitted to *J. Chem. Phys.*

[12] Eppink, A. T. J. B.; Buijsse, B.; Janssen, M. H. M.; van der Zande, W. J.; Parker, D. H. *J. Chem. Phys.* **1998,** *108,* 1305.

[13] Jonah, C. *J. Chem. Phys.* **1971,** *55*, 1915; Zare, R. N. *Mol. Photochem.* **1972,** *4,* 1; Chen K.; Yeung, E. S. *J. Chem. Phys.* **1980,** *72*, 4723.

[14] Lewis, B. R.; Gibson, S. T.; Dooley, P.M. *J. Chem. Phys.* **1994,** *100,* 7012.

[15] Park, H.; Miller, P. J.; Chupka, W. A.; Colson, S. D. *J. Chem. Phys.* **1988**, *89,* 6676.

Downloaded by STANFORD UNIV GREEN LIBR on September 21, 2012 | http://pubs.acs.org
Publication Date: October 18, 2000 | doi: 10.1021/bk-2001-0770.ch004

## Chapter 5

# Image Reconstruction: The Abel Transform

**Benjamin J. Whitaker**

**School of Chemistry, University of Leeds, Leeds LS2 9JT, United Kingdom**

The mathematics underpinning the reconstruction algorithm used in ion imaging experiments is briefly described. The method is illustrated for the simplest case of rapid dissociation in a diatomic molecule but is entirely general. Techniques for removing instrumental blurring are also described. Code for performing velocity reconstruction from ion images is outlined.

## Introduction

The aim of the ion imaging experiment is to obtain the speed and angular distribution of quantum state resolved product species resulting from a photodissociation or scattering process – in short to map the velocity of the products. The subject of this, brief, contribution is to outline the procedure involved in the reconstruction of the velocity distribution from the ion-image; that is a description of the Abel and Hankel transforms. Reconstruction algorithms are necessary because the flux-velocity distribution is three-dimensional but what is actually measured in the experiment is a two-dimensional projection of an ion cloud as it lands on the detector. The questions that naturally arise to anyone encountering ion imaging for the first time is: How does one do this, and does one lose any information in the process?

The easiest way to see how the true velocity distribution can be recovered from an ion image is to consider the case of atomic fragments recoiling from the photodissociation of a diatomic molecule. Here we imagine that the molecule has previously been cooled in a molecular beam expansion so that only one quantum state (v=0, J=0) is present in the beam. After absorption of a photon, conservation of energy and momentum ensure that each fragment travels with a well-defined speed given by the solution to the conservation of momentum and energy equations:

$$m_1\mathbf{v}_1 + m_2\mathbf{v}_2 = 0,$$

$$\frac{(m_1 + m_2)|\mathbf{v}_{\text{rel}}|^2}{2} = h\nu - D_0$$

In Imaging in Chemical Dynamics; Suits, A., et al.;
ACS Symposium Series; American Chemical Society: Washington, DC, 2000.

where $\mathbf{v}_{rel} = \mathbf{v}_1 + \mathbf{v}_2$ is the relative velocity, $D_0$ the bond energy and $h\nu$ the photolysis energy. The fragment atoms will then be found on the surfaces of two expanding spheres centered at the intersection of the laser and molecular beam. For the moment, we imagine this to be a point and leave the investigation of any blurring that might arise due to the fact that both the laser and the molecular beam have a finite width for the time being. At some later time, but before the sphere has grown too large, a second laser, which we have arranged to be loosely focused so that it interacts with all the fragments, is fired. The frequency of the laser is tuned to ionize resonantly only one of the fragments. We can ignore the recoil of the photo-ejected electrons because their momentum transfer to the fragment will be very small, and so we are now left with a sphere of ions expanding at the recoil speed of whichever of the fragments we chose to select. Since we can, in principle, ionize state-selectively any product species by resonantly enhanced multi-photon ionization there is actually no loss of generality by considering atomic fragments.

However, it is well known that the ions are not uniformly distributed over the surface of the sphere because the absorption efficiency of the parent molecule depends on its relative orientation with respect to the polarisation vector of the dissociating light. Specifically, the absorption probability is proportional to the square of the scalar product of the transition dipole moment, $\mu$ of the dissociating molecule, and the electric polarisation vector, $\varepsilon$, of the laser field:

$$I(\vartheta) \propto \langle \mu.\varepsilon \rangle^2$$

If the molecular dissociation is rapid (in comparison to the rotational period of the parent molecule) the angular distribution of the photofragments will be anisotropic. For example, in the case of a diatomic molecule dissociating *via* a parallel transition the angular distribution of the photofragments will be proportional to $\cos^2\vartheta$, where $\vartheta$ is the angle between $\mu$ and $\varepsilon$. Formally, the anisotropy is characterized by(1):

$$I(\vartheta) = \frac{1}{4\pi}[1 + \beta P_2(\cos\vartheta)],$$

where $P_2(\cos\vartheta)$ is the second order Legendre polynomial, $\frac{1}{2}(3\cos^2\vartheta - 1)$. The anisotropy parameter, $\beta$, can vary between 2 and −1, depending on the dissociation timescale but for illustration we will just consider the two limiting cases corresponding the recoil velocity lying parallel or perpendicular to $\mu$ respectively.

## The Abel and Hankel transform

Vertical slices through the 3-D fragment distribution at some arbitrary time after dissociation for these limiting cases ($\beta$ = 2 and −1) are shown in figure 1 (panels a and b). In the figure, the polarisation vector of the dissociating light is aligned vertically. The full 3-D velocity distribution is obtained by rotating the slices around the polarisation axis, and the 2-D ion images that would be observed for these distributions are shown in figures 1c and d respectively. For the more general case of the photodissociation of polyatomic molecule with a finite

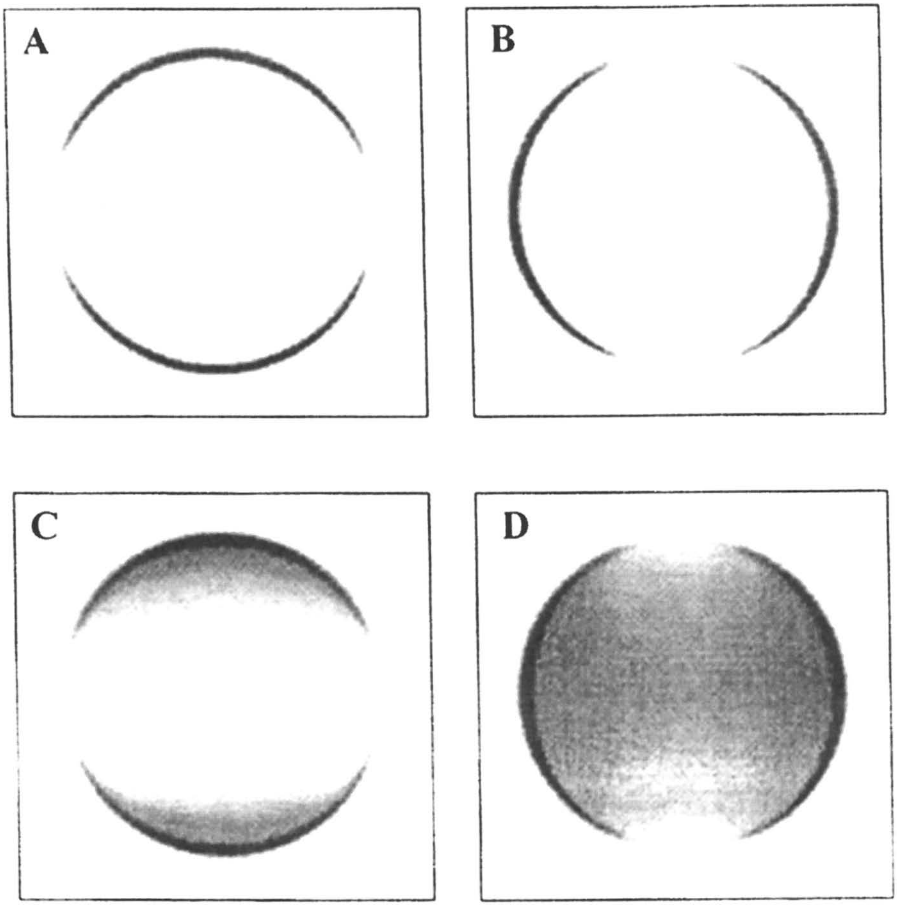

Figure 1. Illustration of the vector correlation between the polarization vector of photolysis light and the recoil direction of an atomic fragment for the cases $\beta = 2$ and $\beta = -1$ (rapid dissociation *via* parallel and perpendicular transitions). Panel A represents a slice through the 3-D velocity distribution for the case $\beta = 2$ and panel B represents the same but for $\beta = -1$. The polarization vector is vertical in both cases. The lower panels represent the corresponding ion-images.

dissociation time the anisotropy will be less pronounced. On the other hand, for a reactive scattering event the products may be almost exclusively forward or backward scattered in the center-of-mass frame. Whatever the case the velocity distribution will have inversion symmetry about a characteristic axis in the image. Note also that even for diatomics in certain circumstances, for example the photolysis of $Br_2$ between 260-580 nm(2), two channels with different anisotropies may be open simultaneously. Because the Br atoms in this case have different speeds, the resultant image is the superposition of two components each looking similar to those depicted in figure 1, panels c and d, but of different diameters. The problem we are faced with is how to recover the velocity distribution, figure 1a or b, from the projected image, (1c or d).

If we write the velocity distribution of the photofragment ions in Cartesian co-ordinates centered on the point of photolysis as $i(x, y, z)$ and take $z$ to be the symmetry axis (*i.e.* the laser polarisation vector), and imagine that the ions are accelerated by the repeller plate and grids in the $y$ direction (as in figure 2), then the measured distribution on the detector is:

$$p(x,z) = \int_{-\infty}^{\infty} i(x,y,z)dy\,.$$

Here we are assuming that the ion optics have been adjusted so that the entire ion cloud arrives within the gate-width of the imaging system. This is achieved by using a quasi Wiley-McLaren(3) arrangement, now usually modified for velocity focusing(4). If we consider just one row of the image, say $f(x; z_0)$, taken along the $x$ axis at some value of $z{=}z_0$, we have:

$$f(x) = \int_{-\infty}^{\infty} s(x,y)dy = 2\int_{0}^{\infty} s(x,y)dy\,, \tag{1.1}$$

where $s(x,y) = i(x,y;z_0)$ is a slice through the 3-D distribution perpendicular to the symmetry axis taken at $z_0$ (as illustrated in figure 2). The function, $s(x,y)$, is obviously cylindrically symmetric and in polar coordinates we can express (1.1) as:

$$f(x) = 2\int_{x}^{\infty} \frac{s(r)r}{\sqrt{r^2 - x^2}}dr \tag{1.2}$$

by a simple change of variables with $r^2 = x^2 + y^2$. This is the Abel transform and it arises frequently in image processing applications when circular symmetry is present(5). The inverse transform can be found by applying the Fourier transform convolution theorem, as described by Bracewell(6), and is given by:

$$s(r) = \frac{1}{\pi}\int_{r}^{\infty} \frac{df\,/\,dx}{\sqrt{x^2 - r^2}}dx\,. \tag{1.3}$$

This can then be used to recover the original distribution, since we now have a prescription for obtaining $s(r; z_0)$ for each row, $f(x; z_0)$, of the projected image.

Solving equation (1.3) is difficult in practice because of the singularity at $r^2 = x^2$, and because the derivative in the integrand tends to magnify noise. The application of the Abel transform, formulated above, also assumes that the input data are symmetric. Of course, because of noise and effects such as mismatch

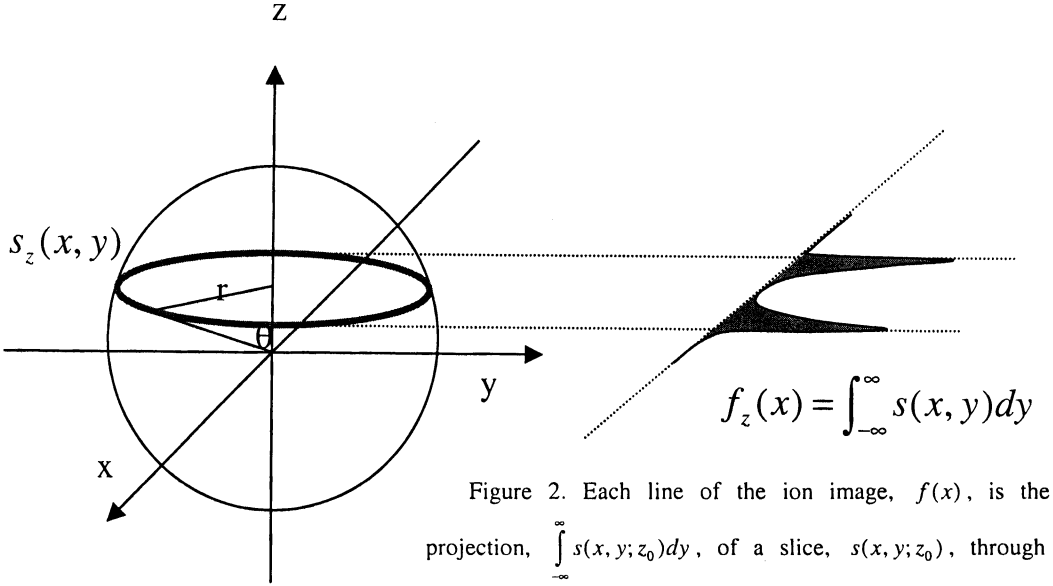

Figure 2. Each line of the ion image, $f(x)$, is the two-dimensional projection, $\int_{-\infty}^{\infty} s(x, y; z_0)dy$, of a slice, $s(x, y; z_0)$, through the cylindrically symmetric three-dimensional velocity distribution. In the figure the symmetry axis lies along $z$, and the ion optics have been arranged so as to project and subsequently focus the ion-cloud onto a detector positioned in the $x,z$ plane. The experiment transforms the ion distribution in the co-ordinates $(r,\vartheta)$ to an image in the co-ordinates $(x,z)$ according to eqn (1.6). The inverse Abel transform or an iterative back-projection method is used to recover the distribution in $(r,\vartheta)$ space from the measured distribution in $(x,z)$ space.

between the ionizing laser bandwidth and the Doppler profile of the fragments, it is frequently the case that real images exhibit some degree of asymmetry. One method of performing the inversion, proposed by Smith and Keefer(7), removes some of these difficulties. It involves taking the Fourier transform of equation (1.1):

$$\mathcal{F}\{f(x)\}=\int_{-\infty}^{\infty}\int_{-\infty}^{\infty} s(\sqrt{x^2+y^2})\exp(-2\pi ixq)dxdy \qquad (1.4)$$

and then noticing that the definition of the zero-order Bessel function of the first kind, $J_0$, is given by:

$$J_0(z)=\frac{1}{2\pi}\int_0^{2\pi}\exp(-iz\cos\vartheta)d\vartheta$$

Changing to polar coordinates and substituting this into equation (1.4) yields:

$$\mathcal{F}\{f(x)\}=2\pi\int_0^{\infty} rs(r)J_0(2\pi rq)dr$$

As noted by Smith and Keefer and by Castleman(8), the right hand side of this equation is the zero-order Hankel transform of *s(r)*. Since the Hankel transform is identical to its inverse, the original distribution *s(r)* can then be recovered by taking the Hankel transform of the Fourier transform of the projected intensity:

$$\begin{aligned}s(r)&=H\left[\mathcal{F}\{f(x)\}\right]\\&=2\pi\int_0^{\infty} qJ_0(2\pi rq)\left[\int_{-\infty}^{\infty} f(x)\exp(-2\pi xq)dx\right]dq\end{aligned} \qquad (1.5)$$

Equation (1.5) has several advantages over the Abel inversion given by (1.3) in that it avoids the difficulty associated with the lower limit of integration and allows one to filter and smooth the data in the Fourier transform step. Computationally, the method used to evaluate equation (1.5) is to apply the Cooley-Tukey fast Fourier transform algorithm(9) on each line of the image and then either to compute the Bessel function convolution by direct summation, or more efficiently, to sum selected Fourier components of the integrand according to an algorithm first given by Candel(10). On a modern personal computer, this is straightforward. Computer code is given in the Appendix which may easily be adapted to most image formats. It is worth noting that if $f(x)$ is an error-free projection of a real and cylindrically symmetric object centered at $x$=0, as originally assumed, it follows that $\mathcal{F}\{f(x)\}$, its Fourier transform, is also a real and even function. This property can be used to check that each line of the image is correctly centered on the symmetry axis, or to correct for any slight skewing in the input image. In the code given in the Appendix this is done by shifting each scan line of the image so as to minimize the imaginary component in $\mathcal{F}\{f(x)\}$. Although the Hankel transform formulation of the image reconstruction algorithm reduces the problems associated with noise in the image it does not completely eliminate them. In particular, because the Bessel function oscillates rapidly close to the origin, noise is magnified along the centerline of the reconstructed velocity distribution.

An alternative strategy(11, 12) is to use a back-projection approach. Here one considers explicitly the Jacobian of the co-ordinate transformation from the velocity distribution space, $(r,\vartheta)$, to that of the image plane, $(x,z)$. In general this is a very complicated function but in the case where, $\rho$, the ratio of the electrostatic energy acquired by the ions in the acceleration region of the mass-spectrometer compared to their initial kinetic energy, is large one can obtain a relatively straightforward analytical expression:

$$f(\rho,x,z)=s(\rho,\vartheta)\frac{\rho}{4\sin\vartheta\sqrt{1-x/x_0}}. \tag{1.6}$$

Here $x_0$ is the maximum value of $x$ that the ions can reach for a given $\rho$ and $\vartheta=\arccos\left(\frac{\sqrt{\rho}z}{2L}\right)$, where $L$ is the distance from the scattering center to the center of the detector. One can then use (1.6) and an iterative procedure to recover $s(\rho,\vartheta)$ from the measured distribution on the detector. For continuous distributions eqn. (1.6) is exact (within the assumption of large $\rho$), however, pixelation of the data introduces some approximations into the inversion. The basic idea is to start with the most energetic particle in the image. This will be found at the outer edge of the recorded image along the line $x=0,z$. One can then deduce, from (1.6), the contribution that particles with this energy will make to the rest of the image and subtract this from the image. Iteratively processing the residual image in this manner one can "peel" the original velocity distribution, ring-by-ring, from the ion image. The back-projection method overcomes the centerline noise problem experienced with the Hankel transform inversion method but can introduce distortion into the recovered velocity distribution if the kinetic energy release is too large.

## Instrument functions and noise

The problems associated with input noise and an additional problem connected with image blurring have been addressed by Strickland and Chandler(13). In the ideal photofragment imaging experiment the fragments come from a point source. This is not achievable in practice since the lasers and molecular beam overlap in a finite volume. To a degree this problem has been overcome through the introduction of the velocity map imaging(4) since now the ion optics are adjusted so that fragments created at different positions across the molecular beam but with the same velocity are imaged onto the same position on to the detector. Furthermore, advances in the image acquisition system, real-time ion counting(14), (15), have significantly improved image fidelity. Nonetheless, because of electrostatic lens aberrations, there may remain some intrinsic blurring, and experimental images are never entirely noise free! This means that the observed distribution of photo-ions, $i(x,y,z)$, is that that would have been formed in a perfect experiment, $o(x,y,z)$ convoluted with some detection function, $h(x,y,z)$. The function, $h$, takes into account the molecular number density and laser power profiles across the interaction volume, and can be called the overlap volume function. Thus:

$$i=o***h$$

where $***$ denotes the three-dimensional convolution.

In the experiment described above the lasers, which are moderately focussed, cross the molecular beam at right angles, so that *h* is approximately a thin cylinder across the molecular beam, as depicted in figure 3. The function *h* can usually be obtained from experiment by ionising and imaging a stable species, such as NO expanded in He, in the molecular beam. In this case there is no recoil velocity and the image formed will be the smallest obtainable.

The size of the overlap volume function in the direction across the lasers can usually be neglected. This is because the laser beam waist in the interaction volume is often much smaller than the molecular beam width. Usually the probe (REMPI) beam is focussed more tightly and thus defines the size of the overlap function. Typical diameters might be 10-100 µm. Since this value is so much less than the molecular beam width (~1-2 mm) we can neglect the effect of *h* in any direction perpendicular to the laser beam propagation direction (*y*, or *z*). So *h* becomes:

$$h(x,y,z) = h'(x)\delta y \delta z$$

and the observed photo-ion distribution is given by the 1-D convolution:

$$i(x,y,z) = o(x,y,z) * h'(x)$$

where $h'(x)$ is called the point spread function (PSF).

Strickland and Chandler(13) have used a technique based on a method introduced by Jansson(16) to deconvolve spectroscopic data. The method is a constrained version of the reblur method of Kawata and Ichioka(17). Each scan line of the observed image can be represented as:

$$i(x;z) = o(x;z) * h'(x;z) + n(x;z)$$

where $o(x)$, $h'(x)$, and $n(x)$ represent lines across the original image, point spread function, and noise function respectively. The algorithm presented by Strickland and Chandler gives an estimate of $o(x)$, indicated as $\hat{o}$. After $k+1$ iterations

$$\hat{o}^{(k+1)} = P\left[\hat{o}^{(k)}\right] + r\left[\hat{o}^{(k)}\right]\left\{i * h' - P\left[\hat{o}^{(k)}\right] * h' * h'\right\} \qquad (1.7)$$

Here the function *r* controls the rate of convergence and *P* is the positivity operator:

$$P\left[\hat{o}^{(k)}\right] = \begin{cases} \hat{o}^{(k)} & \text{if } \hat{o}^{(k)} \geq 0 \\ 0 & \text{otherwise} \end{cases}$$

The iterative procedure is started by setting

$$\hat{o}^{(0)} = i * h'$$

Because the point spread function, $h'$, acts as a low pass filter the deblurring algorithm also has the advantage that it significantly reduces the noise in the reconstructed images. However, these techniques should be used with care because an inappropriate choice of the relaxation function, *r*, can create ringing artifacts in the restored velocity distribution. Strickland and Chandler found that the function(16):

$$r\left[\hat{o}^{(k)}\right] = 2\left[1 - 2\left|\hat{o}^{(k)} - 0.5\right|\right]$$

gave the most reliable results.

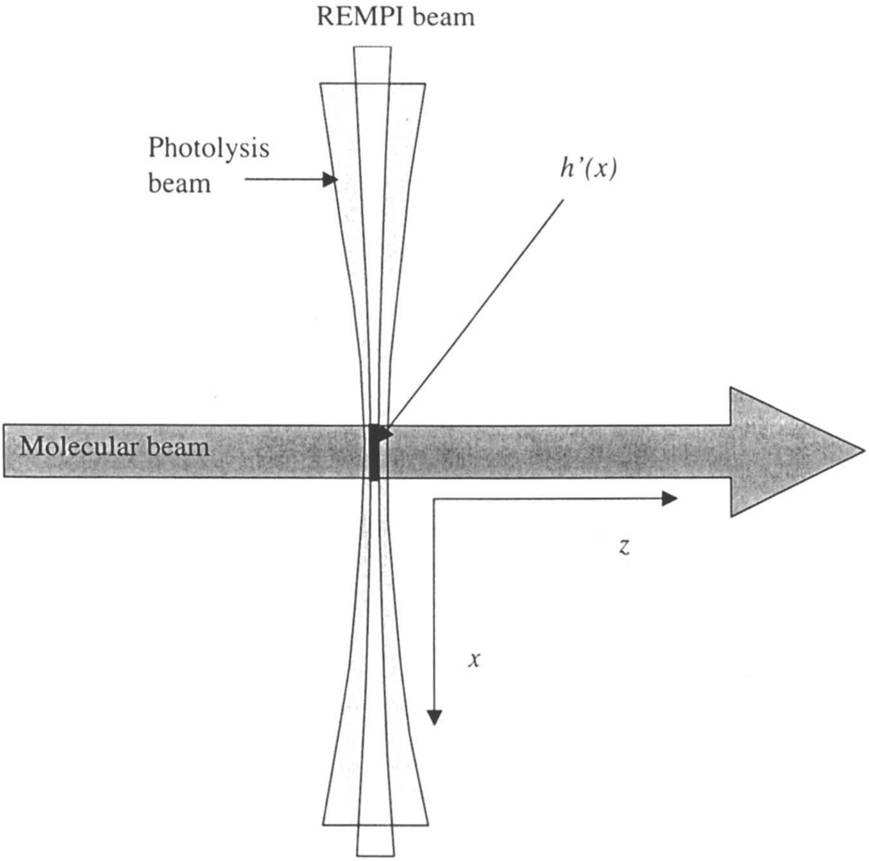

Figure 3. Illustration of the overlap function, *h(x,y,z)*, for the typical case where the ionizing laser beam is more tightly focused than the photolysis laser beam. The overlap function can then be approximated as a function of x only. Velocity map imaging effectively eliminates the effects of the overlap function since ions created at different points across the molecular beam but having the same velocity are imaged at the same point on the detector.

## Conclusions

This contribution has given a brief overview of the mathematics underpinning the recovery of velocity distributions from ion images. There is much more that could have been said but the interested reader should be able to find all they need to know by consulting the original literature. In closing, it is worthwhile to give one warning. It is common practice to symmeterize ion images prior to inversion (that is to fold the image top-to-bottom, left-to-right) with the justification that data must be symmetric so that what one is doing is merely averaging. This is a dangerous and can lead to loss of important dynamical information. For example, experimental images frequently show slight top-bottom asymmetry because of the Doppler effect, *i.e.* fragments moving towards the ionizing laser are ionized with a different efficiency from those moving away. If the anisotropy parameter is a function of the recoil speed this information will be lost by folding the image.

## References

1. Zare, R. N. 1988. *Angular momentum: Understanding spatial aspects in chemistry and physics*: John Wiley
2. Cooper, M. J., Wrede, E., OrrEwing, A., J., Ashfold, M. N. R. 1998. *J. Chem. Soc. Faraday Trans.* 94: 2901
3. Wiley, W. C., McLaren, I. H. 1955. *Rev. Sci. Instrum.* 26: 1150
4. Eppink, A. T. J. B., Parker, D. H. 1997. *Rev. Sci. Instrum.* 68: 3477
5. Dasch, C. R. 1992. *App. Opt.* 31: 1146
6. Bracewell, R. N. 1978. *The Fourier transform and its applications*: McGraw-Hill
7. Smith, L. M., Keefer, D. R. 1988. *J. Quant. Spectrosc. Radiat. Transfer.* 39: 367
8. Castleman, W. 1979. *Digital image processing*: Prentice-Hall
9. Press, W. H., Flannery, B. P., Teukolsky, S. A., Vetterling, W. T. 1988. *Numerical recipes in C*: Cambridge University Press
10. Candel, S. M. 1981. *Comput. Phys. Comm.* 23: 343
11. Bordas, C., Paulig, F., Helm, H., Huestis, D. L. 1996. *Rev. Sci. Inst.* 67: 2257
12. Winterhalter, J., Maier, D., Hornerkamp, J., Schyja, V., Helm, H. 1999. *J. Chem. Phys.* 110: 11187
13. Strickland, R. N., Chandler, D. W. 1991. *Appl. Optics.* 30: 1811
14. Chang, B. Y., Hoetzlein, R. C., Mueller, J. A., Geiser, J. D., Houston, P. L. 1998. *Rev. Sci. Inst.* 69: 1665
15. Cooper, M. J., Jackson, P. J., Rogers, L. J., OrrEwing, A. J., Ashfold, M. N. R., Whitaker, B. J. 1998. *J. Chem. Phys,.* 109: 4367
16. Jansson, P. A. 1987. *Deconvolution with applications in spectroscopy*: Academic Press
17. Katawa, S., Ichioka, Y. 1980. *J. Opt. Soc. Am.* 70: 768

# APPENDIX

The following C code makes use of the Numerical Recipes(9) function library and is designed to run under most variants of UNIX or MSDOS (using the –DMSDOS compile flag). The driving function main() takes a number of command line options as described in the function help(). After allocating temporary working space it then reads each line of the image, which in this implementation is assumed to consist of 512×512 8 bit pixels, but which can easily be modified for other formats. Each horizontal line, scan_line[], of the image is processed in turn according to the prescription given in (1.5), by first calculating the fast Fourier transform (FFT) of each line and then calling the function hankel(). If desired the function hankel() can be replaced the more efficient algorithm given by Candel(10), however on a modern PC this is hardly necessary. Because the each scan line of the image should be symmetric about the center line it is possible with the automatic centering option (-a in the command line) to attempt to compensate for a slight skewing of the image by checking that the imaginary part of the FFT of scan_line[] is close to zero. If it is not the line is shifted by one pixel and the FFT is recalculated in an iterative manner. This option should be used with care and every effort should be made to preprocess the image so as to center and de-skew it prior to using this code.

```
/*
**++
**
**  ABSTRACT:
**
**      Compute transformation from momentum to position space of a 2D image
**      using a Hankel transform. The program makes use of the Numerical
**      recipes function library
**
**  AUTHORS:
**
**      © Ben Whitaker
**      1991
*/

/*
**
**  INCLUDE FILES
**
*/

#include <stdio.h>
#include <math.h>
#ifdef MSDOS
#include <sys\types.h>
#include <sys\stat.h>
#else
#include <sys/types.h>
#include <sys/stat.h>
#endif

/*
**
**  MACRO DEFINITIONS
**
*/
```

```
#define PI 3.14159265358979                         /* or 4.0*atan(1.0) */
#define MAX_SIZE 512

main(argc,argv)
int argc;
char *argv[];
{
       unsigned char pixel;
       char buffer[80],file_in[80],file_out[80],*s;
       int i,j,k,m,n,c,centre,verbose,icount,iauto,iblank;
       float *scan_line,*f,*Re,*Im,*copy_line;      /* pointers to vectors */
       float *vector(),**matrix();                  /* functions returning floats */
       float max,Nyquist,S_Re,S_Im,tmp;
       void free_vector(),free_matrix(),realft(),hankel(),moan(),help();
       FILE *ifp,*ofp,*tfp;
       float **space;
       struct stat f_buf;

       verbose=0;                                   /* set verbosity false */
       centre=0;                                    /* set image centre offset */
       iauto=0;                                     /* switch off auto centre */
       iblank=0;                                    /* switch off blanking option */
       while(--argc>0 && (*++argv)[0]=='-')         /* parse the command line */
              for(s=argv[0]+1;*s!='\0';s++)
                      switch (*s) {
                      case 'v' :                    /* verbose output */
                             verbose=1;             /* set flag */
                             break;
                      case 'h' :                    /* help*/
                             help();
                             break;
                      case 'c' :                    /* fix image centre */
                             s++;
                             for( ; *s>='0' && *s<='9' ; s++) {
                                     centre = 10 * centre + (*s) - '0';
                             }
                             s--;
```

```
                                break;
                        case 'a' :                      /* automatically try to centre image */
                                iauto=1;
                                break;
                        case 'b' :      /* blank out centre line to make things look better */
                                iblank=1;
                                break;
                        default :
                                sprintf(buffer,"hankel: illegal option %c",*s);
                                moan(buffer," ");
                                break;
                        }
        if(argc!=1) {                                   /* should have 2 args left */
                fprintf(stderr,"Usage: hankel [-abc#hv] file\n");
                exit(0);                                /* we don't - so exit politely */
        }

        sprintf(file_in,"%s",*argv);
        if((ifp=fopen(*argv,"rb"))==NULL)
                moan("\nread error on file: ",*argv);
        if((i=stat(*argv,&f_buf)!=0))
                moan("\nread error on file: ",*argv);
        sprintf(file_out,"%s.hkl",*argv);
        if((ofp=fopen(file_out,"wb"))==NULL)
                moan("\nwrite error on file: ",file_out);
#ifdef MSDOS
        if((tfp=fopen("hankel.tmp","w+"))==NULL)
                moan("\nwrite error on file: ","hankel.tmp");
#endif
        n=(int) (sqrt( (double) f_buf.st_size));
        Nyquist=2.0*PI/((float) n);
        if(centre==0)                           /* if -c option not used make a guess */
                centre=n/2;
        if(verbose) {
                fprintf(stderr,"\nread from file: %s",file_in);
                fprintf(stderr,"\nwrite to file: %s",file_out);
                fprintf(stderr,"\npicture size: %d * %d",n,n);
                fprintf(stderr,"\ncentre pixel: %d",centre);
                fprintf(stderr,"\nNyquist frequency: %4.2f",Nyquist);
                if(iauto)
                        fprintf(stderr,"\nautomatic centre image:");
        }

        scan_line=vector(1,n);                /* create some space */
        f=vector(1,n/2);
        Re=vector(1,n/2);
        Im=vector(1,n/2);
#ifndef MSDOS
        space=matrix(1,n,1,n);
#endif
        max=0.0;
        centre = -centre;
        c=centre;
        if(verbose) {
                fprintf(stderr,"\nworking on line: ");
                        for(k=1;k<=47;k++)
                                fprintf(stderr," ");
        }
        for (i=1;i<=n;i++) {                          /* for each row of the picture */
                for (j=1;j<=n;j++) {                  /* stuff each element into scan_line[] */
                        fscanf(ifp,"%c",&pixel);
                        scan_line[j]=(int) pixel;
                }
                realft(scan_line,n/2,1);              /* FFT the data - on exit the array
                                                       * scan_line[1..n] contains the complex
                                                       * discrete FT, with the real part
                                                       * in elements scan_line[2j-1] ; j=1..n/2
                                                       */
                /* now we have to apply the transform theorem
                 *
                 *      g(t-t_0) = G(f)*exp(-i2PIft_0)
                 *
                 */
                icount=0;
                centre=c;
label:
```

```
            if(verbose) {
                    for(k=1;k<=47;k++)
                            fprintf(stderr,"\b");
                    fprintf(stderr,"%4d",i);
            }
            S_Re=0.0;
            S_Im=0.0;

            for (j=1;j<=n/2;j++) {
                    Re[j]= -(scan_line[2*j-1]*(float)cos((double) Nyquist*j*centre) +
                        scan_line[2*j]*(float)sin((double) Nyquist*j*centre));          /* strip out real part */
                    Im[j]= -(scan_line[2*j]*(float)cos((double) Nyquist*j*centre) -
                        scan_line[2*j-1]*(float)sin((double) Nyquist*j*centre));
                                   /* strip out the imaginary part */
                    S_Re+=Re[j];
                    S_Im+=Im[j];
            }                      /* if you did it right Im[j] = 0.0 for all j */
            if(verbose)
                    fprintf(stderr," Re: %10.2f Im: %10.2f centre: %4d",S_Re,S_Im,centre);
            if(S_Im>20.0 && icount<25 && iauto==1) {
                    centre++;
                    icount++;
                    goto label;    /* it's hard to unlearn FORTRAN sometimes */
            }
            if(S_Im<-20.0 && icount<25 && iauto==1) {
                    centre--;
                    icount++;
                    goto label;    /* not again! - who writes this stuff(Ed.) */
            }
            hankel(f,Re,n/2);      /* do the hankel transform on Re[1..n/2]
                                    * and return f[1..n/2] */
            for(j=1 ; j<= n/2 ; j++) {
                    tmp = (f[j] > 0.0) ? 2.0*PI*f[j] : 0.0 ;
#ifndef MSDOS
                    space[i][j]=tmp;
#else
                    fprintf(tfp,"\n%5.1f",tmp);
#endif
```

```
                        if ( tmp > max )
                                max = tmp;
                }

        }

#ifdef MSDOS
        rewind(tfp);
        fscanf(tfp,"\n"); /* line eater */
        for(i=1;i<=n;i++) {
                for(j=1;j<=n/2;j++) {
                        fscanf(tfp,"%f",&tmp);
                        scan_line[j+n/2]=255.0*tmp/max;
                        scan_line[n/2-j]=255.0*tmp/max;
                }
                for(j=1;j<=n;j++) {
                        m = (int) (scan_line[j]);
                        fprintf(ofp,"%c",(char) m);
                }
        }
#else
        for(i=1;i<=n;i++) {
                for(j=1;j<=n/2;j++) {
                        scan_line[j+n/2]=255.0*space[i][j]/max;
                        scan_line[n/2-j]=255.0*space[i][j]/max;
                }
                if(iblank==1) {
                        scan_line[n/2]=0.0;
                }
                for(j=1;j<=n;j++) {
                        m = (int) (scan_line[j]);
                        fprintf(ofp,"%c",(char) m);
                }
        }
#endif
        free_vector(f,1,n/2);        /* clear up the mess we've made */
        free_vector(scan_line,1,n);
        free_vector(Re,1,n/2);
        free_vector(Im,1,n);
#ifndef MSDOS
        free_matrix(space,1,n,1,n);
#else
        remove("h:\hankel.tmp");
#endif
}

/* hankel() performs a hankel transform on a function F given at n points and
 * returns the result as f evaluated at n points. The transformation is
 * evaluated by straightforward addition and is therefore somewhat SLOW. If desired
 * this function can be replaced by one working according to Candel's algorithm
 * [Candel, Comput. Phys. Comm. 23 (1981) 343]
 */
void hankel(f,F,n)
float *f;                            /* f[1..n] is output function */
float *F;                            /* F[1..n] is input function */
int n;                               /* n is number of points */
{
        int i,j;
        float r,q,Nyquist,bessj0();

        Nyquist=1.0/(2.0*n);         /* Nyquist frequency / n */
        for (i=1;i<=n;i++) {
                f[i]=0.0;
                for (j=1;j<=n;j++) {
                        q=Nyquist*(j-1);/* q will run fom zero to Nyquist */
                        r=(float)(i-1);
                        f[i] += q*F[j]*bessj0(2.0*PI*q*r);
                }
        }
}


void moan(s,t)                       /* complain about something */
char *s;
char *t;
{
        fprintf(stderr,"%s%s\n",s,t);
        exit(1);
}

void help()                          /* print a helpful message to stderr */
{
        fprintf(stderr,"Usage: hankel [-a -b -c# -h -v] file\n");
        fprintf(stderr,"       options:\n");
        fprintf(stderr,"              a - auto centre\n");
        fprintf(stderr,"              b - blank centre pixels after transform\n");
        fprintf(stderr,"              c - centre offset, followed by number\n");
        fprintf(stderr,"              h - print this message\n");
        fprintf(stderr,"              v - verbose mode\n");
        fprintf(stderr,"       input  : file name including path of EPIX image\n");
        fprintf(stderr,"       \n");
        fprintf(stderr,"       The output file containing the hankel transform\n");
        fprintf(stderr,"       is sent to the stream file.hkl\n");
        exit(0);
}
```

## Chapter 6

# Photofragment Imaging Studies of Aligned Molecules

**Robert J. Gordon[1], Langchi Zhu[1], Sujatha Unny[1], Yan Du[1], Kaspars Truhins[1], Akihiro Sugita[2], Michio Mashino[2], Masahiro Kawasaki[2], and Yutaka Matsumi[3]**

**[1]Department of Chemistry (m/c 111), University of Illinois at Chicago, 845 West Taylor Street, Chicago, IL 60607–7061**
**[2]Department of Molecular Engineering, Kyoto University, Kyoto 606–8501, Japan**
**[3]Solar Terrestrial Environment Laboratory, Nagoya University, Toyokawa 442–8505, Japan**

Velocity map imaging was used to study the photodissociation of iodobenzene and methyl iodide. Single photon excitation at 266 and 304 nm produced a ringed image of the iodine fragment that is indicative of partitioning of the available energy between internal and translational degrees of freedom. Multiphoton excitation at 532 nm produced a continuous hourglass-shaped image peaked at zero velocity. In a two-color study, a 1064 nm laser aligned the parent $CH_3I$ molecule, and a 304 nm laser dissociated the molecule and ionized the iodine fragment. In this case, the anisotropy parameter was observed to increase monotonically with the intensity of the aligning laser.

## Introduction

Gas phase molecules may be aligned by the electric vector of an electromagnetic field by a variety of mechanisms. In weak fields, alignment arises from the fact that the probability of absorbing a photon is proportional to $|\boldsymbol{\mu}\cdot\mathscr{E}|^2$, where $\boldsymbol{\mu}$ is the transition dipole matrix element and $\mathscr{E}$ is the electric vector of the field (1-3). If the molecule dissociates promptly and the fragments recoil axially, the differential cross section is

In Imaging in Chemical Dynamics; Suits, A., et al.;
ACS Symposium Series; American Chemical Society: Washington, DC, 2000.

given by the familiar expression $I(\theta_r) = 1 + \beta_2 P_2(\cos\theta_r)$, where $\theta_r$ is the angle between the recoil vector and $\mathscr{E}$ in the laboratory frame, and $P_2$ is the second Legendre polynomial (1). The anisotropy parameter $\beta_2$ is equal to $2\langle P_2(\cos\theta_m)\rangle$, where $\theta_m$ is the angle between $\mu$ and the bond axis in the molecular frame, and the brackets denote an average over $\theta_m$. More generally, for an n-photon transition the laboratory distribution of photofragments is given by (4)

$$I(\theta_r) = 1 + \sum_{i=1}^{n} \beta_{2i} P_{2i}(\cos\theta_r). \quad (1)$$

We describe this mechanism of alignment as *passive* because the field simply selects out those molecules that happen to have their transition dipole moments aligned along the electric vector of the field.

In more intense fields (typically $10^{10}$ to $10^{12}$ W/cm$^2$) a qualitatively different alignment mechanism becomes possible (5),(6). The potential energy of a molecule with polarizability tensor $\alpha$ is given by

$$V(\theta,\phi) = -\tfrac{1}{2}\mathscr{E}^2(\alpha_{xx}\sin^2\theta\cos^2\phi + \alpha_{yy}\sin^2\theta\sin^2\phi + \alpha_{zz}\cos^2\theta), \quad (2)$$

where x, y, and z are the principle axes of $\alpha$, $\theta$ is the angle between the z-axis and $\mathscr{E}$, and $\phi$ is the angle of rotation of the molecule about the z-axis. The potential function can be rewritten as

$$V(\theta,\phi) = -\tfrac{1}{2}\mathscr{E}^2[\alpha + \tfrac{1}{2}\eta\sin^2\theta\cos2\phi + \tfrac{1}{2}\Delta\alpha(3\cos^2\theta - 1)], \quad (3)$$

where $\alpha = \tfrac{1}{3}(\alpha_{xx} + \alpha_{yy} + \alpha_{zz})$, $\eta = \alpha_{xx} - \alpha_{yy}$, and $\Delta\alpha = \alpha_{zz} - \alpha$. For a symmetric top or linear molecule, $\eta=0$ and V is a function only of $\theta$. If the depth of the potential energy well is comparable to or greater than the rotational energy, the molecule experiences a torque that aligns it along the electric vector. We refer to this process as *active* alignment because the molecule is physically moved by the electric field.

For active alignment to be observable, the field must be strong enough to align the molecule yet weak enough not to dissociate or ionize it before alignment occurs. This effect was demonstrated by Stapelfeldt and coworkers (7),(8), who used the fundamental of the Nd:YAG laser (1064 nm), with a pulse duration of 3.5 ns and a typical intensity of $10^{12}$ W/cm$^2$. At intensities above the ionization threshold the mechanism once again becomes passive because the probability of ionization depends on the alignment of the molecule with respect to the electric field (9).

In the present paper we present examples of different types of alignment mechanisms in both weak and strong laser fields. We start with weak field, single-photon dissociation of iodobenzene, which displays both direct and predissociative decay. In more intense fields we observe an unusual multiphoton effect. Finally, in a two-color experiment we use a strong infrared laser to align methyl iodide and a weak ultraviolet laser to probe the aligned molecule.

## Experimental Methods

Experiments were performed in laboratories in Chicago and Kyoto using similar apparatuses. A molecular beam of either iodobenzene or methyl iodide was injected by a pulsed nozzle into a differentially pumped vacuum chamber. In most experiments the molecule of interest was entrained in 1 atm of either He or Ar. The molecular beam was irradiated with a harmonic of a Nd:YAG laser and/or a tunable dye laser. The pulse duration was 10 ns in the Chicago experiments and 5 ns in the Kyoto experiments; linear polarization was used throughout. In the single color experiments, the laser, which served both to photodissociate the parent molecule and to photoionize the iodine atom fragment, was focused onto the molecular beam with a 20 cm focal length lens. In the two color experiments (Kyoto), the 1064 nm fundamental of the Nd:YAG laser was used to align the parent molecule, and the counter-propagating 304.67 nm Nd:YAG-pumped dye laser was used to photodissociate the molecule and to detect the $I(^3P_{3/2})$ fragment by 2+1 resonance-enhanced multiphoton ionization (REMPI).

The iodine atoms produced in these experiments were detected by the method of velocity mapping imaging (10). Briefly, the laser(s) and molecular beams intersected at a right angle between a repeller and an extractor electrode. Iodine ions were focused onto a microchannel plate (MCP) mounted at the end of a 70 cm (Chicago) or 55 cm (Kyoto) long flight tube. Electrons ejected from the MCP produced an image on a phosphor screen, which was recorded by a CCD camera and accumulated on a computer. The mass of interest was gated by pulsing the voltage of the front plate of the MCP. The experimentally observed 2D images were back-projected to produce a slice of the 3D image by a method similar to that used in computerized tomography (11). The kinetic energy of the recoiling fragments was calibrated against the known recoil energy of $I(^2P_{3/2})$ obtained by photodissociating either $I_2$ at 532 nm (Chicago) or $CH_3I$ at 304.67 nm (Kyoto).

## Results

Single color, one-photon photodissociation studies of iodobenzene were performed at 304.67 and 304.02 nm, using a tunable dye laser, and at 266 nm, using the fourth harmonic of the Nd:YAG laser. Velocity map images of the product iodine atom are displayed in Figures 1-3. The ringed structures are indicative of parallel transitions ($\beta_2$>0) followed by dissociation that is rapid enough to preserve the spatial anisotropy. The 304.67 and 304.02 nm images are of $I(^2P_{3/2})$ and $I(^2P_{1/2})$, respectively, whereas the 266 nm measurement is not resonant with either spin-orbit state of iodine and may contain contributions from both. State specific measurements with a dye laser tuned near 266 nm are in progress. The relative translational energy distributions at 304.67, 304.02, and 266 nm are plotted in Figures 4a, 4b, and 5a, respectively.

Qualitatively different behavior was observed in the one-color multiphoton experiments. Extensive studies were preformed at 532 nm, using the second harmonic

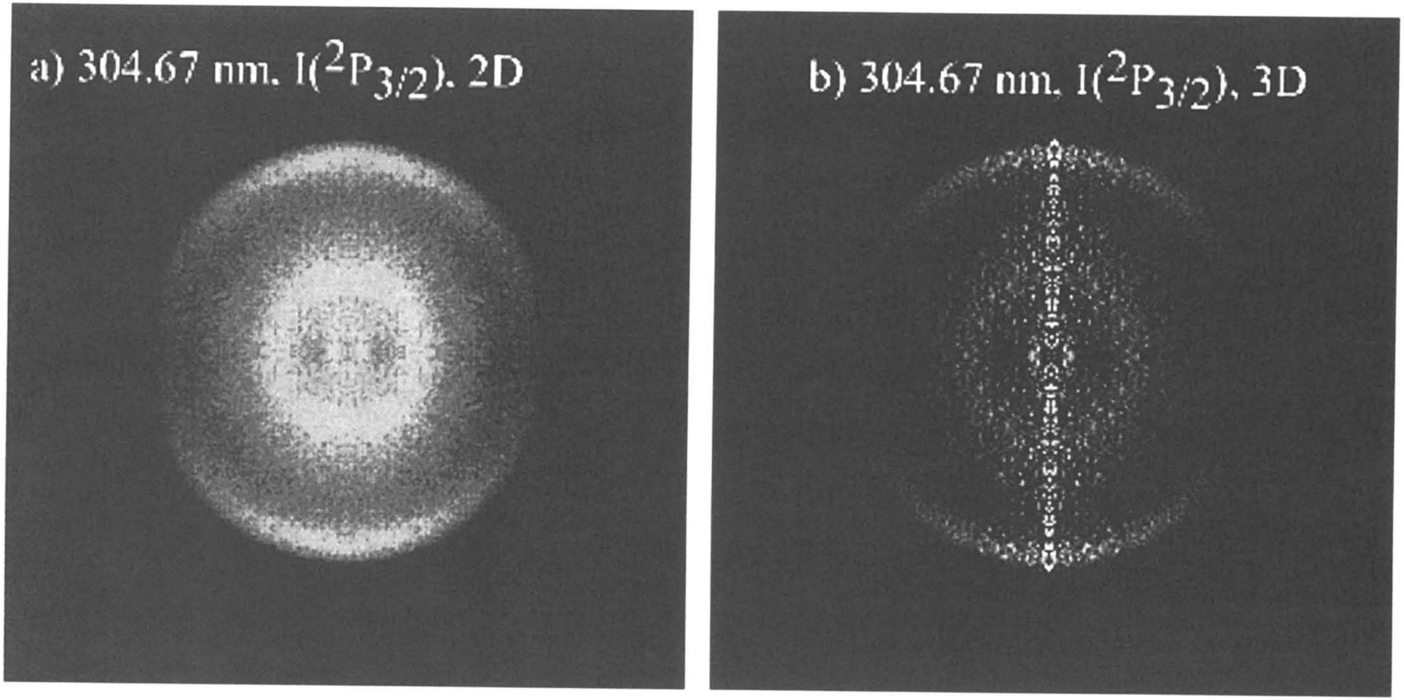

*Figure 1. Image of I($^2P_{3/2}$) produced by photodissociating iodobenzene at 304.67 nm. (a) 2D image. (b) Back-projected 3D image. In these and all subsequent images the laser polarization is vertical.*

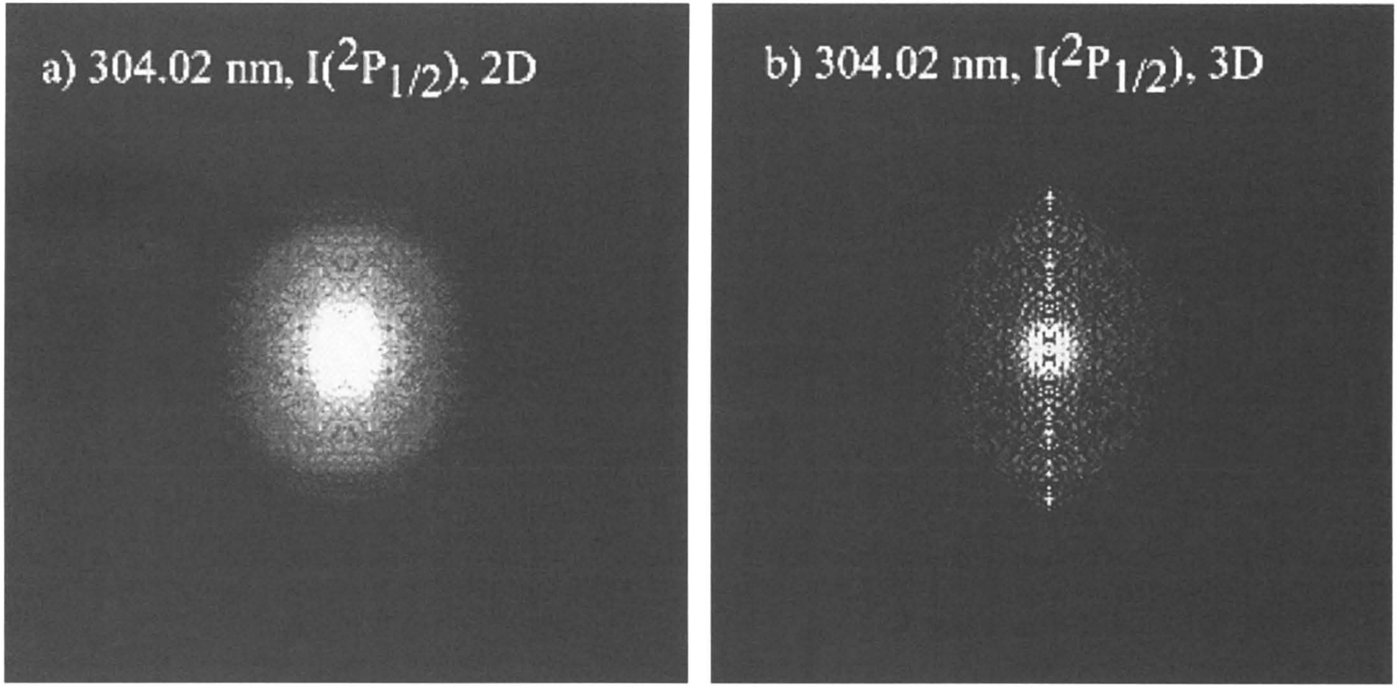

*Figure 2. Image of I($^2P_{1/2}$) produced by photodissociating iodobenzene at 304.02 nm. (a) 2D image. (b) Back-projected 3D image.*

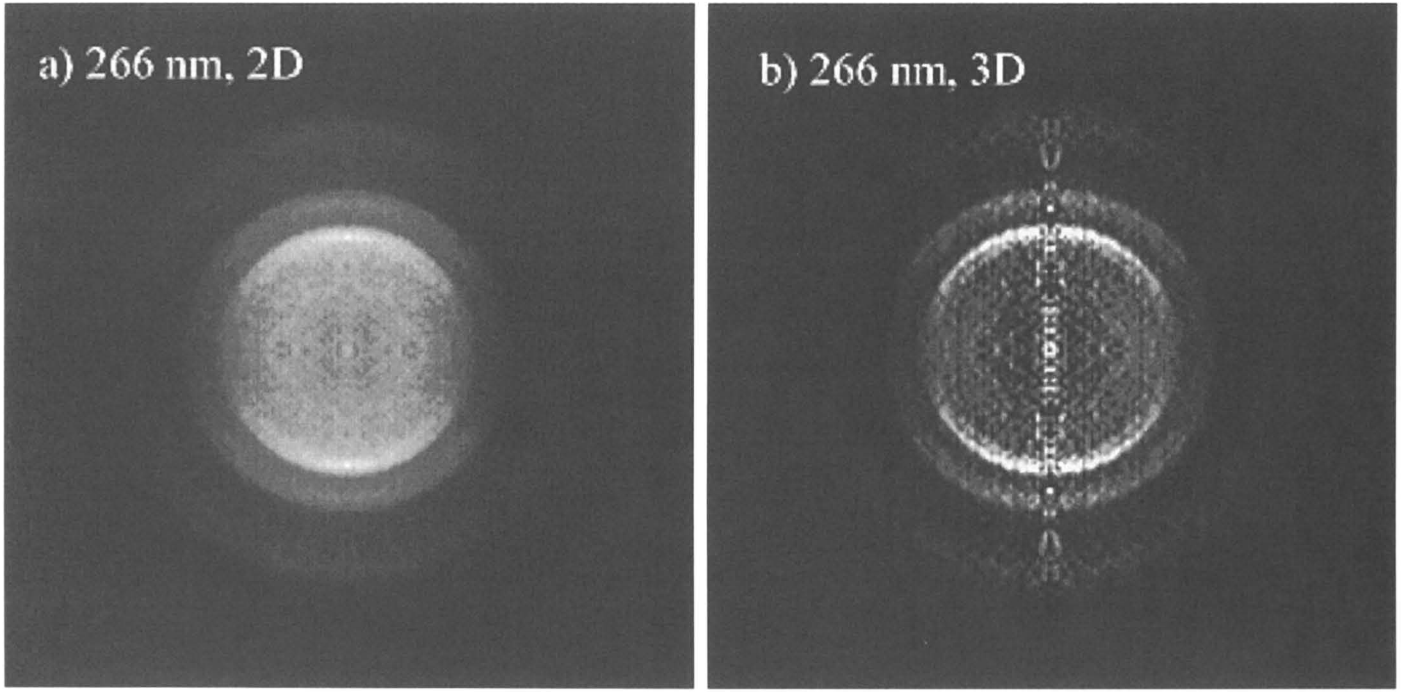

*Figure 3. Image of I atoms produced by photodissociating iodobenzene at 266 nm. (a) 2D image. (b) Back-projected 3D image.*

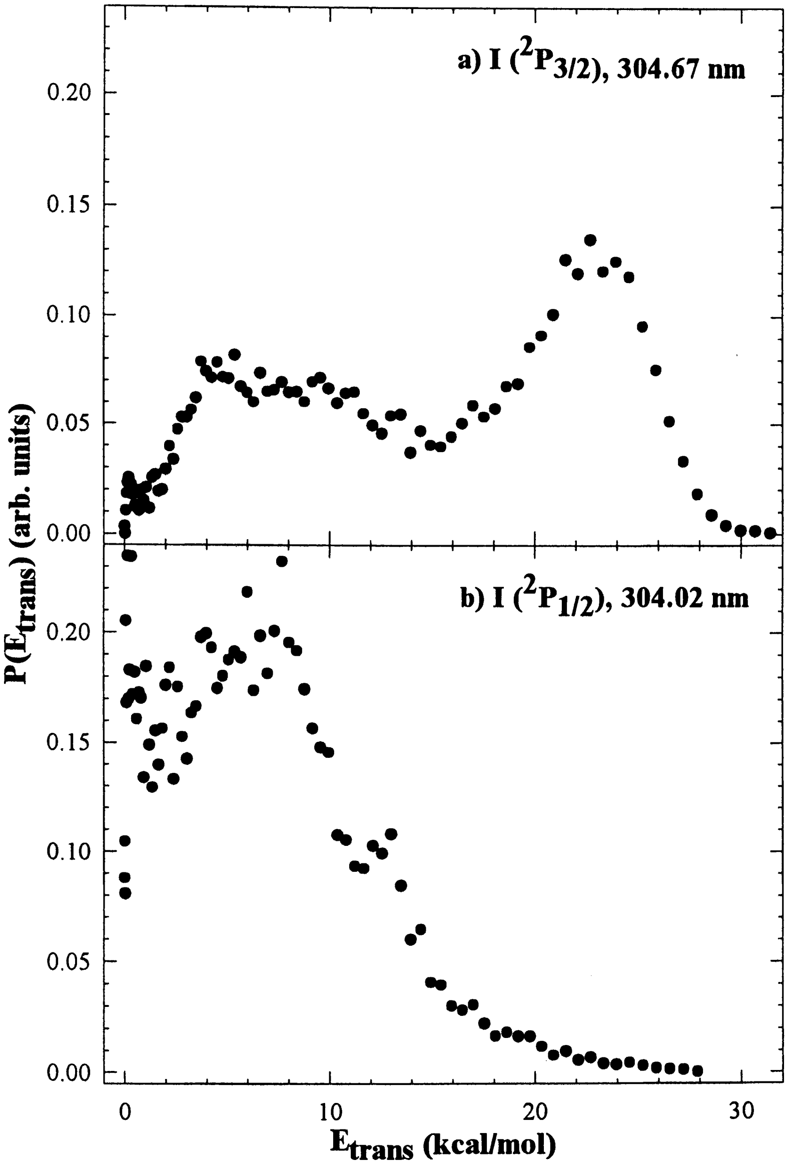

*Figure 4. Relative kinetic energy of the recoiling fragments of iodobenzene. (a) I($^2P_{3/2}$) produced at 304.67 nm. (b) I($^2P_{1/2}$) produced at 304.02 nm.*

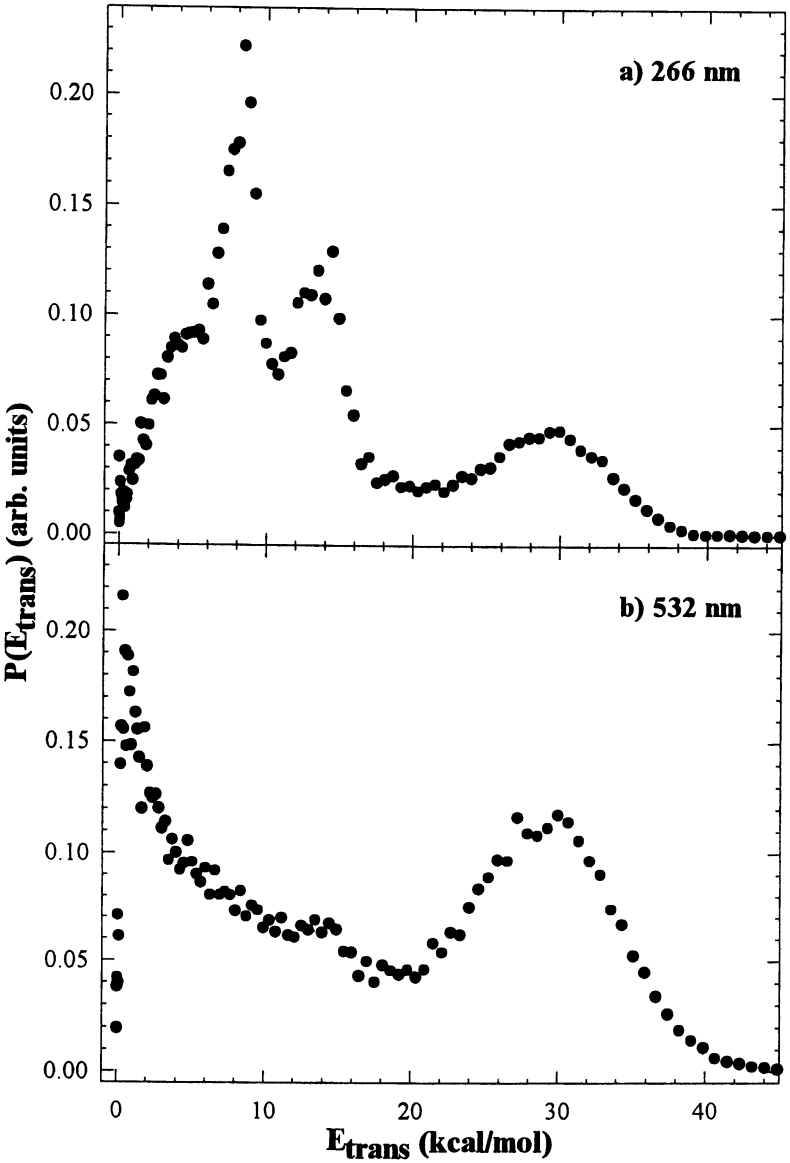

*Figure 5. Relative kinetic energy of the recoiling fragments of iodobenzene produced by (a) 9.2 mJ/cm$^2$ of the fourth harmonic and (b) 68 mJ/cm$^2$ of the second harmonic of the Nd:YAG laser.*

of the Nd:YAG laser. A typical image is shown in Figure 6, and the corresponding kinetic energy distribution is plotted in Figure 5b. The two rings seen in this image are the two-photon counterparts of the two outer rings observed in the 266 nm image. In addition, a continuous pattern peaked at zero velocity is seen superposed on the discrete ring structure. The origin of this extraordinary pattern, which we refer to as an "hourglass" feature, is discussed in the following section. Multiphoton images displaying the hourglass effect were recorded also at 355, 560, 570, 575, 604, and 609 nm. Similar behavior was observed for $CH_3I$ at 532 nm.

Active alignment of $CH_3I$ in a two color experiment is illustrated in Figure 7. The bottom panel displays the variation in $\beta_2$ with the intensity of the aligning (1064 nm) laser. Under our focusing conditions, the laser intensity at 3 mJ/pulse corresponds to $5\text{x}10^{10}$ W/cm$^2$, which is an order of magnitude weaker than that used in ref. (8).

## Discussion

### Single-Photon Photodissociation of Iodobenzene

The discrete structure observed at 304.67, 304.02, and 266 nm is readily attributed to a single-photon photodissociation reaction. Iodobenzene has two chromophores, the non-bonding electrons on the iodine atom and the $\pi$ valence electrons of the phenyl ring. The lowest energy feature observed in the UV absorption spectrum of iodobenzene is a weak, structureless band having a maximum near 260 nm (12). This band is generally attributed to two overlapping transitions, an $n,\sigma^*$ transition produced by the iodine chromophore and a $\pi,\pi^*$ transition produced by the phenyl chromophore. Both transitions have primarily parallel character (13), (14).

The energies of the rings in the 304.67 nm image and of the two outer rings in the 266 nm image are in quantitative agreement with the peak positions observed by El-Sayed and coworkers in their time-of-flight measurements (15), (16). Their analysis led them to conclude that the high energy peak is produced by an $^3n,\sigma^*\leftarrow{}^1X$ transition followed by intersystem crossing to the $^1n,\sigma^*$ potential energy surface, with dissociation occurring in less than one rotational period. They assigned the low energy peak in their spectrum to the $^3\pi,\pi^*\leftarrow{}^1X$ transition, followed by internal conversion, with the available energy being shared between translational motion and internal degrees of freedom of the phenyl radical. This analysis does not take into account the $^{1,3}\pi,\sigma^*$ states, which recent calculations (17) show to be energetically accessible in these experiments. We will explore the possible role played by these states in a future publication.

### Multiphoton Photodissociation of Iodobenzene

The 532 nm images of iodobenzene reveal an unusual hourglass feature superposed on two rings. The rings have the same energies as the two outer rings in the one-photon 266 nm images and undoubtedly have the same physical origin. The hourglass feature is unusual in that it is peaked at zero kinetic energy and has a continuous energy distribution. It was at first tempting to attribute the hourglass to

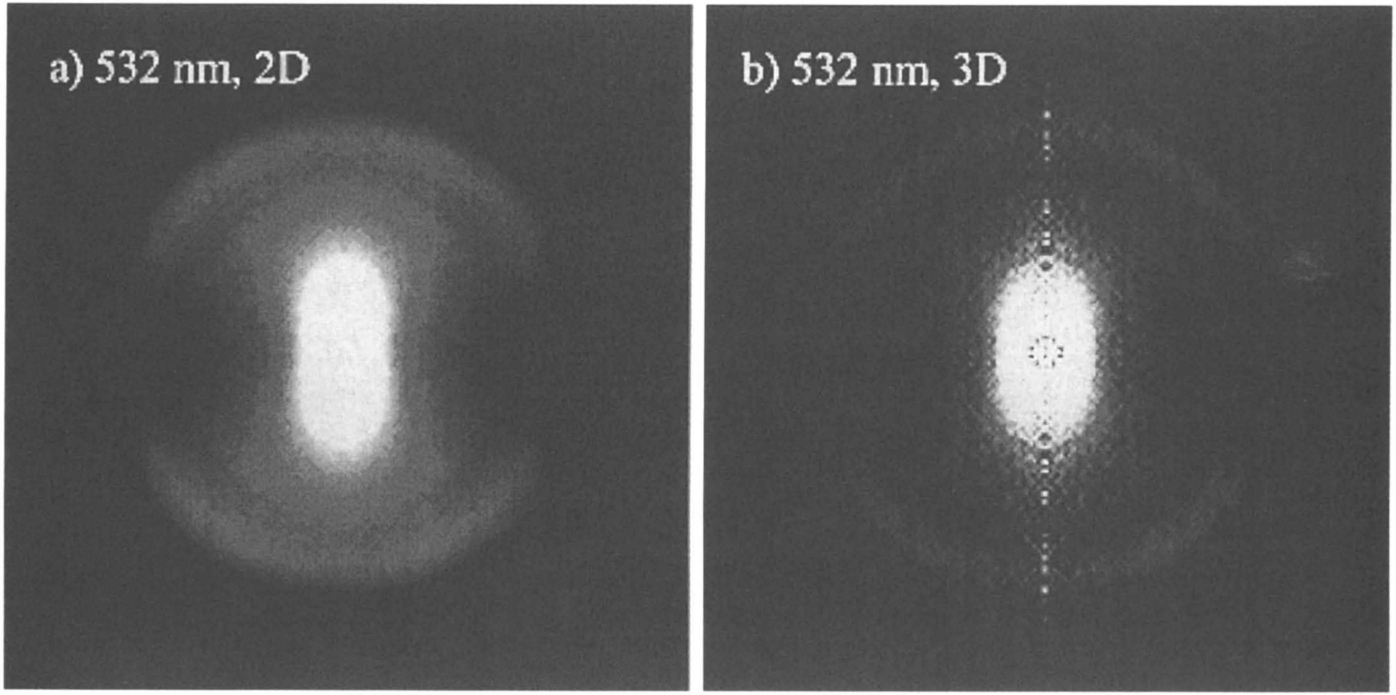

*Figure 6. Image of I atoms produced by photodissociating iodobenzene with 68 mJ/cm$^2$ of 532 nm radiation. (a) 2D image. (b) Back-projected 3D image.*

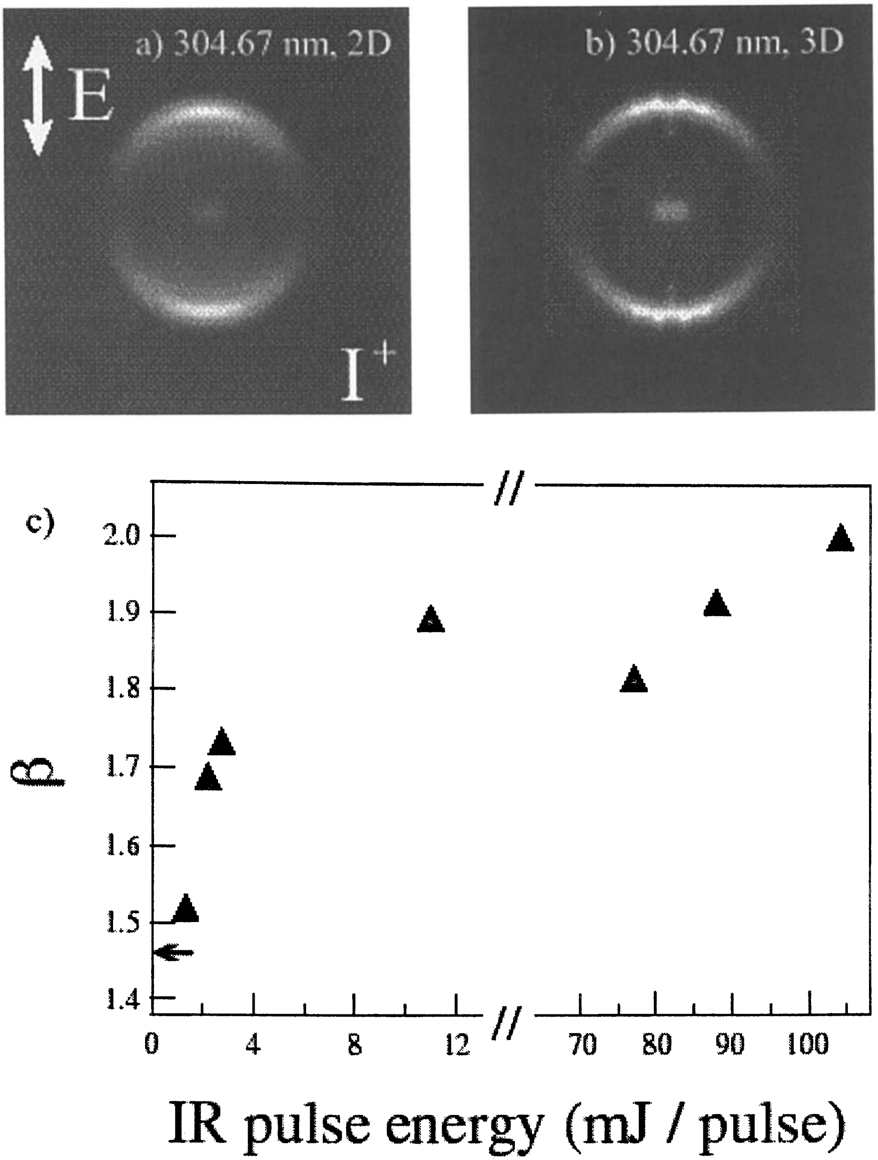

*Figure 7. Image of I($^2P_{3/2}$) produced by photodissociating methyl iodide at 304.67 nm. (a) 2D image. (b) Back-projected 3D image. (c) Variation of $\beta_2$ with IR laser intensity. The arrow indicates the value of $\beta$ averaged over several images in the absence of the aligning laser. Reproduced with permission from Ref. (32). Copyright 2000, American Institute of Physics.*

active alignment of the long-lived, low energy π,π* (or π,σ*) state and the ring structure to the short-lived n,σ* state. (Cheng *et al.* (18) determined that the lifetime of the longer lived state produced at 609 nm to be approx. 400 fs, whereas Dietz *et al.* (19) estimated the lifetime of the antibonding n,σ* state at 266 nm be as short as 20 fs.) But this explanation does not account for the lack of structure in the hourglass or for the zero kinetic energy peak. Conclusive evidence that the hourglass is *not* the result of active alignment is seen in Figure 8, where the intensity dependence of the anisotropy parameters is plotted for the two rings and hourglass. Under our focusing conditions, the laser intensity at 100 mJ/pulse corresponds to approx. $5 \times 10^{11}$ W/cm$^2$. The near independence of $\beta_2$ and $\beta_4$ on laser intensity is inconsistent with an active alignment mechanism. In addition, we altered the rotational temperature of the parent molecule by changing and even eliminating the carrier gas in the nozzle expansion. The lack of a carrier gas effect on the shape of the hourglass further confirms that active alignment is not the primary mechanism.

A variety of other mechanisms were also examined and ruled out. First, we were careful to check (using GC/MS) that there were no trace impurities present that could produce I atoms by absorbing visible light. Second, we considered the possibility of cluster formation, which has been shown to produce a continuous energy distribution peaked at zero (20), (21). Increasing the temperature of the parent molecule by probing different regions of the pulsed molecular beam, and also by eliminating the carrier gas, had no effect. Moreover, it would be difficult to explain why clusters do not produce an hourglass at 266 nm. A third possibility is a dressed state effect such as field-enhanced avoided crossings and bond softening. Broad, anisotropic images have been observed in the high-intensity (~$10^{13}$ W/cm$^2$), above-threshold photoionization and photodissociation of deuterium molecules (22). Such dressed state effects are unlikely in the present case because the laser intensity is much lower and the recoil anisotropy is insensitive to intensity.

Two mechanisms which at present appear to be viable are ladder climbing and dissociative ionization. By ladder climbing we mean ionization of the parent molecule followed by photodissociation of the parent ion, as opposed to ladder switching, in which the neutral molecule dissociates and the fragments are subsequently photoionized. We note that the parent ion was not observed in any of the present experiments. Previous studies of the photoexcitation of iodobenzene showed that the parent ion can be produced only with pulses of ps or shorter duration (23), (24). In experiments with ns pulses, the absence of the parent ion (generated at 248 nm (23), (24)) and the lack of fluorescence by the parent molecule (produced by excitation at 266 nm (19)) were attributed to very rapid predissociation of the $S_1$ state (25). In another experiment, the stable parent ion was produced by electron bombardment and then photodissociated with an Ar$^+$ laser at 514.5 nm. A narrow kinetic energy distribution of the fragments peaked near zero was observed and attributed to a statistical process in which the phenyl fragment retains most of the available energy (26). We propose here that at the higher intensities used in the present experiment the parent ion does form (in competition with two-photon dissociation) but is rapidly dissociated by absorption of additional photons (27), (28).

An alternate possibility is dissociative ionization, in which dissociation and

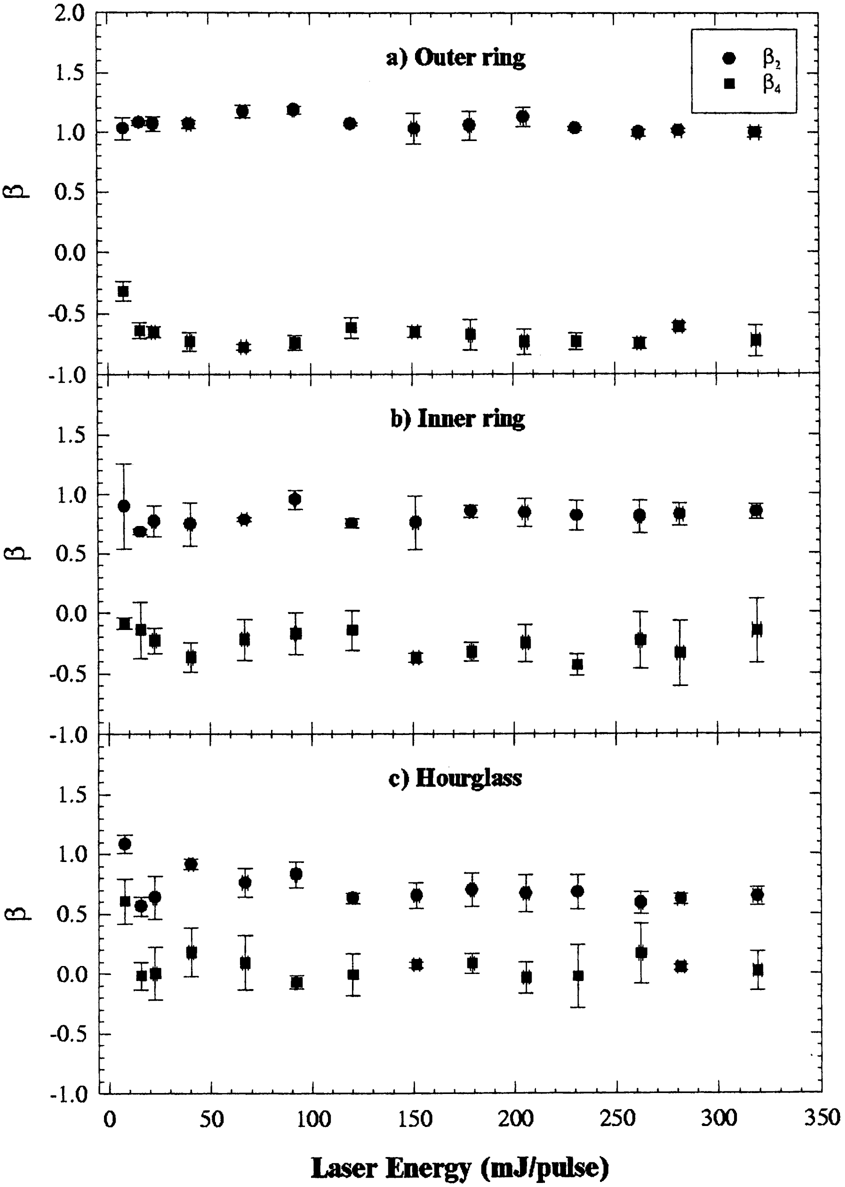

*Figure 8. Intensity dependence of the anisotropy parameters for iodobenzene at 532 nm. Circles are $\beta_2$, and squares are $\beta_4$. Error bars are single standard deviations of multiple images. (a) Outer ring at 29.98 kcal/mol. (b) Inner ring at 14.44 kcal/mol. (c) Hourglass at 6.64 kcal/mol.*

ionization occur in a concerted fashion so that the electron carries off a continuous fraction of the recoil energy. Because of the much lighter mass of the electron, the nuclear kinetic energy peaks near zero. Dissociative ionization in the tunneling regime produced by intense fields ($\geq 10^{14}$ W/cm$^2$) is well known (29). Here we are proposing a lower intensity (though still non-perturbative) mechanism in the multiphoton regime (30). Additional work is required to test these two mechanisms.

### Active Alignment of Methyl Iodide

Active alignment of a molecule with an anisotropic polarizability may be achieved by using a laser to induce a dipole moment in the molecule, which then interacts with the electric field (5),(6). The variation of the β parameters with laser intensity may be readily calculated using classical statistical mechanics (31). The distribution of alignment angles is given by

$$P(\theta) = Ne^{-V(\theta)/kT}, \tag{4}$$

where V(θ) is given by Eq. (3) and N is a normalization constant. Expanding the exponential to first order and combining this result with the probability of absorbing a photon from the dissociation laser, it is readily found (32) that the recoil angular distribution is given by

$$P(\theta_s) = (1/4\pi)\,[1 + \beta_{eff}P_2(\cos\chi)P_2(\cos\theta_s) + (18/35)\beta_2 P_2(\cos\chi)P_4(\cos\theta_s)]. \tag{5}$$

where $\theta_s$ is the angle between the z-axis and the electric vector of the dissociating laser, and $\chi$ is the angle between the electric vectors of the aligning and dissociating lasers. In this equation,

$$\beta_{eff} = \beta_2 + \gamma(1 + 2\beta_2/7 - \beta_2^2/5), \tag{6}$$

where $\beta_2$ is the field-free anisotropy parameter, $\gamma = \mathcal{E}^2\Delta\alpha/2kT$ is a dimensionless control parameter, and T is the rotational temperature. A linear fit of $\beta_{\text{eff}}$ vs. $\mathcal{E}^2$ yields $\gamma$=0.28 at a pulse energy of 3 mJ, in good agreement with the estimated value. The leveling off of $\beta_{\text{eff}}$ at higher pulse energies is attributed to photodissociation of the parent molecule by the aligning laser (32).

## Conclusions

In summary, we have observed three distinct mechanisms for molecular alignment. In a weak, resonant field (266 and 304 nm) iodobenzene undergoes rapid dissociation. Passive alignment results from selection of those molecules that have a transition dipole moment parallel to the electric vector of the laser. The images provide a wealth of information about the photodissociation dynamics of different electronic states of the molecule. A strong field (e.g., 532 nm) also produces passive alignment, but a new physical mechanism occurs producing an hourglass shaped feature peaked at zero kinetic energy. Two possible causes of the hourglass effect in iodobenzene and methyl iodide are ladder climbing and dissociative ionization. Finally, a strong nonresonant field (1064 nm) induces active alignment of methyl iodide. The stable parent molecule is trapped in the potential well that results from the interaction of the anisotropic polarizability of the molecule with the electric field of the laser.

## Acknowledgements

We wish to thank Dr. Attila Berces, Prof. Richard Bersohn, and Dr. Tamar Seideman for many valuable conversations and for their significant assistance in analyzing the data. RJG thanks the U. S. Department of Energy and MK thanks the Ministry of Education of Japan for their support of this research.

## References

1. Zare, R. N. *Bersichte der Bunsen-Gesellschaft* **1982**, *86*, 422.

2. Greene, C. H.; Zare, R., N. *Ann. Rev. Phys. Chem.* **1982**, *33*, 119.

3. Hall, G. E.; Houston, P. L., *Ann. Rev. Phys. Chem.* **1989**, *40*, 375.

4. Gordon, R. J. *Adv. Chem. Phys.*, Prigogine, I. and Rice, S. A. eds., vol. 96, Wiley: New York, 1996, p 1.

5. Seideman, T. *J. Chem. Phys.* **1995**, *1073*, 7887.

6. Freidrich, B.; Herschbach, D. R. *Phys. Rev. Lett.* **1995**, *74*, 4623.

7. Sakai, H.; Salvan, C. P.; Larsen, J. J.; Hilligsøe, K. M.; Hald, K.; Stapelfeldt, H. *J. Chem. Phys.* **1999**, *110*, 10235.

8. Larsen, J. J.; Sakai, H.; Salvan, C. P.; Wendt-Larsen, I.; Stapelfeldt, H. *J. Chem. Phys.* **1999**, *111*, 7774.

9. Posthumus, J. H.; Plumridge, J.; Thomas, M. K.; Codling, K.; Frasinski, L. J.; Langley, A. J.; Taday, P. F. *J. Phys. B: At. Mol. Opt. Phys.* **1998**, *31*, L553.

10. Eppink, A. T. J. B.; Parker, D. H. *J. Chem. Phys.* **1998**, *109*, 4758.

11. Sato, Y.; Matsumi, Y.; Kawasaki, M.; Tsukiyama, K.; Bersohn, R. *J. Phys. Chem.* **1995**, *99*, 16307.

12. Durie, R. A,; Iredale, T.; Jarvie, J. M. S. *J. Chem. Soc. (London)* **1950**, 1181.

13. Dzvonik, M.; Yang, S.; Bersohn, R. *J. Chem. Phys.* **1974**, *62*, 4408.

14. Freedman, A.; Yang, S. C.; Kawasaki, M.; Bersohn, R. *J. Chem. Phys.* **1972,** *80*, 1028.

15. Hwang, H. J.; El-Sayed, M. A. *J. Chem. Phys.* **1992,** *96*, 856 .

16. Freitas, J. E.; Hwang, H .J.; El-Sayed, M. A. *J. Phys. Chem.* **1993,** *97*, 12481.

17. Attila Berces, private communication.

18. Cheng, P. Y.; Zhong, D.; Zewail, A. H. *Chem. Phys. Lett.* **1995,** *237*, 399.

19. Dietz, T. G.; Duncan, M. A.; Liverman, M. G.; Smalley, R. E. *J. Chem. Phys.* **1980**, *73*, 4816.

20. Syage, J. A., *Chem. Phys. Lett.* **1995,** *245*, 605.

21. Tanaka, Y.; Kawasaki, M.; Matsumi, Y. *Chem. Soc. Jap.* **1998**, *71*, 2539.

22. Chandler, D. W.; Parker, D. H. *Adv. Photochem., Vol. 25*, Neckers, D. C.; Volman, D. H.; von Bünau, G., eds.; Wiley: New York, 1999; p 59.

23. Matsumoto, J.; Lin, C.-H.; Imasaka, T. *Anal. Chem.* **1997**, *69*, 4524.

24. Wilkerson, C. W.; Reilly, J. P. *Anal. Chem.* **1990**, *62*, 1804.

25. Tembreull, R.; Sin. C. H.; Li, P.; Pang, H. M.; Lubman, D. M. *Anal. Chem.,* **1985**, *57*, 1186.

26. Yim, Y. H.; Kim, M. S. *J. Phys. Chem.* **1993,** *97,* 12122.

27. Malinovich, Y.; Lifshitz, C. *J. Phys. Chem.* **1986,** *90,* 2200.

28. The dissociation fragments of $C_6H_5I^+$ are $C_6H_5^+$ + I (see ref. (27)). We must therefore assume that the neutral I fragment is subsequently non-resonantly ionized by the same laser field.

29. Seideman, T.; Ivanov, M. Yu.; Corkum, P. B. *Phys. Rev. Lett.* **1995,** *75*, 2819.

30. Levis, R. J.; DeWitt, M. J. *J. Phys. Chem.* **1999**, *103*, 6493.

31. We wish to thank Prof. R. Bersohn for deriving this result.

32. Sugita, A.; Mashino, M.; Kawasaki, M.; Matsumi, Y.; Gordon, R. J.; Bersohn, R. *J. Chem. Phys.* **2000**, *112*, 2164.

## Chapter 7

# Velocity Imaging Studies Using a Vacuum Ultraviolet Laser

William M. Jackson[1], Dadong Xu[1], Roosevelt J. Price[1],
Kevin L. McNesby[2], and Ian A. McLaren[3]

[1]Chemistry Department, University of California,
One Shields Avenue, Davis, CA 95616
[2]Army Research Laboratory, Aberdeen Proving Grounds, Aberdeen, MD 21005
[3]McLaren Research, Mountain View, CA 94043

Velocity ion imaging studies on $C_2H_5Br$, $C_3H_4$, and clusters of $CH_3OH$ using a 118 nm laser are described. A new ion pair process that produces $C_2H_3^+$, $H_2$, and $Br^-$ has been observed in the ethyl bromide studies. Direct ionization of allene produces a $C_3H_3^+$ ion, which may be the result of either direct ionization of the $C_3H_3$ radical by the 118 nm laser or dissociation of a vibrational excited ion by the residual 355 nm radiation. Evidence is presented that in the photoionization of neutral methanol $(CH_3OH)_n$ clusters at 118 nm the protonated cluster ions have very little recoil translation energy as the value of n goes from 2 to 6.

## Introduction

Chandler and Houston originated the ion imaging technique in chemical dynamics (*1*). This method provides information about the mass, angular and velocity distributions of products formed from either photodissociation or chemical reaction. Originally, the kinetic energy resolution was poor but with the modifications suggested by Eppink and Parker (*2*) and further revised by Chang et al. (*3*), it can be improved to about $\Delta E/E$ of 0.055. The ion imaging technique becomes velocity imaging with this modification. Velocity imaging provides the additional advantage that it can be used for imaging positive or negative charged particles by just changing the polarity of the potentials used in the lens system. This even includes electrons if the system has the proper magnetic shielding. Thus, the velocity imaging technique can provide most of the crucial pieces of information needed in chemical dynamics studies.

In Imaging in Chemical Dynamics; Suits, A., et al.;
ACS Symposium Series; American Chemical Society: Washington, DC, 2000.

The advantages described above for the velocity imaging technique are not the only ones that make this technique so exciting. This technique uses pulsed lasers, which means that it is well matched to pulsed molecular beams (*4*). The technique is also very sensitive because the ionization laser can sample the products in the interaction region of the molecular beam where their density is highest. In addition, because of the high electric fields present there, the ions can be collected efficiently. This opens the possibility that a variety of non-linear laser techniques can be combined with velocity imaging to extend its capabilities for chemical dynamics studies. The only disadvantages of the technique are that it cannot be used with continuous lasers or molecular beams and that the 3-D kinetic energy distributions have to be mathematically extracted from the raw 2-D images.

To date most of the chemical dynamics studies utilizing the velocity imaging technique have concentrated on determining specific quantum states of atoms or molecules produced in chemical reactions. Yet, given the advantages of the velocity imaging system it is clear that it can have a much wider applicability than just determining the concentrations of atoms or small molecules in specific quantum states. Four-wave mixing schemes (*5*) can be used to generate high-energy photons in the vacuum ultraviolet region of the spectrum to ionize larger molecular products. Many of the molecular products in elementary chemical reactions are free radicals, which often have lower ionization potentials, IP's, than the molecules from which they are formed. Under these circumstances, it should be possible to ionize the free radical without simultaneously ionizing the parent, which is at a higher concentration. Even when the parent and the product have similar IP's it is still be possible to determine the product if their masses are far enough apart since they can be separated by time-of-flight, (TOF), mass spectrometry. If the geometries of the free radical and its ion are similar, then the Franck-Condon factor for photoionization should be large and hence the ionization probability will be large. The sensitivity for detection of free radical fragments will also depend upon how many quantum states of the radical are populated. This, however, is also a problem with many other techniques for product detection and is an inevitable consequence of trying to determine the products of chemical reactions since they can be produced over a wide area in v-J phase space.

There have been some earlier experiments, which show that velocity imaging can also be used with VUV lasers produced by four-wave mixing to both photodissociate the reactants and photoionize the products with a single laser (*6*). In these experiments, the polyatomic fragments are also observed but the signal is much lower because of the lower photoionization cross sections of molecules relative to atoms and phase space considerations. Yet, these experiments offer a glimmer of hope that velocity imaging may be combined with four wave-mixing schemes to allow one to systematically study the photochemistry on molecules in the VUV region. It could require two VUV lasers for photolysis and detection or one VUV laser for photolysis and other lasers for REMPI detection of the product.

A systematic study of molecular photodissociation using tunable VUV lasers is important for a number of practical and fundamental reasons. Photochemical information about a molecule is often needed at a variety of wavelengths to understand the chemistry occurring in planetary atmospheres, the interstellar medium, and in the various regions of our own atmosphere. Systematic studies also provide information about how direct dissociation competes with indirect dissociation via internal conversion, non-adiabatic transitions or intersystem crossing. These types of studies provide the information, which can be used to test the theories of these processes.

Early studies of the photochemistry of simple molecules in the vacuum ultraviolet (VUV) region showed that electronic excited states of one or more of the products could occur. If the energy is high, then these states can undergo further dissociation. Thus, in principle one can use VUV photolysis of the appropriate parent compound to study free radical dissociation from different excited state surfaces. This method allows one to obtain information about product formation without confronting the difficult task of preparing and isolating the free radical. The free radicals produced by photodissociation will often be vibrationally excited if the geometry of the radical in the excited state is different from the ground state of the radical. When this happens, new information is obtained about the potential surface of the free radical in regions of the potential surface, which are difficult to access from the vibrationless ground state.

The present article describes some of the preliminary results obtained using the velocity imaging technique to study the products formed when molecules are both photodissociated and photoionized in the VUV region with a 118 nm laser. Four-wave mixing the third harmonic of an Nd-YAG in a phase matched medium of Xe and Ar is used to make this laser.

## Experimental

The apparatus that is used in these studies is shown schematically in Figure 1. It is similar to others described in this volume. It consists of a differentially pumped pulsed molecular beam, which is skimmed before entering the main chamber. This main chamber has an ion optics region, a time of flight tube and a detector region. The ion optics collects the charged particles and focuses them through the TOF mass spectrometer perpendicular to the molecular beam onto a multi-channel-plate (MCP) detector. A TOF mass spectrum can be measured in these experiments by using the side window photomultiplier to detect light arising from the phosphor screen when struck by the electrons produced by ions hitting the MCP detector. A two dimensional (2-D) image at a particular fragment mass is observed if the multi-channel plate detector is gated to isolate it from other masses. A 1/2" video camera (Mintron OS-40D or MS-2821E) is focussed onto the phosphor. A Sensoray Model 611 Frame Grabber mounted in a Pentium II-based PC digitizes the resulting video signal. The video signal is also sent to a McLaren Research TM1000CV Video Interface Unit containing programmable timers that are used to trigger the laser, pulsed molecular beam valve, and Microchannel Plate (MCP) gate pulser. These timers are synchronized to the video signal from the camera, to ensure that the ion image is generated on the phosphor during the camera's vertical synchronization period rather than during readout of the CCD.

Data acquisition is performed by custom-written software (CODA32 from McLaren Research, running under Windows 98 on the Pentium II-based PC), which

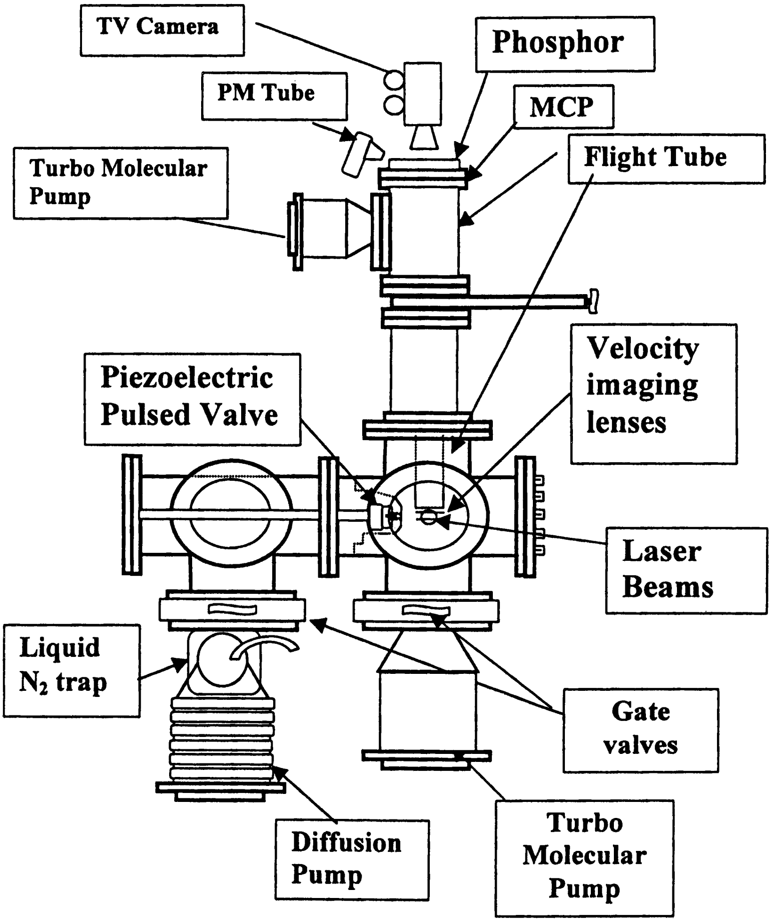
TV Camera
Phosphor
PM Tube
MCP
Turbo Molecular Pump
Flight Tube
Velocity imaging lenses
Piezoelectric Pulsed Valve
Laser Beams
Liquid $N_2$ trap
Gate valves
Diffusion Pump
Turbo Molecular Pump

*Figure 1. A schematic diagram of the apparatus.*

also controls the experimental timing via the TM1000CV. At the full 30 Hz frame rate, ion images are captured, processed, displayed on the PC screen, and accumulated in 32-bit image buffers. The signal processing consists of thresholding and centroiding. Thresholding involves comparison of intensity on each pixel against a user-selected level. Pixels with intensity above this level are retained, while those below this level are treated as noise and set to zero. The centroiding process is based on a method described by Houston's group (*3*) and involves comparison of each non-zero pixel with its neighbors, and assignment of an ion centroid position to the pixel with the local maximum signal value. Houston's group was limited by the speed of their hardware to comparisons with four pixels in the neighborhood above, below, left of, and right of each non-zero pixel. CODA32 can calculate centroids based on arrays of up to 80 nearest neighbors. Each non-zero pixel is considered to be at the center of a 9 x 9 pixel square block, and its value is compared against all other pixels in the block. Other user-selectable options allow comparisons against 8, 24, or 48 neighbors, corresponding to squares of side 3, 5 and 7 pixels respectively.

The centroiding process confers two main benefits. Firstly, inhomogeneities across the surface of the MCP, the phosphor, or the camera CCD array are largely corrected for since the result of the centroid calculation is a single ion count no matter what the individual non-zero pixel values were. Secondly, the spatial resolution of the image is improved since a multi-pixel ion "blob" is reduced to a single-pixel centroid at the position of local maximum value. Algorithms are currently being worked on to allow pseudo-Gaussian centroiding rather than simple neighboring-value comparison, in order to improve the spatial resolution still further. This would potentially allow ion centroid positions to be calculated with a resolution higher than the CCD pixel spacing.

After each experimental acquisition, CODA32 writes disk files representing the accumulated raw (uncentroided) ion image and the accumulated centroided image, both in full-precision binary format and in a Windows Bitmap (BMP) format to allow further processing by the BackPro software (7).

The 2-D image can be converted to a 3-D representation of the recoil velocity of the selected fragment by using the BackPro program (*7*). The translational energy of the fragment and the $\beta$ parameter associated with the photodissociation process can also be determined with this program. The velocity of the fragment, v, is related to the image intensity, I(v, $\theta$), as a function of the speed distribution f(v) and the angular distribution, $\theta$, via (*8*),

$$I\,(v, \theta) = (1/4\,\pi)\, f(v)\{1 + \beta(v)P_2(\cos\theta)\}. \qquad (1)$$

In this equation the angle between the polarization vector of the laser and the recoil velocity of the fragment v is $\theta$, $P_2(\cos\theta)$ is the second Legendre polynomial and $\beta$ is the spatial anisotropy parameter, which varies from −1 to 2. The relative kinetic energy, $E^T_{rel}$, distribution, $P(E^T_{rel})$, can be calculated from the speed distribution by knowing the mass of the counter fragment and then applying the conservation laws. The angular distribution of the image provides information about whether the observed process is direct or indirect and whether one or more electronic states are involved in the photodissociation.

In a typical experiment the gas or gas mixture is mixed in a reservoir behind the pulsed valve so that the composition and the total pressure are known. Time of flight mass spectra of the background gas in the main chamber are taken with and without the Xe and Ar mixture used for creating the VUV light by four wave mixing (*5*)[5]. This then records the ions made by direct and multiphoton ionization of the background gas. A similar experiment is performed with the molecular beam and it is used along with the earlier experiments to obtain a TOF mass spectrum of the beam produced by the VUV laser. Figure 2 is an example of such a TOF mass spectrum of a mixture of acetone, allene and ethyl bromide used to calibrate the time axes of the mass spectrometer. It clearly shows peaks at 110, 108, 58, 43, 40, 29, 28, and 27 corresponding to $C_2H_5{}^{81}Br^+$, $C_2H_5{}^{79}Br^+$, $CH_3COCH_3{}^+$, $COCH_3{}^+$, $C_3H_4{}^+$, $C_2H_5{}^+$, $C_2H_4{}^+$, and $CH_2CH^+$. The separation between the peaks at m/e of 110 and 108, as well as, 29,28, and 27 demonstrates the mass resolution of the system in the velocity imaging mode.

To obtain an image of an ion at a particular m/e ratio the voltage on the MCP detector is first reduced until no signal is observed in the TOF spectra. Then a high voltage pulse, typically a few hundred volts, is added to the offset voltage on the MCP until a signal is observed. The pulse width of this voltage is wide enough to collect all of the ions of interest but narrow enough to exclude unwanted ions. The number of laser shots that will be used to acquire the final image is selected using CODA32 software. Generally, a good image can be obtained in the experiments that are described in this work using from 30,000 to 120,000 shots of the laser. With the 30 Hz laser used in the present experiments, this requires only one to four thousand seconds.

The VUV light at 118 nm is created by frequency tripling (*5*) the 355 nm output from a Spectra Physics Pro 230 Nd-YAG Laser. The 355 nm laser light is focused into a stainless steel cell fitted with a quartz entrance window, a pump out port, vacuum gauges, and a LiF lens at the exit. The cell is filled with ~ 3.7 Torr of Xe. The exact pressure is adjusted to maximize the observed signal. Argon is then added to the cell to further maximize the signal by phase matching. The optimal phase matching mixture generally consists of about ~ 3.7 Torr of Xe and ~ 14.8 Torr of Ar. Only about 3 to 15 mJ of 355 nm Nd-Yag light was used in the experiments described in this article.

## Results and Discussion

### Ethyl Bromide, $C_2H_5Br$

Ethyl bromide was used in the first series of experiments with the velocity imaging apparatus. These experiments were performed to calibrate the imaging detector and to determine if good images could be produced in the apparatus. Earlier experiments by Suto et al. (*9*) have shown that ethyl bromide produces ethyl ions by the following exothermic ion-pair process,

$$C_2H_5Br + h\nu_{118\,nm} \rightarrow C_2H_5{}^+ + Br^- + \Delta H = -60.04 \text{ kcal/mol} \qquad (2)$$

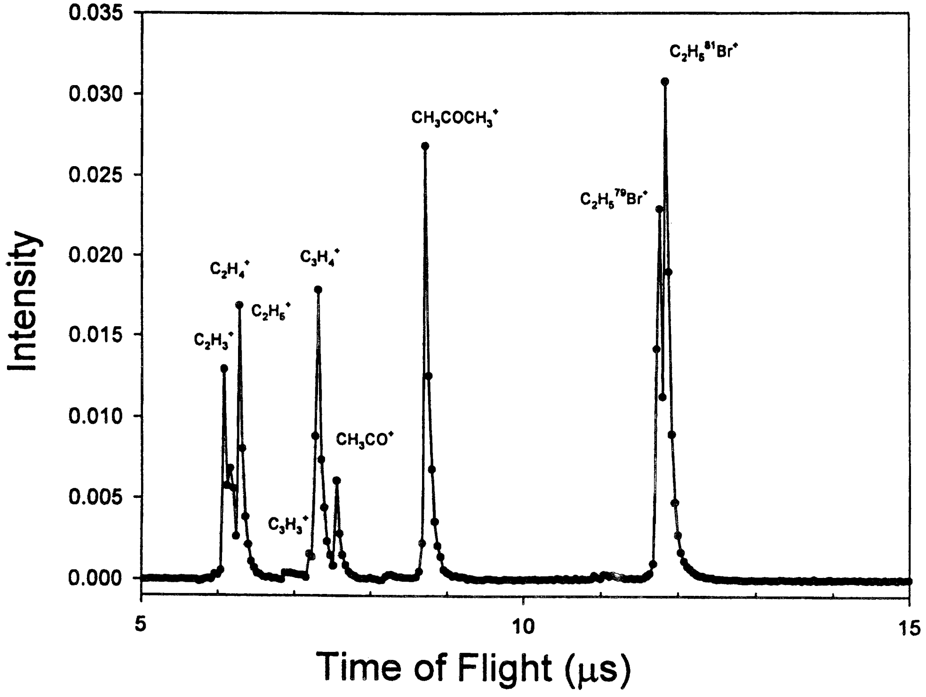

*Figure 2. Allene, acetone and ethyl bromide were used to obtain this calibration TOF Mass Spectrum. Peaks are clearly seen at m/e ratios of 27, 28, 29, 39, 40, 43, 58, 108, and 110 AMU.*

The TOF spectrum in Figure 3 shows that clusters are produced in our system under the conditions described in the previous experiments (*9*). Our nozzle has a diameter of 250 $\mu$ that is a factor of three smaller than the nozzle used in the earlier experiments. This probably accounts for our observations of clusters. When a neat beam of 200 Torr is used, the same figure shows that no clusters are present in the beam. The TOF spectra also show the presence of masses 28 and 27 which were unreported in the previous studies. The peak at mass 27 can be explained by the following exothermic one photon reaction,

$$C_2H_5Br + h\nu_{118\,nm} \rightarrow C_2H_3^+ + H_2 + Br^- \quad \Delta H = -17.24\ kcal/mol \qquad (3)$$

No such one photon exothermic reaction could be found for the mass 28 peak which suggests that two photons may be involved in producing this product.

Images of the 28 and 29 peak, as well as the 27 peak were taken for the neat and seeded beams. These images are shown in Figure 4 and they clearly show that the dissociation processes are isotropic for masses 29 and 28 in a seeded beam but corresponds to a parallel transition in a neat beam. The speed distribution and $\beta$ parameter was extracted from the image of the mass 28 and 29 peaks. A $\beta$ parameter of 1.9 was obtained for the $C_2H_4^+$ and $C_2H_5^+$ ions, which indicates that the angular distribution is parallel to the electric vector of the laser. The velocity distribution is shown in Figure 5 and it is essentially the same as those previously reported (*9*).

The images obtained with the seeded beams are more isotropic and this is born out in the Abel transformation where the $\beta$ parameter is now ~ zero and the speed distribution is distinctly slower. This suggests that somehow before an ion can escape the cluster it must undergo some type of energy transfer. Further, analysis of this and the other observations on this system await a more detailed paper that is currently in preparation.

## Allene, $C_3H_4$

Experiments on allene were performed in order to determine if the images produced by direct ionization of the molecular beam are small and to find out if any radicals produced in the dissociation process can be detected. The TOF spectrum shown in the top of Figure 6 shows that $C_3H_4^+$ is produced when only 3.5 mJ/pulse of 355 nm is used to make 118 nm. The conversion efficiency is about $10^{-5}$, when four-wave mixing in a phased-matched rare gas is used (*10*). Thus, 3.5 mJ/pulse of 355 nm light should yield about 0.035 $\mu$J/pulse of VUV light. The spectrum in the bottom of the figure indicates that there is a shoulder on the low-mass side due to $C_3H_3^+$ when a 9 mJ/pulse of 355 nm light is used. The images and the kinetic energies of the ions derived from these images are shown in Figs. 7 and 8, respectively. At low pulse energies of 355 nm and hence low-pulse energies at 118 nm, the image shows no significant recoil, as one would expect for a direct ionization process. At 9 mJ/pulse the image is much larger and the TOF spectrum indicates that the $C_3H_3^+$ is formed.

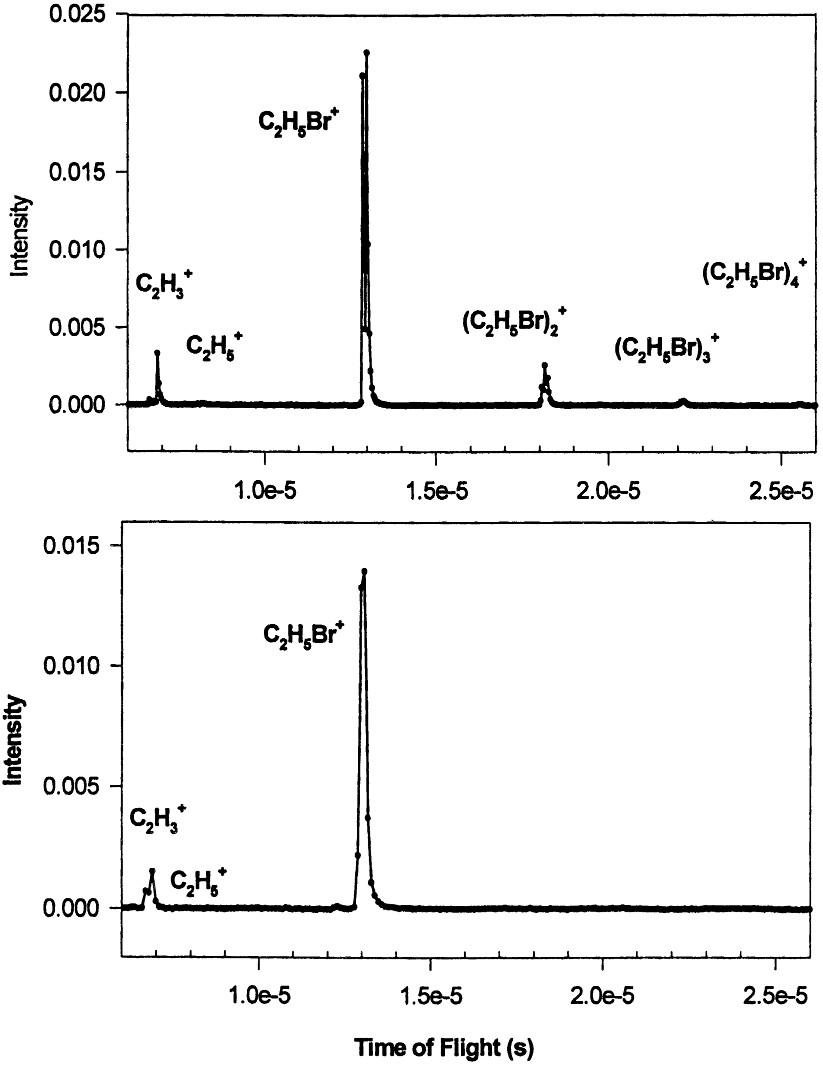

*Figure 3. TOF spectra of the direct photoionization signal from a seeded and neat beam of ethyl bromide using 118 nm light. The top figure is the spectrum from a seeded beam with stagnation pressures of 70 Torr $C_2H_5Br$ in 700 Torr of Ar. The bottom figure is from a neat beam using a stagnation pressure 200 Torr of $C_2H_5Br$.*

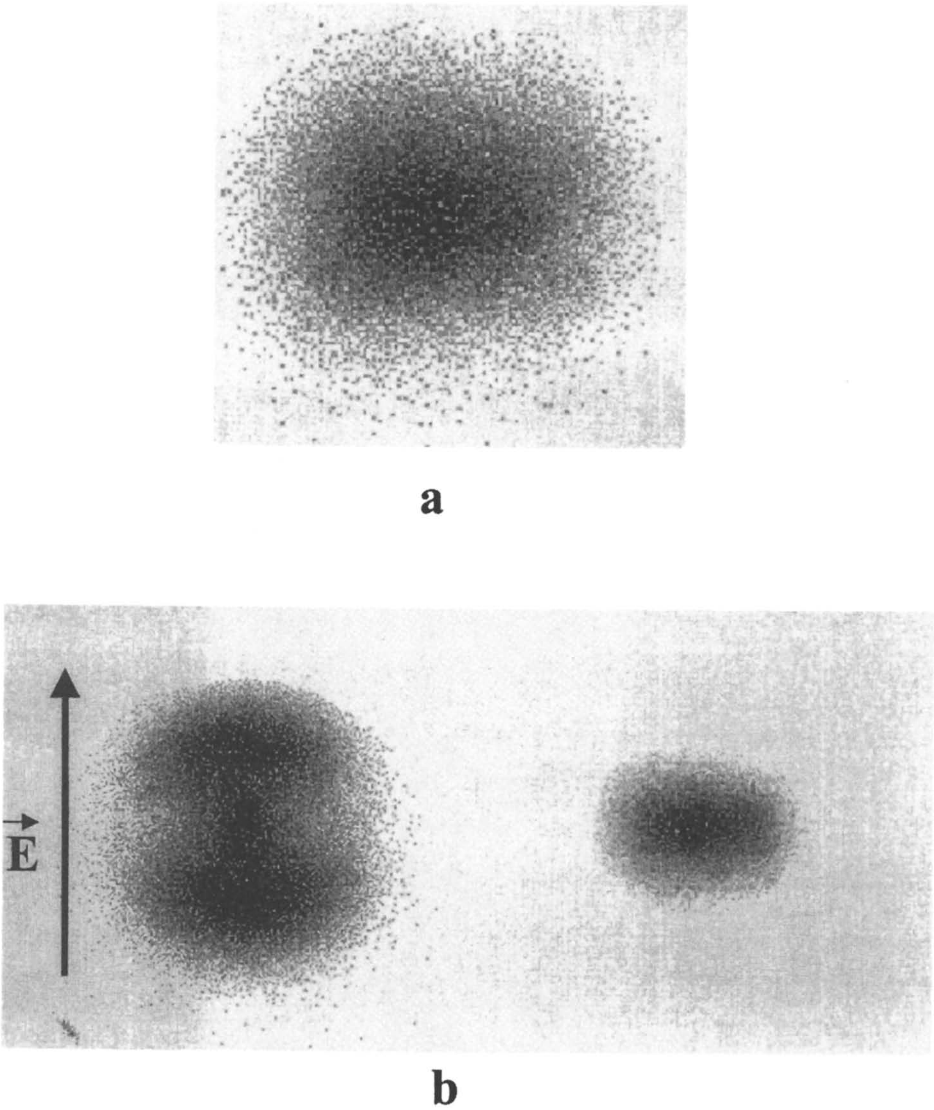

*Figure 4. Velocity mapped images of the fragments from 118 nm photolysis of ethyl bromide under different beam conditions. The image in (a) is for the $C_2H_5^+$ and $C_2H_4^+$ ions from a supersonic beam with stagnation pressures of 70 Torr $C_2H_5Br$ in 700 Torr of argon. In (b) there are two images one for the $C_2H_5^+$ and $C_2H_4^+$ ions and the other for $C_2H_3^+$. A neat beam with a stagnation pressure of 200 Torr of $C_2H_5Br$ was used for (b).*

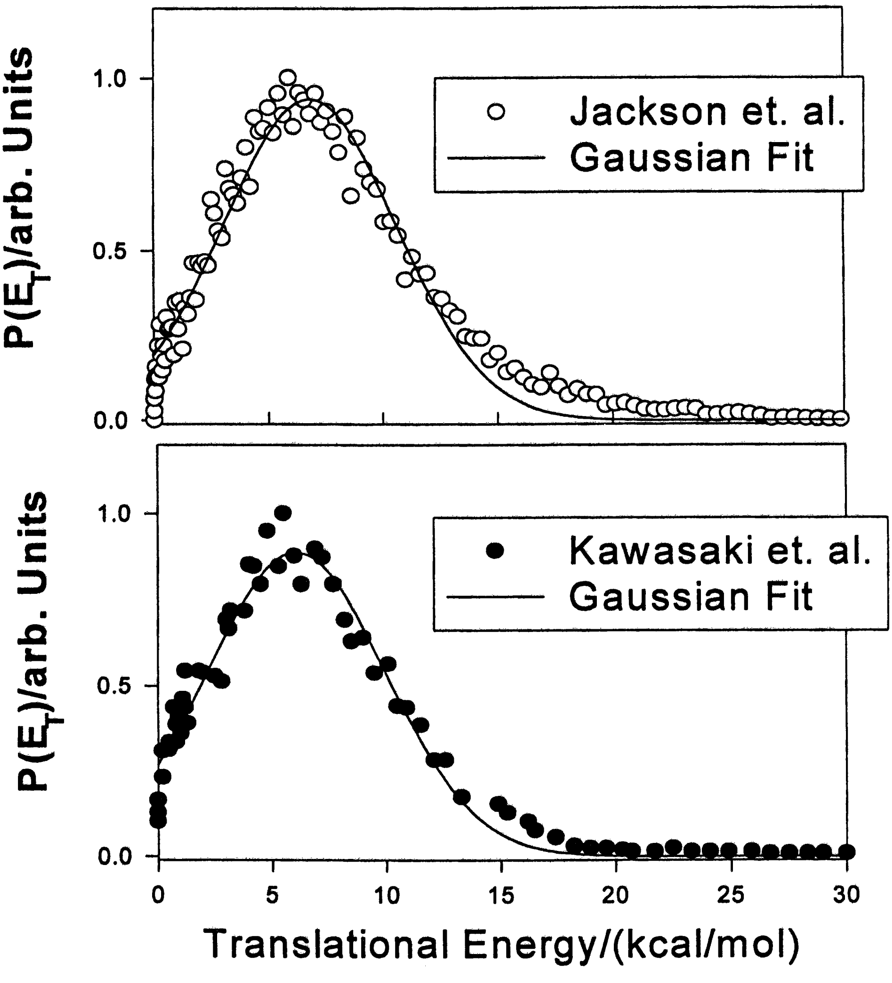

*Figure 5. The translational energy distribution of the $C_2H_5^+$ and the $C_2H_4^+$ ions, which are derived from an image similar to the one in figure 4(b). The curve with the open circles is from the present work and the one with the closed circle is from reference 6.*

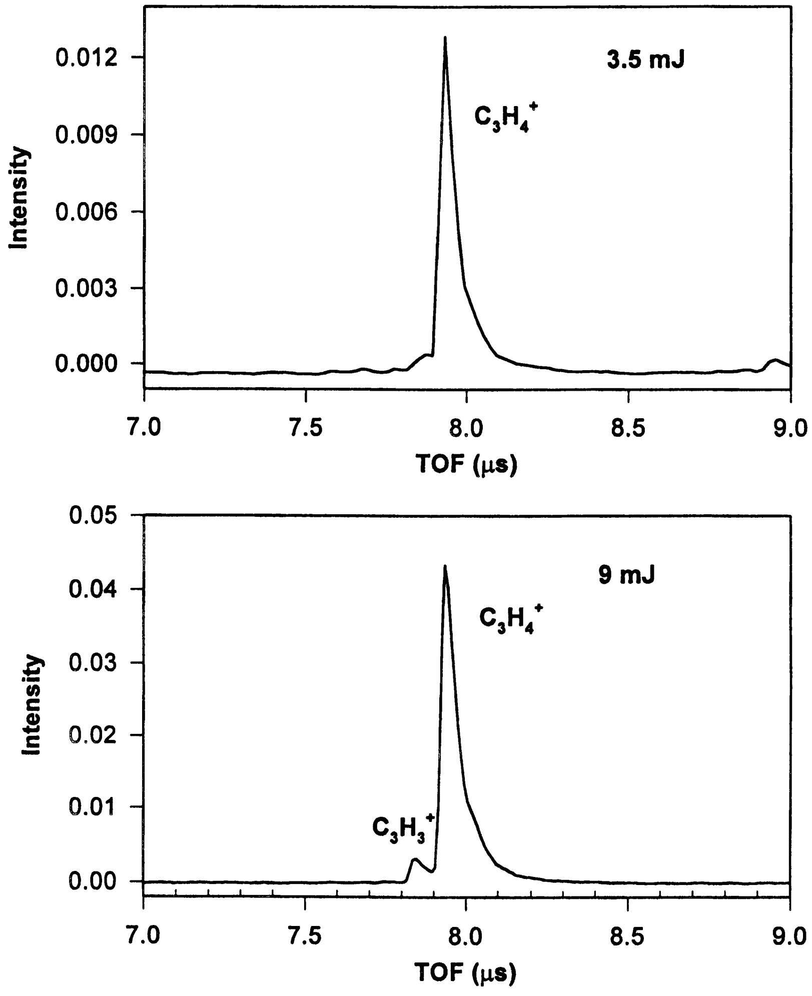

*Figure 6. TOF spectrum of the $C_3H_3^+$ and $C_3H_4^+$ produced in the photolysis of allene at 118 nm formed from a 355 nm laser with pulse energies of 3.5 and 9 mJ/pulse.*

The larger image size of masses 39 and 40 when 9 mJ of 355 nm is used agrees with the notion that the outer part of the image is due to the recoil of the $C_3H_3^+$ radical from an H atom. The translational energy distribution in the top of Figure 8 derived from these images confirms this expectation. This data supports the following mechanism for the production of $C_3H_4^+$ and $C_3H_3^+$.

$$C_3H_4 + h\nu_{118\,nm} \rightarrow C_3H_4^+ + e^- \qquad (4)$$
$$C_3H_4 + h\nu_{118\,nm} \rightarrow C_3H_3^\# + H \qquad (5)$$
$$C_3H_3^\# + h\nu_{355\,nm} \rightarrow C_3H_3^+ + e^- \qquad (6)$$

Reaction 6 is postulated because there is not enough energy in a 118 nm (10.489 eV) photon to produce $C_3H_3^+$ by dissociative ionization. The threshold for this process is 11.595 eV. The photoelectron spectrum of allene shows there is a hot band at 0.104 eV but even with this additional energy there is not enough energy to produce this ion by dissociative ionization. Thus, some type of two-step processes is required to explain the observation of this ion at the higher pulse energies.

The amount of energy required to form the $C_3H_3$ from allene is only 87.8 kcal/mol or 3.81 eV, which leaves enough energy at 6.67 eV to produce the various isomeric forms of this radical. The amount of energy consumed in producing the various forms of $C_3H_3$ will determine how much vibrational energy is left in the radical. This in turn will determine the amount of energy that will be required for a Franck-Condon transition to a particular geometric form of the $C_3H_3$ ion. The intensity of the 355 nm laser beam is almost five orders of magnitude greater than the intensity of the 118 nm laser beam so secondary absorption will be more likely for the former rather than the latter.

Photoelectron spectroscopy clearly shows that there is a shift in the geometry between the ground state of allene and the ground state of the allene ion (*11,12,13*). Well-resolved vibrational structure is observed in the photoelectron spectra of allene (*11,12,13*). This structure has been assigned to two progressions in the ion, namely, the $\nu_4(b_1)$ torsional mode and the $\nu_4(b_1) + \nu_6(b_2)$ combination band. Photoionization of allene at 10.489 eV will excite the $\nu_4(b_1)$ vibration beyond the v' = 5 level and the combination bands beyond the v' = 5 level (*11*). The adiabatic ionization potential, IP, to form the $^2E$ state of the ion is 9.694 eV but the vertical IP is 10.305 eV which also indicates that the transition is to a vibrational excited state of the ion. It is therefore also possible that the mechanism for formation of the $C_3H_3^+$ is given by the following alternate mechanism,

$$C_3H_4 + h\nu_{118\,nm} \rightarrow C_3H_4^{\#+} + e^- \qquad (7)$$
$$C_3H_4^{\#+} + h\nu_{355\,nm} \rightarrow C_3H_3^+ + H \qquad (8)$$

We cannot now distinguish between these two possibilities. High quality ab-initio calculations, such as the ones that we have done in the past, will be needed to answer this question and other questions about the formation of this radical (*14,15*).

## Methanol Clusters

Methanol clusters are known to exist in the gas phase over liquid methanol (*16,17*). Studying these clusters provides a route to the better understanding of the structure of liquids. The TOF mass spectrum that was observed when the 118 nm laser ionized a neat molecular beam of methanol is shown in Figure 9. This spectrum shows that clusters are present in the molecular beam. These clusters and the same TOF spectra were observed even when the stagnation pressure behind the nozzle for a neat beam was varied from 20 to 90 Torr. These results agree with the earlier studies, which showed that methanol clusters are present in the vapor above liquid methanol at room temperature (*18*).

The ionization potential of $CH_3OH$ is too high for the monomer to be ionized at 118 nm, which is why no monomers are observed in the TOF spectra. The clusters have lower ionization potentials, which are below the energy of the 118 nm photon, so that they are all ionized (*18*).

When the methanol monomer or clusters absorb a VUV photon the following reactions are possible,

$$
\begin{array}{lllllll}
(CH_3OH)_n & + h\nu_{118nm} \rightarrow & H(CH_3OH)_{n-1}^+ & + & CH_3O & + & e^- & (9) \\
(CH_3OH)_n & + h\nu_{118nm} \rightarrow & H(CH_3OH)_{n-1}^+ & + & CH_2OH & + & e^- & (10) \\
(CH_3OH)_n & + h\nu_{118nm} \rightarrow & (CH_3OH)_{n-1} & + & CH_2OH & + & H & (11) \\
(CH_3OH)_n & + h\nu_{118nm} \rightarrow & (CH_3OH)_{n-1} & + & CH_3O & + & H & (12) \\
(CH_3OH)_n & + h\nu_{118nm} \rightarrow & (CH_3OH)_{n-1} & + & CH_3 & + & OH & (13) \\
(CH_3OH)_n & + h\nu_{118nm} \rightarrow & (CH_3OH)_{n-1} & + & CH_2(a\ ^1A_1) & + & H_2O & (14) \\
(CH_3OH)_n & + h\nu_{118nm} \rightarrow & (CH_3OH)_{n-1} & + & CH_2(X\ ^3B_1) & + & H_2O & (15) \\
(CH_3OH)_n & + h\nu_{118nm} \rightarrow & (CH_3OH)_{n-1} & + & HCOH & + & H_2 & (16) \\
(CH_3OH)_n & + h\nu_{118nm} \rightarrow & (CH_3OH)_{n-1} & + & CO & + & 2H_2 & (17) \\
(CH_3OH)_n & + h\nu_{118nm} \rightarrow & (CH_3OH)_{n-1} & + & HCO + H_2 & + & H & (18) \\
(CH_3OH)_n & + h\nu_{118nm} \rightarrow & (CH_3OH)_{n-1} & + & H_2C = O & + & 2H & (19) \\
(CH_3OH)_n & + h\nu_{118nm} \rightarrow & (CH_3OH)_{n-1} & + & CO + H_2 & + & 2H & (20) \\
(CH_3OH)_n & + h\nu_{118nm} \rightarrow & (CH_3OH)_{n-1} & + & H_2C = O & + & H_2 & (21)
\end{array}
$$

The IP's of $CH_3OH$, $CH_2OH$, $CH_3O$, $CH_3$, OH, $CH_2\ (X\ ^3B_1)$, $CH_2\ (a\ ^1A_1)$, H, CO, $H_2$, $H_2CO$, HCOH, HCO, and $H_2O$ are 10.84 eV, 7.56 eV, 10.72 eV, 9.84 eV, 13.017 eV, 10.396 eV, ~10.01 eV, 13.598 eV, 14.013 eV, 15.427 eV, 10.88 eV, unknown, 8.12 eV, and 12.6 eV, respectively (*19*).

Reactions 9 and 10 produce ionic protonated methanol clusters that are clearly observed in the TOF spectra. Futrell et al. (*20,21*) suggested that both reactions 9 and 10 have an equal probability. The recent work of Harich et al. (*22*) showed that at 157 nm the photolysis of $CH_3OH$ monomer was complex and that there were two H atom elimination and three $H_2$ molecular elimination channels. They showed that the rate for the H atom elimination channels is almost seven times faster than the $H_2$ elimination channels. In the H atom elimination channels 36% of these go via reaction 11 to produce the $CH_2OH$ radical. This radical has an ionization potential low enough to be ionized at 118 nm. There should be orders of magnitude more monomeric methanol than clusters so there should be large amounts of this radical

*Figure 7. Velocity images of the $C_3H_3^+$ and $C_3H_4^+$ produced in the photoionization of allene at 118 nm at laser energies of 3.5 and 9 mJ/pulse at 355 nm.*

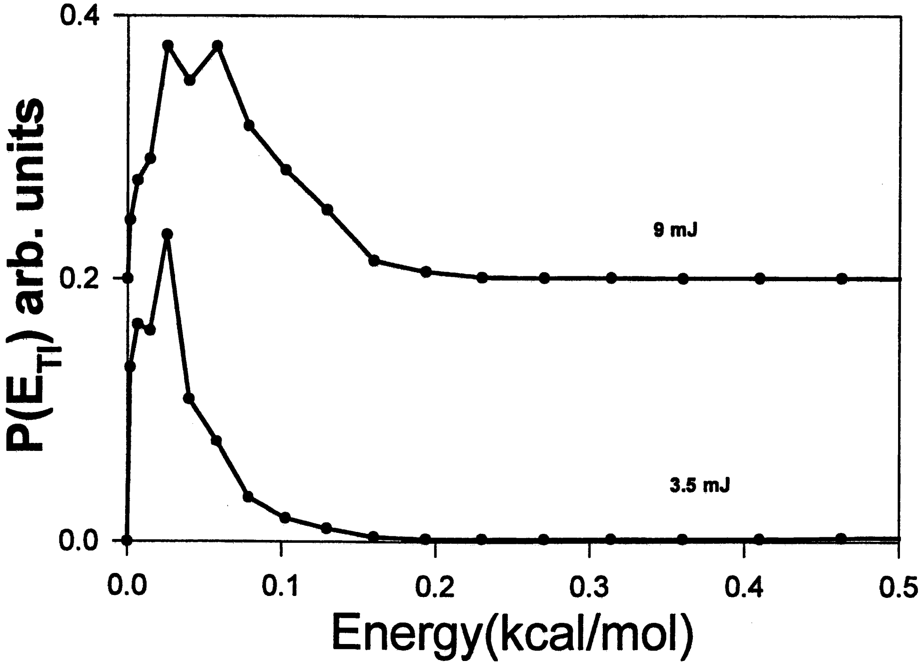

*Figure 8. Translational energy distributions, $P(E_{TI})$, of the $C_3H_3^+$ and $C_3H_4^+$ ions produced in the photoionization of allene at 118 nm at 355 nm laser energies of 3.5 and 9 mJ/pulse. The top curve is for 355 nm pulse energies of 9 mJ/pulse, while the bottom curve is for pulse energies of 3.5 mJ/pulse. These distributions were derived from the images in figure 7.*

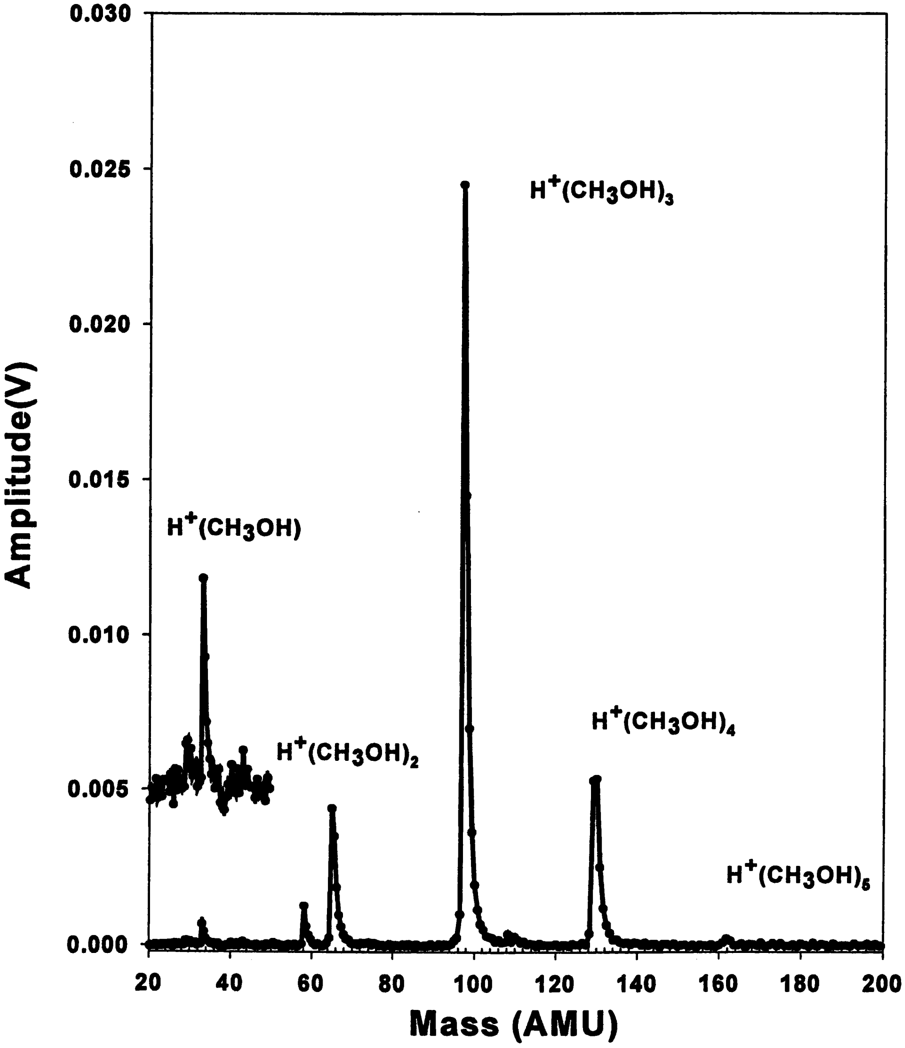

*Figure 9. TOF spectrum of protonated clusters of* $H^+(CH_3OH)_n$, *where n = 1 to 5.*

present in the system. To date, we have not seen any evidence for this product in the TOF spectra at mass 31. The $CH_3$, $CH_2$ (X $^3B_1$), $CH_2$ (a $^1A_1$), and HCO radicals formed in reactions 13, 14, 15, and 18 have IP's low enough to be ionized by a 118 nm photon but none of them have been observed. This could indicate that processes that require ionization by a 118 nm photon are so weak that they are hard to observe. Currently, investigations are under way to determine if longer observation times and/or increases in the VUV laser energy will reveal the presence of some of these reactions.

The images of the protonated monomer, dimer, trimer, tetramer, and pentamer were all measured and they are shown in Figure 10. These images are all at the same magnification so the radii are proportional to the speed of the ions. The radii are all about the same, which indicates that the speeds of the cluster ions are independent of the mass of the cluster. Plots in Figure 11 of the kinetic energy distributions of the ions derived from these images confirm this expectation. This was at first puzzling because previous studies indicated that the mechanism for the formation of the protonated cluster was as follows (*20,21*),

$$(CH_3OH)_n + h\nu_{118nm} \rightarrow (CH_3OH)_n^{+*} + e^- \qquad (22)$$

$$(CH_3OH)_n^{+*} \rightarrow H(CH_3OH)_{n-1}^{+} + CH_3O \qquad (23)$$

This kind of mechanism would imply different radii of the images for different masses if the available energy were the same for all of the protonated clusters. The work of Cook et al. (*18*) however shows that the IP of the clusters decreases from 10.2 to 9.3 eV as the cluster size increases from n = 2 to 5, respectively. This means that the available energy will increase from 0.28 eV to 1.18 eV as the cluster size increases. The image size remains constant because as the available energy increases more energy can go into recoil translational energy.

Ionization of the cluster by reaction 22 should impart very little momentum on the $(CH_3OH)_n^{+*}$ cluster ion. Therefore, the measured kinetic energy of the protonated cluster ions can be used to determine the distribution curve for relative translational energy, $E^T_{rel}$, in the center-of-mass imparted to these ions via reaction 23. Figure 12 is a plot of P ($E^T_{rel}$) vs $E^T_{rel}$, which is determined by multiplying the value of $E_I$ for each point in Figure 11 by the ratio $M_{(CH3OH)n}/ M_{CH3O}$ to obtain a value for $E^T_{rel}$. The $P(E_I)$, which is equal to the $P(E^T_{rel})$, is then plotted at value of $E^T_{rel}$. The energy axis in Figure 12 is much larger than the energy axis in Figure 11; nevertheless, the average value of the recoil translational energy is small because most of the curves peak below 2.0 Kcal/mol.

The maximum translational energies observed in the clusters are also small. They vary from 2.5 to 7.6 Kcal/mol. The energy balance for the reaction is given by equation 24. It allows one to calculate the maximum $E^T_{rel}$ that can occur in each cluster.

$$\begin{aligned} &E_{h\nu} + E_{int}[(CH_3OH)_n] = \\ &\qquad E_{IP}(n) + E_{e^-} + E_{int}[H(CH_3OH)_{n-1}^{+}] + E_{int}[CH_3O] + E^T_{rel} \qquad (24) \end{aligned}$$

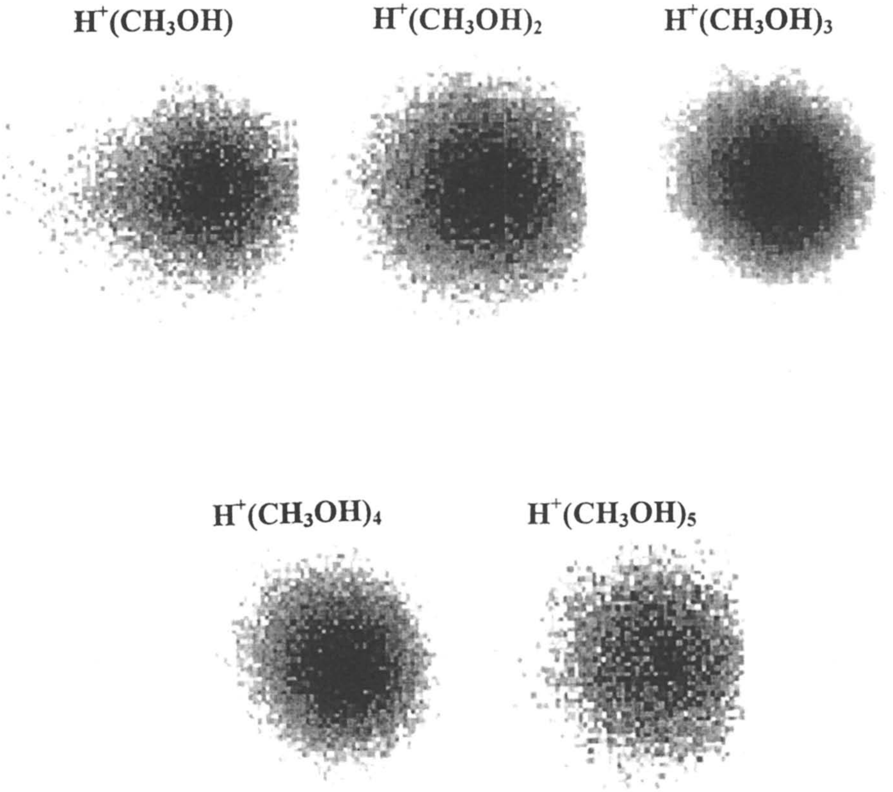

***Figure 10. Velocity images of protonated clusters of methanol produced in the 118 nm photolysis of clusters of $(CH_3OH)_n$ where n goes from n = 2 to 6. Note, the sharp edge on the right hand side of the image is due to edge of the MCP.***

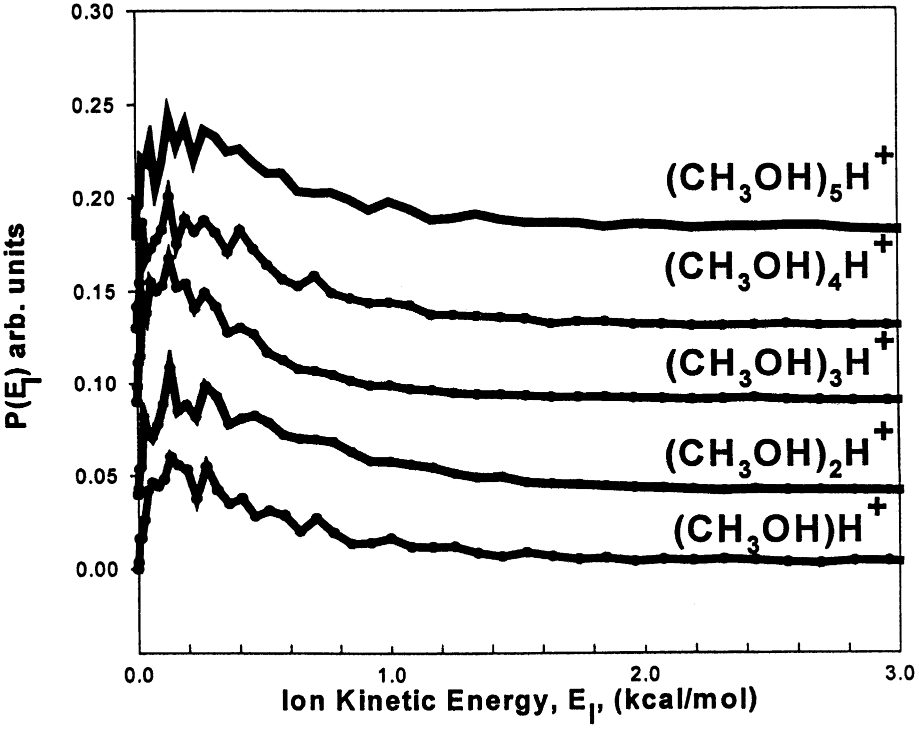

*Figure 11. Ion kinetic energy distributions of protonated clusters produced in the 118 nm photolysis of clusters of $(CH_3OH)_n$ where n goes from n = 2 to 6. Note, the energy only goes up to 3.0 kcal/mol.*

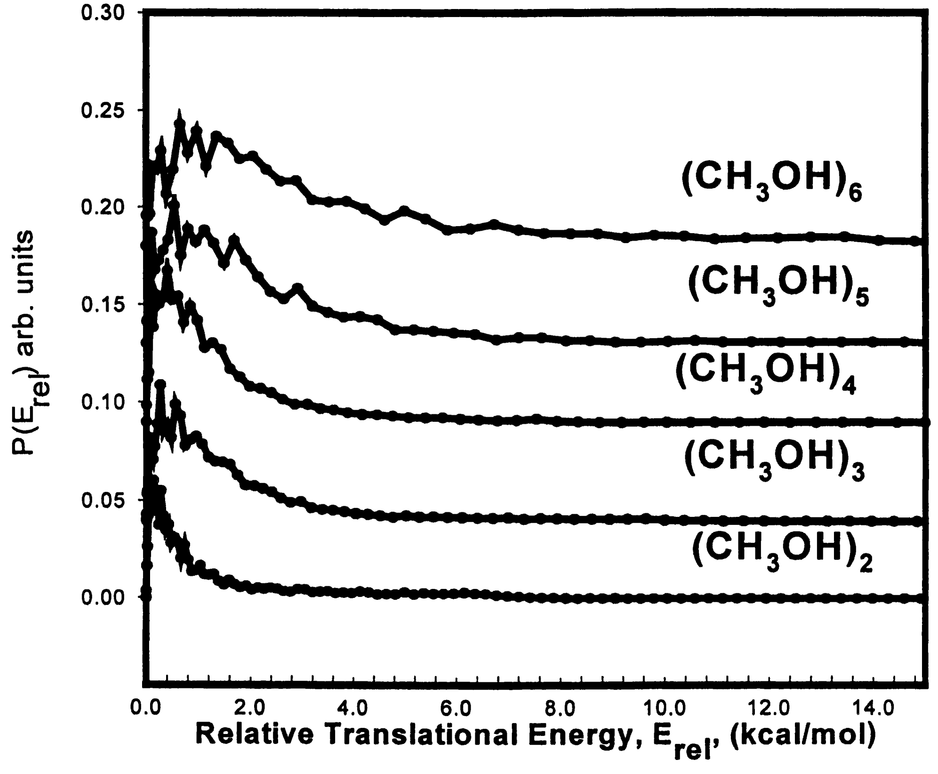

***Figure 12. Relative translational energy distributions of protonated clusters produced in the118 nm photolysis of $(CH_3OH)_n$ clusters where n goes from n = 2 to 6. Note the energy goes up to 14.8 kcal/mol. This assumes the following mechanism,***

$$(CH_3OH)_n + h\nu_{118.2nm} \rightarrow (CH_3OH)_n^{+*} + e^-$$

$$(CH_3OH)_n^{+*} \rightarrow H^+(CH_3OH)_{n-1} + CH_3O$$

In this equation, $E_{h\nu}$, is the energy of a 118 nm photon, $E_{IP}(n)$ is the IP of the n$^{th}$ cluster, $E_{int}[x]$, is the total internal energy of species x, and $E_{e-}$ is the kinetic energy of the recoiling electron. The internal energies of the reactant and the products are not known, but it will be assumed that they balance each other. The $E_{IP}(n)$ for each cluster can be calculated from the work of Cook et al. and the value of $E_{h\nu}$ is defined by the wavelength of the laser. Table 1 summarizes the results of the calculated maximum translational energy, $<^{max}E^{T}_{rel}(n)>_{cal}$ and the observed maximum translational energy, $<^{max}E^{T}_{rel}(n)>_{obs}$ for the clusters with various values of n. The difference between these two values, $\Delta E^{T}_{rel}$, must be the amount of energy that went into either the translational energy of the electron and / or the difference between the internal energies of the reactant and the products. A measurement of the translational energy of the photoelectrons would then be a measure of the internal energy of the clusters. If this is done in a seeded beam then the sum of the internal energy of the products can be determined because the internal energy of the original cluster should be small.

**Table 1. Calculated and Observed Maximum Translational Energies**

| n | $<^{max}E^{T}_{rel}(n)>_{cal}$ (kcal/mol) | $<^{max}E^{T}_{rel}(n)>_{obs}$ (kcal/mol) | $\Delta E^{T}_{rel}$ (kcal/mol) |
|---|---|---|---|
| 2 | 6.6 | 2.5 | 4.1 |
| 3 | 15.9 | 4.6 | 8.7 |
| 4 | 22.8 | 6.0 | 16.8 |
| 5 | 27.4 | 6.7 | 19.6 |
| 6 | 32.0 | 7.6 | 24.4 |

## Conclusions

The experiments reported in this paper illustrate how velocity imaging and a VUV laser can be used to study a variety of chemical reactions. Any reaction that produces an ion such as photoionization or ion pair production provides strong signals for these studies.

A new ion pair reaction, which produces the $C_2H_3^+$ ion, $H_2$ and $Br^-$, has been observed from the 118 nm photolysis of $C_2H_5Br$ for the first time. It has also been shown that another channel is present which probably results from the absorption of a second 355 nm photon. Ion pair production from the photodissociation of ethyl bromide clusters at 118 nm has also been observed. The images from clusters of ethyl bromide are isotropic, whereas the images from the monomers indicate that the ion pair production process is the result of a parallel transition. This switching from a parallel to isotropic dissociation probably occurs because of energy transfer in the cluster.

The photodissociation of allene at 118 nm at higher laser energies produces a $C_3H_3$ free radical and an H atom. Changes in the image size are clearly observed when this radical appears in the TOF flight spectra. This is strong evidence that velocity imaging is capable of measuring the very low recoil velocities associated with the heavier molecules when they lose a light atom or molecule such as an H atom.

The dissociation of methanol clusters that are present in the gas phase was also studied. These studies confirm earlier studies that showed that methanol clusters exist in the vapor phase above the liquid because of hydrogen bonding. It has been shown that very little of the available energy appears as relative translational energy, $E^T_{rel}$, of the protonated cluster and the $CH_3O$ fragment. None of the neutral fragments that should have been present in the system was observed. This may be due to poor Franck-Condon factors and/or lower probabilities for the detection of a neutral fragment. Experiments are continuing to determine what the ultimate sensitivity of this method for neutral fragments.

## Acknowledgements

W.M. Jackson, D. D. Xu, and R. Price wish to thank NASA Planetary Atmosphere Program for its support under grant number NASA-NAG5-4711and Chemistry Division of NSF under grant number NSF-CHE-9713929. K. McNesby thanks the US Army for its support. We also wish to acknowledge the many helpful conversations with Arthur Suits, Musahid Ahmed, and Darcy Peterka of Lawrence Berkeley Laboratories. David Chandler of Sandia National Laboratories also aided us in getting started in this field as well. We also would like to acknowledge the support of Sandia National laboratory for their loan of a turbomolecular pump. Finally, we thank Yutaka Matsumi of Hokkaido University for supplying the software that was used for converting images to speed distributions and for calculating the $\beta$ parameters.

## References

1. Chandler, D. W.; Houston, P. L. *J. Chem. Phys.* **1987**, 87, 1445-1447.
2. Eppink, A. T. J. B.; Parker, D. H. *Rev. Sci. Instrum.* **1997**, 68, 3477-3484.
3. Chang, B-Y.; Hoetzlein, R. C.; Mueller, J. A.; Geiser, J. D.; Houston, P. L. *Rev. Sci.Instrum.* **1998**, 69, 1665-1670.
4. Gentry, W. R. In *Atomic and Molecular Beam Methods*; Scoles, G., Ed.; ISBN 0-19-504280-8; Oxford University Press: New York, 1988; Vol. 1, pp 54 -82.
5. Kung, A. H., Young, J. F.; Harris, S. E. *Appl. Phys. Lett.* **1973**, 22, 301- 302
6. Jackson, W. M.; Price II, R. J.; Xu, D.D.; Wrobel, R. J.; Ahmed, M.; Peterka, D. S.; Suits, A. G. *J. Chem. Phys.* **1998**, 109, 4703-4706.
7. Sato, Y.; Matsumi, Y.; Kawaski, M. . *J. Phys. Chem.* **1995**, 99, 16307-16314.
8. Zare, R. N.; Herschbach, D. R. *Proc IEEE* **1963**, 51, 173- 182

9. Suto, K.; Sato, Y.; Reed, C. L.; Skorohodov, V.; Matsumi, Y.; Kawasaki, M. *J. Phys. Chem. A.* **1997**, 101,1222-1226.
10. Hepburn, J. B. *Chem. Soc. Rev.* **1996**, 25, 281-287.
11. Baltzer P.; Wannberg B.; Lundqvist M.; Karlsson L.; Holland D. M. P.; Macdonald M. A.; von Niessen, W. *Chem. Phys.* **1995**, 196, 551-567.
12. Woywod, C.; Domcke, W. *Chem. Phys.* **1992**, 162, 349-358.
13. Yang, Z. Z., Wang, L.S., Lee, Y. T., Shirley, D. A. Huang, S. Y.; Lester, W. A.; Jr. *Chem.Phys. Letters.* **1990**, 171, 9-13.
14. Jackson, W. M.; Mebel, A.M.; Lin, S. H.; Lee, Y. T. *J. Phys. Chem.* **1997**, 101, 6638-6646.
15. Mebel, A.M.; Jackson, W. M.; Chang, A. H. H.; Lin, S. H. *J. Am. Chem. Soc.* **1998**, 120, 5751-5763.
16. Inskeep, R. G.; Kelliher, I. M.; McMahon, P. E.; Sommers, B. G. *J. Chem. Phys.* **1958**, 28, 1033-1036.
17. Kretsemer, C. B.; Wiede, P. *J. Am. Chem. Soc.* **1954**, 76, 2579-2083.
18. Cook, K. D.; Jones, G. G.; Taylor, J. W. *Int. J. Mass Spectrom. Ion. Phys.* **1980**, 35, 273-292.
19. The NIST Chemistry WebBook, http://webbook.nist.gov/chemistry
20. Ryan, K. R.; Sieck, L. W.; Futrell, J. H. *J. Chem. Phys.* **1964**, 41, 111- 116
21. Sieck, L. W.; Abramson, F. B.; Futrell, J. H. *J. Chem. Phys.***1966**, 45, 2859- 2867
22. Harich, S.; Lin, J. J.; Lee, Y. T.; Yang, X. *J. Chem. Phys.***1999**, 111, 5-9.

## Chapter 8

# Rotational State Resolved Differential Cross–Sections for $O(^1D) + n\text{-}H_2 \rightarrow OH + H$

**X. Liu[1], J. J. Lin[1], S. Harich[1], and X. Yang[1-3]**

**[1]Institute of Atomic and Molecular Sciences, Academia Sinica, Taipei, Taiwan**
**[2]Department of Chemistry, National Tsing Hua University, Hsinchu, Taiwan**

Translational spectroscopy has been instrumental for the mechanistic understanding of elementary chemical reaction processes. Recently, Rydberg "tagging" time-of-flight (TOF) technique have been developed for hydrogen atom detection, which allows us to measure the H atom product TOF spectra with very high translational energy resolution and high sensitivity. The elementary bimolecular reaction, $O(^1D) + n\text{-}H_2 \rightarrow OH + H$, has been investigated at the state-to-state level using this technique. Rotationally resolved reactive differential cross sections have been measured for the $O(^1D) + H_2$ reaction for the first time. The experimental results in this work provide a solid test ground for a quantitative theoretical picture of this bench mark system for insertion mechanism.

## Introduction

Nascent product quantum state distributions in chemical reactions can now be measured routinely using many laser-based techniques such as laser-induced fluorescence (LIF), resonance-enhanced multiphoton ionization (REMPI) etc. For example, in the $O(^1D) + H_2 \rightarrow OH + H$ reaction, the OH radical products are frequently detected using LIF through the $A \leftarrow X$ transition. Quantum state distribution of nascent chemical products, however, only carries part of the product information in a molecular beam experiment. Information on the angular distributions of reaction products is at least as important to the understanding of the

---

[3]Corresponding author (e-mail: xmyang@po.iams.sinica.edu.tw)

In Imaging in Chemical Dynamics; Suits, A., et al.;
ACS Symposium Series; American Chemical Society: Washington, DC, 2000.

whole picture of reactions. In reality, quantum state resolved differential cross section measurements could provide the most detailed mechanistic information on a chemical reaction, and also the most stringent test for a quantitatively accurate theoretical picture for this process.

Product translational spectroscopy in various forms has been used to measure the product angular distributions and angular resolved product translational energy distributions in both unimolecular and bimolecular reaction processes. For example, the velocity mapping imaging technique[1], coupled with REMPI or single photon ionization, has been recently applied to the studies of both unimolecular and bimolecular reactions extensively (see other articles in this book). However, quantum-state resolved differential cross sections are hard to measure experimentally, to say the least. This is largely due to not only the limited translational energy resolution of various translational spectroscopic techniques but also the poor molecular beam conditions under which crossed molecular beam experiments are routinely carried out. Recent development of the H atom Rydberg "tagging" TOF technique[2] has provided us an extremely powerful tool for measurement of state resolved differential cross sections for both unimolecular and bimolecular reactions with unprecedented translational energy resolution and extremely high sensitivity. This technique has been applied successfully to the studies of the important benchmark reaction $H + D_2 \rightarrow HD + H$ recently[34] and many important unimolecular dissociation processes.[5] REMPI with velocity mapping imaging technique is another promising tool to measure state resolved differential cross sections for chemical reactions.

Since H atom products from chemical reactions normally do not carry any internal energy excitation with its first excited state at ~10 eV, the high resolution translational distribution of the H atom products directly reflects the quantum state distribution of its partner product. For example, in the crossed molecular beam studies of the $O(^1D)$ reaction with $H_2$,

$$O(^1D) + H_2 + E_{coll} \rightarrow OH(v, N) + H,$$

total energy and linear momentum should be conserved:

$$E_{avail}(O(^1D) + H_2) + E_{coll} = E_{int}(OH) + E_{trans}(OH) + E_{trans}(H)$$
$$m_{OH} E_{trans}(OH) = m_H E_{trans}(H),$$

where $E_{avail}$ is the total available energy for the reaction at zero collisional energy, while $E_{coll}$ is the collisional energy of the two reactants. $E_{avail}(O(^1D)+H_2)$ is already known exactly, and normally, in a crossed molecular beam condition, $E_{coll}$ is also very well defined. Therefore,

$$E_{int}(OH) = E_{avail} + E_{coll} - (1+m_H/m_{OH})\, E_{trans}(H)$$

Since the reaction available energy $E_{avail}$ and the collisional energy $E_{coll}$, are constants and already well known, the measured laboratory (LAB) H atom product translational energy ($E_{trans}(H)$) distribution can be easily converted into the center-of-mass (CM) OH product internal energy ($E_{int}(OH)$) distribution. With sufficient high translational energy resolution for the H atom product, the OH quantum state distribution can be determined for this photodissociation process by simply measuring the H atom product TOF spectra. OH product angular distribution can also be determined from the H atom product angular distribution since H and OH always run in opposite directions, i.e., $\theta_{OH} \equiv -\theta_H$ in the CM frame. In a crossed molecular beam study of a bimolecular reaction, the translational energy resolution is normally limited by the spread in the collisional energy rather than the intrinsic resolution of Rydberg tagging method itself. Therefore a crucial step to obtain high resolution TOF spectra of H atom products in a crossed beam study is to minimize the collisional energy spread and the internal energy distribution of the reactants. In the photodissociation, higher translational energy resolution can be achieved by detecting H atom products at the perpendicular direction of the molecular beam.

In this article, we will present our recent experimental results on the bimolecular reaction $O(^1D) + H_2 \rightarrow OH + H$ using the H atom Rydberg "tagging" TOF technique. Through these studies, detailed dynamical information can be extracted experimentally for this important system.

## Experimental Methods

H atom Rydberg "tagging" TOF technique was developed in the early 1990s by Welge and coworkers in Bielefeld.[2] The detailed experimental methods used to

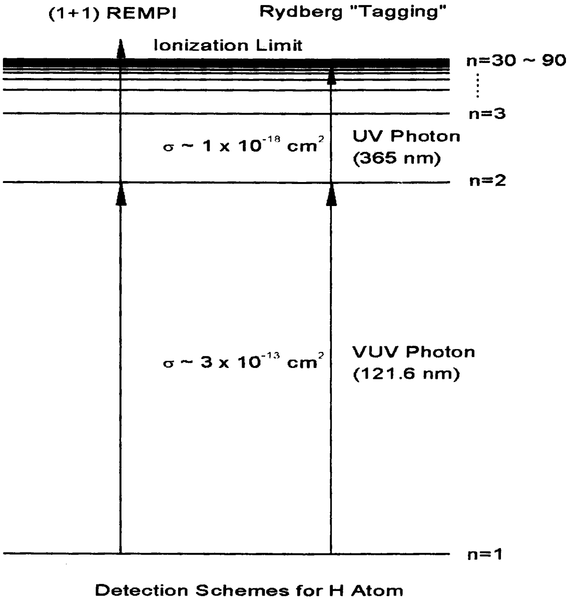

*Figure 1. Detection schemes for H atoms. Rydberg tagging technique is slightly different from the (1+1) REMPI detection scheme in which H atom products are directly ionized, while Rydberg tagging only pumps the H atom to the high Rydberg states.*

study the crossed beam H + $D_2 \rightarrow$ HD + H reaction have been described in great details before.[3] Very detailed descriptions of this technique used for studying molecular photodissociation can also be found in the Ref. 5. The central scheme of this technique is the two step efficient excitation (see figure 1) of the H atom to its high Rydberg levels (n = 25 ~ 90) without ionizing the H atom product directly, which is modified from the (1+1) REMPI technique. Figure 2 shows a spectrum of Rydberg transitions of the H atom from the n=2 level. These high Rydberg H atoms are known to be long lived to millisecond time scale in a small electric field (~20 V/cm). The enhancement of Rydberg H atom lifetimes in a small electric field is believed to be caused by mixing of *l* quantum number in the Rydberg H atom.[6,7] These long-lived neutral H atoms allow us to measure the time-of-flight spectrum of the neutral H atom chemical product with extremely high translational energy resolution (as high as 0.1 % in translational energy has been achieved). The neutral Rydberg H atoms are also quite easy to detect using field ionization. The extremely high translational energy resolution can be achieved by minimizing the physical sizes of the "tagging" region and the field ionization region which ionizes those Rydberg H atoms before reaching the multichannel plate (MCP) ion detector.

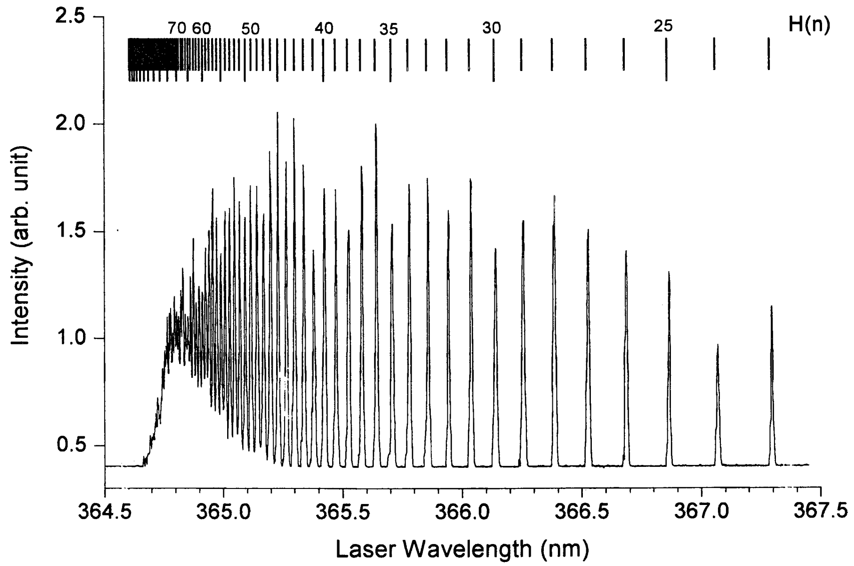

*Figure 2. H atom Rydberg transitions from the n = 2 level to the higher n states.*

The excitation of the ground state H atom product (n=1) is made by the following two step excitation scheme (see figure 1):

$$H\,(n=1) + h\nu\,(121.6\text{nm}) \rightarrow H(n=2) \qquad (1)$$

and

$$H(n=2) + h\nu\ (365\ nm) \rightarrow H(n{\sim}50) \qquad (2)$$

The 121.6 nm VUV light used in the first step excitation is generated using a two photon resonant ($2\omega_1$-$\omega_2$) four wave mixing scheme in the Kr gas cell. $2\omega_1$(212.5 nm) is resonant with the Kr (4p-5p) transition.[8] $\omega_1$ is generated by doubling a dye laser pumped by a Nd:YAG (355 nm) laser, while $\omega_2$ (845 nm) is the direct output of a dye laser pumped by the second harmonic of the same YAG laser. During the experiment, a few mJ of 212.5 nm and 845 nm laser light are generally used. The efficiency of the VUV generation can be enhanced by adding the Ar gas as the phase matching medium in about a 3: 1 ratio between Ar and Kr. By generating about 50 μJ of the 121.6 nm laser light, the first step can be easily saturated since this transition has a huge excitation cross section ($3.0 \times 10^{-13}$ $cm^2$). Following the first step VUV excitation, the H atom products is then sequentially excited to a high Rydberg state with n ≈ 50 using a 365 nm light, which is generated by doubling a dye laser pumped by the same YAG laser. These two excitation lasers have to be overlapped very well in space and time. The neutral Rydberg H atom then flies a certain TOF distance to reach a MCP detector with a fine metal grid (grounded) in the front. After passing through the grid, the Rydberg H atom products are then immediately field-ionized by the electric filed applied between the front plate of the Z-stack MCP detector and the fine metal grid. The signal received by the MCP is then amplified by a fast pre-amplifier, and counted by a multichannel scaler (MCS).

In the crossed beam study of the $O(^1D) + H_2 \rightarrow OH + H$ reaction, two parallel molecular beams ($H_2$ and $O_2$) were generated with similar pulsed valves. The $O(^1D)$ atom beam was produced by the photolysis of 157 nm of the $O_2$ molecule. The $O(^3P)$ atom is also generated, but plays not in the reaction with $H_2$. The $O(^1D)$ beam was then crossed at $90^0$ with the $H_2$ molecular beam. A small aperture is used to define the $O(^1D)$ beam between the $O_2$ and $H_2$ beams. The H atom products were detected using the Rydberg "tagging" TOF method with a rotatable MCP detector.

## Experimental Results

The reaction of $O(^1D) + H_2$ plays a significant role in atmospheric[9] and combustion chemistry.[10] The rate of this reaction has been found to be nearly gas kinetic.[11,12,13,14,15,16,17,18,19,20,21,22,23,24,25,26] This reaction is also a well-known bench mark system for an insertion type chemical reaction. Extensive experimental and theoretical studies have been carried out in order to elucidate the dynamics of this reaction.[27,28,29,30,31,32,33,34,35,36,37,38,39,40,41] Very recent experimental studies show that at the collision energy above ~1.8 kcal/mol, an elusive abstraction mechanism also becomes possible.[42,43,44] At energies below 1.8 kcal/mol, however, this reaction remains the most well known example of an insertion type reaction. Recently, we have studied this reaction using the H atom Rydberg tagging TOF technique. The experiment was carried out at collision energy of ~1.4 kcal/mol which is significantly below the 1.8 kcal/mol barrier for the abstraction mechanism inferred by previous experimental studies. Therefore this investigation would provide an ideal case for the pure insertion type reaction. The purpose of the experiment is to measure the rotationally resolved differential cross sections for this reaction to provide theoreticians a solid test ground for this model system. For the last few decades, experimental research on chemical reaction dynamics has provided extremely insightful information on mechanisms of a range of important chemical reactions. However, accurate measurements on fully rotational state resolved differential cross-sections have been carried out only for a couple of reactions so far: $H + D_2 \rightarrow HD + H$ [3] and $F + H_2 \rightarrow HF + H$ [45,46,47] due to the difficulties and the many limitations in this type of measurements. These reactions are probably the most thoroughly studied systems so far, which have provided excellent examples for understanding the reaction dynamics at the state-to-state level. Through the studies of $O(^1D) + H_2 \rightarrow OH + H$ in this work, we hope to establish this reaction as the true model system for the insertion type reaction at this low energy, and provide a solid test ground for many concepts involving the insertion type at the state-to-state level.

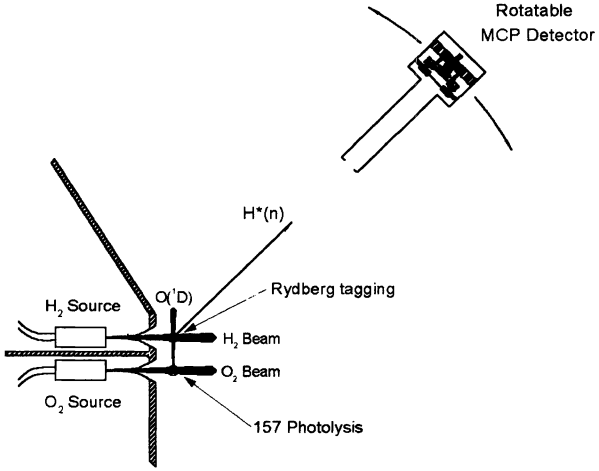

*Figure 3. A simple schematic of the experimental setup for studying the crossed beam* $O(^1D) + H_2 \rightarrow OH + H$ *reaction.*

Figure 3 shows a simple schematic of the experimental setup used for the crossed molecular beam studies of the $O(^1D) + H_2 \rightarrow OH + H$ reaction. As described above, the $O(^1D)$ beam is generated by photolysis of $O_2$ in a molecular beam using a 157 nm $F_2$ laser. This process produces one $O(^1D)$ atom, one $O(^3P)$ atom which has very small reaction cross-section with $H_2$. The $O(^1D)$ beam is then crossed with a normal $H_2$ molecular beam which is produced by a pulsed valve cooled down to liquid nitrogen temperature. This is to reduce the energy uncertainties of the collision energy by minimizing the beam velocity spread. The Newton diagram of the reaction performed in this experiment is shown in figure 4. The velocity of the $O(^1D)$ beam has been measured to be 2050m/s, while the velocity of the $H_2$ beam is 1350 m/s. Normal hydrogen ($n$-$H_2$) is used in this experimental study. It contains both $p$-$H_2$ and $o$-$H_2$ with a ratio of $p$-$H_2$ (mainly J=0): $o$-$H_2$ (mainly J=1) = 1:3 in the molecular beam. The energetic limits of the H atom products that correspond to the different OH vibrational states are described by the different circles in the Newton diagram.

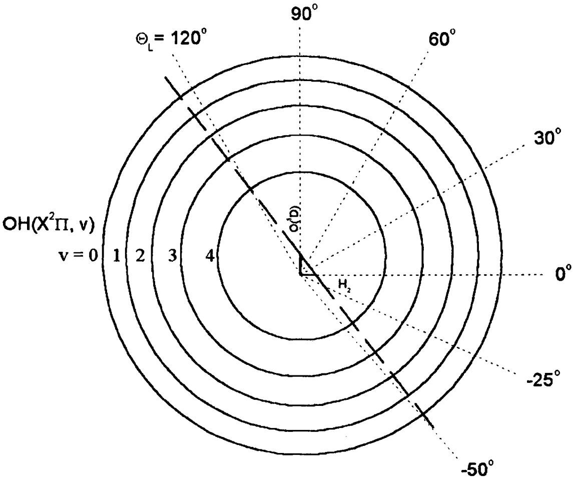

*Figure 4. The Newton diagram for the crossed beam $O(^1D) + H_2 \rightarrow OH + H$ reaction.*

Time-of-flight spectra of the H atom products have been measured at many laboratory angles. Figure 5 shows the TOF spectra at three laboratory angles: $\theta_L$ = 117.5°, 90°, -50°. The laboratory angles at which the TOF spectra are shown are indicative of forward (-50°), backward (117.5°) and sideward scattering (90°). From figure 5, it is quite clear that that these spectra consist of a lot of sharp structures. These sharp structures clearly correspond to the OH quantum state resolved products, indicating that these measured TOF spectra have indeed achieved rotational state resolution for the $O(^1D) + n\text{-}H_2 \rightarrow OH + H$ reaction. From the TOF spectra, the product translational energy distributions at different center-of-mass (CM) scattering angles of the title reaction can be obtained. Figure 6 shows the translational energy distributions obtained from the experimental measured TOF spectra. Since the center-of-mass angles are not constant for a certain laboratory angle at different product (H) velocity (see Newton diagram in figure 4), each of the translational energy distributions obtained from the three different laboratory angles contains information in a range of CM angles. However, the three translational energy distributions still carry the basic information on forward, backward and sideward

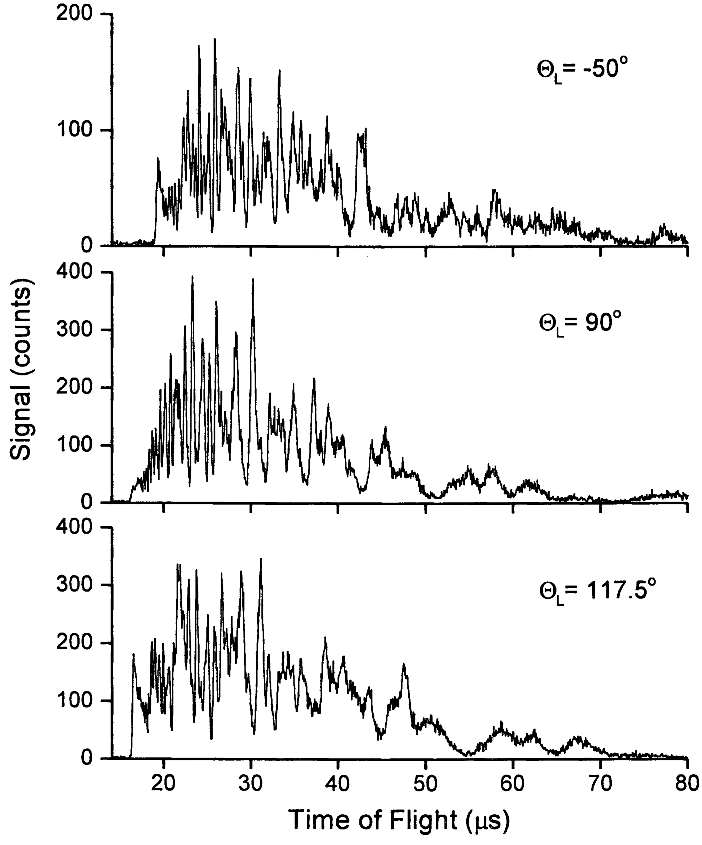

*Figure 5. The time of flight spectra at three different laboratory angles for the H atom products obtained from the crossed beam $O(^1D) + H_2 \rightarrow OH + H$ reaction using the Rydberg tagging TOF technique.*

scattering. From these distributions, it is hopeful that information on ro-vibrational state distributions of the OH product can be obtained from reasonable simulations. The low rotational OH(X, v=0) products, which correspond to the cutoff energy near

46 kcal/mol, are clearly more pronounced at the forward and backward directions than the sideward scattering. The overall features at backward and forward direction scattering are more similar in comparison with the sideward scattering.

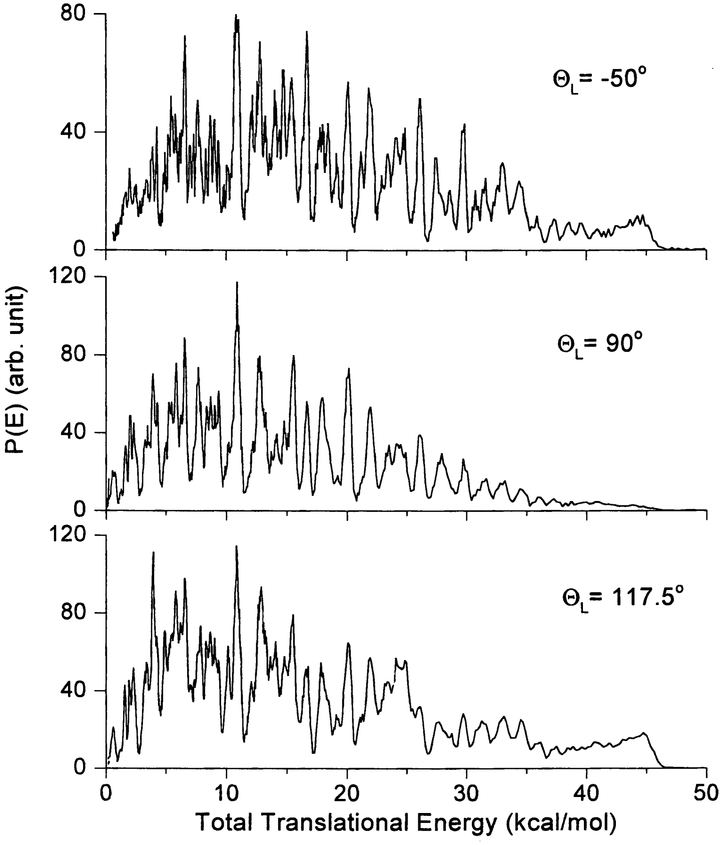

*Figure 6. The total product translational energy distributions converted from the TOF spectra shown in figure 5.*

From modeling of the H detection scheme, angular dependent detection efficiencies can be calculated exactly. Therefore total product angular distribution can be determined by including a correction factor. Figure 7 shows the total H atom product angular distribution. It is quite clear that the total product angular distribution is essentially forward and backward symmetric, which is consistent with previous experimental studies of this at low collisional energies. The detailed symmetry between the forward and the backward scattering in state-to-state details is, however, not so clear. There are, however, marked differences between the forward

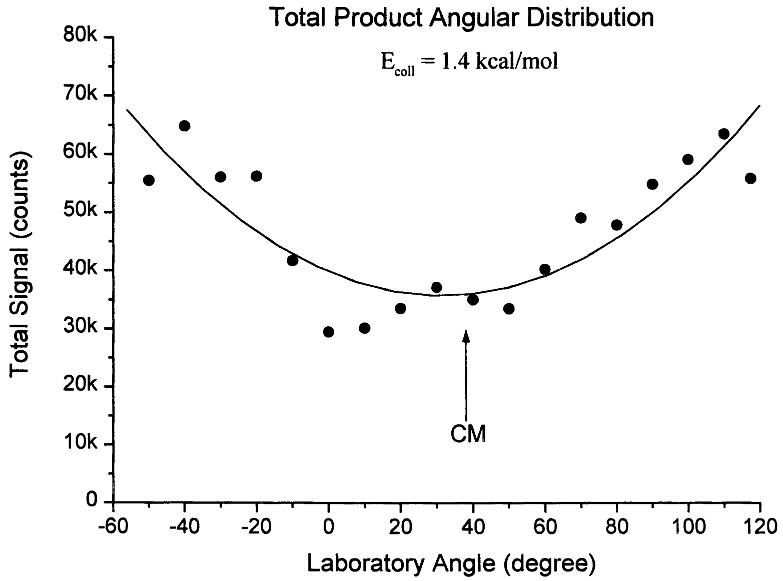

*Figure 7. Angular distribution of total hydrogen atom reaction products.*

and backward H atom kinetic energy distributions or OH quantum state distributions. This is definitely an interesting experimental observation. Another clear observation is that the low rotational excited OH products are more pronounced at the backward and forward directions than at the sideward direction (see figure 6). The angular distribution of the low rotationally excited OH($^2\Pi$, v=0) products is shown in figure 8, which is clearly different from the total product angular distribution. The implications of these interesting results are not immediately clear. It is necessary to point out here that the data presented here are quite preliminary, more detailed analyses are required in order to gain a much clearer picture. Nevertheless, an excellent example has been provided here for the quantum state resolved reactive scattering for an important insertion type reaction. Through more thorough experimental and theoretical investigations, quantitative understandings of this important reaction will be possible.

## Concluding Remark

In this article, we have shown an excellent example of quantum state resolved reactive scattering studies on the important $O(^1D) + H_2 \rightarrow OH + H$ reaction using the

H atom Rydberg "tagging" TOF technique. Rotational state resolved differential cross-sections have been measured for this reaction for the first time. Detailed dynamical information can be learned from the well-controlled experimental investigations. Interesting dynamical phenomena have been observed. The experimental results obtained in this work provide an excellent test ground for theoretical studies of this prototype insertion reaction.

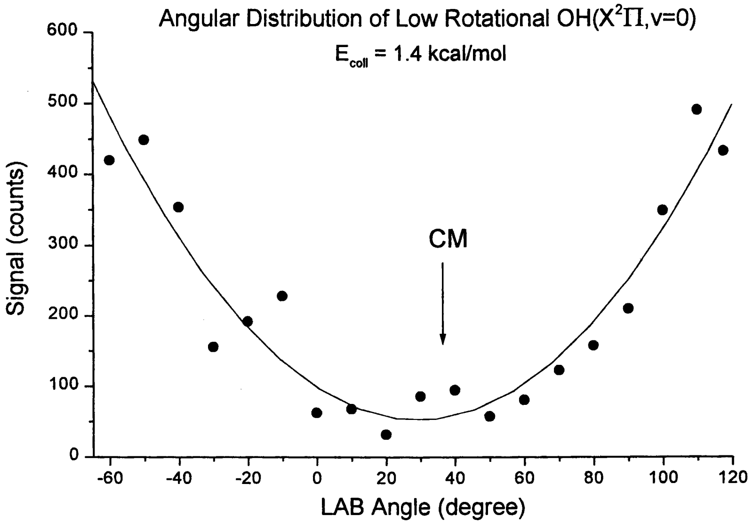

*Figure 8. Angular distribution of H atom products corresponding to low rotationally excited OH($X^2\Pi$, v=0) products.*

## Acknowledgments

This work is supported by the National Science Council, Academia Sinica, and the China Petroleum Company. We also like to thank Prof. Y. T. Lee, Prof. K. Liu and Prof. G. C. Schatz for the helpful discussions.

## References

---

1. Eppink, A., and Parker, D. H., Rev. Sci. Instr. 1997, 68, 3477-3484.
2. Schnieder, L., Meier, W., and Welge, K. H., Ashfold, M. N. R., and Western, C. M., J. Chem. Phys. 1990, 92, 7027-7037.
3. Schnieder, L., Seekamp-Rahn, K., Borkowski, J., Wrede, E., Welge, K. H.,

Aoiz, F. J., Barares, L., D'Mello, M. J., Herrero, V. J., Saez Rabanos, V., and Wyatt, R. E., Science 1995, 269, 207-210.

4. Schnieder, L., Seekamp-Rahn, K., Wrede, E., and Welge, K. H., J. Chem. Phys. 1997, 107, 6175-6195.
5. Ashfold, M. N. R., Mordaunt, D. H., and Wilson, S. H. S., Advances in Photochemistry, Neckers, D. C., Volman D. H., and Bunau, G. v., Eds; John Wiley & Sons, Inc, 1996, vol. 21, p217
6. Chupka, W. A., J. Chem. Phys. 1993, 98, 4520-4530.
7. Wolde, A. ten., Noordam, L. D., Lagendijk, A., Van Linden, H. B., Heuvell, van den, Phys. Rev. A 1989, 40, 485.
8. Marangos, J. P., Shen, N., Ma, H., Hutchinson M. H. R., and Connerade, J. P., J. Opt. Soc. Am. B 1990, 7, 1254.
9. Anderson, G., Ann. Rev. Phys. Chem. 1987, 38, 489, and references therein.
10. Dixon-Lewis, G., and Williams, D. J., Comprehensive Chem. Kinet. 1977, 17, 1.
11. Paraskevopoulos, G., Cvetanovic, R. J., J. Am. Chem. Soc. 1969, 91, 7572-7577.
12. Donovan, R. J., Husain, D., Kirsch, L. J., Chem. Phys. Lett. 1970, 6, 488.
13. Heidner III, R. F., Husain, D., Int. J. Chem. Kinet. 1973, 5, 819-831.
14. Gauthier; M. J. E., and Snelling, D. R., J. Photochem. 1975, 4, 27.
15. Stief, L. J., Payne, W. A., Klemm, R. B., J. Chem. Phys. 1975, 62, 4000-4008.
16. Tully, J. C., J. Chem. Phys. 1975, 62, 1893-1898.
17. Davidson, J. A., Sadowski, C. M., Schiff, H. I., Streit, G. E., Howard, C. J., Jennings, D. A., Schmeltekopf, A. L., J. Chem. Phys. 1976, 64, 57-62.
18. Davidson, J. A. H. I. Schiff, H. I., Streit, G. E., McAfee, J. R., Schmeltekopf, A. L., and Howard, C. J., J. Chem. Phys. 1977, 67, 5021-5025.
19. Wine, P. H., Ravishankara, A. R., Chem. Phys. Lett. 1981, 77, 103-109.
20. Pravilov, A. M., Pauk, V. N., Ryabov, S. E., Kinet. Catal. 1981, 22, 1109.
21. Ogren, P. J., Sworski, T. J., Hochanadel, C. J., and Cassel, J. M., J. Phys. Chem. 1982, 86, 238-242.
22. DeMore, W. B., Sander, S. P., Golden, D. M., Molina, M. J., Hampson, R. F., Kurylo, M. J., Howard, C. J., Ravishankara, A. R., Chemical kinetics and photochemical data for use in stratospheric modeling. Evaluation number 9, JPL Publication 90-1, Pasadena, CA., 1990, p1.
23. Atkinson, R., Baulch, D. L., Cox, R. A., Hampson, Jr., R. F., Kerr J. A., and Troe, J., Evaluated kinetic and photochemical data for atmospheric chemistry. Supplement IV. IUPAC subcommittee on gas kinetic data evaluation for atmospheric chemistry, J. Phys. Chem. Ref. Data 1992, 21, 1125-1568.
24. Matsumi, Y., Tonokura, K., Inagaki, Y., Kawasaki, M., J. Phys. Chem. 1993, 97, 6816-6821.
25. Koppe, S., Laurent, T., Naik, P. D., Volpp, H.-R., Wolfrum, J., Arusi-Parpar, T., Bar, I., and Rosenwaks, S., Chem. Phys. Lett. 1993, 214, 546-552.
26. Laurent, T., Naik, P. D., Volpp, H.-R., Wolfrum, J., Arusi-Parpar, T., Bar, I., and Rosenwaks, S., Chem. Phys. Lett. 1995, 236, 343-349.

27. Whitlock, P. A., Muckerman, J. T., and Fisher, E. R., J .Chem. Phys. 1982, 76, 4468-4489.
28. Schinke, R., and Lester, Jr., W. A., J. Chem. Phys. 1980, 72, 3754-3766.
29. Ransome, S. W., and Wright, J. S., J. Chem. Phys. 1982, 77, 6346-6348.
30. Kuntz, P. J., Niefer, B. I., and Sloan, J. J., J. Chem. Phys. 1988, 88, 3629-3637.
31. Schatz, G. C., Paioannou, A., Pederson, L. A., Harding, L. B., Hollebeck, T., Ho, T. –S., and Rabitz, H., J. Chem. Phys. 1997, 107, 2340-2350.
32. Butler, J. E., Macdonald, R. G., Donalson, D. J., and Sloan, J. J., Chem. Phys. Lett. 1983, 95, 183-188.
33 Butler, J. E., Jursich, G. M., Watson, I. A., and Wiesenfeld, J. R., J. Chem. Phys. 1986, 84, 5365-5377.
34. Buss, R. J., Casavecchia, P., Hirooka, T., Sibener, S. J., and Lee, Y. T., Chem. Phys. Lett. 1981, 82, 386-391.
35 Tsukiyama, K., Katz, B., and Bersohn, R., J. Chem. Phys. 1985, 83, 2889-2893.
36. Matsumi, Y., Tonokura, K., Kawasaki, M., and Kim, H. L., J. Phys. Chem. 1992, 96, 10622-10626.
37. Fritzcharles M. S., and Schatz, G. C., J. Phys. Chem. 90, 3634-3640.
38. Dunne, L. J., Chem. Phys. Lett. 1989, 158, 535-539.
39. Alexander, A. J., Aoiz, F. J., Brouard, M., and Simons, J. P., Chem. Phys. Lett. 2996, 256, 561-568.
40. Badenhoop, K., Koizumi, H., and Schatz, G. C., J. Chem. Phys. 1989, 91, 142-149.
41. Peng, T., Zhang, D. M., Zhang, J. Z. H., and Schinke, R., Chem. Phys. Lett. 1996, 248, 37-42.
42. Che, D.-C., and Liu, K., J. Chem. Phys. 1995, 103, 5164-5167.
43. Hsu, Y. T., and Liu, K., J. Chem. Phys. 1997, 107, 1664-1667.
44. Hsu, Y.-T., Wang, J.-H., and Liu, K., J. Chem. Phys. 1997, 107, 2351-2356.
45. Neumark, D. M., Wodtke, A. M., Robinson, G. N., Hayden, C. C., and Lee, Y. T., J. Chem. Phys. 1985, 82, 3045-3066.
46. Neumark, D. M., Wodtke, A. M., Robinson, G. N., Hayden, C. C., and Lee, Y. T., J. Chem. Phys. 1985, 82, 3067-3077.
47. Faubel, M., Martinez-Haya, B., Rusin, L. Y., Tappe, U., Toennies, J. P., Aoiz, F. J., and Banares, L., Chem. Phys. 1996, 207, 227-243.

## Chapter 9

# Ion Imaging in Surface Scattering

**M. Maazouz[1], J. R. Morris[1, 2], and D. C. Jacobs[1]**

[1]**Department of Chemistry and Biochemistry,**
**University of Notre Dame, Notre Dame, IN 46556**
[2]**Department of Chemistry, Virginia Polytechnic Institute**
**and State University, Blacksburg, VA 24061**

Hyperthermal energy collisions between gas-phase molecular ions and solid surfaces are studied with a novel ion imaging detector that simultaneously records the mass, velocity, and scattering angle of product ions. Image processing techniques are employed to identify, in real time, individual ions appearing within each video frame. Representative ion/surface systems are presented to demonstrate how imaging techniques can be used to extract dynamical information about energy transfer, charge transfer, dissociation, and atom-abstraction processes.

## Introduction

The reaction of hyperthermal energy ions with surfaces is important to a wide variety of applications, e.g., plasma processing in the microelectronics industry, space flight in low-earth orbit, and mass spectrometry. Hyperthermal ions with translational energies ranging from $10^0$ - $10^3$ eV can access reaction pathways that are closed to reagents under thermal conditions. Fundamental processes commonly occurring during ion/surface scattering are energy transfer, electron transfer, dissociative scattering, atom abstraction, sputtering, and ion implantation. In an effort to characterize the detailed dynamics associated with these processes, experiments are performed to probe the atomic motion of the ions as they approach, interact, and scatter from the surface. Novel instrumental techniques are required to detect the scattered products (electrons, neutrals, and ions of various masses) and to resolve their angular and velocity distributions. Scattering data along with theoretical simulations can provide a vivid picture of the complex mechanisms associated with hyperthermal energy gas/surface reactions.

A number of research groups have developed and applied ion detectors with energy-, mass-, and/or angular-resolution in an effort to carefully study ion/surface scattering. Heiland and coworkers measure the time-of-flight distributions of scattered atomic and molecular ions impinging on single-crystal surfaces at keV energies.(*1*) The Kleyn group has utilized an electrostatic sector in conjunction with time-of-flight methods to study the angle-resolved kinetic energy distributions resulting when alkali ions and small molecular ions are scattered from surfaces.(*2, 3, 4*) Akazawa and Murata have utilized a rotatable mass-spectrometer to determine the angular distributions of products in the scattering of $N_2^+$, $CO^+$ and $CO_2^+$ from a Pt(100) surface.(*5, 6*) Cooks and coworkers employed a rotatable hybrid, tandem mass spectrometer of the BEEQ configuration (B, magnet analyzer; E, electrostatic analyzer (ESA); Q, quadrupole mass filter) to study reactions of polyatomic molecules with organic surfaces.(*7*) Winograd combined laser ionization methods with ion-imaging techniques to study the desorption of neutral particles under ion bombardment.(*8*)

Although these pioneering experiments successfully adapted many techniques that were originally developed within the gas-phase dynamics community, the complexity of gas/surface interactions limited researchers from obtaining the detailed dynamics that were routinely achieved in gas-gas scattering experiments. Furthermore, investigations into ion-surface reactions below 100 eV are scarce because of technical difficulties in preparing intense, collimated ion beams. In an attempt to bridge this gap, we have developed an ion/surface scattering apparatus that combines resonance-enhanced multiphoton ionization (REMPI), to prepare an incident beam of state-selected ions, with an ion imaging detector for collecting scattered ions.(*9*)

Ion imaging in gas-phase photodissociation was first employed by Chandler and co-workers to collect two-dimensional images of state-selected photofragments.(*10, 11*) In the surface science community, ion imaging has been used to measure the angular and/or velocity distribution of ions desorbed under electron/photon impact.(*12, 13*) Rabalais developed scattering and recoiling imaging spectroscopy (SARIS) as an analytical tool to accurately assign the structure of adsorbates on surfaces.(*14*) Ion imaging is complementary to time-of-flight methods in that the former records a spatial distribution at one point in time, while the latter records the temporal distribution at one point in space. However, ion imaging detectors generally have a larger solid angle of collection, and they simultaneously record velocity distributions for a wide series of scattering angles.

This chapter introduces a unique two-dimensional velocity, ion-imaging detector specifically designed for surface scattering experiments. In these experiments, one measures the fraction of incident ions which emerge from the surface having a particular mass, velocity, and scattering angle. Image processing algorithms are applied to the data in real-time to identify individual ions within each video frame. Results from various ion/surface systems are presented here to illustrate the capabilities of the ion-imaging detector and to show the type of dynamical information which can be obtained from its use.

## Experimental Design

Scattering is performed in an ultrahigh vacuum chamber equipped with a source of state-selected ions, ion transport optics, a sample manipulator, an ion imaging detector, and standard surface science tools.(*9*) The ion source consists of a differentially-pumped molecular beam crossed by focused pulsed laser. A 20-Hz frequency-doubled, Nd:YAG-pumped dye laser provides 6-ns, tunable ultraviolet light pulses for REMPI. The resulting packets of state-selected ions are accelerated by electrostatic optics, mass filtered, and decelerated before striking the surface.

Both incident and scattered ions are monitored using an ion imaging detector (flyswatter) with near single-ion collection efficiency.(*15*) Figure 1 illustrates the configuration of the flyswatter relative to the final ion transport optics and the surface. The detector's ion optics have been improved since publication of the original design in Ref. 14. Figure 2a provides a cross-sectional view detailing the current arrangement of elements in the flyswatter detector. The flyswatter consists of a normally grounded repeller plate that runs parallel to a permanently grounded grid. The incident ions pass between the repeller and the grid before surface impact, and product ions traverse through this region after scattering from the surface. At a predetermined 'swat delay' relative to the laser trigger, a ~1000 V pulse, of equal polarity as the ions to be detected, is placed on the repeller plate, and a ~1000 V pulse, of opposite polarity, is placed on the flight tube. This action accelerates the ions in a direction normal to the plates while preserving their spatial distribution. After two stages of acceleration, the ions drift through a field-free flight tube before being accelerated into a pair of channel electron multiplier array (CEMA) plates. The 40-mm diameter, image-quality CEMA plates (Galileo) transform an incident ion into ~$10^7$ electrons. These secondary electrons accelerate toward a phosphor screen (Kimball Physics), biased +4 kV relative to the rear CEMA plate. The resulting burst of light (< 300 μm diameter) is captured by a charged coupled device (CCD) camera. The images are sent to a frame grabber board located inside a Macintosh G3 computer, where they are digitized, processed, and stored for analysis.

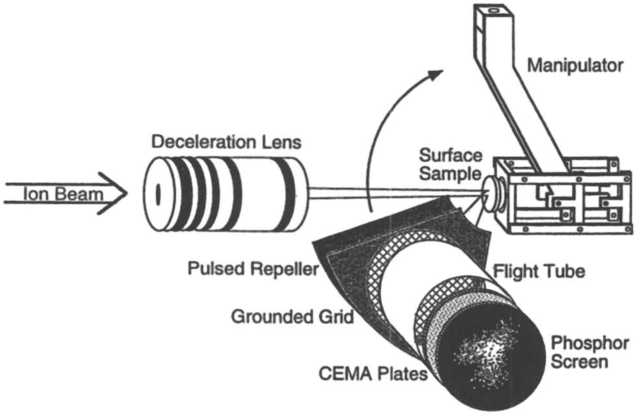

*Figure 1. A schematic of the ion imaging detector (flyswatter). The ion beam exits the Menzinger deceleration lens and is directed toward the surface sample manipulator. Rotation of the detector about the surface increases the range of in-plane acceptance angles to ±55°. (Reproduced with permission from reference 15. Copyright 1992 American Institute of Physics)*

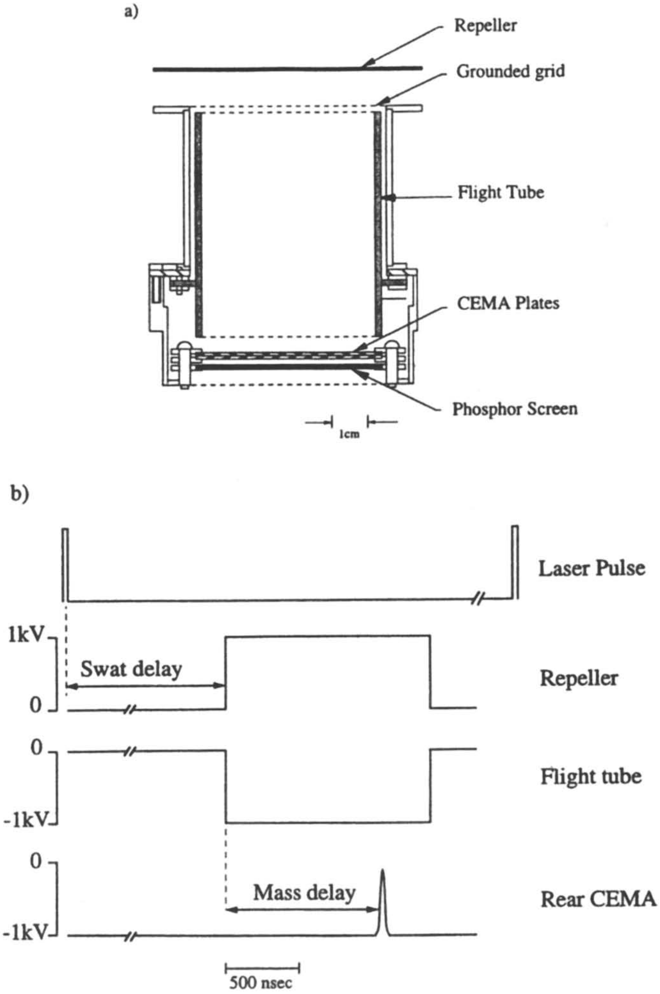
a)
Repeller
Grounded grid
Flight Tube
CEMA Plates
Phosphor Screen
1cm
b)
Laser Pulse
1kV
Swat delay
0
Repeller
0
-1kV
Flight tube
0
Mass delay
-1kV
Rear CEMA
500 nsec

*Figure 2. a) An assembly drawing of the flyswatter detector. b) Sequence of voltage pulses applied to the flyswatter optics.*

Ions of different mass will experience different flight times through the detector. Lighter ions will have a larger velocity than heavier ions upon acceleration into the flight tube; hence, lighter ions will arrive at the CEMA plates earlier in time. The flyswatter exploits this idea to achieve mass-resolution. Wiley and McLaren developed a set of focusing conditions to compensate for the distribution of initial ion positions between the repeller and the grid when the swat pulse fires.(*16*) More advanced optimizations can reduce the broadening associated with the dispersion of initial ion velocities along the direction normal to the repeller.(*17*) By gating the CEMA plates, ions of only one particular mass are allowed to contribute to the resulting image. The pair of CEMA plates are simmered at 1100 VDC. At a preset 'mass delay' relative to the 'swat pulse' on the repeller, an additional 900 V pulse (Directed Energy, Inc.) of 25 ns duration is applied to the rear CEMA plate. During the 'mass pulse', the CEMA plates are biased with a total of 2000 V, and virtually every ion which impacts the CEMA plates produces a spatially localized electron cascade event. In contrast, ions that strike the CEMA plates before or after the mass pulse are amplified with negligible gain, because the CEMA plates have only a 1100 V bias. Consequently, images recorded by the slow, 30-Hz CCD camera represent the spatial distribution of mass-filtered ions recorded at a precise swat delay relative to the initial laser pulse. Figure 2b illustrates the overall pulse sequence applied to the flyswatter optics. Once the flight time, $t_1$, corresponding to detection of ions having mass, $m_1$, is known, any peak, $t_2$, in the time-of-flight spectrum can be accurately assigned to an absolute mass, $m_2$, by the relation:(9)

$$m_2 = m_1\left(\frac{t_2}{t_1}\right)^2 \tag{1}$$

Geometrical constraints must also be considered in the overall analysis. The solid angle of collection for the imaging detector is defined by acceptance angles of ±28° (in-plane) and ±7° (out-of-plane). This corresponds to a collection efficiency of approximately 3.6% of 2π steradians. The detector is mounted on an 8" O.D. rotatable platform (Thermionics). In the most common configuration, both the incident ion beam and the detector lie along the surface normal. Rotation of the detector about the surface extends the range of in-plane acceptance angles to ±55°. In addition, an azimuthal rotation of the surface sample allows for product ion collection within any crystallographic scattering plane.

The critical parameters in operating the flyswatter are the voltage pulse polarities, and the swat and mass delays. The incident ion packet can be detected if the repeller is fired shortly after the ions exit the Menzinger lens and before they leave the detection region. An image of the incident ion packet provides information regarding the spatial integrity of the ion beam as well as a quantitative measure of the number of incident ions. Figure 3 shows three ion images, recorded at successive swat delays, of the incident ion packet as it approaches the surface. For later swat delays, the incident ions have already impacted the surface, and scattered product ions can be detected. Positive and negative scattered ions are distinguished by the polarity of the voltages applied to the repeller pulse, the flight-tube pulse, and the CEMA front plate. Figure 4 shows an image of scattered positive ions recorded at a swat delay of 30 μs. The entire velocity distribution of scattered products is measured by collecting mass-filtered images at a few different swat delays beginning with the time that scattered ions first reach the detector through the time that the slowest ions reach the detection region. Reducing ion images, recorded at various swat delays, to a velocity distribution is described in the "Velocity Analysis" Section below. At periodic intervals during scattering experiments, the swat and mass delays are set to record an image of the incident ion packet. The integrated intensity of the ion packet image is directly proportional to the number of ions incident on the surface, and this quantity is used to normalize the scattered product distributions. The relative ion yield of a given scattered product is calculated as the number of collected product ions, integrated over all velocities within the angular range of the detector, divided by the number of incident ions.

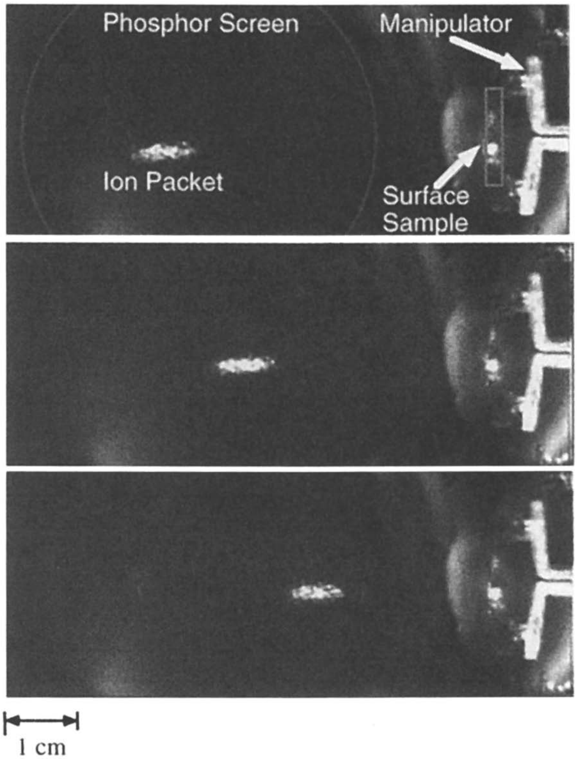
Phosphor Screen
Manipulator
Ion Packet
Surface Sample
1 cm

*Figure 3. Image of incident NO ions approaching the surface. The manipulator, surface sample, and phosphor screen are marked. Swat delays are (a) 20.0 μs, (b) 21.0 μs, and (c) 22.0 μs.*

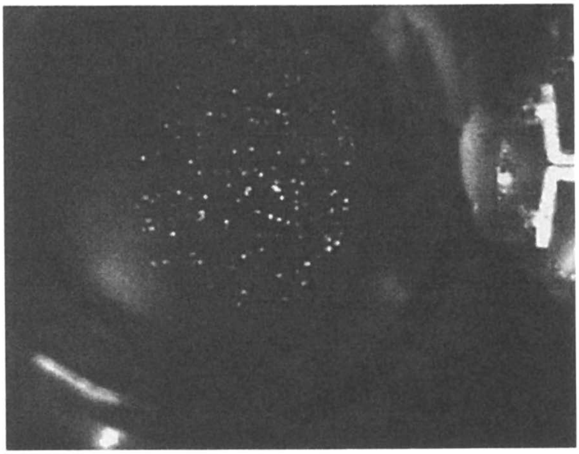

*Figure 4. Image of scattered NO ions at a swat delay of 30 μs.*

## Image Analysis

The images appearing on the phosphor screen are viewed through a standard vacuum window, 25 cm away. A CCD camera (NEC TI-324A) records the image, and a frame grabber board (National Instruments PCI-1408), resident in a Macintosh G3 computer, digitizes the image for analysis. Frame integration on the water-cooled CCD chip is an efficient method to reduce the average amount of dark counts, readout noise, and bit noise associated with frame-grabber digitization. A computer-interfaced timing circuit synchronizes image capturing to the 20-Hz pulsed-laser system. The timing circuit initiates frame integration on the CCD chip and provides an external trigger pulse for the frame grabber board when the CCD camera is ready to transmit its image after a selected number of laser shots (typically 5 - 40). The frame grabber digitizes an entire video frame in 1/30 s and the process of frame-integration on the CCD chip is repeated while the computer processes the last acquired image.

The image analysis software is written in National Instruments' graphical-programming language, LabVIEW–IMAQ. The frame-grabber board passes an 8-bit raw image to the LabVIEW acquisition program. The software converts the 8-bit image to a 16-bit image, subtracts a background image recorded previously, and filters the difference image before thresholding. The table below shows the 9 x 9 Kernel filter that is applied to the image.

**Table I. Kernel for filtering Particles**

| | | | | | | | | |
|---|---|---|---|---|---|---|---|---|
| 0 | 0 | 0 | -1 | -1 | -1 | 0 | 0 | 0 |
| 0 | -1 | -1 | -3 | -3 | -3 | -1 | -1 | 0 |
| 0 | -1 | -3 | -3 | -1 | -3 | -3 | -1 | 0 |
| -1 | -3 | -3 | 8 | 12 | 8 | -3 | -3 | -1 |
| -1 | -3 | -1 | 12 | 20 | 12 | -1 | -3 | -1 |
| -1 | -3 | -3 | 8 | 12 | 8 | -3 | -3 | -1 |
| 0 | -1 | -3 | -3 | -1 | -3 | -3 | -1 | 0 |
| 0 | -1 | -1 | -3 | -3 | -3 | -1 | -1 | 0 |
| 0 | 0 | 0 | -1 | -1 | -1 | 0 | 0 | 0 |

The filter has the effect of amplifying the signal from ions, which illuminate 5 - 9 contiguous pixels, and reducing the intensity of individual hot pixels, which represent background noise. Figure 5a shows an image after background subtraction, and Fig. 5b shows the same image after the Kernel filter has been applied. The filter clearly distinguishes individual ions that are more than 600 μm apart. Ions of different intensity in Fig. 5a appear more equitable in Fig. 5b. The acquisition software then converts the 16-bit filtered image back to an 8-bit image to expedite further processing. A particle-detection routine is applied to the filtered image to identify individual ions. The criterion for an ion is that four or more contiguous pixels must have an intensity greater than a selected threshold value. The *x* and *y* coordinates of all particles meeting the above criterion are recorded in a text file. Digitizing and processing a single video frame (640 x 480 pixels) requires 1.3 s of CPU time. During this processing time, the CCD camera is acquiring the next image via frame-integration on the CCD chip. In a typical experimental run, a few hundred video frames, each representing the scattering of 40 ion packets (laser shots), are digitized and processed.

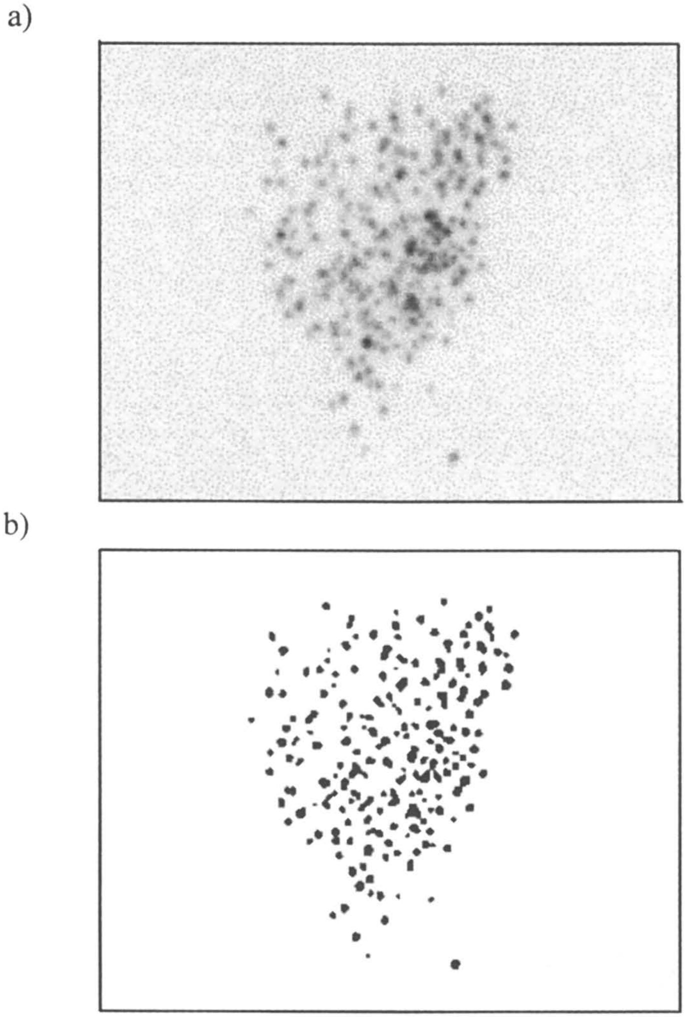

*Figure 5. (a) Image of scattered ions after background subtraction. (b) Same image after filtering and thresholding.*

## Velocity Analysis

To compile a complete velocity distribution of a scattered product, ion images must be gathered at a few different swat delays. This is because scattered ions routinely have broad velocity distributions that extend beyond the dimensions of the image detector for any single swat delay. Real-time processing of the images results in a list of $(x, y)$ coordinates for each detected ion. The list of ion events is transformed into a velocity distribution by a separate velocity analysis program. Characterization of the incident ion packet allows one to determine the $(x, y)$ position and the time at which the incident ion packet strikes the surface. Relative to this reference point, the velocity of all scattered ions can be determined from the distance traveled between the point of surface impact and the scattered ion position, divided by the time lapsed between surface impact and scattered-ion collection (swat delay + mass delay). Appropriate weightings for each ion are calculated from geometrical considerations.(*15*) A 2-D velocity distribution is generated by sorting the recorded ion events into a 2-D velocity grid and assigning the relative intensity in each grid element to the sum of the relevant ion weightings. This can be collapsed to a 1-D velocity distribution by integrating the 2-D velocity distribution over all final scattering angles.

## Results

A variety of ion/surface scattering systems have been studied with the flyswatter detector. Representative systems are briefly presented below to demonstrate how the flyswatter can provide unique data for deciphering the dynamics of complex reaction mechanisms.

Dissociative scattering at surfaces can occur through a number of mechanisms. (*18*) In the scattering of $OCS^+(X\ ^2\Pi)$ on Ag(111), three different anionic fragments are observed. Figure 6 shows the time-of-flight mass spectrum resulting from $OCS^+(X\ ^2\Pi)$ colliding with Ag(111) at 65 eV and normal incidence.(*19*) Equation 1 converts the peaks in the time-of-flight distribution to exact masses. The fragment velocity distributions measured by the flyswatter detector, in conjunction with the dependence of the fragment yields on collision energy, provided evidence for assigning the $O^-$, $S^-$, and $SO^-$ product channels to three distinct fragmentation mechanisms: prompt impulsive dissociation, dissociative neutralization, and atom elimination.

Atom abstraction is an elementary process by which an atom is transferred to or from an incident molecule as the molecule impacts a surface. Hyperthermal energy $NO^+(X\ ^1\Sigma^+)$ ions were found to abstract oxygen from O/Al(111) to produce scattered $NO_2^-$ ions.(*20*) Figure 7 shows the velocity distribution of $NO_2^-$ products formed from $NO^+(X\ ^1\Sigma^+)$ incident on O/Al(111) at 40 eV. The velocity distribution of scattered NO2- products is nonthermal and cannot be described by a Maxwell-Boltzmann distribution at the surface temperature. Moreover, the mean translational energy of scattered $NO_2^-$ increases with $NO^+$ collision energy. These results implicate a direct, Eley-Rideal reaction mechanism, whereby an incident molecule collides with an adsorbed O-atom and reacts without ever becoming thermally accommodated with the surface.

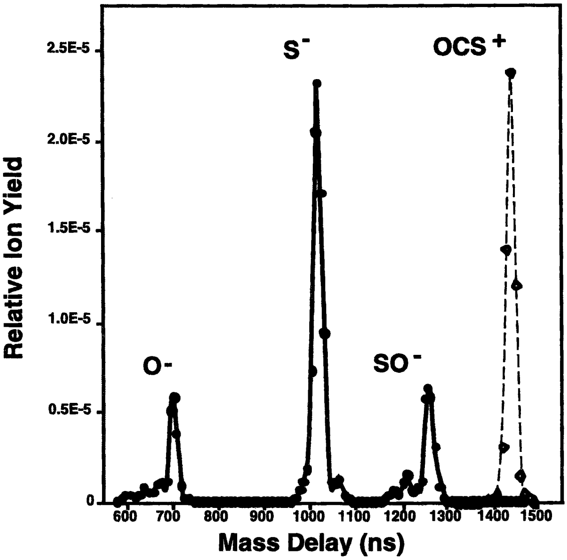

*Figure 6. Time-of-flight mass-spectrum of incident $OCS^+$ ions ( ◊) and scattered negative ions (●) formed through collisions between 65 eV $OCS^+$ and a Ag(111) surface. From left to right, the atomic masses of the four major peaks are 16, 32, 48, and 60 amu. (Reproduced with permission from reference 20. Copyright 1997 American Institute of Physics)*

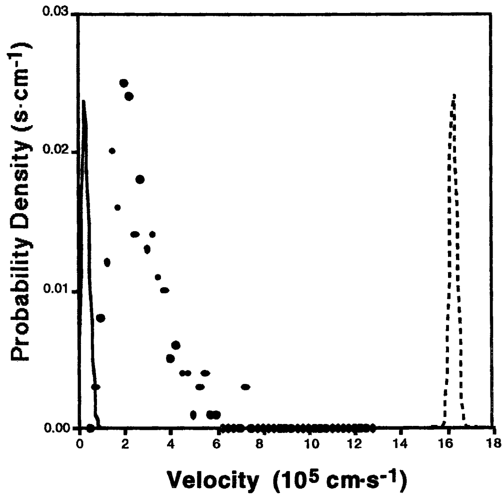

*Figure 7. Velocity distribution for $NO_2^-$ (●) formed from $NO^+$ abstracting an oxygen atom from O/Al(111). For comparison, the plot shows the velocity distribution (dashed line) of incident $NO^+$, and the predicted Maxwell-Boltzmann distribution (solid line) if $NO_2^-$ were thermally equilibrated with the surface at 298 K.*

The scattering of state-selected $NO^+(X\ ^1\Sigma^+$, v=0-6) on GaAs(110) exhibits a variety of fundamental processes: energy transfer, charge transfer, and fragmentation. A dynamical study of $O^-$ product formation was undertaken to explore the interplay between electron transfer and impulsive dissociation events. Vibrational energy in incident $NO^+$ was found to be ten times more effective than collision energy in enhancing the $O^-$ yield.(*9*) Model calculations suggest that electron transfer immediately prior to surface impact creates a quantum mechanical vibrational coherence in the molecule.(*21*) Figure 8 shows the probability density for the $O^-$ product as a function of its final velocity and scattering angle.(*22*) Images were collected for a number of detector orientations to increase the range of acceptance angles. Although $NO^+$ was incident along the surface normal, the scattering distribution in Fig. 8 reveals a striking angular asymmetry, not unlike the asymmetric structure of GaAs(110), shown in the inset of Fig. 8. Trajectory simulations along with an empirical opacity function are able to reproduce the scattering data. The opacity function relates the probability for electron attachment to the oxygen fragment's final surface impact parameter. The probability is found to peak along the lattice rows where dangling bond states reside.

Ion imaging techniques have provided valuable data for understanding the many reaction pathways available to hyperthermal energy, gas/surface collisions. The National Science Foundation (CHE96-15878) is gratefully acknowledged for their support of this work.

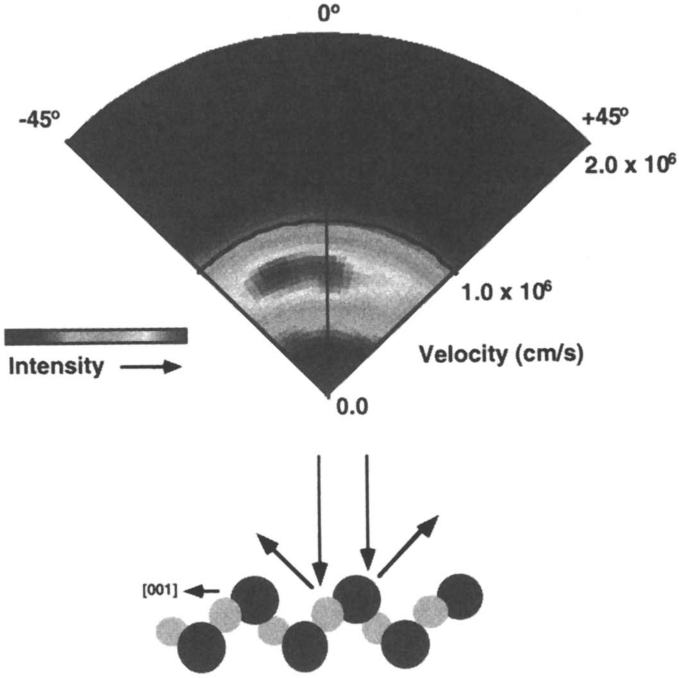

*Figure 8. Probability density for scattered $O^-(^2P)$ fragments as a function of final velocity and scattering angle. $NO^+(X\ ^1\Sigma^+$, v= 1) is incident along the surface normal of GaAs(110) with 45 eV collision energy. The scattering plane lies along the [001] symmetry direction of GaAs(110).*

## References

1. Heiland, W in *Low Energy Ion-Surface Interactions*; Rabalais, J.W.; Ed.; Wiley Series in Ion Chemistry and Physics; Wiley & Sons Inc.: New York, NY, 1994, p. 313-354
2. Reijnen, P.H.F.; Kleyn, A.W. *J. Chem. Phys.* **1989**, *139*, 489-496
3. Horn, TM.; Haochang, P.; van den Hoek, P.J.; Kleyn, A.W. *Surf. Sci.* **1988**, *201*, 573-602
4. Tenner, A.D.; Gillen, K.T.; Horn, T.M.; Los, J.; Kleyn, A.W. *Surf. Sci.* **1986**, *172*, 90-120
5. Akazawa, H.; Murata, Y. *J. Chem. Phys.* **1990**, *92* , 5560-5568
6. Akazawa, H.; Murata, Y. *Surf. Sci.* **1989**, *207* , L971-L979
7. Miller, S.A.; Luo, H.; Jiang, X.; Rohrs, H.W.; Cooks, R.G. *Int. J. Mass Spec. Ion Proc.* **1997**, *160*, 83-105
8. Kobrin, P. H.; Schick, G. A.; Baxter, J. P.; Winograd, N. *Rev. Sci. Instrum.* **1986**, *57*, 1354-1362
9. Martin, J.S.; Greeley, J.N.; Morris, J.R.; Feranchak, B.T.; Jacobs, D.C.; *J. Chem. Phys.* **1994**, *100*, 6791-6812
10. Chandler, D.W.; Houston, P.L. *J. Chem. Phys.* **1987**, *87*, 1445-1447
11. Thoman, J. W.; Chandler, D.W.; Parker, D.H.; Janssen, M.H.M. *Laser Chem.* **1988**, *9*, 27-46
12. Dresser, M.J.; Alvey, M.D.; Yates, J.T. Jr. *J. Vac. Sci. Technol. A* **1986**, *4*, 1446-1450
13. M. Menges et al., Springer Ser. Surf. Sci. 31, 275, Berlin, Springer-Verlag (1992)
14. Kim, C.; Höfner, C.; Rabalais, J. W. *Surf. Sci.* **1997**, *388*, L1085-L1091
15. Corr, D.; Jacobs, D. C. *Rev. Sci. Instrum.* **1992**, *63*, 1969-1972
16. Wiley, M.C.; McLaren, I.H. *Rev. Sci. Instrum.* **1955**, *26*, 1150
17. Chandezon, F.; Huber, B.; Ristori, C. *Rev. Sci. Instrum.* **1994**, *65*, 3344-3353
18. Morris, J. R.; Kim, G.; Barstis, T. L. O.; Mitra, R.; Quinteros, C. L.; Jacobs, D. C. *Nuc. Instrum. Meth. B* **1997**, *125*, 185-193
19. Morris, J. R.; Kim, G.; Barstis, T. L. O.; Mitra, R.; Jacobs, D. C. *J. Chem. Phys.* **1997**, *107*, 6448-6459
20. Maazouz, M.; Barstis, T. L. O.; Maazouz, P.; Jacobs, D. C. *Phys. Rev. Lett.* **2000**, *84*, 1331-1334
21. Qian, J. ; Jacobs, D. C.; Tannor, D. J. *J. Chem. Phys.* **1995**, *103*, 10764-10778
22. Morris, J. R.; Martin, J. S.; Greeley, J. N.; Jacobs, D. C. *Surf. Sci.* **1995**, *330*, 323-336

## Chapter 10

# Recoil Energy Distributions in van der Waals Cluster Vibrational Predissociation

**Laurie M. Yoder[1], John R. Barker[1,3], K. Thomas Lorenz[2], and David W. Chandler[2]**

[1]**Departments of Chemistry and of Atmospheric, Oceanic and Space Sciences, University of Michigan, Ann Arbor, MI 48109–2143**
[2]**Combustion Research Facility, Sandia National Laboratories, Livermore, CA 94551–0969**

The vibrational predissociation of van der Waals dimers produces a kinetic energy of recoil. The distribution of this recoil energy has been investigated in the predissociation of triplet state mixed van der Waals dimers which contain ~2000 to ~8000 cm$^{-1}$ of vibrational energy. One member of a dimer is an aromatic molecule, such as pyrazine or benzene, and the second is a rare gas atom, a diatomic, or a small polyatomic molecule. The recoiling aromatic member was ionized and the recoil energy distribution acquired either by 2–dimensional ion imaging or by a velocity resolved time-of-flight method. The two experimental methods gave comparable results. The resulting probability distributions peak near zero energy and are monotonically decreasing functions of recoil energy. Average center-of-mass recoil energies range from ~100 cm$^{-1}$ to >300 cm$^{-1}$. The results for pyrazine-Ar clusters have been modeled using classical trajectory calculations and the results are compared with the experiments.

## Introduction

The dynamics of van der Waals (VDW) cluster predissociation provide useful insight into intramolecular and intermolecular energy flow. Compared to molecular bonds, VDW bonds are weak and they have low frequencies. Because of this difference, coupling between the VDW degrees of freedom and molecular degrees of freedom is weak and energy flow between them is slow. The so-called "transitional modes", which have been invoked in explanations (*1-3*) of collisional energy transfer, are the

---

[3] Corresponding author.

intermolecular modes in a transient collision complex and are used to describe the relative motions of the collision partners. They can be identified with the VDW modes in a cluster. Thus, one can gain insight into collisional energy transfer by investigating energy disposal in cluster VDW modes.

Numerous fluorescence studies of aromatic-rare gas clusters in the $S_1$ state have determined the vibrational distributions of the free aromatic members following vibrational predissociation of the clusters. Most of the clusters studied [*s*-tetrazine-Ar (*4,5*), benzene-Ar (*6*), aniline-Ar (*7*), *p*-difluorobenzene-Ar (*8*)] show mode selectivity in their final states. Of all energetically available final states, only a few are populated. On the other hand, dissociation of clusters containing p-fluorotoluene produces a statistical distribution which has been attributed to increased intermode coupling via the methyl rotor (*9*).

The fluorescence studies provide information on the final vibrational states of the aromatic member at relatively low densities of states, but do not quantify the recoil energy. Several groups have studied the recoil energy following ground state vibrational predissociation of benzene dimers excited at either 1000 (*10,11*) or 3000 $cm^{-1}$ (*12*). In these experiments the recoiling fragments were detected at an angle of a few degrees from the molecular beam. The resulting recoil distribution is a monotonically decreasing function of energy.

Cluster dissociation has also been investigated computationally. In molecular dynamics simulations of benzene-Ar excited to low vibrational energy, Vacek, *et al.* (*13*) found that the dissociation was very slow, with specific benzene vibrational modes being more efficient than others in transferring energy into the van der Waals modes. Bernshtein and Oref (*14,15*) performed classical trajectory calculations on the benzene-Ar complex excited to 51900 $cm^{-1}$ for various intermolecular potentials. They found that the probability distribution function for energy loss ($\Delta E$) from the benzene partner is roughly exponential in $\Delta E$. The average product translational energy ranges from ~20 $cm^{-1}$ to ~150 $cm^{-1}$ depending on which intermolecular potential is used (*15*).

In the present work recoil energy distributions from vibrational predissociation of aromatic-X van der Waals complexes in the triplet electronic state are reported. Data were obtained using both an ion imaging technique and a velocity-resolved time-of-flight method; the two methods are compared. The vibrationally excited clusters were prepared by optical excitation to the first excited singlet state ($S_1$), followed by spontaneous intersystem crossing to a triplet state (T). The level of vibrational excitation depends on the $S_1$-T energy difference and so the effect of total energy on the final recoil distribution could be tested by using different aromatic molecules (aromatic = pyrazine, methylpyrazine, pyrimidine, benzene, toluene, aniline). The number of degrees of freedom of a cluster, as well as its general structure, could be varied by using different cluster partners (X = Ar, Kr, Xe, $N_2$, $O_2$, $NH_3$, $H_2O$). The experimental results for pyrazine-Ar clusters are compared with results from classical trajectory calculations.

## Experimental Methods

The photophysics of all the aromatic molecules investigated here follow the same pattern. A 1-photon absorption prepares the first excited singlet state ($S_1$) which undergoes intersystem crossing to the lowest triplet state ($T_1$). The $T_1$ origin is lower in energy than the $S_1$ origin; the $S_1$-$T_1$ energy difference varies from 2500 $cm^{-1}$ for pyrimidine (*16,17*) to 8600 $cm^{-1}$ for benzene (*18*). The triplet lifetimes at the $S_1$ origin for the molecules investigated here are on the order of 500 ns to several microseconds (*16-20*). The $T_1$ molecules can be excited into the ionization continuum using 193 nm light (*16-20*); this provides enough energy to ionize all $T_1$ molecules as well as any remaining $S_1$ molecules. The photophysics in the cluster are similar to those of the gas phase. The cluster ($S_1$-$S_0$) transitions are frequency shifted from those of the corresponding monomer band. Like the aromatic monomers, the $S_1$ aromatic-X dimers undergo intersystem crossing to $T_1$ and the vibrational energy in $T_1$ causes the cluster to dissociate. Some of the vibrational energy is used to break the VDW bond and the remaining vibrational energy is partitioned between the internal degrees of freedom of the fragments and the relative recoil energy.

In both the ion imaging and velocity-resolved time-of-flight methods, van der Waals clusters are formed by passing a carrier gas (argon or another cluster partner seeded in argon) at 1.5 atm over the chosen aromatic molecule. The molecular beam is crossed at right angles by two collinear unfocused laser beams from frequency-doubled Nd:YAG (Coherent Infinity) pumped dye lasers (Lambda Physik Scanmate) for ion imaging at Sandia, or an excimer (Lumonics HyperEX-400) pumped frequency-doubled dye laser (Scanmate) and excimer laser (Lumonics) for time-of-flight measurements at Michigan. The delay between the pump and probe lasers is 70 ns. The ions are detected as described below.

## Ion imaging

The ion imaging technique has been used extensively for determining the angular alignment and energy distribution of fragments following small molecule dissociation (*21*). The experimental apparatus for the imaging experiments has been described in detail previously (*21,22*). The molecular beam is directed into the ionization region along the length of the time-of-flight tube (*x*-axis). The beam passes through a hole in the repeller plate into the ionization region where it intersects with the pump and probe lasers. The photoions are accelerated through a hole in the extractor plate into the time-of-flight tube and onto a 2-dimensional microchannel plate detector coupled to a phosphor screen. A CCD camera (Photometrics) integrates the light signal emitted by the phosphor screen for up to 10000 laser shots.

The voltages on the repeller plate and extractor plate were adjusted in order to achieve velocity mapping conditions (*23*). Under these conditions, all ions with the same velocity impinge on the detector at the same position regardless of where the ions were formed in the extraction region. This compensates for the finite size of the molecular beam. Velocity mapping conditions were obtained by imaging a monomer resonance, in which the only transverse velocity present is due to the molecular beam expansion. The size of the monomer spot on the detector was minimized by tuning the extraction voltage. Typical voltages were 1000 V for the repeller plate and 750 V for the extractor plate; these resulted in a time-of-flight of ~13 μs.

The resolution of the ion imaging technique depends on several factors. First, a cold molecular beam is necessary to minimize the velocity spread of the monomer peak. The temperature of the skimmed molecular beam in a series of separate experiments was estimated to be < 5 K based on rovibronic spectra of NO seeded in a beam at the same backing pressure as in the predissociation measurements. The construction of the ion lens must be precise in order to achieve good velocity mapping. The inherent image width of a single ion count must smaller than the desired image resolution.

The spectrometer voltages control the overall time-of-flight and the velocity mapping. For a particular configuration of plates and laser beams, the optimal voltage ratio between repeller and extractor is constant and can be found easily. By decreasing these voltages, a longer flight time is obtained; this allows the recoiling packet of ions to expand and produce a larger image on the detector. The larger image is less affected by the grain of the phosphors and the size of the camera pixels. In the present experiment, the image of a single ion count has approximately the same size as the signal measured for the monomer aromatic (Gaussian width of ~2.5 pixels), where each pixel typically corresponds to ~10 m/s. The resolution could be improved by using a single-ion counting technique (*24*).

The recoil distribution from VDW cluster dissociation is isotropic; it does not depend on the polarization of the pump laser (*22*). The image obtained as described above is a 2-dimensional xy-projection of a 3-dimensional distribution. In an isotropic distribution, the same information can be obtained by observing the 1-dimensional projection along any of the axes with the velocity-resolved time-of-flight method.

## Velocity-resolved time-of-flight

Several groups have studied photodissociation fragments of small molecules using time-of-flight techniques (*25-27*). The time-of-flight experiment is performed in a two-stage Wiley-McLaren (*28*) type mass spectrometer situated on the $x$-axis, which is perpendicular to the molecular beam ($z$-axis). The molecular beam enters the extraction region, where photoions are produced. The ions pass through a charged grid into the acceleration region, then into the field-free 1-meter flight tube. The extraction and acceleration voltages are applied continuously and are set to produce space focusing conditions (*26,28*). Under these conditions, all ions which have the same velocity arrive at the detector at the same time regardless of their spatial origin in the extraction field. The space focusing approximation improves with lower extraction voltages in that the ions may be produced in a larger volume while still maintaining a narrow arrival time distribution. This allows the use of unfocused laser beams of approximately 1-2 mm in diameter. Typical extraction fields used in these experiments range from 20-30 V/cm. The corresponding acceleration voltages to achieve space focusing conditions are 250-350 V/cm. In a given experiment, these conditions are achieved by monitoring the ion peak due to the monomer while the acceleration voltage is adjusted to produce the narrowest time-of-flight profile which does not change position when the $z$-position of the laser is varied.

Charged deflection plates situated near the entrance of the time-of-flight field-free drift tube are used to steer the ion packet and compensate for the velocity of the molecular beam. The ions strike the microchannel plate detector and the resulting amplified signal is viewed on an oscilloscope. The ion signals of approximately 5000 laser pulses are averaged on a digital oscilloscope operating at 2.5 Gsamples/s. The ion signal vs. time profile is stored on a computer.

The ion cloud which arrives at the detector is a *yz*-projection and thus contains velocity components which are perpendicular to the *x*-axis (or time-axis). The desired distribution is not the *yz*-projection, but the 1-dimensional radial distribution corresponding to the limit of zero velocity perpendicular to the *x*-axis. In order to minimize the effect of the perpendicular components, an aperture is placed over the detector, so only the ions with small transverse velocities (the "core") are detected (*25,27*). In the limit of an infinitely small aperture, the projection becomes the radial distribution, but the signal becomes vanishingly small. The resolution of the TOF data is affected by nonideal "core sampling". In the present arrangement, the detector aperture allows ions with a transverse velocity of ~55 m/s to be detected; this effect broadens the distribution by ~5%. To improve the core sampling, the overall time of flight is increased by lowering the extraction and acceleration fields. With a longer time of flight, the ion distribution spreads to a greater extent and the "core" is a more accurate representation of the 1-dimensional distribution. However, at voltages smaller than we used (less than 25 V/cm), effects due to stray fields begin to blur the arrival time distribution. In addition, fewer ions remain in the "core" so the signal averaging statistics become worse.

## Results and Discussion

### Ion imaging

The ion image of triplet monomer pyrazine excited through the Pyr ($S_1 \leftarrow S_0$) 0-0 transition is shown in Figure 1 (upper panel). This image shows the size of the molecular beam when no recoil occurs. The second image (Figure 1, lower panel) is produced by ionizing the triplet pyrazine fragment following predissociation of the Pyr-Xe cluster. The broadening of the signal compared with the monomer image is due to the recoil energy released after predissociation. In order to extract the energy distribution from the image, an inverse Abel transform must be performed, to convert the 2-dimensional projection of the 3-dimensional distribution into the 1-dimensional radial function (*29*). Furthermore, the effects of beam spreading, as manifested in the monomer image, can be removed via a deconvolution technique (*22*).

A pragmatic method was described earlier which minimizes the effects of experimental noise on the deconvolution and Abel transformation (*22*). Basically, the intensity is plotted as a function of the distance of each pixel relative to the center of the molecular beam image. The resulting monotonically decaying profile is nonlinear-least-squares fitted to a smooth analytical function with well known transformation properties. In this case, the empirical function is a summation of Gaussian functions, which can be transformed analytically. The use of an analytical function in the transformation instead of the actual experimental data eliminates the noise inherent in numerical transformations. Following deconvolution and transformation, the probability distribution of recoil energy is obtained.

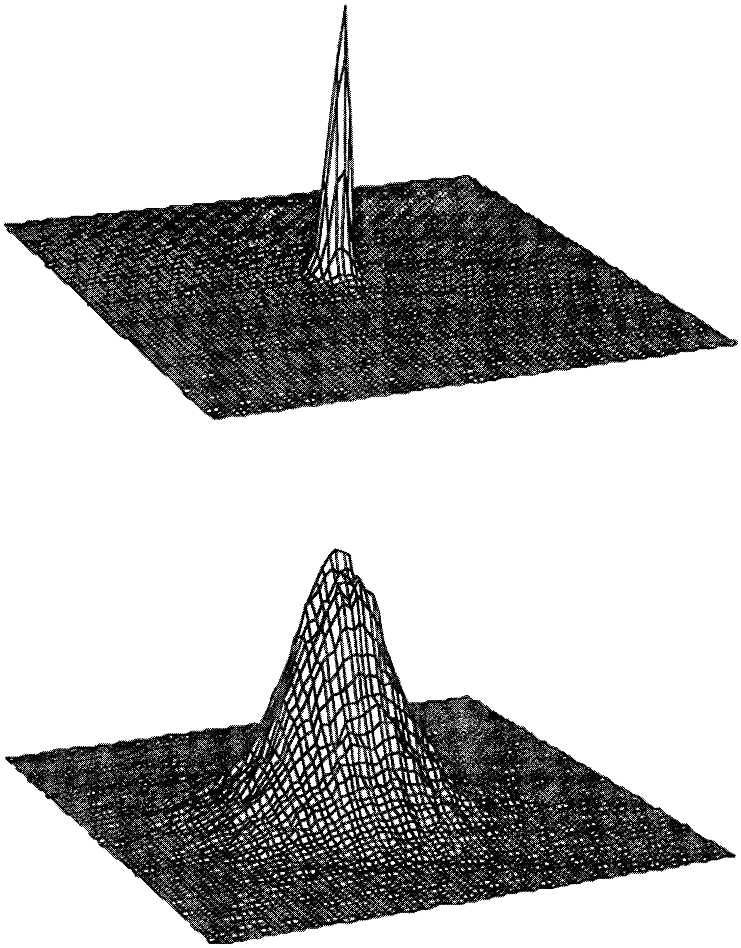

***Figure 1.*** *(upper) Ion image from excitation of monomer pyrazine which shows the size of the molecular beam. (lower) Ion image of the pyrazine fragment after Pyr-Xe cluster predissociation. Each grid line in the figure corresponds to the spacing of one pixel.*

## Velocity-Resolved Time-of-Flight

A typical TOF profile for dissociation of Pyr-Ar is shown in Figure 2 along with the corresponding pyrazine molecular beam profile. Both profiles are roughly Gaussian in shape. The cluster profile is fitted to a summation of Gaussian functions. Analytical deconvolution is performed to remove the effects of the molecular beam size and the core sampling approximation. The details will be described in a forthcoming publication. The recoil velocity is directly proportional to the arrival time $t$ relative to $t_0$, the center of the distribution (*26,28*):

$$v_x = \frac{q\varepsilon(t_0 - t)}{m} \tag{1}$$

The extraction field is given by $\varepsilon$, $q$ is the charge and $m$ is the mass. The resulting velocity distribution is then converted into an energy probability distribution.

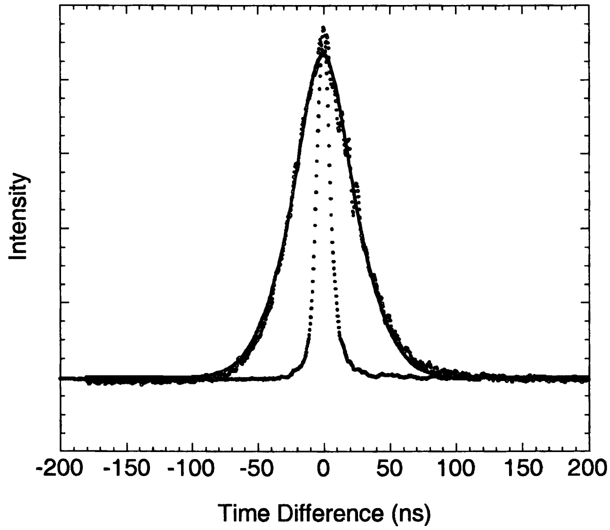

*Figure 2. Time-of-flight profiles for monomer pyrazine (filled circles) and pyrazine fragment after Pyr-Ar cluster predissociation (open circles). The solid line through the cluster profile is the nonlinear least squares fit to the sum of two Gaussian functions.*

Recoil probability distributions obtained using the two methods are shown in Figure 3. All of the measured recoil distributions were found to have a maximum probability near zero energy and to decay monotonically with increasing energy. The TOF probability distributions are approximately exponential, while the imaging distributions have a higher probability tail at high energy. The two data analysis procedures differ in the way they treat the high velocity data. In the imaging analysis, the fitting function consisted of four Gaussian terms, one of which had a large width to fit the high velocity tail. The TOF data were too noisy to include more than two terms in the fitting function. The statistical uncertainties (±σ) shown in Figure 3 become relatively larger at high recoil energies, so the difference between the two distributions may not be significant. The average recoil energy for the two methods is nearly the same. The Pyr-Ar average recoil is 101±6 $cm^{-1}$ for imaging and 89±11 $cm^{-1}$ for TOF. The average recoil energy from Pyr-Xe is slightly higher at 125 $cm^{-1}$. These results are similar to the average center-of-mass recoil energy following ground state photodissociation of benzene dimers which contained ~1000 $cm^{-1}$ of vibrational energy: 78±10 $cm^{-1}$ (*10*) and 50 $cm^{-1}$ (*11*). The VDW interaction in the benzene dimers is different than in the rare gas complexes due to hydrogen bonding with the π-cloud and due to the presence of additional vibrational degrees of freedom, however, at very low benzene excitation energy, the recoil energies are similar.

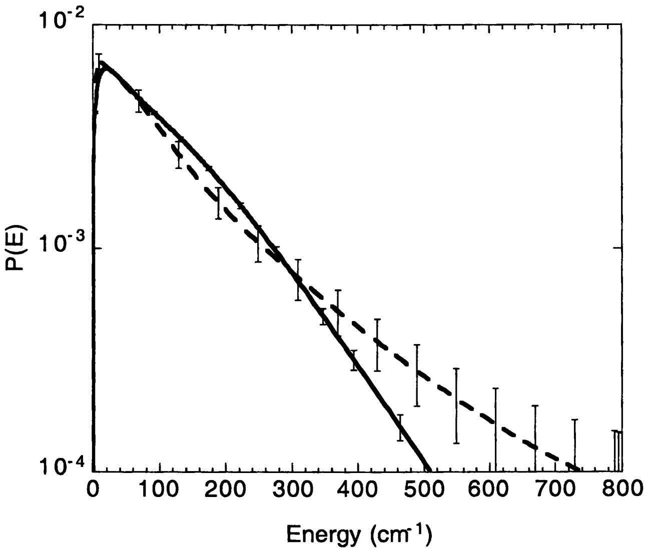

*Figure 3. Normalized relative recoil probability distributions for predissociation of Pyr-Ar. The solid line is from the velocity-resolved time-of-flight and the dashed line is from the ion imaging experiment.*

The ion imaging technique and the velocity-resolved time-of-flight technique, while giving the same recoil results in these experiments, have differences in their velocity selectivity and sensitivity. One of the most striking differences between the two methods is the large increase in information obtained through imaging. The ion image detects all ions which are formed so it is equally sensitive to all velocities. On the other hand, the TOF profile records only the ions within the central core. As the radial distance from the center increases, the fraction of ions in the core decreases, thus reducing the sensitivity to higher velocities. In photodissociation experiments in which the fragment distribution is anisotropic, the ion imaging method is far superior because the entire distribution is imaged at once; to perform the same experiment in the TOF apparatus would require rastering the ion packet across the detector and signal averaging multiple profiles (*26*).

## Discussion

In order to investigate the dependence of the recoil energy distribution on the vibrational energy content and density of states of the donor, several other aromatic molecules were investigated using the TOF technique. Table I lists the relevant spectroscopic data and the density of states of pyrazine, pyrimidine, 2–methylpyrazine, benzene, toluene, and aniline at the $S_1$ energy origin. The structure of the argon cluster of each of these aromatic molecules is expected to be the same: the argon is located above the center of the ring. The average recoil energy of each Ar complex is listed in Table I.

In their work on $S_1$ p-difluorobenzene-Ar and p-fluorotoluene-Ar complexes Gilbert, *et al.* (*9*) found that the product states following vibrational predissociation are qualitatively different. The p-fluorotoluene fragments have a nonselective statistical distribution of final vibrational states, while the final distribution of p–difluorobenzene states is highly selective. Gilbert, *et al.* attributed the differences to increased coupling among modes in p-fluorotoluene via the methyl rotor. The analogous comparison between the recoil energy of 2-methylpyrazine and pyrazine and benzene and toluene (Table I and Figure 4) suggests that the presence of the methyl rotor may have a small effect in increasing the average recoil energy. Clearly, however, the density of states of the donor and the presence of a methyl rotor are not strong factors in determining recoil energy.

**Table I. Properties of Aromatic-Ar van der Waals Clusters**

| *Molecule* | *$E_{vib}$ at $S_1$ origin ($cm^{-1}$)* | *log ($\rho$)$^a$* | *Ar Cluster Spectral Shift ($cm^{-1}$)* | *VDW Well Depth (K)* | *Ar Cluster $<E_T>$ ($cm^{-1}$)* |
|---|---|---|---|---|---|
| Pyrimidine | 2543 | 1.2 | -41 | | 98±14 |
| Pyrazine | 4056 | 3.1 | -28 | 436$^b$ | 101±11 |
| Methylpyrazine | ~4056 | 4.6 | -32 | | 134±3 |
| Aniline | ~7200 | 5.6 | -54 | 448$^c$ | 206±40 |
| Benzene | ~8600 | 5.8 | -22 | 401$^c$ | 130±5 |
| Toluene | ~8800 | 8.0 | -26 | 408$^c$ | 153±40 |

[a] $\rho$ = density of $T_1$ vibrational states at $S_1$ energy origin.

[b] Reference 30.

[c] Reference 31.

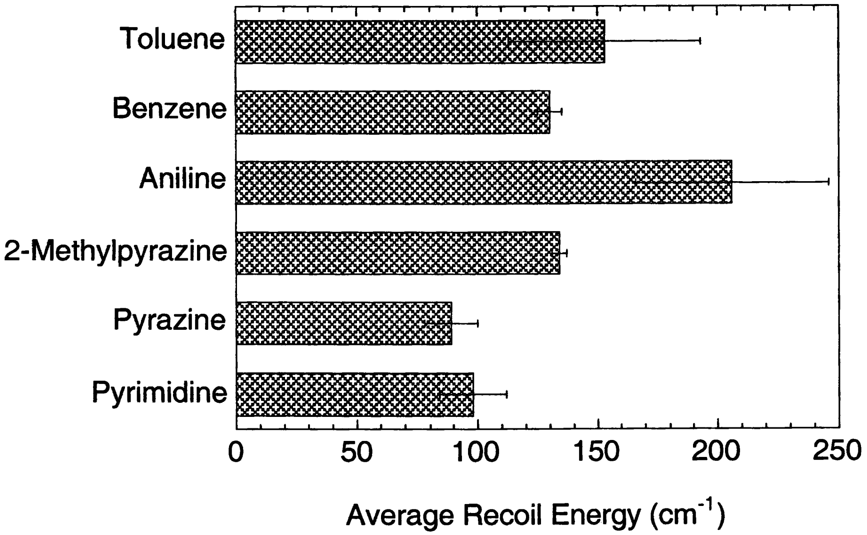

*Figure 4. Average recoil energy from the predissociation of aromatic-Ar van der Waals clusters.*

The triplet state vibrational energy also appears to have a only a small effect on recoil energy. The aromatics with lower vibrational energy in $T_1$ have only slightly lower values of average recoil compared to those with higher vibrational energy (Figure 4). Surprisingly, aniline, with characteristics intermediate between the benzenes and pyrazines, has significantly larger recoil energy.

The average recoil energy is also found to depend on the cluster partner. For a given aromatic molecule, clusters with monatomic and diatomic partners have similar recoil energies (Figure 5). This may be due to structural similarities between them. Like monatomic partners, the homonuclear diatomics are expected to form van der Waals bonds with the π-orbital centered above the ring (*32*). Dramatic differences are seen, however, in the average recoil energy from Pyr-$NH_3$ and Pyr-$H_2O$ clusters, which are about three times greater than those from the corresponding monatomic clusters. This may be due to a fundamental difference in the cluster bond. The ammonia and water molecules can form hydrogen bonds both with a nitrogen atom in the ring and with the out-of-plane π-orbital (*33,34*). The extremely large recoil from these hydrogen bonded complexes may be due to a change in geometry (in-plane bonding instead of out-of-plane bonding), or a difference in bond strength. The hydrogen bond strength, however, calculated to be 689 $cm^{-1}$ for singlet state Pyr-$NH_3$ (*33*), is similar to the estimated bond strength of singlet state Pyr-Xe, 700 $cm^{-1}$ (*17*), so bond dissociation energy alone does not account for the difference, if bond strengths are similar in singlet and triplet states.

The VDW cluster may be useful as a model of a half-collision to provide information about full collisions. The ergodic collision theory (*1*) has been proposed to model collisional energy transfer. This model assumes that the vibrational energy distribution in the collision complex reaches statistical equilibrium before the collision partners separate, and overestimates the energy transfer (*1*). Likewise, in the VDW cluster predissociation described here, a completely statistical model predicts that much more energy should be found in the recoil coordinate than is observed (*22*). This indicates that there is a dynamical constraint which limits vibrational-to-translational energy transfer in clusters, even given their relatively long lifetimes.

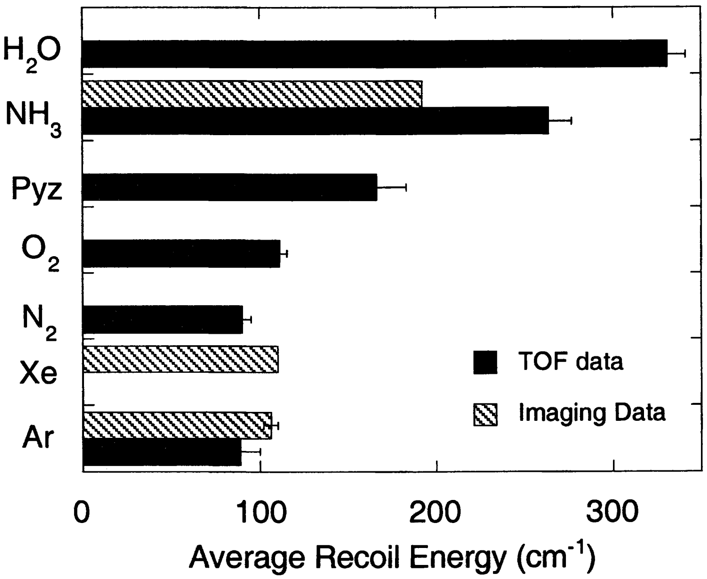

*Figure 5. Average recoil energy from the predissociation of pyrazine-X van der Waals clusters.*

### *Classical Trajectory Calculations*

The dynamics of pyrazine-Ar cluster dissociation may be modeled using classical trajectory calculations. In the present work, the pyrazine intramolecular potential surface was obtained by modifying the force constants used by Lenzer, *et al.* (*35*) for benzene to achieve reasonable agreement between the calculated and experimental vibrational frequencies. The geometry and frequencies of ground state pyrazine (*36*) were used since complete data for the triplet state are unavailable. There is evidence that the $T_1$ geometry resembles the ground state (*37*), but the vibrational frequencies are somewhat lower in $T_1$ (*38*). Atom-atom pair-wise Lennard-Jones potentials were used for the intermolecular potential with benzene-Ar parameters. This intermolecular potential predicts the deepest potential wells 3.2 Å above and below the center of the ring and four shallow wells in the plane of the ring beside the two nitrogen atoms and beside the two C-C bonds. This is similar to the potential surface for the benzene-Ar cluster (*15*). The initial vibrational energy in excess of the zero point energy was placed in the high frequency C-H stretching modes, as expected following intersystem crossing (*39*). The initial rotational temperature was assumed to be 0 K.

Approximately 3000 trajectories were run for pyrazine-Ar clusters at each excitation energy (4000 cm$^{-1}$ and 8500 cm$^{-1}$) to obtain the average recoil and rotational energies. A slightly modified version of the public domain computer program VENUS96 (*40*) integrated the equations of motion using the above potential surface. The program output was modified to analyze cluster lifetimes for a sample of approximately half of the trajectories. Each trajectory was terminated when the separation between cluster fragments was 16 Å. Above ~1000 trajectories the average energy disposal and lifetime results did not change.

The calculated recoil energy distributions are compared to the experimental data in Figure 6. Both calculated distributions are approximately exponential and the average recoil energy for 4000 cm$^{-1}$ initial energy is 114 cm$^{-1}$, lower than that calculated for 8500 cm$^{-1}$ excitation (142 cm$^{-1}$). The agreement with the experiment is surprisingly good. In a typical trajectory, the excited pyrazine vibrates as the energy in the C-H stretches randomizes throughout the other modes. The low frequency van der Waals modes do not couple efficiently to the higher frequency molecular modes, so the energy transfer process is slow. Eventually the VDW bend and stretch modes become excited and the argon atom leaves its potential well above the plane of the pyrazine molecule. The argon atom "hops" around on the pyrazine surface, sampling the shallow in-plane potentials and both equilibrium positions prior to dissociation. The dissociation kick and subsequent recoil take place over a very short time compared to the total trajectory lifetime, so we identify the cluster lifetime with the trajectory lifetime. The trajectory lifetime distribution for each excitation energy is shown in Figure 7. The lower initial energy trajectories tend to have longer lifetimes $\tau$ with $<\tau>$ = 132 ps compared with $<\tau>$ = 81 ps for the higher initial energy trajectories. In both cases, the recoil distribution does not depend on trajectory lifetime. Bernshtein and Oref reach a similar conclusion in their benzene-Ar cluster dissociation calculations (*15*). In each case, the final dissociation kick depends only on the instantaneous vibrational phases of the molecule, not on its past history.

The calculations allow us to investigate aspects of the vibrational predissociation which are not observable in the experiments. In both our time of flight and ion imaging experiments, the cluster lifetime, discussed above, cannot be measured. The rotational state distribution following dissociation is also experimentally unavailable because all of the triplet state aromatic molecules are ionized regardless of vibrational or rotational state. The trajectory calculations, however, provide some information on rotational energy. The final rotational energy distributions for both excitation energies are nearly the same as the corresponding translational energy distributions. The distributions are approximately exponential, with the average rotational energy of 140 cm$^{-1}$ from the clusters with 8500 cm$^{-1}$ internal vibrational energy and 117 cm$^{-1}$ rotational energy from clusters with 4000 cm$^{-1}$ initial energy. The results are consistent with classical equipartition of energy in the VDW modes, in which the energy is equally partitioned among the final three translational and three rotational degrees of freedom. This may indicate that the vibrational energy is statistically distributed among the VDW modes of the complex.

Bernshtein and Oref (*14,15*) performed classical trajectory calculations on benzene-Ar clusters excited to much higher energy (51900 cm$^{-1}$). The Lennard-Jones potential for benzene-Ar interaction is very similar to the pyrazine-Ar potential, so we expect the results to be similar. They find the average trajectory lifetime to be 36.3 ps for 51900 cm$^{-1}$ excitation and 94.2 ps for 30864 cm$^{-1}$ excitation (*15*). This trend of increasing lifetime with decreasing internal energy is consistent with our results. A more quantitative comparison between our results and those of Bernshtein and Oref is difficult to make, since the criteria for terminating trajectories and the initial excitation conditions differ from ours. The recoil energy calculated for benzene-Ar excited to 51900 $cm^{-1}$ is ~150 $cm^{-1}$ (*15*), similar to our calculated values of 114 and 142 $cm^{-1}$ for pyrazine excited to 4000 and 8500 $cm^{-1}$, respectively.

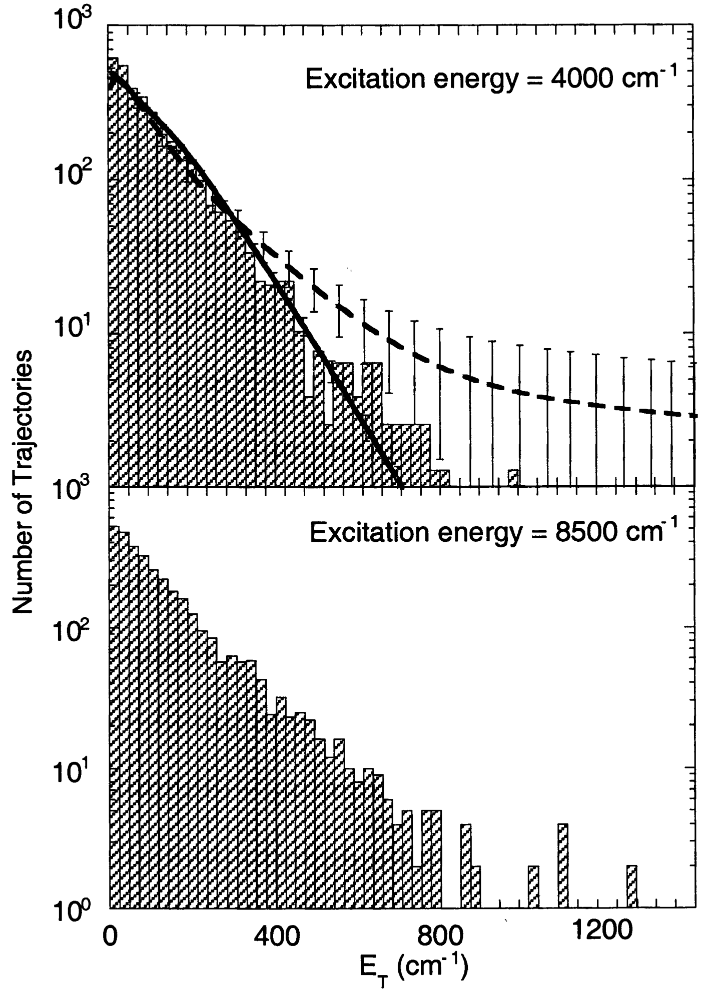

*Figure 6. Translational energy histograms from classical trajectory calculations. The solid line in the top panel is the time-of-flight experimental data and the dashed line in the top panel is the ion imaging experimental data. The experimental probability distributions are renormalized to compare with the trajectory results.*

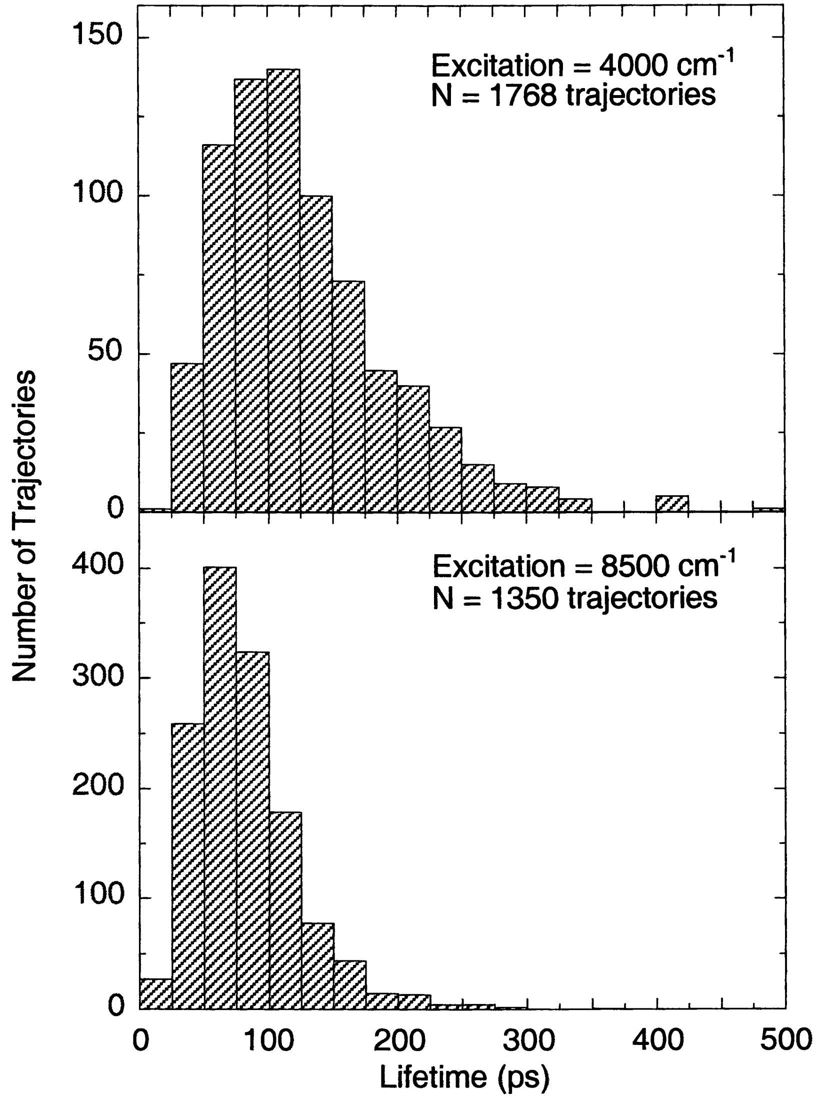

*Figure 7. Cluster lifetime histograms from classical trajectory calculations.*

Continuing work will focus on trajectory calculations for other aromatic clusters. The effect of the methyl rotor on the translational energy distribution and on the cluster lifetime will be determined for methylpyrazine. In addition, calculations on hydrogen bonded clusters will be performed to compare with the experimental data. Future work with picosecond lasers would be necessary to test the predicted cluster lifetime dependence.

## Conclusions

Both the ion imaging and velocity-resolved time-of-flight methods can be used to obtain quantitative measurements of the recoil energy from the vibrational predissociation of van der Waals clusters. The ion imaging technique is preferred because the entire distribution of fragments can be monitored, rather than only the core sample obtained with the time-of-flight method.

Recoil energy probability distributions were obtained for clusters containing pyrazine, methylpyrazine, pyrimidine, benzene, toluene, and aniline. All of the distributions peak near zero recoil and decrease approximately exponentially with increasing energy. The average recoil energy is similar in magnitude for clusters containing rare gas atoms and polyatomic molecules. Recoil from pyrazine clusters hydrogen bonded to ammonia or water was ~3 times greater. The density of states and the initial vibrational energy in the aromatic molecule appear to have only small effects on the recoil energy distribution. Classical trajectory calculations were performed for the pyrazine-Ar complex using a Lennard-Jones potential. The predicted recoil distribution agrees well with the experimental data.

### Acknowledgments

We thank Dr. David Neyer, Dr. Carl Hayden, and Prof. Joe Cline for helpful discussions. Thanks go to Prof. I. Oref for communicating results prior to publication. Thanks also go to Mark Jaska for his expert technical aid. Financial support was provided by the US Department of Energy, Office of Basic Energy Sciences. LMY thanks the Horace H. Rackham School of Graduate Studies for a Predoctoral Fellowship.

## References

1. Nordholm, S.; Schranz, H. W. *Adv. Chem. Kin. Dyn.* **1995,** *2A,* 245.
2. Oref, I.; Tardy, D. C. *Chem. Rev.* **1990,** *90,* 1407.
3. Tardy, D. C.; Rabinovitch, B. S. *Chem. Rev.* **1977,** *77,* 369.
4. Brumbaugh, D. V.; Kenny, J. E.; Levy, D. H. *J. Chem. Phys.* **1983,** *78,* 3415.
5. Ramaekers, J. J. F.; van Dijk, H. K.; Langelaar, J.; Rettschnick, R. P. H. *Faraday Discuss. Chem. Soc.* **1983,** *75,* 183.
6. Stephenson, T. A.; Rice, S. A. *J. Chem. Phys.* **1984,** *81,* 1083.
7. Nimlos, M. R.; Young, M. A.; Bernstein, E. R.; Kelley, D. F. *J. Chem. Phys.* **1989,** *91,* 5268.
8. Jacobson, B. A.; Humphrey, S.; Rice, S. A. *J. Chem. Phys.* **1988,** *89,* 5624.
9. Gilbert, B. D.; Parmenter, C. S.; Su, M.-C.; Oh, H.-K.; Zhao, Z.-Q. *Appl. Phys. B* **1994,** *59,* 397.
10. Johnson, R. D.; Burdinski, S.; Hoffbauer, M. A.; Giese, C. F.; Gentry, W. R. *J. Chem. Phys.* **1986,** *84,* 2624.
11. Nishiyama, I.; Hanazaki, I. *Chem. Phys. Lett.* **1985,** *117,* 99.

12. Vernon, M. F.; Lisy, J. M.; Kwok, H. S.; Krajnovich, D. J.; Tramer, A.; Shen, Y. R.; Lee, Y. T. *J. Phys. Chem.* **1981,** *85,* 3327.
13. Vacek, J.; Hobza, P.; Jortner, J. *J. Phys. Chem. A* **1998,** *102,* 8268.
14. Bernshtein, V.; Oref, I. *Chem. Phys. Lett.* **1999,** *300,* 104.
15. Bernshtein, V.; Oref, I., *private communication.*
16. Dietz, T. G.; Duncan, M. A.; Pulu, A. C.; Smalley, R. E. *J. Phys. Chem.* **1982,** *86,* 4026.
17. Knee, J.; Johnson, P. *J. Phys. Chem.* **1985,** *89,* 948.
18. Duncan, M. A.; Dietz, T. G.; Liverman, M. G.; Smalley, R. E. *J. Phys. Chem.* **1981,** *85,* 7.
19. Dietz, T. G.; Duncan, M. A.; Smalley, R. E. *J. Chem. Phys.* **1982,** *76,* 1227.
20. Knee, J. L.; Johnson, P. M. *J. Chem. Phys.* **1984,** *80,* 13.
21. Heck, A. J. R.; Chandler, D. W. *Annu. Rev. Phys. Chem.* **1995,** *46,* 335.
22. Yoder, L. M.; Barker, J. R.; Lorenz, K. T.; Chandler, D. W. *Chem. Phys. Lett.* **1999,** *302,* 602.
23. Eppink, A. T. J. B.; Parker, D. H. *Rev. Sci. Instrum.* **1997,** *68,* 3477.
24. Chang, B.-Y.; Hoetzlein, R. C.; Mueller, J. A.; Geiser, J. D.; Houston, P. L. *Rev. Sci. Instrum.* **1998,** *69,* 1665.
25. Ogorzalek Loo, R.; Hall, G. E.; Haerri, H.-P.; Houston, P. L. *J. Phys. Chem.* **1988,** *92,* 5.
26. Syage, J. A. *J. Chem. Phys.* **1996,** *105,* 1007.
27. Simpson, W. R.; Orr-Ewing, A. J.; Rakitzis, T. P.; Kandel, S. A.; Zare, R. N. *J. Chem. Phys.* **1995,** *103,* 7299.
28. Wiley, W. C.; McLaren, I. H. *Rev. Sci. Inst.* **1955,** *26,* 1150.
29. Bracewell, R. N. *The Fourier Transform and Its Applications;* WCB McGraw-Hill: Boston, MA, 1986; pp. 262-266.
30. Bevilacqua, T. J.; Weisman, R. B. *J. Chem. Phys.* **1993,** *98,* 6316.
31. Mourits, F. M.; Rummens, F. H. A. *Can. J. Chem.* **1977,** *55,* 3007.
32. Nowak, R.; Menapace, J. A.; Bernstein, E. R. *J. Chem. Phys.* **1988,** *89,* 1309.
33. Wanna, J.; Menapace, J. A.; Bernstein, E. R. *J. Chem. Phys.* **1986,** *85,* 1795.
34. Del Bene, J. E. *Chem. Phys.* **1976,** *15,* 463.
35. Lenzer, T.; Luther, K.; Troe, J.; Gilbert, R. G.; Lim, K. F. *J. Chem. Phys.* **1995,** *103,* 626.
36. Hewett, K. B.; Shen, M.; Brummel, C. L.; Philips, L. A. *J. Chem. Phys.* **1994,** *100,* 4077.
37. Donckers, M. C. J. M.; Schwencke, A. M.; Groenen, E. J. J.; Schmidt, J. *J. Chem. Phys.* **1992,** *97,* 110.
38. Kok, P.; Groenen, E. J. J.; van Amersfoort, P. W.; van der Meer, A. F. G. *J. Chem. Phys.* **1997,** *106,* 2984.
39. Freed, K. F. in *Radiationless Processes in Molecules and Condensed Phases*; Fong, F.K.; Ed.; Topics in Applied Physics; Springer-Verlag: Berlin, 1976; pp. 23-168.
40. Hase, W. L.; Duchovic, R. J.; Hu, X.; Komornicki, A; Lim, K. F.; Lu, D.-H.; Peslherbe, G. H; Swamy, K. N.; Vande Linde, S. R.; Varandas, A.; Wang, H.; Wolf, R. J.; *VENUS96*, Quantum Chemistry Program Exchange Program No. 671.

## Chapter 11

# New Directions in Reaction Dynamics Using Velocity Map Imaging

**Musahid Ahmed, Darcy S. Peterka, and Arthur G. Suits**

**Chemical Sciences Division, Ernest Orlando Lawrence Berkeley National Laboratory, Berkeley, CA 94720**

We present several recent examples of application of the velocity map imaging technique from our laboratories in Berkeley. Results are shown for the following systems: photodissociation of vinyl radical at 243nm; reactive scattering of chlorine atoms with ethanol in crossed beams; use of imaging as an aid to identifying novel molecules; and dissociative ionization of sulfur hexafluoride using synchrotron radiation. These examples are chosen to demonstrate the versatility of the method in application to a a broad range of problems in chemical dynamics.

## Introduction

The ion imaging technique, pioneered by David Chandler and Paul Houston(*1*), has become a powerful, broadly applicable tool for the study of chemical reaction dynamics. In this chapter we present several recent applications of the technique in our laboratories in Berkeley, with an aim to showcase the versatility of the method. This chapter is organized as follows: we first present an overview of the crossed-beam imaging apparatus used in most of these studies; we then introduce one example of the use of the imaging technique to characterize H loss from hydrocarbon radicals; we then describe recent applications of the method to study reactive scattering; the following section highlights our use of photoelectron imaging to aid in identification of a novel metastable tetraoxygen species, and finally we point to new directions for imaging in a recent example using intense vacuum ultraviolet undulator radiation from the Chemical Dynamics Beamline at the Advanced Light Source in Berkeley.

## Experimental

The crossed-beam imaging apparatus used in the bulk of the studies presented here is shown schematically in Figure 1. The design is based on that of Houston et al.(*2*) with some modifications. The main chamber is a modified six-way 12" conflat cross, with four additional 2-3/4" conflat ports at 45° to the main ports in one plane. Four keying rings have been welded just inside the four main ports, on which are bolted the source differential cones. All components have been manufactured to key together so that there is no adjustment of the molecular beam sources. The differential cones are configured so that a mechanical chopper motor can be mounted to chop the molecular beam pulses to 5 microseconds or less, for the crossed-beam experiments or studies using undulator radiation. The source regions have ports for access of lasers to the nozzle regions for photolytic radical production. The molecular beam sources, typically fixed at 90° but capable of operating in a counterpropagating configuration, are each pumped by 700 l/s high-throughput compound turbomolecular pumps (Osaka TG-703M), while the main chamber is pumped by a 1000 l/s magnetic bearing turbomolecular pump (Seiko-Seiki STP-1000). The latter pump is backed by an oil-free scroll pump (Galiso-Nuvac NDP-18HV) providing a completely oil-free system in the ionization region. The molecular beams cross at the center of the main chamber on the axis of a momentum-focusing time-of-flight mass spectrometer. The products are ionized either by REMPI using UV lasers, or direct one-photon ionization using VUV undulator radiation or frequency tripled laser light, typically introduced via the smaller ports at 45°. Product ions are accelerated by repeller and acceleration fields into a ½ meter flight tube perpendicular to the plane of the beams. Product ions strike the position-sensitive detector, which is an 80-mm diameter dual microchannel plate coupled to a phosphor screen (Galileo 3075FM). Mass-selected images were obtained by pulsing the microchannel plate, typically pulsing from a DC value of -1100V to -1900V, with 1 microsecond duration. The detector is viewed by an integrating fast-scan video camera system typically employing thresholding in conjunction with a binary video look-up table. Current experiments are performed using a TMS-1000 video integration system (McLaren Research) that is capable of finding centroids of the ions spots for several hundred ions per frame in real-time. This approach also contributes to considerably improved experimental resolution.

All of the laser-based studies described here were performed using the "velocity map imaging" (VELMI) technique developed by Eppink and Parker(*3*), and discussed in some detail in Chapter X of this volume. The VELMI approach, in contrast to "traditional" ion imaging relying on space focusing conditions, allows one to focus all ions onto the detector plane strictly according to their momentum in that plane, regardless of their point of origin. This is nicely illustrated in Figure 2, in which a molecular beam of $O_2$ is crossed by a laser beam. The laser is also ionizing background gas, which shows up in the space-focused image as a long stripe, directly reflecting the spatial profile of the laser in the chamber. The molecular beam in Figure 2A also shows a width determined by the spatial profile of the overlap between the laser and molecular beam. The appearance of the analogous VELMI image in Figure 2B is dramatically altered owing to the absence of any spatial blurring of the

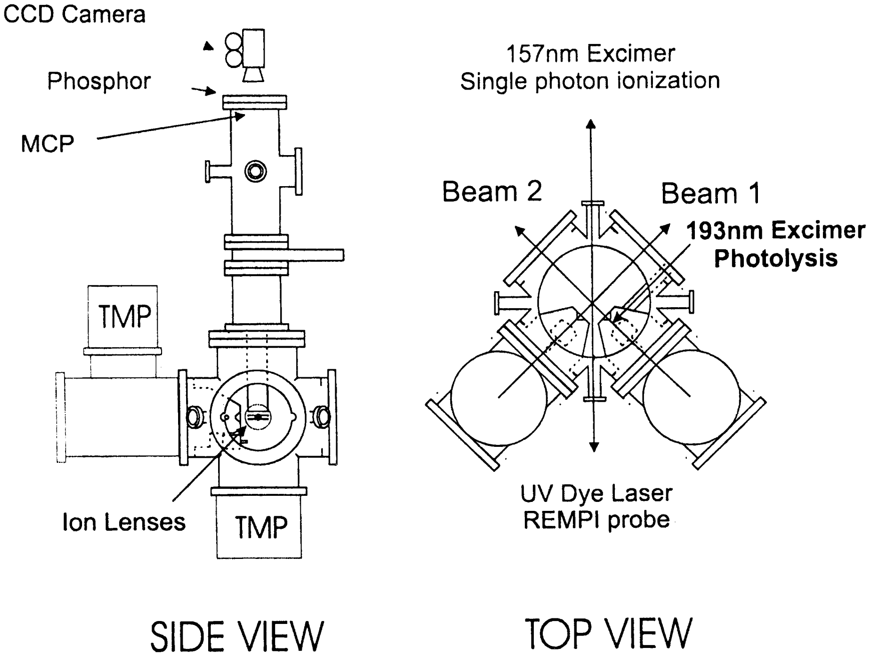
CCD Camera
Phosphor
MCP
TMP
Ion Lenses
TMP
SIDE VIEW
157nm Excimer
Single photon ionization
Beam 2
Beam 1
193nm Excimer
Photolysis
UV Dye Laser
REMPI probe
TOP VIEW

*1. Schematic view of crossed-beam imaging apparatus.*

native velocity distributions. The background gas is fully imaged according to its room temperature velocity distribution, regardless of the spatial profile of the ionization laser. The molecular beam profile is also clearly improved, showing the complete absence of the spatial blurring that is so apparent in Figure 2A.

## Imaging Radical Dissociation Dynamics

In 1965, R. G. W. Norrish asserted that combustion research followed two principal lines of investigation(*4*), one of which is "to find the nature of the chain centers, and intermediate products, and to examine quantitatively their reactions, and also involves analytical photochemical and spectroscopic studies". Following in that vein we have started a project to study the photodissociation of free radicals in molecular beams using velocity map imaging (VELMI). The study of the dynamics of photodissociation can give detailed information on the nature of the potential energy surfaces and the coupling between them, the structure of the transition state, and the identity and thermodynamics of the dissociation pathways. In this section we highlight some of our results on the photodissociation of the vinyl radical.

The molecular beams apparatus has been described in the previous section and in previous publications(*5,6*). A modification for the radical studies was to install a closed cycle He cryo-pump to minimize hydrocarbon background in the detection chamber. The radical beam was generated by photolysis of a suitable precursor by the focussed 193 nm output of a ArF excimer laser, at the nozzle of a Proch-Trickl piezoelectric pulsed valve. After the radical beam was collimated by a skimmer, it was crossed by a second photolysis/probe (one color) laser beam on the axis of a momentum focusing (VELMI) time-of-flight mass spectrometer. The product H atoms formed from the radical photodissociation were ionized using a one color (2+1) resonant enhanced multiphoton ionization (REMPI) scheme. The probe light around 243 nm was generated by doubling the output of an injection-seeded Nd-YAG pumped dye laser (Laser Analytical Systems LDL) operating at 729 nm in $\beta$- barium borate (BBO), then mixing the resultant UV light with the dye fundamental in a second BBO crystal.

The $H^+$ ion was accelerated toward a 80-mm detector and imaged as described above. All images were accumulated while scanning across the Doppler profile of the H atom, since the line width of the laser light was narrower than the Doppler spread of the detected atom. A raw image of H atoms formed in the photodissociation of the vinyl radical is shown in Figure 3(a). The direction of the molecular beam is from the upper right to the bottom left of the image, and the laser propagation direction is through the center of the image from right to left. The extremely bright spot near the center are the H atoms formed in the photolysis of vinyl chloride. The rest of the image is composed of H atoms formed via vinyl radical photodissociation. There is also structure in the outer edges of the image: two rings which can be seen in Figure 3(a) are marked. In addition, there is another very slow feature. This was studied in greater detail by reducing the acceleration fields to expand the image, and scanning the Doppler profile across this feature only. Figure 3(b) shows this magnified image

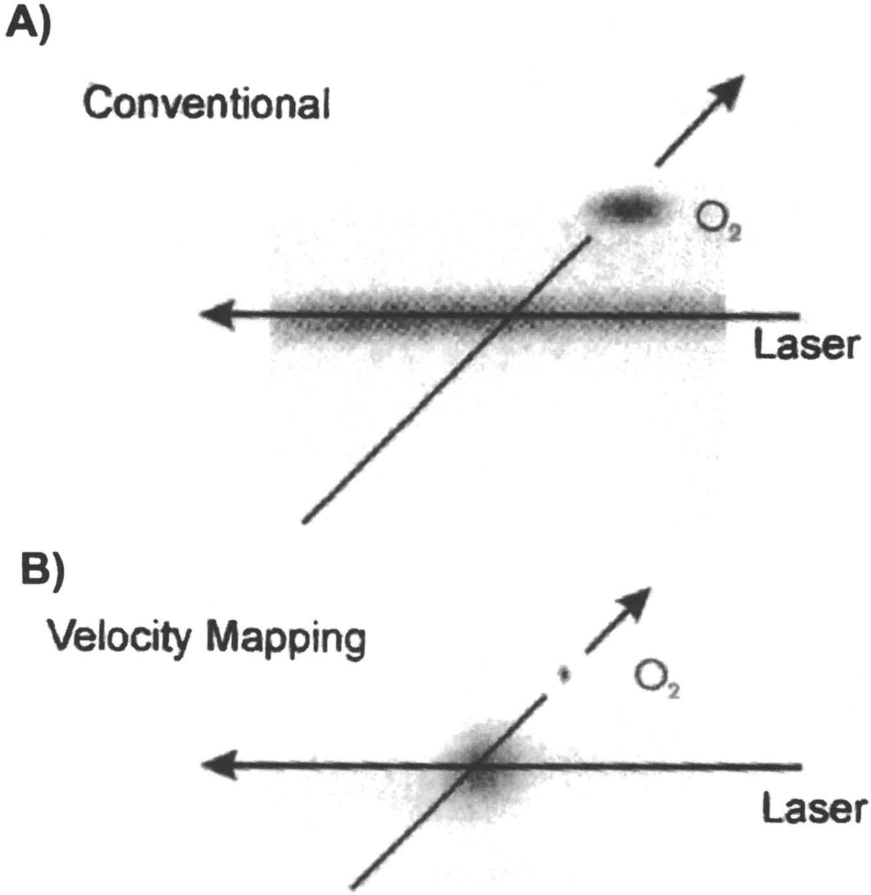
A)
Conventional
$O_2$
Laser
B)
Velocity Mapping
$O_2$
Laser

*2. Conventional ion imaging and VELMI contrasted.*

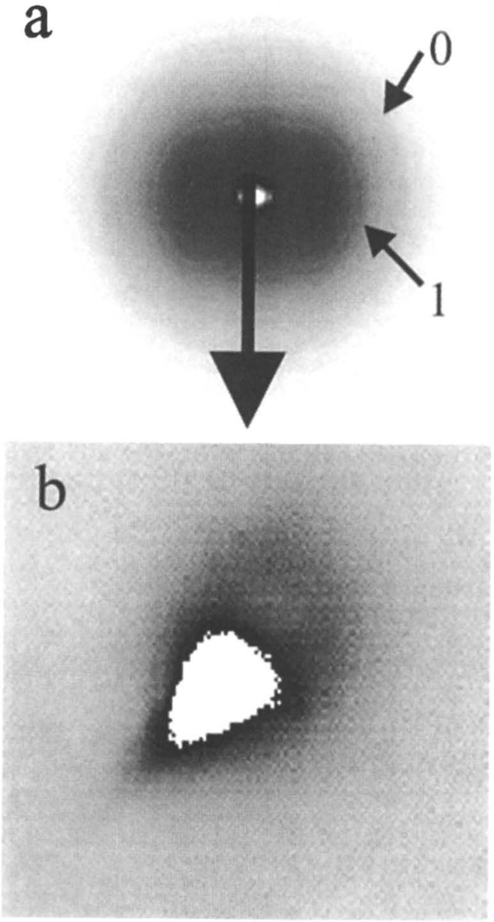

*3. a) Image of H atom from 243nm dissociation of vinyl radical b) magnified portion of slow component; c,d) P(E)'s from images at left.*

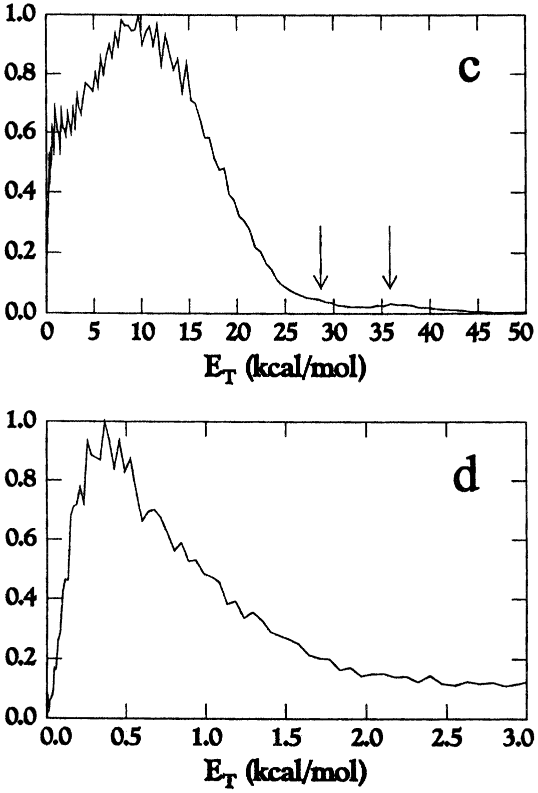

Figure 3. *Continued.*

of the inner area of the H atom distribution. Offset from the bright spot of H atoms formed via vinyl chloride dissociation at the nozzle, we see an added ring corresponding to extremely slow H atoms. The offset between the H atom spot and the center of this ring indicates that there is velocity slippage between the entrained H atoms and the vinyl radicals formed in the beam.

Figure 3(c) shows the translational energy distribution ($P(E_T)$) for the H atom obtained from the inverse Abel transformed image of Figure 3(a). The translational energy distributions were calibrated by measuring the speed of H atoms formed from the photodissociation of $H_2S$. The most noticeable feature is that the translational energy is peaked away from zero (maximum at 9.5 kcal/mol) and that the two rings mentioned above at the outer edges show up as little humps at 28.4 and 36.7 kcal/mol. Figure 3(d) is the translational energy distribution for the inner ring obtained from the inverse Abel transformed image shown in Figure 3(b), peaking at 0.4 kcal/mol.

Figure 4 shows an energy diagram for the excited states of vinyl radical accessible with the absorption of a 243 nm (117.61 kcal/mol) photon, and their correlation to various vinylidene + H and acetylene + H dissociation channels. From the translational energy release distributions, we can explore both the dynamics and the energetics of these various decay pathways. Examination of our $P(E_T)$) from Figure 4(a) shows that we have a small peak at 36.7 kcal/mol which corresponds to the $C_2H_3 \rightarrow H_2CC(^1A_1)$ + H channel. Less than 1.1% of the products appear at a higher $E_T$ (below the threshold for vinylidene formation) and these in fact may arise from 'hot band' contributions. The bulk of the translational energy distribution appears at much lower energy, however, showing that most off the available energy remains in internal degrees of freedom of the $C_2H_2$ product. The correlations in Figure 4 shows that the available product channels are only accessible from the excited states after twisting of the molecule, after which internal conversion to the ground state may precede dissociation.

The energy diagram in Figure 4 also indicates that based on most recent calculations(*7,8*), apart from forming ground state vinylidene and acetylene, there are no other channels available for H atom formation with the available photon energy of 117.6 kcal/mol. However, we do observe an additional channel giving rise to very slow H atoms. Examination of Figure 4 shows that the nearest state available to give rise to such slow H atoms must be the lowest triplet state of acetylene $C_2H_2$ ($\tilde{a}\ ^3B_2$). This state correlates directly to the excited states, and involves little geometry change from the excited radical to the product. The associated dynamics are thus likely to be direct. The excitation energy for this triplet state relative to ground state acetylene has never been measured experimentally; our results imply a term energy of 28900 $cm^{-1}$. This is significantly below the best available theoretical values(*7,8*); the discrepancy could be attributable to photolysis of the small fraction of vibrationally excited radicals in the beam. Future studies at higher dissociation energies should readily resolve this question.

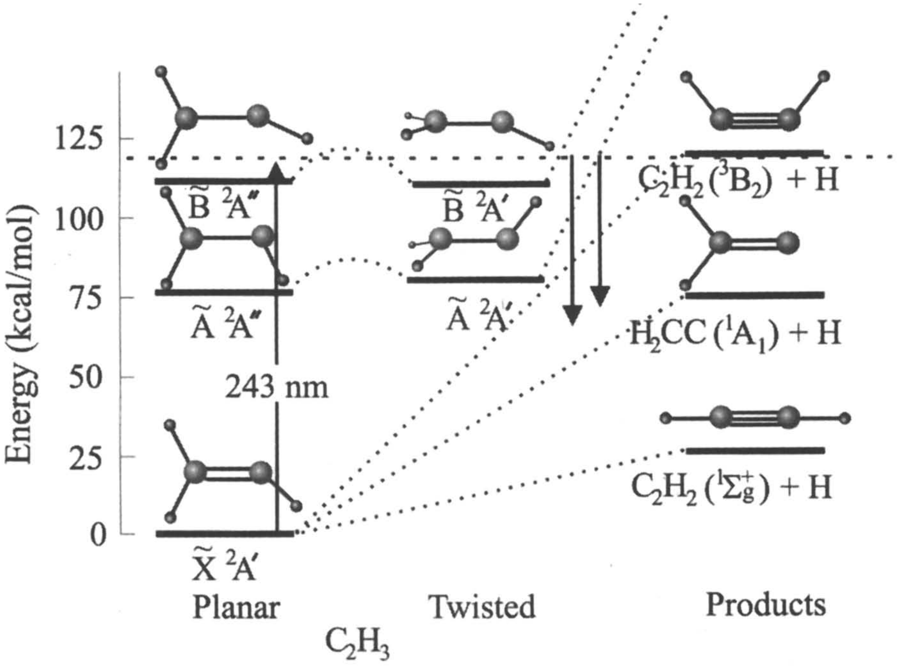
Energy (kcal/mol)
125
100
75
50
25
0
$\tilde{B}\ ^2A''$
$\tilde{A}\ ^2A''$
$\tilde{X}\ ^2A'$
243 nm
$\tilde{B}\ ^2A'$
$\tilde{A}\ ^2A'$
$C_2H_2\ (^3B_2)$ + H
$H_2CC\ (^1A_1)$ + H
$C_2H_2\ (^1\Sigma_g^+)$ + H
Planar
Twisted
Products
$C_2H_3$

4. *Schematic energy diagram for vinyl radical and dissociation to $C_2H_2$+H.*

## Reactive Scattering: $Cl+C_2H_5OH \rightarrow HCl+C_2H_4OH$

In this section we illustrate the power of the imaging technique in application to the study of chemical reactions in crossed molecular beams. The crossed-beam technique has long been recognized as the premier means of obtaining detailed insight into elementary chemical reactions, and we recently reported the first reactive scattering study using velocity map imaging (VELMI), an investigation of the reaction dynamics of the $O(^1D) + D_2 \rightarrow OD + D$ system(*9*). Crossed-beam imaging has several distinct advantages that make it an important addition to the chemical dynamicist's repertoire. These advantages include: 1) the freedom from kinematic constraints that often preclude the study of certain systems by traditional means; 2) the inherent multiplexing nature of the method, in which all recoil energies and all angles are obtained simultaneously; 3) the direct nature in which the data is recorded (effectively in the center-of-mass frame) and can be inverted, yielding the full double differential cross sections, both without tedious fitting procedures and without need for intuition to guide the fitting. Of course these advantages do not come without some cost; in the following section we summarize some of the challenges facing application of the method that have hampered its more widespread use.

The most significant difficulty with application of ion imaging methods to reactive scattering is the issue of sensitivity. For crossed-beam reactions to be practical, they require large cross sections, significant number densities of reactants, and sensitive probe techniques. The first two requirements are difficult to satisfy simultaneously; most reactions with sizable cross sections involve atomic or radical species that are not easy to produce in intense beams. Most applications of the ion imaging technique rely on laser-based multiphoton ionization processes for detection, typically 2+1 resonance-enhanced multiphoton ionization (2+1 REMPI). These probes have limited sensitivity owing to 1) the low cross sections for the two-photon excitation step, and 2) the small ionization volumes that are necessary to drive the non-linear two-photon excitation. A review of the literature shows only a few examples of crossed-beam reactive scattering studies employing ion imaging(*9-11*), and all of these have relied on 1+1 REMPI detection, precisely because of the challenges associated with 2+1 REMPI probes.

Abstraction reactions of hydrogen atoms from hydrocarbons are of great importance in combustion, and a fundamental understanding of the dynamics of these processes is important since the reactivity of the different radical products may vary widely. There has been an explosion of studies with the advent of laser technology and development of new techniques in studying such processes, particularly for the reactions of O and Cl with saturated hydrocarbons. Although alcohols have become important as alternative fuels in recent years, and there have been a few kinetic studies focussing on H abstraction from alcohols by O, Cl, and OH, it is perhaps surprising that there have been no experimental dynamics studies performed on the bimolecular reactions of alcohols, except for an earlier crossed-beam LIF study of $O(^3P)$ + $C_2H_5OH$(*12*). In this section we present results from a study the dynamics of H abstraction from alcohols using crossed molecular beams in conjunction with velocity map imaging (*13,14*).

The Cl beam was generated by photodissociation of oxalyl chloride [$(ClCO)_2$] seeded in He, using the 193 nm output of a ArF excimer laser (60 mJ, 10 Hz Lambda Physik) at the nozzle of a Proch-Trickl piezoelectric pulsed valve. The molecular beam of $(ClCO)_2$ was generated by passing helium through a bubbler containing oxalyl chloride, held at 6° C. The photodissociation dynamics of oxalyl chloride have recently been examined in our labroratory and photodissociation at 193nm yields predominantly Cl, $Cl^*$ and CO(*15*). The Cl atom beam velocity and spread was monitored using (2+1) REMPI of $Cl(^2P_{3/2})$ via the $4p^2D_{3/2} \leftarrow\leftarrow 3p^2P_{3/2}$ transition at 235.336nm. The UV photodissociation of oxalyl chloride also generates the spin-orbit excited $Cl^*(^2P_{1/2})$ which was monitored using the $4p^2P_{1/2} \leftarrow\leftarrow 3p^2P_{1/2}$ transition at 235.205nm. The $Cl^*$/Cl ratio was 1:50 and 1:62 for oxalyl chloride seeding in He and Ar respectively, or better than 98% ground state Cl, using relative linestrengths for the transitions as discussed in reference (*5*). We believe the efficient quenching is likely induced by many Cl-CO collisions. Ethanol seeded 2% in He was expanded through another Proch-Trickl pulsed valve, collimated by a single skimmer and the beams were allowed to interact on the axis of the velocity focusing time-of-flight mass spectrometer. The collision energy was reduced by seeding the oxalyl chloride in Ar.

Light from a 157nm excimer laser (1-2 mJ, 10Hz, Lambda-Physik) was focussed loosely into the interaction region of the two crossed beams and used to ionize the hydroxyalkyl radical reaction product. The ions were accelerated toward a 80-mm diameter dual microchannel plate (MCP) detector coupled to a fast phosphor screen (P-47) and imaged on a fast scan charge-coupled device camera with integrating video recorder (Data Design AC-101M). Camera threshold and gain were adjusted in conjunction with a binary video look-up table to perform integration of single ion hits on the MCP free of video noise. As discussed above, the recorded image is actually a 2-dimensional (2-D) projection of the nascent 3-dimensional (3-D) velocity distribution, and established tomographic techniques were used to reconstruct the 3-D distribution. Typical accumulation time for a single collision energy was about 30 minutes.

Figure 5 shows a raw image of the product formed at mass 45, $CH_3CHOH$, from the reaction of Cl with ethanol probed at 157nm. The relative velocity vector is vertical in the plane of the figure, and the Newton diagram for the scattering process has been superimposed on the image. There is substantial photodissociation of ethanol at 157nm, which also produces $CH_3CHOH$. This shows up as the small ring centered at the ethanol beam. As is immediately apparent from the image, this creates a problem in extracting information for forward scattering relative to the incoming alcohol beam. We subtracted an image recorded with the 193nm laser off from a reactive scattering image to remove the photodissociation contribution from the reactive scattering image. Unfortunately, the intense photochemical signal creates substantial noise and corresponding uncertainty in the reactive flux formed between 0-50°. However we can extract the full double-differential cross-section reliably from the rest of the image.

The abstraction of an H atom from ethanol by the Cl atom can give rise to three different radicals as shown below:

$$CH_3CH_2OH + Cl \rightarrow CH_3CHOH + HCl \qquad \Delta H = -9.3\ \text{kcal/mol} \qquad (1)$$

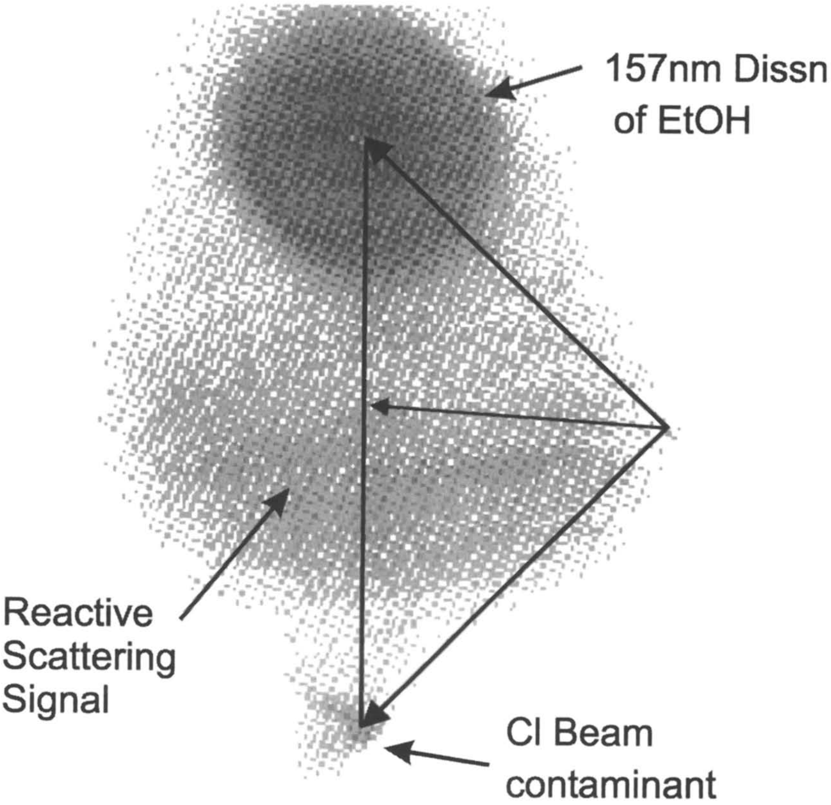

*5. Raw image of hydroxyethyl radical product of Cl+ethanol reaction.*

$$\rightarrow CH_2CH_2OH + HCl \qquad \Delta H = 0.5 \text{ kcal/mol} \qquad (2)$$

$$\rightarrow CH_3CH_2O + HCl \qquad \Delta H = 4.5 \text{ kcal/mol} \qquad (3)$$

In our experiment we will not observe the ethoxy radical channel (3), since its ionization energy of 10.29 eV(*16*) is way above that available from a 157nm photon (7.89 eV). The ionization energies for the 1-hydroxyethyl and 2- hydroxyethyl radical formed in process (1) and (2) are 6.64 eV(*17*) and ~8.2 eV(*16*) respectively. However the I.E. for 2-hydroxyethyl is by no means conclusive. Ruscic and Berkowitz(*16*) quote a figure of 8.18±0.08, but they infer an I.P of ~7.7 eV depending on the thermodynamic cycle and bond dissociation energies employed in generating the result. A G-2 theoretical result(*18*) posits 7.58 eV as the adiabatic ionization energy for the 2-hydroxyethyl radical. Khatoon *et al.* (*19*) carried out an end product analysis experiment to measure the rates of this reaction and also derive the branching ratio for the formation of the three different radicals. They conclude for the reaction of Cl with alcohols no abstraction from the OH group was observed and that the abstraction from the alkyl groups followed the thermodynamically favoured route by forming mainly secondary radicals. With this in mind we can tentatively say that the mass 45 detected is the 1-hydroxyethyl radical.

Reactive scattering experiments with ethanol were performed at two collision energies $E_{coll}$ = 6.0 kcal/mol and 9.7 kcal/mol. Figure 6A and 6B shows the subtracted images for these two collision energies, respectively. It is apparent from both images that the reactive flux does not extend out to the thermodynamic limit. The average translational energy release is 38 and 32% of the available energy for $E_{coll}$ = 6.0 kcal/mol and 9.7 kcal/mol, respectively. The upper panel in Figure 7 shows the translational energy distribution obtained from the reconstructed data at $E_{coll}$ = 6.0 kcal/mol and 9.7 kcal/mol. The corresponding angular distributions are shown in the lower panel. As was apparent in the raw images, we see a large enhancement in sideways scattering with an increase in collision energy. There is also significant coupling between translational energy release and the angular distribution, particularly at the lower collision energy.

T. Khatoon *et al.*(*19*) studied the kinetics and mechanism of reaction of Cl with ethanol ($7.2 \times 10^{13}$ $cm^3$/mol s) and 1- and 2- propanol. For the reaction of Cl atoms with alcohols, the authors saw no abstraction from the OH group, abstraction from the alkyl groups followed the thermodynamically favored route by forming mainly secondary radicals. J. Edelbuttel-Einhaus et al.(*20*) report a rate constant of $4.72 \times 10^{13}$ $cm^3$/mol s and obtain a branching ratio of 1:20 between reaction 4 and 3 confirming that the 1-hydroxyethyl radical is predominantly formed.

These results clearly show the importance of a direct reaction mechanism likely involving a near-collinear Cl-H-C transition state. Additional insight is provided by the effect of collision energy on the dynamics. At low collision energy, scattering is predominantly in the backward hemisphere. With an increase in collision energy the scattering is enhanced in the sideways direction with no concomitant increase in the translational energy release. The angular distributions for ethanol at the higher collision energy begins to resemble that of methanol, suggesting that finite impact parameter collisions begin to play a role, or deviations from collinearity may be more important. The translational energy release in reduced in the sideways direction,

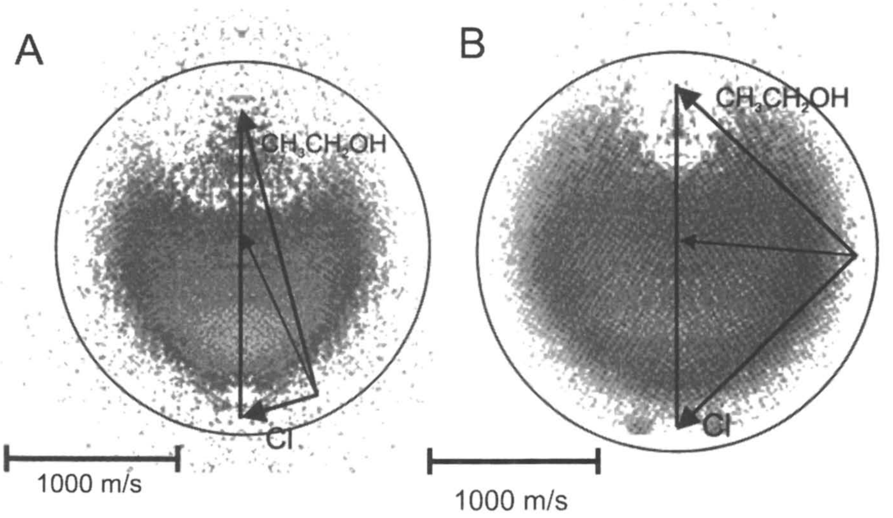

6. *Images of reactively scattered hydroxyethyl radical from reaction of Cl with ethanol at relative collision energies of 6.0 (A) and 9.7 (B) kcal/mol.*

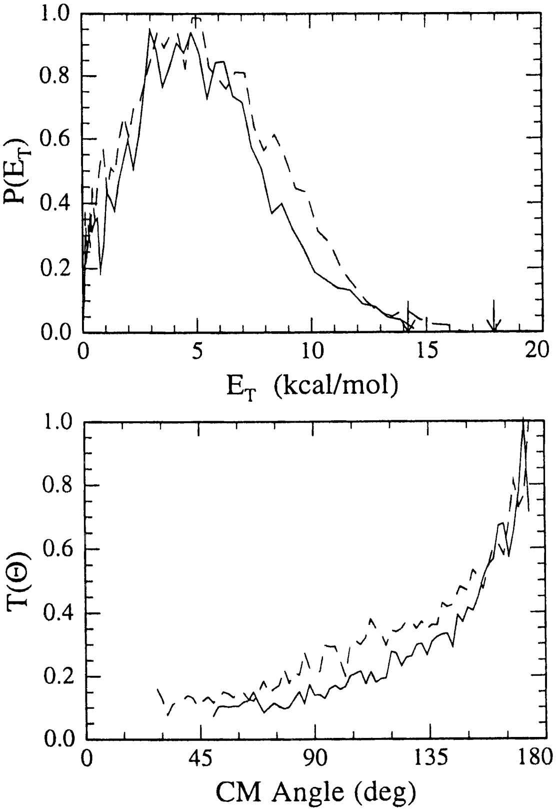

*7. Translational energy distribution (top) and CM angular distribution (bottom) for Cl+ethanol reaction at 6.0 (solid) and 9.7 (dashed) kcal/mol.*

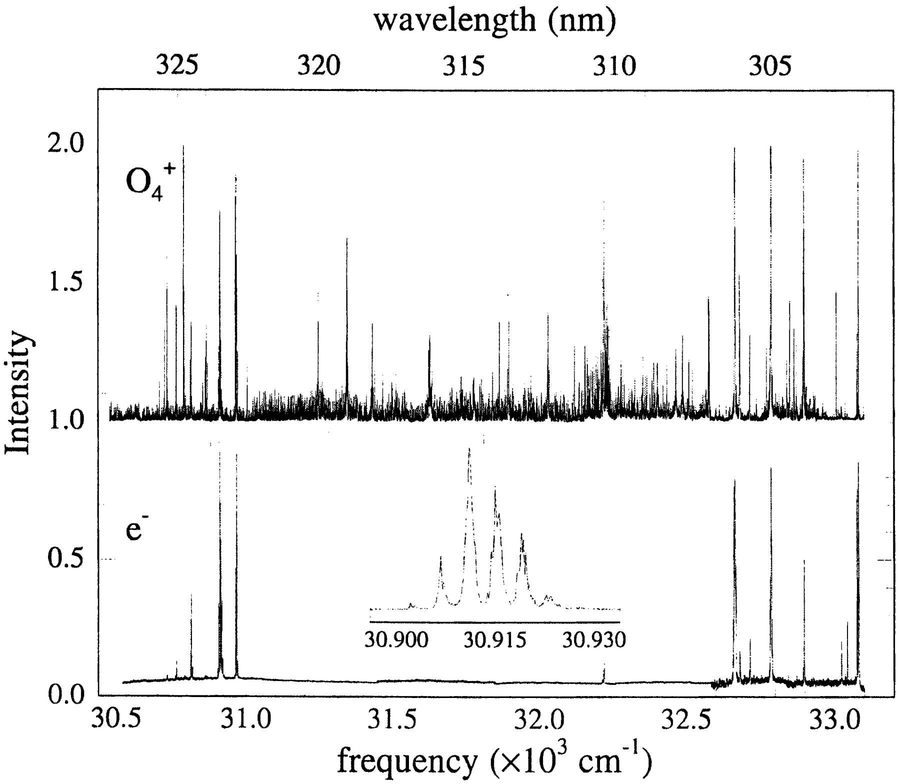

8. *Photoelectron and m/e=64 PIY spectra of $O_2$ beam through a DC discharge.*

implying greater internal energy in the larger impact parameter collisions. This is consistent with greater rotational excitation for these side-ways scattered products.

The energies of the C-H bonds in ethanol and propane are very similar, furthermore the structures resemble each other. This allows us to compare the results for Cl-$C_2H_5OH$ with Cl-$C_3H_8$. We do not observe the large impact parameter dominated forward scattering reported in the case of propane(*21*). However, for the low impact parameter sideways-backward scattering there is qualitative agreement with our results. Blank et al. (*21*)saw strong coupling between their angular and translational energy distributions, again this is in agreement with our observations. These authors(*21*) found a much larger fraction of available energy in translation than in the Cl-ethanol reaction, and this fraction changed little with collision energy ($<E_T>/E_{avail}$ = 0.53, 0.52, 0.48 for $E_{coll}$ = 8.0, 11.5, 31.6 kcal/mol).

It is surprising, given the similarity in the sideways-backward scattering between the Cl-alcohol and Cl-hydrocarbon systems, that we do not observe the forward scattering component seen by Suits and co-workers in their Cl-hydrocarbon experiments(*21,22*). As mentioned before we cannot extract quantitative information about forward scattering events since the extensive photodissociation of the parent alcohol blinds us in this sector. However any forward scattering will be superimposed on the photodissociation signal and this should be readily observable in our experiment. A possible explanation for the difference between our experiment and those performed on the Cl-hydrocarbon systems may lie in the source of Cl atoms used in the two sets of experiments. We used a photolytic source and have carefully characterised the Cl beam to be of predominantly ground state Cl atoms. In the Cl-hydrocarbon experiments(*21,22*) the Cl atom beam was generated by thermal dissociation of $Cl_2$ in a heated nozzle maintained at 1500-1550°C. A Boltzmann distribution as stated by the authors predicts that ca. 15% of the chlorine atoms will be formed in spin-orbit excited state, Cl ($^2P_{1/2}$). While the excited state component of the Cl beam was not explicitly determined, the authors assumed that the supersonic expansion would relax the spin-orbit excited component of the beam. Recently Liu and co-workers have seen enhanced reactivity with spin-orbit excited Cl and F atoms(*23*) (*24*). They find the spin-orbit excited atoms show very different dynamical behavior compared to their ground state counterparts. We tentatively suggest that the forward scattering seen in the crossed-beam Cl-hydrocarbon systems may arise from the participation of the spin-orbit excited component of their Cl beam. Efforts are underway in this laboratory to study the effect of spin-orbit excitation on the reaction dynamics of alcohols and hydrocarbons. These results demonstrate the power of VELMI combined with single-photon VUV ionization. Work is currently underway in our laboratory on reactions with other alcohols, and analogous reactions of O and OH should be quite feasible. With judicious choice of chemical system and probe light sources, the detailed and systematic investigations of the dynamics of many polyatomic reactions should be routine.

## Identification of novel species: $O_4^*$

In a recent report from our laboratory(*25*), 1+1 resonant photoionization spectra were reported for an energetic, metastable $O_4$ species produced in a DC discharge. Intense spectra were observed throughout the region from 280 to 325 nm. In the absence of plausible alternatives accounting for all the observations, an energetic covalent $O_4$ species was considered the most likely candidate. Our subsequent studies(*26,27*), including rotationally resolved photoion and photoelectron yield spectra as well as photoelectron imaging results suggest instead that the identity of this energetic $O_4$ species is a novel complex involving one ground state $O_2$ molecule and one in the metastable $c(^1\Sigma_u^-)$ state. This system nicely illustrates the versatility of the imaging technique for application to novel problems.

Interest in tetraoxygen molecules dates to a 1924 paper by G. N. Lewis(*28*); since then, studies of $O_2$ dimers have enjoyed a long history of investigation(*29-31*). Theoretical studies of covalently bound $O_4$ species began with Adamantides' 1980 prediction of a bound cyclic ($D_{2d}$) form(*32*). This stimulated considerable further theoretical effort as this cyclic $O_4$, nearly 4 eV higher in energy than two $O_2$ molecules, appeared to be a promising candidate for a high energy density material(*33-35*). Subsequent theoretical studies have also identified a $D_{3h}$ form analogous to $SO_3$ at a somewhat higher energy(*36,37*). Photodetachment studies on $O_4^-$ have also provided detailed insight into the various decay processes available to this species at lower energy(*38*). Although experimentalists have long observed evidence of van der Waals' complexes of ground state $O_2$ molecules, no evidence has been found supporting the theoretical predictions of covalent $O_4$ species.

The photoelectron yield and m/e=64 photoion yield (PIY) spectra Figure 8. The fact that we can achieve 1+1 ionization in this region implies two important things: 1) the discharge must produce an initial $O_4$ complex with at least 4 eV internal energy, and 2) there must be an excited state roughly 4 eV above this through which the ionization takes place. The rotational spacing in Figure 8, however, is roughly 3.8 $cm^{-1}$, not consistent with any of the predicted geometries for the covalent forms of $O_4$. Additional insight is provided by the representative photoelectron images and kinetic energy spectra recorded on a number of resonant lines that are shown in Figure 9. With few exceptions, these are dominated by single, low-energy peaks in the photoelectron spectrum, precisely what one would expect for ionization via Rydberg states. It seemed at first difficult to reconcile several of these observations: both the photoelectron spectra and the rotational spacing suggested some kind of excited van der Waals complex, but it seemed unlikely that these would only ionize to give $O_4^+$; however, no other ions were observed in these spectra. A careful consideration of the potential curves, particularly in light of the illuminating studies of charge transfer to $O_2$ conducted by van der Zande and coworkers(*39,40*), produced the following picture accounting for all the observations, summarized in Figure 10. If we begin with a van der Waals complex between $O_2$ $X(^3\Sigma_u^-)$ and $O_2$ $c(^1\Sigma_u^-)$, a fully allowed electronic transition localized on the c state molecule(*41*) takes us to a complex involving the

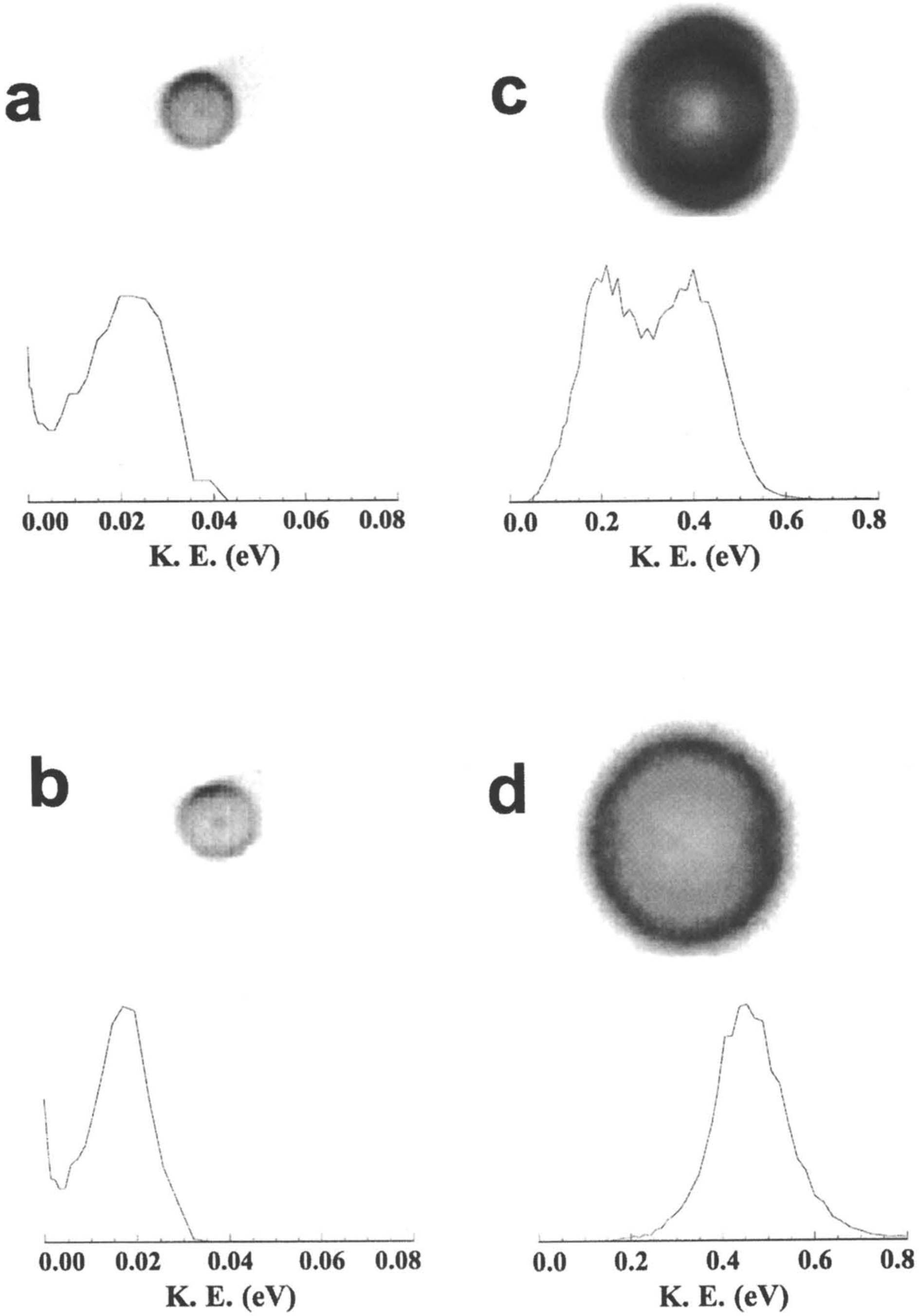

9. *Photoelectron images recorded on various lines in the spectra of Figure 8: a)323.48nm; b)306.12nm; c)296.79nm; and d) 294.89nm.*

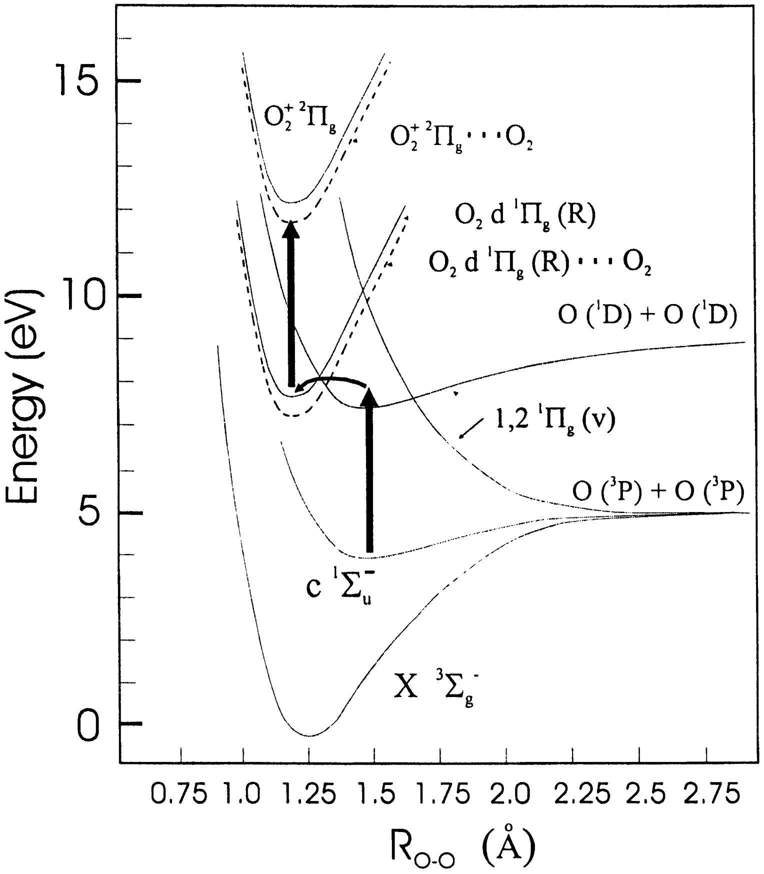

*10. Relevant potential curves adapted from references 40 and 41 ( see text).*

$1(^1\Pi_g)$ state. This state can either predissociate to give oxygen atoms (and an $O_2$ molecule), or couple to the $d(^1\Pi_g)$ Rydberg state, or the system can dissociate to two $O_2$ molecules. It is likely that all of these occur, no doubt with a strong dependence upon the initially excited vibrational level. If the Rydberg complex is formed, it can then ionize easily in this wavelength region, and the ionization will be dominated by $\Delta v=0$ transitions owing to the diagonal Franck-Condon factors between the Rydberg and the ion. If this picture is accurate for $O_4$, it is surprising that no $O_2^+$ is seen; this implies some significant differences for the ionization dynamics in the complex as opposed to the free $O_2$ molecule. In fact, it is precisely in the nature of these Rydberg-valence interactions that we can expect a profound impact of the formation of the van der Waals complex. This is because the Rydberg state will be greatly stabilized in the complex-nearly to the extent of the 0.45 eV bond in $O_2$--$O_2^+$. The valence state curves will be little-perturbed in comparison. The location of the Rydberg and ion curves for the complex are shown as dashed lines in Figure 10. This provides a reasonable explanation for the absence of the $O_2^+$ in these experiments despite the likelihood that the number density of free $O_2$ $c(^1\Sigma_u^-)$ molecules is much greater than those involved in complexes. The fate of the free $O_2$, upon excitation to the $1(^1\Pi_g)$ state, is either predissociation via the $2(^1\Pi_g)$ state, or by the triplet states interacting with the d state.

Many of the experimental results can be satisfactorily accounted for by invoking this complex. The rotational spacing in the long wavelength region, about 3.5 $cm^{-1}$, is very near $4B_e$ for the $c(^1\Sigma_u^-)$ state ($B_e$ = 0.9 $cm^{-1}$). This would be expected, for example, for a T-shaped complex wherein one of the rotational constants will resemble that of one of the $O_2$ molecules. The photoelectron spectra, dominated by single peaks, arise owing to the fact that the ionization takes place from a complex involving the $d(^1\Pi_g)$ Rydberg state so that $\Delta v=0$ transitions dominate as mentioned above. Finally, the absence of $O_2^+$ is likely explained by the very different Rydberg-valence interactions in the complex as opposed to the free $O_2$. This picture also accounts for some unusual spectra reported in a closely related study by Helm and Walter(*42*). Their experiments were similar to the studies of van der Zande et al.(*39,40*) but used charge transfer to $O_4^+$ rather than $O_2^+$. They reported clearly resolved vibrational structure in the $O_2$ product kinetic energy distributions following charge transfer from cesium, which they reluctantly ascribed to coincident formation of two $O_2$ molecules in v=29, a rather unlikely process, to account for the vibrational spacing of 800 $cm^{-1}$ observed in the $O_2$ kinetic energy release distributions. Our alternative interpretation of their results suggests simply the reverse of the ionization process outlined above: electron transfer from cesium populates the Rydberg state around 7.6 eV, which then couples efficiently to the metastable $O_2$ $X(^3\Sigma_u^-)$--$O_2$ $1(^1\Pi_g)$ complex. We suggest the structure in the kinetic energy release distributions of Helm and Walter simply reflects the vibrational structure in the metastable state. For the Herzberg states, the vibrational frequencies are all on the order of 800 $cm^{-1}$; the vibrational frequency in the $1(^1\Pi_g)$ state is likely to be similar.

## Imaging dissociative ionization dynamics in $SF_6$

We present a final recent example of ion imaging studies in Berkeley pointing to important new opportunities using tunable synchrotron radiation in imaging studies of reaction dynamics. In this study, the technique of photofragment imaging has been adapted to use on a VUV undulator beamline at the Advanced Light Source(*43*), affording a new approach to the study of dissociative ionization processes. The technique allows direct inversion of the raw data to yield angular and translational energy distributions for the product ions. The method is here applied to study the dissociative ionization of $SF_6$ at photon energies from 15 to 28 eV. The experiment allows for detailed characterization of the angular and translational energy distributions of the fragments, providing insight into the decay mechanisms of these excited ionic states.

These experiments were performed in a new endstation recently added to the Chemical Dynamics Beamline(*44*). The apparatus is schematically illustrated in the inset to Figure 11. Briefly, it features a molecular beam source pumped by a 2000 L/s magnetic bearing turbomolecular pump. The molecular beam is skimmed once before entering the ionization chamber, pumped by two 400 L/s magnetic bearing turbomolecular pumps. Product ions are accelerated by repeller and acceleration fields into a 0.5 meter flight tube perpendicular to the plane of the beams. They then strike a position-sensitive detector, which is a 40-mm diameter dual microchannel plate coupled to a phosphor screen . Photionization yield (PIY) spectra were obtained by integrating the ion TOF peaks as a function of photon energy. Mass-selected images were obtained by pulsing the microchannel plate, typically pulsing from a DC value of −1100 to −1900 V, with 300 nanosecond duration. The detector is viewed by an integrating fast-scan video camera system employing thresholding in conjunction with a linear video look-up table. Typical accumulation times were 10 minutes for each image. The molecular beam was produced by passing neat $SF_6$ through a piezoelectric pulsed valve operating at 90 Hz with 100 microsecond pulses. Time-of-flight mass spectra were recorded by placing a photomultiplier tube to view the detector. The polarization of the undulator radiation is purely linear, and parallel to the plane of the detector.

The images recorded are 2-dimensional projections of the 3-dimensional recoiling product ion sphere. The translational energy, speed and angular distributions were reconstructed from the projection using standard techniques. Images of $SF_5^+$, $SF_4^+$ and $SF_3^+$ were recorded (when observed) at various photon energies from to 16.0 to 24 eV, although only results for $SF_5^+$ will be presented here. These are not coincidence experiments, and the dissociation processes are not presented for energy selected ions. However, to estimate contributions from particular electronic states, difference images were generated for $SF_5^+$ during analysis. This involved collecting two images one below and one above the rise of a feature in the PIY curve and then subtracting them. This approach is intended to provide an overview of the dynamics in a given region, roughly corresponding to a threshold experiment, but clearly it is not a truly energy-selected measurement.

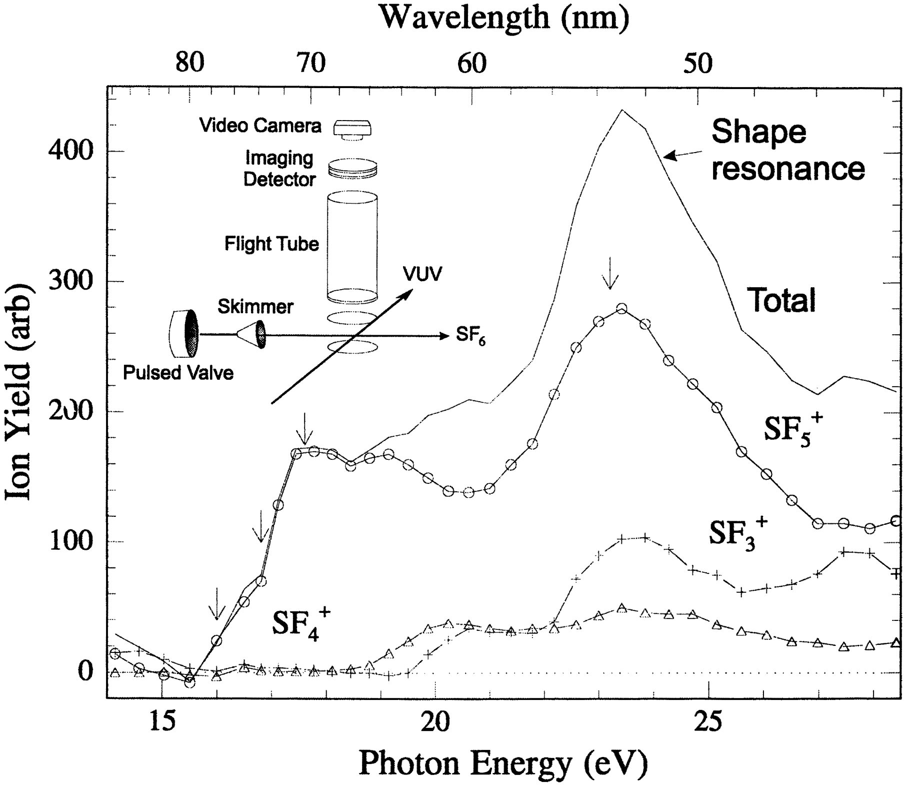

*11. Photoion yield spectra for $SF_6$.*

The PIY spectra for the various product ions are shown in Figure 11. Arrows in the figure indicate photon energies at which images were recorded to obtain translational energy and angular distributions. The onset for $SF_5^+$ is found near 15.5 eV, consistent with previous reports (see ref. (*45*) and references therein) It shows additional onsets at 17 eV, 20 eV, some decrease beginning near 19 eV, and a very prominent resonant feature at 23 eV. $SF_4^+$ shows an onset around 18.5 eV, again consistent with previous reports, and shows only modest changes up to 30 eV. $SF_3^+$ appears at 20 eV, and exhibits the same resonant feature seen in $SF_5^+$ near 23 eV.

An image for $SF_5^+$ at 16 eV, and difference images at 16.8, 17.6, and 23.2 eV are shown in Figure 12. From these images, we obtain the translational energy distributions shown in Figure 13. These energy distributions show surprisingly little change with the changing excitation energy throughout this region. As mentioned above, these results are not obtained for energy-selected ions. Instead, we derive the translational energy distributions from difference images taken in an effort to isolate the contribution for a given region of onset. At 16 eV the average translational energy release is 0.62 eV, and extends to a maximum of 1.8 eV. At 16.8 and 17.6 eV the average release is ~0.55 eV with a maximum energy of 1.4 eV, while at 23.2 eV the average energy release is 0.66 eV with a maximum release of ~1.7 eV.

The angular distributions are shown for $SF_5^+$ for the four representative photon energies in Figure 13. These were fitted to the familiar expression: $I(\Theta) \propto 1 + \beta P_2(\cos(\Theta))$ to obtain the $\beta$ parameters(*46*). The $\beta$ values obtained are: 0.94 at 16 eV, 1.23 at 16.8 eV, 1.24 at 17.6 eV, and reach a maximum of 1.31 at 23.2 eV.

The detailed kinetic energy distributions shown in Figure 13 are the first obtained for dissociative ionization of $SF_6$, and noteworthy in the level of detail achieved. The average of the distributions agree reasonably well with the low resolution measurements previously reported. These distributions are remarkably independent of ionization energy, possibly suggesting a late barrier to decomposition of $SF_6^+$ to $SF_5^+$ + F. Consideration of the geometry changes involved provides a plausible picture of the dissociation pathway. Stretching of one of the S-F bonds in $SF_6^+$ yields an $SF_5^+$ ion initially in a square pyramidal geometry. However, recent ab initio calculations(*47,48*) confirm that the structure of $SF_5^+$ is clearly trigonal bipyramidal ($D_{3h}$), so that extensive rearrangement must occur during the dissociation process. The kinetic energy release likely reflects fairly efficient conversion of the energy of this barrier into product repulsion. The fact that the kinetic energy distributions are similar for several excited states of the $SF_6^+$ ion may indicate that internal conversion to the ground state of the ion precedes dissociation. This is also consistent with the similarities in the angular distributions.

Our observed anisotropic $SF_5^+$ angular distributions augment the picture of the dynamics sketched above. All of the $SF_5^+$ distributions show considerable anisotropy consistent with a parallel dissociation; that is, the fragments show a strong tendency to dissociate on an axis parallel to the polarization of the VUV radiation. This may seem surprising for such a highly symmetrical molecule (point group $O_h$.) Ionization through the $\tilde{X}$, $\tilde{A}$ and $\tilde{B}$ states of $SF_6^+$ are ($1t_{1g}^{-1}$}) and [($5t_{1u}^{-1}$})+($1t_{2u}^{-1}$)] ionizations respectively(*45*). These all represent removal of 2p lone pair electrons from the fluorine atoms(*49*), so it is perhaps not so surprising that a more local view of the

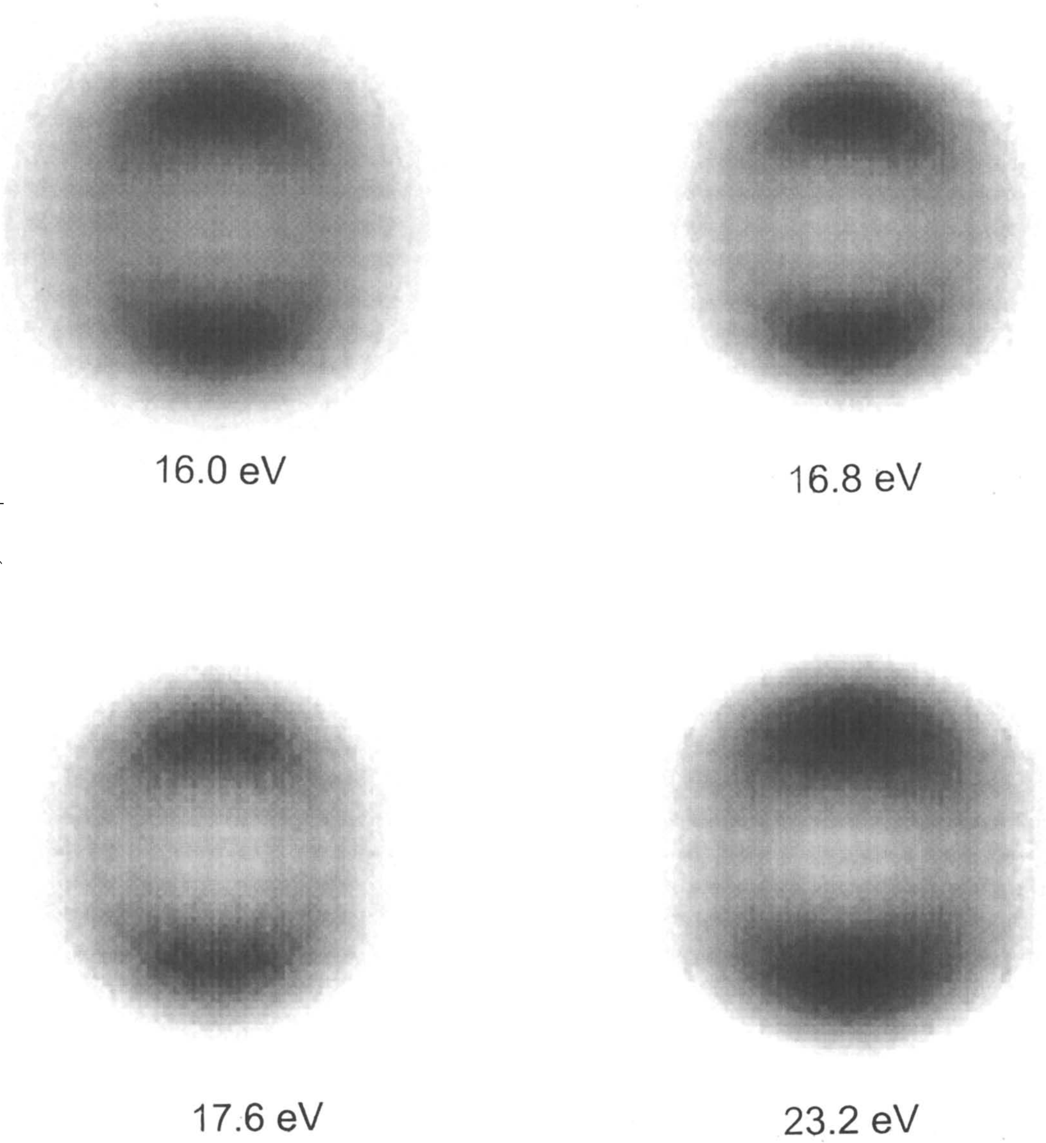

16.0 eV

16.8 eV

17.6 eV

23.2 eV

*12. Images of $SF_5^+$ from dissociative ionization of $SF_6$ at the indicated energies.*

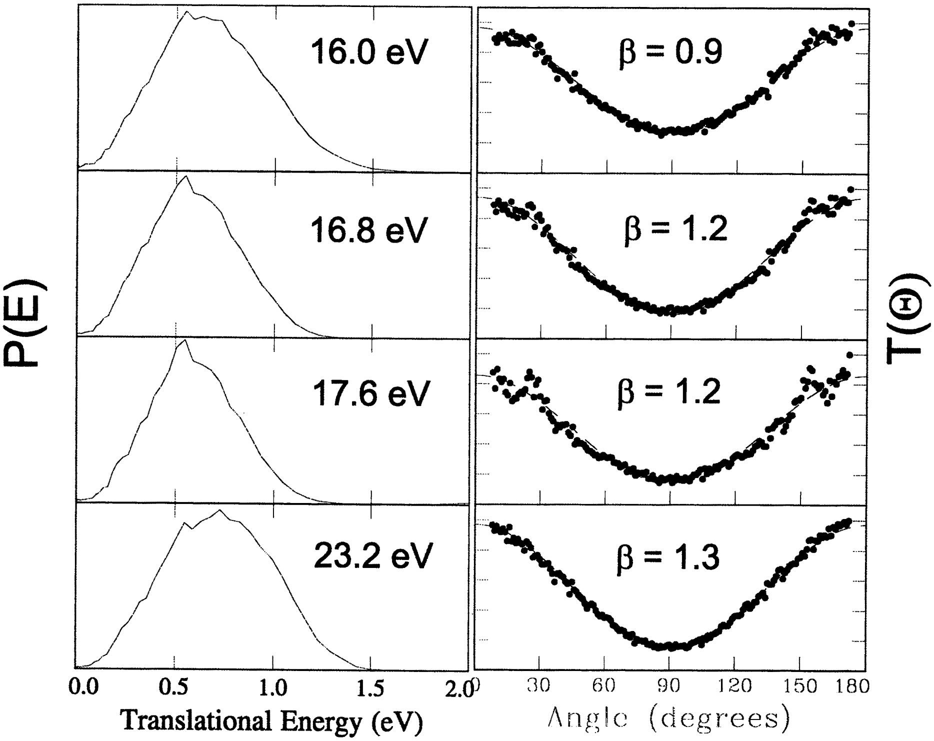

*13. Translational energy (left) and angular distributions (right) for $SF_5^+$ from images in Figure 12.*

ionization and subsequent dissociation is appropriate. The angular distributions further show that the autoionization via the shape resonance must be very rapid. Photoelectron spectra at these photon energies would be useful to identify the $SF_6^+$ state(s) formed in the ionization step. All of these angular distributions show that the $SF_6^+$ dissociation is very rapid, occurring on a timescale short compared to its rotational period. These studies also provide insight into the dynamics underlying the productions of $SF_4^+$ and $SF_3^+$; interested readers are directed to reference (*44*) for a full account of these studies. This preliminary investigation provides only a glimpse of what will be possible as imaging methods are combined routinely with intense, tunable VUV synchrotron radiation. This promises to be an important new direction for the technique.

## Conclusion

In this chapter we have highlighted several recent examples of the applications of ion imaging techniques to a broad range of problems in chemical reaction dynamics, from radical photochemistry to crossed-beam reactions, from identification of novel molecules to studies of dissociative ionization dynamics. We believe the only limits to the application of the method are the limits of the dynamicist's imagination, and we look forward in eager anticipation of further developments over the coming decade.

*Acknowledgments.*
This work was supported by the Director, Office of Energy Research, Office of Basic Energy Sciences, Chemical Sciences Division of the U.S. Department of Energy under contract No. DE-ACO3-76SF00098. The ALS is supported by the Director, Office of Energy Research, Office of Basic Energy Sciences, Materials Sciences Division of the U.S. Department of Energy under the same contract.

## Literature Cited

1. Chandler, D. W.; Houston, P. L. *J. Chem. Phys.* **1987**, *87*, 1445.
2. Bontuyan, L. S.; Suits, A. G.; Houston, P. L.; Whitaker, B. J. *J. Phys. Chem.* **1993**, *97*, 6342.
3. Eppink, A.; Parker, D. H. *Rev. Sci. Instrum.* **1997**, *68*, 3477.
4. Norrish, R. G. W. In *Tenth symposium (International) on Combustion*; Combustion Institute, Pittsburgh, PA, 1965; pp 1.
5. Ahmed, M.; Blunt, D.; Chen, D.; Suits, A. G. *J. Chem. Phys.* **1997**, *106*, 7617.
6. Ahmed, M.; Peterka, D. S.; Suits, A. G. *J. Chem. Phys.* **1999**, *110*, 4248.
7. Lundberg, J. K.; Field, R. W.; Sherrill, C. D.; Seidl, E. T.; Xie, Y.; Schaefer, H. F. *J. Chem. Phys.* **1993**, *98*, 8384.

8. Yamaguchi, Y.; Vacek, G.; Schaefer, H. F. *Theoretica Chimica Acta* **1993**, *86*, 97.
9. Ahmed, M.; Peterka, D. S.; Suits, A. G. *Chem. Phys. Lett.* **1999**, *301*, 372.
10. Suits, A. G.; Bontuyan, L. S.; Houston, P. L.; Whitaker, B. J. *J. Chem. Phys.* **1992**, *96*, 8618.
11. Kitsopoulos, T. N.; Buntine, M. A.; Baldwin, D. P.; Zare, R. N.; Chandler, D. W. *Science* **1993**, *260*, 1605.
12. Dutton, N. J.; Fletcher, J. W.; Whitehead, J. C. *J. Phys. Chem.* **1985**, *89*, 569.
13. Ahmed, M.; Peterka, D. S.; Suits, A. G. *Chem. Phys. Lett.* **2000**.
14. Ahmed, M.; Peterka, D. S.; Suits, A. G. *Phys. Chem. Chem. Phys.* **2000**.
15. Hemmi, N.; Suits, A. G. *J. Phys. Chem. A* **1997**, *101*, 6633.
16. Ruscic, B.; Berkowitz, J. *J. Chem. Phys.* **1994**, *101*, 10936.
17. Dyke, J. M.; Groves, A. P.; Lee, E. P. F.; Niavaran, M. H. Z. *J. Phys. Chem. A* **1997**, *101*, 373.
18. Curtiss, L. A.; Lucas, D. J.; Pople, J. A. *J. Chem. Phys.* **1995**, *102*, 3292.
19. Khatoon, T.; Edelbuttel-Einhaus, J.; Hoyermann, K.; Wagner, H. G. *Ber. Bunsenges. Phys. Chem.* **1989**, *93*, 626.
20. Edelbuttel-Einhaus, J.; Hoyermann, K.; Rohde, G.; Seeba, J. In *J. Proc. Symp (Int.) Combust.*, 1992; Vol. 24; pp 661.
21. Blank, D. A.; Hemmi, N.; Suits, A. G.; Lee, Y. T. *Chem. Phys.* **1998**, *231*, 261.
22. Hemmi, N.; Suits, A. G. *J. Chem. Phys.* **1998**, *109*, 5338.
23. Lee, S. H.; Lai, L. H.; Liu, K. P.; Chang, H. *J. Chem. Phys.* **1999**, *110*, 8229.
24. Liu, K. P. , 1999.
25. Bevsek, H. M.; Ahmed, M.; Peterka, D. S.; Sailes, F. C.; Suits, A. G. *Farad. Disc.* **1997**, 131.
26. Peterka, D. S.; Ahmed, M.; Suits, A. G.; Wilson, K. J.; Korkin, A.; Nooijen, M.; Bartlett, R. J. *J. Chem. Phys.* **1999**, *110*, 6095.
27. Peterka, D. S.; Ahmed, M.; Suits, A. G.; Wilson, K. J.; Korkin, A.; Nooijen, M.; Bartlett, R. J. *J. Chem. Phys.* **1999**, *111*, 5279.
28. Lewis, G. N. *J. Am. Chem. Soc.* **1924**, *46*, 2027.
29. Dianov-Klonov, V. I. *Opt. Spectrosc.* **1959**, *6*, 290.
30. Leckenby, R. E.; Robins, E. J. *Proc. R. Soc. London, Ser. A* **1965**, *265*, 389.
31. Long, C. A.; Ewing, G. E. *J. Chem. Phys.* **1972**, *58*, 4824.
32. Adamantides, V.; Neisius, D.; Verhaegen, G. *Chem. Phys.* **1980**, *48*, 215.
33. Seidl, E. T.; Schaefer, H. F. *J. Chem. Phys.* **1988**, *8*, 7043.
34. Seidl, E. T.; Schaefer, H. F. *J. Chem. Phys.* **1992**, *96*, 1176.
35. Dunn, K. M.; Scuseria, G. E.; Schaefer, H. F. *J. Chem. Phys.* **1990**, *92*, 6077.
36. Roeggen, I.; Nilssen, E. W. *Chem. Phys. Lett.* **1989**, *157*, 409.
37. Hotokka, M.; Pyykko, P. *Chem. Phys. Lett.* **1989**, *157*, 415.
38. Hanold, K. A.; Continetti, R. E. *Chem. Phys.* **1998**, *239*, 493.
39. van der Zande, W. J.; Koot, W.; Los, J. *J. Chem. Phys.* **1988**, *89*, 6758.
40. van der Zande, W. J.; Koot, W.; Los, J. *J. Chem. Phys.* **1989**, *91*, 4597.
41. Saxon, R. P.; Liu, B. *J. Chem. Phys.* **73**, *73*, 876.
42. Helm, H.; Walter, C. W. *J. Chem. Phys.* **1993**, *98*, 5444.

43. Heimann, P. A.; Koike, M.; Hsu, C. W.; Blank, D.; Yang, X. M.; Suits, A. G.; Lee, Y. T.; Evans, M.; Ng, C. Y.; Flaim, C.; Padmore, H. A. *Rev. Sci. Instrum.* **1997**, *68*, 1945.
44. Peterka, D. S.; Ahmed, M.; Ng, C. Y.; Suits, A. G. *Chem. Phys. Lett.* **1999**, *312*, 108.
45. Creasey, J. C.; Lambert, I. R.; Tuckett, R. P.; Codling, K.; Frasinski, L. J.; Hatherly, P. A.; Stankiewicz, M. *J. Chem. Soc. Faraday Trans.* **1991**, *87*, 1287.
46. Zare, R. N. *Mol. Photochem.* **1972**, *4*, 1.
47. Cheung, Y. S.; Li, W. K.; Chiu, S. W.; Ng, C. Y. *J. Chem. Phys.* **1994**, *101*, 3412.
48. Cheung, Y. S.; Chen, Y. J.; Ng, C. Y.; Chiu, S. W.; Li, W. K. *J. Am. Chem. Soc.* **1995**, *117*, 9725.
49. Berkowitz, J. *Photoabsorption, Photoionzation and Photoelectron Spectroscopy*; Academic Press: New York, 1979.

Downloaded by STANFORD UNIV GREEN LIBR on September 21, 2012 | http://pubs.acs.org
Publication Date: October 18, 2000 | doi: 10.1021/bk-2001-0770.ch012

## Chapter 12

# Extracting Rotational State-to-State Differential Cross-Sections from Velocity-Mapped Ion Imaging Data

**K. Thomas Lorenz[1], Michael S. Westley[2], and David W. Chandler[1]**

[1]Sandia National Laboratories, P.O. Box 969,
MS 9055, Livermore, CA 94551–0969
[2]Department of Chemistry, Cornell University, Baker Laboratory,
P.O. Box 159, Ithaca, NY 14853–1301

Rotational state-resolved differential cross sections (DCS) for j-changing collisions are a sensitive measure of the intermolecular potential. Crossed-molecular beam, velocity-mapped imaging has recently been used to measure this quantity. We present ion images for the rotational energy transfer process HCl (j = 0) + Ar → HCl (j′ = 2, 3) + Ar at a center-of-mass energy of ~538 $cm^{-1}$. These images are presented to illustrate an iterative technique for the extraction of DCS's from crossed molecular beam / ion imaging data.

## Introduction

Rotational energy transfer (RET) processes serve as an important pathway for the redistribution of energy in the equilibration of combustion products. However, the cross section for RET can vary greatly for different collision partners and reaction conditions. A more complete understanding of energy transfer processes can be facilitated by establishing an intermolecular potential energy surface (PES) for the system of interest, since an accurate and detailed PES allows for the inference of reaction mechanisms and the calculation of reaction rates and cross sections. Molecular beam scattering techniques have allowed chemists to study single elementary chemical events, obtaining fundamental information such as angular distributions of products, energetics of reactions, and internal state distributions of products. This detailed level of measurement has made it possible for experimentalists to validate calculated potential energy surfaces.

Velocity mapped ion imaging is a method that couples laser spectroscopy with crossed molecular beam scattering, thereby providing the selectivity of laser spectroscopy and the velocity resolution of crossed molecular beams. The marriage of laser and crossed molecular beam techniques to measure nascent product distributions and differential cross sections is a long one. Several excellent reviews are available (*1*,*2*). Recently ion imaging has been used in several studies to measure DCS's of bimolecular processes (*3*). Suits et al. (*4*) first used the imaging technique to measure DCS's for inelastic scattering of NO with Ar, in an experimental arrangement similar to that used here. The measurement of DCS's for reactive scattering was demonstrated first by Kitsopoulos et al. (*5*) and more recently by M. Ahmed et al. (*6*).

Downloaded by STANFORD UNIV GREEN LIBR on September 21, 2012 | http://pubs.acs.org
Publication Date: October 18, 2000 | doi: 10.1021/bk-2001-0770.ch012

With this paper we use the velocity mapping ion optics to obtain high resolution images of inelastically scattered HCl and describe a method for extraction of the differential cross section from the ion images. Specifically, we present representative results of a crossed molecular beam / ion imaging study for inelastic scattering of the j-changing collisions of Ar + HCl (j = 0 ) at a center of mass collision energy of 538 $cm^{-1}$. The ion images are a two-dimensional projection of the three-dimensional distribution of state selected scattered products. We extract the differential cross sections from these data to demonstrate an iterative approach to determining the DCS. These state-to-state (partial) DCS's provide a sensitive means of testing the quality of the Ar - HCl potential surface

## Experimental

The apparatus consists of two doubly-skimmed, pulsed molecular beams intersecting at 90°. The distance from nozzle to scattering center is ~130 mm. For this work, both target and collider beams are formed using pulsed pinhole valves (General Valve, Series 9, 0.78 mm aperture) operating at 30 Hz. A 2% HCl in Ar mixture is used as the target beam. The collider beam is neat Argon. Typical pressures used behind the nozzles are 25 psig for Ar and 10 psig for the HCl/Ar mix. Typical base pressure (sources off) in the scattering chamber is $\sim 2\times10^{-8}$ torr. Scattered products are photoionized and extracted using standard ion extraction lenses in a mass spectrometer arrangement lying orthogonal to the molecular beams and scattering plane. The ionization laser beam is focused with a 0.53 m focal length lens and propagated in the plane of the molecular beams, which is located between the repeller and extractor of the ion optics. Ionized products are extracted through a set of ion lenses set for velocity mapping conditions (*7*, *8*) and accelerated onto a 2-dimensional position-sensitive detector. Ions of a single mass are selectively detected and imaged by pulsing the front plates of the MCP array using a pulsed voltage source having rise and fall times of approximately 10 ns. The experimental geometry allows us to detect ions from all scattered velocities; however, different velocities are detected with different efficiencies.

The $H^{35}Cl$ scattered products are state selectively ionized using (2 + 1) resonant enhanced multi-photon ionization (REMPI) *via* the Q-branch of the E $(^1\Sigma^+) \leftarrow$ X $(^1\Sigma^+)$ transition (*9* - *11*). This transition is insensitive to rotational alignment, allowing us to disregard any biases in detectivity of one j-alignment over another in the scattered HCl trajectories. The rotational temperature of the HCl before scattering is determined by analysis of the REMPI spectrum of the unscattered HCl/Ar molecular beam. Taking into account the line strengths of the j = 0 and j = 1 transitions, this spectrum represents a rotational temperature of ~ 6 Kelvin, i.e., more than 97% of the HCl molecules in the molecular beam begin in the ground rotational state.

Ideally, one would measure the differential cross sections at a well-defined collision energy. In practice, a near delta-function collisional energy distribution is not attainable with our crossed molecular beams. The typical velocity spread we observe is 5 – 10 % (FWHM). This velocity spread corresponds to an energy spread of 9 - 18% (FWHM) for our collision system and geometry. The velocity spread of the molecular beams in this work is measured by placing the HCl/Ar mix in both molecular beams and setting the laser frequency to detect HCl (j = 0). An image is taken for each molecular beam. After determining the magnification factor of the ion optics (M=20% from both modeling and measurement), the location of the beam-spot centers and the flight time of the ions provide a direct measure of the mean velocity and velocity spread of each molecular beam. We determine for our experiment values of v = 580 m/s and Δv = 70 m/s (FWHM) for the mean beam velocity and velocity spread, respectively. These beam velocity spreads correspond to a collision energy spread of 140 $cm^{-1}$ (FWHM) in the center-of-mass frame.

## Modeling of the Experiment

The objective of the data analysis is to extract a quantitative DCS for each j-changing collision. To do this, we must understand in detail how the experiment samples the different velocity vectors of the scattered products, and how those different velocities are projected onto the detector. This is equivalent to determining the apparatus function. A Newton diagram representing the reactant and product velocity vectors for this system is shown in Fig. 1. The lab-frame velocities are depicted as dotted arrows. Note that the center-of-mass velocity in the lab-frame is along the laser propagation axis. By subtracting the velocity of the center-of-mass of the system, one can represent the kinematics in the center-of-mass (CM) frame. These vectors are drawn as solid arrows. In the CM frame the HCl approaches the collision center from the right of the figure and the Ar approaches from the left. The relative velocity vector indicating the approach velocity of the HCl reactant colliding with Ar is shown pointing to the left. This is the direction for forward scattered HCl products and indicates where the deflection angle, θ, has a value of zero. Those HCl products that incur a large change of momentum and are back-scattered to θ = 180° have their final velocity vectors pointing to the right in this figure. Side-scattered products point either up or down in this orientation. This scattering orientation is identical for all the experimental images shown in this paper. The maximum speed for each rotational product-state is represented by a concentric circle about the scattering center. The size of the circles decreases as the available translational energy is taken up by the rotational motion of the HCl rotor.

Downloaded by STANFORD UNIV GREEN LIBR on September 21, 2012 | http://pubs.acs.org
Publication Date: October 18, 2000 | doi: 10.1021/bk-2001-0770.ch012

Downloaded by STANFORD UNIV GREEN LIBR on September 21, 2012 | http://pubs.acs.org
Publication Date: October 18, 2000 | doi: 10.1021/bk-2001-0770.ch012

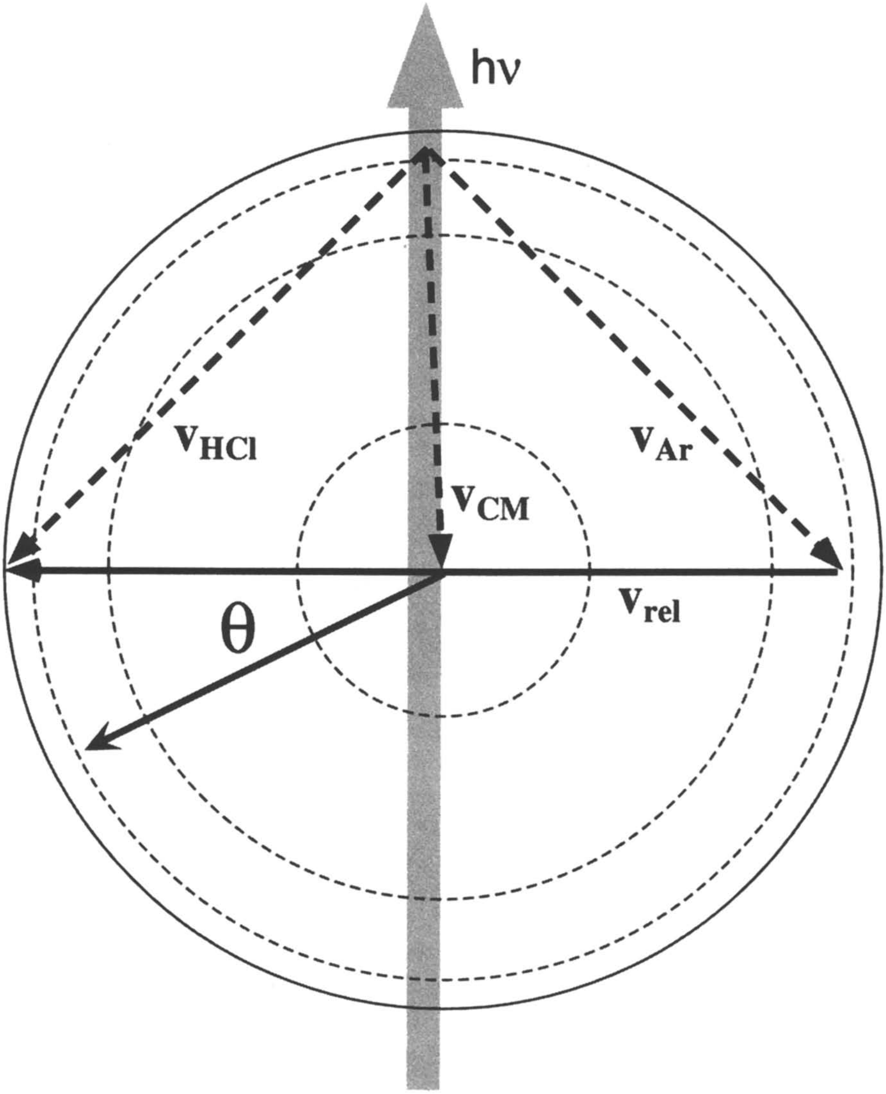

*Figure 1. A Newton diagram for the inelastic scattering of HCl seeded in Ar with a molecular beam of neat Ar. The dashed lines represent the lab frame velocity of the two molecular beams. The solid lines show the relative velocity and velocity of scattered products in the center-of-mass frame. The angle, θ, indicates the polar scattering angle. The dashed circles represent the expected size of the scattering sphere for product states j = 2, 4 and 6.*

Downloaded by STANFORD UNIV GREEN LIBR on September 21, 2012 | http://pubs.acs.org
Publication Date: October 18, 2000 | doi: 10.1021/bk-2001-0770.ch012

Scattered collision products are photoionized and projected onto a detector parallel to and located above the scattering plane. An experimental image nearly represents a projection of the center-of-mass scattering distribution of the ionized products. However, because of the quasi-CW nature of the molecular beams and their concurrent velocity spreads the ion images are not simple projections of a single scattering sphere. The measured scattering distribution is a sum of many discrete scattering events originating at different times from a distribution of molecular beam velocities. Additionally, the laser detects molecules with different scattering velocities with different efficiencies. In order to extract quantitative differential cross sections from the images, a model "apparatus function" must be calculated and used to normalize the intensities on the images.

Ion images for the state-to-state j-changing collisions $j = 0 \rightarrow j' = 2$ and 3 are shown in Fig. 2 as panels A and B, respectively. The highest intensity on the images represents nearly 2000 ion counts. Each image has an integration time of approximately 60 minutes. There are several characteristics of these images that must be addressed in any model of the experiment. Note in the $j' = 3$ image (Fig. 2B) that the intensity at the top of the image ($\theta = -90°$) is significantly greater than the intensity at the bottom of the image ($\theta = +90°$). In addition, the signal is broader and more diffuse at the bottom of the image, while at the top it appears sharper. Finally, there is a small, oval-shaped spot at $\theta = 0°$ and 180° in many of these images. The spot at $\theta = 180°$ is due to a small amount of HCl left over in the Ar molecular beam from the laser alignment procedure. Signal from trace amounts of residual HCl in the collider beam is not removed by our background subtraction procedure and therefore accumulates with image integration. This spot does not overlap the scattering signal in any of our images and therefore is only a cosmetic anomaly. The residual beam spot at $\theta = 0°$ does overlap the scattering signal in the $j' = 2$ image and to a lesser degree the $j' = 3$ image. We estimate that this spot affects the first 5 degrees of the DCS in the $j' = 2$ image and less in the $j' = 3$ image.

The source of the non-uniformity in intensity and velocity spread about the images resides in the temporal and velocity spread of the two molecular beams, as well as the incomplete spatial overlap of the laser beam with the scattered products. This is because there is a correlation between the recoil velocity of the scattered products in the CM-frame and the velocity of their CM in the lab-frame. The high energy collisions resulting from collisions from fast HCl molecules with fast Ar atoms have both larger CM collision energy and larger velocity of the CM. In contrast, the low energy collisions have a recoil velocity that is lower and a smaller CM velocity in the lab-frame. This correlation, averaged over the many interactions of the two molecular beam velocity distributions, creates a higher velocity spread for fast lab-frame products and a lower velocity spread for slow lab-frame products. This kinematic effect resulting from non-zero velocity spreads in the molecular beams gives the images their characteristic asymmetric appearance.

Downloaded by STANFORD UNIV GREEN LIBR on September 21, 2012 | http://pubs.acs.org
Publication Date: October 18, 2000 | doi: 10.1021/bk-2001-0770.ch012

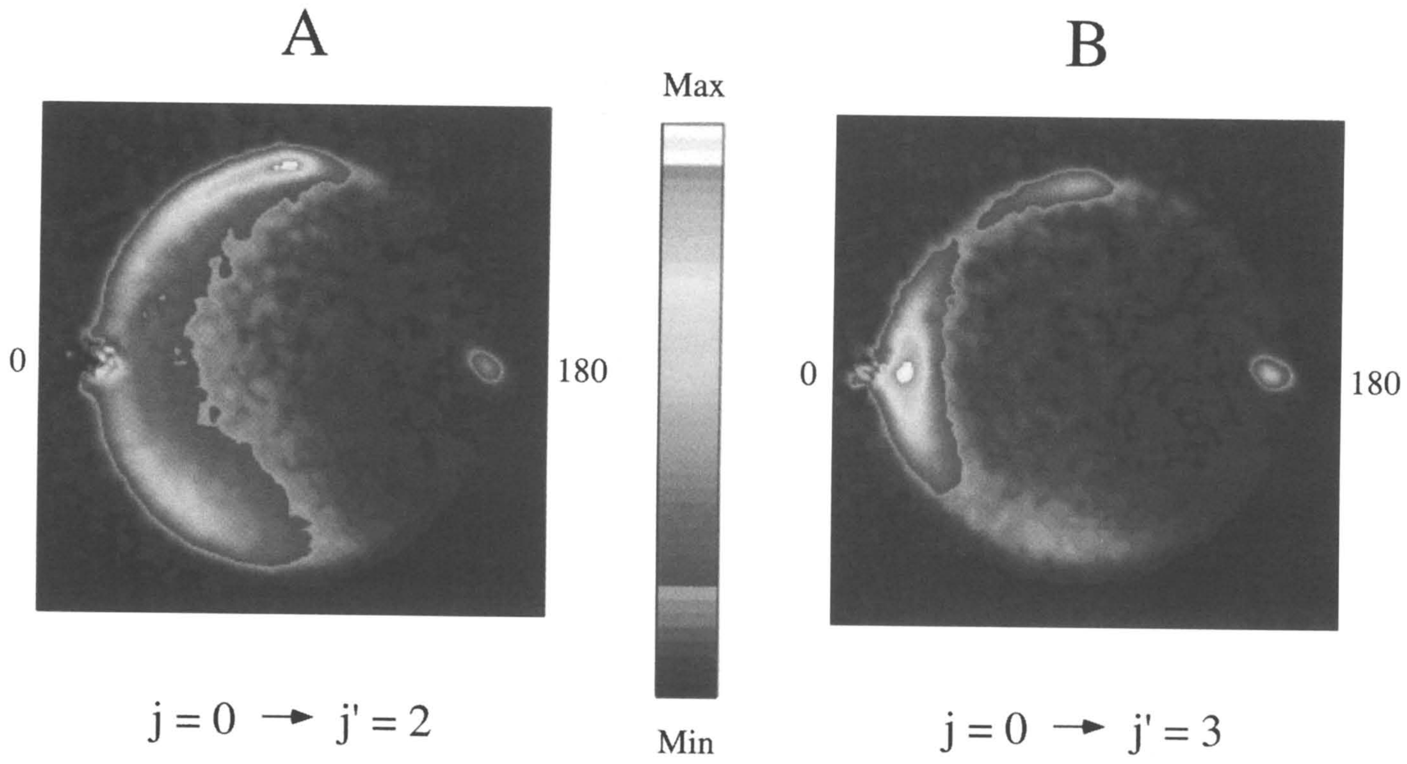

*Figure 2. Experimental ion images of scattering spheres for inelastic scattering of HCl ($j = 0$) + Ar → HCl ($j' = 2, 3$) + Ar. Images A and B correspond to $j' = 2$ and $j' = 3$, respectively.*

Downloaded by STANFORD UNIV GREEN LIBR on September 21, 2012 | http://pubs.acs.org
Publication Date: October 18, 2000 | doi: 10.1021/bk-2001-0770.ch012

The temporal overlap of the molecular beams is on the order of 50 μs (FWHM). At some time within this temporal envelope, a 3 ns laser pulse intersects the distribution of scattered products. The extent to which the focused laser volume overlaps the distribution of scattered products is modeled by summing over time the overlap of the scattering density with the laser intensity. Imagine at time $t_{laser}$, the laser beam intersects the scattering distribution, a portion of which results from a scattering sphere that was born several microseconds earlier. This scattering sphere will have expanded, and its center-of-mass will have traveled away from the laser focus / molecular beam interaction volume. The laser beam will therefore ionize scattered products from this sphere unequally because it overlaps only part of the sphere. The scattering sphere born just prior (a few nanoseconds) to the laser beam's intersection will be the smallest (spatially), and its CM will have moved the least distance in the lab-frame. The laser will therefore ionize all scattered products from this smaller scattering sphere equally, irrespective of velocity. Summing ions formed from many different scattering spheres, originating at different times and scattering points within the scattering volume, generates an apparatus function. The effect of having a large temporal spread in the molecular beams and a short laser pulsewidth is to bias the detection towards particles scattered with low lab-frame velocities and those moving directly along the laser axis. This creates a large intensity spike at the top of the images where the lab-frame velocities of the scattered particles is near zero. In addition, the products having velocities directed to each side of the image at θ = 0° and 180° tend to fly out of the laser beam volume where they are not detected as efficiently.

## Determination of the Apparatus Function

The two-dimensional velocity-mapped images collected in this study are the product of the state-to-state total cross sections and the angular dependent scattering probability function, and an additional angular dependent apparatus function term that includes the flux-to-density build-up of scattered products and their angular dependent detection efficiencies. The time-integrated intensity, I, on the image at some time t after scattering begins for a given center-of-mass collision energy, E*, can be expressed as

$$I(v_x, v_y, v_z; j \rightarrow j', t)_{Lab} = A\,\sigma(j \rightarrow j')P(\theta,\phi)\,F_{app}(v_x, v_y, v_z; j \rightarrow j', t), \quad (1)$$

where the intensity given in the lab-frame depends upon the state-to-state total cross section σ(j → j′), and its angular probability P(θ, ϕ) in the center-of-mass frame, an amplitude factor *A*, which is proportional to the molecular beam intensities, and an instrument dependent "apparatus function", $F_{app}$(j → j′). The apparatus function includes the experimental geometry, the temporal and velocity distributions of the molecular beams, and the laser beam's spatial and frequency distributions. The apparatus function accounts for the averaging over velocities in the molecular beams, averaging over scattering volume and scattering time, and the ionization efficiency over all scattering trajectories. The only factor in Eq. 1 that includes an angular probability for the scattering event is P(θ, ϕ). Any anisotropy present in the experiment – such as detection biases, or scattering asymmetries due to velocity and temporal spreads in the molecular beams, but not present in the differential cross section, must therefore be included in $F_{app}$.

The three-dimensional distribution of ionized scattering products is extracted from the interaction region and accelerated along the TOF axis finally to be projected onto our two-dimensional detector. The intensity of ions impinging upon the detector is a function of (x,y) or alternatively (r, θ) such that

$$I_{image}(r,\theta)=\sum_{v_z} I(v_x,v_y,v_z) \tag{2}$$

is defined as the spatial intensity distribution of scattering signal in our experimental ion images. We can absorb the σ and A terms in Eq. 1 into a new apparatus function $F'_{app}$, as they serve only as intensity scaling factors to the DCS. The resulting relation can be combined with Eq. 2 to give a simple expression for deconvolving the relative DCS's from the experimental images – the product of the relative differential cross section, $DCS_0(\theta,\phi)$ and $F_{app}$. Strictly speaking, the experimental image is the projection of many scattering spheres resulting from the spread in the molecular beam velocities. Therefore, the intensity at a given polar angle θ, in the image, has contributions from a small spread in θ from scattering spheres having different radial velocities and center-of-mass velocities. This blurring in θ is not easily deconvoluted in a direct fashion, which makes the relationship between the relative differential cross section and the experimental image approximate. The experimental image intensity is given by

$$I_{image}(r,\theta)\approx DCS_0(\theta,\phi)\ F'_{app}, \tag{3}$$

where $F'_{app}$ is the newly defined apparatus function, and each term is dependent upon the initial and final rotational states as well as the center-of-mass collision energy. Once $F'_{app}$ is known, then $DCS_0(\theta,\phi)$ can be extracted approximately from the experimental images by factoring out the angle dependent intensity of the apparatus function. Ideally, one would want to image a distribution of scattered products that is isotropic. This isotropic scattering distribution would provide $F'_{app}$ directly. We do not know of a bimolecular collision system that provides this type of product distribution. However, three independent simulations were written to model $F'_{app}$, each using an independent mathematical approach. Both isotropic DCS's and structured or model DCS's were input into the three simulations. The resulting simulated scattering images were in excellent agreement with one another. We are therefore confident that we understand the dynamics necessary to correctly model $F'_{app}$.

Figure 3 is a flowchart for the scattering simulation program developed for the apparatus described in this paper. The first section of the code calculates a three-dimensional array of intensities for the scattered product molecules. After inputting all fitting parameters, the program samples a discrete velocity group from each molecular beam's velocity distribution and calculates the mean recoil velocity and velocity spread for the products, and a velocity for the center-of-mass of the products.

Downloaded by STANFORD UNIV GREEN LIBR on September 21, 2012 | http://pubs.acs.org
Publication Date: October 18, 2000 | doi: 10.1021/bk-2001-0770.ch012

Downloaded by STANFORD UNIV GREEN LIBR on September 21, 2012 | http://pubs.acs.org
Publication Date: October 18, 2000 | doi: 10.1021/bk-2001-0770.ch012

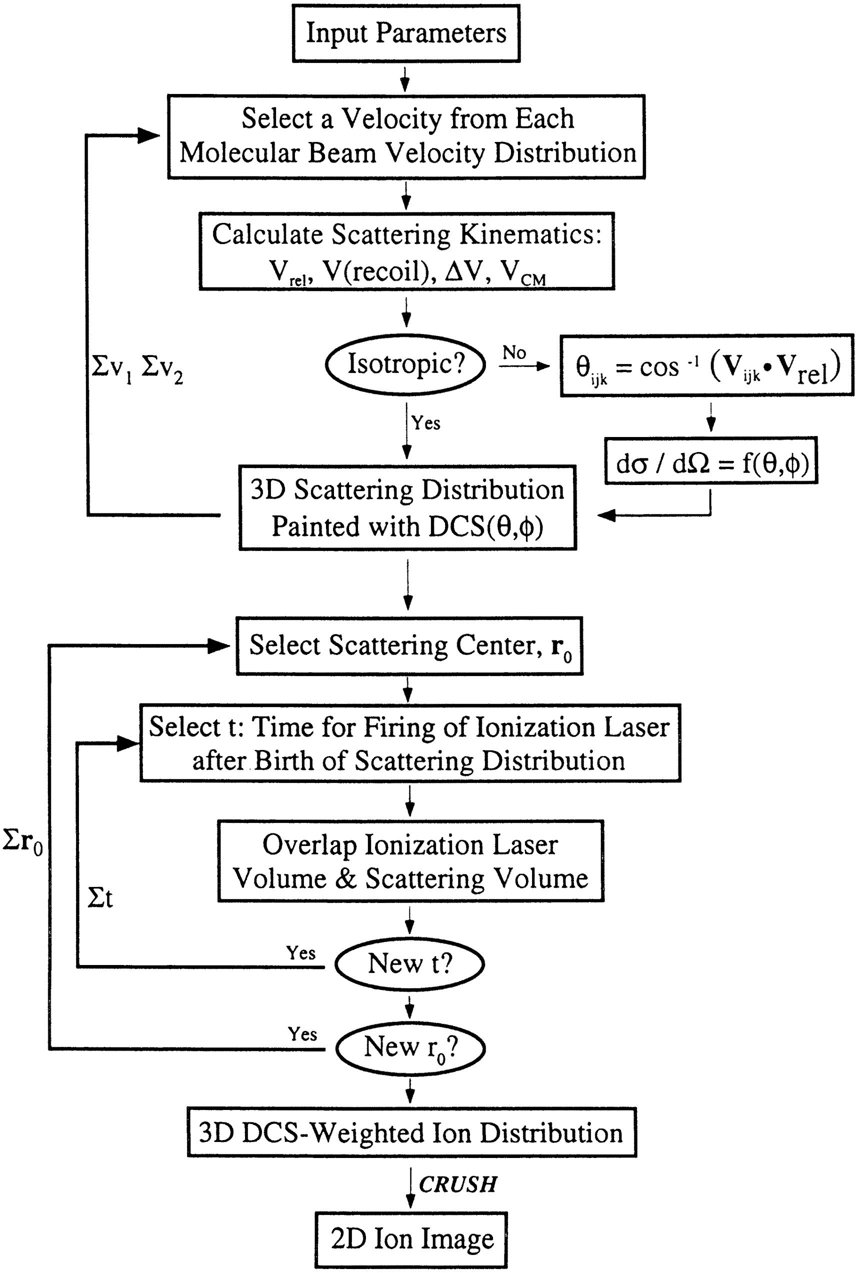
Input Parameters
Select a Velocity from Each Molecular Beam Velocity Distribution
Calculate Scattering Kinematics: $V_{rel}$, V(recoil), ΔV, $V_{CM}$
Isotropic?
No
$\theta_{ijk} = \cos^{-1}(\mathbf{V}_{ijk} \cdot V_{rel})$
$d\sigma / d\Omega = f(\theta,\phi)$
Yes
$\Sigma v_1\ \Sigma v_2$
3D Scattering Distribution Painted with DCS(θ,ϕ)
Select Scattering Center, $\mathbf{r}_0$
Select t: Time for Firing of Ionization Laser after Birth of Scattering Distribution
Overlap Ionization Laser Volume & Scattering Volume
$\Sigma r_0$
$\Sigma t$
Yes
New t?
Yes
New $r_0$?
3D DCS-Weighted Ion Distribution
CRUSH
2D Ion Image

***Figure 3. Flow chart describing the procedure used to generate the simulated ion images. This procedure, with a DCS($\theta,\phi$) = 1, produces the apparatus function for the molecular beam machine. Reprinted with permission from reference 13.***

Then the deflection angle θ about the relative velocity vector is calculated for each velocity in this scattering distribution in order to weight that velocity for cases where a forward simulation of a non-isotropic differential cross section is desired. For the case of calculating an angle-independent apparatus function, every velocity as a function of scattering angle is equally weighted. An overall weighting proportional to the product of the weights of the two chosen beam velocities is then applied to this scattering array. The program picks two more molecular beam velocity groups, and repeats the calculation of another scattering sphere in order to integrate over all velocity combinations within the two molecular beam velocity distributions and create a single intensity array for the scattered product velocities. The second section of the program simulates the overlap of the laser beam with the scattered HCl products generating a distribution of scattering centers and scattering times to create a three-dimensional distribution of ions that will be projected onto the detector. A position $\boldsymbol{r}_0$ within the scattering volume relative to the laser beam waist is chosen for the scattering center. Then a time t is chosen before the laser fires, allowing for expansion of the scattering sphere before the laser intersects the scattering sphere. Since the scattering arrays are in velocity coordinates, each velocity must be converted to spatial coordinates in the lab-frame before calculating the ionization probability – or spatial overlap with the laser volume. An ionization probability is calculated for each scattering trajectory and an integrated intensity is assigned to that trajectory for a given image. The spatial profile of the laser is described by

$$I(x,y,z)=\frac{1}{1+\left(\frac{z}{Z_R}\right)^2}\exp\left(-\frac{x^2+y^2}{\omega_0^{\,2}\left[1+\left(\frac{z}{Z_R}\right)^2\right]}\right) \tag{4}$$

where $Z_R$ is the Rayleigh range, $\omega_0$ is the Gaussian beam waist (FWHM), and z is the propagation direction of the laser beam. The spatial coordinates $x(\boldsymbol{r}_0, t)$ (y and z are defined in the same manner) within the laser volume for a given velocity trajectory are expressed as

$$x(\bar{r},t)=\left[v_x - v_x(CM)\right]\, t\,, \tag{5}$$

where the vector $\boldsymbol{r}_0$ represents the position of the scattering interaction relative to the laser beam waist, $v_x(CM)$ is the velocity of the center-of-mass moving in the lab-frame and t is the time elapsed between the birth of the scattering sphere and the firing of the laser. We cycle this procedure through all velocities within the three-dimensional array and then loop back to choose another scattering center, $\boldsymbol{r}_0$. After integrating over the scattering time and the scattering volume, a two-dimensional projection is calculated; the scattering sphere is projected onto the image plane by summing the $v_z$ column of values for each $(v_x, v_y)$ pixel, where the $v_z$ coordinate is identified with the time-of-flight axis in the lab-frame. An approximation is made in our current simulations, which uses a single scattering center but redefines the laser beam waist to be the width of the scattering volume. This approximation asserts that particles scattering outwards from a single point through a larger laser beam volume

Downloaded by STANFORD UNIV GREEN LIBR on September 21, 2012 | http://pubs.acs.org
Publication Date: October 18, 2000 | doi: 10.1021/bk-2001-0770.ch012

is effectively equivalent to particles scattering from a large volume into and through a laser beam having a very small waist. This approximation speeds the simulation routine by omitting the loop over scattering centers.

The extraction procedure is shown in Fig. 4 for an ideal scattering system having a narrow collisional energy distribution and a correspondingly narrow distribution of recoil speeds. An isotropic differential cross section, DCS(θ, φ) = 1, is input into the scattering simulation to produce Image 4B. This image simulation of our apparatus function clearly shows the non-uniform intensities associated with the detectivity biases and molecular beam spreads discussed previously. There is a roll-off of the intensity for very low and high deflection angles, a significant intensity spike at the top of the image where lab-frame velocities are low, and an asymmetry in the recoil velocity spread around the circumference of the scatter signal. Image A is a simulation using a model, non-isotropic differential cross section. In this case the DCS shows significant forward scattering intensity along with three rotational rainbow peaks at larger deflection angles. This intensity pattern is mirrored in Image 4A, but it is distorted. Removal of the instrument dependent asymmetries is accomplished by dividing Image 4A by Image 4B, pixel-by-pixel. This division produces Image 4C, a deconvolved image of the same dimensionality, having a pattern of stripes that varies in intensity along the relative velocity coordinate. These stripes are projections of annular scattering cones, Δθ, mapped into cos(θ) coordinates. The angular scattering distribution can be recovered by integrating the intensities down the vertical stripes and rebinning the data onto a θ-axis. This technique works well for simulated images with narrow velocity spreads and no noise, but is less satisfactory when used with experimental images. A more robust approach is to use the intensity distributions around the rim of the scattering signal where the signal-to-noise ratio is highest in the data. Concentric lines bounding an annulus centered at the mean recoil velocity for this system are overlaid onto the images to show a typical region used for extracting the angular intensity distributions from the data and apparatus function images. A FORTRAN routine converts each image's pixel positions from Cartesian coordinates to cylindrical coordinates, I(r, θ) and then steps around an annulus in increments of θ, integrating the signal intensity as a function of r in each increment. This partial integration is described by

$$R(\theta)=\int_{r_1}^{r_2} I(r,\theta)r\,dr \qquad (6)$$

where $r_1$ and $r_2$ are user defined inner and outer radii, and the angular increments Δθ vary between 2° and 3°. The resulting angular distributions for the simulated apparatus function and the experimental data are shown as $R_{sim}(\theta)$ and $R_{data}(\theta)$, respectively. An angular distribution, $I_{extract}(\theta)$, can be extracted from the "experimental image" using the relationship for the annular distribution intensities

$$\frac{R_{data}(6)}{R_{sim}(\theta)} = I_{extract}(\theta) \sim DCS_0(\theta,\phi) \qquad (7)$$

to give the angular scattering intensity, $I_{extract}(\theta)$. This extracted distribution closely resembles the DCS used to simulate Image B. However, this technique does not

Downloaded by STANFORD UNIV GREEN LIBR on September 21, 2012 | http://pubs.acs.org
Publication Date: October 18, 2000 | doi: 10.1021/bk-2001-0770.ch012

Downloaded by STANFORD UNIV GREEN LIBR on September 21, 2012 | http://pubs.acs.org
Publication Date: October 18, 2000 | doi: 10.1021/bk-2001-0770.ch012

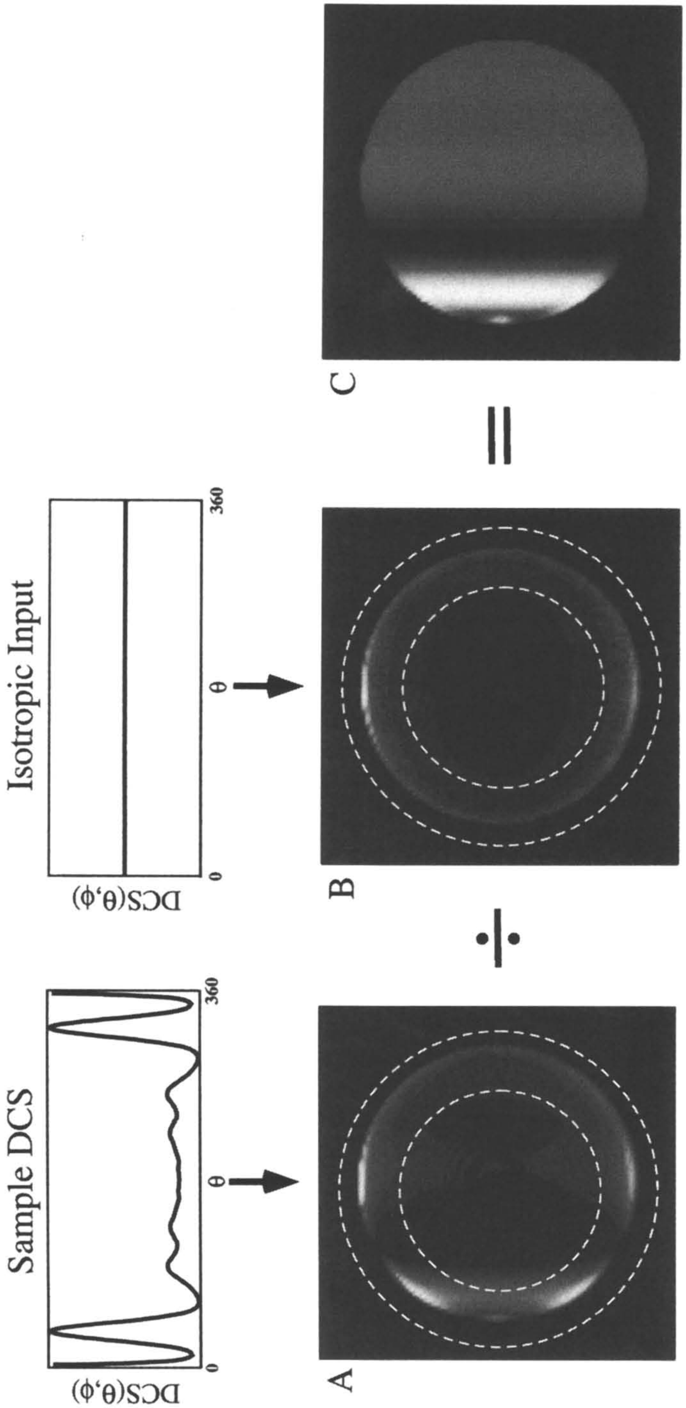
Sample DCS
DCS(θ,φ)
0
θ
360
A
÷
Isotropic Input
DCS(θ,φ)
0
θ
360
B
=
C

Downloaded by STANFORD UNIV GREEN LIBR on September 21, 2012 | http://pubs.acs.org
Publication Date: October 18, 2000 | doi: 10.1021/bk-2001-0770.ch012

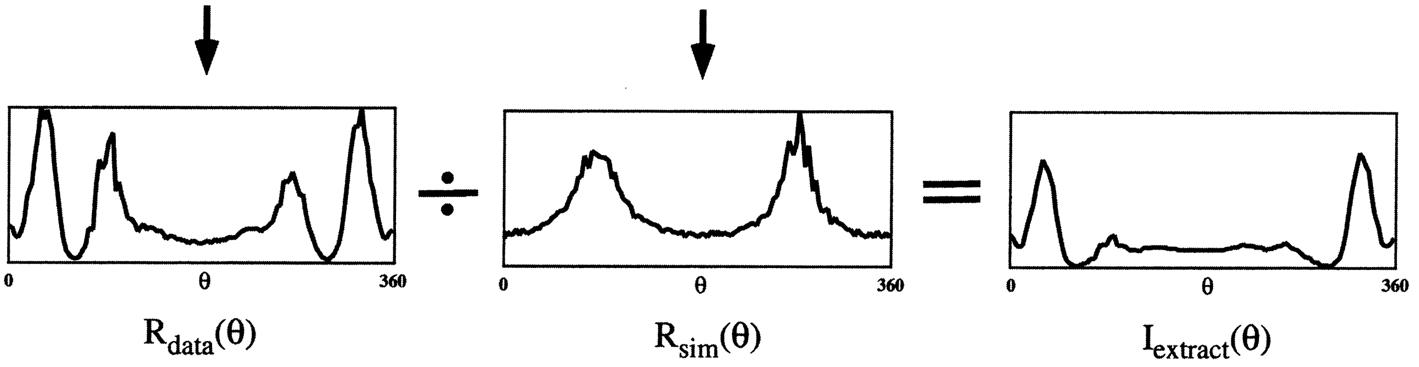

*Figure 4. (A) Simulated image with sample DCS; (B) simulated image for an isotropic differential cross section (DCS) input, i.e. the apparatus function; and (C) the image resulting from the normalization of image B by image A. Below each image is the intensity pattern obtained by integrating around the image in the annulus shown on each image. To the extent that, $I_{extract}(\theta)$ looks like the input sample DCS, this procedure is capable of a direct extraction of the DCS. Adapted with permission from reference 13.*

Downloaded by STANFORD UNIV GREEN LIBR on September 21, 2012 | http://pubs.acs.org
Publication Date: October 18, 2000 | doi: 10.1021/bk-2001-0770.ch012

extract the scattering signal in the image perfectly. Sharp features in the intensity distribution or features at very low and very high deflection angles (θ = 0, 180°) can be washed out due to the finite pixel resolution in the images and finite annulus width. Within these constraints, we can use a technique of performing successive extractions with corresponding correction factors to force $I_{extract}(\theta)$ to converge to the best fit of the normalized differential cross section, $DCS_0(\theta,\phi)$.

Once an initial angular scattering distribution is extracted, it can be used as the differential cross section for a new simulated image. If our extraction technique is perfect, the new image will be identical to the experimental image (without the noise), and the angular scattering distribution of the original data and the new simulated scattering distribution will also be identical. In as much as the extraction technique is not equally sensitive across the angular range of scatter, the two intensity distributions will differ. We will use this difference as a correction factor and apply it to the previous extracted distribution. In other words, we can write

$$DCS^{i}_{trial}(\theta) = DCS^{i-1}_{trial}(\theta)\, C^{i-1}_{correction}(\theta) \qquad (8)$$

where the i'th correction factor $C_{correction}$ is given by

$$C^{i}_{correction}(\theta) = \frac{R_{data}(\theta)}{R^{i}_{sim}(\theta)}, \qquad (9)$$

and $R_{data}(\theta)$ represents the angular distribution for an annulus in the original experimental image, and $R^{i}_{sim}(\theta)$ represents the angular distribution for an annulus in the simulated image that was produced using the previous extracted $DCS_{trial}(\theta)$ as the input differential cross section. With successive iterations, the angular scattering distributions converge to the relative differential cross section, $DCS_0(\theta,\phi)$. A similar iterative technique was used by Shapiro et al. (*12*) to remove laboratory averaging from measured DCS's in elastic scattering. The annular distributions in θ converge to the solid-angle differential cross section in Ω = f(θ, ϕ) because the projected image of the scattering sphere contains all the scattering trajectories of the three-dimensional distribution. By simulating the $I^{1}_{extract}(\theta)$ again as a new $DCS_{trial}(\theta)$ input for the apparatus function, one can find a correction factor for the extraction, which is multiplied by the previous $DCS^{i}_{trial}(\theta)$ to give a new $DCS^{i+1}_{trial}(\theta)$. Successive iterations, until $C_{correction}(\theta)$ converges to unity across θ, force the extracted angular intensities defined in Eq. 7 to converge to the best fit of the relative differential cross section. We therefore write

$$DCS^{i}_{trial}(\theta)\Big|_{i\to N} \Rightarrow DCS_0(\theta,\phi) \qquad (10)$$

where we observe an N as small as 3 in favorable cases where the features of the differential cross section are not finely structured.

In Fig. 5, we demonstrate how we extract the DCS from a simulated experimental image that was made using the sample DCS shown in Fig. 4. Figure 5A shows this sample $DCS(\theta,\phi)_{in}$ used to model our simulated data, as well as the 1st, 4th and 6th trial DCSs extracted from the images. Note that the first extracted DCS recovers even the

Downloaded by STANFORD UNIV GREEN LIBR on September 21, 2012 | http://pubs.acs.org
Publication Date: October 18, 2000 | doi: 10.1021/bk-2001-0770.ch012

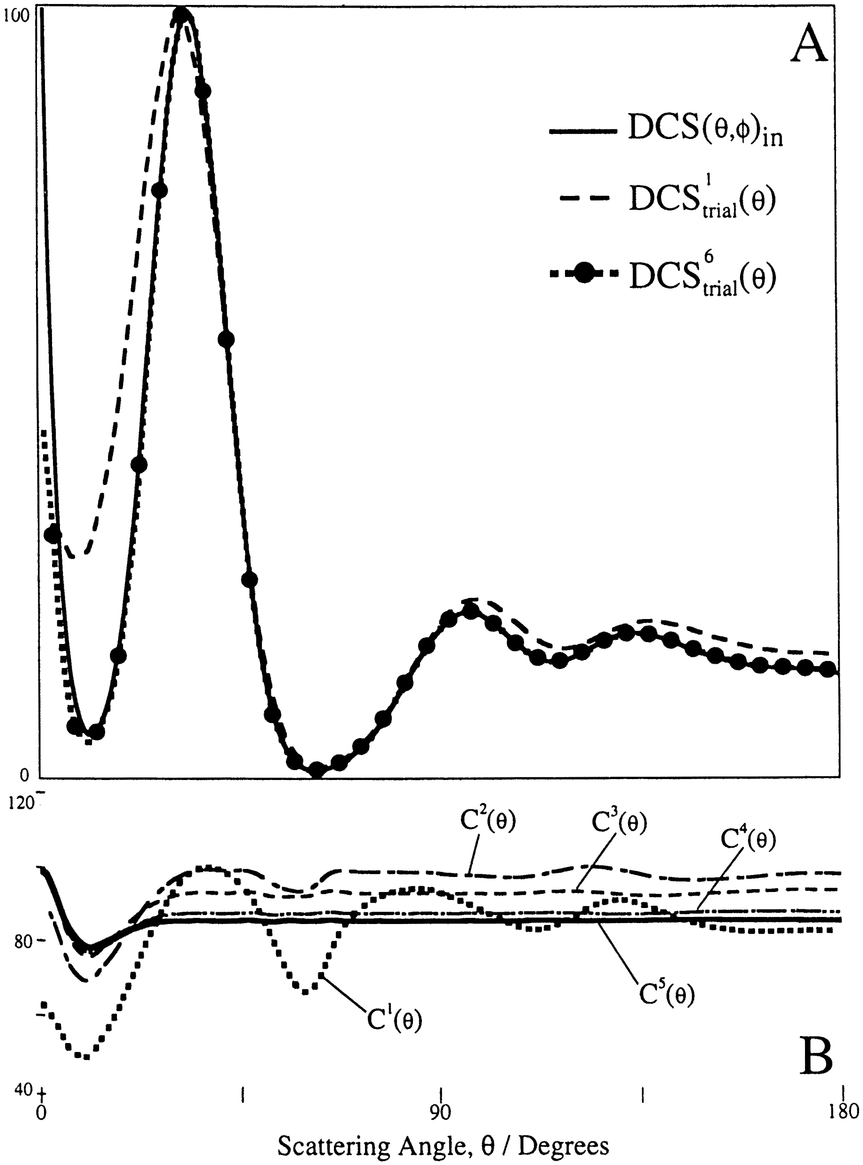

*Figure 5. Solid line shows the sample input DCS from figure 4. Dashed line is $I_{extract}(\theta)$ from Figure 4 representing the first iteration in a procedure to extract the true DCS. The dashed line with markers represents the 7th iteration in the procedure described in the text for extracting the true DCS from the data. The lower panel shows the correction factor for each iterative step as a function of angle. By the sixth iteration [$C^6(\theta)$], only a small correction at low angle is needed. Adapted with permission from reference 13.*

Downloaded by STANFORD UNIV GREEN LIBR on September 21, 2012 | http://pubs.acs.org
Publication Date: October 18, 2000 | doi: 10.1021/bk-2001-0770.ch012

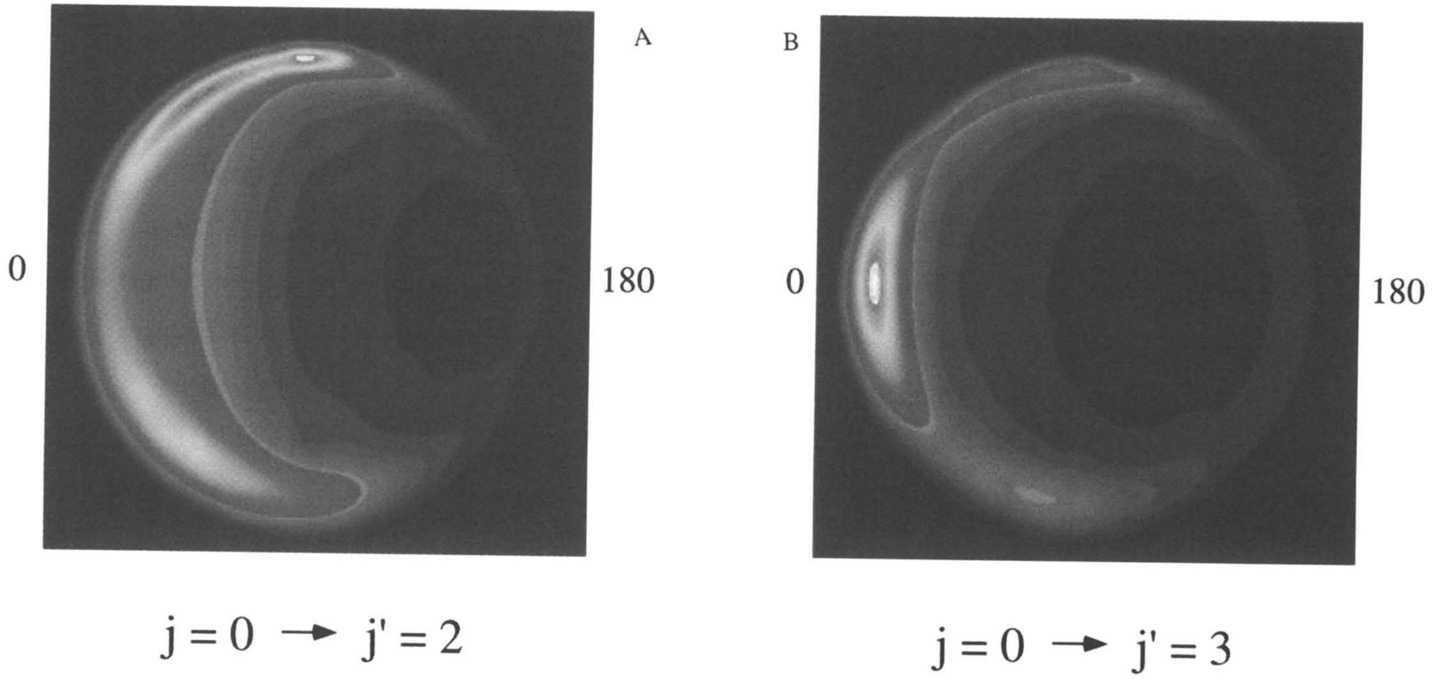

*Figure 6. Panel A is the simulated ion image obtained for HCl ($j = 0$) + Ar → HCl ($j' = 2$) + Ar. Panel B is the simulated ion image for HCl ($j = 0$) + Ar → HCl ($j' = 3$) + Ar. These images were obtained using the apparatus function and the DCS extracted by the iterative procedure described in the text. To the extent that these images are identical to images in Fig. 2 we understand the apparatus function and have extracted the true DCS.*

broad features of the original DCS well – the main rainbow and the back-scattered rainbows. However, the sharp forward scattered intensity and subsequent dip is washed out with the first extraction. By the 7th extraction all the principal features are nearly quantitatively recovered across $\theta$, with the exception of the area of $\theta = 0 - 3°$. In Fig. 5B several of the angle dependent correction factors $C^i(\theta)$ are shown. The initial correction factor shows quite a bit of structure where the initially extracted DCS produced an image having an angular intensity in its annulus different from the original image. The 6th correction factor is flat everywhere across $\theta$ except for the forward scattering region. More iterations will force convergence of the extracted DCS to the original sample DCS, to the extent of the limits imposed by the resolution of the chosen annulus width, the apparatus or the pixelated images (in the case of a simulated image). In Fig. 6, we show simulated images of our experimental data for the $j = 0 \rightarrow j' = 2$ and 3 scattering channel using as input differential cross section the final extracted $DCS_{trial}(\theta)$ from the data. These simulated images should be compared to the experimental images of Fig. 2. There is excellent agreement between the features of the simulated image and the experimental image.

## Summary

We have used 2 + 1 resonance enhanced multiphoton ionization together with a crossed-molecular beam / ion imaging apparatus to measure velocity mapped images of inelastically scattered HCl from Ar. The machine-dependent intensities can be removed from the experimental images by factoring out the angular intensity of an apparatus function from the angular intensity of the data. An iterative method for extracting the state-selected differential cross section for each rotational state of HCl produced in the collision produces an angular distribution, $I(\theta)$, that closely resembles the normalized differential cross section, $DCS_0(\theta,\phi)$.

### Acknowledgements

The authors are grateful to G.C. McBane for his helpful discussions and assistance, and Mr. Mark Jaska for his valuable technical assistance. This work is supported by the U.S. Department of Energy, Office of Basic Energy Sciences, Division of Chemical Sciences. M.S.W. also acknowledges support from the U.S. Department of Energy under Grant DE-FG02-88ER13934.

## Literature Cited

1. M. Alagia, N. Balucani, P. Casavecchia, D. Stranges, and G.G. Volpi, *J. Chem. Soc.-Faraday Trans.*, **1995**, *91*, 575.
2. C.B. Moore and I.W.M. Smith, *J. Phys. Chem.*, **1996**, *100*, 12848.
3. A.J.R. Heck and D.W. Chandler, *Ann. Rev. Phys. Chem.*, **1995**, *46*, 335.

Downloaded by STANFORD UNIV GREEN LIBR on September 21, 2012 | http://pubs.acs.org
Publication Date: October 18, 2000 | doi: 10.1021/bk-2001-0770.ch012

4. A.G. Suits, L.S. Bontuyan, P.L. Houston and B.J. Whitaker, *J. Chem. Phys.*, **1992**, *96*, 8618.
5. T.N. Kitsopoulos, M.A. Buntine, D.P. Baldwin, R.N. Zare and D.W. Chandler, *Science*, **1993**, *260*, 1605.
6. M. Ahmed D.S. Peterka and A.G. Suits, *Chem. Phys. Lett.*, **1999**, *301*, 372.
7. A.T.J.B. Eppink and D.H. Parker, *Rev. Sci. Instrum.*, **1997**, *68*, 3477.
8. D.H. Parker and A.T.J.B. Eppink, *J. Chem. Phys.*, **1997**, *107*, 2357.
9. R. Callaghan, S. Arepalli, and R.J. Gordon, *J. Chem. Phys.*, **1987**, *86*, 5273.
10. P.J. Dadigian, D.F. Varley, R. Liyanage, R.J. Gordon and R.W. Field, *J. Chem. Phys.*, **1996**, *105*, 10251.
11. T. A. Spiglanin, D.W. Chandler and D.H. Parker, *Chem. Phys. Lett.*, **1987**, *137*, 414.
12. M. Shapiro, R.B. Gerber, U. Buck and J. Schleusener, *J. Chem. Phys.* **1977**, *67*, 3570.
13. K. Thomas Lorenz, Michael S. Westley and David W. Chandler, *Phys. Chem. Chem. Phys.*, in press.

Downloaded by STANFORD UNIV GREEN LIBR on September 21, 2012 | http://pubs.acs.org
Publication Date: October 18, 2000 | doi: 10.1021/bk-2001-0770.ch012

## Chapter 13

# Simulation and Analysis of Image Data from Crossed Beam Experiments

**George C. McBane**

**Department of Chemistry, The Ohio State University, Columbus, OH 43210**

Simulation of images expected from velocity mapping of crossed molecular beams is described. A general expression for the expected image is derived. Simplifying approximations and methods of forward convolution fitting are discussed. The analysis of a state to state experiment on Ne–CO rotationally inelastic scattering is shown as an example.

## Introduction

In a traditional crossed molecular beam experiment (*1*), a detector with a small aperture is located far away from the intersection volume of two collimated beams. Most molecules scattered from the intersection do not move toward the detector, and are lost. Such molecules represent an opportunity for improved experimental design; if they could be detected without sacrificing the angular information provided by the small-angular-acceptance detectors, the signal collection rate could be increased enormously. The potential advantages of ion imaging (discussed extensively in this volume) to crossed beam experiments have been apparent at least since its first application to photodissociation (*2*). In an ion imaging experiment, products scattered into all directions are photoionized in the intersection volume. Electrostatic fields then direct all the ions onto a position sensitive detector; the arrival positions of the ions provide information about the velocity vectors of the original scattered molecules.

Applications of ion imaging to crossed beam experiments have been slow in coming. The first example was provided by Bontuyan et al. (*3*), who studied Ar + NO inelastic scattering with 1+1 resonance enhanced ionization of NO; further work on the same system was reported by Yonekura et al. (*4*). The H + $H_2$ reaction was investigated by Kitsopolous et al. (*5*). Peterka et al. studied the $O(^1D)$ + $D_2$ reaction (*6*). Several more papers are in press (*7–10*).

In Imaging in Chemical Dynamics; Suits, A., et al.;
ACS Symposium Series; American Chemical Society: Washington, DC, 2000.

## The Idealized Experiment

In an ideal crossed beam experiment with ion imaging detection, two molecular beams with sharp velocities and no angular divergence would intersect. Scattered product molecules would then be photoionized with an efficiency independent of their positions and velocities. The ions would be propelled by external electric fields (and not repelled by one another!) onto a detector in a way that permitted the postcollision velocity vector of each arriving ion to be determined accurately. In the simplest case, the undetected sibling products would have only one accessible internal state.

Under these circumstances, the two-dimensional distribution of intensities appearing on the detector may be directly interpreted to give the differential cross section (DCS) for scattering. If the relation between initial velocity and ion arrival position is a simple projection of the velocity vector onto the plane of the detector, and the detector plane is parallel to the initial relative velocity vector, the resulting ion image will be a disk with a sharp edge. The brightness of the disk in any annulus about its center, as a function of angular displacement from the initial relative velocity vector, gives the DCS.

No real experiment duplicates these ideal conditions. Real experiments have finite velocity distributions in the molecular beams, nonuniform photoionization probabilities, and imperfect correlations between ion arrival positions and velocities of scattered molecules. They may also be complicated by internal state distributions of undetected products. This article describes the effects of these nonidealities, their incorporation into realistic simulations of experiments, and useful ways of analyzing data in their presence.

## Real Experiments: Simulation

In photodissociation experiments, it is not too difficult to realize the equivalent of the "ideal experiment" described above. If the photolysis volume is small, the detection volume is large, and Doppler selectivity in the photoionization and space charge effects are negligible, then the ion image of photodissociation products can be inverted directly to give the speed and angular distribution of the products. The inverse Abel transform widely used in imaging studies of photodissociation is an example of such a direct inversion (*11*).

In the crossed beam case, even with sharp velocity distributions in the beams, the Abel transform is not usually available. The pulsed molecular beams used in the experiments have durations long compared to the flight times of scattered molecules across the detection volume. Molecules moving along the probe laser beam can be formed rather early in the molecular beam pulse and still be detected, while molecules formed that early but moving perpendicular to the probe laser will not be detected. The cylindrical symmetry present in the COM-frame velocity vector distribution is consequently not retained in the distribution of ions produced by the probe laser. The inverse Abel transform, which requires this symmetry, is therefore not valid. Other direct methods might still work in this case, but finite velocity spreads in the molecular beams add an additional averaging that removes the rigorous validity of any direct deconvolution method. Experimenters are left with two choices: assume (incorrectly) the absence of velocity spreads, apply a direct method, and try to assess the importance of the resulting errors; or use a fitting procedure that incorporates the experimental averages. The latter approach has been widely used in traditional time of flight crossed beam studies. The next sections develop the corresponding analysis for ion imaging of crossed beam products.

## General Expression for Observed Intensity Distribution

The data in an ion imaging experiment are the intensities in the pixels of an image. Each pixel covers a small part, usually rectangular, of the two-dimensional detector. This description is useful whether the data were collected directly as pixel intensities in an "analog" mode or were obtained by digitizing individual ion arrival positions and then histogramming them into a 2D image (*12*).

In collisions with well defined relative velocity $g = |\mathbf{v}_1 - \mathbf{v}_2|$, the density of products scattered per unit time from initial state $i$ to final state $f$ into center of mass (COM) scattering angles $\theta$ and $\phi$ is

$$\frac{dn_{\mathrm{p}}(\theta, \phi, i \rightarrow f)}{dt} = \frac{d\sigma}{d\omega}(\theta, \phi, g, i \rightarrow f) g n_1 n_2, \tag{1}$$

where $\frac{d\sigma}{d\omega}$ is the state to state differential cross section and $n_1$ and $n_2$ are the densities of beams 1 and 2 at the intersection point. The state label $i \rightarrow f$ will be suppressed in further expressions; experiments that are not state to state will require an additional average over initial states and sum over final states in the equations below.

In most crossed beam experiments with pulsed laser detection, the molecular beams are also pulsed; then, $n_1$ and $n_2$ are distributions in position, velocity, and time. The signal depends on the density distribution of products at the time the probe laser fires, called $t = 0$; times before the probe are negative. A molecule scattered at position $\mathbf{r}_{\mathrm{s}}$ with laboratory-frame velocity $\mathbf{v}$ at time $t$ ($< 0$) will be at position $\mathbf{r}_{\mathrm{s}} - \mathbf{v}t$ at $t = 0$. The velocity $\mathbf{v}$ is a function of the initial velocity vectors of the colliding reactants $\mathbf{v}_1$ and $\mathbf{v}_2$, and the scattering angles $\theta$ and $\phi$. To find the product densities at $t = 0$, one adds all the contributions from earlier scattering times and positions of molecules that could contribute to the density at $\mathbf{r}$ at $t = 0$:

$$\begin{aligned} n_{\mathrm{p}}(\theta, \phi, \mathbf{r}, \mathbf{v}_1, \mathbf{v}_2, t = 0) &= \int_{-\infty}^{0} dt \int d\mathbf{r}_{\mathrm{s}} \frac{d\sigma}{d\omega}(\theta, \phi, g) g n_1(\mathbf{v}_1, \mathbf{r}_{\mathrm{s}}, t) n_2(\mathbf{v}_2, \mathbf{r}_{\mathrm{s}}, t) \\ &\quad \times \delta(\mathbf{r} - (\mathbf{r}_{\mathrm{s}} - \mathbf{v}t)) \\ &= \int_{-\infty}^{0} dt \frac{d\sigma}{d\omega}(\theta, \phi, g) g n_1(\mathbf{v}_1, \mathbf{r} + \mathbf{v}t, t) n_2(\mathbf{v}_2, \mathbf{r} + \mathbf{v}t, t) \end{aligned} \tag{2}$$

The distribution of product *ions* is given by the density of product molecules times the ionization probability $P_{\rm I}$, which is a function of both the position (through the spatial dependence of the laser intensity) and the velocity (through the Doppler shift). ($P_{\rm I}$ probably also depends on $f$, the final state of the molecule, because of different absorption probabilities for different final states.) The number of product ions with a particular $\theta$ and $\phi$, produced by scattering from beams with initial velocities $\mathbf{v}_1$ and $\mathbf{v}_2$ is

$$N_{\rm I}(\theta,\phi,\mathbf{v}_1,\mathbf{v}_2) = \int_V d\mathbf{r}\, n_{\rm p}(\theta,\phi,\mathbf{r},\mathbf{v}_1,\mathbf{v}_2,t=0)P_{\rm I}(\mathbf{r},\mathbf{v}), \tag{3}$$

where the integration over $\mathbf{r}$ must include both the molecular beam intersection volume and the volume from which ions can be collected and sent toward the detector. The total number of product ions with COM scattering angles $\theta$ and $\phi$ is found by integrating over the velocity distributions in the two molecular beams:

$$\begin{aligned} N_{\rm I}(\theta,\phi) &= \int d\mathbf{v}_1 \int d\mathbf{v}_2\, N_{\rm I}(\theta,\phi,\mathbf{v}_1,\mathbf{v}_2) \\ &= \int d\mathbf{v}_1 \int d\mathbf{v}_2 \int_V d\mathbf{r} \int_{-\infty}^{0} dt\, \frac{d\sigma}{d\omega}(\theta,\phi,g)g \\ &\quad \times n_1(\mathbf{v}_1,\mathbf{r}+\mathbf{v}t,t)n_2(\mathbf{v}_2,\mathbf{r}+\mathbf{v}t,t)P_{\rm I}(\mathbf{r},\mathbf{v}) \end{aligned} \tag{4}$$

In a velocity mapped imaging experiment, the observed quantity is the number of ions arriving in a particular pixel. If the velocity mapping optics are perfect, the arrival positions of the ions depend only on their velocity components in the detector plane (that is, perpendicular to the time of flight axis). To find the pixel intensities one must transform Eq. (4) to Cartesian velocity coordinates ($v_x$ and $v_y$). The transformation to Cartesian coordinates inserts a Jacobian that has a very simple form: it is proportional to $1/|v_z|$, the reciprocal of the velocity component along the time of flight axis. For each $\mathbf{v}_1, \mathbf{v}_2$ pair, there are at most two values of $v_z$ that contribute to the signal at a particular $(v_x, v_y)$, one from the "upper half" of the Newton sphere and one from the lower half. (If the velocity projection $(v_x, v_y)$ lies outside the Newton sphere, no ions will arrive there; if it lies exactly at the edge of the Newton sphere, there is only one $\mathbf{v}$ that will contribute, namely $(v_x, v_y, 0)$.) The two contributions simply add, and the intensity in a single pixel is obtained by integrating over its surface. Then

$$\begin{aligned} N_{\rm I}(v_x,v_y) = \int_{\Delta v_x} dv_x \int_{\Delta v_y} dv_y \int d\mathbf{v}_1 \int d\mathbf{v}_2 \int_V d\mathbf{r} \int_{-\infty}^{0} dt\, g \left|\frac{\partial\theta\,\partial\phi}{\partial v_x \partial v_y}\right| \\ \times \left[\frac{d\sigma}{d\omega}(\theta^+,\phi^+,g)n_1(\mathbf{v}_1,\mathbf{r}+\mathbf{v}^+t,t)n_2(\mathbf{v}_2,\mathbf{r}+\mathbf{v}^+t,t)P_{\rm I}(\mathbf{r},\mathbf{v}^+)\right. \\ \left. + \frac{d\sigma}{d\omega}(\theta^-,\phi^-,g)n_1(\mathbf{v}_1,\mathbf{r}+\mathbf{v}^-t,t)n_2(\mathbf{v}_2,\mathbf{r}+\mathbf{v}^-t,t)P_{\rm I}(\mathbf{r},\mathbf{v}^-)\right], \end{aligned} \tag{5}$$

where $\mathbf{v}^+$ and $\mathbf{v}^-$ are the "upper half" and "lower half" velocity vectors. The $x$ and $y$ components of $\mathbf{v}^+$ and $\mathbf{v}^-$ are the same; their $z$ components will be equal in magnitude but opposite in sign if the COM velocity is perpendicular to the TOF axis. $\theta^+$ amd $\phi^+$ are the upper-half COM scattering angles; $\theta^+ = \theta^-$ if the relative velocity is perpendicular to the TOF axis.

If the velocity mapping optics are not perfect, then the arrival position of an ion may depend on both its velocity $\mathbf{v}$ and its position of formation $\mathbf{r}$. An explicit projection procedure is then required to reduce the five variables $\theta$, $\phi$, and $\mathbf{r}$ to the detector position variables $x_\mathrm{d}$ and $y_\mathrm{d}$. The projection is straightforward if the function giving $x_\mathrm{d}$ and $y_\mathrm{d}$ in terms of $\theta$, $\phi$, and $\mathbf{r}$ is known.

Equation 5 is a general expression for the final two-dimensional velocity distribution in terms of the differential cross section and quantities determined by the apparatus. It may be compared to the similar expression given by Buck for a more traditional crossed beam apparatus with a detector located far from the scattering center, eq (18.23) of Ref. 13. There are several minor differences, but the Jacobian is quite different in the two cases. In the traditional experiment the COM solid angle subtended by the detector varies strongly as the laboratory scattering angle changes. In the imaging experiment the COM solid angles vary simply with the distance of the pixel away from the COM velocity; the strong variation of angular resolution with scattering angle characteristic of the traditional experiment is no longer present.

## Simplifying Approximations

Equation 5 is a twelve-dimensional integral. Most programs that simulate images from crossed beam experiments make approximations that reduce its dimensionality before attempting the integration. This section describes the approach followed in my own simulations of CO scattering experiments; it is similar to that used by several other groups.

In the crossed beam imaging apparatus at Sandia, the two molecular beams are very tightly collimated, with half-angles of 0.23°, and cross at right angles. Their speed ratios are modest ($S = 15$–$20$). Under these circumstances the distributions of relative velocities $\mathbf{v}_1 - \mathbf{v}_2$ and of COM velocity vectors $\mathbf{v}_\mathrm{COM}$ are almost entirely determined by the spread in speeds of the two molecular beams rather than their angular spreads. We can therefore reduce the six-dimensional integral over the molecular beam velocities $\mathbf{v}_1$ and $\mathbf{v}_2$ to a two-dimensional one over their magnitudes alone. This reduction is not usually available; in experiments with looser collimation the angular spread of the beams will make important contributions to the distribution of COM and relative velocities (*14*).

A second approximation is that the pixels are sufficiently small that only the Jacobian from Eq. (5) varies significantly over the small region defined by $\Delta v_x$, $\Delta v_y$. All the other quantities can be evaluated at the values of $v_x$ and $v_y$ that describe the center of the pixel. This approximation is reasonable if features in the experimental images are large compared to single pixels.

With these two approximations Eq. (5) reduces to

$$N_I(\bar{v}_x, \bar{v}_y) = \int dv_1 \int dv_2\, g \bar{J}(v_1, v_2, \bar{v}_x, \bar{v}_y) \times \left[\frac{d\sigma}{d\omega}(\bar{\theta}^+, \bar{\phi}^+, g) F(v_1, v_2, \mathbf{v}^+) + \frac{d\sigma}{d\omega}(\bar{\theta}^-, \bar{\phi}^-, g) F(v_1, v_2, \mathbf{v}^-)\right] \quad (6)$$

where the barred variables represent quantities evaluated at the center of a particular pixel, and

$$\bar{J}(v_1, v_2, \bar{v}_x, \bar{v}_y) = \int_{\bar{v}_x - \Delta v_x}^{\bar{v}_x + \Delta v_x} dv_x \int_{\bar{v}_y - \Delta v_y}^{\bar{v}_y + \Delta v_y} dv_x \left| \frac{\partial\theta\, \partial\phi}{\partial v_x \partial v_y} \right| \quad (7)$$

$$F(v_1, v_2, \mathbf{v}) = \int_V d\mathbf{r} \int_{-\infty}^{0} dt\, n_1(v_1, \mathbf{r} + \mathbf{v}t, t) n_2(v_2, \mathbf{r} + \mathbf{v}t, t) P_I(\mathbf{r}, \mathbf{v}). \quad (8)$$

Eq 6 is simple enough to evaluate in practical programs. Either Monte Carlo or deterministic (e.g., nested Gaussian quadrature) methods may be used.

## Implementation

This section describes a particular program, called Imsim, that evaluates Eq. (6) and has been used in extraction of state to state differential cross sections for Ne–CO rotationally inelastic scattering.

Evaluation of Eq. (6) requires specification of the functions $n_1$, $n_2$, $P_I$, $\frac{d\sigma}{d\omega}$, and $\left|\frac{\partial\theta\,\partial\phi}{\partial v_x \partial v_y}\right|$. In the Imsim program the molecular beam densities are assumed to have Gaussian profiles in the radial spatial dimension, in time (though with a temporal peak that might not fall at $t = 0$), and in speed. The ionization probability is proportional to the intensity of a focused Gaussian laser beam at the Doppler-shifted absorption frequency $\nu_{\text{abs}}$ and at the position $\mathbf{r}$, raised to a power given by the number of photons in the absorption. The Jacobian in the perfect velocity mapping case is

$$\left| \frac{\partial\theta\, \partial\phi}{\partial v_x \partial v_y} \right| = \frac{2}{|\mathbf{u}_f|^2 (|\mathbf{u}_f|^2 - u_x^2 - u_y^2)^{\frac{1}{2}}}, \quad (9)$$

where $\mathbf{u}_f$ is the final velocity in the COM frame, and $u_x$ and $u_y$ are its components in the plane perpendicular to the TOF direction. A user-supplied function evaluates the differential cross section so any reasonable shape can be used.

The outer integration over $v_1$ and $v_2$ is performed with trapezoidal rule quadrature, using typically 30 speeds for each beam. The Jacobian integral is expressed analytically (*15*) and evaluated for each pixel at each $v_1/v_2$ pair. The integrand of the three-dimensional integral over space is very strongly peaked if the laser beam is tightly focused. In Imsim this integral is performed with Gaussian quadratures that incorporate all the spatial dependence of the laser intensity into the Gaussian weighting functions (*16,17*), so that relatively few spatial quadrature points are required (125 points at each $t$ is typical). The integral over time is performed with Gauss-Legendre quadrature; a finite lower integration limit is chosen for each pixel so that scattering at earlier times contributes negligibly to the signal.

As just described, an accurate image simulation requires on the order of $10^6$ evaluations of the integrand (primarily the product of molecular beam densities) for each pixel; a typical image might be $100 \times 100$ pixels for a total of $10^{10}$ integrand evaluations. These evaluations will dominate the computation time. If each evaluation requires 100 floating point operations, then on a 100 MFLOPS computer the simulation will take about three hours.

If the molecular beam densities have the same speed distribution for every position and time, that is, if $n(v, \mathbf{r}+\mathbf{v}t, t) = s(v)\rho(\mathbf{r}+\mathbf{v}t, t)$, the simulation time can be reduced enormously by a simple trick. The speed distribution $s$ may be removed from the four-dimensional integration in the definition of $F$. For a specified pixel, the only remaining effect of $v_1$ and $v_2$ within the integral is to determine the position and diameter of the Newton sphere and therefore the $z$-component of $\mathbf{v}$. The four-dimensional integral over $\mathbf{r}$ and $t$ for a single pixel may then be regarded as a function of a single parameter, $v_z$. If the integral is determined accurately for a representative set of $v_z$ at each pixel, its value for other nearby $v_z$ (implying other values of $v_1$ and $v_2$) can be determined by interpolation. The integral is a smooth function of $v_z$, so that six representative $v_z$ support an accurate cubic spline interpolation. The number of 4D integral evaluations per pixel has then been reduced from 900 (for 30 speeds in each molecular beam) to six, with a corresponding reduction in run time. Typical simulations with Imsim using this trick require about five minutes; the run time is dominated by evaluations of $\bar{J}$.

## Real Experiments: Data Analysis

### Qualitative Analysis

One of the main attractions of imaging experiments is that the appearance of the image data immediately suggests simple qualitative interpretations. For instance, in rotationally inelastic scattering, the positions of rotational rainbow peaks are usually immediately apparent, and their changes in a series of images corresponding to different $\Delta j$ can be followed easily. In the most common geometry, with the TOF axis perpendicular to the molecular beam plane, each position on the outer edge of the Newton circle in the image corresponds roughly to a single scattering angle. The positions (though not the relative intensities) of sharp features in the DCS, and its overall shape, can usually be estimated directly from the image with an angular accuracy of 10° or better. For qualitative interpretation this is sometimes all that is required.

A crude estimate of the DCS may be obtained by simply measuring the intensity near the edge of the image as a function of angular displacement about the COM velocity from the initial product velocity. This estimate is accurate if the detection probabilities of all scattered molecules are the same. Most experiments do not meet that condition, and the resulting errors in intensities in the DCS can be large. (The corresponding requirement is easy to meet in photodissociation experiments, so that an equivalent analysis of photodissociation data is often reasonable.)

A better estimate may be obtained by performing a simulation for an *isotropic* DCS, then dividing that image into the observed image pixel by pixel. In the absence of velocity spreads in the two molecular beams, the quotient image would show a series of stripes of constant intensity perpendicular to the relative velocity vector. The pixel values in the stripes would give the DCS at the corresponding values of $\cos\theta$. The unique mapping between $\theta$ and pixel position is destroyed by the velocity spreads, but this method will still provide an initial estimate of the DCS that is better than that from a direct interpretation of uncorrected pixel intensities.

## Linear Fitting

Integration is a linear operation. If the DCS in Eq. (6) is written as a linear combination of basis functions, a set of basis images may be obtained by performing simulations using each basis function as the DCS. Then the predicted image for any linear combination of basis functions is the corresponding linear combination of basis images. Narrow functions in angle space make good basis functions; Gaussians, triangles, and rectangles could all be used. Once the basis images have been generated, no further multidimensional integrals are required, and the simulated image for each new set of weighting coefficients can be assembled in milliseconds rather than minutes.

If the experiment does not resolve $m_j$ states so that the DCS has no $\phi$ dependence, and the desired quantity is the DCS averaged over the experimental distribution of relative speeds $g$, then the desired function $d\sigma/d\omega$ is a function of $\theta$ alone. If everything in Eq. (6) except the DCS is known, then its extraction from the data (i.e., determination of the optimum set of weighting coefficients in the DCS expansion) is a linear fitting problem. The data do not always determine the DCS at every angle very well, so it is usually an ill-conditioned problem. Methods from the field of inverse problems are needed to bias the result toward physically reasonable values in some regions. "By-hand" fitting, Tikhonov regularization (*18*), and van Cittert iteration (*19*) have all been used.

## Nonlinear Fitting

If quantities other than the differential cross section—for example, the wavelength offset of the laser or the detector location and orientation—need to be fit to the data rather than specified in advance, then the problem is no longer a linear one. Iterative, rather than direct, methods must be applied. A program that uses a nonlinear optimization algorithm to adjust the few nonlinear parameters in an outer loop, with a simulation, a linear DCS fit, and computation of the resulting $\chi^2$ in its function-evaluation routine, often works well.

In some nonlinear problems, it is possible to generate new basis functions at each iteration without new simulations. When this kind of basis-image construction is available it is usually much faster than performing new simulations for each set of trial nonlinear parameters. For example, if the absolute wavelength of the probe laser is unknown, its value might be a nonlinear fitting parameter. If the laser beam is parallel to the detector, and velocity mapping is used, each pixel corresponds to a known velocity component along the laser beam. Corrections for Doppler weighting can therefore be applied to each basis image by multiplying a Doppler weighting function pixel by pixel into the basis images.

Other experimental parameters that often need to be fit are the orientation and position of the detector and the velocity-to-detector-position mapping factor (the effective flight time). These quantities specify the relation between laboratory frame velocity $(\bar{v}_x, \bar{v}_y)$ and pixel position in the image. It is reasonable to compute $N_I(\bar{v}_x, \bar{v}_y)$ at a suitably fine grid of $(\bar{v}_x, \bar{v}_y)$ points, then interpolate in that 2D grid to obtain simulated images for new values of detector position and effective flight time. This interpolation scheme again permits the parameters to be fit without new simulations at each iteration. It was used in the analysis of Ne–CO scattering data described next.

## Example: Analysis of Ne + CO Inelastic Scattering

The left panel of Figure 1 shows an experimental image obtained by 2+1 REMPI of scattered CO in a crossed beam Ne + CO experiment with velocity mapping. This image was obtained at Sandia National Laboratory; a detailed description of the apparatus and experimental procedures will be published elsewhere (*8*). The two molecular beams crossed at right angles; the probe laser traveled in the same plane and bisected the two oncoming molecular beams. Molecules scattered into $j_f = 10$ were ionized and the ions were accelerated perpendicular to the beam plane by velocity mapping optics. The initial CO rotational temperature was about 2 K. The speeds of the CO and Ne beams were 560 and 785 m/s, respectively, for a collision energy of 456 $\text{cm}^{-1}$. The 215 nm laser beam was focused at the molecular beam crossing point by a 0.5 m lens and was linearly polarized in the molecular beam plane.

The center panel of Figure 1 shows a simulated image with an isotropic DCS and other parameters chosen to represent the experiment. This image demonstrates the importance of the "kernel functions" that multiply the DCS in Eq. (5). The Jacobian causes the bright outer ring and dimmer center of the image; the velocity spread in the beams produces the fuzziness at the outer edge, which is more pronounced at the bottom of the image; the ionization probability and integration over time produce the bright spot near the top of the image and the slight weighting in a vertical stripe through the center. A naive analysis that simply used the intensity as a function of angle about the center as an estimate of the DCS would give very poor results, especially if the measurements were made around the upper edge of the image.

The right panel of Figure 1 shows a simulated image obtained from a nonlinear fit. The DCS was modeled as a piecewise linear function with values defined at 5° intervals; the basis functions were therefore narrow triangles. A set of basis images was

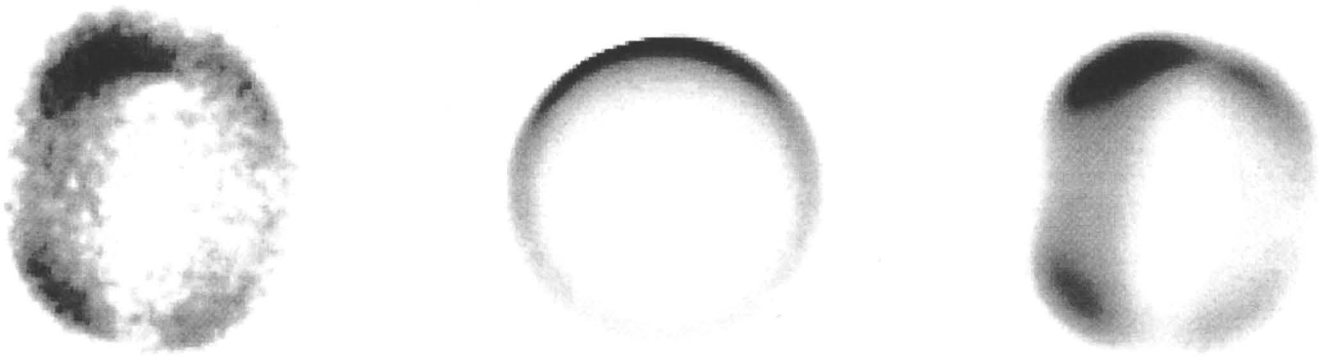

Figure 1: Left panel: experimental image for $j_f = 10$. Center panel: simulated image for isotropic differential cross section. Right panel: fitted image.

generated by simulation using no Doppler weighting and estimates of the other experimental parameters. A least squares fit was then performed; the wavelength offset of the laser, the detector position and orientation, and the effective flight time were varied in a nonlinear fitting loop. At each iteration, a new set of basis images was determined by interpolation, weightings for the Doppler effect were applied, and a linear fit of the DCS alone was performed with first order regularization. The best fit yielded detector position and effective flight time values that differed by less than 5% from the initial estimates. Figure 2 shows several 1D profiles through the data and best-fit images. Figure 3 shows the extracted DCS.

All the major features of the experimental image have been captured, but systematic disagreements between the fitted image and the data remain. Some of these disagreements come from imperfections in the velocity mapping; in particular, there appear to be some space charge effects in the bright spot at the top of the experimental image, the experimental image is blurrier than the simulation, and the main ring is not quite round. Angular momentum polarization was neglected during this fit. The effects of angular momentum polarization of the scattered molecules will be discussed briefly below.

## Further Applications

This section examines two points that were hidden in the discussion above by the assumption of complete initial and final quantum state resolution. One is the effect of angular momentum polarization on the images. The second is the possibility of unresolved internal energy distributions in the unprobed product.

### Polarization Effects

Scattered molecules with a given $j$ will usually have nonisotropic distributions of their angular momentum vectors. Laser ionization probes are sensitive to the angular momentum distribution, so if the molecules arriving in different pixels have different angular momentum distributions the relative pixel intensities will be affected. This dependence is both a nuisance and an opportunity; it must be accounted for even if one simply wants to measure a degeneracy averaged differential cross section, but it provides a rich source of dynamical information beyond the DCS if it can be exploited well.

It is straightfoward to include the effects of any known angular momentum polarization in simulations. Formulas cited in the excellent review by Orr-Ewing and Zare (*20*) may be incorporated easily into the $P_I$. On the other hand, the problem of extracting an unknown angular momentum distribution from images measured with different polarizations or geometries has not yet been fully addressed for the crossed-beam problem.

The Ne-CO analysis described above assumed that the scattered molecules were not polarized. One way to estimate the likely error introduced by that assumption is to perform additional fits assuming limiting nonisotropic polarizations, and see how

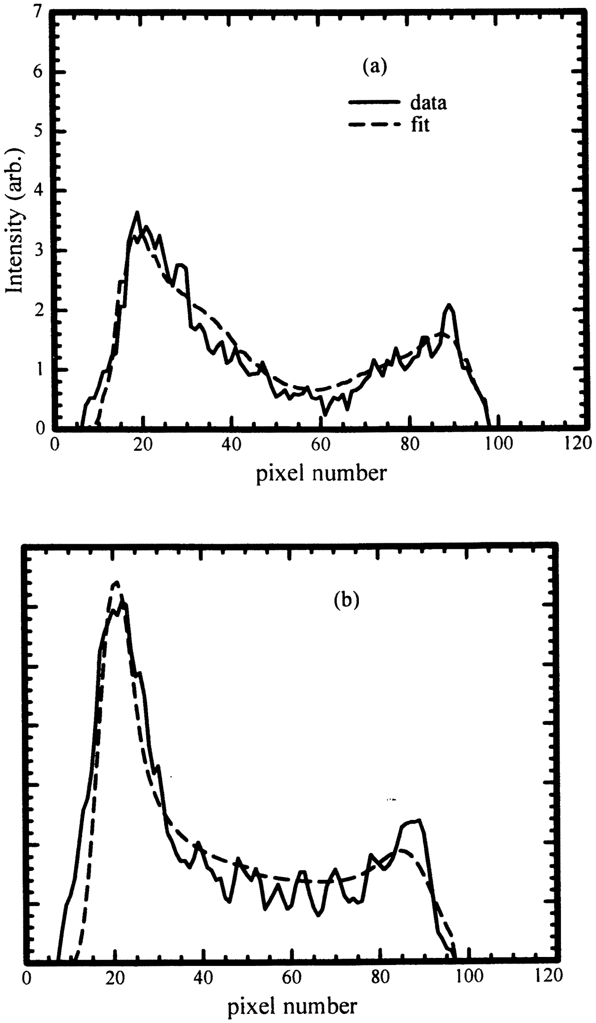

Figure 2: Line profiles through data and best-fit images. (a) diagonal trace from upper left to lower right of image; (b) vertical trace at column 54 (through brightest part of image).

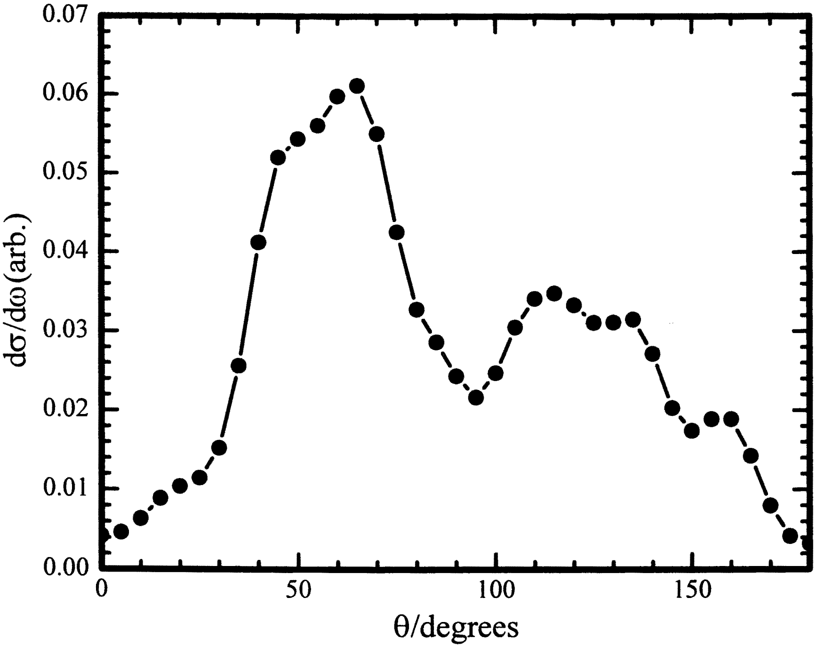

Figure 3: Fitted differential cross section.

much the extracted DCS changes. In the present example, three fits were performed: one assuming no polarization, one assuming limiting positive alignment ($m_j = j$ and $m_j = -j$ equally populated, with all other $m_j$ unpopulated; the quantization vector is taken along the final COM frame velocity vector of the CO), and one assuming limiting negative alignment (only $m_j = 0$ populated). The most likely actual outcome of the scattering process is modest negative alignment. For the geometry of the experiment, negative alignment tends to enhance the intensity at extreme forward and backward scattering, while not affecting sideways scattering. Since this DCS does not have much intensity near the poles, the neglect of polarization effects does not introduce significant error.

### Unresolved Internal Energy Distributions

If the unprobed collider has accessible internal energy states, then the observed image will be a superposition of different images corresponding to different Newton sphere diameters. The object of the data analysis (discounting the distribution of collision energies) would be the two-dimensional energy-angle distribution. In photodissociation experiments this distribution is usually obtained with an inverse Abel transform. Suits et al. have applied this analysis to one crossed-beam study of the $O(^1D) + D_2$ reaction (*6*); they used a very short oxygen atom beam and a loosely focused probe laser to reduce selective detection effects. In cases where the selective detection effects are stronger, one can imagine an extraction procedure in the spirit of the Abel transform: analyze the outermost ring, using only the data at the edge; simulate an image with the resulting DCS; subtract that image from the data, leaving a residual image with a smaller diameter, and work inwards. In such a procedure, small errors will propagate inward and grow, so the results will get steadily worse at higher internal energies. A general solution to this problem is not yet known.

## Acknowlegements

K. Thomas Lorenz and David W. Chandler acquired the experimental data with Department of Energy support. The author has benefited from conversations with David Chandler, Thomas Lorenz, Gregory Hall, and Michael Westley. Michael Westley provided the analytic Jacobian integral code.

## References

[1] *Atomic and Molecular Beam Methods;* Scoles, G., Ed.; Oxford University Press: New York, 1988.

[2] Chandler, D. W.; Houston, P. L. *J. Chem. Phys.* **1987,** *87,* 1445.

[3] Bontuyan, L. S.; Suits, A. G.; Houston, P. L.; Whitaker, B. J. *J. Phys. Chem.* **1993,** *97,* 6342–6350.

[4] Yonekura, N.; Gebauer, C.; Kohguchi, H.; Suzuki, T. *Rev. Sci. Inst.* **1999,** *70,* 3265–3270.

[5] Kitsopoulos, T. N.; Buntine, M. A.; Baldwin, D. P.; Zare, R. N.; Chandler, D. W. *Science* **1993,** *260,* 1605–1610.

[6] Ahmed, M.; Peterka, D. S.; Suits, A. G. *Chem. Phys. Lett.* **1999,**.

[7] Lorenz, K. T.; Westley, M. S.; Chandler, D. W. *Phys. Chem. Chem. Phys.* **2000,** submitted.

[8] Lorenz, K. T.; Chandler, D. W.; McBane, G. C. in preparation.

[9] Ahmed, M.; Peterka, D. S.; Suits, A. G. *Phys. Chem. Chem. Phys.* **2000,** in press.

[10] Ahmed, M.; Peterka, D. S.; Suits, A. G. *Chem. Phys. Lett.* **2000,** in press.

[11] Heck, A. J. R.; Chandler, D. W. *Annu. Rev. Phys. Chem.* **1995,** *46,* 335–372.

[12] Chang, B.-Y.; Hoetzlein, R. C.; Mueller, J. A.; Geiser, J. D.; Houston, P. L. *Rev. Sci. Inst.* **1998,** *69,* 1665–1670.

[13] Buck, U. In *Atomic and Molecular Beam Methods,* Vol. I; Scoles, G., Ed.; Oxford University Press: New York, 1988; Chapter 18.

[14] Buck, U. In *Atomic and Molecular Beam Methods,* Vol. I; Scoles, G., Ed.; Oxford University Press: New York, 1988; Chapter 20.

[15] Westley, M. S. private communication.

[16] Gautschi, W. *ACM Trans. Math. Soft.* **1994,** *20,* 21–62.

[17] Elhay, S.; Kautsky, J. *ACM Trans. Math. Soft.* **1987,** *13,* 399–415.

[18] Press, W. H.; Teukolsky, S. A.; Vetterling, W. T.; Flannery, B. P. Numerical Recipes in C: the Art of Scientific Computing, 2nd ed.; Cambridge University Press: New York, 1992; Chapter 18.

[19] Shapiro, M.; Gerber, R. B.; Buck, U.; Schleusener, J. *J. Chem. Phys.* **1977,** *67,* 3570–3576.

[20] Orr-Ewing, A. J.; Zare, R. N. *Ann. Rev. Phys. Chem.* **1994,** *45,* 315–366.

Downloaded by STANFORD UNIV GREEN LIBR on September 21, 2012 | http://pubs.acs.org
Publication Date: October 18, 2000 | doi: 10.1021/bk-2001-0770.ch014

## Chapter 14

# Velocity Mapping of Reaction Products: The Cl + $C_2H_6 \rightarrow$ HCl + $C_2H_5$ Reaction

**Peter C. Samartzis[1, 2], Derek J. Smith[2], and Theofanis N. Kitsopoulos[1, 2]**

**[1]Department of Chemistry, University of Crete, 714 09 Heraklion, Greece**
**[2]Institute of Electronic Structure and Laser, Foundation of Research and Technology–Hellas, 711 10 Heraklion, Greece**

Ion imaging techniques have been a useful tool for studying the dynamics of unimolecular and bimolecular processes. In this contribution we apply the refined imaging method of velocity mapping towards the investigation of the bimolecular reaction of atomic chlorine with ethane. Images for state selected reaction products HCl(υ=0,J=0,1) are obtained from which velocity distributions are extracted. Our results are in qualitative

## Introduction

In order to understand the dynamics of a chemical reaction, detailed knowledge concerning both the reactants and the products such as velocity vectors, state-selected internal energy distributions, and correlations between these quantities are essential. Ion imaging experiments have been used to investigate a limited number of reactions such as A+BC$\rightarrow$AB+C thereby demonstrating both the strengths and weaknesses of the method (*1*). Both single beam and crossed molecular beam scattering setups have been used in conjunction with ion imaging detection of products. In the former, reactants or their precursors are premixed and co-expanded through a pulsed nozzle thus forming a single molecular beam. A photolysis laser is used to generate hot-atom reactants that subsequently react with other molecules in the beam. A suitable delay (10-100 ns) allows a sufficient density of products to build up, after which a second probe laser, is used to state selectively ionize the reaction products. Such imaging experiments have been reported for the H+HI$\rightarrow H_2$+I reaction (*2,3*), however, no information concerning the angular distribution of the products could be extracted, mainly because of the mass combination between reactants and products. A crossed molecular beam configuration was used to study reactions of the type

In Imaging in Chemical Dynamics; Suits, A., et al.;
ACS Symposium Series; American Chemical Society: Washington, DC, 2000.

Downloaded by STANFORD UNIV GREEN LIBR on September 21, 2012 | http://pubs.acs.org
Publication Date: October 18, 2000 | doi: 10.1021/bk-2001-0770.ch014

$A+B_2 \rightarrow AB+B$ reaction (*4,5*) that allowed determination of the non-state selective differential cross section, by probing the atomic product. In all crossed molecular-beam reactive scattering experiments, when resonance enhanced multiphoton ionization (REMPI) is used to state-selectively detect the products, the sensitivity of the process becomes an issue. Typical product densities per quantum state are $10^4$-$10^5$ $cm^{-3}$ hence approaching the sensitivity limits of REMPI. In addition, with the exception of (1+1) REMPI, in all other situations the probe laser is focused creating a very small interaction volume that yields extremely low count rates.

The current publication deals with the reaction of atomic chlorine with ethane producing hydrogen chloride and an ethyl radical:

$$Cl + C_2H_6 \rightarrow HCl + C_2H_5 \qquad (1)$$

This reaction has been studied by Kandel *et al.* (*6,7,8*) at the collision energy of 0.24 ± 0.03 eV using single-beam time-of-flight Doppler measurements to extract the velocity and angular distributions of the detected HCl or $C_2H_5$ products. It was concluded that the $C_2H_5$ reaction product has almost no internal energy excitation and little effect on the dynamics of the reaction. HCl is produced mostly in its J=0 state with smaller amounts formed in higher rotational states. These *photoloc* experiments offer the advantage of high product number densities as they are performed only a few mm from the nozzle orifice. In this report, we have adapted a similar method to our imaging apparatus and demonstrate the potential of this new configuration for probing reactive scattering processes. Our experiment is performed at a collision energy of 0.358 eV and velocity map images for the HCl (υ=0,J=0,1) product are recorded.

## Experimental

A schematic of the experimental apparatus is shown in Figure 1. The major modification to the apparatus compared to the configuration used for unimolecular photofragmentation studies (*9*) is the removal of the skimmer and mounting of the ion optics (*10,11*) directly in front of the nozzle. By doing so, differential pumping is being sacrificed for increasing the number density of the reactants and consequently that of the reaction products. A slight differential pumping between the source and detector regions is achieved by a 15mm hole. When a mixture of 10% $Cl_2$ (Merck, 99.8%) in ethane (Aldrich, 99+ %) is expanded through the pulsed nozzle operating at 10Hz, backing pressure ~1000 Torr, the source and detector chamber pressures are $10^{-5}$ and $10^{-6}$ torr respectively. The repeller is mounted concentrically onto the nozzle faceplate and has a 2mm orifice. Both nozzle and repeller are at the same voltage in order to eliminate discharging during the gas pulse firing.

Two counter-propagating lasers intersect the molecular beam perpendicularly approximately 5mm from the repeller plate. The photolysis laser beam is the focused (f=300mm) non-polarized output of an excimer laser (Lumonics HyperEX 400) operating at 308nm, which photodissociates $Cl_2$. HCl(v,J) product is detected via (2+1) REMPI through the $F^1\Delta_2$ state, (*12,13,14*) using the focused (f=250mm)

Downloaded by STANFORD UNIV GREEN LIBR on September 21, 2012 | http://pubs.acs.org
Publication Date: October 18, 2000 | doi: 10.1021/bk-2001-0770.ch014

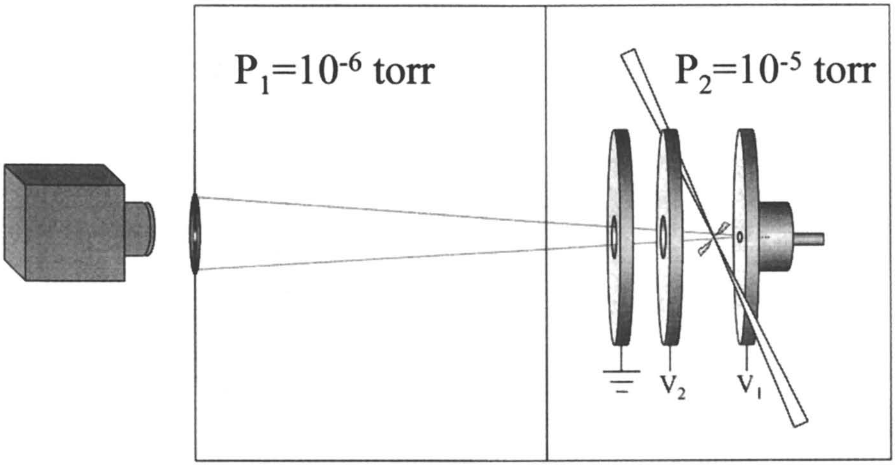

*Figure 1. Apparatus schematic. Counter-propagating lasers intersect a pulsed molecular beam. The pump (photolysis) beam produces atomic chlorine that reacts with ethane. HCl product is state-selectively photoionized by the probe laser. The resulting ions are detected with a 2-D position sensitive imaging detector after passage through a linear TOF mass spectrometer.*

frequency-doubled output of an Nd:YAG-pumped optical parametric oscillator (Spectra-Physics Pro190, MOPO 730D10). The timing of the experiment is controlled using a digital delay pulse generator (Stanford Research Systems, model DG535). The probe pulse is delayed by 30–90 ns with respect to the photolysis pulse, in order to allow a sufficient density of HCl products to buildup prior to the REMPI detection.

The resultant ions are accelerated by a suitable electric field needed for velocity mapping (*10*) and are detected using a position sensitive imaging detector. Background images are obtained when no molecular beam is present (nozzle off). The experiment is performed with sufficient care as to avoid space-charge effects.

Downloaded by STANFORD UNIV GREEN LIBR on September 21, 2012 | http://pubs.acs.org
Publication Date: October 18, 2000 | doi: 10.1021/bk-2001-0770.ch014

## Results

In order to extract quantitative data from the 2-D images one needs to reconstruct the 3-D velocity distribution. For photodissociation experiments, in which linearly polarized lasers are commonly used, the configuration is such that the photolysis and probe polarization vectors are parallel to each other and to the imaging plane. The resulting photofragment angular distribution is cylindrically symmetric and thus an inverse Abel transform can be applied to extract the 3D distribution (*1*). In the present experiment, the photolysis laser is unpolarized, i.e., the electric field of the laser is cylindrically symmetric with respect to the propagation direction. Therefore, the resulting Cl-atom photofragment and the product HCl(v,J) angular distributions will also be cylindrically symmetric with respect to this direction and hence we can once again apply the inverse Abel transformation to extract scattering information (*15*).

Figure 2a shows quadrant-averaged 2-D projections of the associated 3-D spatial distributions of $H^{35}Cl$ ions. The photolysis laser propagation direction and the axis perpendicular to it define the quadrants. The inverted images are shown in Figure 2b for v=0, J=0,1. Two main features can be observed in every image: an intense spot in the center and an anisotropic distribution at the outer edge. Performing the experiment under the same experimental conditions but without the photolysis laser at 308 nm and probing $H^{35}Cl$ ($\upsilon=0$, J), we still observe the intense peak in the center of the image but the surrounding anisotropic distribution is completely gone. This suggests that 308 nm laser is involved in the production of the translationally energetic species observed in the outer regions of the image. We therefore conclude that the central spot is from residual HCl present in the molecular beam prior to the photolytic initiation of the reaction – likely due to impurities in the $Cl_2$ bottle and primary reactions in the mixing tank. Tuning the probe laser off the HCl REMPI lines and with the 308nm laser on, provides an image without any of the two features, suggesting that the observed $H^{35}Cl^+$ ion distribution is in fact that of selected rotational states.

Integration of the inverted images by radius gives the HCl speed distributions for each of the rotational states probed (Figure 3). For the speed calibration we used the $Cl^*$ fragment distribution, probed through the (2+1) REMPI line at 240.170 nm (*16*).

Downloaded by STANFORD UNIV GREEN LIBR on September 21, 2012 | http://pubs.acs.org
Publication Date: October 18, 2000 | doi: 10.1021/bk-2001-0770.ch014

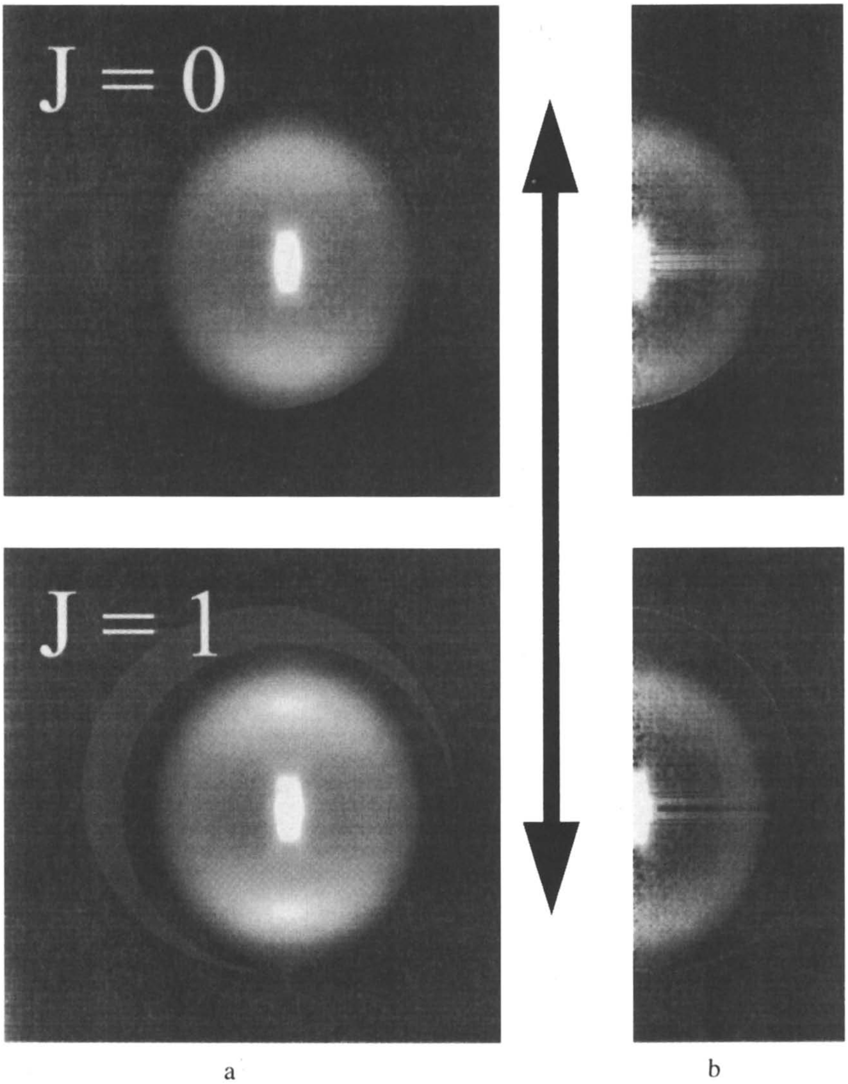

*Figure 2. (a) Averaged 2-D ion projections of HCl for $v=0$, $J=0,1$. The energetic outer ring is the HCl reaction product, whereas the central spot is produced from residual HCl in the parent molecular beam. (b) Reconstructed images of the 2-D projections, via inverse Abel transformation.*

Downloaded by STANFORD UNIV GREEN LIBR on September 21, 2012 | http://pubs.acs.org
Publication Date: October 18, 2000 | doi: 10.1021/bk-2001-0770.ch014

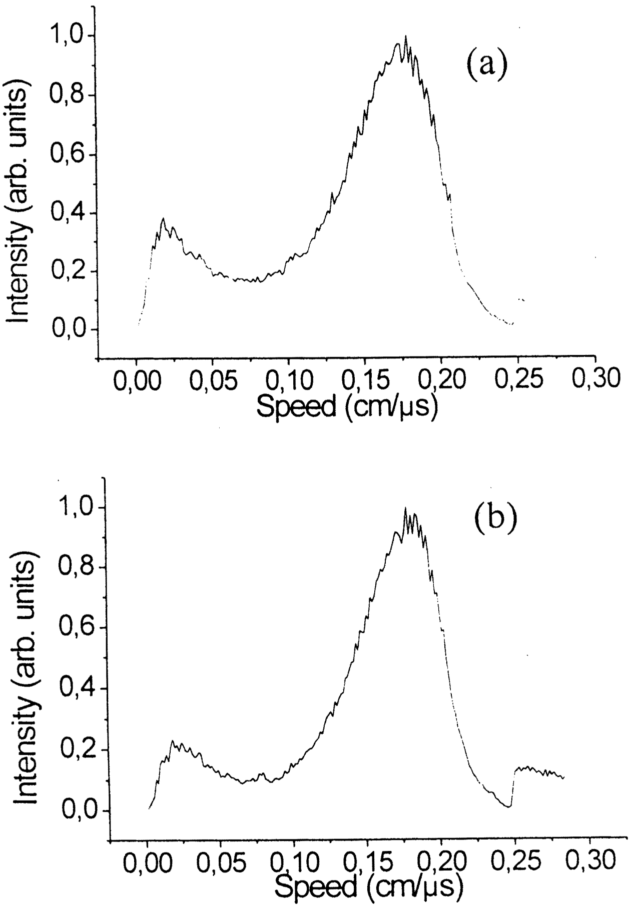

*Fig. 3. Speed distributions of HCl by rotational state (a) J=0 (b) J=1. The vertical line indicates the position of the center of mass for this reaction.*

## Discussion

The photolysis laser wavelength at 308 nm defines the speed of Cl reactants and hence the collision energy of the reaction. At this wavelength essentially only ground spin-orbit state of Cl is produced (*11*), and the kinetic energy release of Cl fragments after photodissociation is 0.776 eV. This dictates collision energy of 0.358 eV and a maximum allowed speed for HCl products of 2185 m/s assuming no internal excitation in any of the reaction products. For the calculation of the above values we have used 4.433 eV for the bond dissociation energy of HCl (*17*) and 4.31 eV for the C-H bond dissociation energy in ethane (*18*).

The uncertainty in the collision energy for the reaction in the current experimental setup is determined by several factors. One consideration is the bandwidth of the photolysis laser which in this case is ~0.013 eV (XeCl excimer). That means that the error in the photofrgament kinetic energy is ±0.0065 eV. If a narrow band laser is use for the photolysis (0.2 $cm^{-1}$), then this uncertainty becomes negligible. A second factor is the velocity slip between the $Cl_2$ precursor reactant molecule and the ethane molecules. Although during a co-expansion of two gases one expects their velocities to be matched, velocity *slipping* is not uncommon (*19*). However, this is usually a small percentage (~1%) of the average beam velocity, so once again we expect this error in the collision energy to be small. Hence we observe that the uncertainty in the collision energy for this photoloc method is on the order of a 1-2 percent (upper limit) of the reaction collision energy.

Although a detailed quantitative analysis of extracting differential cross section from images of the type presented here will be presented in a future paper (*20*), some qualitative conclusions can be drawn. If the HCl products are primarily forward scattered, then we expect the laboratory speed distribution to peak at values greater than the center-of-mass speed $v_{cm}$ (~1110 m/s). For side scattering the distribution would peak at speeds near $v_{cm}$, while for back scattering the HCl speed distributions will peak at speeds less than $v_{cm}$. For the $H^{35}Cl$ products, the observed speeds range from 1150 to 2190 m/s. Based on our qualitative argument, our such a speed distribution suggests that the HCl(v=0, J=0,1) product is primarily forward scattered.

Our observation is in contrast to the previous work of Kandel *et al.* (*6,7,8*) where for the same internal states of HCl products, a more isotropic scattering was observed. The main difference in these two studies is the collision energy, and specifically our study is performed at much higher collision energy (~1.5 times greater). This increase in collision energy and assuming a stripping type Hydrogen abstraction reaction (*6*) could explain the discrepancy. In other words, a faster approaching Cl atom could strip the H-atom with greater ease and at larger impact parameters. Both factors favor a forward scattering HCl product. It is also noticeable that there is not any significant difference in the peak width of the ion distributions between the J=0 and 1 rotational states of HCl probed, as observed in previous studies (*6*).

Downloaded by STANFORD UNIV GREEN LIBR on September 21, 2012 | http://pubs.acs.org
Publication Date: October 18, 2000 | doi: 10.1021/bk-2001-0770.ch014

## Conclusions

We have illustrated the potential of applying velocity mapping to the investigation of bimolecular reactions in a *photoloc* type experimental arrangement. Our results have been qualitatively analyzed and indicate a forward scattering HCl(v=0, J=0,1) product for a collision energy of 0.358 eV. These results are consistent with previous observations, however quantitative comparisons require further experimentation and complete analysis of the images obtained with this imaging configuration.

Downloaded by STANFORD UNIV GREEN LIBR on September 21, 2012 | http://pubs.acs.org
Publication Date: October 18, 2000 | doi: 10.1021/bk-2001-0770.ch014

## Literature Cited

1. Heck, A.J.R. and Chandler, D.W. *Annu. Rev. Phys. Chem.* **1995**, *46*, 335.
2. Buntine, M.A.; Baldwin, D.P.; Zare, R.N.; Chander, D.W. *J. Chem. Phys.* **1991**, *94*, 4672
3. Chandler, D.W.; Kitsopoulos, T.N.; Buntine, M.A.; Baldwin, D.P.; McKay, R.I.; Heck, A.J.R. and Zare, R.N. In *Gas-Phase Chemical Reaction Systems: Experiments and Models 100 Years after Max Bodenstein*; Wolfrum, J.; Volpp, H.-R.; Rannacher, R.; Warnatz, J., Ed.; Springer Series in Chem. Phys.; Springer Berlin: Heidelberg 1996.
4. Kitsopoulos, T.N.; Buntine, M.A.; Baldwin, D.P.; Zare, R.N.; Chander, D.W. *Science* **1993**, *260*, 1605-1610.
5. Ahmed, M.; Peterka, D.S.; Suits, A.G.; *Chem. Phys. Lett.* **1999**, 301, 372.
6. Kandel, A.S.; Rakitzis, P.T.; Lev-On, T.; Zare, R.N. *J. Chem. Phys.* **1996**, *105*, 7550.
7. Kandel, A.S.; Rakitzis, P.T.; Lev-On, T.; Zare, R.N. *Chem. Phys.Lett.* **1997**, 265, 121.
8. Kandel, A.S.; Rakitzis, P.T.; Lev-On, T.; Zare, R.N. *J. Phys. Chem. A* **1998**, *102*, 2270.
9. Samartzis, P. C.; Sakellariou, I., Gougousi, T. and Kitsopoulos, T. N. *J. Chem. Phys.* **1997**, *107*, 43.
10. Eppink, A.T.J.B. ; Parker, D.H. *Rev. Sci. Instrum.* **1997**, *68*, 3477.
11. Samartzis, P. C.; Gougousi, T.; Kitsopoulos, T. N. *Laser Chem.* **1998**, *17*, 185.
12. Green, D.S.; Bickel, G.A.; Wallace, S.C. *J. Mol. Spectros.* **1991**, *150*, 388.
13. Green, D.S.; Bickel, G.A.; Wallace, S.C. *J. Mol. Spectros.* **1991**, *150*, 354.
14. Green, D.S.; Bickel, G.A.; Wallace, S.C. *J. Mol. Spectros.* **1991**, *150*, 303.
15. We are ignoring possible alignment effects for now.
16. NIST Atomic Spectra Database Data, URL http://physics.nist.gov/cgi-bin/AtData/main_asd
17. Huber, K.P. and G. Herzberg, *Constants of Diatomic Molecules*, Van Nostrand Reihnhold Co: New York, 1979; p285.
18. Marshall, P. *J. Phys. Chem.*, **1999**, *103*, 4560-4563 and references therein.
19. D.R. Miller; *Atomic and Molecular Beam Methods Vol I;* G. Scoles Ed.; Oxford Univ. Press: Oxford 1988.
20. Samartzis P.C.; Smith D.J.; Rakitzis T.P. and Kitsopoulos T.N. (in preparation).

## Chapter 15

# Imaging the Atomic Orientation and Alignment in Photodissociation

**Eloy R. Wouters[1,3], Musahid Ahmed[1], Darcy S. Peterka[1], Allan S. Bracker[1,4], Arthur G. Suits[1,5], and Oleg S. Vasyutinskii[2,5]**

**[1]Chemical Sciences Division, Ernest Orlando Lawrence Berkeley National Laboratory, Berkeley, CA 94720**
**[2]Ioffe Physico-Technical Institute, Russian Academy of Sciences, 194021 St. Petersburg, Russia**

A rigorous theoretical connection is established between experimental measurements of the photofragment orientation and alignment and the underlying photodissociation dynamics. Laboratory and molecular-frame angular momentum state multipoles are derived as a function of photofragment recoil angles. These state multipoles are expressed in terms of orientation and alignment anisotropy parameters, which contain information on excited state symmetries, coherence effects, and nonadiabatic interactions. To demonstrate the power of our theoretical method, it is applied to experimental data obtained with velocity map ion imaging and Doppler techniques in both diatomic (RbI and $Cl_2$) and polyatomic systems ($NO_2$ and $N_2O$). Strong recoil-frame alignment and orientation has been observed, as well as coherence effects and long-range nonadiabatic interactions.

## Introduction

Vector correlations in the photodissociation of molecules have attracted the interest of experimentalists for a long time (*1*). Initially (*2, 3*), the correlation of

---

[3]Current address: School of Chemistry, Cantock's Close, University of Bristol, Bristol BS8 1TS, United Kingdom

[4]Current address: Naval Research Laboratory, Code 6876, 4555 Overlook Avenue SW, Washington DC 20375

[5]Corresponding authors (e-mail: AGSuits@lbl.gov and Osv.Pms@pop.ioffe.rssi.ru)

the fragments' recoil velocity vector **v** with the laser polarization direction **e** was probed, *i.e.*, the photofragment angular distribution or velocity anisotropy, characterized by the familiar anisotropy parameter $\beta$.[†] More recently, another important vector correlation has been measured, that between the **e** vector and the projection of the angular momentum **J** of the photofragments on the space-fixed **Z** axis (*4–7*). These vector correlations are characterized by the moments of the magnetic sublevel distribution: the population, which is independent of the magnetic sublevel $m_j$ distribution, the orientation, which is proportional to the dipole moment of the ensemble and implies a nonstatistical $m_j$ distribution, or the alignment, which is proportional to the quadrupole moment of the ensemble and implies a nonstatistical $|m_j|$ distribution (*8*). Important information about the dissociation dynamics, the shape of the potential curves, the symmetries of excited states and the role of nonadiabatic interactions can be obtained from a detailed analysis of these vector correlations. Another notable aspect is the correlation between the photofragment recoil direction **v**, and the photofragment angular momentum **J**, or the angular distribution of the angular momentum polarization (*9–12*). This has been studied in considerable detail for photofragment rotational angular momentum, where the experiments can sometimes provide insight into the broad features of the dissociation dynamics and the nature of the transition state.

Investigations of this **v**–**J** correlation for photofragment atomic orbital polarization, have begun recently in several groups, using either the ion imaging technique (*13–15*), in which these effects can be dramatically evident, or Doppler (*16–18*) or ion time-of-flight profiles (*19*). These studies have the potential to provide insight into the underlying photophysics in the frame of the molecule. In much of the recent literature, coherences, *i.e.*, the off-diagonal elements of the density matrix, are assumed to vanish and only the diagonal elements of the density matrix, the magnetic sublevel populations, are inferred. Lately however, studies in our laboratory (*20–23*), and in the Zare laboratory (*24–26*) have shown that these coherence effects are by no means negligible, and in fact may be used to provide new insights into the photodissociation dynamics. These studies build on the theoretical foundation provided by Siebbeles, Vasyutinskii and coworkers (*27, 28*), however, each experimental group has provided a similar description of the photodissociation mechanism in terms of a different set of alignment parameters. In this chapter we will provide the reader with a comparison of the two sets, and equations to convert the one set into the other. We feel that this will solve the confusion that the two comparable sets might have created.

As an overview of our recent work, in this chapter we will first describe the theoretical apparatus developed for photofragment orientation and alignment. In this comprehensive frame work, photodissociation processes will be expressed in terms of orientation and alignment anisotropy parameters, each related to a specific dissociation mechanism. A demonstration of its power will be shown in a few experimental applications: orientation has been measured in the photodissociation of RbI; photofragment alignment is analyzed in the case of diatomic photodissociation ($Cl_2$), as well as in the photodissociation of polyatomics ($NO_2$ and $N_2O$). For a detailed discussion of those examples we refer the reader to our recent publications (*20–23, 29*).

---

[†] This parameter will be called $\beta_0$ in this chapter for reasons explained below.

## Theory: Two-photon ion imaging spectroscopy of polarized atomic photofragments

### Photofragment orientation and alignment angular distributions

*Laboratory frame*

In this chapter, we consider a generic molecular photodissociation event in which a molecule $AB$ produces fragments $A$ and $B$ with angular momenta $j_A$ and $j_B$, respectively. Each fragment can either be an atom or a molecular radical. The differential excitation cross section matrix elements $\sigma^{(j_A)}_{m'm}(\theta, \phi)$ give the probability of photofragment $A$ flying in a direction specified by the polar angles $\theta, \phi$ with components $m, m'$ of $j_A$ along the space-fixed **Z** axis (see Figure 1). The diagonal elements of the matrix ($m = m'$) give the probability of producing the fragment with a specific angular momentum $j_A$ and component $m$, while the off-diagonal elements ($m \neq m'$) describe the coherence between states with different $m$ quantum numbers (*8*). The initial and the final total angular momenta of the molecule are $J_i$ and $J$, respectively.

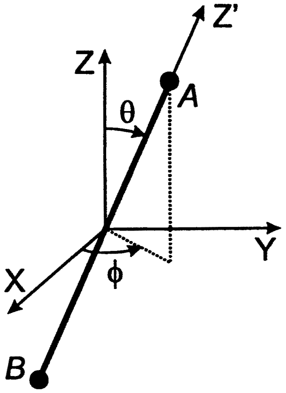

*Figure 1. Space-fixed reference frame for a diatomic molecule AB.*

It is convenient to express the excitation matrix elements $\sigma^{(j_A)}_{m'm}(\theta, \phi)$ in terms of the angular momentum polarization irreducible cross sections $\sigma^{(j_A)}_{KQ}(\theta, \phi)$ $\equiv \sigma_{KQ}(\theta, \phi)$, which are spherical tensors of rank $K$ and component $Q$ where

$Q = -K...K$ *(8, 30, 31)*

$$\sigma_{KQ}(\theta,\phi) = \sum_{m',m} (-1)^{j-m}(2K+1)^{1/2} \begin{pmatrix} j_A & j_A & K \\ m & -m' & -Q \end{pmatrix} \sigma^{(j_A)}_{m'm}(\theta,\phi). \quad (1)$$

The photofragment differential cross section (eq 1) for one-photon fragmentation, obtained with first-order perturbation theory for electric dipole transitions in the axial recoil approximation, is *(27)*[†]

$$\sigma_{KQ}(\theta,\phi) = \frac{3\sigma_0(2K+1)^{1/2}}{4\pi} \sum_{k_d,q_d,Q'} \sum_{q,q'} (-1)^{K+q'} E_{k_d q_d}(\mathrm{e}) \times \frac{f_K(q,q')}{f_0(0,0)+2f_0(1,1)} (2k_d+1)^{1/2} \times \begin{pmatrix} 1 & 1 & k_d \\ q' & -q & -Q' \end{pmatrix} D^{K*}_{QQ'}(\phi,\theta,0) D^{k_d}_{q_d Q'}(\phi,\theta,0), \quad (2)$$

where $\sigma_0 = \langle \sigma_{00}(\theta,\phi) \rangle$ is a zeroth-order fragmentation cross section integrated over angles $\theta$ and $\phi$, $D^K_{QQ'}(\phi,\theta,0)$ are Wigner functions *(32)*, and $E_{k_d q_d}(\mathrm{e})$ is an element of the polarization matrix[‡] of the dissociation light *(30, 31, 34, 35)*. The cross sections $\sigma_{KQ}(\theta,\phi)$ in eq 2 relate to the case of an isotropic distribution of the parent molecule angular momenta. The expression in eq 2 is valid for any experimental geometry and any polarization of the dissociation light. Although eq 2 was determined in reference *(27)* for the photoprocess in which one of the fragments is produced with its total angular momentum $j_B = 0$, the photofragment angular distributions are the same for cases where the two fragments $A$ and $B$ have angular momentum each different from zero [see reference *(36)*].

In principle, the multipole rank $K$ ranges from $K = 0$ to $K = 2j_A$ *(8)*, although usually only the lowest order terms [$K = 0$ (photofragment density), $K = 1$ (orientation), and $K = 2$ (alignment)] dominate experimental data (see the section on absorption below). Eq 2 evidently shows that each fragment's irreducible photodissociation cross section $\sigma_{KQ}$ can be treated separately from all others. This is an important advantage of the state multipole representation. Another important result from eq 2 is that each cross section $\sigma_{KQ}$ has a unique space angular distribution and can in principle be separately determined experimentally. Note, that the determination of all independent photofragment cross sections (state multipoles) in an experiment is equivalent to the complete quantum mechanical photodissociation experiment, which provides the researcher with all quantum mechanical amplitudes and phases that arise from theory. The terminology of the "complete experiment" was introduced by Fano *(37)* and is widely used in photoionization reaction studies *(38)*. Recent developments in techniques and theory provide, in principle, the possibility for carrying out complete experiments in photodissociation and reaction dynamics as well.

---

[†] The notation $\sigma_{KQ}(\theta,\phi)$ corresponds to $T_{KQ}(\Theta_k,\Phi_k)$ in reference *(27)*.

[‡] The values of the polarization matrix elements $\Phi_{kq}(\mathrm{e}) \equiv (-1)^{k+1} E_{kq}(\mathrm{e})$ for different light polarizations are also given in reference *(33)*.

The values $f_K(q,q')$ in eq 2 are ***dynamical functions***, which contain all the information on the transition dipole moments and fragmentation dynamics. The dynamical functions for the case $j_B = 0$ in their full quantum mechanical form are presented in (*27*) while the dynamical functions for the case of arbitrary $j_A$, $j_B$ obtained in the quasiclassical approximation are presented in references (*21, 33*). The indices $q, q'$ are cyclic components of the molecular electric dipole moment with respect to the recoil axis. They can only take the values 0 and ±1, corresponding to parallel or perpendicular electronic transitions, respectively. The case $q \neq q'$ corresponds to simultaneous coherent excitation of different $\Omega, \Omega'$ excited molecular states (*5, 39*). As shown by Glass-Maujean and Beswick (*39, 40*) the "coherent" type dynamical functions corresponding to excitation of two different dissociation continua, contain energy-dependent photodissociation phases which result in oscillations of experimental polarization signals on the photon energy scale. The observation of this effect has recently been reported for photofragment alignment (*41-43*) and orientation (*24*). Dynamical functions obey the following symmetry relations (*33*):

$$f_K(q,q') = (-1)^K f_K(-q,-q') = (-1)^{q-q'} f_K^*(q',q). \tag{3}$$

We first consider the photofragment polarization cross sections (eq 2) in the laboratory frame. It is more convenient to work with the fragment state multipoles $\rho_{KQ}(\theta,\phi)$, obtained by normalizing $\sigma^j_{KQ}(\theta,\phi)$ by the total zeroth-order fragmentation cross section $\sigma_0$, which is proportional to the total number of fragments. This yields

$$\rho_{KQ}(\theta,\phi) = \frac{\sigma_{KQ}(\theta,\phi)}{(2j_A+1)^{1/2}\sigma_0}. \tag{4}$$

The fragment state mutipoles with $K = 1$ and $K = 2$ in eq 4 have a clear physical meaning, being proportional to the mean fragment dipole and quadrupole moment, respectively (*8*). They are related to the fragment orientation and alignment parameters $A_{KQ}(\theta,\phi)$ by the usual transformation formulas (*30*)

$$A_{1Q} = \frac{1}{\sqrt{3}}\frac{\mathrm{Re}[\rho_{1Q}]}{\rho_{00}}, \tag{5}$$

$$A_{2Q} = \left[\frac{(2j_A+3)(2j_A-1)}{5j_A(j_A+1)}\right]^{1/2}\frac{\mathrm{Re}[\rho_{2Q}]}{\rho_{00}}. \tag{6}$$

Using eqs 2 and 4 one can obtain expressions for the specific differential photofragment state multipoles and for definite experimental geometries. For example, the case $K = 0$, $Q = 0$ leads to the following well known [see, *e.g.*, reference (*30*)] angular distributions for the number of photofragments:

Geometry I: Dissociation light is linearly polarized along the **Z** axis:

$$\rho_{00}(\theta,\phi) = \frac{1}{4\pi\sqrt{2j_A+1}}[1+\beta_0 P_2(\cos\theta)] \tag{7}$$

Geometry II: Dissociation light is linearly polarized along the **Y** axis:

$$\rho_{00}(\theta,\phi) = \frac{1}{4\pi\sqrt{2j_A+1}}[1 - \frac{\beta_0}{2}(1 - 3\sin^2\theta\sin^2\phi)], \tag{8}$$

where the $\beta_0$ parameter can be written in terms of zeroth-order dynamical functions as (*27*)

$$\beta_0 = \frac{2[f_0(0,0) - f_0(1,1)]}{f_0(0,0) + 2f_0(1,1)}. \tag{9}$$

We use the notation $\beta_0$ here instead of the more commonly used $\beta$ to emphasize that this anisotropy parameter describes the angular contribution of the zeroth-order state multipole.

The case $K = 1$, $Q = 0, \pm 1$ in eq 2 leads to the following expressions for photofragment orientation

Geometry I:

$$\rho_{10}(\theta,\phi) = 0, \tag{10}$$

$$\rho_{11}(\theta,\phi) = -\frac{3\sqrt{3}}{4\pi\sqrt{2}\sqrt{2j_A+1}}\gamma_1'\sin\theta\cos\theta i e^{i\phi}.$$

Geometry II:

$$\rho_{10}(\theta,\phi) = -\frac{3\sqrt{3}}{8\pi\sqrt{2j_A+1}}\gamma_1'\sin^2\theta\sin 2\phi, \tag{11}$$

$$\rho_{11}(\theta,\phi) = -\frac{3\sqrt{3}}{4\pi\sqrt{2}\sqrt{2j_A+1}}\gamma_1'\sin\theta\cos\theta\sin\phi.$$

Geometry III: Dissociation light is right hand circularly polarized and propagates along the **Z** axis:

$$\rho_{10}(\theta,\phi) = \frac{3\sqrt{3}}{4\pi\sqrt{2j_A+1}}[\alpha_1\cos^2\theta + \frac{\gamma_1}{2}\sin^2\theta], \tag{12}$$

$$\rho_{11}(\theta,\phi) = -\frac{3\sqrt{3}}{4\pi\sqrt{2}\sqrt{2j_A+1}}\sin\theta\cos\theta e^{i\phi}[\alpha_1 - \frac{\gamma_1}{2} - \frac{i\gamma_1'}{2}].$$

The following relation holds in general:

$$\rho_{K-Q}(\theta,\phi) = (-1)^Q\rho^*_{KQ}(\theta,\phi). \tag{13}$$

The values $\alpha_1, \gamma_1, \gamma_1'$ in eqs 10–12 are rank $K = 1$ angle-independent anisotropy parameters which are normalized first-order dynamical functions (*28*):

$$\alpha_1 = \frac{f_1(1,1)}{f_0(0,0) + 2f_0(1,1)},$$

$$\gamma_1 = \frac{2\mathrm{Re}[f_1(1,0)]}{f_0(0,0)+2f_0(1,1)}, \qquad (14)$$
$$\gamma_1' = \frac{2\mathrm{Im}[f_1(1,0)]}{f_0(0,0)+2f_0(1,1)}.$$

These parameters have a clear physical meaning as they represent contributions to photofragment orientation from different dissociation mechanisms. In particular, the parameter $\alpha_1$ represents contribution to the photofragment orientation from incoherent excitation via a perpendicular transition† while the parameter $\gamma_1$ represents contribution from coherent excitation of a parallel and a perpendicular transition. The parameter $\gamma_1'$ also describes the coherent excitation of a parallel and a perpendicular transition, but it contributes only to the part of the fragment orientation which vanishes after averaging over all recoil angles.

The ranges of these parameters listed in Table I were calculated assuming maximum possible orientation of the atomic fragment in the molecular frame (*28*). They do not depend on the specifics of the molecule (which can be either diatomic or polyatomic) and have the advantage that for any type of reaction the parameters cannot be outside the ranges; one must therefore in general not assume to be able to measure these extrema in an actual experiment.

**Table I. Physical range of the rank $K = 1$ *anisotropy* parameters.**

| *Parameter* | *Extrema* |
|---|---|
| $\alpha_1$ | $\pm\frac{2-\beta_0}{6}\left[\frac{j}{j+1}\right]^{1/2}$ |
| $\gamma_1$ | $\pm\frac{2}{3}\left[\frac{j(1+\beta_0)(2-\beta_0)}{2(j+1)}\right]^{1/2}$ |
| $\gamma_1'$ | $\pm\frac{2}{3}\left[\frac{j(1+\beta_0)(2-\beta_0)}{2(j+1)}\right]^{1/2}$ |

By integrating eqs 12 over the angles $\theta$, $\phi$ and using eq 5 one obtains

$$\langle A_{10}\rangle = \alpha_1 + \gamma_1, \qquad (15)$$

where the angle brackets indicate averaging over the recoil angles $\theta$ and $\phi$. The angular distributions of a laboratory frame fragment angular momentum $Z$ component $\rho_{10}(\theta,\phi) \sim (j_A)_Z$ corresponding to the three different dissociation mechanisms described above, are presented in Figure 2.

The eqs 10–12 clearly show that the photofragment orientation can be produced either with circularly or linearly polarized dissociation light. However,

---

†Pure parallel excitation does not result in any fragment orientation in the axial recoil approximation (*44*).

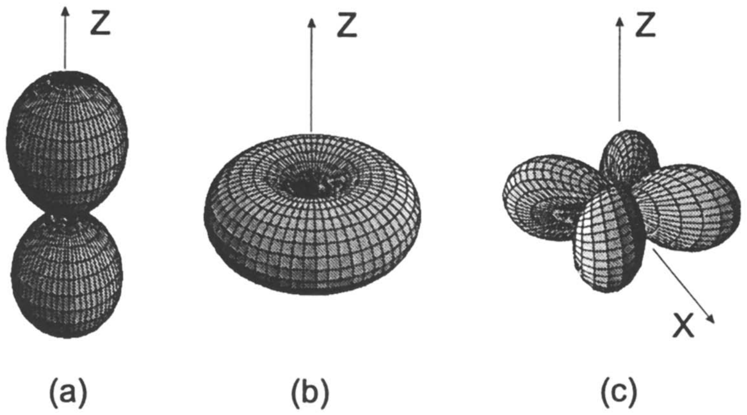

*Figure 2. Laboratory frame orientation distributions. The state multipole component* $\rho_{10}(\theta,\phi) \sim j_z$ *is related to three possible dissociation mechanisms: (a)* $\langle \mathbf{j}_{\|}\rangle_z \sim \cos^2\theta$*, related to* $\alpha_1$*; (b)* $\langle \mathbf{j}'_{\perp}\rangle_z \sim \sin^2\theta$*, related to* $\gamma_1$*; and (c)* $\langle \mathbf{j}_{\perp}\rangle_z \sim \sin^2\theta\sin 2\phi$*, related to* $\gamma'_1$*. Cases (a) and (b) correspond to circularly polarized dissociation light propagating along the* **Z** *axis (Geometry III); case (c) to light linearly polarized along the* **Y** *axis (Geometry II).*

excitation by circularly polarized light can in general lead to all three dissociation mechanisms described above, while excitation by linearly polarized light can result only in the coherent mechanism of orientation related to the $\gamma'_1$ parameter. Note that a contribution to fragment orientation from this mechanism in the case of light linearly polarized along the **Z** axis (eq 10) has opposite sign and is twice as large as the contribution in the case of circularly polarized light propagating along the same axis (eq 12). Actually, the mechanisms related to the $\alpha_1$, $\gamma_1$ parameters and related to the $\gamma'_1$ parameter are quite different: the first two result from the *helicity* (photon spin orientation) of the dissociation light, while the third results from the *alignment* of the light polarization vector **e**.

Angular distributions of fragment orientation have already been observed experimentally. The orientation effect following photodissociation of $Cl_2$, ICl, and OCS by linearly polarized light was recently reported by Rakitzis, Zare, Kitsopoulos, and coworkers (*19, 24, 26, 45*). The orientation of Rb fragments produced in photodissociation of RbI by circularly polarized light was observed by Korovin and coworkers (*29*).

The case $K = 2$, $Q = 0, \pm1, \pm2$ in eq 2 leads to the following expressions for photofragment alignment (*21*)

Geometry I:

$$\rho_{20}(\theta,\phi) = \frac{\sqrt{5}V(j_A)}{4\pi\sqrt{2j_A+1}}\Big\{P_2(\cos\theta)[s_2 - 2\alpha_2 P_2(\cos\theta)]$$

$$
\begin{aligned}
&-3\gamma_2 \sin^2\theta\cos^2\theta - \frac{3}{4}\eta_2 \sin^4\theta\Big\}, \\
\rho_{21}(\theta,\phi) &= -\frac{\sqrt{15}V(j_A)}{4\sqrt{2}\pi\sqrt{2j_A+1}}\sin\theta\cos\theta e^{i\phi}\Big\{[s_2 - 2\alpha_2 P_2(\cos\theta)] \\
&+\gamma_2(2\cos^2\theta - 1) + \frac{1}{2}\eta_2\sin^2\theta\Big\}, \qquad (16) \\
\rho_{22}(\theta,\phi) &= \frac{\sqrt{15}V(j_A)}{8\sqrt{2}\pi\sqrt{2j_A+1}}\sin^2\theta e^{2i\phi}\Big\{[s_2 - 2\alpha_2 P_2(\cos\theta)] \\
&+2\gamma_2\cos^2\theta - \frac{1}{2}\eta_2(1+\cos^2\theta)\Big\}.
\end{aligned}
$$

Geometry II:

$$
\begin{aligned}
\rho_{00}(\theta,\phi) &= \frac{1}{4\pi\sqrt{2j_A+1}}[1 - \frac{\beta_0}{2}(1 - 3\sin^2\theta\sin^2\phi)], \\
\rho_{20}(\theta,\phi) &= \frac{\sqrt{5}V(j_A)}{4\pi\sqrt{2j_A+1}}\Big\{P_2(\cos\theta)\Big[s_2 + \alpha_2[P_2(\cos\theta)(1-\cos 2\phi) + \cos 2\phi]\Big] \\
&+\frac{3}{2}\gamma_2\sin^2\theta\cos^2\theta(1-\cos 2\phi) \\
&+\frac{3}{8}\eta_2\sin^2\theta[\sin^2\theta + (1+\cos^2\theta)\cos 2\phi]\Big\}, \qquad (17) \\
\rho_{21}(\theta,\phi) &= -\frac{\sqrt{15}V(j_A)}{4\sqrt{2}\pi\sqrt{2j_A+1}}\sin\theta\cos\theta e^{i\phi} \\
&\times\Big\{\Big[s_2 + \alpha_2[P_2(\cos\theta)(1-\cos 2\phi) + \cos 2\phi]\Big] \\
&-\frac{\gamma_2}{2}[\cos 2\theta(1-\cos 2\phi) + i\sin 2\phi] \\
&-\frac{\eta_2}{4}[(1-\cos 2\phi)\sin^2\theta + 2\cos 2\phi - 2i\sin 2\phi]\Big\}, \\
\rho_{22}(\theta,\phi) &= \frac{\sqrt{15}V(j_A)}{8\sqrt{2}\pi\sqrt{2j_A+1}}e^{2i\phi}\Big\{\sin^2\theta\Big[s_2 + \alpha_2[P_2(\cos\theta)(1-\cos 2\phi) + \cos 2\phi]\Big] \\
&-\gamma_2\sin^2\theta[\cos^2\theta(1-\cos 2\phi) + i\sin 2\phi] \\
&+\frac{\eta_2}{4}[(1+\cos^2\theta)\sin^2\theta + (1+\cos^2\theta)^2\cos 2\phi - 4i\cos^2\theta\sin 2\phi]\Big\},
\end{aligned}
$$

where the values $s_2$, $\alpha_2$, $\gamma_2$, and $\eta_2$ in eqs 16, 17 are rank $K = 2$ angle-independent anisotropy parameters which are normalized second-order dynamical functions (*28*):

$$
\begin{aligned}
s_2 &= V(j_A)^{-1}\frac{f_2(0,0) + 2f_2(1,1)}{f_0(0,0) + 2f_0(1,1)}, \\
\alpha_2 &= V(j_A)^{-1}\frac{f_2(1,1) - f_2(0,0)}{f_0(0,0) + 2f_0(1,1)},
\end{aligned}
$$

$$\gamma_2 = 2\sqrt{3}V(j_A)^{-1}\frac{\mathrm{Re}[f_2(1,0)]}{f_0(0,0)+2f_0(1,1)}, \tag{18}$$
$$\gamma_2' = 2\sqrt{3}V(j_A)^{-1}\frac{\mathrm{Im}[f_2(1,0)]}{f_0(0,0)+2f_0(1,1)},$$
$$\eta_2 = \sqrt{6}V(j_A)^{-1}\frac{f_2(1,-1)}{f_0(0,0)+2f_0(1,1)},$$

with $V(j){=}5\{j(j+1)/[(2j+3)(2j-1)]\}^{1/2}$.

The parameters and their physical range are listed in Table II. The ranges were calculated assuming maximum possible alignment of the atomic fragment in the molecular frame (*28*). They do not depend on the specifics of the molecule, which can either be diatomic or polyatomic, and have the advantage that for any type of reaction the parameters cannot be outside the ranges; these most likely will be smaller in less general cases, as in the experimental examples further on. Note, that the ranges presented in our publications (*21-23*) for the $\eta_2$ and $\gamma_2$ anisotropy parameters differ from those given in Table II. The reason is that

**Table II. Range of the rank $K = 2$ *anisotropy* parameters.**

| | *Range* | |
|---|---|---|
| $s_2$ | $-\frac{1}{5} \cdots \frac{2j-1}{5(j+1)}$ | if $j$ is an integer |
| | $-\frac{(2j-1)(2j+3)}{20j(j+1)} \cdots \frac{(2j-1)}{5(j+1)}$ | if $j$ is a half-integer |
| $\alpha_2$ | $-\frac{2j+\beta_0(j-1)}{10(j+1)} \cdots \frac{2j+\beta_0}{10(j+1)}$ | if $j$ is an integer |
| | $-\frac{(2j-1)[2(2j+1)+\beta_0(2j-1)]}{40j(j+1)} \cdots \frac{(2j-1)(2j+\beta_0+1)}{20j(j+1)}$ | if $j$ is a half-integer |
| $\gamma_2$ | $-\frac{1}{5}\left[\frac{(1+\beta_0)(2-\beta_0)}{2}\right]^{1/2} \cdots \frac{1}{5}\left[\frac{(1+\beta_0)(2-\beta_0)}{2}\right]^{1/2}$ | if $j{=}1$ |
| | $-\frac{2j-1}{5(j+1)}\left[\frac{(1+\beta_0)(2-\beta_0)}{2}\right]^{1/2} \cdots \frac{2j-1}{5(j+1)}\left[\frac{(1+\beta_0)(2-\beta_0)}{2}\right]^{1/2}$ | if $j{>}1$ |
| $\gamma_2'$ | $-\frac{1}{5}\left[\frac{(1+\beta_0)(2-\beta_0)}{2}\right]^{1/2} \cdots \frac{1}{5}\left[\frac{(1+\beta_0)(2-\beta_0)}{2}\right]^{1/2}$ | if $j{=}1$ |
| | $-\frac{2j-1}{5(j+1)}\left[\frac{(1+\beta_0)(2-\beta_0)}{2}\right]^{1/2} \cdots \frac{2j-1}{5(j+1)}\left[\frac{(2j-1)(1+\beta_0)(2-\beta_0)}{2(j+1)}\right]^{1/2}$ | if $j{>}1$ |
| $\eta_2$ | $-\frac{(2-\beta_0)}{10} \cdots \frac{(2-\beta_0)}{10}$ | if $j{=}1$ |
| | $-\frac{(2j-1)(2-\beta_0)}{10(j+1)} \cdots \frac{(2j-1)(2-\beta_0)}{10(j+1)}$ | if $j{>}1$ |

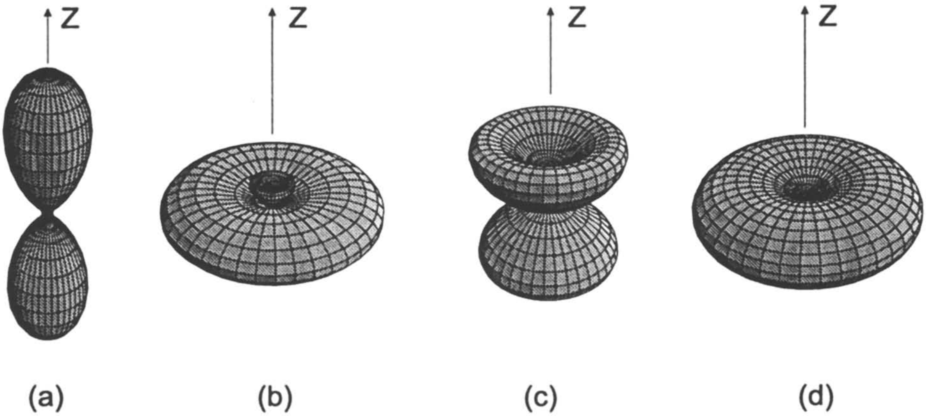

*Figure 3. Laboratory frame alignment distributions for dissociation light linearly polarized along the* **Z** *axis (Geometry I). The state multipole component* $\rho_{20}(\theta,\phi) \sim (3j_z^2 - j^2)$ *is related to four possible dissociation mechanisms: (a)* $\langle 3j_z^2 - j^2\rangle_{\parallel} \sim P_2(\cos\theta)(\cos^2\theta)$*, related to* $s_2/\alpha_2 = -1$*; (b)* $\langle 3j_z^2 - j^2\rangle_{\perp} \sim P_2(\cos\theta)(\sin^2\theta)$*, related to* $s_2/\alpha_2 = 2$*; (c)* $\langle 3j_z^2 - j^2\rangle_{\parallel,\perp} \sim \sin^2\theta\cos^2\theta$*, related to* $\gamma_2$*; and (d)* $\langle 3j_z^2 - j^2\rangle_{\perp,\perp} \sim \sin^4\theta$*, related to* $\eta_2$*.*

the ranges in references (*21–23*) were calculated using eq 7 of reference (*27*) using the simplest model of adiabatic photodissociation for the case of $j_B = 0$. Moreover, these were the maximum possible values of the ranges as a function of $\beta_0$. However, the ranges in Table II are not connected with any particular model of dissociation as they were calculated just from the maximum possible fragment alignment in the molecular frame as function of $\beta_0$. The limits in Table II are not symmetric since the limiting values of atomic angular alignment are not symmetric either [see, *e.g.*, reference (*30*)].

Parameters $\alpha_2$, $\gamma_2$, and $\eta_2$ represent contributions to the photofragment alignment which do not vanish after averaging over all recoil angles. Parameter $\alpha_2$ describes the alignment due to incoherent excitation ($q = q'$), via both parallel and perpendicular transitions. Parameter $\gamma_2$ describes alignment from a coherent superposition of parallel and perpendicular excitation. This parameter is important when two excited electronic states with electronic projections $\Omega$ equal to ±1 and 0 have comparable excitation probabilities. Parameter $\eta_2$ relates to a coherent superposition of two perpendicular transitions. This may occur for two states separated in energy as in the parallel/perpendicular case. However, a more common possibility is simultaneous excitation of the degenerate $\Omega = \pm 1$ "lambda doublet" components of an $|\Omega| = 1$ state [see reference (*6*)], since both states automatically have equal excitation probabilities. By integrating the equation for $\rho_{20}(\theta,\phi)$ from eq 16 over the recoil angles $\theta$, $\phi$, one obtains

$$\langle A_{20}\rangle = -2(\alpha_2 + \gamma_2 + \eta_2) \tag{19}$$

The parameters $s_2$ and $\gamma_2'$ in eq 18 represent a contribution to the alignment components which vanishes after averaging over all recoil angles. The parameter

$s_2$ describes the contribution due to incoherent excitation via both parallel and perpendicular transitions. The parameter $\gamma_2'$ is not present in eqs 16 and 17 and is included in eq 18 for completeness. As shown in reference (*27*), it represents a coherent superposition of parallel and perpendicular excitation when the dissociation light is circularly polarized. The angular distributions of a laboratory frame fragment angular momentum $Z$ component $\rho_{20}(\theta,\phi) \sim (3j_z^2 - j^2)$ corresponding to the four different dissociation mechanisms described above, are presented in Figure 3. Angular distributions of fragment alignment have been observed by several groups both for diatomic (*15, 16, 20, 26*) and triatomic (*13, 14, 22*) molecules.

The anisotropy parameters with the rank $K$ ranging from $K = 0$ to $K = 2j_A$ represent a total set of laboratory frame quantum mechanical variables which can be determined from experiment and contain the complete information about the dissociation dynamics. The parameters in eqs 9, 14, 18 can be directly determined from an experiment on randomly oriented parent molecules. This set is an alternative to the widely used Dixon bipolar moments (*9*), having the advantage of giving more direct insight into the dissociation mechanisms, especially for low $j$ values. The conversion between the anisotropy parameters and the bipolar moments of the rank $K = 2$ is given in Table A1 of reference (*28*). Note that this table presents the bipolar moments in the laboratory frame. Transformation to the molecular frame is given by factor 2/5, as shown by Dixon (*9*).

Recently Rakitzis and Zare (*25, 46*) introduced another set of ***polarization*** parameters $\mathbf{a}_Q^{(K)}(p)$ which are expressed in the molecular frame. The relationship between the ***anisotropy*** (*28*) and ***polarization*** (*46*) parameters of the rank $K = 2$ are presented in Table III. The parameters $\mathbf{a}_Q^{(K)}$ can be directly measured from molecular frame experiments (*19*) on initially aligned parent molecules. As shown in the next section, each set of parameters contains the same information about the molecular frame orientation and alignment.

### *Molecular frame*

The power of ion imaging and other techniques that are used to measure the angular distribution of angular momentum polarization is that they readily lead to an understanding of the dynamics in the frame of the molecule. In order to examine the angular momentum polarization in the molecular frame (see Figure 1), it is convenient to normalize the cross sections by the zeroth-order differential fragmentation cross section $\sigma_{00}(\theta,\phi)$, which is proportional to the number of fragments flying in the direction defined by the angles $\theta,\phi$. The expression for the molecular frame state multipoles $\rho_{KQ'}^{mol}(\theta,\phi)$ is given by

$$\rho_{KQ'}^{mol}(\theta,\phi) = \frac{\sigma_{KQ'}(\theta,\phi)}{(2j_A+1)^{1/2}\sigma_{00}(\theta,\phi)}, \tag{20}$$

where the indices $Q'$ are the components of multipole rank $K$ along the recoil axis $\mathbf{Z}'$. Using eqs 4 and 20, we obtain the relationship between the laboratory

**Table III. Relationship between the *anisotropy* and the *polarization* rank $K = 2$ parameters.**

| *Dynamical function expression* | *Anisotropy parameter (28)* | *Polarization parameter (46)* |
|---|---|---|
| $\frac{f_2(0,0)}{f_0(0,0)+2f_0(1,1)}$ | $\frac{V(j_A)}{3}(s_2 - 2\alpha_2)$ | $\frac{(1+\beta_0)}{6}\mathbf{a}_0^{(2)}(\parallel)$ |
| $\frac{f_2(1,1)}{f_0(0,0)+2f_0(1,1)}$ | $\frac{V(j_A)}{3}(s_2 + \alpha_2)$ | $\frac{(1-\beta_0/2)}{6}\mathbf{a}_0^{(2)}(\perp)$ |
| $\frac{\mathrm{Re}f_2(1,0)}{f_0(0,0)+2f_0(1,1)}$ | $\frac{V(j_A)}{2\sqrt{3}}\gamma_2$ | $-\frac{\sqrt{2}}{12}\mathrm{Re}\left[\mathbf{a}_1^{(2)}(\parallel,\perp)\right]$ |
| $\frac{\mathrm{Im}f_2(1,0)}{f_0(0,0)+2f_0(1,1)}$ | $\frac{V(j_A)}{2\sqrt{3}}\gamma_2'$ | $-\frac{\sqrt{2}}{12}\mathrm{Im}\left[\mathbf{a}_1^{(2)}(\parallel,\perp)\right]$ |
| $\frac{f_2(1,-1)}{f_0(0,0)+2f_0(1,1)}$ | $\frac{V(j_A)}{\sqrt{6}}\eta_2$ | $-\frac{(1-\beta_0/2)}{3}\mathbf{a}_2^{(2)}(\perp)$ |

and molecular frame state multipoles (*21*)

$$\rho_{KQ}(\theta,\phi) = (2j_A+1)^{1/2}\rho_{00}(\theta,\phi)\sum_{Q'} D^{K*}_{QQ'}(\phi,\theta,0)(\rho^{mol}_{KQ'}), \tag{21}$$

The expression for the molecular frame state multipoles (eq 20) in terms of the $K = 0, 1, 2$ anisotropy parameters (eqs 9, 14, 18) can be obtained comparing eq 21 with eqs 12, 16 and rewriting eq 4 as

$$\rho^{mol}_{00} = \frac{1}{\sqrt{2j_A+1}}. \tag{22}$$

One then obtains:

$$\begin{aligned}
\rho^{mol}_{10} &= \frac{3\sqrt{3}}{\sqrt{2j_A+1}}\frac{\alpha_1\cos\theta}{[1-\frac{1}{2}\beta_0 P_2(\cos\theta)]},\\
\mathrm{Re}[\rho^{mol}_{11}] &= \frac{3\sqrt{6}}{4\sqrt{2j_A+1}}\frac{\gamma_1\sin\theta}{[1-\frac{1}{2}\beta_0 P_2(\cos\theta)]},\\
\mathrm{Im}[\rho^{mol}_{11}] &= \frac{3\sqrt{6}}{4\sqrt{2j_A+1}}\frac{\gamma_1'\sin\theta\cos\theta}{[1-\frac{1}{2}\beta_0 P_2(\cos\theta)]},
\end{aligned} \tag{23}$$

and

$$\rho^{mol}_{20} = \frac{\sqrt{5}V(j_A)}{\sqrt{2j_A+1}}\frac{[s_2 - 2\alpha_2 P_2(\cos\theta)]}{[1+\beta_0 P_2(\cos\theta)]},$$

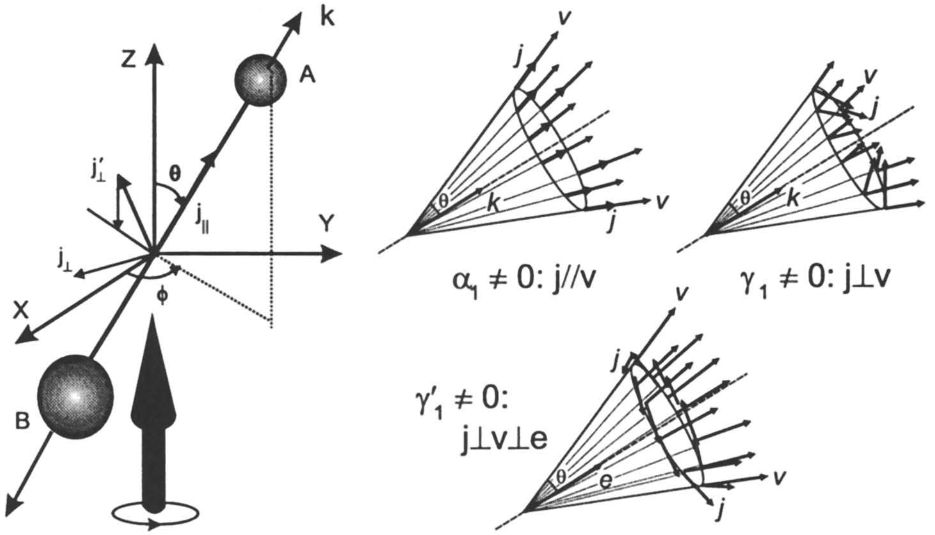

*Figure 4. Molecular frame model of photofragment orientation and molecular frame angular momentum distributions.*

$$\mathrm{Re}[\rho_{21}^{mol}] = -\frac{\sqrt{30}V(j_A)}{2\sqrt{2j_A+1}}\frac{\gamma_2 \sin\theta\cos\theta}{[1+\beta_0 P_2(\cos\theta)]}, \tag{24}$$

$$\rho_{22}^{mol} = -\frac{\sqrt{30}V(j_A)}{4\sqrt{2j_A+1}}\frac{\eta_2 \sin^2\theta}{[1+\beta_0 P_2(\cos\theta)]}.$$

Eqs 23 are derived for circularly polarized dissociation light propagating along the **Z** axis while eqs 24 are derived for dissociation light that is linearly polarized along the **Z** axis. The corresponding angular dependency of the molecular frame orientation and alignment parameters $A_{1Q'}^{mol}$ and $A_{2Q'}^{mol}$ can be easily obtained from eq 23 and 24 using the relations 5 and 6.

Three possible dissociation mechanisms of the fragment orientation can be described by a simple vector model (*27*) presented in Figure 4. The rank $K = 1$ diagonal state multipole in eq 23 corresponds to the component of the total fragment angular momentum along the recoil axis **v**: $\rho_{10}^{mol} \sim (j_A)_{\|}$ and is proportional to the $\alpha_1$ parameter. It is real and related to an incoherent perpendicular transition in the parent molecule.

The off-diagonal state multipole $\rho_{11}^{mol}$ corresponds to the molecular frame $Q' = +1$ cyclic component of $j_A$: $\rho_{11}^{mol} \sim (j_A)_{\perp}$ which is perpendicular to the recoil axis. This state multipole can be complex, its real part is proportional to the $\gamma_1$ parameter and its imaginary part is proportional to the $\gamma_1'$ parameter. Both parts are related to a coherent superposition of a parallel and a perpendicular transition in the parent molecule. Only the imaginary part contributes to the photofragment orientation produced by linearly polarized or unpolarized light.

The corresponding vector equation can be presented as (*27*)†

$$\mathbf{j} = j_{\|}\mathbf{v} + \frac{j_{\perp}(\mathbf{v}\times\mathbf{Z})}{\sin\theta} + \frac{j'_{\perp}[(\mathbf{v}\times\mathbf{Z})\times\mathbf{v}]}{\sin\theta} \qquad (25)$$

One can see from Figure 4 and from eq 25 that the coherent excitation when $\gamma_1 \neq 0$ produces a component $j_{\perp}$ which is perpendicular to the recoil direction and lies in the **v**–**Z** plane, while the coherent excitation when $\gamma'_1 \neq 0$ produces a component $j'_{\perp}$ which is perpendicular to the **v**–**Z** plane. The molecular frame angular momentum distributions related to all three possible dissociation mechanisms are also presented in Figure 4.

The rank $K = 2$ state multipole $\rho_{20}^{mol}$ is related to incoherent parallel and perpendicular transitions, while the multipoles $\rho_{22}^{mol}$ and $\rho_{21}^{mol}$ are related to coherent superposition of two perpendicular transitions or a parallel and a perpendicular transition, respectively. The multipoles $\rho_{20}^{mol}$ and $\rho_{22}^{mol}$ are real, while the multipole $\rho_{21}^{mol}$ can be complex, although only its real part contributes to the photofragment alignment produced by linearly polarized or unpolarized light.

According to eq 24, if parallel and perpendicular optical transitions occur simultaneously all molecular frame orientation and alignment state multipoles depend on the angle $\theta$ between the recoil axis **v** and the **Z** axis.

In the limit of a *pure perpendicular* transition, $2\alpha_2 = s_2$ (see eq 18), $\beta_0 = -1$ and $\gamma_2 = 0$. Then only the state multipoles $\rho_{20}^{mol}$ and $\rho_{22}^{mol}$ in eq 24 can be nonzero and their values do not depend on the angle $\theta$. Using eqs 24, 6, and the reference Table III the corresponding limiting values of the molecular frame alignment parameters $A_{2Q'}^{mol}(\perp)$ can be presented as

$$A_{20}^{mol}(\perp) = 5s_2 = \frac{5}{2}V(j_A)^{-1}\mathbf{a}_0^{(2)}(\perp) \qquad (26)$$

$$A_{22}^{mol}(\perp) = -\frac{5}{\sqrt{6}}\eta_2 = \frac{5}{2}V(j_A)^{-1}\mathbf{a}_2^{(2)}(\perp)$$

For a *pure parallel* transition, $\alpha_2 = -s_2$ (eq 18), $\beta_0 = 2$, $\gamma_2 = \eta_2 = 0$. Only the state multipole $\rho_{20}^{mol}$ can be nonzero and its value does not depend on the angle $\theta$. The corresponding limiting value of the molecular frame alignment parameter $A_{20}^{mol}(\|)$ can be presented as

$$A_{20}^{mol}(\|) = 5s_2 = \frac{5}{2}V(j_A)^{-1}\mathbf{a}_0^{(2)}(\|) \qquad (27)$$

Note that according to eqs 23, 24 the real part of the $\rho_{21}^{mol}$ state multipole as well as all rank $K = 1$ state multipoles are $\theta$-dependent for any values of $\beta_0$.

The above results can be important not only for investigation of photodissociation dynamics, but also for reaction dynamics because the rank $K = 2$ state multipoles each represents a component of the characteristic shape of the electron cloud in the recoiling atom, as shown in Figure 5. Although the shapes

---

† Note the typographical error in eq 23 of reference (*27*) where the denominators $\sin\theta$ were omitted and also note the redefinitions with respect to reference (*27*): $j_{\perp} \rightleftharpoons j'_{\perp}$, $\Theta_k \to \theta$.

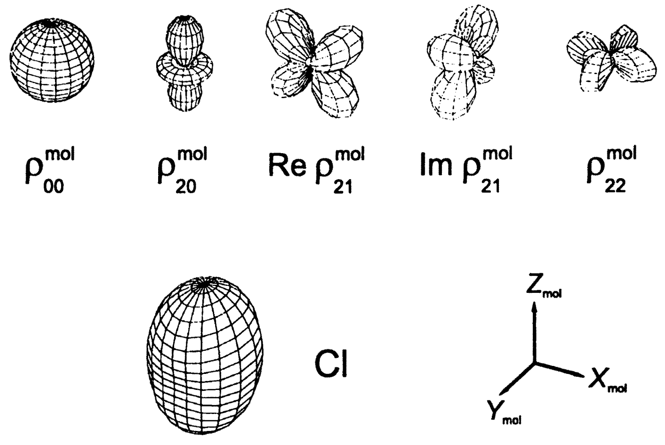

*Figure 5. Components of the angular distribution of electron density, associated with each state multipole $\rho^{mol}_{KQ'}$. On the bottom is the distribution for a pure perpendicular transition, using $\alpha_2$ and $\eta_2$ obtained for chlorine (Table IV), eq 20 of this chapter, and eq 4.6.21 of reference (8). For this pure transition, the shape does not depend on recoil angle.*

are independent of recoil angle, their relative contributions are not, and this angular dependence is different for each state multipole. Thus in general, the shape of the electron cloud will vary with recoil direction.

It should also be emphasized that the rank $K = 1$ state multipoles do not affect at all the shape of the electron cloud in the recoiling atom, that is, oriented photofragments preserve the spherical symmetry of the angular distribution of the electron cloud. Tensors with odd rank are proportional to the corresponding magnetic multipoles, and describe the distribution of electric currents within the atoms (*8*).

## Absorption of light by atomic photofragments

To extract orientation and alignment information from measurements that use two-photon excitation as a probe of diatomic photofragments, we have adapted the approach of Kummel and coworkers (*47,48*) to the case of atoms and made some convenient modifications. The general expression describing the intensity of absorption of the probe light by the photofragments is (*21*)

$$I = C \sum_{Kk_1k_2} S^{k_2}_{Kk_1} \left[ (\rho_K \otimes E_{k_1})_{k_2} \cdot E_{k_2} \right], \tag{28}$$

where the tensor product is easily calculated according to

$$\left[ (\rho_K \otimes E_{k_1})_{k_2} \cdot E_{k_2} \right] = \sum_{Q,q_1,q_2} (-1)^{K-k_1} \sqrt{2k_2 + 1}$$

$$\begin{pmatrix} K & k_1 & k_2 \\ Q & q_1 & -q_2 \end{pmatrix} E_{k_1 q_1} \rho_{KQ} E_{k_2 -q_2} \tag{29}$$

Here $E_{k_1 q_1}$ and $E_{k_2 -q_2}$ are polarization matrices with ranks $k_1$ and $k_2$, which correspond to the first and second photons, respectively. The proportionality constant $C$ depends on the intensity of the probe light. The factor $S^{k_2}_{Kk_1}$ depends on all quantum numbers of the initial, intermediate and final states involved in the two-photon process, but not on the projections of any tensors:

$$\begin{aligned} S^{k_2}_{Kk_1}(j_i\gamma_i; j_f\gamma_f) =& (-1)^{K+1}\sqrt{(2K+1)(2k_1+1)} \\ & \times \sum_{j_e\gamma_e j'_e\gamma'_e} (-1)^{j_f+j'_e} \begin{Bmatrix} j_i & 1 & j_e \\ j_i & 1 & j'_e \\ K & k_1 & k_2 \end{Bmatrix} \begin{Bmatrix} j_e & j'_e & k_2 \\ 1 & 1 & j_f \end{Bmatrix} \\ & \times S(\gamma_i j_i, \gamma_e j_e, \gamma'_e j'_e, \gamma_f j_f). \end{aligned} \tag{30}$$

The quantum numbers $j_i$, $j_e$ and $j_f$ designate total angular momentum of initial, excited (intermediate or "virtual") and final states of the photofragment, respectively. The $\gamma_i$, $\gamma_e$, and $\gamma_f$ are sets of all other fragment quantum numbers excluding projections. The presence of both $j_e$ and $j'_e$ as well as $\gamma_e$ and $\gamma'_e$ is a result of coherent sums over different intermediate excited states. The factor $S(\gamma_i j_i, \gamma_e j_e, \gamma'_e j'_e, \gamma_f j_f)$ contains reduced matrix elements and the energy denominator of second order time-dependent perturbation theory:

$$\begin{aligned} & S(\gamma_i j_i, \gamma_e j_e, \gamma'_e j'_e, \gamma_f j_f) = \\ & \frac{\langle \gamma_f j_f \| d \| \gamma_e j_e \rangle \langle \gamma_f j_f \| d \| \gamma'_e j'_e \rangle^* \langle \gamma_e j_e \| d \| \gamma_i j_i \rangle \langle \gamma'_e j'_e \| d \| \gamma_i j_i \rangle^*}{(E_{ei} - h\nu + i\Gamma/2)(E_{e'i} - h\nu - i\Gamma/2)}. \end{aligned} \tag{31}$$

Eqs 28–31 can be used for any polarization of the probe light and any experimental geometry. They are equivalent to those given by Kummel and coworkers (*48*) and by Docker (*49*), except that all projection information and laser polarization dependence have been factored out. The practical convenience of this modification lies in the complete separation between the scalar linestrength factor $S^{k_2}_{Kk_1}$ and the tensor quantities in the photon-atom dot product. In this form, the qualitative dependence of the signal on laser polarization can be studied without reference to linestrengths.

We now write expressions for the 2+1 Resonance-Enhanced Multiphoton Ionization (2+1 REMPI) signal for four experimental geometries, corresponding to the linear probe laser polarization along the axes **X**, **Y**, **Z**, and to the right/left hand circularly polarized dissociation light propagating along the **Z** axis. Later on, we will define these signals as $I_X$, $I_Y$, $I_Z$, and $I^z_R/I^z_L$, respectively. Using eqs 28 and 29, with polarization tensor components

$$E_{00} = -\frac{1}{\sqrt{3}};\ E_{1q} = 0;\ E_{20} = \frac{2}{\sqrt{6}};\ E_{21} = 0;\ E_{22} = 0 \quad \text{for} \quad \mathrm{e} = e_Z$$

$$E_{00} = -\frac{1}{\sqrt{3}};\ E_{1q} = 0;\ E_{20} = -\frac{1}{\sqrt{6}};\ E_{21} = 0;\ E_{2\pm 2} = \pm\frac{1}{2} \quad \text{for} \quad \mathrm{e} = e_X,\ e_Y$$

$$E_{00} = -\frac{1}{\sqrt{3}};\ E_{10} = \frac{1}{\sqrt{2}};\ E_{20} = -\frac{1}{\sqrt{6}};\ E_{21} = 0;\ E_{2\pm 2} = 0 \quad \text{for} \quad \mathrm{e} = e_R,$$

we obtain

$$I_Z = C\left[P_0\rho_{00} + P_2\rho_{20} + P_4\rho_{40}\right] \tag{32}$$

$$\begin{aligned} I_{X,Y} = C\Bigg[P_0\rho_{00} - \frac{P_2}{2}\left\{\rho_{20} \mp \sqrt{6}\mathrm{Re}[\rho_{22}]\right\} \\ +\frac{P_4}{8}\left\{3\rho_{40} \mp 2\sqrt{10}\mathrm{Re}[\rho_{42}] + \sqrt{70}\mathrm{Re}[\rho_{44}]\right\}\Bigg] \end{aligned} \tag{33}$$

$$I^z_{R,L} = C\left[P^c_0\rho_{00} \pm P^c_1\rho_{10} + P^c_2\rho_{20} \pm P^c_3\rho_{30} + P^c_4\rho_{40}\right] \tag{34}$$

where

$$\begin{aligned} P_0 &= \frac{1}{3}\left(S^0_{00} + 2S^2_{02}\right), \\ P_2 &= -\frac{\sqrt{2}}{3}\left(S^2_{20} + \frac{1}{\sqrt{5}}S^0_{22} + \frac{2}{\sqrt{7}}S^2_{22}\right), \\ P_4 &= \frac{4}{3\sqrt{14}}S^2_{42}, \\ P^c_0 &= \frac{1}{3}\left(S^0_{00} + \frac{3}{2}S^1_{01} + \frac{1}{2}S^2_{02}\right), \\ P^c_1 &= \frac{1}{3\sqrt{2}}\left(S^0_{11} - \sqrt{3}S^1_{10} - S^2_{11} + \sqrt{\frac{3}{5}}S^1_{12}\right), \\ P^c_2 &= \frac{\sqrt{2}}{6}\left(S^2_{20} + \frac{1}{\sqrt{5}}S^0_{22} - \frac{3}{\sqrt{5}}S^1_{21} - \frac{1}{\sqrt{7}}S^2_{22}\right), \\ P^c_3 &= \frac{1}{2\sqrt{7}}\left(S^2_{31} - \sqrt{\frac{3}{5}}S^1_{32}\right), \\ P^c_4 &= \frac{1}{3\sqrt{14}}S^2_{42}. \end{aligned} \tag{35}$$

Here $P_K$, $P^c_K$ are linestrength factors for linearly and for circularly polarized probe light, respectively. The laboratory frame state multipoles $\rho_{KQ}$ in eqs 28, 29, 32–34 are not written as a function of recoil angles, but the expressions are general and valid both for the angle-dependent state multipoles $\rho_{KQ}(\theta, \phi)$ and for their angle-averaged values. The $-$ and $+$ of $\mp$ in eq 33 correspond to the **X** and **Y** probe polarizations, respectively, while the $-$ and $+$ of $\pm$ in eq 34 correspond to the right and left circularly polarized light, respectively. The multipole rank $K = 4$ in eqs 32–34 corresponds to the maximum possible rank that can be measured with a two-photon detection technique. It is seen from eqs 32–34 that linearly polarized probe light is sensitive only to even rank state multipoles with $K = 0, 2, 4$ while circularly polarized probe light is sensitive to all rank $K$ state multipoles from $K = 0$ to $K = 4$.

General relationships between the linestrength factors corresponding to linearly and circularly polarized light can be derived for the case where $j_i \neq j_f$, or $L_i \neq L_f$, with $L_i$ and $L_f$ the orbital moments for initial and final states of the fragments, respectively. Using the expression for the linestrength factors given in the Appendix, one obtains

$$P_0^c = \frac{3}{2}P_0; \qquad P_2^c = -\frac{3}{2}P_2; \qquad P_4^c = \frac{1}{4}P_4. \tag{36}$$

In an ion image, Doppler profile, or TOFMS profile, the spatial modulations that result from photofragment orientation, alignment, and from higher rank state multipoles are generally small compared to the total signal. For this reason, it is useful to isolate the orientation and alignment contributions by taking linear combinations of the signal collected in different geometries, in such a way that the population term $\rho_{00}(\theta,\phi)$ cancels. Similarly, by combining measurements along all three Cartesian axes, the orientation and alignment terms can be eliminated. These expressions are

$$\begin{aligned}\frac{I_Z(\theta,\phi) - I_{X,Y}(\theta,\phi)}{\langle I_X\rangle + \langle I_Y\rangle + \langle I_Z\rangle} = \frac{\sqrt{2j_A+1}}{2}\Bigg[\frac{P_2}{P_0}\Big(\rho_{20}(\theta,\phi) \mp \frac{\sqrt{6}}{3}\mathrm{Re}[\rho_{22}(\theta,\phi)]\Big) \\ +\frac{P_4}{12P_0}\Big(5\rho_{40}(\theta,\phi) \pm 2\sqrt{10}\mathrm{Re}[\rho_{42}(\theta,\phi)] \\ -\sqrt{70}\mathrm{Re}[\rho_{44}(\theta,\phi)]\Big)\Bigg]\end{aligned} \tag{37}$$

$$\frac{I_X(\theta,\phi) - I_Y(\theta,\phi)}{\langle I_X\rangle + \langle I_Y\rangle + \langle I_Z\rangle} = \frac{\sqrt{(2j_A+1)}}{3}\left[\frac{\sqrt{6}P_2}{P_0}\mathrm{Re}[\rho_{22}(\theta,\phi)] - \frac{\sqrt{10}P_4}{2P_0}\mathrm{Re}[\rho_{42}(\theta,\phi)]\right] \tag{38}$$

$$\frac{I_R^z(\theta,\phi) - I_L^z(\theta,\phi)}{\langle I_X\rangle + \langle I_Y\rangle + \langle I_Z\rangle} = \frac{2\sqrt{(2j_A+1)}}{3}\left[\frac{P_1^c}{P_0}[\rho_{10}(\theta,\phi)] + \frac{P_3^c}{P_0}[\rho_{30}(\theta,\phi)]\right] \tag{39}$$

$$\frac{I_X(\theta,\phi) + I_Y(\theta,\phi) + I_Z(\theta,\phi)}{\langle I_X\rangle + \langle I_Y\rangle + \langle I_Z\rangle} = \sqrt{2j_A+1}\rho_{00}(\theta,\phi). \tag{40}$$

In deriving the expressions 37–40 we neglected the terms of the rank $K = 4$ comparing to those of the rank $K = 0$ in all denominators and in the numerator of eq 40. These equations have been normalized by $\langle I_X\rangle + \langle I_Y\rangle + \langle I_Z\rangle$, the sum of the total intensities along all three Cartesian axes which is proportional to the total number of fragments. Each term such as $\langle I_X\rangle$ represents an integral over the coordinates of the corresponding spatially-resolved intensity $I_X(\theta,\phi)$. In practice, in the case of a cylindrically symmetric fragment angular momentum distribution, all three terms in the denominator can be obtained from spatially-resolved measurements in only two of the three geometries, because the two geometries with the probe polarization perpendicular to the photolysis polarization will have equal total intensities.

Another important form of the rank $K = 1, 2, 3$ independent expression can be obtained from eqs 33, 34 and 36 as

$$\frac{I_X(\theta,\phi) + I_Y(\theta,\phi) - \frac{1}{3}\left[I_R^z(\theta,\phi) + I_L^z(\theta,\phi)\right]}{\langle I_X\rangle + \langle I_Y\rangle - \frac{1}{3}\left[\langle I_R^z\rangle + \langle I_L^z\rangle\right]} = \sqrt{2j_A+1}\rho_{00}(\theta,\phi). \tag{41}$$

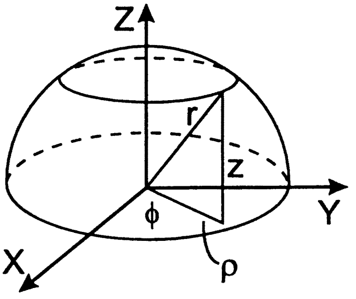

*Figure 6. Clarification of variables in 3D to 2D transformation (eq 42). The* **Z** *axis is parallel to the axis of the TOF tube.*

Here again the terms of the rank $K = 4$ were neglected comparing to those of the rank $K = 0$ both in the numerator and denominator. Although eq 41 is valid only under the condition $j_i \neq j_f$, or $L_i \neq L_f$, it has an undeniable advantage compared to eq 40 because determination of fragment population for any fragment angular space distribution can be carried out by changing only the probe laser polarization, without moving the laser beam direction. Note, that the value in the right part of eq 41 is a scalar. Therefore, this expression will have the same form for any other direction of propagation of the probe light with only appropriate change of the $X, Y$ and $Z$ sub- and superscript indices.

## Orientation and alignment image basis functions

In most ion imaging studies to date, investigators sought to obtain recoil energy and angular distributions, using the inverse-Abel transform to directly invert their images to obtain the original three-dimensional ion spatial distribution (*50*). However, this approach can only be used if the image is a projection of a cylindrically symmetric distribution, where the symmetry axis lies parallel to the two-dimensional surface. In general this condition is not met when crossed laser polarizations are employed, so the inverse-Abel transform cannot be used. Instead, we use the expression (*21*)$^{\dagger}$

$$M(\rho,\phi) = \int_{\rho}^{\infty} \frac{g(r)dr}{\sqrt{1-\rho^2/r^2}} \left[ f\left[\arcsin(\rho/r),\phi)\right] + f\left[(\pi - \arcsin(\rho/r)),\phi\right] \right] \quad (42)$$

where $M(\rho,\phi)$ is an orientation or alignment image, $\rho$ and $\phi$ are polar coordinates ($\phi$ is the same as in three dimensions), and $r$ is the length of the photofragment radius vector. These variables are labeled clearly in Figure 6. The function $f(\arcsin(\rho/r),\phi) \equiv f(\theta,\phi)$ for $0 \leq \theta \leq \pi/2$ describes the angular dependence of the intensity distribution and can be substituted with one of the REMPI intensity combinations in eqs 37–41. The function $g(r)$ describes

---

[†] Eq 42 is a generalization of eq 35 from reference (*21*) for the case when the function $f(\theta,\phi)$ is not symmetric over the reflection in the $X - Y$ plane.

the radial dependence of the three-dimensional distribution.[†] Unlike the Abel transform, eq 42 is not a true integral transform and cannot be inverted. Nevertheless, it may still be used for "forward-convolution" fitting of image data.

For monoenergetic photofragments, $g(r) = \delta(r - r_0)$, where $r_0 = v_0\tau$, $v_0$ is the photofragment velocity, and $\tau$ is the flight time of the ions. For this special case, we can evaluate the integral in eq 42 analytically. Later we will consider the case when the influence of rank $K = 3, 4$ state multipoles in eqs 37–39 can be neglected in comparison with the $K = 1, 2$ state multipoles.

Using eq 37 together with eqs 16 or 17 for $f$ (in dissociation Geometries I or II, respectively) and substituting $\sin\theta = \rho/r_0$ gives the alignment images (*21*):

Geometry I: Dissociation light is linearly polarized along the **Z** axis:

$$\begin{aligned}\frac{M_Z(t,\phi) - M_Y(t,\phi)}{\langle M_Z\rangle + 2\langle M_Y\rangle} = \frac{C'}{\sqrt{1-t^2}}\frac{P_2}{P_0}\Big\{&[s_2 - 2\alpha_2 + 3\alpha_2 t^2][1 - t^2(1+\sin^2\phi)]\\ &-2\gamma_2 t^2(1-t^2)(1+\sin^2\phi)\\ &-\frac{\eta_2}{4}t^2[3t^2 + (2-t^2)\cos(2\phi)]\Big\},\end{aligned} \tag{43}$$

Geometry II: Dissociation light is linearly polarized along the **Y** axis:

$$\begin{aligned}\frac{M_Z(t,\phi) - M_Y(t,\phi)}{\langle M_Y\rangle + 2\langle M_Z\rangle} = \frac{C'}{\sqrt{1-t^2}}\frac{P_2}{P_0}\Big\{&[s_2 + \alpha_2(1 - 3t^2\sin^2\phi)]\\ &\times[1 - t^2(1+\sin^2\phi)]\\ &+2\gamma_2 t^2\sin^2\phi[2 - t^2(1+\sin^2\phi)]\\ &+\frac{\eta_2}{2}[t^2(2-t^2)\cos(2\phi) + 1 - t^2\\ &+t^4(1 - \frac{\sin^2(2\phi)}{4})]\Big\},\end{aligned} \tag{44}$$

where $C' = \sqrt{5}V(j_A)/4\pi$ and $\langle M_Y\rangle$, $\langle M_Z\rangle$ are total image intensities for the two probe light polarizations. The variable $t$ is the radial coordinate normalized to the maximum possible radius, *i.e.* $t = \rho/r_0$. The resulting shapes of these equations are linear combinations of the "basis" images in Figure 7 that were obtained at limiting values of the alignment parameters.

One can see from eqs 34, 39 that circularly polarized light is sensitive to the $\rho_{10}$ component of the photofragment orientation which is parallel to the detection direction. In practice, physical restrictions in the experimental apparatus usually prevent use of the **Z** axis as the propagation direction for the probe laser, as in our definition this axis coincides with the TOF direction (see Figure 6). Therefore we first consider the experimental geometries where both dissociation and probe laser beams are orthogonal to the **Z** axis:

---

[†] Most analyses of **v**–**J** correlation data assume the separability $h(r,\theta,\phi)=f(\theta,\phi)g(r)$. However in general, angular momentum polarization will depend on recoil speed, so this separation will not be valid.

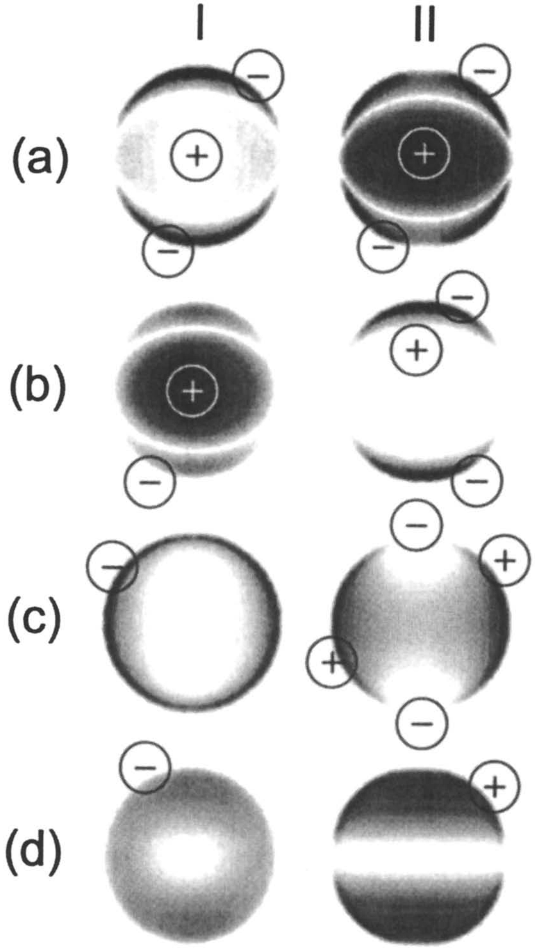

*Figure 7. Alignment image basis functions: plots of* $M_Z(t,\phi) - M_Y(t,\phi)$ *(eqs 43 and 44) for dissociation polarization Geometries I and II [dissociation laser parallel and perpendicular to the TOF (or:* $\mathbf{Z}$*) axis, respectively]. The linestrength factor ratio* $P_2/P_0$ *was not included, so that these basis images are independent of the particular probe transition. For display purposes, each image has been normalized independently. Cases (a)–(d) correspond to the following mechanistic limits: (a) incoherent perpendicular excitation, (b) incoherent parallel excitation, (c) coherent perpendicular excitation, (d) coherent parallel and perpendicular excitation. The corresponding values of the alignment anisotropy parameters are discussed in the text.*

(a). If dissociation and probe beams are circularly polarized and counterpropagate along the **X** axis the expressions 39 and 12 can be used to determine the three-dimensional image in the light reference frame **X′Y′Z′** where the **Z′** axis is parallel to the dissociation beam propagation. Using the angular transformation (*32*) to the laboratory **XYZ** frame (see Figure 6) and the transformation eq 42 yields the following orientation image

$$\frac{M_R^x(t,\phi) - M_L^x(t,\phi)}{\langle M_Z\rangle \ + \ \langle M_Y\rangle \ - \frac{1}{3}\left[\langle M_R^x\rangle + \langle M_L^x\rangle\right]} = \frac{C''}{\sqrt{1-t^2}}\frac{P_1^c}{P_0}\left[\alpha_1 t^2\cos^2\phi + \frac{\gamma_1}{2}(1 - t^2\cos^2\phi)\right] \tag{45}$$

where $C'' = 3\sqrt{3}/2\pi$. This equation has been normalized by $\langle M_Z\rangle + \langle M_Y\rangle - \frac{1}{3}\left[\langle M_R^x\rangle + \langle M_L^x\rangle\right]$, the combination of the total intensities related to linearly and circularly polarized probe light which is proportional to the total number of fragments (see eq 41). The corresponding orientation image basis functions and experimental geometry are shown in Figure 8(a). Eq 45 is derived for the case when the dissociation beam is left hand circularly polarized. A flip of its helicity results just in a change of the sign of the expression as a whole. Note, that the above experimental geometry leads to axial symmetry of the photofragment angular momentum distribution and thus can also be analyzed using the conventional inverse-Abel transform technique.

If linearly polarized light is used for photodissociation, the choice of experimental geometry is especially important, since for certain geometries the three-dimensional photofragment angular momentum distribution in eq 39 becomes antisymmetric with respect to reflection in the $X - Y$ plane. This then would lead to zero orientation signal after applying the transformation of eq 42. The cause of this antisymmetry lies with the angular distribution associated with the $\gamma_1'$ anisotropy parameter (see Figures 2 and 4). In particular, all geometries obeying the conditions $\mathbf{e}\|\mathbf{Z}$, or $\mathbf{e}\perp\mathbf{Z}$ and ($\mathbf{k}_{pr}\perp\mathbf{Z}$), where $\mathbf{k}_{pr}$ is the direction of the circularly polarized probe beam, give zero contributions to the orientation image. However, if $\mathbf{e}$ or $\mathbf{k}_{pr}$ do not lie in the $X - Y$ plane, the image can be nonzero. Below we present the expressions for difference images obtained for several important experimental geometries. Each of these was derived using eqs 11 and 39 in an appropriate reference frame **X″Y″Z″**, followed by a rotation to the **XYZ** frame using familiar equations (*32*). The resulting difference images are as follows:

(b). The dissociation and probe beams counterpropagate along the **X** axis, with the dissociation light linearly polarized at 45° with respect to the **Z** axis [see Figure 8(b)]

$$\frac{M_R^x(t,\phi) - M_L^x(t,\phi)}{\langle M_Z\rangle \ + \ \langle M_Y\rangle \ - \frac{1}{3}\left[\langle M_R^x\rangle + \langle M_L^x\rangle\right]} = \frac{C''\gamma_1'}{2\sqrt{1-t^2}}\frac{P_1^c}{P_0}\left[1 - \frac{t^2}{2}(3 - \cos 2\phi)\right]. \tag{46}$$

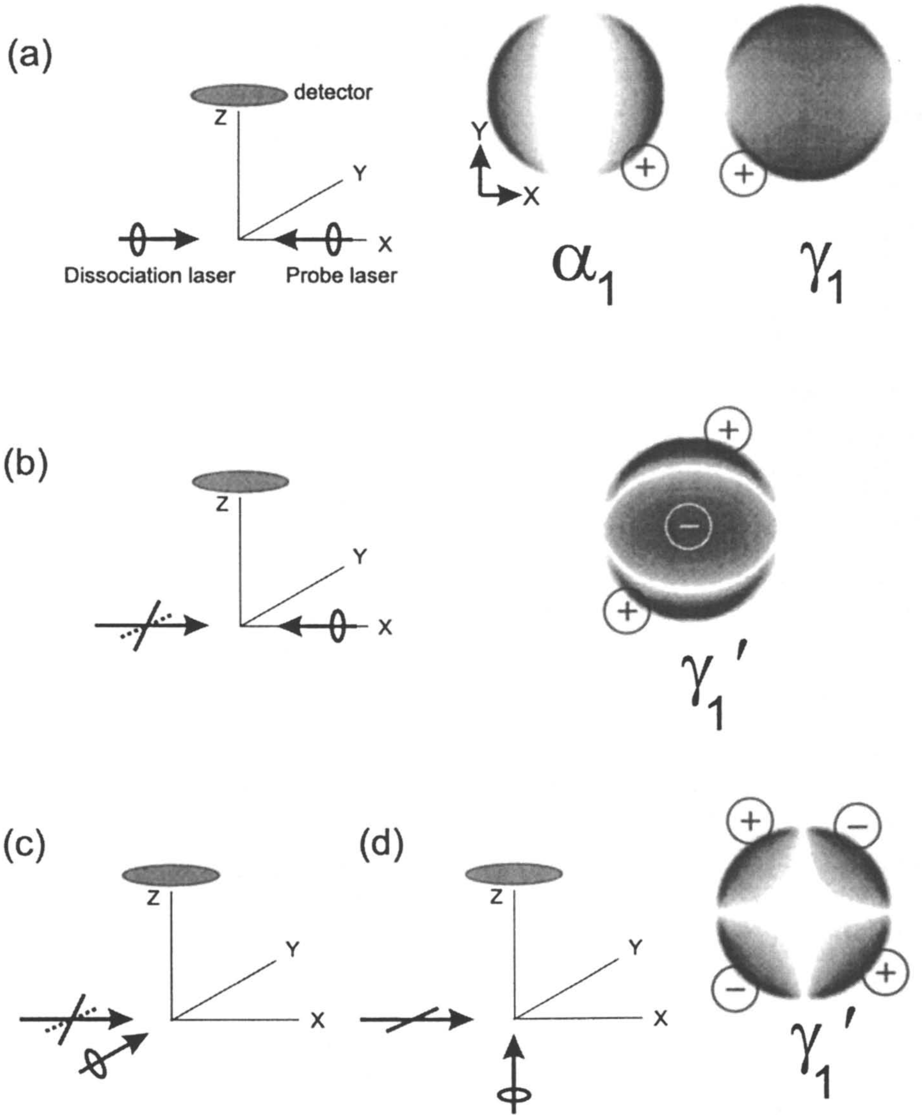
(a)
detector
Z
Y
X
Dissociation laser
Probe laser
Y
X
+
+
$\alpha_1$
$\gamma_1$
(b)
Z
Y
X
+
−
+
$\gamma_1'$
(c)
Z
Y
X
(d)
Z
Y
X
+
−
−
+
$\gamma_1'$

*Figure 8. Orientation image basis functions [plots of $M_R(t,\phi) - M_L(t,\phi)$] in four different geometries, together with the associated orientation parameters. Geometries (c) and (d) both yield the same shape basis image.*

(c). The dissociation and probe beams propagate along the **X** and the **Y** axis, respectively. The polarization vector of the linearly polarized dissociation light makes an angle of 45° with the **Z** axis [see Figure 8(c)]

$$\frac{M_R^y(t,\phi) - M_L^y(t,\phi)}{\langle M_X\rangle \ + \ \langle M_Z\rangle \ - \frac{1}{3}\left[\langle M_R^y\rangle + \langle M_L^y\rangle\right]} = \frac{C''\gamma_1'}{4\sqrt{1-t^2}}\frac{P_1^c}{P_0}t^2\sin 2\phi. \qquad (47)$$

An image similar to that of eq 47 has recently been observed (*45*).

(d). The dissociation and probe beams propagate along the **X** and the **Z** axis, respectively, and the dissociation light is linearly polarized along the **Y** axis [see Figure 8(d)]

$$\frac{M_R^z(t,\phi) - M_L^z(t,\phi)}{\langle M_X\rangle \ + \ \langle M_Y\rangle \ - \frac{1}{3}\left[\langle M_R^z\rangle + \langle M_L^z\rangle\right]} = -\frac{C''\gamma_1'}{2\sqrt{1-t^2}}\frac{P_1^c}{P_0}t^2\sin 2\phi \qquad (48)$$

Note that the basis images represented by eq 48 and eq 47 have the same shape but differ in sign and in intensity (by a factor 2).

The basis images described by eqs 43–48 provide a powerful means for interpreting the orientation and alignment contribution to photofragment ion image data, since each of the orientation and alignment mechanisms discussed previously is associated with a unique radial and angular dependence in the images. The image "basis" functions shown in Figure 7 and Figure 8 are graphs of eqs 43–48 for limiting values of the rank $K = 1, 2$ anisotropy parameters. Linear combinations of these shapes can be used to simulate the contribution of rank 2 alignment to photofragment ion image data for dissociations that are initiated with linearly polarized light and that produce fragments with a single recoil velocity. These shapes are the final result of the theoretical approach discussed in this and the preceding sections. In the following we will present several experimental examples of photofragment orientation and alignment using the formalism presented in this chapter.

## Experimental examples

### Photofragment orientation by circularly polarized light: photodissociation of RbI at 266 nm

In this section we present an experimental study of the angular distribution of oriented photofragments produced by circularly polarized light which has recently been reported by Korovin and coworkers (*29*). The experiment focuses on RbI photodissociation at 266 nm which produces spin-oriented ground state Rb atoms (see Figure 9). As shown in the theoretical section, the underlying dissociation dynamics in this case are described by the anisotropy parameters $\alpha_1$ and $\gamma_1$ which both contribute to the experimental signal (see eq 12).

The experimental data is obtained using a new technique: Doppler-resolved paramagnetic Faraday detection. This technique explores the photofragment

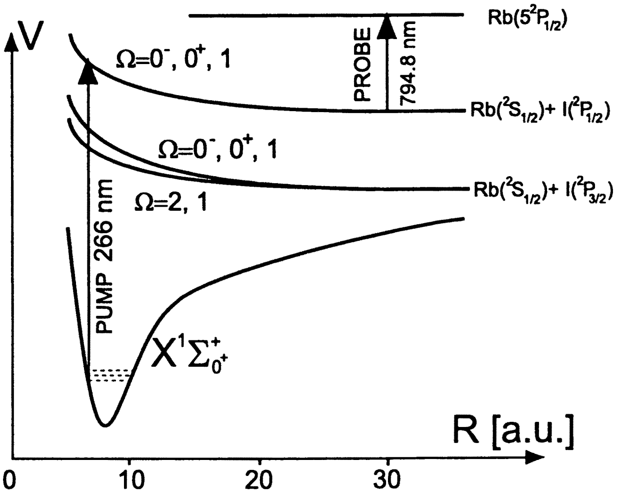

*Figure 9. Potential curves of the molecule RbI. The pump-probe scheme used in the experiment is also indicated.*

magnetic optical birefringence of a vapor and is based on the fact that the gyrotropic component of the atomic polarizability causes the electric field of the probe light to be rotated by a certain angle after the light is passed through a polarized vapor. Compared with resonance techniques, it has the advantage of reducing the influence of saturation effects and of thick optical layers on experimental data (*28*).

The experiment was carried out using a pump-probe scheme: RbI vapor in bulk condition was illuminated by pulsed laser radiation dissociating the molecules into ($5^2S_{1/2}$) rubidium atoms and metastable ($5^2P_{1/2}$) iodine atoms. The nascent spin-oriented rubidium atoms were detected by a probe beam that crossed the pump laser beam at 90°. The probe radiation source was a commercial cw tunable diode laser (TUI Optics, DL 100) providing an output power of approximately 6 mW. The laser linewidth of about 1 MHz was much smaller than the width of the Doppler-broadened atomic absorption profile, on the order of 1000 MHz. The linearly polarized probe light was analyzed by a linear polarizer after passing through the cell and was detected by a photomultiplier. By tuning the probe laser frequency within the atomic absorption line the spin orientation of a group of rubidium atoms was determined with a certain velocity vector. An additional external magnetic field of $B_0 = 1.55$ G was applied to the reaction volume to separate population and Faraday detection signals and to increase the experimental signal-to-noise ratio.

The experimental results are presented in Figure 10. The upper curve is the Doppler resolved absorption line of the Rb fragments while the lower curve is the Faraday signal resulting from the fragment orientation. The Faraday

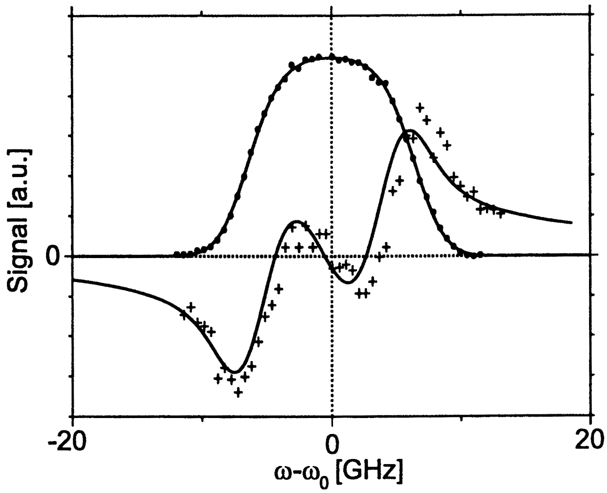

*Figure 10. Experimental absorption (+) and dispersion (•) Doppler profiles of spin-oriented rubidium photofragments. $\omega = 2\pi\nu$, where $\nu$ is the probe laser frequency. Solid lines are fits (see text).*

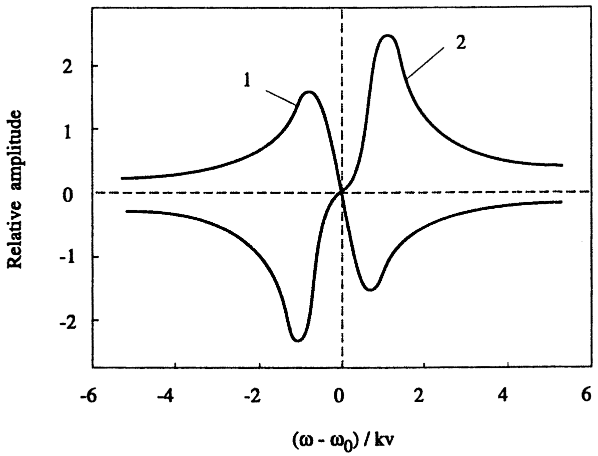

*Figure 11. Dispersion cross sections corresponding to incoherent (1) and coherent (2) mechanisms for photofragment orientation. The experimental dispersion signal is a superposition of curves 1 and 2.*

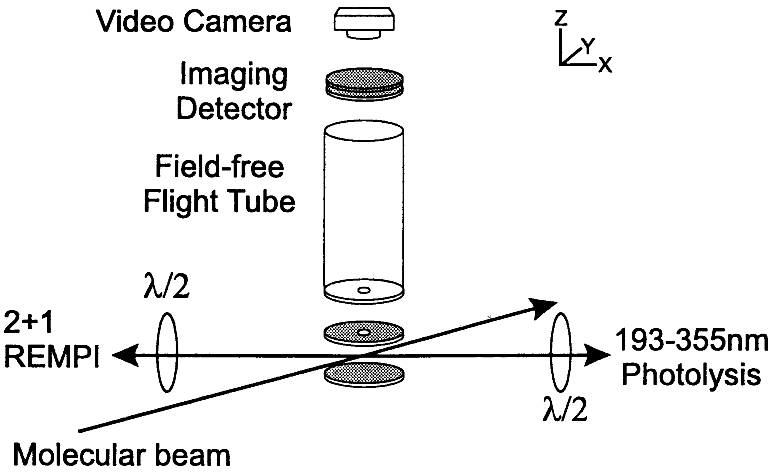

*Figure 12. Schematic view of the experimental apparatus. The Cartesian axis definition in this figure is used throughout the chapter.*

signal can be presented as a superposition of two theoretical curves shown in Figure 11, each related to a certain dissociation mechanism (*28, 29*). These are: (1) incoherent excitation into the $\Omega = 1$ molecular state and (2) excitation into the coherent superposition of the $\Omega = 1, 0^+$ molecular states. The ratio of the corresponding rank $K = 1$ anisotropy parameters was found to be $\alpha_1/\gamma_1 \approx -0.33$.

These results show evidence of a contribution to RbI photodissociation from the coherent excitation mechanism and indicate opposite directions of the net photofragment orientation vectors for incoherent and coherent dissociation mechanisms.

## Photofragment alignment studied with ion imaging

### *Experimental procedure*

In general, in order to study the polarization angular distribution, one must simultaneously measure recoil velocity vectors and the correlated angular momentum polarization. In our study, we have used two-dimensional photofragment ion imaging (*51*) and 2+1 REMPI for this purpose.

Figure 12 shows a schematic diagram of our molecular beam apparatus, described in detail in a recent publication (*52*). This velocity map ion imaging apparatus consists of a time-of-flight mass spectrometer and a position-sensitive detector. A skimmed molecular beam enters the interaction region of the mass spectrometer, where it crosses counter-propagating 30 Hz photolysis and probe laser beams at 90°. The initial laser pulse is slightly focused at the interaction center and dissociates a small fraction of the molecules. After a delay of 10–

20 ns, the nascent atomic photofragments are state-selectively ionized by the probe pulse via a 2+1 REMPI transition. During image acquisition, the wavelength of the probe laser light is repeatedly scanned over the Doppler profile of the line to sample the entire velocity distribution. The polarizations of the two lasers were >99% linear (90% when an excimer laser with a pile-of-plates polarizer was used as photolysis source), as measured with a Glan-Taylor prism polarizer. Each polarization could be rotated with an appropriate half-wave plate.

The photofragments are ionized between repeller and attractor plates, which are set at voltages corresponding to velocity-map imaging conditions (*53*). The ion packet travels through a field free flight tube and strikes dual microchannel plates, which are gated at the flight time of the atomic ions. Electrons emerging from the back of the microchannel plate strike a phosphor screen to produce images of the spatial distribution of the ionized photofragments. Images were collected with a CCD camera and signal-averaged at each of four geometries of the dissociation and probe laser polarizations. To further improve the signal-to-noise ratio, we used an image processor to combine the raw data images with their horizontal and vertical reflections. A photomultiplier tube behind the phosphor screen was used to measure the total image intensity. This was used to obtain mass spectra, to optimize signal, and to measure the total alignment in the laboratory frame.

### *Imaging the chlorine atoms from photodissociation of $Cl_2$ at 355 nm*

We have measured ion images for chlorine dissociation into ground state $Cl(^2P^o_{3/2})$ atoms probed via both the $^2S^o_{1/2}$ and $^2D^o_{5/2}$ intermediate states, using the four different combinations of laser polarizations discussed earlier, *i.e.* the dissociation and probe laser polarizations both parallel and perpendicular to the **Z** axis (ion flight axis); both lasers were counterpropagating along the **X** axis. The shape of the data images is predominantly influenced by the population distribution $\rho_{00}(\theta, \phi)$, described by the $\beta_0$ parameter, which is close to the limiting value of $-1$ for this perpendicular transition (*2, 54–58*). There is a small difference between images measured with different probe laser polarizations which is a consequence of angular momentum alignment.

From these raw data images, we wish to obtain alignment images as prescribed by eqs 43 and 44. In an ideal experiment, where no intensity-altering conditions change between the **Z** and **Y** measurements, it would be possible to directly subtract the measured images. Because of slow drifts in experimental conditions, this is nearly impossible in practice, unless one carries out a shot-to-shot rotation of the probe laser polarization and collects two separate images in parallel. As an alternative, we normalize the experimental images, and perform a subtraction weighted by a trial value for $I_{\|}/I_{\perp}$, the ratio of the total intensity in the two images. Then we calculate the alignment images by optimizing the alignment parameters (or equivalently, the relative weightings of basis functions shown in Figure 7) using the Singular Value Decomposition (SVD) technique. $I_{\|}/I_{\perp}$ is iteratively improved by repeated fitting and recalcu-

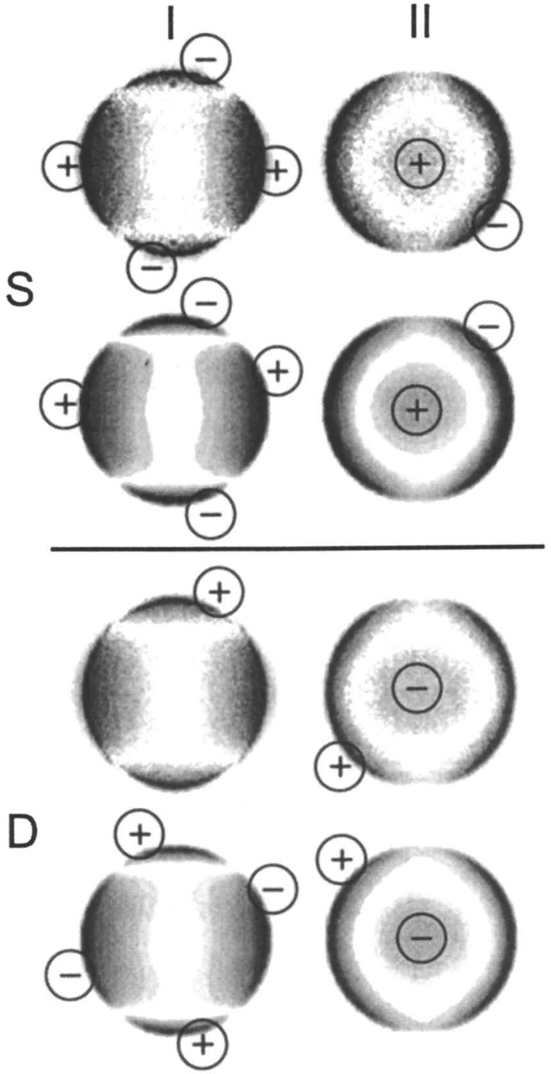

*Figure 13. Comparison of difference images (alignment images) obtained for Geometries I and II with results of simulations. The top half contains images for the ${}^2S^o_{1/2}$ probe state, the bottom half those for the ${}^2D^o_{5/2}$ state. The first and third rows contain the experimental data, the second and fourth rows the simulated images. These simulations were obtained by an SVD fit using the four basis images of Figure 7, which yielded the values listed in Table IV (second column). Note the sign difference between the ${}^2S^o_{1/2}$ and ${}^2D^o_{5/2}$ probe state difference images, which is due to opposite signs of the linestrength factor ratio for those transitions.*

**Table IV. Alignment anisotropy parameters for Cl($^2P^o_{3/2}$) obtained from an SVD fit to ion image data, for the photodissociation of $Cl_2$ at 355 nm probed via the $^2S^o_{1/2}$ and $^2D^o_{5/2}$ REMPI states. The digits in parentheses are the one-standard-deviation uncertainty in the last digits of the given value. The theoretical range and interpretation of the alignment parameters is also tabulated.**

| *Parameter* | *Best fit* | *Range* | *Interpretation* |
|---|---|---|---|
| $s_2$ | −0.074(9) | −0.16...0.16 | incoherent ‖ and ⊥ |
| $\alpha_2$ | −0.032(3) | −0.08...0.08 | incoherent ‖ and ⊥ |
| $\eta_2$ | 0.075(20) | −0.30...0.30 | coherent ⊥ |
| $\gamma_2$ | 0.001(16) | −0.15...0.15 | coherent ‖ and ⊥ |
| $s_2/\alpha_2$ | 2.3(3) | −1...2 | |
| $\langle A_{20}\rangle$ | −0.09(8) | −0.8...0.8 | $-2(\alpha_2 + \gamma_2 + \eta_2)$ |

lation of the alignment images until a self-consistent result is obtained. In doing so, we are recognizing that $I_{\parallel}/I_{\perp}$ is proportional to $\langle A_{20}\rangle = -2(\alpha_2 + \gamma_2 + \eta_2)$ (eq 19), so in effect, the unknowns which we wish to obtain by fitting appear on both sides of eqs 43 and 44. We found that even extreme initial trial values of $I_{\parallel}/I_{\perp}$ converge quickly to the same set of alignment anisotropy parameters and final value of $I_{\parallel}/I_{\perp}$.

Figure 13 (first and third rows) shows the alignment images, obtained from the raw data, using the best-fit value for $I_{\parallel}/I_{\perp}$ together with the best-fit simulated images (second and fourth rows). The features of the measured images are very well represented in these fits. The alignment parameters obtained by fitting the data for both probe states were averaged and are shown in Table IV. The size of the error margins represents the standard deviation associated with averaging four (nominally) equivalent image quadrants in multiple data sets for both $^2S^o_{1/2}$ and $^2D^o_{5/2}$ probe states. This uncertainty reflects the spatial inhomogeneity of the images and the modest effects of changes in experimental conditions during the course of the investigation. The ranges of the parameters are also listed in Table IV. Note, that in this specific case, as said before, the range of some of the parameters is slightly smaller than calculated for the general case (Table II). From the alignment anisotropy parameters in Table IV, we can also obtain a value for $\langle A_{20}\rangle$, using eq 19. This value compares favorably with the value obtained from the independent measurement of $I_{\parallel}/I_{\perp}$.

The fits include substantial contributions from basis images (a) and (c) of Figure 7, which correspond to incoherent and coherent perpendicular excitation, respectively. This identifies something quite new for chlorine—a coherent contribution to the photoexcitation. Coherence effects have been seen before in total alignment measurements [*e.g.* for the calcium dimer (*5, 6*)], but these measurements are not capable of fully separating coherent and incoherent contributions to the alignment. Whereas total alignment measurements give the sum $\alpha_2 + \gamma_2 + \eta_2$, v–j correlation measurements make it possible to determine each alignment anisotropy parameter individually. At first glance, the contri-

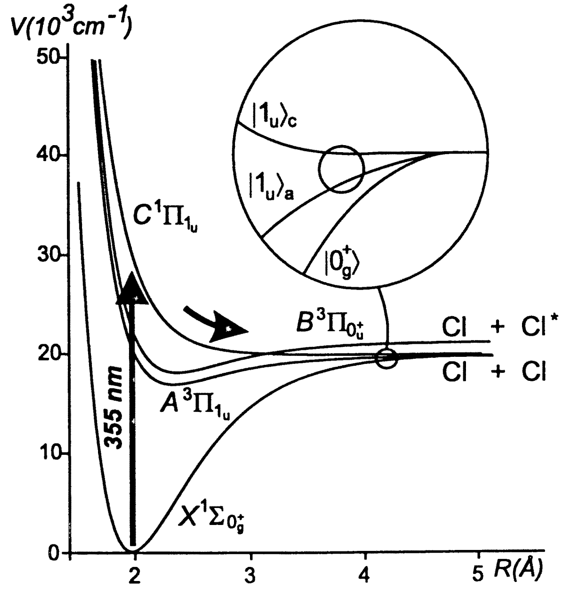

*Figure 14. Schematic potential energy curves of the chlorine molecule. The inset shows the asymptotic state labels and possible long-range interactions.*

bution to photofragment alignment from coherent perpendicular excitation may seem unsurprising. The $C^1\Pi_{1_u}$ state of chlorine, which is believed to be the primary absorber, contains a degenerate pair of $|\Omega|=1$ states. One might conclude therefore, that coherent excitation of these states followed by adiabatic dissociation, is all that is required to explain the observed coherence effect. In fact, the coherent contribution to alignment also requires the occurrence of nonadiabatic transitions during separation of the two chlorine atoms. To understand this fact, it is necessary to take a closer look at the physics of photofragment alignment.

We start by considering a purely adiabatic dissociation, which is sufficient to qualitatively explain the incoherent contribution to alignment. The two lowest molecular states of $1_u$ symmetry, $|1_u\rangle_a$ and $|1_u\rangle_c$ correlate adiabatically with the states $A^3\Pi_{1_u}$ and $C^1\Pi_{1_u}$ of $Cl_2$, respectively (see Figure 14). It can be shown (*21*) that photodissociation via the $A^3\Pi_{1_u}$ excited molecular state does not produce photofragment alignment. In contrast, photodissociation via the $C^1\Pi_{1_u}$ excited molecular state leads to photofragment alignment due to an incoherent dissociation mechanism, although no alignment is produced by a coherent mechanism. These results are a direct consequence of the symmetry of the long-range molecular wavefunctions that were obtained under the assumption of a purely adiabatic dissociation. The degree of photofragment alignment that can be obtained through photodissociation via the $C^1\Pi_{1_u}$ excited state is described by the alignment anisotropy parameters $\alpha_2$, $s_2$, and $\eta_2$ (eq 18), which

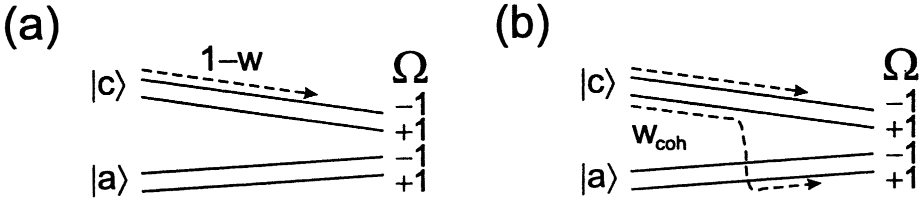

*Figure 15. Nonadiabatic, alignment producing, transitions for incoherent (a) and coherent (b) excitation.*

have the values (*21*) $\alpha_2 = s_2/2 = -2/25, \eta_2 = 0$. Converting to molecular frame alignment parameters using eqs 6 and 20, one obtains $A_{20}^{mol} = 10\alpha_2 = -4/5$; $A_{22}^{mol} = 0$. This value of the molecular frame alignment parameter $A_{20}^{mol}$ is equal to its most negative possible value [see, *e.g.*, reference (*30*)], showing that the $m_j = \pm 1/2$ fragment magnetic sublevels are equally populated while the $m_j = \pm 3/2$ magnetic sublevels are empty. Thus both fragments' angular momenta are mainly perpendicular to the molecular axis.

Although the ratio $s_2/\alpha_2$ obtained from our measurements is similar to the calculation, the individual values are considerably smaller. The adiabatic analysis also predicts a value of zero for $\eta_2$, at odds with our measurements. In order to explain the measured alignment, one must therefore consider the role of nonadiabatic interactions between the nascent $C^1\Pi_{1_u}$ state and the $A^3\Pi_{1_u}$ state. Since there are no avoided crossings involving these two states, nonadiabatic transitions can occur only at relatively long range, where the energy gap between the $A^3\Pi_{1_u}$ and $C^1\Pi_{1_u}$ states becomes comparable in magnitude to the matrix elements which describe their nonadiabatic coupling. We define $w$ as the probability of the nonadiabatic transition. For incoherent excitation of a $|C, \Omega\rangle$ substate followed by dissociation, the molecule can remain in the same substate, transfer to the $|A, \Omega\rangle$ substate, or appear in a coherent superposition of both. Only the first of these dissociation channels [see Figure 15(a)] leads to a nonzero dynamical function $f_2(1,1)$, resulting in a photofragment alignment component $A_{20}^{mol}$ as discussed previously. The probability of this channel is $(1-w)$. For coherent excitation of the $|C, \Omega{=}\pm1\rangle$ substates, the molecule can end up in the same substates, a coherent superposition of the $|A, \Omega{=}\pm1\rangle$ substates, or a coherent superposition of $|C, \Omega{=}\pm1\rangle$ and $|A, \Omega{=}\mp1\rangle$. Only the third channel [see Figure 15(b)] results in a nonzero value for the dynamical function $f_2(1,-1)$, which is related to the photofragment alignment component $A_{22}^{mol}$. This component is proportional to the "coherent" off-diagonal nonadiabatic transition matrix element $w_{\text{coh}}$.

The anisotropy parameters $\alpha_2$ and $\eta_2$, which describe the contribution to photofragment alignment resulting from incoherent and coherent excitation, respectively, can be calculated (*21*) as $\alpha_2 = s_2/2 = -2(1-w)/25$, $\eta_2 =$

$-4\sqrt{6}w_{\text{coh}}/25$. The corresponding molecular frame alignment parameters (eqs 6 and 20) are $A_{20}^{mol} = -4(1-w)/5$, $A_{22}^{mol} = 4w_{\text{coh}}/5$. Comparing the above expressions for the alignment anisotropy parameters to the values obtained in the experiment, we can draw conclusions about the mechanisms responsible for the Cl photofragment alignment. The first important contribution to the experimental signals is the incoherent excitation mechanism: the photofragment alignment produced by incoherent excitation of the molecular $C^1\Pi_{1_u}$ state is shown to be negative and equal to approximately half of its most negative possible value. This deviation from the extremum is a consequence of the homogeneous nonadiabatic transition from the $C^1\Pi_{1_u}$ state of the chlorine molecule to the $A^3\Pi_{1_u}$ state. We can calculate the probability of this nonadiabatic transition to be $w = 0.60(4)$. The second important contribution to the experimental signals is the coherent excitation mechanism. The coherence is initiated by optical excitation to components $\Omega = \pm1$ of the $C^1\Pi_{1_u}$ state, however a nonadiabatic transition later in the dissociative process is required for the coherence to have observable consequences. This nonadiabatic transition produces a system that dissociates along two indistinguishable pathways (the $C^1\Pi_{1_u}$ and $A^3\Pi_{1_u}$ asymptotic curves), which can interfere to produce modulations—interference fringes—in the alignment angular distribution. The contribution to molecular frame alignment from coherent excitation is negative and proportional to the "coherent" nonadiabatic probability $w_{coh}$, calculated to be $w_{coh} = -0.19(5)$.

Analyzing the experimental results with the methods described in this chapter leads to a much deeper understanding of this already well known system. We have shown that the atomic alignment is a consequence of both incoherent and coherent perpendicular excitation to the $C^1\Pi_{1_u}$ state of chlorine. In order to explain the coherent contribution to alignment and the non-maximal value of the incoherent contribution, we have shown that a nonadiabatic transition to the $A^3\Pi_{1_u}$ state must have occurred in the asymptotic region of the chlorine potential energy curves.

### *Imaging the oxygen atoms from photodissociation of $NO_2$ at 213 nm*

For another application of our theoretical model we have measured the angular distribution of the angular momentum polarization in a polyatomic molecule, nitrogen dioxide. The focus of this study is on the ground state oxygen atoms, $O(^3P_j)$ that are among the products in the photodissociation of $NO_2$ at 212.8 nm. The three different fine-structure components, $j = 0, 1, 2$ are probed with 2+1 REMPI transitions near 226 nm (*59*), in each of which the three closely spaced upper-state fine-structure components are encompassed in the scan across the Doppler profile. We first measured the total laboratory frame alignment for all three fine-structure components, to be able to scale the image data accurately. Table V shows a negligible alignment for the $O(^3P_2)$ ground state, strong alignment for the $O(^3P_1)$, and the expected absence of alignment for the $O(^3P_0)$ state. Note, that for a detailed quantitative analysis of this data in terms of the alignment parameters, line-strength factors for the probe transitions are required which are not yet available. However, qualitative insight may be obtained

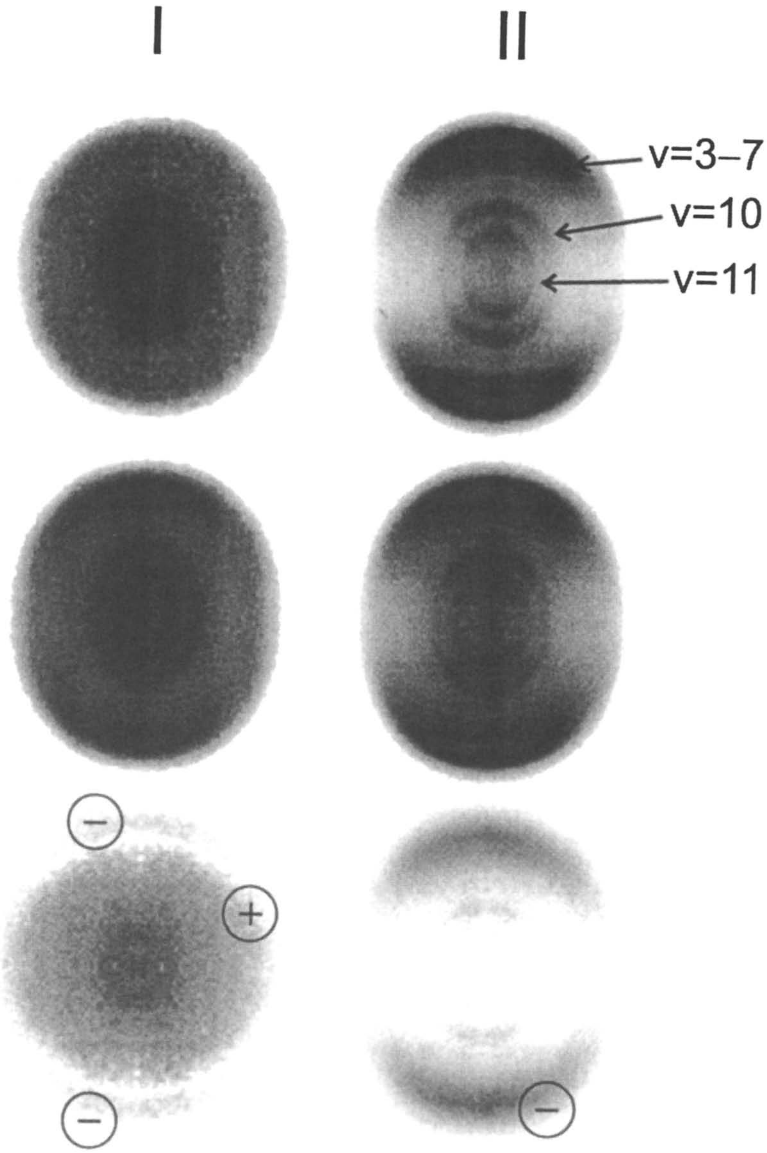

*Figure 16. Grey scale data images for $O(^3P_1)$ from photodissociation of $NO_2$ at 212.8 nm for Geometries I and II, with probe laser polarization along the **Z** axis (first row) and along the **Y** axis (second row). The vibrational levels of the NO co-fragment that correspond to the different rings in the image are also indicated. The difference images are presented in the third row.*

**Table V. Total alignment in the laboratory frame for the three spin-orbit states of $O(^3P_j)$ from photodissociation of $NO_2$ at 212.8 nm. The digits in parentheses are the one-standard deviation uncertainty in the last digits of the given value.**

| *State* | $(I_{\parallel} - I_{\perp})/(I_{\parallel} + 2I_{\perp})$ |
|---|---|
| $O(^3P_2)$ | 0.010(41) |
| $O(^3P_1)$ | 0.088(25) |
| $O(^3P_0)$ | 0.016(33) |

**Table VI. Alignment parameters for $O(^3P_1)$ from photodissociation of $NO_2$ at 212.8 nm obtained from fits to the difference images. The digit(s) in parentheses are the one-standard deviation uncertainty in the last digit(s) of the given value.**

| *Parameter* | *Best fit* | *Range* | *Interpretation* |
|---|---|---|---|
| $s_2$ | 0.044(12) | −0.2 … 0.1 | incoherent ∥ and ⊥ |
| $\alpha_2$ | −0.036(12) | −0.1 … 0.2 | incoherent ∥ and ⊥ |
| $\eta_2$ | 0.0049(80) | −0.30 … 0.30 | coherent ⊥ |
| $\gamma_2$ | −0.019(8) | −0.21 … 0.21 | coherent ∥ and ⊥ |

from the results directly, as we have shown in the $Cl_2$ case.

Ion image data for the $O(^3P_1)$ product are shown in Figure 16 for the four different combinations of photolysis and probe polarizations. The internal energy distribution of the NO co-fragment is present as different rings, each corresponding to one or more vibrational levels of NO. The apparent bi-modal kinetic energy release distribution likely arises from a dissociation via crossing to another potential energy surface. Again, we isolate the angular distribution of the orbital angular alignment from the larger population signals by subtracting ion images for different probe polarizations, shown in the lower panel of Figure 16. As in the present case the image data show the presence of a bi-modal translational energy distribution, we have chosen to fit the images by examining the angular behavior of the outer ring for both the basis images and the experimental images. For simplicity, the inner rings are thus neglected in this analysis. A good fit is readily obtained, and the resulting parameters are presented in Table VI. In the absence of further information on the probe transition line-strength factors, these are strictly relative values. However, estimates of the line-strength factors suggest that the absolute quantities are likely to be somewhat larger than the values indicated.

The total alignment is significant only for the $O(^3P_1)$ state, and in this case it is substantial. As is apparent from the results in Table VI, the dominant

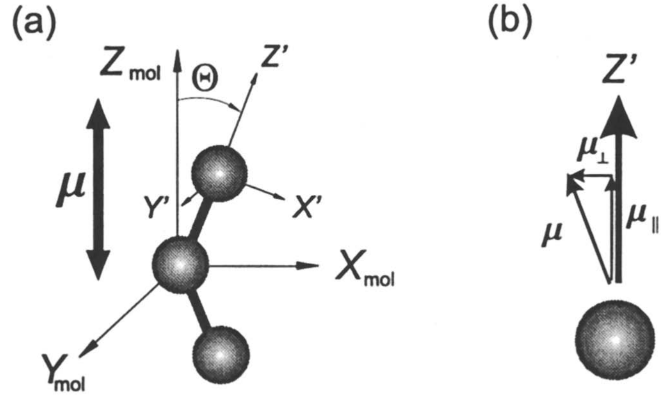

*Figure 17. Schematic view of $NO_2$ showing the relative orientation of the transition moment $\mu$, in (a) the molecular frame and (b) the recoil frame.*

mechanism responsible for this alignment is an incoherent parallel excitation of the parent molecule. This is implied by the ratio $s_2/\alpha_2$ which is close to $-1$. Furthermore, this contribution reaches nearly half its limiting value. In addition to this incoherent contribution, there is also a coherent component to the alignment, as indicated by the non-zero $\gamma_2$ value. For photolysis of $NO_2$ at 212.8 nm, the dominant excitation is to the $2^2B_2$ excited state, and the transition moment is in the plane of the molecule parallel to the line joining the oxygen atoms (*60*). The N–O bond in the ground state equilibrium geometry makes an angle of 23° with this transition moment (see Figure 17). In the recoil frame of the oxygen atom, the transition moment has both parallel and perpendicular components, *i.e.*, projections both on $\mathbf{Z}'$ and on $\mathbf{X}'$. This is precisely the means by which coherences can be generated in the angular momentum distribution of the recoiling oxygen atom. These coherences result in a loss of cylindrical symmetry of the electron cloud about the recoil direction. This is illustrated in Figure 18: the shape of the electron cloud, as implied by the measured alignment parameters, is dominated by the incoherent alignment distribution (the elongated shape at all angles). The coherent distribution is most pronounced at $\Theta = 45°$, where $\gamma_2$ reaches a maximum. There, the azimuthal distortion of the electron cloud bears the imprint of the original molecular plane: on the long time scale of the experiment, and even in the asymptotic region, the oxygen atom "remembers" the original plane of the molecule. This is probably a common feature of polyatomic photodissociation and not specific to $NO_2$.

It is interesting to contrast these observations to the coherence effects observed in diatomic molecules [see before and also references (*19, 24*)]. There, the coherent excitation of two dissociative states of different symmetry leads to interference, and yields an electron cloud in the recoiling atom that possesses azimuthal symmetry (see Figure 5). This is then observed as oscillations in

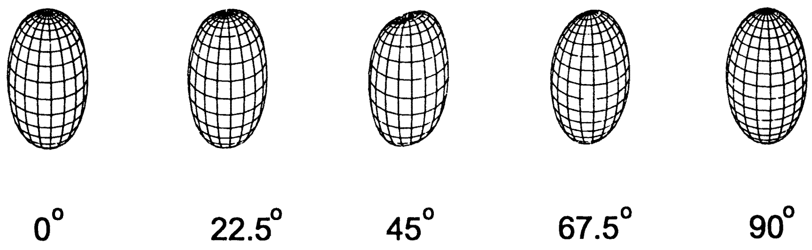

*Figure 18. Recoil-frame electron charge cloud distributions for the O($^3P_1$) atom based on the measured alignment parameters at indicated values of the angle Θ between the molecular axis $\mathbf{Z}_{mol}$ and the recoil direction $\mathbf{Z}'$.*

the angular distributions when probe with polarized radiation. In the polyatomic case, the mechanism is formally the same: coherent excitation of states of different symmetry (in the recoil frame that is) leads to interference. However, the presence of states of distinct symmetry arises directly from the nuclear symmetry in the molecule.

### *Imaging the oxygen atoms from photodissociation of $N_2O$ at 193 nm*

As another experimental example of our theoretical approach we have measured the orbital alignment of excited state oxygen atoms, O($^1D_2$), from the photodissociation of $N_2O$ at 193.3 nm. Owing to its importance in the atmosphere and its use as a precursor producing O($^1D_2$) for reactive scattering experiments, the photodissociation of $N_2O$ in the deep ultraviolet has been the subject of numerous studies (*14, 61–65*). Despite the abundance of studies in this wavelength region, a consensus on the detailed dissociation dynamics and alignment has yet to emerge, and no one to date has considered the role of coherences in the O($^1D_2$) product. Vertical electronic excitations in $N_2O$ from the equilibrium geometry are both optically forbidden and energetically inaccessible in the vicinity of 200 nm. However, as can be seen in the schematic potential curves of Figure 19, based on extensive calculations by Hopper (*66*), optical transitions become both allowed and energetically accessible when the molecule is bent, a well-known aspect of $N_2O$ photochemistry. In the linear geometry, there are two singlet excited surfaces that may play a role in this process, the $A(^1\Sigma^-)$ and the $B(^1\Delta)$. The $A$ state becomes the $1A''$ in $C_s$, with a minimum near 130°. The $B$ state represents a Renner-Teller pair with the lower component, $2A'$ in $C_s$, also exhibiting a minimum near 130° while the second component is the $2A''$ surface, with a minimum at the linear geometry. One of the outstanding questions in $N_2O$ photochemistry is the relative contributions of these excited states to this transition. The fact that the anisotropy parameter $\beta_0$ is positive has been taken as evidence that the $2A'$ transition dominates, and the deviation from the limiting value of 2, among other things, has sometimes been adduced

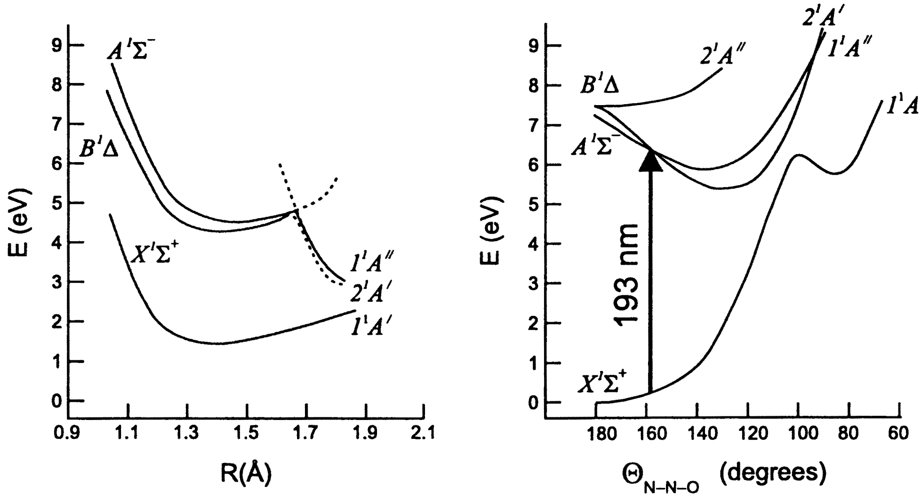

*Figure 19. Schematic potential curves for $N_2O$ adapted from reference (66). The potential energy dependence on N–O bond distance is shown on the left. Note the curve crossing region at an N–N–O angle of 130°. On the right is the dependence on bending angle for fixed bond distances: N–N 1.1 Å and N–O 1.4 Å. The arrow indicates the angle for which 193 nm excitation is energetically allowed.*

as evidence that the $1A''$ state also may play a role. For the $1A''$ state, the anisotropy parameter would be $-1$ in the impulsive limit regardless of bending. A distinct advantage of the detailed study of orbital alignment is that it can be a probe of the excited state symmetries, allowing us to address these questions directly.

For the $O(^1D_2)$ product, state multipoles up to rank $K \leq 2j = 4$ are necessary for a complete description of the orbital polarization. However, we confine ourselves to a detailed analysis of the dominant rank 0 and 2 contributions. The odd multipoles may be present but are not probed when only linear polarizations are used. To further decrease the significance of rank 4 alignment terms in our ion images, we have chosen to probe the $O(^1D_2)$ alignment via the $^1F_3$ intermediate state as for this probe transition the detection efficiency for quadrupole components to the alignment, as expressed in the linestrength factor ratio $P_4/P_0$, is the lowest of all three possible probe transitions. For this transition, we measured the total laboratory frame alignment to be $I_{\|}/I_{\perp} = 0.88 \pm 0.14$. As the error bar is relatively small, we can directly use this value to scale the image data accurately. For the $O(^1D_2)$ atom there is no net nuclear or electron spin, so that there is no corresponding depolarization of the alignment on the timescale of the probe. Therefore, we obtain for the total alignment $\langle A_{20} \rangle = -0.11$, which represents a relatively small laboratory frame alignment. Nevertheless,

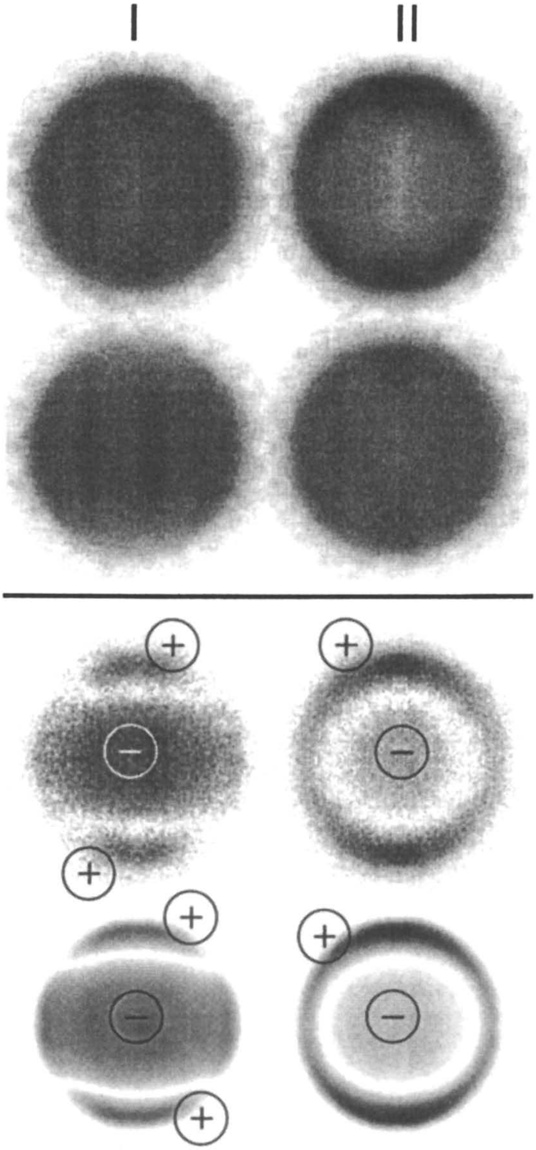

*Figure 20. Data images for $O(^1D_2)$ from photodissociation of $N_2O$ at 193.3 nm. Upper panel, experimental data for photolysis Geometries I and II, and probe laser polarizations along* **Z** *and* **Y** *axis (first and second row, respectively). Lower panel, difference images obtained from data and the corresponding SVD fit (third and fourth row, respectively), representing alignment angular distributions.*

**Table VII. Alignment parameters for $O(^1D_2)$ from photodissociation of $N_2O$ at 193.3 nm obtained from fits to the difference images. The digit(s) in parentheses are the one-standard deviation uncertainty in the last digit(s) of the given value.**

| *Parameter* | *Best fit* | *Range* | *Interpretation* |
|---|---|---|---|
| $s_2$ | −0.082(13) | −0.2...0 | incoherent ‖ and ⊥ |
| $\alpha_2$ | 0.022(14) | −0.05...0.2 | incoherent ‖ and ⊥ |
| $\eta_2$ | 0.017(5) | −0.30...0.30 | coherent ⊥ |
| $\gamma_2$ | −0.003(10) | −0.12...0.12 | coherent ‖ and ⊥ |

the imaging technique allows us to identify a large recoil-frame alignment, as shown below, despite the fact that the angle-averaged alignment is small.

The data images are shown in Figure 20 for the four combinations of photolysis and probe polarizations, along with their difference images. As before, these alignment images were fitted to the four basis images using the SVD technique. To account in a first order approximation for the smearing out of the images due to the broad velocity distribution (*62*) and the finite experimental resolution, we have convoluted the basis images with a Gaussian distribution to match the experimental images. The resulting best-fit simulated images are also shown in Figure 20. The values for the alignment parameters extracted from the analysis are summarized in Table VII. These alignment images are dominated by a strong $s_2$ and somewhat weaker $\alpha_2$ contribution, implying incoherent parallel and perpendicular components to the excitation. This may well reflect the different components of the $2A' \leftarrow 1A'$ excitation in the recoil frame. It is important to note that both singlet transitions are strictly forbidden for the linear molecule. The orientation of the transition moment is thus an important, nontrivial question, even for the $2A' \leftarrow 1A'$ excitation. The assumption that the transition moment is aligned along the N–O bond direction is clearly invalid for this transition. Qualitative estimates suggest that the transition moment is directed at large angles from the N–O bond axis for N–N–O angles near linear, and it is only when the molecule is sharply bent that the transition moment begins to align with the N–O bond. Examination of the potential curves of Hopper (*66*) and the more recent ones by Brown *et al.* (*67*), can provide a rough estimate of the degree of bending necessary to make the transition energetically allowed. For fixed bond distances, excitation to the $2A'$ surface at 193 nm becomes possible for bond angles 10–20° from linear as indicated in Figure 19. The value of 0.5 for $\beta_0$ corresponds, in the prompt limit for a single transition, to recoil at an angle of 45° from the transition moment. Although it is possible to achieve this angle for the $2A' \leftarrow 1A'$ transition, by invoking excitation from near-linear geometries at which the transition moment may be up to 45° from the N–O bond, a coherent contribution of the $1A'' \leftarrow 1A'$ could also play a role. The impact of a contribution from this transition will be to reduce the effective $\beta_0$ value.

The large $s_2$ value is a manifestation of the predominant incoherent, intrinsic vector correlation that vanishes after averaging over recoil angles. The $s_2/\alpha_2$ ratio shows that most of the alignment is produced via the parallel transition, consistent with the overall positive $\beta_0$ parameter. We can transform these results to the molecular frame using eq 24 and find that the molecular-frame diagonal alignment parameter $\langle A_{20}^{mol} \rangle$ is always negative, which implies that the corresponding angular momentum vector **J**, for any recoil direction, is mainly perpendicular to the recoil axis. In addition to the dominant incoherent contributions to the orbital alignment, a perpendicular coherence is clearly observed, as seen as a nonzero $\eta_2$ value. This can be accounted for in several ways: (a) coherent excitation of the perpendicular components of the $2A' \leftarrow 1A'$ transition, (b) coherent excitation of the pure perpendicular $1A'' \leftarrow 1A'$ transition, or (c) through simultaneous, coherent excitation of the perpendicular component of the $2A' \leftarrow 1A'$ transition and the pure perpendicular $1A'' \leftarrow 1A'$ transition. The destiny of either one of these coherent superpositions depends on the details of the following dynamics leading to the observed value of the $\eta_2$ alignment parameter, which will require further theoretical study.

In conclusion, we have observed strong recoil-frame orbital alignment in the $O(^1D_2)$ product following photodissociation of $N_2O$ at 193.3 nm. We have analyzed the results using our rigorous quantum mechanical theory to obtain alignment anisotropy parameters having direct physical significance. The results provide detailed insight into the dynamics of the photodissociation process and the nature of the electronic transitions responsible for the initial excitation. The alignment is dominated by strong incoherent parallel and perpendicular contributions which reflect mainly the two components of the $2A' \leftarrow 1A'$ transition. In addition, we find evidence of a contribution from a coherence between two perpendicular transitions, quite possibly the perpendicular components of the $2A' \leftarrow 1A'$ transition, subject to more detailed theoretical scrutiny.

## Conclusion

A technique for extracting information on dissociation dynamics from measurements of the recoil angular distribution of atomic photofragment orientation and alignment has been developed. By applying this method to experimental data, one obtains a set of orientation and alignment anisotropy parameters, which describe excited state symmetries, coherence effects, and nonadiabatic transitions.

To demonstrate the power of this analysis, we have undertaken studies of polarized atoms, that are produced by molecular photodissociation of diatomics (RbI and $Cl_2$) and polyatomics ($NO_2$ and $N_2O$). Analyzing the experimental results with the methods described in this chapter leads to a much deeper understanding of these systems. Strong alignment and orientation effects were seen, as well as coherences and long-range nonadiabatic interactions. The analysis emphasizes the application to ion imaging experiments, however, it can be readily adapted to other common experimental techniques that combine two-photon excitation with measurement of the photofragment spatial or velocity distribution, as was shown in the experimental example of RbI.

## Acknowledgements

This work was supported by the Director, Office of Energy Research, Office of Basic Energy Sciences, Chemical Sciences Division of the U.S. Department of Energy under Contract No. DE-AC03-76SF00098, and by a Cooperative Grant from the Civilian Research and Development Foundation, CRDF Award No. RP1-223.

## Appendix: Transformation of the expression for the linestrength factors $P_K$

The expression for the linestrength factors $P_K$ (eqs 30, 31, and 35) can be transformed as follows. Since the atomic dipole moment operators in eq 31 do not depend on the electron spin $S$, eq 31 can be rewritten as (*32*)

$$\begin{aligned} S(j_i\gamma_i, j_e\gamma_e, j'_e\gamma'_e, j_f\gamma_f) =& (-1)^{j_e+j'_e+L_e+L'_e+2j_i}(2J_i+1)(2J_e+1)(2J'_e+1) \\ &\times(2J_f+1)\left\{\begin{array}{ccc} L_e & S & j_e \\ j_f & 1 & L_f \end{array}\right\}\left\{\begin{array}{ccc} L_e & S & j_e \\ j_i & 1 & L_i \end{array}\right\} \\ &\times\left\{\begin{array}{ccc} L'_e & S & j'_e \\ j_i & 1 & L_i \end{array}\right\}\left\{\begin{array}{ccc} L'_e & S & j'_e \\ j_f & 1 & L_f \end{array}\right\} \\ &\times\frac{\langle L_f\|d\|L_e\rangle\langle L_f\|d\|L'_e\rangle^*\langle L_e\|d\|L_i\rangle\langle L'_e\|d\|L_i\rangle^*}{(E_{ei}-h\nu+i\Gamma/2)(E_{e'i}-h\nu-i\Gamma/2)}. \end{aligned} \tag{49}$$

When the light is linearly polarized along the laboratory **Z** axis, or right/left circularly polarized and propagates along the **Z** axis, the cyclic projections of the light polarization vector **e** in the laboratory frame have the simplest form $q = 0$, or $q = +1, -1$, respectively. Only the $Q = 0$ components of the fragment state multipoles differ from zero in this case (see eqs 32, 34). Using the definition of the light polarization matrix $E_{kq}(\mathbf{e})$ (*30*) and the summation rule 7 from chapter 12.1 of reference (*32*) one can rewrite the tensor product (eq 29) as

$$\begin{aligned} [(\rho_K \otimes E_{k_1})_{k_2} \cdot E_{k_2}] =& (-1)^{K+k_2}\rho_{K0}(2k_1+1)^{1/2}(2k_2+1) \\ &\times\sum_{q_1,q_2}\left(\begin{array}{ccc} 1 & 1 & k_1 \\ q & -q & q_1 \end{array}\right)\left(\begin{array}{ccc} k_1 & K & k_2 \\ -q_2 & 0 & -q_2 \end{array}\right) \\ &\times\left(\begin{array}{ccc} k_2 & 1 & 1 \\ q_2 & q' & -q' \end{array}\right) \\ =& (-1)^{K+k_2}\rho_{K0}(2k_1+1)^{1/2}(2k_2+1) \\ &\times\sum_{T,t}\sum_{R,r}(2T+1)(2R+1)\left(\begin{array}{ccc} 1 & 1 & T \\ q & q' & t \end{array}\right) \end{aligned} \tag{50}$$

$$\times \begin{pmatrix} T & K & R \\ -t & 0 & -r \end{pmatrix} \begin{pmatrix} R & 1 & 1 \\ r & -q & -q' \end{pmatrix}$$

$$\times \left\{ \begin{matrix} 1 & 1 & k_1 \\ 1 & 1 & k_2 \\ T & R & K \end{matrix} \right\}$$

where $q, q' = 0, \pm 1$.

Carrying out the summation over indices $k_1$ and $k_2$ in eq 28 using the summation rules 12 and 27 from chapter 12.2 of reference (*32*), yields

$$\sum_{k_1,k_2} (-1)^{k_2}(2k_1+1)(2k_2+1) \left\{ \begin{matrix} j_i & 1 & j_e \\ j_i & 1 & j'_e \\ K & k_1 & k_2 \end{matrix} \right\} \left\{ \begin{matrix} 1 & 1 & k_1 \\ 1 & 1 & k_2 \\ T & R & K \end{matrix} \right\} \tag{51}$$

$$\times \left\{ \begin{matrix} j_e & j'_e & k_2 \\ 1 & 1 & j_f \end{matrix} \right\}$$

$$= (-)^{T+K+j'_e-j_i+1} \left\{ \begin{matrix} j_f & 1 & j_e \\ 1 & j_i & T \end{matrix} \right\} \left\{ \begin{matrix} j_f & 1 & j'_e \\ 1 & j_i & R \end{matrix} \right\} \left\{ \begin{matrix} j_i & j_i & K \\ T & R & j_f \end{matrix} \right\}$$

Finally, the summation over $j_e$ and $j'_e$ in eq 30 is performed by twice applying the summation rule 18 from chapter 12.2 of reference (*32*). This yields eq 32, 34 with the linestrength factors given by

$$P_K(q) = (-1)^{j_i+j_f}(2j_i+1)(2j_f+1)(2K+1)^{1/2} \sum_{T,R,q_1} (2T+1)(2R+1)$$

$$\times \begin{pmatrix} 1 & 1 & T \\ q & q & -q_1 \end{pmatrix} \begin{pmatrix} T & K & R \\ q_1 & 0 & -q_1 \end{pmatrix} \begin{pmatrix} R & 1 & 1 \\ q_1 & -q & -q \end{pmatrix}$$

$$\times \left\{ \begin{matrix} j_i & j_i & K \\ T & R & j_f \end{matrix} \right\} \left\{ \begin{matrix} T & L_i & L_f \\ S & j_f & j_i \end{matrix} \right\} \left\{ \begin{matrix} R & L_i & L_f \\ S & j_f & j_i \end{matrix} \right\}$$

$$\times \mathcal{L}(\bar{\gamma}_i L_i, \bar{\gamma}_f L_f), \tag{52}$$

where

$$\mathcal{L}(\bar{\gamma}_i L_i, \bar{\gamma}_f L_f) = \tag{53}$$

$$\sum_{\bar{\gamma}_e, \bar{\gamma}'_e} \sum_{L_e, L'_e} \left\{ \begin{matrix} T & L_i & L_f \\ L_e & 1 & 1 \end{matrix} \right\} \left\{ \begin{matrix} R & L_i & L_f \\ L'_e & 1 & 1 \end{matrix} \right\} S(\bar{\gamma}_i L_i, \bar{\gamma}_e L_e, \bar{\gamma}'_e L'_e, \bar{\gamma}_f L_f),$$

and $P_K(0) \equiv P_K$, $P_K(\pm 1) \equiv P_K^c$. The factor $S(\bar{\gamma}_i L_i, \bar{\gamma}_e L_e, \bar{\gamma}'_e L'_e, \bar{\gamma}_f L_f)$ is defined in eq 31, $L$ and $S$ are fragment electron orbital and spin angular momenta, respectively. The symbol $\bar{\gamma}$ denotes the set of all other fragment quantum numbers other than $j$, $L$, and $S$.

Similar expressions for the linestrength factors have been recently analyzed by Mo and Suzuki (*68*), who also discussed the following calculation rules. By considering the symmetry properties of the $3j$ and $6j$ symbols (*32*), it can be seen from eq 52 that in case of circularly polarized light, $R$ and $T$ can take only the values $R = T = 2$, whereas for the case of linearly polarized light in general, $R$ and $T$ can take the values 0 or 2. However, when $j_i \neq j_f$ or $L_i \neq L_f$, both $R$ and $T$ are restricted to the value 2 for any light polarization. This allows for a determination of the relative values of the linestrength factors $P^c_\kappa$ for any $j, L$ values and $P_\kappa$ when $j_i \neq j_f$ or $L_i \neq L_f$, without computing the radial integrals. In case of atoms without a nuclear spin the relations $j_i = L_i$, $j_f = L_f$ should be used in eq 52.

Note that the summation over $j_e$ and $j'_e$ can be performed with only minimal loss of accuracy of eq 30, because usually the denominator in eq 31 depends only slightly on the spin-orbit splittings between the energy levels of $|\bar{\gamma}_e S L_e j_e\rangle$ and $|\bar{\gamma}_e S L_e j'_e\rangle$.

## Literature Cited

1. (a) Zare, R.N.; Herschbach, D.R., *Proc. IEEE* **1963**, *51*, 173; (b) Ling, J.H.; Wilson, K.R., *J. Chem. Phys.* **1976**, *65*, 881; (c) Greene, C.H.; Zare, R.N., *Annu. Rev. Phys. Chem.* **1982**, *33*, 119; (d) Bernstein, R.B.; Herschbach, D.R.; Levine, R.D., *J. Phys. Chem.* **1987**, *91*, 5365; (e) Hall, G.E.; Sivakumar, N.; Chawla, D.; Houston, P.L.; Burak, I., *J. Chem. Phys.* **1988**, *88*, 3682; (f) Ashfold, M.N.R.; Lambert, I.R.; Mordaunt, D.H.; Morley, G.P.; Western, C.M., *J. Phys. Chem.* **1992**, *96*, 2938; (g) North, S.W.; Hall, G.E., *J. Chem. Phys.* **1996**, *104*, 1864.
2. Busch, G.E.; Mahoney, R.T.; Morse, R.I.; Wilson, K.R., *J. Chem. Phys.* **1969**, *51*, 449.
3. (a) Busch, G.E.; Wilson, K.R., *J. Chem. Phys.* **1972**, *56*, 3626; (b) Busch, G.E.; Wilson, K.R., *J. Chem. Phys.* **1972**, *56*, 3638; (c) Zare, R.N., *Mol. Photochem.* **1972**, *4*, 1.
4. (a) Van Brunt, R.J.; Zare, R.N., *J. Chem. Phys.* **1968**, *48*, 4304; (b) Rothe, E.W.; Krause, U.; Düren, R., *Chem. Phys. Lett.* **1980**, *72*, 100; (c) Vasyutinskii, O.S., *Sov. Phys. JETP Lett.* **1980**, *31*, 428.
5. Vigué, J.; Grangier, P.; Roger, G.; Aspect, A., *J. Physique Lett.* **1981**, *42*, L531.
6. Vigué, J.; Beswick, J.A.; Broyer, M., *J. Physique* **1983**, *44*, 1225.
7. (a) Kato, H., *Faraday Discuss. Chem. Soc.* **1986**, *82*, 1; (b) Kleiber, P.D.; Wang, J.-X.; Sando, K.M.; Zafiropulos, V.; Stwalley, W.C., *J. Chem. Phys.* **1991**, *95*, 4168.
8. Blum, K., *Density Matrix Theory and Applications*; Plenum: New York, 2nd edition, 1996.
9. Dixon, R.N., *J. Chem. Phys.* **1986**, *85*, 1866.
10. Hall, G.E.; Sivakumar, N.; Houston, P.L.; Burak, I., *Phys. Rev. Lett.* **1986**, *56*, 1671.
11. Houston, P.L., *J. Phys. Chem.* **1987**, *91*, 5388.
12. Gordon, R.J.; Hall, G.E., *Adv. Chem. Phys.* **1996**, *96*, 1.
13. Mo, Y.; Katayanagi, H.; Heaven, M.C.; Suzuki, T., *Phys. Rev. Lett.* **1996**, *77*, 830.

14. Suzuki, T.; Katayanagi, H.; Mo, Y.; Tonokura, K., *CPL* **1996**, *256*, 90.
15. Eppink, A.T.J.B.; Parker, D.H.; Janssen, M.H.M.; Buijsse, B.; van der Zande, W.J., *J. Chem. Phys.* **1998**, *108*, 1305.
16. Wang, Y.; Loock, H.P.; Cao, J.; Qian, C.X.W., *J. Chem. Phys.* **1995**, *102*, 808.
17. North, S.W.; Zheng, X.S.; Fei, R.; Hall, G.E., *J. Chem. Phys.* **1996**, *104*, 2129.
18. Costen, M.L.; North, S.W.; Hall, G.E., *J. Chem. Phys.* **1999**, *111*, 6735.
19. Rakitzis, T.P.; Kandel, S.A.; Zare, R.N., *J. Chem. Phys.* **1998**, *108*, 8291.
20. Bracker, A.S.; Wouters, E.R.; Suits, A.G.; Lee, Y.T.; Vasyutinskii, O.S., *Phys. Rev. Lett.* **1998**, *80*, 1626.
21. Bracker, A.S.; Wouters, E.R.; Suits, A.G.; Vasyutinskii, O.S., *J. Chem. Phys.* **1999**, *110*, 6749.
22. Ahmed, M.; Peterka, D.S.; Vasyutinskii, O.S.; Suits, A.G., *J. Chem. Phys.* **1999**, *110*, 4115.
23. Ahmed, M.; Wouters, E.R.; Peterka, D.S.; Vasyutinskii, O.S.; Suits, A.G., *Faraday Discuss.* **1999**, *113*, 425.
24. Rakitzis, T.P.; Kandel, S.A.; Alexander, A.J.; Kim, Z.H.; Zare, R.N., *Science* **1998**, *281*, 1346.
25. Rakitzis, T.P.; Zare, R.N., *J. Chem. Phys.* **1999**, *110*, 3341.
26. Rakitzis, T.P.; Kandel, S.A.; Alexander, A.J.; Kim, Z.H.; Zare, R.N., *J. Chem. Phys.* **1999**, *110*, 3351.
27. Siebbeles, L.D.A.; Glass-Maujean, M.; Vasyutinskii, O.S.; Beswick, J.A.; Roncero, O., *J. Chem. Phys.* **1994**, *100*, 3610.
28. Picheyev, B.V.; Smolin, A.G.; Vasyutinskii, O.S., *J. Phys. Chem.* **1997**, *101*, 7614.
29. Korovin, K.O.; Picheyev, B.V.; Vasyutinskii, O.S.; Valipour, H.; Zimmermann, D., *J. Chem. Phys.* **2000**, *112*, 2059.
30. Zare, R.N., *Angular Momentum*; World Scientific: New York, 1988.
31. Happer, W., *Rev. Mod. Phys.* **1972**, *44*, 169.
32. Varshalovich, D.A.; Moskalev, A.N.; Khersonskii, V.K., *Quantum Theory of Angular Momentum*; World Scientific: Singapore, 1988.
33. Kupriayanov, D.V.; Vasyutinskii, O.S., *Chem. Phys.* **1993**, *171*, 25.
34. Alexandrov, E.B.; Chaika, M.P.; Khvostenko, G.I., *Interference of atomic states*, Springer, Berlin, 1993.
35. Auzinsh, M.; Ferber, R., *Optical Polarization of Molecules*; Cambridge University Press: Cambridge, 1995.
36. Vasyutinskii, O.S., *Opt. Spectrosc* **1983**, *54*, 524.
37. Fano, U., *Rev. Mod. Phys.* **1957**, *29*, 74.
38. See, *e.g.*, (a) Bederson, B., *Comments At. Mol. Phys.* **1969**, *1*, 65; (b) Kessler, J., *Comments At. Mol. Phys.* **1981**, *10*, 47; and (c) *Symposium on Photo-dynamics and Reaction Dynamics of Molecules at IAMS*; Okazaki, Japan, July 1999.
39. Glass-Maujean, M.; Beswick, J.A., *J. Chem. Soc. Faraday Trans.* **1989**, *85*, 983.

40. Glass-Maujean, M.; Beswick, J.A., *Phys. Rev. A* **1988**, *38*, 5660.
41. Glass-Maujean, M.; Frohlich, H.; Beswick, J.A., *Phys. Rev. Lett.* **1988**, *61*, 157.
42. Siebbeles, L.D.A.; Beswick, J.A., *J. Chem. Soc. Faraday Trans.* **1992**, *88*, 2565.
43. Flemming, E.; Wilhelmi, W.; Schmoranzer, H.; Glass-Maujean, M., *J. Chem. Phys.* **1995**, *103*, 4090.
44. Vasyutinskii, O.S., *Sov. Phys. JETP* **1981**, *54*, 855.
45. Rakitzis, T.P.; Samartzis, P.C.; Kitsopoulos, T.N., *J. Chem. Phys.* **1999**, *111*, 10415.
46. Rakitzis, T.P.; Hall, G.E.; Costen, M.L.; Zare, R.N., *J. Chem. Phys.* **1999**, *111*, 8751.
47. Kummel, A.C.; Sitz, G.O.; Zare, R.N., *J. Chem. Phys.* **1986**, *85*, 6874.
48. Kummel, A.C.; Sitz, G.O.; Zare, R.N., *J. Chem. Phys.* **1987**, *88*, 6707.
49. Docker, M.P., *Chem. Phys.* **1988**, *125*, 185.
50. Strickland, R.N.; Chandler, D.W., *Appl. Opt.* **1991**, *30*, 1811.
51. Whitaker, B.J., In *Research in Chemical Kinetics*, Compton, R.G.; Hancock, G., editors; Vol. 1; pp 307–346; Elsevier: Amsterdam, 1994.
52. Ahmed, M.; Blunt, D.A.; Chen, D.; Suits, A.G., *J. Chem. Phys.* **1997**, *106*, 7617.
53. Eppink, A.T.J.B.; Parker, D.H., *Rev. Sci. Instr.* **1997**, *68*, 3477.
54. Diesen, R.W.; Wahr, J.C.; Adler, S.E., *J. Chem. Phys.* **1969**, *50*, 3635.
55. Li, L.; Lipert, R.J.; Lobue, J.; Chupka, W.A.; Wilson, S.D., *Chem. Phys. Lett.* **1988**, *151*, 335.
56. Matsumi, Y.; Tonokura, K.; Kawasaki, M., *J. Chem. Phys.* **1992**, *97*, 1065.
57. Samartzis, P.C.; Sakellariou, I.; Gougousi, T.; Kitsopoulos, T.N., *J. Chem. Phys.* **1997**, *107*, 43.
58. Peyerimhoff, S.D.; Buenker, R.J., *Chem. Phys.* **1981**, *57*, 279.
59. Bamford, D.J.; Dyke, M.J.; Bishel, W.K., *Phys. Rev. A* **1987**, *36*, 3497.
60. Uselman, W.M.; Lee, E.K.C., *J. Chem. Phys.* **1975**, *65*, 1948.
61. (a) Alexander, A.J.; Aioz, F.J.; Brouard, M.; Simons, J.P., *Chem. Phys. Lett.* **1996**, *256*, 561; (b) Alexander, A.J.; Aioz, F.J.; Bañares, L.; Brouard, M.; Burak, I.; Fujimura, Y.; Short, J.; Simons, J.P., *Chem. Phys. Lett.* **1996**, *262*, 589; (c) Alexander, A.J.; Aioz, F.J.; Bañares, L.; Brouard, M.; Short, J.; Simons, J.P., *J. Phys. Chem. A* **1997**, *101*, 7544.
62. Felder, P.; Haas, B.-M.; Huber, J.R., *Chem. Phys. Lett.* **1991**, *186*, 177.
63. Springsteen, L.L.; Satyapal, S.; Matsumi, Y.; Dobeck, L.M.; Houston, P.L., *J. Phys. Chem.* **1993**, *97*, 7239.
64. Shafer, N.; Tonokura, K.; Matsumi, Y.; Tasaki, S.; Kawasaki, M., *J. Chem. Phys.* **1991**, *95*, 6218.
65. Hansico, T.F.; Kummel, A.C., *J. Phys. Chem.* **1993**, *97*, 7242.
66. Hopper, D.G., *J. Chem. Phys.* **1984**, *80*, 4290.
67. Brown, A.; Jimeno, P.; Balint-Kurti, G.G., *J. Phys. Chem. A* **1999**, *103*, 11089.
68. Mo, Y.; Suzuki, T., *J. Chem. Phys.* **1998**, *109*, 4691.

Downloaded by STANFORD UNIV GREEN LIBR on September 21, 2012 | http://pubs.acs.org
Publication Date: October 18, 2000 | doi: 10.1021/bk-2001-0770.ch016

## Chapter 16

# Femtosecond Time-Resolved Photoelectron Imaging

**Toshinori Suzuki[1], Li Wang, and Hiroshi Kohguchi**

**Institute for Molecular Science, Myodaiji, Okazaki 444-8585, Japan**

Femtosecond time-resolved photoelectron imaging (FS-PEI) was applied to ultrafast dephasing processes in pyrazine. For $S_1$ state, known as the best example for intermediate case in radiationless transition, FS-PEI visualized the decay of optically-prepared singlet character in 100 ps and corresponding build-up of triplet character, for the first time. Photoexcitation to the $S_2$ state exhibited dephasing to $S_1$ within our time-resolution (400 fs) and subsequent decay to $S_0$ in 20 ps.

## Introduction

Molecular photodissociation dynamics has been studied extensively by measuring quantum state and scattering distributions of products.[1,2] However, undoubtedly, the most unambiguous experimental elucidation of reaction mechanism is by real-time observation of the reaction. The best example for it is femtosecond pump-probe fluorescence spectroscopy on non-adiabatic dissociation dynamics of NaI by Zewail and coworkers.[3,4]

In a pump-probe experiment, a probe pulse projects the wave packet motion on an excited state surface to a higher electronic state. Therefore, the prerequisite for this approach is precise knowledge on this higher state. However, most of higher excited states have complicated surface crossings and spectroscopic data on these states are very limited.

Considering this difficulty in pump-probe experiments between neutral states, photoelectron spectrocopy[5-9] seems more advantageous, since it projects the dynamics onto a cation potential that is accurately characterized by spectroscopy and/or computationally tractable. Other advantages of photoelectron spectroscopy are (1) capability of detecting both singlet and triplet states, enabling direct observation of intersystem crossing and internal conversion processes, (2) high sensitivity due to efficient collection of electrons by electromagnetic fields, and (3) applicability of ultrafast laser with fixed wavelength. As with Raman spectroscopy, a laser wavelength can be fixed while electron energies are dispersed to observe vibrational dynamics.

[1] Corresponding author (email: suzuki@ims.ac.jp).

Downloaded by STANFORD UNIV GREEN LIBR on September 21, 2012 | http://pubs.acs.org
Publication Date: October 18, 2000 | doi: 10.1021/bk-2001-0770.ch016

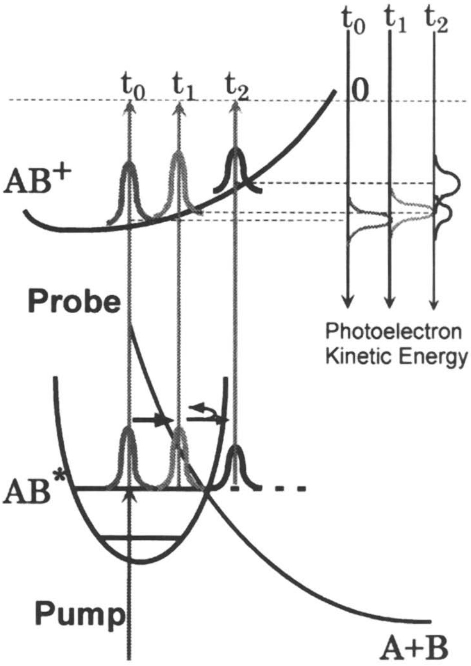

*Figure 1. Photoelectron spectroscopy of wave-packet motion.*

As for the analysis of photoelectron scattering distribution, the time-of-flight (TOF) method has been widely with pulsed light sources (Table I). However, a standard TOF method has a poor collection efficiency of electrons, which are also highly susceptible to stray fields. The magnetic bottle spectrometer developed by Kruit and Read significantly improved the efficiency, but angular resolution was sacrificed.[10] Photoelecton imaging (PEI) pioneered by Helm *et al.*,[11] on the other hand, achieves the highest collection efficiency of electrons while providing routine measurements of speed and angular distributions of photoelectrons.

This work combines PEI with femtosecond pump-probe technique, for the first time, and examines its performance through observation of ultrafast dephasing in an isolated molecule.

Since the pioneering work by Frad, Lahmani, Tramer and Tric,[12,13] the $S_1(^1B_{3u})$ state of pyrazine has been the best-known example of an intermediate case in molecular radiationless transition.[12-15] It was predicted[13] that coherent excitation of an intermediate case molecule exhibits biexponential fluorescence decay *I(t)*,

$$I(t) \propto \left|\langle s|\psi(t)\rangle\right|^2 = \sum_{n\neq m}\sum A_n A_m^* \alpha_n \alpha_m^* e^{-i(\varepsilon_n-\varepsilon_m)t} e^{-[(\gamma_n+\gamma_m)/2]t} + \sum_n |A_n|^2 |\alpha_n|^2 e^{-\gamma_n t}$$

where the fast decay is the ultrafast dephasing of an optically-prepared singlet state into the mixed singlet-triplet character (the first term of the above formula) and the slow decay is the depopulation of this mixed state (the second term).[12,13]

*Table I. Comparison of Photoelectron Spectroscopic Methods*

| ***Method*** | ***Resolution (meV @ 1eV)*** | ***Acceptance Angle (steradian)*** | ***Angular Dist. Measurement*** | ***CW light*** |
|---|---|---|---|---|
| ***Electrostatic*** | >5 | $10^{-2}$-$10^{-3}$ | Inefficient | OK |
| ***TOF*** | >3 | $10^{-3}$-$10^{-4}$ | Inefficient | No |
| ***Magnetic bottle*** | >10 | 2π | Not Possible | No |
| ***Imaging*** | >20 | 4π | Routine | OK |

The biexponential fluorescence decay of $S_1$ pyrazine was extensively studied in the 1980's, and lengthy debate ensured as to whether the fast component experimentally observed was due to dephasing predicted or Rayleigh-Raman scattering. With the development of picosecond laser spectroscopy, convincing evidences for dephasing ($\tau$~100ps) have been obtained,[16-21] and the consistency was also found with molecular eigenstate spectroscopy pioneered by Kommandeur, Meerts and coworkers.[22,23] However, it is noted that these works only observed time-evolution of the singlet character of the excited state, $|\langle s|\psi(t)\rangle|^2$, and the dynamics in the triplet manifold, $|\langle l|\ \psi(t)\rangle|^{2}$ has not been observed. The present work revisits this classic problem by femtosecond time-resolved photoelectron imaging and sheds light on the dark triplet manifold.

Internal conversion from $S_2$ state of pyrazine has been considered in a pioneering theoretical work on femtosecond photoelectron spectroscopy by Seel and Domke.[24] Although our experimental time-resolution (450 fs) is much lower than the estimated electronic dephasing time of 30 fs,[24] we applied FS-PEI to this problem and attempted to extract dynamical information.

## Experimental

### A. [1+2'] ionization of pyrazine via $S_1$ state

A solid-state femtosecond laser system consists of a diode-pumped Ti:sapphire oscillator, 10Hz YAG-pumped Ti:sapphire regenerative amplifier, and optical parametric amplifier. Tunable UV light ($\lambda$< 323 nm) and the second harmonic (396 nm) of Ti:sapphire fundamental were optically delayed and irradiated onto the molecular beam. The cross correlation of the pump-probe pulses was about 400 fs. The pump pulse excites pyrazine in a molecular beam 0.3-3% seeded in He (a stagnation pressure 1 atm to the vacuum) up to the $S_1$ $0^0$ level and a probe pulse further ionizes them. The photoelectrons are accelerated by an electric field parallel to the molecular beam and projected onto a position-sensitive imaging detector. The acceleration field provides two-dimensional space focussing, so that the image only reflects the linear momentum of the electron parallel to the detector face.[25] The field-free region (44 cm) of the TOF spectrometer was shielded with a $\mu$-metal tube to avoid external magnetic fields that might otherwise deflect the electron trajectories. The imaging detector consists of a microchannel plate (MCP), a phosphor screen, and a charge-coupled device (CCD) camera. The video signal (25 frames/sec) is transferred to a computer on which a real-time image processing calculates the center of gravity of each light spot to enhance imaging resolution and counts the number of electrons arrived at each pixel over a number of laser shots. The electron images thus

Downloaded by STANFORD UNIV GREEN LIBR on September 21, 2012 | http://pubs.acs.org
Publication Date: October 18, 2000 | doi: 10.1021/bk-2001-0770.ch016

obtained were inverted to electron speed-angular distribution by inverse Abel transforms.

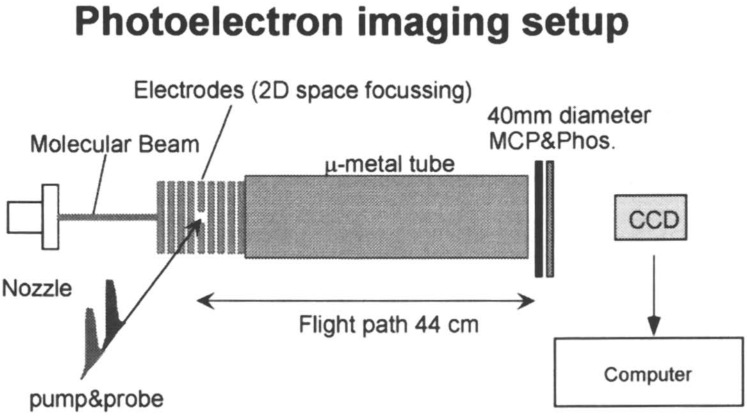
Photoelectron imaging setup
Electrodes (2D space focussing)
40mm diameter MCP&Phos.
Molecular Beam
μ-metal tube
CCD
Nozzle
Flight path 44 cm
Computer
pump&probe

*Figure 2. Schematic diagram of photoelectron imaging apparatus.*

The probe wavelength of 396 nm energetically allows two-photon ionization from both the singlet and triplet states (IP=74 908 cm$^{-1}$).[26] The power density of our pump laser at the interaction region was less than $10^{10}$ W/cm$^2$, while that of the probe laser was about $5 \times 10^{10}$ W/cm$^2$. For these power densities, ponderomotive shift of the photoelectron kinetic energies and the alignment of ground-state molecule in the laser field can be neglected. We also measured the $S_1 \leftarrow S_0$ spectrum of pyrazine in the molecular beam by a nanosecond laser and ascertained good rovibrational cooling and negligible clustering. The bandwidth of our pump pulse (110 cm$^{-1}$) does not allow selection of rotational lines but excludes excitation to other vibronic levels than $0^0$.

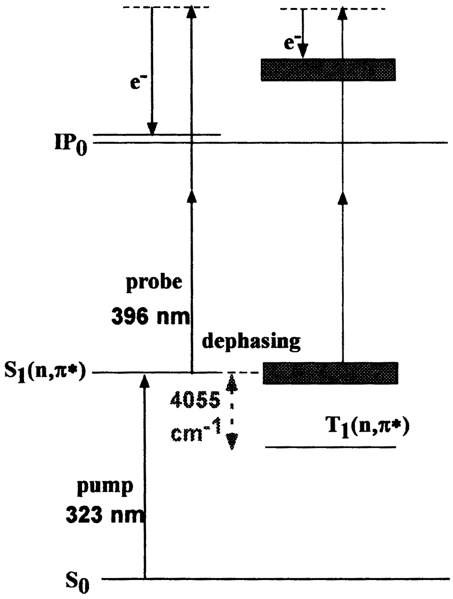
e⁻
e⁻
IP0
probe
396 nm
dephasing
S1(n,π*)
4055
cm-1
T1(n,π*)
pump
323 nm
S0

*Figure 3. [1+2'] REMPI of pyrazine.*

Downloaded by STANFORD UNIV GREEN LIBR on September 21, 2012 | http://pubs.acs.org
Publication Date: October 18, 2000 | doi: 10.1021/bk-2001-0770.ch016

### B. [1+1'] ionization of pyrazine *via* $S_2$ state

The third harmonic (262 nm) of Ti:sapphire laser was used to excited pyrazine to $S_2$ state and 220 nm light ionized them. The probe pulse was generated by non-linear mixing of the UV light from OPA with the Ti:sapphire fundamental. All other experimental procedures are the same with the $S_1$ case.

## Results and Discussion

### A. $S_1$ State of Pyrazine

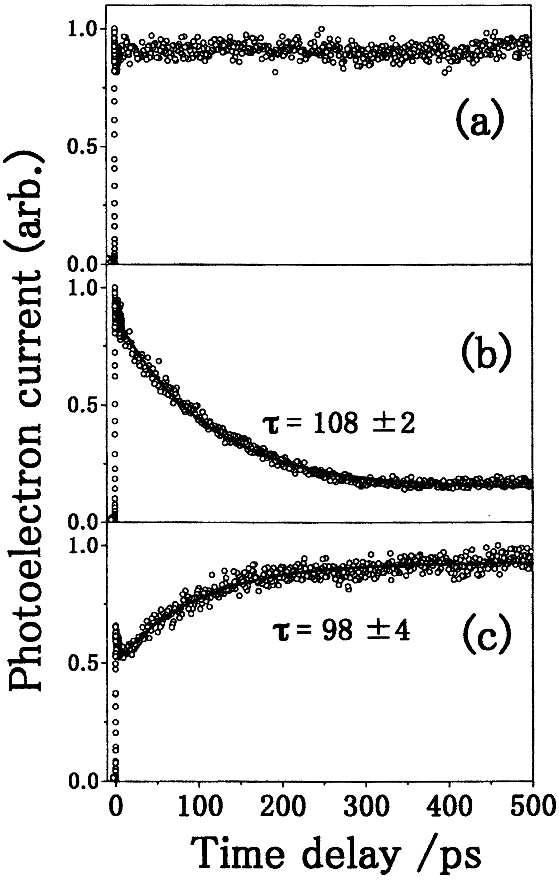

*Figure 4. (a) Time dependence of total photoelectron signal in femtosecond [1+2'] REMPI of pyrazine via the $S_1[^1B_{3u}(n,\pi^*)]$ $0^0$ level. The pump and probe wavelengths are 323 and 396 nm, respectively. (b) Photoelectron signal for the kinetic energy E > 630 meV. (c) Photoelectorn signal for the kinetic energy E< 630 meV.*

Downloaded by STANFORD UNIV GREEN LIBR on September 21, 2012 | http://pubs.acs.org
Publication Date: October 18, 2000 | doi: 10.1021/bk-2001-0770.ch016

Figure 4 shows the photoelectron intensity observed as a function of time delay in [1+2'] ionization of pyrazine *via* $S_1$ State. As seen in Fig. 4(a), the total electron current (= integral photoionization cross section) shows no time-dependence, which apparently contradicts the fast fluorescence decay data reported previously.[16-21] Note, however, that photoionization can occur both from the singlet and triplet manifolds. Therefore, Fig. 4(a) simply implies that population decay from the mixed singlet-triplet states does not occur in this time range. The depopulation of the mixed states takes place in 300-400 ns.[27]

Figure 5 shows the snapshots of photoelectron speed and angular distributions. Inspection of these images immediately reveals the ionization from the singlet and triplet characters as the outer and inner rings, respectively. Ionization from the triplet results in low photoelectron energy, because the triplet states isoenergetic to the singlet have large vibrational energies (4055 $cm^{-1}$ in the case of $T_1$),[28] and Franck-Condon overlap favors ionization to highly vibrationally-excited states in the cation. (The bright spot in the middle of the image is due to the low energy tail of the inner ring. Photoelectrons with near zero kinetic energy are concentrated in the center of the image with a weighting factor that scales with the kinetic energy of electron or the image radius squared.) The singlet character decays in less than 200 ps, and the triplet character builds up correspondingly. The selective measurements of time-dependent singlet and triplet characters were performed by observing light spots in the outer and inner parts of images on the phosphor with masks and a photomultiplier tube. The results are shown in Fig. 4(b) and 4(c). The high energy electron decayed with τ = 108±2 ps, in excellent agreement with fast fluorescence decay observed previously, while the low energy electron increased correspondingly with τ = 98±4 ps (Fig. 4(c)).

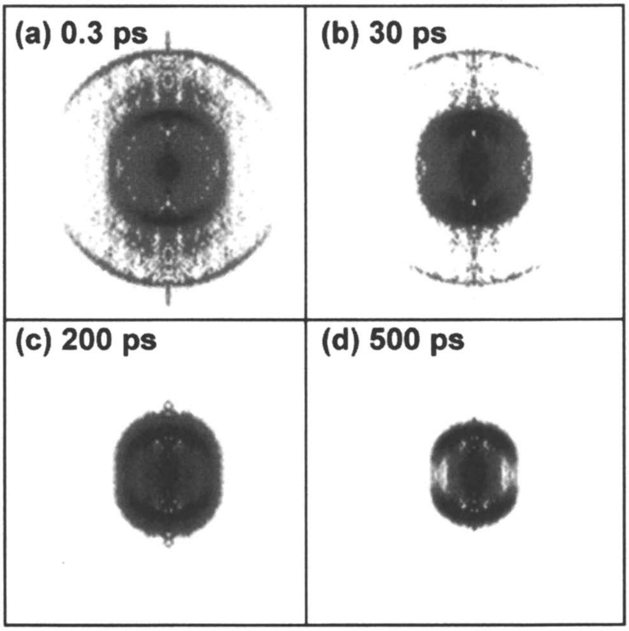

*Figure 5. Inverse Abel transforms (512 × 512 pixels) of photoelectron images of [1+2'] REMPI of pyrazine via the $S_1[^1B_{3u}(n,\pi^*)]$ $0^0$ level at the time delays of (a) 0.3, (b) 30, (c) 200, and (d) 500 ps. The original images were integrated for 36 000 laser shots.*

Downloaded by STANFORD UNIV GREEN LIBR on September 21, 2012 | http://pubs.acs.org
Publication Date: October 18, 2000 | doi: 10.1021/bk-2001-0770.ch016

The result clearly demonstrates that the coherent decay of singlet character is compensated by the build-up of the triplet character; $S_{coh}(t)$=-$L_{coh}(t)$.[13] This is because the decay from the excited state manifold to the ground state is negligible in this time range. Similar experiment on pyrazine-$d_4$ revealed essentially the same behavior with slightly shorter dephasing lifetime, $\tau$ = 80 ps.

El-Sayed has speculated that efficient intersystem crossing in pyrazine ($\Phi_{ISC}$=1) is mediated by $T_2(\pi,\pi^*)$, since direct spin-orbit coupling is not allowed for $S_1(n,\pi^*)$ - $T_1(n,\pi^*)$ but allowed for $S_1(n,\pi^*)$-$T_2(\pi,\pi^*)$.[29] This idea has been widely accepted by researchers, although it has not been fully proved. Quantum mechanical electronic structure calculations have been performed on pyrazine,[30,31] but the energies of $^{1,3}(n,\pi^*)$ states in diazine are strongly influenced by through-bond interaction between the two nitrogen atoms.[32,33] *Ab initio* calculations considering extensive configuration interaction including $\sigma$-orbitals are required to answer this question.[34]

Careful inspection of the snapshots reveals that the ring due to triplet states shrinks in time; the time delay of 30 ps is a critical point where the two rings in the triplet part are equal in intensity. This suggests the possibility that relaxation occurs in the triplet manifold. The time evolution of the system can be examined more quantitatively in photoelectron kinetic energy distributions presented in Fig. 6. The feature at 160 meV appears instantaneously with the light pulse, but it is overtaken by the growth of another peak at 100 meV. The peak at 100 meV is assigned to ionization from $T_1(n,\pi^*)$. If the peak at 160 meV is assigned to ionization from $T_2(\pi,\pi^*)$, the time evolution of $S_1(n,\pi^*)$, $T_2(\pi,\pi^*)$, and $T_1(n,\pi^*)$ provides experimental evidence for intersystem crossing mediated by $T_2(\pi,\pi^*)$ suggested by El-Sayed.[28]

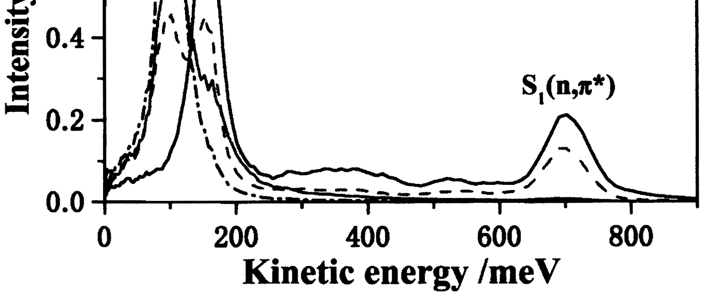

*Figure 6. Photoelectron kinetic energy distributions in femtosecond [1+2'] REMPI of pyrazine via the $S_1[^1B_{3u}(n,\pi^*)]$ $0^0$ level at the time delays of 0.3, 30, 200, and 500 ps.*

Downloaded by STANFORD UNIV GREEN LIBR on September 21, 2012 | http://pubs.acs.org
Publication Date: October 18, 2000 | doi: 10.1021/bk-2001-0770.ch016

However, assignment of the peak at 160 meV to a higher excited (Rydberg) state resonant by $h\nu$(323 nm)+ $h\nu$(396 nm) can not be excluded. We are performing [1+1'] photoelectron imaging to examine it further.

The angular anisotropy of the photoelectron distribution slightly varied with time delay, but the $\beta$ values at 60 ps were 1.1 and 1.7 for the singlet and triplet channels, respectively. As Piancastelli *et al.* have shown for one-photon ionization of pyrazine from the ground state,[35] the anisotropy is expected to change with photoelectron energy, especially for the ejection of $\pi$ electrons. Therefore, the interpretation of the anisotropy observed at one ionization wavelength is not possible at the point.

Finally, although our experiment employed a static electric field (< 700 V/cm) to extract photoelectrons toward the detector, the Stark effect on the short time dynamics of pyrazine can be excluded. Previous works have shown that noticeable Stark shift of the level structure is only induced by an order of magnitude higher field strength (>10kV/cm).[35,36] The dephasing rate we obtained is in excellent agreement with the previous fluorescence decay data under field free conditions.[16-21]

### B. $S_2$ state of Pyrazine

The second excited singlet state of pyrazine $S_2[^1B_{2u}(\pi,\pi^*)]$ is located 7000 cm$^{-1}$ above the $S_1[^1B_{3u}(n,\pi^*)]$ state. The $S_2(\pi,\pi^*)\leftarrow S_0$ absorption band is broad due to ultrafast $S_2 \rightarrow S_1$ electronic dephasing. Seel and Domcke have reported the theory of femtosecond time-resolved photoelectron spectroscopy for this dephasing process.[24]

We excited pyrazine in a molecular beam with 262 nm light to the vicinity of the zero vibrational level in $S_2(\pi,\pi^*)$ and subsequently ionized the excited molecules with 220 nm light. As shown in Fig. 7, the total photoelectron (and parent mass) signal decayed with the lifetime of 22±1 ps. Similar measurement on pyrazine-d4 showed the lifetime of 39±1 ps.

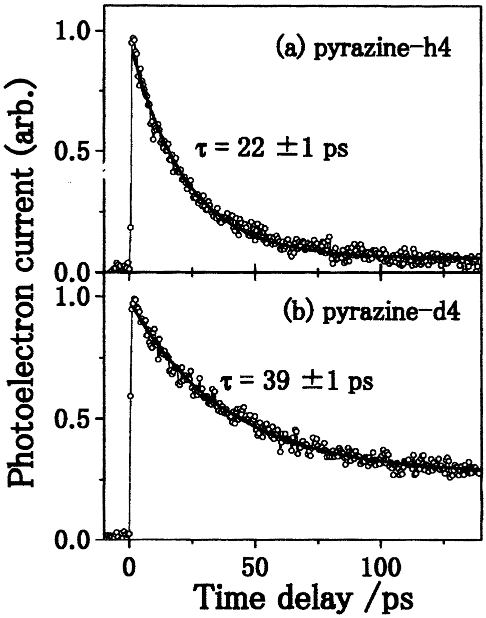

*Figure 7. The decay of total photoelectron intensity in [1+1'] REMPI via $S_2$ state of (a) pyrazine and (b) deuterated pyrazine.*

Downloaded by STANFORD UNIV GREEN LIBR on September 21, 2012 | http://pubs.acs.org
Publication Date: October 18, 2000 | doi: 10.1021/bk-2001-0770.ch016

The observed lifetime for pyrazine-h4 is in agreement with the lifetime, < 50 ps, of the higher vibronic level of $S_1$ studied by Yamazaki *et al*, [18] from which we assign the observed decay to the electronic relaxation from the $S_1$ manifold after ultrafast dephasing from $S_2$, although the latter is undetectable with our apparatus. The intersystem crossing yield from $S_1$ pyrazine is known to sharply fall off near 280 nm,[18] so the observed decay is ascribed to $S_1 \rightarrow S_0$ internal conversion. The longer lifetime observed for pyrazine-d4 is ascribed to the reduction of the Franck-Condon overlap for the accepting modes between $S_1$ and $S_0$.

Downloaded by STANFORD UNIV GREEN LIBR on September 21, 2012 | http://pubs.acs.org
Publication Date: October 18, 2000 | doi: 10.1021/bk-2001-0770.ch016

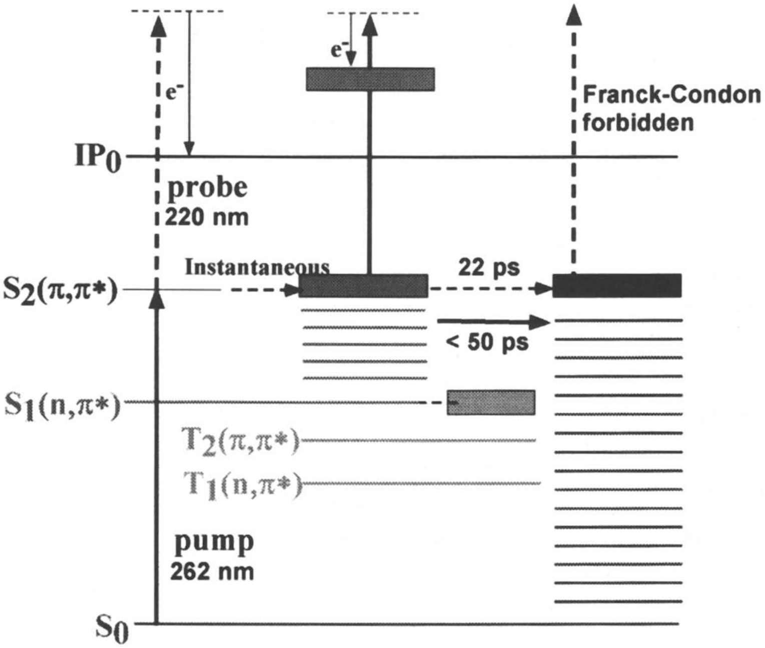

*Figure 8. Instantaneous formation of $S_1$ from $S_2$ and its subsequent decay to $S_0$.*

## Conclusion and Outlook

The present work demonstrated high performance of time-resolved photoelectron imaging for the study of excited state dynamics. The two-dimensional position sensitive detection allows visualization of speed-angular distribution of photoelectrons routinely, and the pump-probe technique provides snap-shots of the distribution as a function of time.

The energy resolution is enhanced by center-of-gravity calculation for light spots captured by a CCD camera, and thresholding/counting method corrects non-uniform sensitivity of the position sensitive detector. The energy resolution $\Delta E/E=0.05$ is easily achievable with this method. Modification of an electrode design will provide ΔE/E<0.02.

Introducing VUV femtosecond probe laser, excited wavefunction can be projected to various electronic states of cation, by which time-dependent electron configuration in the course of reaction can be extracted. In addition, the high harmonics of femtosecond lasers will allow excitation of molecule to the dissociative states in the cation, where the coincidence measurement of electrons and daughter ions provides photoelectron scattering distribution in the 'molecular frame' (fixed-in-space technique).[38] This technique will eliminate angular averaging of photoelectron distribution in the laboratory frame and provide extremely detailed information on the excited state wavefunctions. With these extensions, time-resolved photoelectron imaging will be an extremely useful tool for the study of chemical dynamics in isolated molecules and molecular clusters.

Downloaded by STANFORD UNIV GREEN LIBR on September 21, 2012 | http://pubs.acs.org
Publication Date: October 18, 2000 | doi: 10.1021/bk-2001-0770.ch016

## Acknowledgment

This work was supported by Grant-in-Aid from the Ministry of Education, Science, Sports and Culture of Japan (Nos. 09440208, 11440183, and 11359005). We also acknowledge support from PRESTO administrated by Japan Science and Technology Corporation.

## References

1. Bush, G.E.; Wilson, K.R. *J. Chem. Phys.* **1972**, *7*, 3626; *ibid.* 3638.
2. Schinke, R. *Photodissociation Dynamics, Cambridge Monographs on Atomic, Molecular and Chemical Physics*; Cambridge University Press, Cambridge, 1993.
3. Rose, T.S.; Rosker, M.J.; Zewail, A.H. *J. Chem. Phys.* **1989**, *91*, 7415.
4. Zewail, A.H. *Femtochemistry I and II*, World Scientific, Singapore, 1994.
5. Dobber, M.R.; Buma, W.J.; de Lange, C.A. *J. Phys. Chem.* **1995**, *99*, 1671.
6. Cyr D.R.; Hayden C.C. *J. Chem. Phys.* **1996**, *104*, 771.
7. Greenblatt B.J.; Zanni M.T.; Neumark D.M. *Science* **1997**, *276*, 1675.
8. Blanchet V.; Stolow A. *J. Chem. Phys.* **1998**, *108*, 4371.
9. Schultz T.; Fischer I. *J. Chem. Phys.* **1998**, *109*, 5812.
10. Kruit, P.; Read, F.H. *J. Phys. E: Sci. Instrum.* **1983**, *16*, 313.
11. Helm, H.; Bijerre, N.; Dyer, M.J.; Huestis, D.L.; Saeed, M. *Phys. Rev. Lett.* 1993, *70*, 3221.
12. Frad, A.; Lahmani, F.; Tramer, A.; Tric, C. *J. Chem. Phys.* **1974**, *60*, 4419.
13. Lahmani, F.; Tramer, A.; Tric, C. *J. Chem. Phys.* **1974**, *60*, 4431.
14. Bixon, M.; Jortner J. *J. Chem. Phys.* **1968**, *48*, 715.
15. Avouris, P.; Gelbert, W.M.; El-Sayed, M.A. *Chem. Rev.* **1977**, *77*, 793 and references therein.
16. McDonald, D.E.; Fleming, G.R.; Rice, S.A. *Chem. Phys.* **1981**, *60*, 335.

17. Okajima, S.; Saigusa, H.; Lim, E. *J. Chem. Phys.* **1982**, *76*, 2096.
18. Yamazaki, I.; Murao, T.; Yamanaka, T.; Yoshihara, K. *Faraday Discuss. Chem. Soc.* **1983**, *75*, 395.
19. Lorincz, A.; Smith, D.D.; Novak, F.; Kosloff, R.; Tannor, D.J.; Rice, S.A. *J. Chem. Phys.* **1985**, *82*, 1067.
20. Knee, J.L.; Doany, F.E.; Zewail, A.H. *J. Chem. Phys.* **1985**, *82*, 1042.
21. Felker P.M.; Zewail, A.H. *Chem. Phys. Lett.* **1986**, *128*, 221.
22. van der Meer, B.J.; Jonkman, H. Th.; Kommandeur, J.; Meerts, W.L.; Majewski, W.A. *Chem. Phys. Lett.* **1982**, *92*, 565.
23. de Lange, P.J.; Drabe, K.E.; Kommandeur, J. *J. Chem. Phys.* **1986**, *84*, 538.
24. Seel M.; Domcke, W. *J. Chem. Phys.* **1991**, *95*, 7806.
25. Eppink, A.T.J.B.; Parker, D.H. *Rev. Sci. Instrum.* **1997**, *68*, 3477.
26. Zhu, L.; Johnson, P. *J. Chem. Phys.* **1993**, *99*, 2322.
27. Ohta, N. *J. Phys. Chem.* **1996**, *100*, 7298 and references therein.
28. Innes, K.K.; Giddings, L.E. Jr. *Discuss. Faraday Soc.* **1963**, *35*, 192.
29. El-Sayed, M.A. in *Molecular Luminescence*, edited by E.C. Lim, Benjamin, New York, 1969.
30. Hackmeyer, M.; Whitten, J.L. *J. Chem. Phys.* **1971**, *54*, 3739.
31. Wadt, W.R.; Goddard, W.A.; Dunning, T.H. *J. Chem. Phys.* **1976**, *65*, 438.
32. Hoffmann, R. *Acc. Chem. Res.* **1971**, *4*, 1 and references therein.
33. Gleiter, R.; Heilbronner, E.; Hornung, V. *Helv. Chim. Acta* **1972**, *55*, 255.
34. CASSCF/DZ level of calculations provide incorrect energetic ordering of $^3(\pi,\pi^*)$ and $^3(n,\pi^*)$ states.
35. Piancastelli, M.N.; Keller, P.R.; Taylor, J.W.; Grimm, F. A.; Carlson, T.A. *J. Am. Chem. Soc.* **1982**, *105*, 4349.
36. Okruss, M.; Penn, F.; Hase, A. *J. Mol. Struct.* **1995**, *348*, 119.
37. Ohta N.; Takemura, T. *Chem. Phys. Lett.* **1990**, *169*, 611.
38. Shigemasa, E.; Adachi, J.; Oura, M.; Yagishita, A. *Phys. Rev. Lett.* **1995**, *74*, 359.

Downloaded by STANFORD UNIV GREEN LIBR on September 21, 2012 | http://pubs.acs.org
Publication Date: October 18, 2000 | doi: 10.1021/bk-2001-0770.ch016

# Chapter 17

# Photoisomerization and Photodissociation Dynamics of the NCN, CNN, and HNCN Free Radicals

Ryan T. Bise, Alexandra A. Hoops, Hyeon Choi,
and Daniel M. Neumark[1]

Department of Chemistry, University of California, Berkeley, CA 94720
and Chemical Sciences Division, Lawrence Berkeley
National Laboratories, Berkeley, CA 94720

The photodissociation spectroscopy and dynamics of the NCN, CNN and HNCN radicals have been investigated by fast beam photofragment translational spectroscopy. For all three radicals, $N_2$ loss was determined to be the dominant dissociation channel. However, minor CN channels were observed for the NCN and CNN radicals. Dissociation energies have been measured directly for each radical, providing substantially improved heats of reaction. The translational energy distributions for NCN and HNCN show well-resolved structure corresponding to vibrational excitation of the $N_2$ photofragment. For CNN, the vibrational structure of the $N_2$ photoproduct could not be resolved due to extensive rotational excitation of this fragment. The photofragment branching ratios and translational energy distributions suggest that the NCN and HNCN radical dissociate through cyclic intermediate states of approximate $C_{2v}$ symmetry while the CNN radicals dissociate via bent intermediate states.

## I. Introduction

The NCN, CNN, and HNCN radicals have all been proposed as important intermediates in both combustion and interstellar chemistry.(1-4) The CNN and HNCN radicals have been suggested as possible intermediates in the formation of NO, providing low-energy pathways for the cleavage of molecular nitrogen to produce N atoms, which are subsequently oxidized to produce nitric oxide.(2) In an effort to further characterize the potential energy surfaces of these radicals, we have

---

[1] Corresponding author.

In Imaging in Chemical Dynamics; Suits, A., et al.;
ACS Symposium Series; American Chemical Society: Washington, DC, 2000.

investigated their photodissociaton dynamics. These radicals possess multiple low-lying excited states and fragmentation pathways, see Table I, providing potentially rich systems for photodissociation measurements. While the formation of molecular nitrogen from CNN seemingly involves simple bond cleavage, substantial bond rearrangement is required for the HNCN and NCN radicals. Using the technique of fast beam photofragment translational spectroscopy we have obtained structured photodissociation cross-sections, product branching ratios, and detailed internal energy distributions, yielding accurate dissociation energies and insight into isomerization pathways and fragmentation mechanisms of these radicals.

## II. Experimental

The fast beam photofragment translational spectrometer, Figure 1, has been described in detail elsewhere;(5-7) only a brief description will follow. In this experiment, we generate a clean source of neutral radicals by mass-selectively photodetaching a beam of stable negative ions. The neutrals are then photodissociated by a second laser.

Vibrationally and rotationally cold negative ions are prepared using a pulsed discharge source,(8) then accelerated to 8 keV, and separated temporally by a Bakker time-of-flight (TOF) mass spectrometer.(9,10) The ion of interest is selectively photodetached by a pulsed laser. To produce vibrationally cold neutral radicals, the detachment energy, based upon the recent photoelectron studies of Clifford *et al.*(11,12) and Taylor *et al.*(13), is set ≤ 100 meV above threshold. In the case of NCN, a detachment energy of 2.8 eV was selected to produce NCN in the $\tilde{X}\,^3\Sigma_g^-$ state exclusively, while a detachment energy of 4.03 eV was used to populate both the $\tilde{X}\,^3\Sigma_g^-$ and $\tilde{a}\,^1\Delta_g$ states.(14) Undetached ions are deflected out of the beam path.

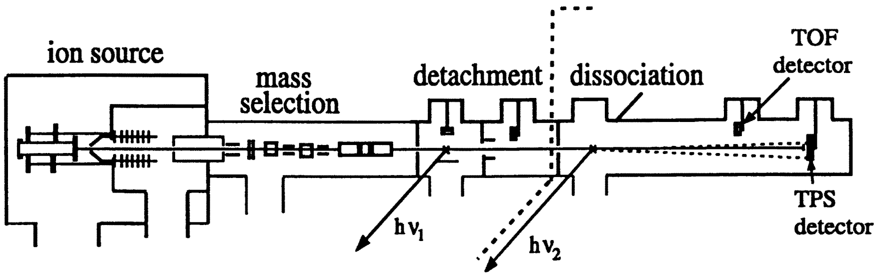

*Figure 1. Fast radical beam translational spectrometer. The dotted line separates the radical production section on the left from the photodissociation experiment on the right.*

In the dissociation region, the neutrals are intersected by an excimer-pumped dye laser with frequency doubling capabilities. When resonant with a predissociative transition, a fraction of the neutral molecules dissociate yielding photofragments detected directly by either the retractable TOF or TPS (time and position sensing) microchannel plate detector assemblies in Figure 3. An aluminum strip is positioned at the center of each detector to prohibit any undissociated radicals from impacting the detector, so that any observed signal is from recoiling photofragments.

The spectroscopy of the dissociative electronic state is examined by monitoring the total yield of photofragments at the TOF detector as the dissociation laser is scanned. Once the dissociation spectroscopy has been examined, a second type of experiment, which probes the dissociation dynamics, can be performed. In this detection scheme both photofragments from a single parent radical are detected in coincidence using a time-and-position sensitive (TPS) detector of the type developed by de Bruijn and Los,(15) located at either 1 or 2m from the interaction region. Our implementation of this detection scheme has been described in detail elsewhere.(5,6) The TPS detector records the positions and difference in time of arrival of the two photofragments from a single dissociaton. This information is then used to determine the photofragment masses, their relative translational energy $E_T$, and the scattering angle $\theta$ between the relative velocity vector and the electric vector of the polarized dissociation laser. The photofragment mass resolution is m/Δm ≈ 10 while the translational energy resolution for these experiments is $\Delta E_T / E_T = 2.0$.

## III. Results

### A. NCN

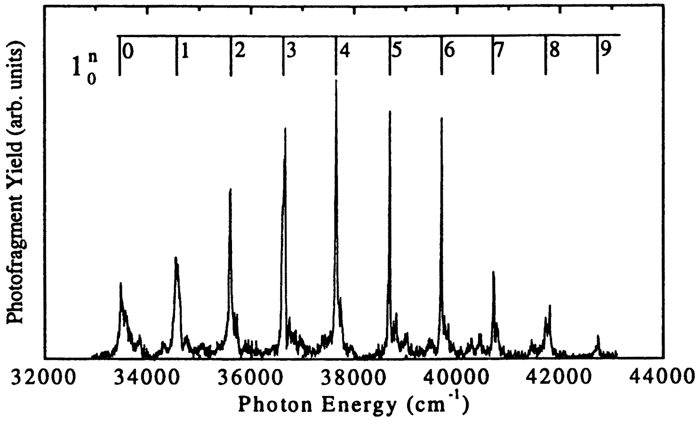

*Figure 2. Photofragment Yield Spectrum of the* $\tilde{B}\,^3\Sigma_u^- \leftarrow \tilde{X}\,^3\Sigma_g^-$ *band. The vibrational comb denotes the symmetric stretch* $1_0^n$ *progression.*

### *1. Photofragment Yield Spectrum*

The photofragment yield (PFY) spectra for the $\tilde{B}\,^3\Sigma_u^- \leftarrow \tilde{X}\,^3\Sigma_g^-$, $\tilde{c}\,^1\Pi_u \leftarrow \tilde{a}\,^1\Delta_g$, and $\tilde{d}\,^1\Delta_u \leftarrow \tilde{a}\,^1\Delta_g$ bands of NCN have been described in detail in a previously.(14) Briefly, the PFY spectra of the $\tilde{B}\,^3\Sigma_u^- \leftarrow \tilde{X}\,^3\Sigma_g^-$ band is shown in Figure 2, covering 33000-43000 cm$^{-1}$. We observe a progression with a peak spacing of ≈ 1050 cm$^{-1}$, in accordance with absorption studies by Kroto and coworkers(16) and by Milligan *et al.*(17) This progression has been assigned to the symmetric stretch ($1_0^n$). The relative intensities of the PFY transitions are similar to those for the matrix absorption measurements of Milligan *et al.*,(17) suggesting that the quantum yield for photodissociaton is ~ 1.

By increasing the photodetachment energy to 4.03 eV, both the $\tilde{X}\,^3\Sigma_g^-$ and $\tilde{a}\,^1\Delta_g$ states of the NCN radical are populated with an intensity ratio of approximately 2:1,(13) allowing us to probe the photodissociation spectroscopy of the singlet manifold. An intense feature centered around 30045 cm$^{-1}$, Figure 3a, agrees well with the $\tilde{c}\,^1\Pi_u \leftarrow \tilde{a}\,^1\Delta_g$ (000-000) band observed previously by Kroto.(18) Additional

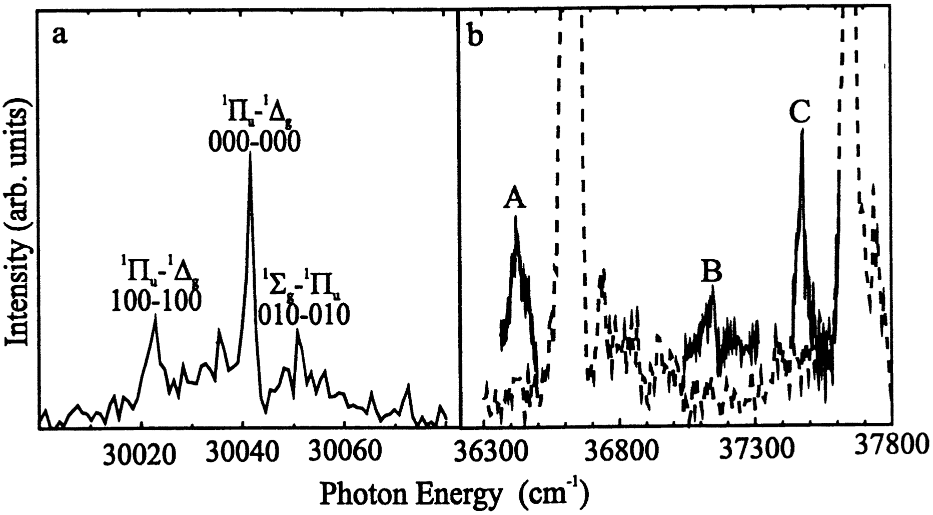

*Figure 3a) PFY spectra of the $\tilde{c}\,^1\Pi_u \leftarrow \tilde{a}\,^1\Delta_g$ origin band. b) PFY spectra from 36,300 to 37,800 cm$^{-1}$. The solid line denotes features observed with a photodetachment energy of 4.03 eV while the dashed line indicates features observed with a photodetachment energy of 2.82 eV. The features A, B and C are assigned to the $\tilde{d}\,^1\Delta_u \leftarrow \tilde{a}\,^1\Delta_g$ band.*

vibronic transitions are also labeled. Higher energy singlet transitions were observed between 36200 to 37800 cm$^{-1}$, labeled A, B and C in Figure 3b. These transitions have been assigned to the $\tilde{d}\,^1\Pi_u \leftarrow \tilde{a}\,^1\Delta_g$ band by Kroto and coworkers(16) based upon kinetic information and vibrational structure. Our photodetachment technique confirms that these transitions originate form the $\tilde{a}\,^1\Delta_g$ state. Despite extensive efforts, we have been unable to detect dissociation signal from the $\tilde{A}\,^3\Pi_u \leftarrow \tilde{X}\,^3\Sigma_g^-$ band, consistent with the long radiative lifetime of 185 ns reported by Smith *et al.*(19)

**Table I. Heats of Reaction at 0 K for the NCN, CNN, and HNCN radicals.**

| *Reactant* | | *Product Channel* | *$\Delta H_{rxn,0}$ (eV)* |
|---|---|---|---|
| NCN ($\tilde{X}\,^3\Sigma_g^-$) | | | |
| | (Ia) | $N_2(X^1\Sigma_g^+) + C(^3P)$ | 2.54 ± 0.03 |
| | (Ib) | $N_2(X^1\Sigma_g^+) + C(^1D)$ | 3.80 ± 0.03 |
| | (Ic) | $CN(X^2\Sigma^+) + N(^4S)$ | 4.56 ± 0.03 |
| CNN ($\tilde{X}\,^3\Sigma^-$) | | | |
| | (IIa) | $N_2(X^1\Sigma_g^+) + C(^3P)$ | 1.22 ± 0.03 |
| | (IIb) | $N_2(X^1\Sigma_g^+) + C(^1D)$ | 2.47 ± 0.03 |
| | (IIc) | $CN(X^2\Sigma^+) + N(^4S)$ | 3.24 ± 0.03 |
| | (IId) | $N_2(X^1\Sigma_g^+) + C(^1S)$ | 3.90 ± 0.03 |
| | (IIe) | $CN(A^2\Pi) + N(^4S)$ | 4.39 ± 0.03 |
| | (IIf) | $CN(X^2\Sigma^+) + N(^2D)$ | 5.62 ± 0.03 |
| HNCN($\tilde{X}\,^2A''$) | | | |
| | (IIIa) | $N_2(X^1\Sigma_g^+) + CH(X^2\Pi)$ | 2.78 ± 0.03 |
| | (IIIb) | $HCN(\tilde{X}\,^1\Sigma^+) + N(^4S)$ | 2.87 ± 0.05 |
| | (IIIc) | $HNC(\tilde{X}\,^1\Sigma^+) + N(^4S)$ | 3.45 ± 0.05 |
| | (IIId) | $N_2(X^1\Sigma_g^+) + CH(a^4\Sigma^-)$ | 3.50 ± 0.03 |
| | (IIIe) | $H(^2S) + NCN(\tilde{X}\,^3\Sigma_g^-)$ | 3.72 ± 0.04 |
| | (IIIf) | $NH(X^3\Sigma^-) + CN(X^2\Sigma^+)$ | 4.86 ± 0.06 |

All values are based upon this work and NIST-JANAF thermochemical tables.(20)

### 2. *Photofragment mass distributions*

At the photon energies explored in this study three possible dissociation channels are accessible, see Table I. All three channels are accessible following excitation of the $1_0^n$, $n \geq 4$ transitions of the $\tilde{B}\,^3\Sigma_u^- \leftarrow \tilde{X}\,^3\Sigma_g^-$ band. The photofragment masses are calculated from the relative recoil distance of the coincident photofragments from the center of the neutral beam. This enables us to largely, but not completely, distinguish C + $N_2$ from N + CN products, since our product mass resolution is only ~ 10. At excitation energies less than 4.9 eV, photofragment mass ratios of 12:28 were observed, consistent with products C + $N_2$. To improve our detection efficiency of low energy photofragments, the recoil flight length was increased from 1 to 2 m (see ref. (14)). At photon energies > 4.9 eV, the photofragment mass ratio of low translational energy fragments was found to be 14:26, indicating the onset of a new N + CN dissociation channel. The photofragment mass distributions were found to be 12:28 for the $\tilde{c}^1\Pi_u \leftarrow \tilde{a}^1\Delta_g$ and $\tilde{d}^1\Pi_u \leftarrow \tilde{a}^1\Delta_g$ bands at all recoil energies.

*3. Translational energy distributions*

The translational energy distributions for the $N_2$ + C mass channel resulting from

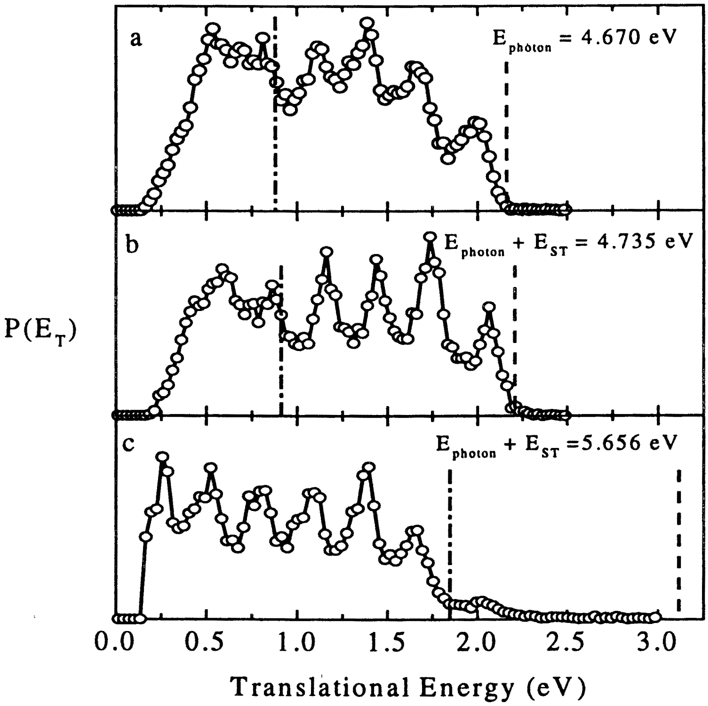

*Figure 4. $P(E_T)$ distributions for the $N_2$ + $C(^3P)$ channel of NCN resulting from the a) $\tilde{B}^3\Sigma_u^- \leftarrow \tilde{X}^3\Sigma_g^-$ b) $\tilde{c}^1\Pi_u \leftarrow \tilde{a}^1\Delta_g$ and c) $\tilde{d}^1\Delta_u \leftarrow \tilde{a}^1\Delta_g$ transitions. The dashed and dot-dashed vertical lines denote $E_T^{max}$ for $C(^3P)$ and $C(^1D)$ products. $E_{photon}$ denotes the photon energy and $E_{ST}$ is the singlet-triplet splitting = 1.010 ±0.010 eV.(13)*

excitation of the $\tilde{B}\,^3\Sigma_u^- \leftarrow \tilde{X}\,^3\Sigma_g^-$, $\tilde{c}\,^1\Pi_u \leftarrow \tilde{a}\,^1\Delta_g$ and $\tilde{d}\,^1\Pi_u \leftarrow \tilde{a}\,^1\Delta_g$ transitions are shown in Figures 4a, b, and c respectively. All three transitions display a sharp onset at high translational energy and well-resolved peaks separated by approximately 290 meV, corresponding to excitation of the $N_2$ product vibration. The full width at half maximum (FWHM) of each peak is approximately 150 meV with an asymmetric tail extending toward low translational energy. The $P(E_T)$ distributions for the $\tilde{B}\,^3\Sigma_u^- \leftarrow \tilde{X}\,^3\Sigma_g^-$ and $\tilde{c}\,^1\Pi_u \leftarrow \tilde{a}\,^1\Delta_g$ transitions become less resolved for low kinetic energy regions ($E_T < 0.8$ eV), while the $P(E_T)$ resulting from excitation of the $\tilde{d}\,^1\Pi_u \leftarrow \tilde{a}\,^1\Delta_g$ transition displays resolved structure to translational energies as low as 0.2 eV.

The steep falloff in intensity of the $P(E_T)$ distributions toward the high energy side is characteristic of the maximum available translational energy, $E_T^{max}$, corresponding to photofragments with zero internal energy. By subtracting this thermodynamic limit from the known photon energies, we can directly determine the dissociation energy, $D_0$. The $E_T^{max}$ values for the $\tilde{B}\,^3\Sigma_u^-$ $P(E_T)$ distributions yield $D_0 = 2.54 \pm 0.03$ eV. For the singlet manifold, the singlet-triplet splitting $E_{ST}(\tilde{a}\,^1\Delta_g\text{-}\tilde{X}\,^3\Sigma_g^-) = 1.010 \pm 0.010$ eV(13) is added to the photon energy. The $\tilde{c}\,^1\Pi_u$ state displays a sharp threshold at the $E_T^{max}$ for ground state $C(^3P)$ products while the $P(E_T)$ distribution for the $\tilde{d}\,^1\Pi_u$ state increases sharply near the threshold value for $C(^1D)$ products. The small shoulder which extends about 0.3 eV past this $E_T^{max}$ value in Figure 4c is due to a small contribution from a weak $\tilde{B}\,^3\Sigma_u^- \leftarrow \tilde{X}\,^3\Sigma_g^-$ transition which dissociates to ground state $C(^3P)$ products.

In addition to the $C + N_2$ channel, excitation of the $1_0^n$, $n \geq 6$ transitions of the $\tilde{B} \leftarrow \tilde{X}$ band produced a minor N + CN dissociation channel. The $P(E_T)$ distributions for the low $E_T$ regions of the $1_0^6$, $1_0^7$, and $1_0^9$ transitions display sharp narrow features (FWHM ≈ 100 meV) with a photofragment mass ratio 14:26. The peak positions shift with photon energy; consistent with opening of the $N(^4S) + CN(\tilde{X}\,^2\Sigma^+)$ channel. Further, the $P(E_T)$ distributions for the $1_0^7$ and $1_0^9$ transitions display two sharp features with a spacing of ≈ 250 meV, attributed to vibrational excitation of the CN fragment. We estimate the relative yield of the CN + N channel for the $1_0^6$, $1_0^7$ and $1_0^9$ transitions to be ~ 25 ± 10%. The angular distributions for the $N_2 + C$ product channel for all three electronic transitions were all found to be nearly isotropic with $\beta \approx 0$, while the N + CN channel was found to have an anisotropic angular distribution described by $\beta = 0.9$.

### B. CNN

#### *1. Photofragment yield spectra*

The photofragment cross sections for the $\tilde{A}\,^3\Pi \leftarrow \tilde{X}\,^3\Sigma^-$ and $\tilde{B}\,^3\Sigma^- \leftarrow \tilde{X}\,^3\Sigma^-$ bands are shown in Figures 5. A broad feature, with a width of ≈ 100 $cm^{-1}$ is observed near 23850 $cm^{-1}$ in good agreement with the rotationally resolved origin band observed by Curtis et al.(21) Weaker features at 200 and 300 $cm^{-1}$ to the blue of the origin are most likely due to sequence bands involving vibrationally excited levels of the ground state. Based upon rotational contours and a comparison with LIF studies by Bondybey et al.(22), features at 25044 and 25236 $cm^{-1}$ can be reasonably assigned to the ($02^+0$-000) and (100-000) bands. At higher energies, strong broad transitions with two major progressions of 1000 $cm^{-1}$ are observed, in agreement with the matrix absorption measurements of Jacox.(23) These progressions are assigned to the symmetric stretch $1_0^n$, and combination band $1_0^n 3_0^1$ progressions of the $\tilde{B}\,^3\Sigma^- \leftarrow \tilde{X}\,^3\Sigma^-$ band with $\omega_1'$=1000 $cm^{-1}$ and $\omega_3'$=1455 $cm^{-1}$.

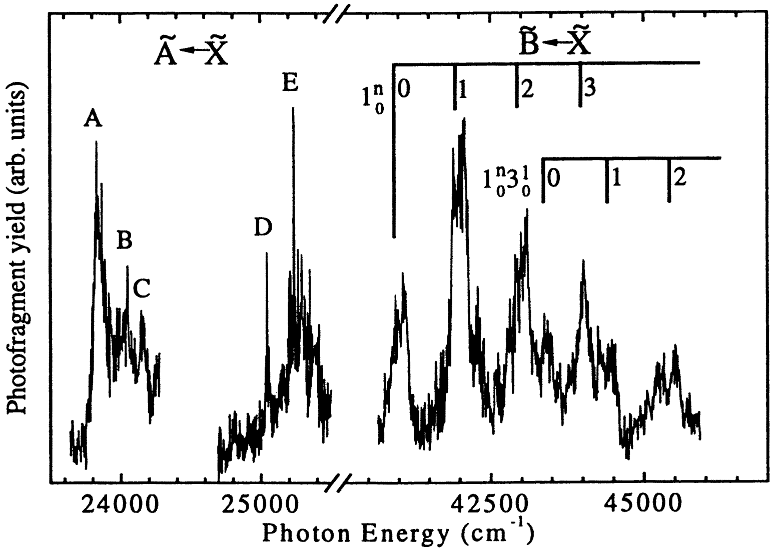

*Figure 5. PFY spectra of the $\tilde{A}\,^3\Pi \leftarrow \tilde{X}\,^3\Sigma^-$ and $\tilde{B}\,^3\Sigma^- \leftarrow \tilde{X}\,^3\Sigma^-$ bands of CNN. The labeled transitions of the $\tilde{A}\,^3\Pi \leftarrow \tilde{X}\,^3\Sigma^-$ band are mentioned in the text. The $1_0^n$ and $1_0^n 3_0^1$ progressions are labeled with a comb.*

#### *2. Photofragment mass distributions*

At the photon energies examined in the $\tilde{A}\,^3\Pi \leftarrow \tilde{X}\,^3\Sigma^-$ band between 2.95-3.22 eV, only C($^3$P) and C($^1$D) products are energetically available and an expected 12:28 mass ratio is observed. The higher energy $\tilde{B}\,^3\Sigma^- \leftarrow \tilde{X}\,^3\Sigma^-$ band transitions between

5.1 – 6.0 eV have multiple dissociation pathways available. At translational energies less than 0.8 eV the mass distributions broaden and a shift to higher (lower) mass is observed for the light (heavy) photofragment, indicating that a CN channel contributes.

### *3. Translational Energy Distributions*

Selected translational energy distributions from the $\tilde{A}\,^3\Pi \leftarrow \tilde{X}\,^3\Sigma^-$ and $\tilde{B}\,^3\Sigma^- \leftarrow \tilde{X}\,^3\Sigma^-$ bands are shown in Figures 6a and b. The P($E_T$) distribution resulting form excitation of the $\tilde{A}\,^3\Pi \leftarrow \tilde{X}\,^3\Sigma^-$ (100-000) band, Figure 6a, shows bimodal structure with a high energy component which extends towards ~ 2 eV and a low energy component which is peaked at 0.6 eV. The sharp falloff in signal at 1.91 eV, defines the maximum translation energy for ground state C($^3$P) products, yielding $D_0 = 1.22 \pm 0.03$ eV. The onset of this feature occurs at higher translational energy than the threshold for C($^1$D) products and is therefore due to internally excited C($^3$P) products.

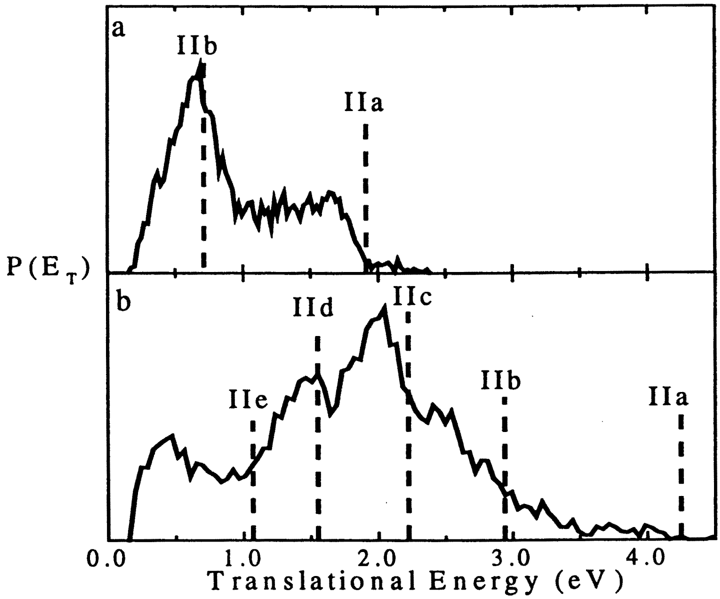

*Figure 6. Representative P($E_T$) distributions for the a) $\tilde{A}\,^3\Pi \leftarrow \tilde{X}\,^3\Sigma^-$ and b) $\tilde{B}\,^3\Sigma^- \leftarrow \tilde{X}\,^3\Sigma^-$ transitions of CNN. The thresholds for the product state energies listed in Table I are indicated with vertical dashed lines.*

The P($E_T$) distribution resulting from the $\tilde{B}\,^3\Sigma^-$ state at 5.46 eV is remarkably different from the $\tilde{A}\,^3\Pi$ state. The observed structure, with features between 0.5 and

1.0 eV in width, is much too broad to attribute to individual vibrational states of either $N_2$ or CN products. Furthermore, these features neither coincide with the thermodynamic thresholds for available product states nor shift with excitation energy making their assignment ambiguous. The low energy feature peaking near 0.5 eV has a fragment mass ratio of 14:26, suggesting that N + CN products are responsible for this feature.

Angular distributions for the $\tilde{A}\,^3\Pi$ state were found to be nearly isotropic with $\beta \approx 0$, indicating a long-lived excited state. The $\tilde{B}\,^3\Sigma^- \leftarrow \tilde{X}\,^3\Sigma^-$ transitions yield anisotropic photofragment angular distributions described by $\beta \approx 1.6$, consistent with a parallel electronic transition moment and a short-lived excited state.

## C. HNCN

### *1. Photofragment yield spectra*

The HNCN PFY spectra for the photon energies between 28850-29200 $cm^{-1}$ and between 30500-34500 $cm^{-1}$ have been observed. The lower energy band (not shown) corresponds to the $\tilde{B}\,^2A' \leftarrow \tilde{X}\,^2A''$ transition observed previously in rotationally resolved absorption studies by Herzberg and Warsop(24) and in more recent LIF studies by Wu *et al.*(25) Rotational analysis of this band(24) indicates that the NCN backbone is essentially linear and the HNC bond angles for the $\tilde{X}\,^2A''$ and $\tilde{B}\,^2A'$ states are 116.5° ± 2.7° and 120.6° ± 2.5° respectively.

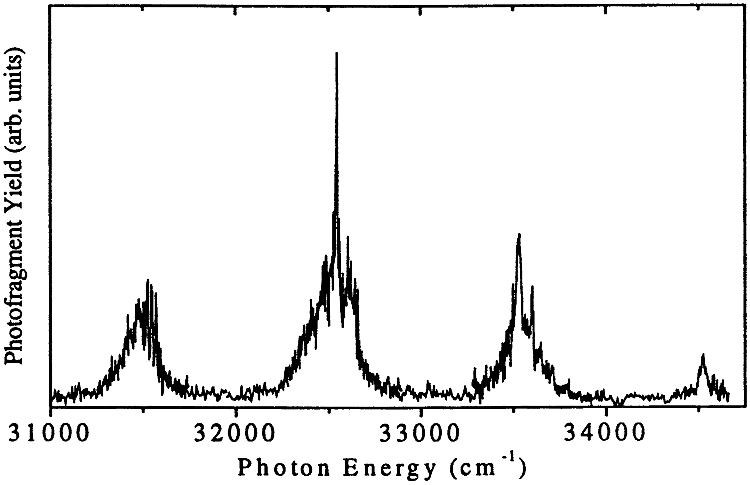

*Figure 7. PFY spectra of the* $\tilde{C}\,^2A'' \leftarrow \tilde{X}\,^2A''$ *band of HNCN.*

The higher energy transitions, shown in Figure 7, have been reported in the absorption studies of Basco and Yee(26) and Kroto and coworkers.(16) The vibrational progression of ~ 1000 $cm^{-1}$ does not shift upon deuteration, indicating that the active mode does not include H-atom motion and has been assigned to the NCN "symmetric" stretch. The transition centered at 31520 $cm^{-1}$ shows subband structure with a spacing of ~ 24 $cm^{-1}$, which is halved upon deuteration. The vibrational features to the blue do not display the same subband structure.(27)

### 2. *Photofragment mass distributions*

Prior to this work, the most accurate value for the heat of formation of HNCN, $\Delta H_{f,0\ K}$(HNCN) = 3.34 ± 0.17 eV, was determined by Clifford *et al.*(11). The uncertainty in the heat of formation is larger than the energy separation of product channels IIIa and IIIb. Therefore, the photofragment mass ratios are essential to identify the photoproducts. An unambiguous assignment of the products required photolysis of the deuterated species, DNCN. For DNCN, the CD + $N_2$ and N + DCN channels have the same photofragment mass ratio of 2:1. Figure 8 shows the fragment mass distributions for DNCN and HNCN. The width of the mass distributions for HNCN is identical to that for DNCN indicating only one mass channel contributes. The light mass for HNCN is shifted one mass unit lower than DNCN, establishing CH + $N_2$ as the product channel.

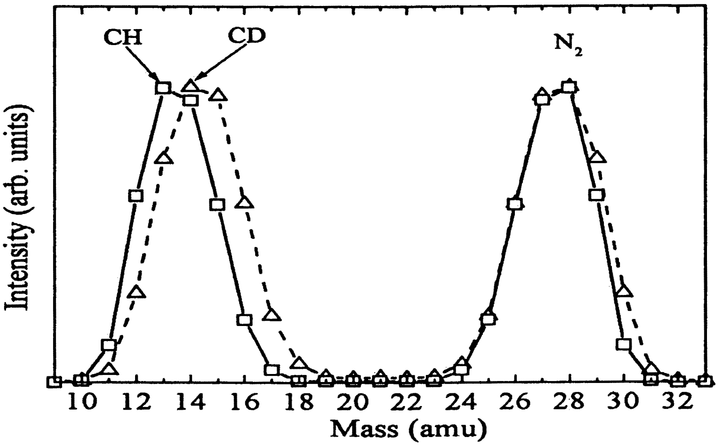

*Figure 8. Fragment mass distributions for HNCN (squares) and DNCN (triangles).*

### 3. *Translational energy distributions*

The P($E_T$) distributions for CH + $N_2$ products are shown in Figure 9. The distributions show a steep falloff at high translational energy defining $E_T^{max}$, yielding values of 2.78 ± 0.03 eV and 3.35 ± 0.03 eV for $D_0$ and $\Delta H_{f,0\ K}$(HNCN)respectively. The distributions are highly structured with peaks separated by approximately 290 meV, corresponding to the $N_2$ photofragment vibration. Excitation at 3.603 eV leads to almost no vibrational excitation of the $N_2$ fragment with the n=1 vibrational state representing less than 20% of the distribution. The widths of these features are ~ 120 meV. As the photon energy is increased to 3.909 eV, the vibrational exictation increases and the peak widths broaden to 180 meV. At photon energies of 4.035 and 4.157 eV, the widths continue to broaden and the vibrational distribution peaks at n=1.

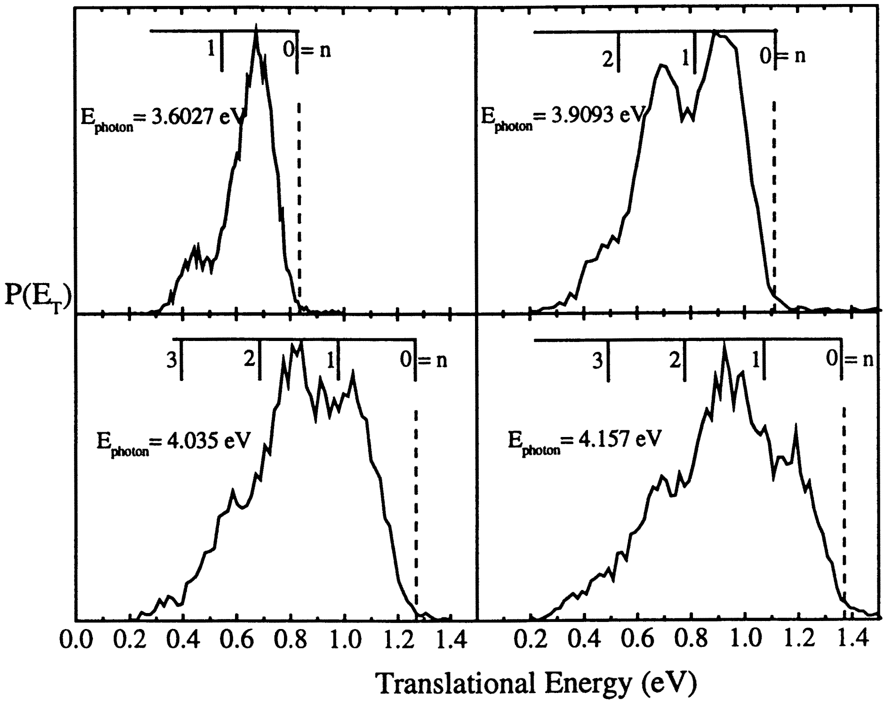

*Figure 9. P($E_T$) distributions for the CH + $N_2$ dissociation channel of the HNCN radical. $E_{photon}$ denotes the transition energy and the combs correspond the vibrational energy levels of the $N_2$ photofragment.*

## IV. Discussion

The P($E_T$) distributions for the NCN, CNN, and HNCN radicals reveal that the mechanism of photofragmentation is complicated and involves considerable geometry changes along the dissociation pathway. The dynamics of the NCN radical are particularly surprising. The excited states for the NCN radical are all linear, yet the dominant reaction pathways are the $N_2$ loss channels indicating that strongly bent or cyclic transition states are involved in the dissociation pathway. The C($^3$P) products are the dominant dissociation channel (≥ 90%) for the $\tilde{c}\,^1\Pi_u$ state, even though spin allowed C($^1$D) products are energetically accessible by more than 0.9 eV, while only C($^1$D) products are observed from the $\tilde{d}\,^1\Delta_u$ state.

All of the NCN P($E_T$) distributions reveal well resolved structure corresponding to $N_2$ vibrational excitation. The extended vibrational excitation in the $N_2$ photoproduct is consistent with a bent or cyclic intermediate state with the N-N bond forming and C-N bonds breaking at relatively large N-N distances. The rotational distributions peak between 20-40 quanta. The limited rotational excitation suggests that the dissociation at the transition state does not produce significant torque on the $N_2$ photofragment, consistent with a cyclic, $C_{2v}$-type dissociation pathway.

Recent calculations by Martin *et al.*(28) on the linear, bent and cyclic structures of NCN and CNN provide support for a $C_{2v}$ dissociation mechanism. Their calculations within the $C_{2v}$ point group have located a local minimum energy structure with $^3A_2$ symmetry and a transition state with $^3B_1$ symmetry at respective energies of 3.01 and 4.76 eV above the linear ground state of NCN, see Figure 10. The $\tilde{X}\,^3\Sigma_g^-$

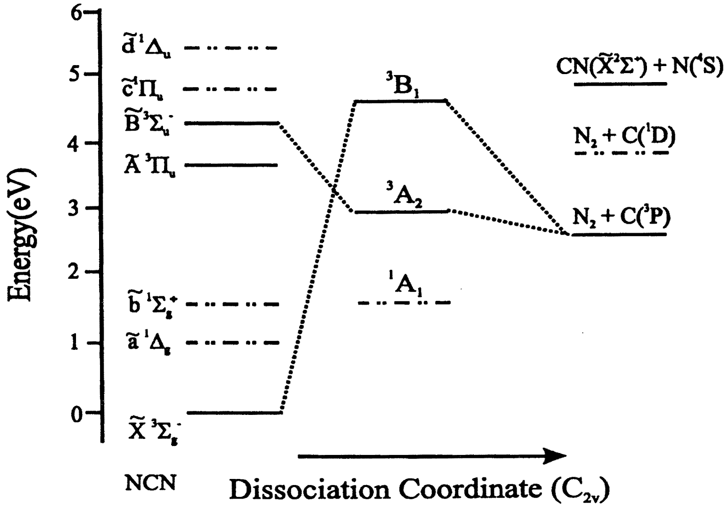

*Figure 10. Energy level and correlation diagram of the relevant electronic states of the NCN radical along a $C_{2v}$ dissociation coordinate. The energetic positions of the $\tilde{a}^1\Delta_g$, $\tilde{b}^1\Sigma_g^+$, $\tilde{A}^3\Pi_u$, $\tilde{B}^3\Sigma_u^-$, $\tilde{c}^1\Pi_u$, and $\tilde{d}^1\Delta_u$ states are based upon previous experimental spectroscopic studies discussed in the text. The $^1A_1$, $^3A_2$, and $^3B_2$ states are from ab inito calculations by Martin and coworkers (Ref. 27) and the product state energies are from NIST-JANAF thermochemical tables (Ref. 20).*

state adiabatically correlates to the $^3B_1$ state while the $\tilde{B}\,^3\Sigma_u^-$ state correlates to the $^3A_2$ state, providing a low-energy pathway through a cyclic intermdiate to products $N_2$ + C($^3$P). The $\tilde{A}\,^3\Pi_u$ state, although above the dissociation asymptote, cannot dissociate since it does not correlate with the lower energy $^3A_2$ state and does not have enough energy to access cyclic intermediates of either $^3B_1$ or $^3A_1$ symmetry.

The formation of C($^3$P) products from the $\tilde{c}\,^1\Pi_u$ state clearly indicates that the dissociation mechanism involves intersystem crossing (ISC) to a triplet surface. The

$\tilde{c}\,^1\Pi_u \leftarrow \tilde{a}\,^1\Delta_g$ band has been rotationally resolved by Kroto(18) with an instrument resolution of 0.1 $cm^{-1}$ and appears to be instrument limited, indicating that the lifetime of the $\tilde{c}\,^1\Pi_u$ state is > 50 ps. Additionally, the $\tilde{B}\,^3\Sigma_u^-$ and $\tilde{c}\,^1\Pi_u$ states display similar $P(E_T)$ distributions with increasing rotational excitation for higher vibrational states of $N_2$, washing out vibrational structure for $E_T < 0.6$ eV. The long lifetime, spin-forbidden products, and rotational distribution suggest that the $\tilde{c}\,^1\Pi_u$ state first intersystem crosses to the $\tilde{B}\,^3\Sigma_u^-$ state prior to dissociation.

The $\tilde{d}\,^1\Delta_u$ state, in contrast to the $\tilde{c}\,^1\Pi_u$ leads to spin-allowed $C(^1D)$ dissociation products. Although the $N(^4S) + CN(X\,^2\Sigma^+)$ products are energetically accessible by 1.08 eV, these spin-forbidden products are not observed. Unlike the $\tilde{B}\,^3\Sigma_u^-$ or $\tilde{c}\,^1\Pi_u$ states, the rotational excitation of the $N_2$ fragment from the $\tilde{d}\,^1\Delta_u$ state does not appear to increase substantially with increased vibrational excitation. Resolved vibrational structure is obscured at $E_T$ values as low as 0.3 eV. This notable dissimilarity in the $P(E_T)$ distributions implies that singlet and triplet dissociation surfaces have different contours.

While the dominant photodissociation products observed in this study are $N_2$ + C, the CN + N channel has been observed from the $\tilde{B}\,^3\Sigma_u^-$ state at photon energies > 4.9 eV, comprising 25 ± 10% of the total dissociation signal. The rotational distribution peaks at $J = 10$, less than half that observed for the $N_2$ loss channels. The limited rotational excitation and positive photofragment anisotropy ($\beta$=0.9) are consistent with collinear dissociation. The ability of the $N_2$+$C(^3P)$ channel to dominate when linear dissociation channels are available proves that the coupling of the linear excited states to intermediate cyclic states is highly efficient.

Unlike the NCN radical, the CNN radical can access either $N_2$ or CN products through simple bond cleavage. Since both the $\tilde{A}\,^3\Pi$ and $\tilde{B}\,^3\Sigma^-$ states are linear, one might expect the dissociation to proceed along a linear pathway producing only low rotational quantum levels for the diatomic fragment. However, rotational excitation of the $N_2$ fragment is so large that it obscures the underlying vibrational structure. The extensive rotational excitation ($J > 40$) suggests that the CNN radical dissociates via a bent transition state, which produces torque onto the molecular fragment.

Analogous to the NCN radical, the HNCN radical displays resolved vibrational structure of the $N_2$ photofragment. Formation of $CH(^2\Pi)$ + $N_2$ products from HNCN requires significant structural rearrangement involving an H atom shift to the central C and bending of the NCN backbone to allow N-N bond formation. The $N(^4S)$ channels are not observed, indicating that isomerization is much faster than intersystem crossing. It is particularly surprising that we are able to resolve vibrational structure since two diatomic photofragments are produced and hence, a large number of product rotational states are accessible. The limited rotational excitation implies a cyclic transition state, just like NCN.

Several theorists have investigated the role of cyclic $HCN_2$ in the reaction of $CH(^2\Pi) + N_2 \rightarrow N(^4S) + HCN$,(29-36) and propose that a bound *c*-$HCN_2$

intermediate allows the above spin-forbidden reaction to occur.(30) Walch calculates the minimum energy structure of *c*-$HCN_2$ to be 0.55 eV below the CH + $N_2$ asymptote and estimates the exit barrier to be 0.79 eV above this asymptote.(35) We observe photofragment signal from the origin of the $\tilde{B}\,^2A' \leftarrow \tilde{X}\,^2A''$ band ($T_0$ = 28993.766 $cm^{-1}$),(25) indicating that the exit barrier must be ≤ 0.8 eV, in good agreement with the results of Walch. We cannot directly determine the barrier to isomerization of HNCN to *c*-$HCN_2$; however, this barrier must also be located ≤ 0.8 eV above the dissociation limit. The HNCN radical is energetically more stable than $HCN_2$ and *c*-$HCN_2$ by 1.74 ± 0.05 eV(27,37) and 2.23 ± 0.09 kcal/mol(35) respectively, suggesting that this radical may play an important role in the reaction of $N_2$ + $CH(^2\Pi)$, particularly at higher temperatures where passage over activation barriers becomes more facile.

## V. Conclusions

The photodissociation spectroscopy and dynamics of the CNN, NCN, and HNCN free radicals have been investigated by fast beam photofragment spectroscopy. For all of these systems, we have observed dissociation from multiple excited states. In addition to refining the thermodynamics of these radicals, the photofragment internal energy distributions indicate that these radicals isomerize to cyclic or bent intermediate states prior to dissociation. We hope that future theoretical studies of the isomerization pathways of these radicals and direct spectroscopic investigation of the diazirinyl radical (*c*-HCNN) and diazirinylcarbene (*c*-CNN) will allow a more thorough investigation of the global potential energy surface.

## Acknowledgements

This research is supported by the Director, Office of Energy and Research, Office of Basic Energy Sciences, Chemical Sciences Division, of the U.S. Department of Energy under Contact No. DE-AC03-76F00098.

## References

1. Jennings, K. R.; Linnett, J. W. *Trans. Faraday Soc.* **1960**, *56*, 1737.
2. Fenimore, C. P. in *Procedings of the Thirteenth Symposium (International) on Combustion* The Combustion Institute, Pittsburgh, Pa, 1971; pp 373.
3. Yamamoto, S.; Saito, S. *J. Chem. Phys* **1994**, *101*, 10350.
4. O'Dell, C. R.; Miller, C. O.; Cochran, A. L.; Cochran, W. D.; Opal, C. B.; Barker, E. S. *Astrophys. J.* **1991**, *368*, 616.
5. Continetti, R. E.; Cyr, D. R.; Osborn, D. L.; Leahy, D. J.; Neumark, D. M. *J. Chem. Phys* **1993**, *99*, 2616.

6. Leahy, D. J.; Osborn, D. L.; Cyr, D. R.; Neumark, D. M. *J. Chem. Phys* **1995**, *103*, 2495.
7. Osborn, D. L.; Choi, H.; Mordaunt, D. H.; Bise, R. T.; Neumark, D. M.; Rohlfing, C. M. *J. Chem. Phys* **1997**, *106*, 3049.
8. Osborn, D. L.; Leahy, D. J.; Cyr, D. R.; Neumark, D. M. *J. Chem. Phys* **1996**, *104*, 5026.
9. Bakker, J. M. B. *J. Phys. E* **1973**, *6*, 785.
10. Bakker, J. M. B. *J. Phys. E* **1974**, *7*, 364.
11. Clifford, E. P.; Wenthold, P. G.; Lineberger, W. C.; Petersson, G. A.; Ellison, G. B. *J. Phys. Chem. A* **1997**, *101*, 4338.
12. Clifford, E. P.; Wenthold, P. G.; Lineberger, W. C.; Petersson, G. A.; Broadus, K. M.; Kass, S. R.; Kato, S.; DePuy, C. H.; Bierbaum, V. M.; Ellison, G. B. *J. Phys. Chem. A* **1998**, *102*, 7100.
13. Taylor, T. R.; Bise, R. T.; Asmis, K. R.; Neumark, D. M. *Chem. Phys. Lett.* **1999**, *301*, 413.
14. Bise, R. T.; Choi, H.; Neumark, D. M. *J. Chem. Phys.* **1999**, *111*, 4923.
15. de Bruijn, D. P.; Los, J. *Rev. Sci. Instrum.* **1982**, *53*, 1020.
16. Kroto, H. W.; Morgan, T. F.; Sheena, H. H. *Trans. Faraday Soc.* **1970**, *66*, 2237.
17. Milligan, D. E.; Jacox, M. E.; Bass, A. M. *J. Chem. Phys* **1965**, *43*, 3149.
18. Kroto, H. W. *Can. J. Phys.* **1967**, *45*, 1439.
19. Smith, G. P.; Copeland, R. A.; Crosley, D. R. *J. Chem. Phys* **1989**, *91*, 1987.
20. Chase Jr., M. W. *J. Chem. Phys. Ref. Data* **1998**, *Monograph 9*, 1.
21. Curtis, M. C.; Levick, A. P.; Sarre, P. J. *Laser Chem.* **1988**, *9*, 359.
22. Bondybey, V. E.; English, J. H. *J. Chem. Phys.* **1977**, *67*, 664.
23. Jacox, M. E. *J. Mol. Spec.* **1978**, *72*, 26.
24. Herzberg, G.; Warsop, P. A. *Can. J. Phys.* **1963**, *41*, 286.
25. Wu, W.; Hall, G.; Sears, T. J. *J. Chem. Soc., Faraday Trans.* **1993**, *89*, 615.
26. Basco, N.; Yee, K. K. *Chem. Commun.* **1968**, *3*, 150.
27. Bise, R. T.; Hoops, A. A.; Neumark, D. M. *manuscript in preparation* .
28. Martin, J. M. L.; Taylor, P. R.; Francois, J. P.; Gijbels, R. *Chem. Phys. Lett.* **1994**, *226*, 475.
29. Manaa, M. R.; Yarkony, D. R. *J. Chem. Phys* **1991**, *95*, 1808.
30. Manaa, M. R.; Yarkony, D. R. *Chem. Phys. Lett.* **1992**, *188*, 352.
31. Martin, J. M. L.; Taylor, P. R. *Chem. Phys. Lett.* **1993**, *209*, 143.
32. Seideman, T. *J. Chem. Phys* **1994**, *101*, 3662.
33. Seideman, T.; Walch, S. P. *J. Chem. Phys* **1994**, *101*, 3656.
34. Tao, F.-M.; Klemperer, W.; McCarthyy, M. C.; Gottlieb, C. A.; Thanddeus, P. *J. Chem. Phys* **1994**, *100*, 3691.
35. Walch, S. P. *Chem. Phys. Lett.* **1993**, *208*, 214.
36. Walch, S. P. *J. Chem. Phys* **1995**, *103*, 4930.
37. Bise, R. T.; Hoops, A. A.; Choi, H.; Neumark, D. M. *manuscript in preparation* .

## Chapter 18

# Three-Body Dissociation Dynamics of Transient Neutral Species: Dissociative Photodetachment of $O_6^-$

**A. K. Luong, T. G. Clements, and R. E. Continetti**[1]

**Department of Chemistry and Biochemistry, University of California at San Diego, 9500 Gilman Drive, La Jolla, CA 92093–0314**

The three-body dissociation dynamics of the transient $O_6$ molecules produced by the photodetachment of $O_6^-$ at 388 and 258 nm were studied by photoelectron-photofragment coincidence (PPC) spectroscopy. Photodetachment of a negatively charged precursor, with coincident energy analysis of the photoelectron, allowed production of energy-selected transient neutral complexes. Measurement of the times and positions-of-arrival of all the particles (one electron and three molecular fragments) in coincidence provides a kinematically complete description of the three-body decay dynamics of $O_6$. Molecular-frame differential cross sections, showing the angular correlations between the photofragments, are presented and interpreted in terms of a spectator model for the addition of a third $O_2$ to $O_4^-$.

The dynamics of three-body dissociation and recombination processes of neutral species is an area of chemical dynamics that remains to be explored in detail. This is in spite of the fact that three-body recombination and dissociation reactions play important roles in a number of situations, including complex combustion and atmospheric chemical processes. There have been a number of studies of three-body photodissociation processes, reviewed in some detail recently by Gericke and Maul.(*1*) These studies have typically involved non-coincident detection of one or more of the photofragments, with inferences made on the overall three-body dissociation dynamics. We have established a research effort aimed at characterizing the three-body dissociation dynamics of neutral species by coincident detection of the photofragments following dissociative photodetachment of stable cluster anions. The

---

[1] Corresponding author.

In Imaging in Chemical Dynamics; Suits, A., et al.;
ACS Symposium Series; American Chemical Society: Washington, DC, 2000.

work reported here expands on a previous preliminary report on the three-body dissociation dynamics of $O_6^-$ at 532 nm.(*2*)

Coincidence measurements of multiple fragments has proven to be a valuable tool in understanding many-body dissociation processes such as ion and photon-induced dissociative ionization.(*3,4*) These include the pioneering kinematically complete experiments on double photoionization by Schmidt-Bocking and co-workers.(*5*) A recent extension of coincidence studies of three-body dissociation dynamics, in addition to that from our own laboratory, is the study of the dissociation dynamics of excited states of $H_3$ produced by charge-exchange neutralization of $H_3^+$ by Helm and co-workers.(*6*) Since the decay of complex systems may yield multiple fragments, which may or may not originate from the same reaction channel, experiments can either implement techniques for detection of all the products or employ relatively simple models during data analysis to remove ambiguities from a lack of knowledge of the correlation between product states. In the case of three-body dissociation dynamics, there are several detection schemes that permit kinematically complete descriptions of the system.(*1*) For example, if the dissociation yields three particles with equal momenta in a synchronous dissociation, it is only necessary to detect one of the particles and deduce the dynamics based on conservation of momentum. In the general case, however, one does not know *a priori* the distribution of momenta among the particles nor the relative recoil angles of these particles. To completely kinematically characterize such processes, it is essential to measure and identify at least two out of the three fragments in coincidence, with momentum conservation providing the information on the third particle.

In our laboratory, photoelectron and photofragment spectroscopy methods are combined to study the three-body dissociation dynamics of transient neutral species. An anion precursor is produced in a fast ion beam and mass selected. This is followed by photodetachment and coincidence detection of the photoelectron. The photoelectron kinetic energy fixes the internal energy of the transient neutral, and any subsequent dissociation of the nascent neutral can be studied using the multiple-photofragment translational spectroscopy technique.(*7*) Using the fast-ion-beam technique and a multiparticle detector these experiments allow detection of all the products: a free electron and three photofragments. We refer to this combination of photoelectron and photofragment translational spectroscopies as photoelectron-photofragment coincidence (PPC) spectroscopy. PPC spectroscopy provides the capability to simultaneously measure the kinetic energies and recoil angles of the photoelectron and fragments resulting from individual events, thereby obtaining a complete kinematic description of the decay process. An application of PPC spectroscopy to the study of three-body dissociation dynamics will be illustrated by studies of $O_6^-/O_6$.

Previous experimental studies on the small homogeneous cluster anions of $O_2$ have revealed that both dissociative photodetachment and photodissociation processes yielding $O_2^-$ occur over a wide range of photon energies.(*8,9,10*) Mass spectrometric studies,(*11*) confirmed by our own photodissociation studies,(*12*) have shown that $O_4^-$ is 0.46 ± 0.02 eV more stable than $O_2(^3\Sigma_g^-) + O_2^-(^2\Pi_g)$. However, the addition of a third $O_2$ to $O_4^-$ stabilizes the system only by 0.11 eV.(*11*) A recent theoretical study (*13*) of $O_4^-$ predicts a rectangular $^2A_u$ ground state in $D_{2h}$ symmetry, with the excess electron delocalized over the two $O_2$ moieties. This is consistent with our observation that $O_4^-$ undergoes DPD with a remarkably constrained product internal energy distribution, producing a Franck-Condon vibrational distribution with little rotational excitation of the products.(*14,15*) There have been no comparable theoretical studies of the structure of $O_6^-$.

Photodestruction and photodissociation cross-section measurements on $O_6^-$ by Johnson and co-workers (*9,10*) showed a much larger cross-section for the photodissociation of $O_6^-$ relative to $O_4^-$ at longer wavelengths. They attributed this significant difference in the photochemistry of $O_4^-$ and $O_6^-$ to a charge-transfer-to-solvent interaction between the $O_4^-$ core and the "solvating" $O_2$. Subsequent studies in our laboratory recorded photoelectron and photofragment time-of-flight spectra for $O_6^-$ at 532, 355 and 266 nm.(*16*) These experiments showed that the DPD dynamics of $O_6^-$ do not differ considerably from $O_4^-$, but confirmed the significant difference in photodissociation dynamics at longer wavelengths. The recent development of the photoelectron-multiple-photofragment coincidence technique finally allowed detailed measurements of the energy and angular distributions for three-body dissociative photodetachment of $O_6^- + h\nu \rightarrow O_2 + O_2 + O_2 + e^-$.(*2*) Our first application of this technique focused on the photodestruction dynamics of $O_6^-$ at 532 nm, confirming the similarity between the DPD dynamics of $O_4^-$ and $O_6^-$. This study also clearly showed that $O_6^-$ exhibits two photodissociation channels at this wavelength: one producing $O_2(^3\Sigma_g^-) + O_2(^1\Delta_g) + O_2^-(^2\Pi_u, v=0,1)$, and a second one yielding $2O_2(^3\Sigma_g^-) + O_2^-(^2\Pi_u, v>3)$. This is in contrast to $O_4^-$, which only undergoes photodissociation to $O_2(^1\Delta_g) + O_2^-(^2\Pi_u,v=0,1)$ at 532 nm.(*12*)

At shorter wavelengths, the study of $O_6^-$ photoelectron and time-of-flight spectra by Li *et al.* showed that the DPD and photodissociation dynamics of $O_6^-$ do not differ considerably from $O_4^-$.(*16*) The objective of the present work is to more completely characterize the DPD dynamics of $O_6^-$ using photoelectron-multiple-photofragment coincidence spectroscopy. It is found that the DPD of $O_6^-$ at 388 and 258 nm is a direct process governed by the photochemistry of an $O_4^-$ core with a spectator $O_2$. The three-body dissociation of the transient $O_6$ species is rapid, and examination of the dynamics as revealed in the center-of-mass angular distributions of the three coincident photofragments allows inferences on the cluster structure to be made.

## Experiment

The experimental apparatus is described in detail in a recent publication,(*17*) and is comprised of four differentially pumped regions as shown in **Figure 1**. Anions are generated in the source chamber by intersecting a 1 kHz pulsed supersonic expansion of $O_2$ with a 1 keV electron beam. The ion beam enters the acceleration region through a conical skimmer and is accelerated to 4 keV. The ions are mass-selected by time-of-flight, and guided into the interaction/detection region. The ion beam is then crossed by a focused linearly polarized laser beam at 90 degrees, under conditions that yield on average 0.1 photodetachment events per laser shot. The position and time-of-arrival of the photodetached electron is measured by one of two microchannel-plate-based wedge-and-strip-anode electron detectors placed

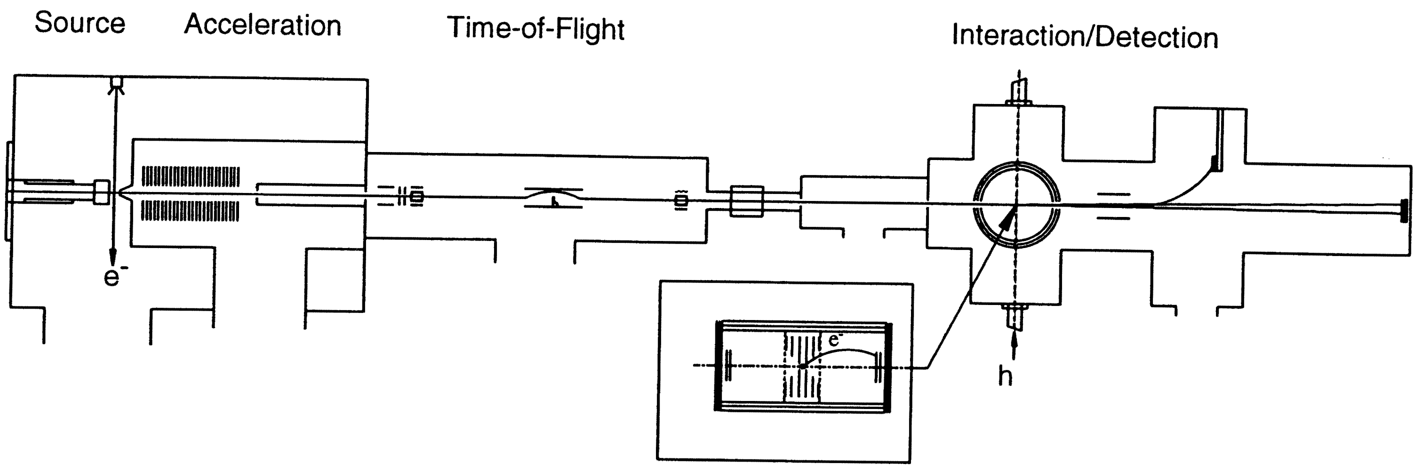
Source
Acceleration
Time-of-Flight
Interaction/Detection
e⁻
e⁻
h

*Figure 1.* Schematic of the apparatus.

perpendicular to the beam path and opposite of each other. To correct for the Doppler broadening in the electron kinetic energy distribution introduced by the large-solid-angle of acceptance by the electron detector, the laboratory kinetic energy obtained by recording the time- and position-of-arrival of the electron is adjusted by subtracting the component that is due to the ion beam velocity.(*18*) This method yields a center-of mass electron kinetic energy (eKE) resolution ΔE/E ~5% at 1.3 eV. Ions remaining in the beam are electrostatically deflected into an ion detector.

Neutral particles leaving the interaction region continue to fly until they impinge on a time- and position-sensitive multiparticle detector located 104 cm downstream. The multiparticle detector uses a stack of three resistance-matched microchannel plates for particle amplification backed by an anode consisting of four separate crossed-delay-line (*19*) quadrants. Each quadrant is instrumented to detect up to two particles as long as the time-of-arrival difference is greater than the electronics dead-time of 10 ns. From the time and position of arrival, the center-of-mass translational energy ($E_T$) and product recoil angles are determined, as discussed further below. In the three-body dissociation dynamics study of the $O_6$ system, the detector demonstrated a photofragment translational energy resolution of $\Delta E_T/E_T$ ~15% at 0.7 eV.(*17*)

Recorded events are sorted by the number of particles detected. The results reported here include photoelectron-photofragment energy correlation spectra, N($E_T$,eKE), for which one electron and three photofragments are recorded. The three-body dissociation dynamics for a distribution of neutral precursor internal energies can also be examined by analyzing events with only three coincident photofragments. Statistics governed by the efficiency of the photoelectron and photofragment spectrometers, the count rate of the experiment, and a check on conservation of linear momentum during data analysis ensure the correlation of the detected particles from individual events.(*7*) A false coincidence rate of ~2% is estimated for three-body dissociation events in the present experiments.

Once the events are sorted, the three-body dissociation dynamics can be analyzed. Based on the known center-of-mass (CM) velocity of the parent beam and the times and positions-of-arrival of the particles, the laboratory frame velocities are calculated and transformed into a CM frame such that the velocity of a reference particle is directed along the positive x-axis. Subsequent fragment mass calculations are based on the CM frame velocities, the known parent mass, and conservation of linear momentum. In the $O_6^-/O_6$ system under study in the present work, energetic considerations dictate that DPD will produce $3O_2 + e^-$, so the low fragment mass resolution (*17*) (m/Δm ~ 2.5) inherent in this technique is not a problem. The fragment masses and CM velocities are then used to calculate the kinetic energy of each fragment, the sum of which generates the CM translational energy ($E_T$) spectrum for the dissociation process.

Since the recoil angles of all three particles are recorded, a spectrum showing the correlation of the product recoil angles in the CM frame can also be generated. This is plotted in the form of a molecular-frame differential cross section (MF-DCS), (*4,20*) constructed by creating a two-dimensional histogram of all the events such that the recoil velocity of the reference particle (chosen to be the fastest particle in the present study) is histogrammed along the positive x-axis and the velocity vectors of the other two particles histogrammed where they lie in the plane of the three-body breakup. When the dissociation process is rapid relative to molecular rotation, the MF-DCS records the initial recoil velocity vectors in the dissociating molecule, permitting insights into the structure of the system at the time of dissociation. As will be discussed below, the dissociative photodetachment of $O_6^-$ presents such a case.

## Results

In the following sections, first the photoelectron-photofragment kinetic energy correlation spectra for $O_4^-$ and $O_6^-$ at 388 nm are presented. These are followed by the MF-DCS results for $O_6^-$ at 532, 388 and 258 nm. The 532 nm results were obtained in an earlier study, but this is the first time they are presented and interpreted in terms of the MF-DCS.

### 1. Photoelectron-photofragment kinetic energy correlation spectra

The N($E_T$, eKE) spectra for $O_4^-$ and $O_6^-$ at 388 nm are shown in **Figure 2**. The $O_4^-$ spectrum is very similar to one previously measured at 355 nm, (*15*) with the exception that the photoelectron spectrum is shifted by the difference in photon energies, as expected in a DPD process. The diagonal lines in the $O_4^-$ spectrum represent the maximum kinetic energies for the production of (I) $2O_2(X\,^3\Sigma_g^-) + e^-$ and (II) $O_2(a\,^1\Delta_g) + O_2(X\,^3\Sigma_g^-) + e^-$. Diagonal structures observed below limits I and II show that DPD occurs to a distribution of $O_2$ vibrational states in both product channels, but with low rotational excitation as discussed in greater detail in reference 15. Evidence for a photodissociation channel (III) producing $O_2(^3\Sigma_g^-) + O_2^-(^2\Pi_u, v>3)$ is seen in the horizontal lines along the $E_T$ axis correlated with the two resolved peaks below 0.5 eV in the photoelectron spectrum. These features arise when a vibrationally excited $O_2^-$ product undergoes autodetachment, leading to an electron with a well-defined kinetic energy. A completely analogous spectrum is observed for $O_6^-$, as observed in Figure 2(b). Now the diagonal lines labeled I and II represent the maximum kinetic energy ($KE_{MAX}$) available for production of $3O_2(X\,^3\Sigma_g^-) + e^-$, $O_2(a\,^1\Delta_g) + 2O_2(X\,^3\Sigma_g^-) + e^-$, and $O_2(b\,^1\Sigma_g^+) + 2O_2(X\,^3\Sigma_g^-) + e^-$, respectively. The value for $KE_{MAX} = 2.18$ eV at limit I is based on the binding energy of 0.11 eV for $O_6^-$ relative to $O_4^- + O_2$, the dissociation energy of $O_4^-$ to $O_2 + O_2^-$ (0.46 eV), the EA of $O_2$ (0.45 eV) and the photon energy at 388 nm (3.20 eV).(*7,21*)

Both spectra in Figure 2 exhibit structure consistent with direct DPD, where photodetachment of the anion precursor accesses a repulsive potential energy surface. The diagonal ridges are separated by ~0.19 eV, which is the vibrational energy spacing of $O_2$. Hence, each ridge correlates to dissociation from different vibrationally adiabatic repulsive states of either $O_4$ or $O_6$, yielding $O_2$ with a specific vibrational state distribution. The products, $O_2(a^1\Delta_g) + 2O_2(X^3\Sigma_g^-) + e^-$, are represented by the faint ridges lying below the diagonal line labeled II. Finally, there are faint features parallel to the x-axis (III) that are superimposed on the higher $E_T$ feature below limit II. These result from photodissociation of $O_6^-$ to form neutral

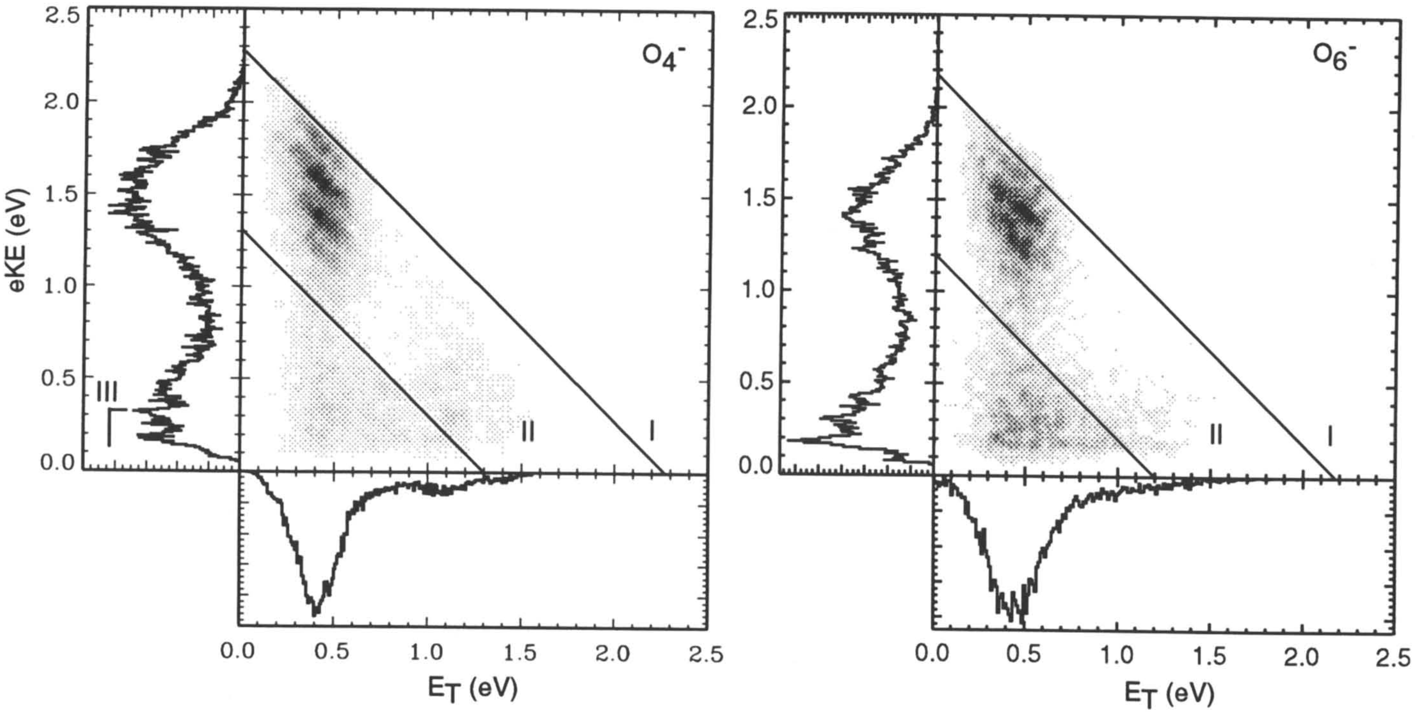

*Figure 2.* N($E_T$, eKE) spectra of $O_4^-$ and $O_6^-$ at 388 nm.

$O_2$ and vibrationally excited $O_2^-(v=5,6)$. It can be seen clearly from Figure 2 that there are only minor differences in the product distributions for either photodissociation or DPD in $O_4^-$ and $O_6^-$ at 388 nm. The N($E_T$,eKE) correlation spectra give direct insights into both the product state distributions in DPD and photodissociation, and also give dynamical insights –e.g., whether the process is a direct dissociative photodetachment or a sequential photodissociation/autodetachment event. In the case of three-body dissociation processes, an additional level of dynamical information can be obtained by considering the product angular correlations, or the MF-DCS, as discussed in the next section.

## 2. Molecular Frame Differential Cross Section

The direct dissociation of $O_6$ on a repulsive potential energy surface following photodetachment of the parent $O_6^-$ anion must occur promptly relative to molecular rotation, so the observed MF-DCS for the DPD of $O_6^-$ is expected to have a strong correlation with the geometry at the time of dissociation. What is found in the MF-DCS is that two fast and one slow $O_2$ are found for the DPD of $O_6^-$ over a wide range of wavelengths, as shown in the velocity-space MF-DCS observed for $O_6^-/O_6$ at 532, 388, and 258 nm in **Figure 3**. These MF-DCS spectra are integrated over all eKE, so there is not a fixed energy available to the dissociating $O_6$. Arrows are drawn to the centroid of the distribution of center-of-mass velocities for each photofragment in **Figure 3**. As mentioned in section 2, the fastest particle is histogrammed along the x-axis, with the slowest particle in the upper half-plane and the second fastest particle placed in the lower half-plane. Note that these distributions are thus molecular-frame distributions averaged over any dependence on the electric vector of the laser. At all three wavelengths, the MF-DCS shows that the two fastest particles exhibit a strong angular correlation, and are nearly scattered at 180° in the center-of-mass frame. The slow $O_2$, on the other hand, is observed to exhibit a very low recoil velocity near the center-of-mass and is scattered over a wide range of angles.

The wavelength dependence of the MF-DCS spectra is primarily determined by the appearance of different DPD pathways at the higher photon energies. All three spectra, however, contain signatures arising from photodissociation and photodissociation/autodetachment processes. It is easiest to examine these features in terms of the one-dimensional histogram of the reference particle along the x-axis of the MF-DCS spectra in **Figure 3**. At 532 nm, the dominant peak observed arises from DPD to $3O_2(X\,^3\Sigma_g^-) + e^-$. The small peak at larger velocity ( $\approx 1.5\times10^5$ cm/sec ) is due to photodissocation to $O_2(X^3\Sigma_g^-) + O_2(a\,^1\Delta_g) + O_2^-(\,X\,^2\Pi_u$, v=0,1), followed by photodetachment of the $O_2^-(\,X\,^2\Pi_u$, v=0,1) by a second photon. At 388 nm, the dominant DPD peak contains contributions from both channels (I) and (II) discussed in the previous section. The shoulder at velocities larger than $1.5\times10^5$ cm/sec primarily comes from the horizontal lines observed in the N($E_T$,eKE) correlation spectra arising from photodissociation processes yielding $O_2^-(\,X\,^2\Pi_u$, v > 3) which undergoes rapid autodetachment. At 258 nm the lower velocity peak at $\approx 1.1\times10^5$ cm/sec results from DPD to the ground state products, $3O_2(X\,^3\Sigma_g^-) + e^-$ and the higher velocity peak at $\approx 1.6\times10^5$ cm/sec corresponds to DPD to channel (II); $O_2(a\,^1\Delta_g)$ +

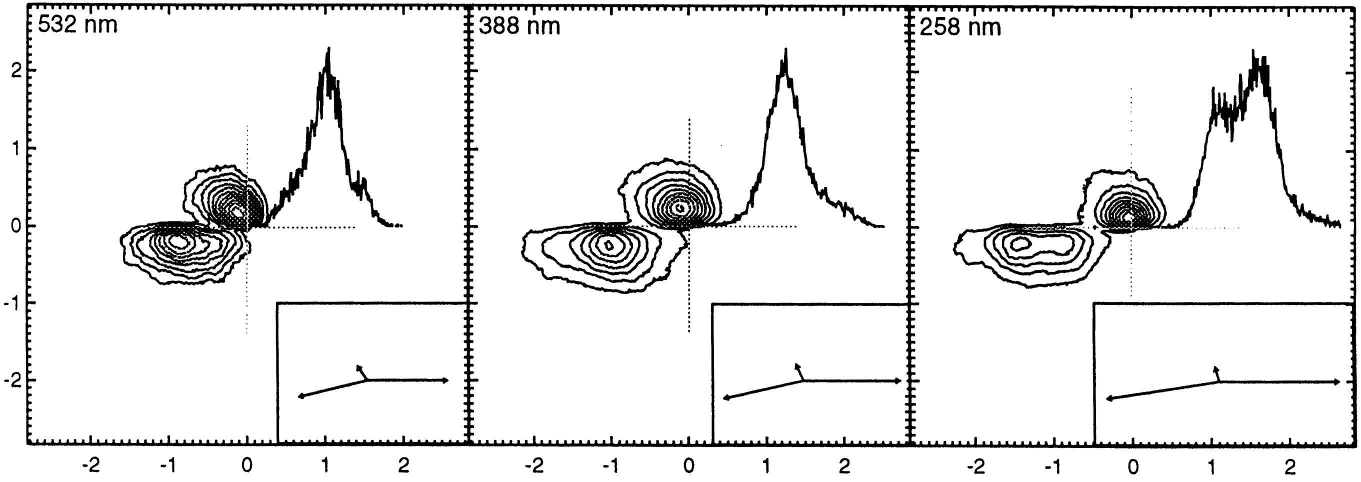

*Figure 3.* MF-DCS spectra observed for the DPD of $O_6^-$ at 532, 388, and 258 nm in center-of-mass velocity space. Units for the axes are $10^5$ cm/sec.

$2O_2(X^3\Sigma_g^-) + e^-$, but on a more repulsive excited state surface than observed in the 388 nm experiment. This is analogous to the previous observations by Hanold *et al.*(*15*) on $O_4^-$ at 266 nm. The fact that the changes in product state distributions as a function of wavelength can be so clearly seen in the velocity distribution of either of the two faster particles emphasizes the point that the third, slow $O_2$ product generated upon DPD of $O_6^-$ is really a spectator, playing only a minor role in the partitioning of momentum in the dissociation.

To take full advantage of the information contained in the coincidence data recorded in these experiments, it is instructive to examine the MF-DCS for defined ranges of the total kinetic energy release, $E_{TOT}$ = eKE + $E_T$. The MF-DCS for different regions in the N($E_T$,eKE) correlation spectrum can be selected from the whole coincidence data set by restricting the energy range of the accepted data. Restrictions on $E_{TOT}$ correspond to different diagonal limits on **Figure 2** and different internal energy ranges for the nascent $O_6$ cluster and the three $O_2$ products. In **Figure 4** energy-selected MF-DCS spectra generated from the 388 nm data in Figure 2 are shown. In frames A and B, spectra generated in the ranges $0 < E_{TOT} < 1.1$ eV and $1.1 < E_{TOT} < 2.2$ eV are shown, respectively. The spectrum in frame A thus contains contributions from both DPD channel (II) and the photodissociation/autodetachment channel (III), while the spectrum in frame B contains contains contributions from DPD channel (I), and at higher $E_T$, contributions from the photodissociation/autodetachment channel (III). The effect of channel (III) on the spectra can be seen by imposing a further constraint on the data, accepting only data in the above $E_{TOT}$ ranges *and* with $E_T < 0.8$ eV. These spectra, shown in frames C and D, illustrate the effect of the high $E_T$ component of channel III on the MF-DCS.

## Discussion

The observed features in the N($E_T$, eKE) spectrum of $O_4^-$ and $O_6^-$ at 388 nm are remarkably similar to those of $O_4^-$ at 355 nm studied by Hanold *et al.* (*15*) Aside from the shift towards lower eKE due to the combined effects of the difference in photon energy between 355 and 388 nm (0.29 eV) and the stability of $O_6^-$ relative to $O_4^- + O_2$ (0.11 eV), all the characteristics are retained. However, there is some broadening of the features in the correlation spectrum of $O_6$, which is more dramatic for the products in channel (II): $O_2(a^1\Delta_g) + 2O_2(X^3\Sigma_g^-) + e^-$. This is in spite of the fact that the eKE resolution in this time-of-flight measurement is expected to be higher for the slower electrons corresponding to this product channel. The narrow distribution of each ridge in the correlation spectrum of $O_4^-$ at 355 nm was attributed to low rotational excitation of the $O_2$ products resulting from dissociation of a highly symmetrical structure of the $O_4$. Hence, the broadening of the still resolvable diagonal ridges the $O_6^-$ N($E_T$, eKE) may be due to increased rotational excitation of the products resulting from dissociation of an $O_6$ species which may have lower symmetry than $O_4$. It is also noted that while channel III in $O_6^-$ appears to be enhanced relative to the analogous channel in $O_4^-$, the relative intensity of the autodetachment features are very similar in both spectra, consistent with the previous photoelectron spectroscopy studies by Li *et al.*(*16*) Thus, the photodestruction dynamics of $O_6^-$ at 388 nm exhibit

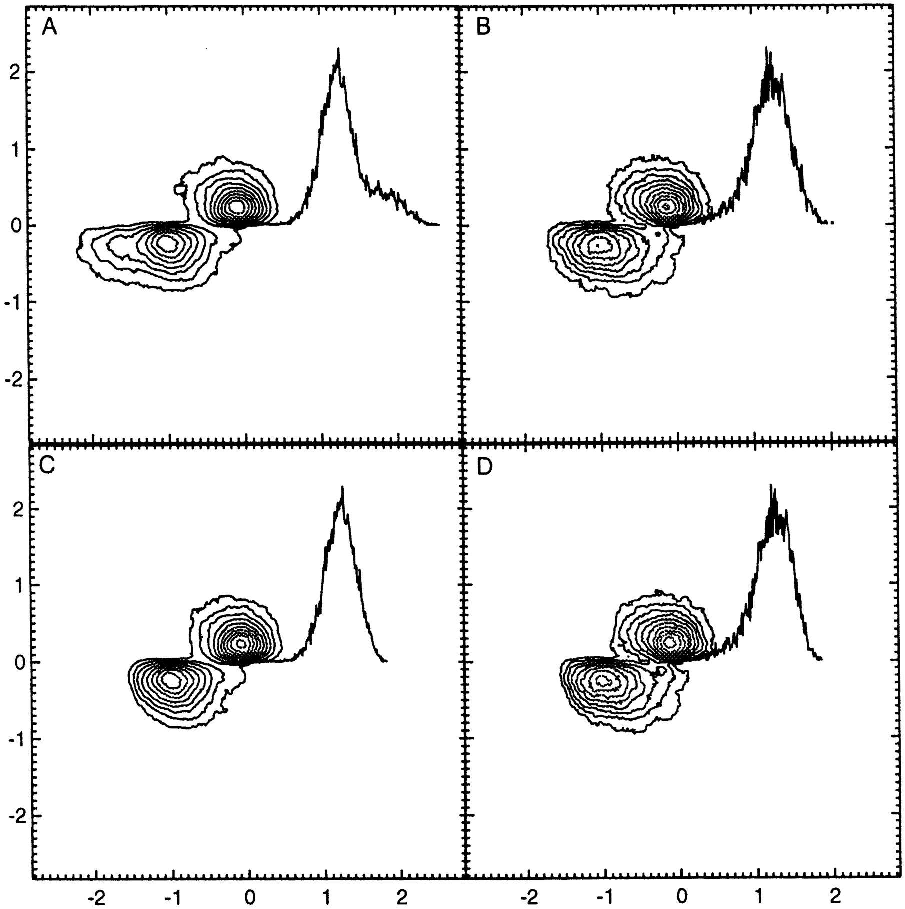

*Figure 4.* Total energy gated MF-DCS images of $O_6$ at 388 nm, where A is $1.1 < E_{total} < 2.2$ eV, B is $0.0 < E_{total} < 1.1$ eV, C is $1.1 < E_{total} < 2.2$ eV and $E_T < 0.8$ eV, and D is $0.0 < E_{total} < 1.1$ eV and $E_T < 0.8$ eV, respectively. Units on the axes are $10^5$ cm/sec.

the overall effect of increased internal excitation in the products, appearing as broadened features and enhancement of channel III in the N($E_T$,eKE) spectrum compared to $O_4^-$.

The MF-DCS spectra observed at all wavelengths are consistent with an $O_6$ precursor in which the photochemistry is determined by the $O_4^-$ core. The additional $O_2$ molecule is truly a spectator and does not participate significantly in the partitioning of momentum in the dissociation. While this is the most likely explanation of both the relatively small stabilization of $O_6^-$ relative to $O_4^-$ + $O_2$ and the observed dynamics, alternate explanations, involving symmetric $O_6^-$ species, cannot be completely ruled out. If, for example, the three $O_2$ formed a planar complex with the centers-of-mass of each $O_2$ in a linear configuration, a dissociation producing two fast and one slow $O_2$ is easy to envision. The end $O_2$ moieties would receive most of the kinetic energy, with the central $O_2$ left behind at the center-of-mass upon dissociation. It is noted in the MF-DCS spectra, however, that in fact the spectator $O_2$ is receiving some momentum in the dissociation. We propose that it is more likely that this comes about from a structure in which the third $O_2$ is added above the plane of the $O_4^-$ core. It is hoped that in the future, high-level quantum chemistry calculations can be carried out to help resolve the question of the structure of $O_6^-$. Such calculations will without question be difficult due to the small binding energy, open-shell electronic configuration and the necessity for the inclusion of large basis sets to deal with the excess electron.

While the significant similarities between the N($E_T$, eKE) spectra for $O_4^-$ and $O_6^-$ and the MF-DCS spectra discussed above suggest that the third $O_2$ only plays a role as a spectator molecule in the photochemistry of $O_6^-$, it is important to note that some unanswered questions remain in this regard. First, in our previous study of the DPD of $O_6^-$ at 532 nm, we applied a simple local-mode Franck-Condon simulation applied to analyze vibrational structure in the $E_{TOT}$ spectrum of $O_6^-$ at 532 nm.(*2*) The 532 nm data showed that the $O_2$ products exhibited higher vibrational excitation in the DPD of $O_6^-$ than $O_4^-$, which is not expected in the spectator limit. Also, as Johnson and co-workers previously discussed,(*9*) and as we noted at 532 nm,(*15,16*) new ionic photodissociation channels appear in $O_6^-$ at the longer wavelengths. In the 388 and 258 nm results reported here, differences in DPD vs. ionic photodissociation in $O_4^-$ and $O_6^-$ are much less striking, although there is a tendency towards larger photodissociation branching ratios.(*16*) To develop a unified understanding of these observations a more detailed theoretical treatment of the potential charge-transfer-to-solvent transitions at longer wavelengths would be of interest. A determination of the multiplicity of the ground state of $O_6^-$, be it doublet or quartet, or a distribution thereof, is also a matter of interest.

## Conclusion

In this work, we have focused on the three-body DPD of $O_6^-$, and showed some of the observables measured and insights gained into the three-body dissociation dynamics of the transient $O_6$ species. This study confirms previous conclusions that the addition of a third $O_2$ to $O_4^-$ does not alter the DPD dynamics significantly from that of $O_4^-$ at the wavelengths of 532, 388 and 258 nm. The MF-DCS spectra were discussed in terms of the three-body dissociation dynamics and used to gain insights into the geometry of the transient neutral species at the time of break-up. The results suggest that the most likely geometry of the anionic precursor $O_6^-$ is an $O_4^-$ core with a weakly bound spectator $O_2$ attached. While theoretical calculations to understand the structure and dynamics of anionic clusters and the corresponding transient neutral species are difficult, it is hoped that the new levels of experimental detail being gained on the three-body dissociation dynamics of these systems will provide motivation. These are fundamental questions which need to be answered, we believe, to provide a solid foundation for the understanding of the transition from gas-phase to condensed-phase dynamics.

## Acknowledgment

This work was supported by the Air Force Office of Scientific Research under Grant F49620-96-1-0220 and DURIP Grant F49620-97-1-0255. AKL is supported by an AFOSR AASERT grant F49620-97-1-0387. REC is a Camille Dreyfus Teacher-Scholar, an Alfred P. Sloan Research Fellow and a Packard Fellow in Science and Engineering.

## Literature Cited

1. C. Maul and K.H. Gericke, Int. Rev. Phys. Chem. **16**, 1 (1997).
2. K.A. Hanold, A.K. Luong and R.E. Continetti, J. Chem. Phys. **109**, 9215 (1998).
3. U. Werner, K. Beckord, J. Becker and H.O. Lutz, Phys. Rev. Lett. **74**, 1962 (1995).
4. S. Hsieh and J.H.D. Eland, J. Phys. B **30**, 4515 (1997).
5. R. Dörner, H. Bräuning, O. Jagutzki, V. Mergel, M. Achler, R. Moshammer, J.M. Feagin, T. Osipov, A. Bräuning-Demian, L. Spielberger, J.H. McGuire, M.H. Prior, N. Berrah, J.D. Bozek, C.L. Cocke, and H. Schmidt-Bocking, Phys. Rev. Lett. **81** (1998) 5776.
6. U. MJller, Th. Eckert, M. Braun and H. Helm, Phys. Rev. Lett. **83** (1999) 2718.
7. R. E. Continetti, Adv. Ser. Phys. Chem.: Photoionization and Photodetachment, ed. C. Y. Ng, World Scientific, 1999 (in press).
8. L. A. Posey, M. J. Deluca, and M. A. Johnson, Chem. Phys. Lett **131** (1986) 170
9. M.J. DeLuca, C.C. Han and M.A. Johnson, J. Chem. Phys. **93** (1990) 268
10. C.C. Han and M.A. Johnson, Chem. Phys. Lett. **189** (1992) 460.
11. K. Hiraoka, J. Phys. Chem. **89** (1988) 3190.
12. C.R. Sherwood, K.A. Hanold, M.C. Garner, K.M. Strong and R.E. Continetti, J. Chem. Phys. **105**, (1996) 10803.

13. A. Aquino, S.P. Walch and P.R. Taylor, J. Chem. Phys. (submitted).
14. K.A. Hanold, M.C. Garner and R.E. Continetti, Phys Rev. Lett. **77** (1996) 3335
15. K.A. Hanold and R.E. Continetti, Chem. Phys. **239** (1998) 493.
16. R.Li, K.A. Hanold, M.C. Garner, A.K. Luong and R.E. Continetti, Disc. of the Faraday Soc., **No. 108**, 115 (1998).
17. K. A. Hanold, A. K. Luong, T. G. Clements and R. E. Continetti, Rev. Sci. Instrum. **70** (1999) 2268.
18. K.A. Hanold, C.R. Sherwood, M.C. Garner and R.E. Continetti, Rev. Sci. Instrum. **66** (1995) 5507.
19. M. Lampton, O. Siegmund and R. Raffanti, Rev. Sci. Instrum. **58** (1987) 2298.
20. A.K. Luong, T.G. Clements and R.E. Continetti, J. Phys. Chem. **103** (1999) 10237.
21. M.J. Travers, D.C. Cowles and G.B. Ellison, Chem. Phys. Lett. **164** (1989) 449.

## Chapter 19

# Fragmentation of $Na_n^+$ Clusters by He Impact: Non-Adiabatic Aspects

**D. Babikov[1], Y. J. Picard, F. Aguillon[2], M. Barat, J-C. Brenot, H. Dunet, J. A. Fayeton, V. Sidis, and M. Sizun**

**Laboratoire des Collisions Atomiques et Moléculaires, UMR 8625, Bât. 351,**
**Université Paris Sud, 91405 Orsay, France**

Abstract:

Collision induced fragmentation of small $Na_n^+$ clusters by He atoms is investigated both experimentally and theoretically in the 100 eV center-of-mass collision energy range. The experiment is based on the determination of the velocity vectors of the fragments using a multi-coincidence technique. The non-adiabatic theoretical treatment is based on a common trajectory approximation for the collision itself, and on a Trajectory Surface Hopping (TSH) calculation to account for the post collisional effects. Three important fragmentation mechanisms are observed: the dissociation may follow a significant momentum transfer between the He atom and a $Na^+$ core in a binary encounter. Conversely, a small momentum transfer to a hot cluster can lead to the formation of a superexcited metastable cluster, which dissociates with a statistical behavior. Finally, the electronic excitation induced by the He atom can bring the cluster into a dissociative state. In these mechanisms, the role of electron pairing is very important.

[1] Current address: Department of Chemistry, University of Illinois, 845 West Taylor Street, Chicago, IL 60637.
[2] Corresponding author.

In Imaging in Chemical Dynamics; Suits, A., et al.;
ACS Symposium Series; American Chemical Society: Washington, DC, 2000.

Fragmentation of clusters by making them collide with atoms is a way of studying the dynamics of energy deposition and its subsequent distribution in polyatomic molecules. Schematically, there are two main mechanisms by which collision induced fragmentation can occur. The first mechanism involves momentum transfer from the relative collision motion to the internal degrees of freedom of the cluster. A particularly simple example of this mechanism is when the projectile atom hits, in a close binary encounter, an atom of the cluster and kicks it out. Another simple example is when an initial binary kick is followed by successive caroms; the transferred energy is shared among several degrees of freedom of the cluster and may yield delayed fragmentation as evaporation. The second mechanism involves an electronic transition to a (pre) dissociative state of the cluster, which automatically entails its fragmentation.

We present here both experimental and theoretical description of the fragmentation of small sodium ion clusters. The experimental apparatus, based on the multicoincidence detection of both neutral and charged particles, allows the simultaneous determination of the velocity vectors of three fragments of the cluster produced by the collision, and the determination of the mass of the ionic fragment. Following previous work on collision induced dissociation (CID) of diatomic molecules ($Na_2^+$ [1,2], $K_2^+$ and $NaK^+$ [3]), this technique is applied to investigate fragmentation of small ionic sodium clusters ($Na_n^+$, $2<n<10$). Simultaneously, the theoretical description of the fragmentation by He impact of $Na_3^+$ is carried out. This theoretical investigation is based on a Diatomic in Molecule (DIM) description of the Potential Energy Surfaces (PESs), improved by explicit incorporation of three-center integrals to efficiently account for the He-cluster interaction. The dynamical calculation takes advantage of the short duration of the collision with respect to the vibrational periods of the cluster. The collision itself and the subsequent fragmentation can thus be described at different levels of approximation, leading to an efficient description of this four-body process. Although they are not as complete as the experimental data, the theoretical results help understand many of the measured phenomena.

## Experimental technique

The experimental technique, presented in Fig.1, is based on the determination of the velocity vectors of the various fragments detected in coincidence. Briefly [2,4], a mass selected cluster ion beam crosses at 90 deg. a cold He target beam produced by a supersonic expansion. The relative cluster-He energy is in the 100eV range. The ionic and neutral fragments are separated in an electrostatic analyzer and detected on two position sensitive detectors (PSDs.) The electrostatic analyzer can be tuned to select an ionized fragment of a given mass, but the mass of the neutral fragments cannot be directly determined by the present technique. In the general case, this leads to an ambiguity. However, in two important cases, we obtain the complete description of the collision: *(i)* if one neutral fragment is detected in coincidence with the ionic fragment, the $Na_n^+ \rightarrow Na_{n-1}^+ + Na$ channel is unambiguously described; *(ii).* ) if two

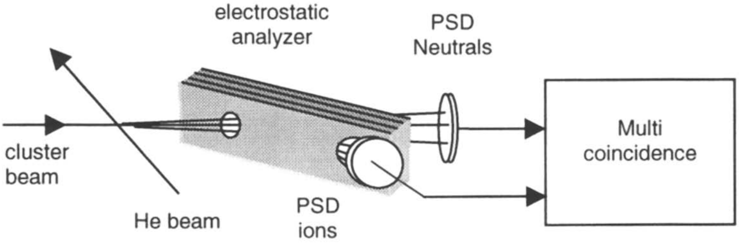

*Fig1: scheme of the experiment*
Copyright 1999 American Institute of Physics.

neutral fragments are detected in coincidence with the ionic fragment, the $Na_n^+ \rightarrow Na_{n-2}^+ + Na + Na$ channel is also unambiguously described. The latter triple coincidence experiments are possible thanks to the very short dead time of the neutral PSD (20 ns).

## Theoretical treatment

The theoretical method used has been described in a previous publication [5] and will only be briefly summarized here. The PESs have been obtained using the DIM formalism. In order to keep the DIM basis at a reasonable size, the He-cluster interaction has been obtained by explicit incorporation of three-center integrals (He-Na-Na') which assumes a non-local separable potential for He[6]. A geometry dependent analytical expression has been assumed for these integrals; it has been optimized by comparing a DIM calculation of the $Na_2^+$-He system with a previous *ab initio* calculation [7] on the same system. Each diabatic state obtained by the DIM method is partially adiabatized by a proper rotation of the basis set. This rotation depends only on the geometry of the $Na_3^+$ cluster, and is chosen to be the one which diagonalizes the Hamiltonian when the He atom is at infinity. Then, the basis used is adiabatic with respect to the intra-cluster motion, and diabatic with respect to the collision He-cluster motion.

The dynamical calculation is carried out in two steps. The first one deals with the collision itself. Because the cluster-atom encounter is so fast ($t_{coll} \sim 10^{-15}$s) compared to the cluster vibrations ($t_{vib} \sim 10^{-13}$s), we confidently use a frozen approximation during this first step. As the collision energy is very large with respect to the energy gap between electronic states, the collision motion is expected not to depend on the cluster electronic state. Then, we use a common trajectory approximation to describe the collision motion. The results of interaction of such a frozen cluster with He atom then are *(i)* population of the electronically excited states of $Na_3^+$ cluster and *(ii)* gain of momentum by clamped cluster's nuclei. The second dynamical step describes the fragmentation of the cluster, which takes place when the He atom has gone. Unlike in the first step, the dissociation trajectory is expected to strongly depend on the electronic state of the cluster. Nevertheless, one has to allow for electronic transitions during the dissociation process. So, we have used in this second step the TSH procedure of Parlant and Gislason [8]. We start this TSH procedure independently for each electronic state that was significantly populated during the He- $Na_3^+$ collision, and the final probability of each branch is multiplied by the initial population of the relevant electronic state.

## Experimental results

A first but important aspect of the cluster fragmentation is the relative fragmentation probabilities for the various pathways, identified by the ionic fragment size. The role of the electron pairing is clearly seen in Fig.2. Except in the n=3 case, the fragmentation preferentially produces the ionic fragment with the largest size having an even number of electrons. The reason for such a behavior is found in two trends of the fragmentation: first, the charge tends to be located on the bigger fragment and second the electrons tend to be paired inasmuch as possible. $Na_4^+$ has an odd number of electrons. So there is always at least one odd numbered fragment in any channel, and the most favorable channel is $Na_3^+$ + Na. Conversely, $Na_5^+$ has an even number of electrons. Its dissociation in the $Na_4^+$ + Na channel produces two electronically odd numbered fragments, which seems less favorable than the $Na_3^+$ + $Na_2$, which produces two even fragments. This behavior is also reflected in the exothermicity of the corresponding channels[9].

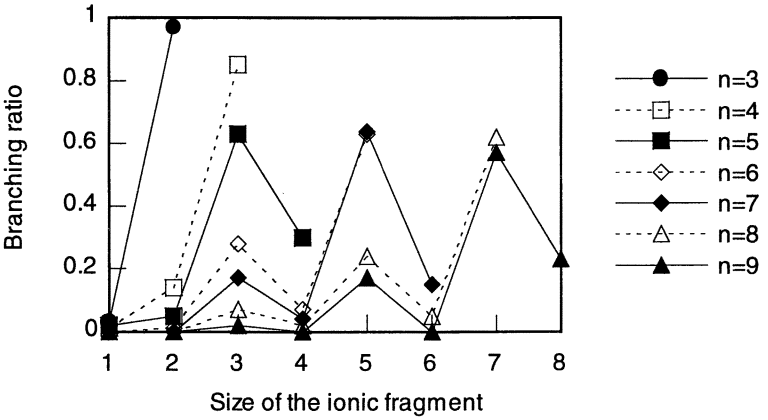

*Figure 2 : Relative probabilities for the various fragmentation pathways of the $Na_n^+$ clusters.*
Copyright 1999 American Institute of Physics.

To go further in the description of the fragmentation dynamics, one can look at the correlation between locations on the vertical axis Z of the two detected fragments, abbreviated as the "ZZ correlation". The meaning of this correlation has been discussed in detail in [10]. In brief, points localized inside the bottom-left and top-right squares indicate a large deviation of the cluster center-of-mass, a signature of an *impulsive* character of the fragmentation process. Conversely, points inside the other

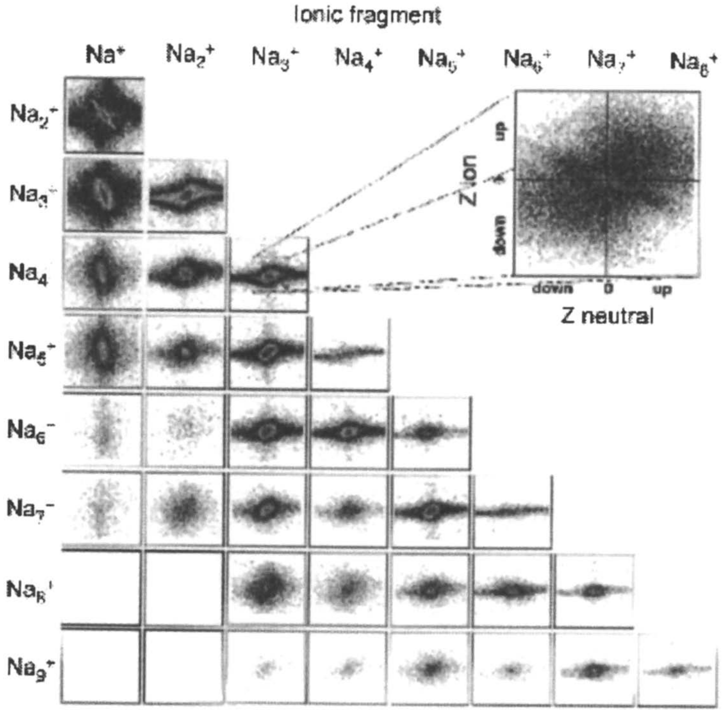

*Figure 3 : ZZ correlation patterns. Rows:* $Na_n^+$ *parent clusters. Columns: identified ionic fragment. Insert: enlarged view of the "bulky" part of the* $Na_4^+ \rightarrow Na_3^+ + Na$ *pattern showing the two components corresponding to electronic and indirect impulsive mechanisms (IM2). Reprinted with permission from Ref. [9].* Copyright 1999 American Institute of Physics.

squares show dissociation without significant deviation of the cluster center-of-mass, a feature of the *electronic* mechanism. A glance at Fig.3 reveals four typical structures: *(i)* backslash structures which reveal an electronic mechanism; *(ii)* a thin almost horizontal slash, indicating a dominant impulsive character, shows the ejection of a neutral fragment with a large velocity; *(iii)* a thin almost vertical slash, indicating a dominant impulsive character, shows the ejection of a ionic fragment with a large velocity; and finally *(iv)* a bulky pattern corresponding to fragments with small fragmentation velocities.

The first column of Fig.3 corresponds to the ejection of a single $Na^+$ ion, the most endothermic pathway; it is always the less populated channel (Fig.2). Asymptotically, this means that this channel always corresponds to an electronically excited state, because one always obtains a more stable configuration by moving the charge to any other fragment (except if all the fragments are atoms). Then, it is not really surprising that the corresponding ZZ patterns are dominated by a nearly vertical linear structure characteristic of fragmentation induced by an electronic transition. The slope increasing with the size of the cluster is given by the mass ratio between the two fragments, a feature that points out the negligible momentum transfer. In addition to the dominant structure, the ZZ correlation shows additional fuzzy features appearing outside the main structure as particularly salient for the $Na_3^+ \rightarrow Na^+$ channel. The interpretation of this fuzzy structure will be given in the theoretical part of the paper.

The $Na^+_n \rightarrow Na^+_{n-1} + Na$ channels located on the diagonal of Fig.3 and corresponding to ejection of a *unique* Na atom are unambiguously identified. They all show a slash structure corresponding to the ejection of a fast neutral Na atom; all but the n=5 and n=7 also show a bulky structure. Within the bulky structure, one can distinguish an electronic backslash structure for n=4, 6 and 8. The slash structure is attributed to momentum transfer between He and a Na atom during a close encounter, followed by the ejection of the kicked Na atom. This can be seen on the so-called $\varepsilon$-$\chi$ correlation diagram, which shows the fragmentation probability as a function of the relative energy of the fragments $\varepsilon$ and the center of mass deflection angle $\chi$ (Fig4). Superimposed to the correlation diagram is the prediction of the binary He-Na elastic moment transfer model, hereafter referred to as impulsive model 1 (IM1). This simple model assumes an elastic collision between He and one of the Na; the other Na atoms are only spectators. The relative energy of the fragments $\varepsilon$ is simply the energy transferred to the kicked Na core minus the energy needed to break the bond between that Na and the rest of the cluster (which depends on the initial cluster temperature). For the $Na_5^+ \rightarrow Na_4^+ + Na$, it is clear in Fig.4 that the $\varepsilon$-$\chi$ correlation diagram is roughly located along this IM1 line, thus indicating an IM1 mechanism. The angular behavior of this fragmentation process [9] is very close to the prediction of the IM1 model. Such an impulsive mechanism is compatible with the weakness (if not the lack) of a vertical slash structure indicating production of a fast $Na^+$ ion. As already mentioned, this channel is energetically disfavored; once kicked by the He, it is very likely that the fast Na core brings adiabatically one electron.

Things are not so obvious for the $Na_4^+ \rightarrow Na_3^+ + Na$ channel. Indeed, only one part of the $\varepsilon$-$\chi$ correlation diagram closely follows the IM1 prediction. The main part of the cross section is found near the origin; besides, this part corresponds to the bulky structure in the ZZ correlation diagram. In the case of $Na_4^+ \rightarrow Na_3^+ + Na$, this structure is the superimposition of *(i)* an electronic contribution (EM) [9], which is due to the unpaired electron in $Na_4^+$, which makes this cluster electronically active,

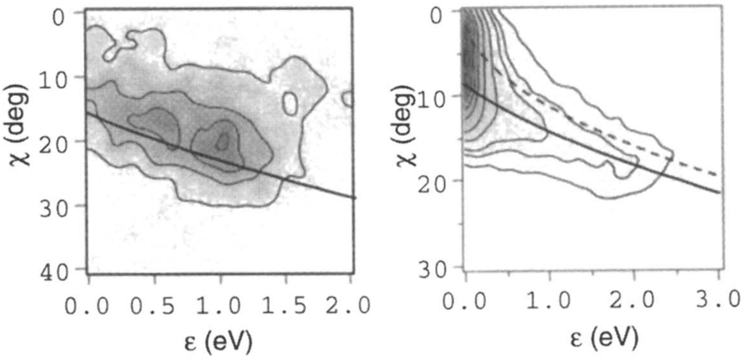

*Figure 4: ε-χ correlation diagram for the channel $Na_5^+ \rightarrow Na_4^+ + Na$ (left frame) and channel $Na_4^+ \rightarrow Na_3^+ + Na$. The full lines give the prediction of the IM1 model with a cluster in its ground state. The dashed line gives the prediction of the same model for a cluster excited up to its dissociation limit.*

and *(ii)* of an indirect impulsive mechanism (IM2) typical of an initially hot clusters, as will be shown in the following. Note that the absence of the bulky structure in the $Na_5^+ \rightarrow Na_4^+ + Na$ ZZ correlation diagram does not necessarily mean that the $Na_5^+$ clusters are cold while the $Na_4^+$ clusters are hot. Both of them, probably produced by evaporation of a bigger cluster after the ionization [11], are certainly hot, but the mechanism which specifically requires a hot cluster leads to the channel $Na_5^+ \rightarrow Na_3^+ + Na_2$, where a ZZ bulky structure is actually observed. Note that the above comparison between $Na_4^+$ and $Na_5^+$ would have been identical for the pairs $Na_6^+$ - $Na_7^+$ or $Na_8^+$ - $Na_9^+$.

Finally, one can examine the channels corresponding to the inner part of the triangle shown in Fig.3. All these channels exhibit strong similarities with those discussed above. For example, the quasi-horizontal slash of the "ZZ" correlation suggests again a fragmentation induced by a direct impulsive mechanism. However the loss of more than one Na atomic fragment cannot be explained by such IM1 alone. Actually this behavior is understood if one further assumes that, after the ejection of the fast Na atom, the hit cluster is left warm enough to evaporate additional Na or $Na_2$ fragments from the remaining $Na^+_{n-1}$. This is confirmed by the fact that all the $Na_n^+ \rightarrow Na_{n-2}^+$ detected events corresponding to this IM1 structure produce one fast neutral Na and one slow neutral Na. Moreover, these IM1 three body fragmentation processes are more probable for the odd value of n. Indeed, the cluster obtained after impulsive ejection of the fast Na atom has an odd value of electrons if n is odd, and is then less stable. The bulky structures involve two contributions similarly to the release of a unique Na atom: *(i)* a two step (IM2) mechanism involving a redistribution of the momentum initially given by a binary He-Na collision; *(ii)* an EM mechanism responsible for the backslash structure. For the $Na_n^+ \rightarrow Na_{n-2}^+$ pathways, both mechanisms produce a dimer fragment. The EM contribution is dominant for the cluster with an odd number of electrons, while the IM2 contribution is dominant for the cluster with an even number of electrons. The trend for the IM2 mechanism to produce low energy fragments will be explained in the theoretical section.

## Theoretical results

At the present time, the theoretical calculations have been carried out only for n=2[7] and n=3[5]. Only the results corresponding to n=3 will be presented here. Fig.5 shows a cut of the three relevant adiabatic PESs obtained in a T shape geometry when the He atom is at infinity. One can note that *(i)* only the ground state shows a minimum, the first excited state has a two fragment dissociative valley, and the second excited state is purely repulsive; *(ii)* there are two intersections between the electronic states. The ground and first excited state show an avoided crossing at large Na-$Na_2$ distance. The two intersecting states are $Na_2^+$ + Na and $Na_2$ + $Na^+$. $Na_2^+$ + Na is the ground state of the system. This breaks the "electron pairing rule" but for this cluster, this pairing rule is not compatible with the "charge localization on the bigger fragment" rule. That could be the reason why the two electronic states are so close to each other. The first and second excited state present a true crossing, which is a conical intersection occurring in equilateral shape.

As mentioned before, the description of the fragmentation process is made simpler by the fact that, at the collision energy studied here (263eV for the theoretical calculation), the cluster fragmentation occurs only after the collision. The He-cluster encounter can induce *(i)* electronic excitation of the cluster and *(ii)* momentum transfer between He and Na core(s). However, one complication arises from the crossings in the PESs, which induce non-adiabatic transitions between the cluster electronic states during the dissociation stage. Then, the description of the dynamics of the fragmentation amounts to answering two questions: *(i)* what is the state of the cluster just after the collision? and *(ii)* what is its final state? As there are three electronic states and three possible channels:

channel A: $Na_3^+ \rightarrow Na_2^+ + Na$
channel B: $Na_3^+ \rightarrow Na^+ + Na_2$
channel C: $Na_3^+ \rightarrow Na^+ + Na + Na$,

we will present our results using a 3x3-matrix, each column corresponding to an electronic state after the collision and each line to a given channel

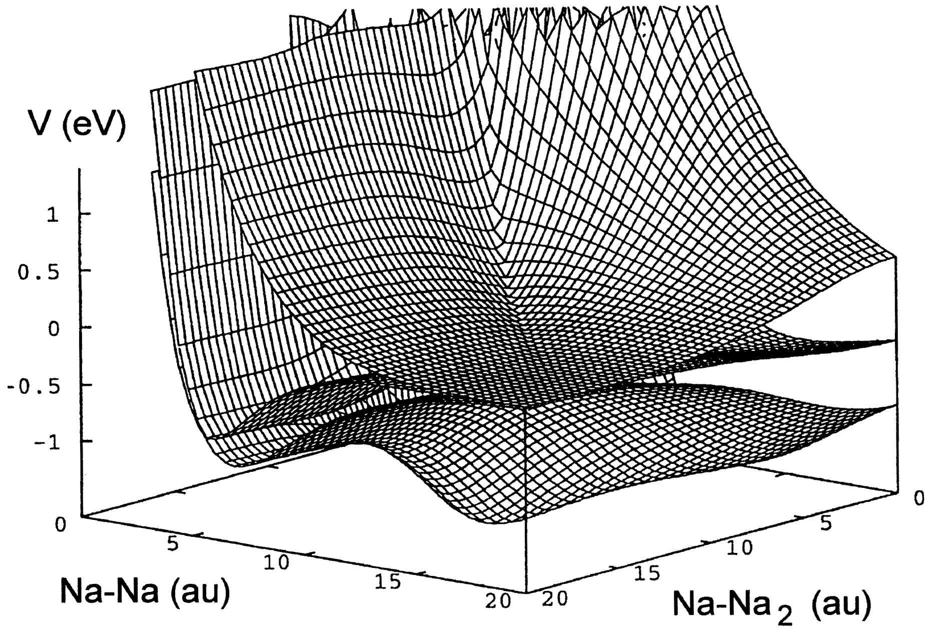

Figure 5: Perspective view of the three lowest PESs of $Na_3^+$ in C2v geometry.

Fig.6 shows the ε-χ correlation diagram matrix obtained by assuming that the ionic cluster is initially in its rovibronic ground state, together with the available experimental results (the B channel is experimentally not accessible: because the detection efficiency is far from 1, when only one neutral fragment is detected, it is not possible to ensure that it is an $Na_2$ fragment and not an Na fragment with the second Na fragment missing). The A1 frame shows almost exactly the same behavior as the simple IM1 mechanism. The C1 frame shows two components. The main one, also aligned with the IM1 prediction, corresponds to He-Na followed by Na-Na' collisions, while the small widespread components correspond to two successive He-Na collisions. The EM mechanisms are not pure electronic mechanisms, since they correspond to a noticeable deflection angles, i.e. to a significant impulsive momentum transfer. The analysis of the He trajectories shows that the coupling between electronic state by the He atom is efficient when He passes *through* the cluster. This is barely possible without touching one of the Na cores. Then, even EM mechanisms have a significant impulsive component. The latter result is not compatible with the ZZ correlation diagram measured (Fig.3), which show a nice backslash structure corresponding to a pure EM mechanism. More generally, the agreement with the experimental data is far from being satisfactory. For example, the main experimental structure of channel A at low energy and low angle is completely missing in the theoretical results; another point is the ratio between channels A and B+C (fig.3) which is much too large in the theoretical results.

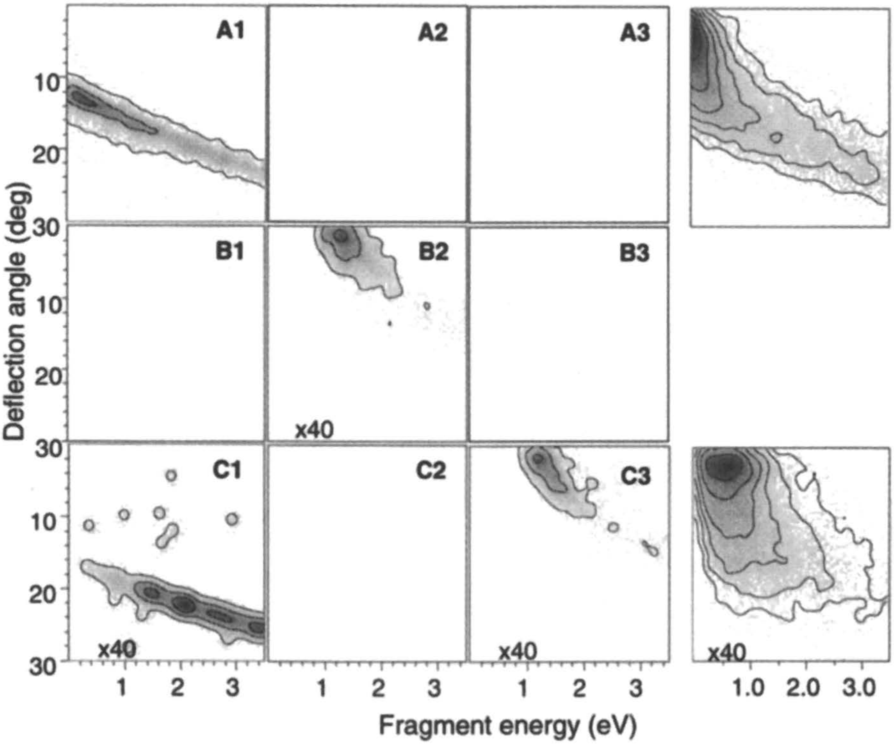

*Figure 6: Matrix of the $\varepsilon$-$\chi$ correlation diagrams for the ground rovibrational state $Na_3^+$ induced fragmentation. The lines refer to the three channels (A, B and C from top to bottom). From the left to the right, the first three columns are the theoretical result corresponding to the ground, first excited and second excited electronic states as populated by the collision with the He atom. The rightmost column shows the corresponding experimental results.*

As suggested by the prediction of the IM1 model on a hot cluster (Fig.4b), these drawbacks can be overcome by assuming that the cluster is initially hot. Besides, one knows that the clusters are obtained by evaporation from bigger clusters; then, they are probably in a high vibrational state. Then, we have performed the theoretical calculation assuming a 1eV vibrational energy for the parent cluster. The resulting matrix of the $\varepsilon$-$\chi$ correlation diagrams is shown in Fig.7. The agreement with the experimental results is much better than for a cold cluster. In particular, the important low $\varepsilon$ - low $\chi$ structure is reproduced, and the ratio between the $Na^+$ and the $Na_2^+$ pathways is close to the experimental one. The $\varepsilon$-$\chi$ correlation diagram for the channel

C (three-body fragmentation) is only qualitatively correct. The reason for this relative discrepancy is probably the poor quality of the second excited PES. We have made pinpoint comparisons of the DIM PESs of the isolated $Na_3^+$ cluster with *ab initio* potentials obtained at the interaction configuration level; this comparison shows that the first excited DIM PES is too low and not repulsive enough, while the second excited DIM PES is too high and too repulsive. Then, the C3 results should be shifted to the left, leading in an improved agreement with the experiment.

The analysis of the trajectories, which contribute to the low $\varepsilon$ - low $\chi$ structure in the A1 frame, which also corresponds to the bulky structure of the ZZ correlation diagram, is very fruitful. These trajectories correspond to situations where the hot cluster gains a small amount of energy by impulsive momentum transfer during the collision with He. After the collision, its vibrational energy is just slightly above the dissociation energy, and the cluster can survive quite a long time in this super-excited state: this is the simplest description of the IM2. Then, it is clear the ZZ bulky structure cannot appear in some fragmentation pathways, e.g. in the $Na_5^+ \rightarrow Na_4^+ + Na$ pathway (see Fig.3). Indeed, because of the relative exothermicities, a superexcited $Na_5^+$ cluster dissociates much more easily by dimer evaporation than by monomer evaporation.

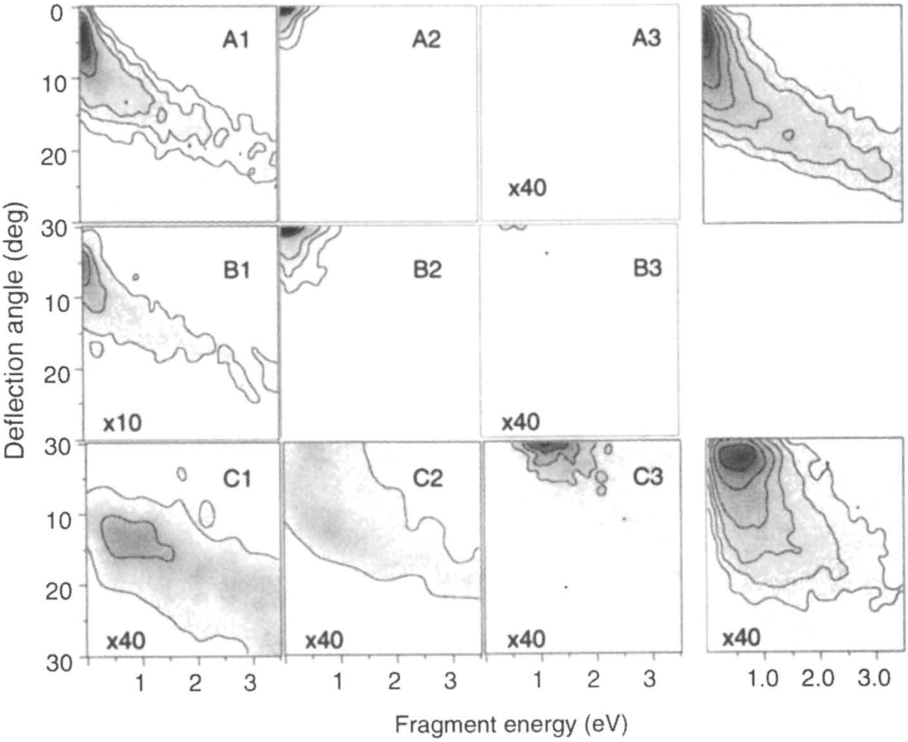

*Figure 7: Same as Fig.6, except that the internal energy of the $Na_3^+$ cluster is now 1eV.*

Another important result of Fig.7 is the pure character of the EM mechanism: in contrast with the cold cluster case, the fragmentation in frames B2 and C3 takes place at $\chi=0$, i.e. without any impulsion transfer. The reason for that is that hot cluster geometries are very elongated. It is thus much easier for the He atom to pass through the cluster –which is almost necessary to induce electronic excitation- without touching the Na cores. There is another difference between EM production for cold and hot cluster: the relative energy of the fragments is much smaller for hot cluster than for cold clusters. This is also due to the fact that EM mechanism occur preferentially with elongated cluster: when the R Jacobi coordinate is large, the excited PESs are closer to the ground PES, and the energy release is smaller.

Finally the last main difference between cold and hot clusters situations is the importance of post-collisional non-adiabatic transitions: there is a significant part of the population in the A1 or B2 frame. One can note that these non adiabatic transitions between the ground and the first excited state only affect the location of the electric charge, and not the dynamics of the nuclei, very probably because the avoided crossing seam between the two surfaces is reached in almost asymptotic regions. Consequently, although the main part of the events detected in channel A are purely impulsive, a small amount (i.e. the contribution of the A2 frame) has the characteristics of an EM process. Conversely, the B channel has mainly the characteristics of an EM mechanism but the B1 contribution to the B mechanism has the characteristics of an impulsive process. These two effects are observed in the experimental results.

## Conclusion

From the present analysis of the various fragmentation pathways, a first finding is that release of $Na^+$ fragments, at least for the smallest (n=3-5) clusters, primarily involves electronic transitions towards dissociative states. In contrast, all other channels are populated via momentum transfer in binary collisions with a $Na^+$ core through one step and two step dynamics. This latter mechanism becomes dominant for large clusters (table I) and shows up through two distinct mechanisms: either ejection of a fast atomic fragment, which can be followed by the evaporation of slower fragments (IM1) or a heating of the hit cluster via Na-Na collisions before evaporation (IM2). Therefore fragmentation dynamics in the 100 eV CM collision energy range seems at variance with that operating at low eV energies where only evaporative mechanisms are generally invoked.

The role of electron pairing in the fragmentation process was already pointed out by Nonose *et. al.* [12] in the preferential "adiabatic" release of a $Na_2$ dimer following $Na_9^+$ dissociation. Such a behavior is also found here at higher collision energy. Among the numerous examples of these pairing effects, the relative contribution of the EM mechanism is more important when the number n of atoms of the ionic cluster is even.

Finally, one must emphasize the key role of the initial cluster temperature: theoretical analysis of the $Na_3^+$ fragmentation shows that the IM2 mechanism does not even exist for cold clusters, and that the EM mechanism is much weaker than for hot clusters. Further calculation on bigger cluster and/or experiments on cold clusters are necessary to check whether this behavior is general (as we believe), or is typical of the $Na_3^+$ cluster.

## References

1. J.C. Brenot, H. Dunet, J.A. Fayeton, M. Barat and M. Winter, Phys. Rev. Lett. **77**, 1246 (1997).
2. J.A. Fayeton, M. Barat, J.C. Brenot, H. Dunet, Y.J. Picard, R Schmidt and U. Saalmann, Phys. Rev. A **57**, 1058 (1998).
3. M. Barat, J.C. Brenot, H. Dunet J.A. Fayeton and Y.J. Picard, Eur. Phys. J. **1**, 271 (1998).
4. M. Barat, J.C. Brenot, H. Dunet, J.A. Fayeton, Y.J. Picard, D. Babikov and M. Sizun, Chem. Phys. Lett. **306**, 233 (1999).
5. D. Babikov, M. Sizun, F. Aguillon and V. Sidis, Chem. Phys. Lett. **306**, 226 (1999).
6. V. Sidis, C. Kubach, D. Fussen, Phys. Rev. A **27**, 2431 (1983).
7. D. Babikov, F. Aguillon, M. Sizun and V. Sidis, Phys. Rev. A **59**, 330 (1999).
8. G. Parlant and E. A. Gislason, J. Chem. Phys. **109**, 4815 (1998).
9. M. Barat, J.C. Brenot, H. Dunet, J.A. Fayeton and Y.J. Picard, J. Chem. Phys. **110**, 10758 (1999).
10. M. Barat, J.C. Brenot, H. Dunet and J.A. Fayeton, Z. Phys. D **40**, 323 (1997).
11. L. Bewig, U. Buck, C. Mehlmann and M. Winter, J. Chem. Phys. **100**, 2765 (1994).
12. S. Nonose, H. Tanaka, T. Mizuno, N.J. Kim, K. Someda and T. Kondow, J. Chem. Phys. **105**, 9167 (1996).

## Chapter 20

# 3-D Coincident Imaging Spectroscopy for Ions and Electrons

**R. Dörner[1], T. Weber[1], M. Achler[1], V. Mergel[1], L. Spielberger[1], O. Jagutzki[1], F. Afaneh[1], M. H. Prior[3], C. L. Cocke[2], and H. Schmidt-Böcking[1]**

**[1]Institute für Kernphysik, Universität Frankfurt, August Euler Strasse 6, D-60486 Frankfurt, Germany**
**[2]Department of Physics, Kansas State University, Manhattan, KS 66506**
**[3]Lawrence Berkeley National Laboratories, Berkeley, CA 94720**

Novel imaging techniques allow the coincident determination of the vector momenta of several ions and electrons from ionizing interactions of photons or charged particles with atoms or molecules. These devices combine 4 $\pi$ solid angle with high resolution in momentum space. They deliver multidimensional images of the multi-particle breakup processes. Electrostatic and pulsed electric fields, magnetic fields and multi-hit capable micro-channel plate detectors are combined in such devices. We focus on some technical aspects and discuss an application to study single ionization in ion-atom collisions.

## Introduction

The investigation of few-particle transitions in atoms or molecules induced by photons or charged particles are a fascinating test ground for our understanding of many-body dynamics in quantum mechanics. Such dynamics of Coulomb systems is the governing factor for much of the structure and evolution in our everyday world. Atomic and molecular many-particle reactions are characterized by fully differential cross sections (FDCS), i.e. cross sections differential in all observables of the final state. In an ionization process of an atom this typically corresponds to the vector momenta, spins and internal excitation of all reaction products. Such FDCS provide the most stringent test for theory. Any integration over observables often masks important characteristics of the process. In turn, experimental FDCS in the best case directly unveil mechanisms of the many-particle transition. Tremendous progress in measuring such FDCS have been made in the field of (e,2e) collisions (see [1, 2, 3] for reviews) and $(\gamma, 2e)$ experiments by detecting two electrons with traditional spectrometers in coincidence (see e.g. [4, 5, 6, 7, 8, 9, 10, 11, 12] ). Coincident momentum space imaging for atomic and molecular reactions which is the subject of this article differs from coincident electron detection techniques mainly by the fact that it covers the full final state phase space of the reaction and that it can be used for the study of ion-atom collisions. Technically it also differs from most of the chemistry imaging work reported in this book by the fact that coincident single particle counting is used.

The basic principles for 3-dimensional coincident momentum space imaging are identical for ion and electron detection. They are based on a small reaction volume (typically below 1 mm$^3$) from which the fragments are guided by electric and magnetic fields to large area position sensitive detectors. The momenta of electron and ion can then be calculated from the time of flight and the position where the particles hit the detectors.

## General considerations for momentum space imaging

The dynamic range of typical energies, momenta and particle masses which is of relevance in the different fields of application of momentum space imaging is several orders of magnitude. We list some examples:

- Slow ion-atom collisions: For reactions like

$$10keVp + He \rightarrow p + He^{1+} + e^- \qquad (1)$$

  typical momenta of the electrons are below 0.6 a.u. (atomic units) corresponding to 5 eV, the momenta of the He$^{1+}$ ions are below 20 a.u. corresponding to an ion energy of 740 meV [13].

- Fast Ion-atom collisions: For reactions like

$$1MeVp + He \rightarrow p + He^{1+} + e^- \qquad (2)$$

  electrons of up to few hundred eV are of interest and ion momenta are in the range of 1 a.u. corresponding to only 1.9 meV ion energy (this holds for other projectils with similar velocity as well).

- VUV photon-atom interaction: For example

$$80eV\gamma + He \rightarrow He^{2+} + 2e^- \qquad (3)$$

  results in electrons below 1 eV (higher photon energies however lead to higher electron energies) and ion momenta of about 0.2 a.u. or energies of 0.07 meV [14].

- Ionization of atoms by femtosecond lasers in the 10$^{14}$-10$^{15}$ W/cm$^2$ regime leads to typical electron energies below 1 keV and ion momenta below 10 a.u. [15, 16].

- Ionization of molecules by ion, photon or laser impact leads to electron energies similar to the ionization of an atom but to ion energies reaching up to 10 eV.

The task is to find field configurations which guide particles with masses from the electron mass up to several $10^5$ times the electron mass and energies from a few $\mu$eV up to several 100 eV towards the position sensitive detectors. The general ingredients used to achieve a projection of these very different particles are the combination of static electric and magnetic fields for the electrons and static and pulsed electric fields with lenses for the ion imaging.

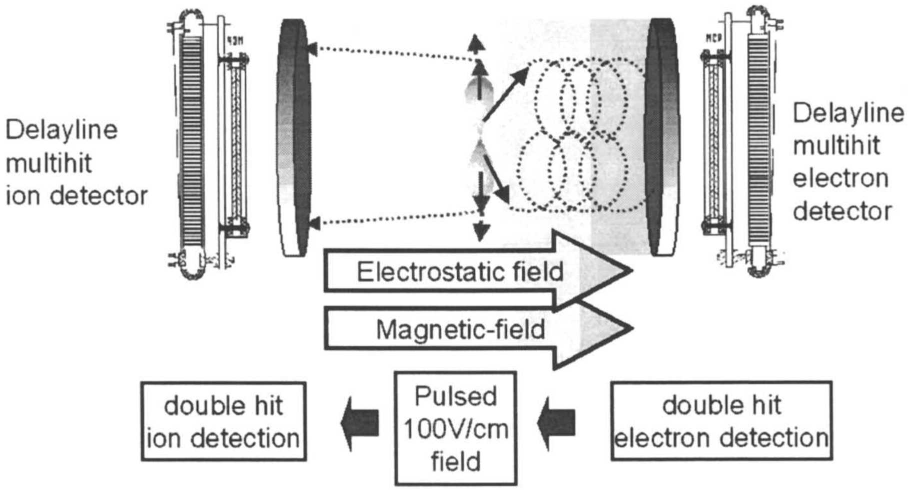

Figure 1: *Schematic of coincident momentum space imaging spectrometer for the investigation of multiple ionization of molecules. A superposition of a weak (few V/cm) electrostatic field and a magnetic field guides the electrons from the reaction volume onto a position sensitive channel plate detector with delayline readout, which is capable of decoding the position of multiple hits. After arrival of the electrons the electric field is pulsed to 80 V/cm to collect the heavy fragment of the molecule onto a second position sensitive detector. Positions and times-of-flight of all particles are recorded in event mode.*

The schematic of a spectrometer used for the investigation of double ionization of $D_2$ by 80 eV photons is shown in figure 1. For this application electron energies range from 0-20 eV and equal mass ions with about 9.5 eV energy each are expected. To achieve $4\pi$ solid angle for the electrons an electrostatic field of about 3V/cm and a magnetic field of 10 gauss was used. The low electrostatic field was necessary first to spread the two electrons out in time over about 100 nsec to circumvent multihit dead time of the detector and second to improve the momentum resolution in the time-of-flight direction. After the electrons reached the detector the electric field was pulsed to about 80 V/cm to collect the ionic fragments.

## Momentum and spatial width of the target

A general limit for the resolution achievable is given by the internal momentum distribution in the target. At room temperature the thermal motion of helium corresponds to 4.6 a.u. of momentum, thus some cooling technique is essential. With the use of supersonic gas jet targets the momentum spread can be easily improved by about a factor of 100, giving a limit of around 0.05 a.u. or 4.6 $\mu$eV. For heavier targets this gets much worse, for two reasons. First typically the speed ratio of supersonic jets is best for helium and worse for heavier gases and the gas nozzles cannot be cooled to 30 K as it can be done for helium. Second the thermal energies stay constant, thus the momenta increase with the square root of the mass. For studies of molecular breakup this is mostly not a severe limitation, since the typical momenta are large, for ionization studies of heavier atoms this becomes a limitation. The use of laser cooled trapped atoms instead of supersonic beams [17] will yield a great improvement in resolution.

Besides the momentum spread of the target also the spatial extension of the target needs to be considered. For ion imaging 3-dimensional focussing has been effectively used to circumvent this problem. In the direction of the electric field a proper choice of acceleration and field free regions can be chosen to make the time-of-flight independent of the starting point of the trajectory [18]. In the two dimensions perpendicular to the electric field electrostatic lenses can be used to focus particle trajectories starting at different positions in the reaction volume to the same position on the detector. The field geometries must be chosen such that the focal plane of the time-of-flight focussing coincides with the focal plane of the lens. Ideally one aims for non dispersive focusing. In electrostatic lenses this requires in general that the energy of the particle when passing the lens is similar for all particles. This means that the energy acquired in the extraction field before entering the lens should by large compared to the energy from the collision. For reactions with atoms where typical ion energies are in the meV regime, this is already achieved with typical extraction field of a few V/cm. For electrons and ions from molecular breakup however very high extraction fields (several 100 V/cm) are necessary. Such high fields effect the momentum measurement in the time-of-flight direction. A field of 1 V/cm corresponds to a difference of flight time of 125nsec for singly charge particles starting with zero or 1 a.u. momentum respectively. This scales linearly with the extraction voltage. Thus fields in the range of 100 V/cm result in no or extremely bad momentum resolution in the time-of-flight direction. Therefore a combination of high resolution in the time-of-flight direction and focussing is hard to achieve for higher energetic particles.

## Magnetic Guiding Fields for Electrons

Electrons with very low energy (up to a few eV) can be efficiently projected onto the detector with fields which are low enough to archive reasonable resolution in the time-of-flight direction. However, the electron detector need to be placed close (a few cm) to the interaction volume to provede a solid angle close to $4\pi$. To guide also electrons with higher momenta transverse to the electric field Moshammer and Ullrich introduced electron imaging with a homogenous magnetic field superimposed parallel to the electric extraction field [19, 20]. The magnetic field forces the electrons into spiral trajectories and thus prevents them from leaving the spectrometer. The revolution time does not depend on the electron momentum. It scales linearly with the magnetic field. By measuring the time-of-flight and the position of impact on the detector the two momentum components perpendicular to the field can be deduced. For time-of-flights which coincide with integer multiples of the revolution time the electrons return to the projection of their starting point on the detector, independent of their momenta. For such times the information regarding the perpendicular momentum is lost.

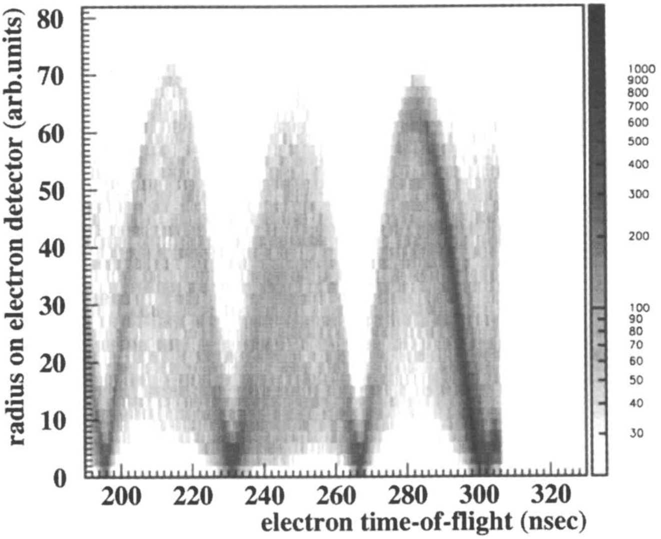

Figure 2: *Distance of electron impact from center of electron detector versus time-of-flight of the electron. The time-of-flight zero increases from right to left, zero is in channel 336. The magnetic field is about 10 gauss, the electrons are from double ionization of $D_2$ by 80 eV photon impact. The nodes correspond to full turns of the electrons in the magnetic field.*

Figure 2 shows the radial distance from the projected position of the reaction volume as a function of the time-of-flight of the electrons. The nodes of the distribution spaced by the revolution time are clearly seen. This gives a highly accurate online calibration of the magnetic field. A magnetic field of 10 Gauss yields a revolution time of 32 nsec. It collects electrons of up to 40 eV onto a detector of 80mm active diameter. The electron spectrometer configuration with electric and magnetic field yields a unique combination of $4\pi$ solid angle up to relatively high electron energies and high resolution in all three dimensions by effectively decoupling the transverse and longitudinal motions. A practical limit for the magnetic field strength and thus the maximum acceptable transverse momentum is given by the revolution frequency. With a typical time-of-flight resolution of 0.5 nsec at fields higher than about 30-40 Gauss (8-10- nsec revolution time) the resolution in the transverse momentum decreases strongly.

## Applications to ion-atom collisions

There are already many examples for multiphoton ionization of molecules in this book. Therefore we choose single ionization in ion-atom collisions as an example to illustrate the power of coincident momentum space imaging for unveiling the driving mechanism of a few-body process. In general single ionization (as equations 1 or 2) is a three-body momentum exchange process. One can approximate it by splitting it in three separate two-body momentum exchange processes between projectile-electron, projectile-ion and electron-ion. Although all three pair-wise interactions are always present, there are paradigmatic cases where one of the three dominates. As example for the dominance of the projectile-ion momentum exchange we discuss 10 keV impact energy and as example where projectile-electron is important we show 0.5 MeV impact energy. These data have been measured by coincident imaging of the momentum vector of the electron and the recoiling ion. The momentum change of the projectile is determined for each event using momentum conservation.

Figure 3 shows the final state momenta of reaction 1, corresponding to a collision velocity of 0.63 a.u.. Thus contrary to most of the chemical 'collisions' discussed in this book here the velocity is of the same order of magnitude as the orbital velocity of the electrons. The electron is not ejected by additional laser assistance, but dynamically from the collision itself. The figure shows that only little momentum is transferred to the electron while the main momentum exchange is between the projectile and the recoiling ion. As the proton approaches the helium atom for a short time a quasi-molecule is formed in which the electron acts as 'glue' which pulls the recoiling ion in the forward direction. As this quasi-molecule breaks apart, in most of the cases the electron relaxes to a bound state of either the projectile or the target. This major channel is not shown in the figure. Only in about 10 % of the collisions is the electron promoted into a continuum state. This channel is shown in figure 3. As can be expected from the above picture of a quasi-adiabatic electron promotion, the momentum exchange between the two

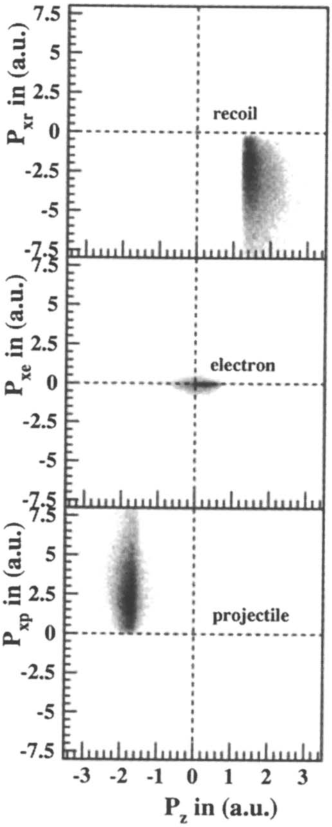

Figure 3: *Projection of the momentum transfer vectors of the* $He^{1+}$ *recoil-ion (upper) electron (middle) and projectile (lower) in the final state onto the plane defined by the projectile beam and the momentum vector of the recoil-ion for 10 keV/u* $p+He \rightarrow He^{1+}+e^{-}+p$*. The* $+p_z$ *axis is parallel to the incoming projectile direction, the* $+p_y$ *axis is parallel to the final transverse momentum component of the recoil-ion. The grey scale represents the corresponding doubly differential cross section* $d^2\sigma/(dk_x dk_{||})$ *on a linear scale (similar to [21]).*

nuclei is dominant, the electron is stranded with very little momentum in between the two centers.

If the projectile velocity is raised to 6.3 a.u. the momentum exchange pattern changes completely (figure 4). Here the projectile passes so fast that no quasi-molecule can be formed. Ionization becomes the main reaction channel. One of the mechanisms leading to the emission of the electron is now a binary encounter between the fast projectile and the bound electron. This can be seen in figure 4 from the partly back to back emission of projectile and electron. The recoiling ion is, contrary to figure 3 no longer pulled in the forward direction.

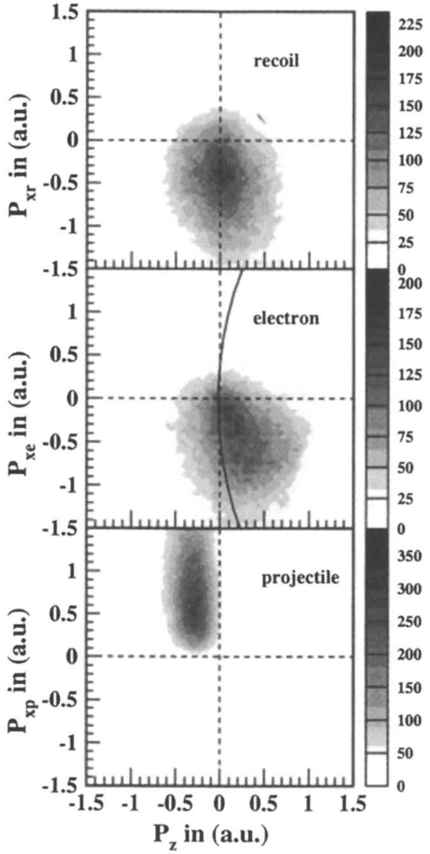

Figure 4: *0.5 MeV/u $p + He \rightarrow He^{1+} + e^- + p$. Projection of the momentum transfer vectors of $He^{1+}$ recoil-ion (upper) electron (middle) and projectile (lower) in the final state onto the plane defined by the projectile beam and the scattered projectile. The $+p_z$ axis is parallel to the incoming projectile direction, the $+p_y$ axis point in the direction of the scattered projectile. The grey scale represents the corresponding doubly differential cross section $d^2\sigma/(dk_x dk_{||})$ on linear scale. The circular arc in the middle figure shows the location of the binary encounter ridge for electrons (from [22]).*

A great amount of coincident 3-dimensional momentum space imaging studies have been performed in the previous 10 years. They include electron impact ionization of atoms [23, 24], single photon double ionization of atoms from threshold [14, 25, 26, 27, 28, 29] to 100 keV [30, 31] and ion impact on atoms from keV protons [13] to GeV/u $U^{92+}$ [32] projectiles, capture and transfer reactions [33, 34], multiphoton double and triple ionization by femto second laser pulses [15, 16] and single photon double ionization of fixed in space molecules [35]. An overview can be found in [36]. The unprecedented resolution and completeness of many of those investigations allowed the resolution of some long-standing puzzles in atomic collision physics but at the same time raised even more fundamental questions.

## Acknowledgements

The work was financially supported by DFG, BMBF and by the Division of Chemical Sciences, Basic Energy Sciences, Office of Energy Research, U.S.Department of Energy. H.B. and R.D. acknowledge support from the Alexander von Humboldt foundation. F.A. greatfully acknowledges support by the DAAD. We also acknowledge financial support from Max Planck Forschungspreis of the Humboldt foundation. We acknowledge helpful discussion with our colleagues Y.D. Wang, S. Keller, R. Dreizler, C. Whelan, J. Walters, H. Khemliche.

## References

[1] M.A. Coplan et al. *Rev.Mod.Phys.*, 66:985, 1994, and References therein.

[2] I.E. McCarthy and E. Weigold. *Rep. Prog. Phys.*, 54:789, 1991.

[3] A. Lahmam-Bennani. *J. Phys*, B24:2401, 1991.

[4] O. Schwarzkopf, B. Krässig, J. Elmiger, and V. Schmidt. *Phys. Rev. Lett.*, 70:3008, 1993.

[5] O. Schwarzkopf, B. Krässig, V. Schmidt, F. Maulbetsch, and J. Briggs. *J. Phys.*, B27:L347–50, 1994.

[6] O. Schwarzkopf and V. Schmidt. *J. Phys.*, B28:2847, 1995.

[7] A. Huetz, P. Lablanquie, L. Andric, P. Selles, and J. Mazeau. *J. Phys.*, B27:L13, 1994.

[8] G. Dawber, L. Avaldi, A.G. McConkey, H. Rojas, M.A. MacDonald, and G.C. King. *J. Phys.*, B28:L271, 1995.

[9] P. Lablanquie, J. Mazeau, L. Andric, P. Selles, and A. Huetz. *Phys. Rev. Lett.*, 74:2192, 1995.

[10] J. Viefhaus, L. Avaldi, F. Heiser, R. Hentges, O. Gessner, A. Rüdel, M. Wiedenhöft, K. Wielczek, and U. Becker. *J. Phys.*, B29:L729, 1996.

[11] J. Viefhaus, L. Avaldi, G. Snell, M. Wiedenhöft, R. Hentges, A. Rüdel, F. Schäfer, D. Menke, U. Heinzmann, A. Engelns, J. Berakdar, H. Klar, and U. Becker. *Phys. Rev. Lett.*, 77:3975, 1996.

[12] J.P. Wightman, S. Cveejanovic, and T.J. Reddish. *J. Phys.*, B31:1753, 1998.

[13] R. Dörner, H. Khemliche, M.H. Prior, C.L. Cocke, J.A. Gary, R.E. Olson, V. Mergel, J. Ullrich, and H. Schmidt-Böcking. *Phys. Rev. Lett*, 77:4520, 1996.

[14] R. Dörner, J. Feagin, C.L. Cocke, H. Bräuning, O. Jagutzki, M. Jung, E.P. Kanter, H. Khemliche, S. Kravis, V. Mergel, M.H. Prior, H. Schmidt-Böcking, L. Spielberger, J. Ullrich, M. Unverzagt, and T. Vogt. *Phys. Rev. Lett.*, 77:1024, 1996. see also erratum in Phys. Rev. Lett. 78. 2031 (1997).

[15] Th. Weber et al. *Phys. Rev. Lett*, , submitted for publication.

[16] R. Moshammer et al. *Phys. Rev. Lett*, , submitted for publication.

[17] S. Wolf and H. Helm. *Phys. Rev.*, A56:R4385, 1997. .

[18] W.C. Wiley and I.H. McLaren. *Rev. Sci. Instr.*, 26:1150, 1955. .

[19] R. Moshammer, M. Unverzagt, W. Schmitt, J. Ullrich, and H. Schmidt-Böcking. *Nucl. Instr. Meth.*, B 108:425, 1996.

[20] H.Kollmus, W. Schmitt, R. Moshammer, M. Unverzagt, and J. Ullrich. *Nucl. Instr. Meth.*, B124:377, 1987.

[21] R. Dörner, V. Mergel, L. Spielberger, M. Achler, Kh. Khayyat, T. Vogt, H. Bräuning, O. Jagutzki, T. Weber, J. Ullrich, R. Moshammer, M. Unverzagt, W. Schmitt, H. Khemliche, M.H. Prior, C.L. Cocke, J. Feagin, R.E. Olson, and H. Schmidt-Böcking. *Nucl. Instr. Meth.*, B127:225–31, 1997.

[22] Th. Weber. Master's thesis, Diploma Thesis, University Frankfurt, 1998. unpublished.

[23] O. Jagutzki, L. Spielberger, R. Dörner, s: Nüttgens, V. Mergel, H. Schmidt-Böcking, J. Ullrich, R.E. Olson, and U. Buck. *Zeitschrift für Physik*, D36:5, 1996.

[24] A. Dorn, R. Moshammer, C.D. Schröter, T. Zouros, W. Schmitt, H. Kollmus, R. Mann, and J. Ullrich. *Phys. Rev. Lett*, 82:2496, 1999.

[25] R. Dörner, T. Vogt, V. Mergel, H. Khemliche, S. Kravis, C.L. Cocke, J. Ullrich, M. Unverzagt, L. Spielberger, M. Damrau, O. Jagutzki, I. Ali, B. Weaver, K. Ullmann, C.C. Hsu, M. Jung, E.P. Kanter, B. Sonntag, M.H. Prior, E. Rotenberg, J. Denlinger, T. Warwick, S.T. Manson, and H. Schmidt-Böcking. *Phys. Rev. Lett.*, 76:2654, 1996.

[26] R. Dörner, H. Bräuning, J.M. Feagin, V. Mergel, O. Jagutzki, L. Spielberger, T. Vogt, H. Khemliche, M.H. Prior, J. Ullrich, C.L. Cocke, and H. Schmidt-Böcking. *Phys. Rev.*, A57:1074, 1998.

[27] H.P Bräuning, R. Dörner, C.L. Cocke, M.H. Prior, B. Krässig, A. Bräuning-Demian, K. Carnes, S. Dreuil, V. Mergel, P. Richard, J. Ullrich, and H. Schmidt-Böcking. *J. Phys.*, B30:L649, 1997.

[28] H.P Bräuning, R. Dörner, C.L. Cocke, M.H. Prior, B. Krässig, A. Kheifets, I. Bray, A. Bräuning-Demian, K. Carnes, S. Dreuil, V. Mergel, P. Richard, J. Ullrich, and H. Schmidt-Böcking. *J. Phys.*, B31:5149, 1998.

[29] V.Mergel, M. Achler, R. Dörner, Kh. Khayyat, T. Kambara, Y. Awaya, V. Zoran, B. Nyström, L.Spielberger, J.H. McGuire, J. Feagin, J. Berakdar, Y. Azuma, , and H. Schmidt-Böcking. *Phys. Rev. Lett.*, 80:5301, 1998.

[30] L. Spielberger, O. Jagutzki, B. Krässig, U. Meyer, Kh. Khayyat, V. Mergel, Th. Tschentscher, Th. Buslaps, H. Bräuning, R. Dörner, T. Vogt, M. Achler, J. Ullrich, D.S. Gemmel, and H. Schmidt-Böcking. *Phys. Rev. Lett.*, 76:4685, 1996.

[31] L. Spielberger, H. Bräuning, A. Muthig, J.Z. Tang, J. Wang, Y. Qui, R. Dörner, O. Jagutzki, Th. Tschentscher, V. Honkimäki, V. Mergel, M. Achler, Th. Weber, Kh. Khayyat, J. Burgdörfer, J. McGuire, and H. Schmidt-Böcking. *Phys. Rev.*, 59:371, 1999.

[32] R. Moshammer, J. Ullrich, W. Schmitt, H. Kollmus, A. Cassimi, R. Dörner, R. Dreizler, O. Jagutzki, S. Keller, H.-J. Lüdde, R. Mann, V. Mergel, R.E. Olson, T. Prinz, H.Schmidt-Böcking, and L Spielberger. *Phys. Rev. Lett*, 79:3621, 1997.

[33] V. Mergel, R. Dörner, J. Ullrich, O. Jagutzki, S. Lencinas, S. Nüttgens, L. Spielberger, M. Unverzagt, C.L. Cocke, R.E. Olson, M. Schulz, U. Buck, E. Zanger, W. Theisinger, M. Isser, S. Geis, and H. Schmidt-Böcking. *Phys. Rev. Lett*, 74:2200, 1995.

[34] V. Mergel, R. Dörner, M. Achler, Kh. Khayyat, S. Lencinas, J. Euler, O. Jagutzki, S. Nüttgens, M. Unverzagt, L. Spielberger, W. Wu, R. Ali, J. Ullrich, H. Cederquist, A. Salin, R.E. Olson, Dž. Belkić, C.L. Cocke, and H. Schmidt-Böcking. *Phys. Rev. Lett*, 79:387, 1997.

[35] R. Dörner, H. Bräuning, O. Jagutzki, V. Mergel, M. Achler, R. Moshammer, J. Feagin, A. Bräuning-Demian, L. Spielberger, J.H. McGuire, M.H. Prior, N. Berrah, J. Bozek, C.L. Cocke, and H. Schmidt-Böcking. *Phys. Rev. Lett.*, 81, 1998.

[36] R. Dörner, V. Mergel, O. Jagutzki, L. Spielberger, J. Ullrich, R. Moshammer, and H. Schmidt-Böcking. *Physics Reports*, page in print, 1999.

## Chapter 21

# State-to-State Dissociation of Molecular Ions

**D. Zajfman**

**Department of Particle Physics, Weizmann Institute of Science, Rehovot, 76100, Israel**

## Abstract

State selective measurement of the dissociation of molecular ions is made possible using molecular fragment imaging technique. We present a specific example which involve the simplest molecular ion $HD^+$, and its dissociation by low energy electron impact. The technique demonstrates that it is possible to follow the reaction path of the dissociation process of each initial vibrational state, as long as the population of these states are known. The population is measured using the Coulomb Explosion Imaging technique, and the measurement takes place in a storage ring, to allow for change of the vibrational population as a function of storage time.

## Introduction

The last 20 years have seen tremendous progress in our understanding of elementary chemical reactions. Molecular-beam experiments have provided very detailed information about the dynamics of inelastic and reactive collisions [1]. Supersonic expansion, leading to a strong reduction of the temperature relevant for the molecular level population, has been widely exploited in experiments dealing with neutral molecules in their vibrational ground state. Much greater experimental difficulties are encountered in producing molecules and molecular ions in well defined excited states and studies of their collision dynamics, important in such areas as high-temperature combustion media or atmospheric processes under nonequilibrium conditions [2], are scarce.

Although the production of beams of molecular ions in a well defined vibrational state has been shown to be possible (more specifically for neutral molecular beams) using complex laser pumping systems, it is a technological challenge to develop such techniques for any molecular ion, since the method usually requires a well suited set of electronic states so that the vibrational population transfer can be done efficiently. In the following we shall demonstrate a different technique for measuring vibrational-state specific reaction rates, with a specific application to the dissociative recombination (DR) process of $HD^+$ [3]. It will be shown that the technique is not limited to DR reaction, but can be applied to a large variety of reactions. The methods presented here are based on advanced molecular imaging techniques and we will also present some new development in the field of three dimensional imaging.

In the following Sections, the basic method for measuring state selected reaction rates, with emphasis on the DR process of $HD^+$ and the storage ring environment is explained. Then a description of the three-dimensional detection techniques used in these experiments will be be given followed by the results of the Coulomb explosion imaging as well as of the DR for $HD^+$. From these results, the vibrational state-selective DR rate coefficients can be extracted. The last Section present some future thoughts about future experiments.

## The Dissociative Recombination of $HD^+$

Dissociative recombination (DR) [4] of molecular ions with free electrons is an elementary reactive collision strongly sensitive to vibrational excitation. In many partly ionized gas-phase environments, the process removes charged particles and produces neutral fragments carrying considerable kinetic energy and often also internal excitation. It is therefore very important in astrophysics and planetary science; for example, the DR of $O_2{}^+$ molecules is responsible for the production of the so-called green-light emission (airglow) in the earth ionosphere [5,6]. For a molecular ion $AB^+$ in an initial vibrational state $\nu$, the DR reaction is described as [7,8]:

$$AB^+(\nu) + e^- \rightarrow A(n) + B(n') \qquad (1)$$

where $n$ and $n'$ are the final quantum states of the fragments A and B respectively. The DR reaction is usually characterized by its rate coefficient $\alpha(E_e)$, where $E_e$ is the kinetic energy of the electron in reaction (1).

For many years, the main problem in laboratory study of this process has been the extreme sensitivity of DR to the initial vibrational state of the molecular ion. During the last few years, the heavy-ion storage ring technique has been used to produce infrared active molecular ion beam in their ground vibrational state [9]. In this technique, a vibrationally excited molecular ion beam is generated by a standard (hot) ion source, and injected into the storage ring where it is stored for a time which is long enough to allow for complete vibrational relaxation through infrared transitions between the various vibrational states. Rotational cooling has also been demonstrated using this technique, the limit here being the blackbody radiation of the storage ring walls (300 K) [10]. After full relaxation is obtained, the beam is merged with an intense, cold electron beam (see Fig. 1), which is produced within an electron cooler device [11] at a velocity similar to that of the ion beam. Due to the kinematical transformation between the energies in the laboratory frame of reference to the center of mass frame of reference, a strong reduction is obtained in energy spread, and resolution down to few meV are usually obtained in the study of DR reactions. The heavy-ion storage ring technique has led to many breakthroughs in the field of DR, and has considerably enhanced the theoretical understanding of this process [9].

An important step forward for the storage-ring techniques, would be the possibility to measure the DR cross section also for individual excited vibrational states, i.e., not only for the ground state. A reaction well suited for initiating these studies is the DR of $HD^+$ with low-energy electrons (experimental energy spread ~10 meV). $HD^+$ is the simplest molecular ion subject to vibrational relaxation by infrared emission. Its DR with low-energy electrons can be depicted as

$$HD^+(\nu) + e^- \rightarrow \begin{array}{c} H(1s) + D(nl) \\ \text{or} \\ H(nl) + D(1s) \end{array} \qquad (2)$$

where

$nl$ denotes the orbital of the electron in the atomic fragments. Starting with the capture of an electron by the molecular ion, a rearrangement of the whole electronic cloud leads to a transfer of kinetic energy to the dissociating nuclei. The DR from lower lying vibrational states $\nu$ of $HD^+$ predominantly starts by electron capture in the $^1\Sigma_g^+$ doubly excited, dissociating state of neutral HD (Fig. 2). This state crosses all the vibrational levels of $HD^+$ at different locations. The recombination rate therefore strongly depends on the vibrational excitation of the ion. For higher vibrational excitation, an additional effect involving the next $^3\Pi_g$ dissociative curve and higher dissociative Rydberg states can be expected. It is important to point out that the $^1\Sigma_g^+$ as well as the $^3\Pi_g$ doubly excited states cross an infinite number of Rydberg states (shown in the inset in Fig. 2) and that the dissociating flux coming from these dissociating states can branches to these Rydberg levels, producing different degrees of electronic excitation in the product, depending either on the initial vibrational state or on the initial electron energy. Fig. 2 also illustrates that measurement of the kinetic energy release $E_k$ identifies both the initial and the final state of the reaction.

The main ideas behind the experimental technique is to measure, on one hand, the final states of the DR reaction for a beam of vibrationally excited $HD^+$, and on the other hand, to measure the vibrational population of the beam using the Coulomb Explosion Imaging (CEI) technique. Both experiments require to measure the kinetic energy release of the dissociation fragments.

The experiments were carried out at the Max-Planck-Institut für Kernphysik, Heidelberg, Germany using the Test Storage Ring (TSR) (see Fig. 1 [11]. A 2.0-MeV $HD^+$ beam produced by a standard Penning ion source was injected into the TSR; typically $10^7$ particles circulated in the ring with a lifetime of $\sim$ 10 s. The vibrational cooling time of $HD^+$ is about 300 ms, depending on the initial vibrational excitation created in the ion source. The circulating beam was merged with a 3.5-cm diameter, quasimonochromatic electron beam over a length of 1.5 m, providing electrons at a typical density of $2\times10^6$ $cm^{-3}$ and a temperature of 10 meV in the comoving reference frame. Recombination fragments produced in this interaction region were detected as a function of the storage time $t$ using an imaging microchannel plate located 6 m downstream [12], yielding the state-specific recombination rates $r_\nu(t)$. The level populations $N_\nu(t)$ were measured as a function of storage time from injection ($t = 0$) to complete relaxation ($t > 300$ ms), by extracting a part of the beam from the ring toward the CEI setup (see Fig. 1). The combination of these results then yields the DR rate coefficient $\alpha_\nu$ for molecular ions in a vibrational state $\nu$ as

$$\alpha_\nu = K\, r_\nu(t)/N_\nu(t) \tag{3}$$

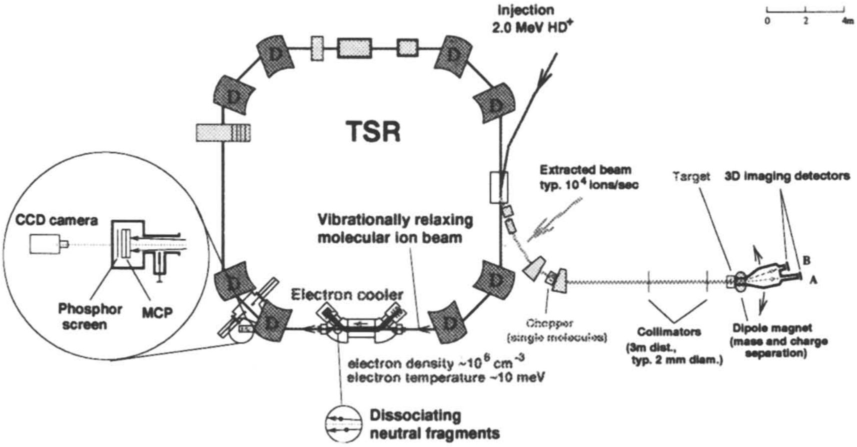
Injection
2.0 MeV HD⁺
0 2 4m
TSR
D
Extracted beam
typ. 10⁴ ions/sec
Target
3D imaging detectors
CCD camera
Vibrationally relaxing
molecular ion beam
Electron cooler
Phosphor screen
MCP
Chopper
(single molecules)
Collimators
(3m dist.,
typ. 2 mm diam.)
Dipole magnet
(mass and charge separation)
B
A
electron density ~10⁶ cm⁻³
electron temperature ~10 meV
Dissociating
neutral fragments

FIG. 1. Schematic drawing of the TSR storage ring, including the extraction towards the dedicated beam line for the Coulomb explosion imaging (CEI) of the molecular ions.

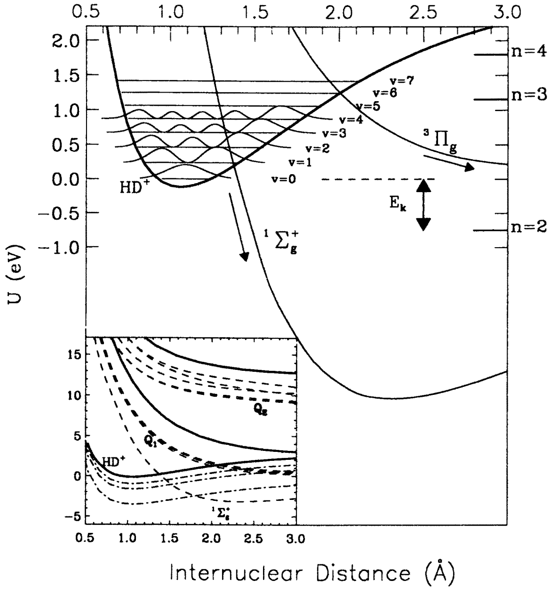

FIG. 2. Potential energy curves for $HD^+$ and HD. For $HD^+$ only the ground electronic state is shown together with the position of its vibrational levels and some corresponding vibrational wave-functions squared. For HD, some of the Rydberg states ($Q_1$ and $Q_2$ series) are shown.

with a normalization constant $K$ independent of $t$ and $\nu$. The experiment aims to determine rate coefficients relative to $\alpha_{\nu=0}$, therefore absolute normalizations of $r_\nu(t)$ and $N_\nu(t)$ are not required.

## Three-dimensional Molecular Fragments Imaging

As pointed out in the previous section, in order to measure the final state for the DR of $HD^+$, it is necessary to measure the kinetic energy release of the DR fragments, as well as the kinetic energy of the fragments after the Coulomb explosion imaging. Because of the fast velocity of the beam, the detector must have very good spatial resolution (better than $100\mu m$) and very good time resolution ($\approx$ 100 ps). The detector must also be able to measure *simultaneously*, i.e., with no dead-time at all, the position and time of impact of few particles.

For the detection and amplification of the original signal, most of the detectors use standard micro-channel plates (MCP) with various schemes of anodes. As the requirement is to measure the position and time of impact of all the fragments simultaneously, the standard technique of resistive anode [13,14] is useless as it allows the measurement of the time and position of a single particle only. Hence, different techniques have been developed, such as the segmented anode [15,16], the crossed-wire anode [17], and direct imaging using phosphor screen and video techniques together with pick-up wires [18]. Very often, the detector geometry (and/or the anode geometry) have been adapted to a specific experimental situation or problem.

In the present experiments, the basic imaging technique is based on the use of CCD video camera to measure the positions of impact, providing a two-dimensional image of the dissociation event, together with a time pick-up technique, which measure the time differences between the impact of the different fragments. Two different pick-up techniques were used.

### The CEI detector

The CEI detector consist of a two-stage microchannel plate with a CsI-coated, aluminized mylar foil located in front of the detector, in order to achieve nearly 100% detection efficiency on the MCP. Behind the MCP the amplified electron pulse generated by the particle impact is accelerated onto a P-20 phosphor layer that resides on top of a $17\,\mu m$ thin kapton foil. The electrons impact creates visible light spot which are imaged by a CCD camera, which, after digitization (see below), yield the transverse ($x$ parallel and *y* perpendicular to the magnet deflection plane) coordinates of the particle impact positions. The video signal from each of the two cameras is fed into a Frame Threshold Suppressor (FTS), a VME module developed at the Weizmann Institute of Science [18] which digitizes each video frame by a 10 MHz, 8bit ADC and produce a list of pixels whose intensity exceeds a programmable threshold. Under typical condition, the pixel diameter of the CCD correspond to 200 $\mu$m on the phosphor screen surface. Since the impact position of a particle is taken as an intensity weighted average over 20-50 pixels, the resolution in the transverse coordinates amounts to $\sim$ 100 $\mu$m .

The time difference between the various particle impact is measured using strip electrodes which are printed on the kapton foil located on the phosphor screen. These strips are use to pick up the fast timing signals induced for each bunch of electrons hitting the phosphor screen [19]. The printed circuit has been photochemically created from a 17 $\mu$m thin copper coating on top of the kapton foil, and is made of 93 wires (100 $\mu$m wide, 1.0 mm apart) for the rectangular detector and 64 wires (1.85 mm apart) for the circular detector; the wire orientation is vertical, i. e. perpendicular to the deflection plane of the postdeflector. The detector described in ref. [18], used freely stretched thin wires (50 $\mu$m diameter) in front of the phosphor screen instead of the printed wires behind the phosphor screen in the present setup. It was found that this new last configuration produces stronger signal than in the previous design. In order to avoid efficiency losses when two particles hit the same anode wire, the circular detector has 32 additional anode wires (3.75 mm apart) on the back side of the kapton foil at right angle to the wires on the front side (parallel to the deflection plane of the postdeflector). The time resolution achieved with this setup can be measured as the uncertainty of the time difference between a start and a stop signal from the same particle, neglecting the small contribution from the drift time spread in the MCP. This measurement yield a value (averaged over the wires) of 130 ps (FWHM) with a one standard deviation spread of 30 ps.

## The DR imaging detector

Fig. 3 shows a schematic view of this new multi-particle 3-D imaging detector. The particles are detected by a 40 mm diameter two-stage MCP, and, subject to the detection efficiency of the MCP, each impact produces a light spot of $\sim$ 1-1.5 mm diameter on a P-20 phosphor screen located behind the MCP. The spatial position of each impact is extracted by digitizing

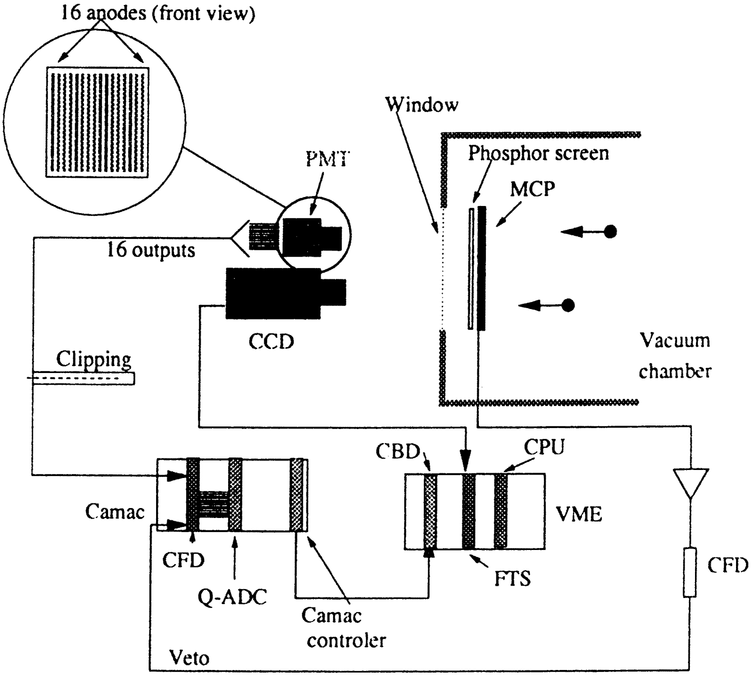
16 anodes (front view)
PMT
16 outputs
CCD
Clipping
Window
Phosphor screen
MCP
Vacuum chamber
CBD
CPU
VME
FTS
CFD
Camac
CFD
Q-ADC
Camac controler
Veto

FIG. 3. Schematic drawing of the 3-D imaging detector setup. The inset on the upper left corner shows the geometry of the anode strips in the photomultiplier. PMT: Photomultiplier, CCD: Charge Coupled Device camera, CFD: Constant Fraction Discriminator, Q-ADC: Charge Analog Digital Converter, CBD: CAMAC Branch Driver, FTS: Frame Threshold Suppressor.

the images formed on the phosphor screen using a standard CCD camera, focused on the phosphor screen through a vacuum window (as for the CEI detector). The video output is digitized by a fast frame grabber device which is read out by a VME computer [18]. Upon analysis, the 2-D position of each impact is determined using a peak finding procedure. The time of arrival of each impact on the surface of the detector is obtained using a multi-anode PMT (Hamamatsu Model R5900U-00-L16), located *outside* the vacuum chamber.

The image of the phosphor screen is focused on the PMT using standard lens optics. The present multi-anode PMT has 16 independent anodes (shaped as narrow strips, or wires), each of area of 16×0.8 $mm^2$, separated by 0.2 mm dead space between each pair. Other geometries are available such as square pads (4×4 or 8×8 independent pads). If each light spot created on the phosphor screen by the impact of a single particle is focused on a different anode, the time of impact of a few fragments can be measured simultaneously by analyzing the 16 outputs of the PMT. For the sake of clarification, we emphasize again that both the 2-D position and the time of all impacts are measured simultaneously. In order to obtain the position and the relative time of arrival of each fragment on the detector surface for one single molecular dissociation (event) at a time, the MCP-phosphor screen assembly is operated in the so-called trigger mode [20,21]. In this mode of operation, the potential of the phosphor screen, which is used to accelerate the electrons from the MCP output plate to the screen itself is lowered to the MCP potential (fall time of about 1 $\mu$s) as soon as an "event" is detected on the screen. The trigger for this is the logical "OR" signal generated by the constant fraction discriminators connected to the anode outputs (see Fig. 3). The high-voltage is turned back on as soon as the video output has been stored in the frame grabber. This ensures that only one event is digitized at a time, and that the measured coordinates (space and time), as obtained from the CCD and the PMT respectively, can be correlated to a single dissociation event.

## Dissociative Recombination of $HD^+(\nu=0)$

In this section we present the results for the DR of $HD^+(\nu = 0)$ for electron energy in the range $0<E_e<2.5$ eV. In such a case, the initial vibrational state of the molecular ion beam is known, and the imaging data provided by the DR detector is used to determine the reaction path of the reaction, i.e.

the final quantum state of the fragments (see Eq. 2). For low energy electron ($E_e$ <1.16 eV), the only energetically allowed states are when one of the two fragments (H or D) are in the ground electronic state (1s) and the other is either in the 1s or 2(s,p) state. However, above this energy, more and more states are opening, and the experiment allows to follow the way the wave packet formed in the doubly excited state ${}^1\Sigma_g^+$ by the electron capture split among the various final states, through a series of infinite avoided crossings with the Rydberg states of HD (see Fig. 2).

The results from the imaging detector are shown in Fig. 4. From the relative position $d_{2D}$ and the time difference $\Delta t$ between the impacts for each pair of H and D fragments, their three-dimensional distance $d_{3D}$ upon arrival at the detector can be determined using the relation $d_{3D}^2 = (v_0 \Delta t)^2 + d_{2D}^2$, where $v_0$ is the beam velocity and $v_0 \Delta t$ and $d_{2D}$ are assumed to be small compared to the distance from the dissociation point to the detector. The kinetic energy release $E_k$ in the c.m. frame is represented by the difference between the c.m. electron energy $E_e$ and the internal (electronic) energy of the fragments, measured relative to the initial (rovibrational) energy level of $HD^+$. Recombination events associated with a kinetic energy release $E_k$ yield the three-dimensional fragment distance

$$d_{3D} = L\,(M/\sqrt{m_1 m_2})\,\sqrt{E_k/E_0}, \tag{4}$$

where $E_0$ is the ion beam energy, $L$ the distance from the dissociation point to the detector, $M$ the molecular ion mass, and $m_1$ and $m_2$ are the fragment masses. The distribution of the measured three-dimensional distances $d_{3D}$ for events with given fixed $E_k$ is broadened in this experiment by the finite extension of the interaction region (1.5 m $\approx$ 23% of the average distance $L_0$ = 6.47 m) and by the 170-ps time resolution ($\approx$ 17% of the typical relative time difference of $\approx$ 1 ns).

The three-dimensional distance spectra as measured for three different electron energies in a time interval of 1–15 s after the injection are shown in Fig. 4. Background substraction and correction for the efficiency of the photomultiplier, considering its detailed anode structure, have been applied [22]. The expected relative distances $d_{3D}$ for recombination into the different final channels $n = 2, 3, 4$, calculated for $HD^+$ ions in the rovibrational ground state and for $L = L_0$, are marked with an arrow. As can be seen, the different contributions show up as separate peaks centered close to the calculated positions, which confirms both the relaxation of the ions stored in the ring and the resolution obtained in the fragment imaging.

At $E_e = 0$ (Fig. 4(a)), only a single peak is found, demonstrating than only the $n = 2$ final channel is populated. At $E_e = 1.81$ eV (Fig. 4(b))

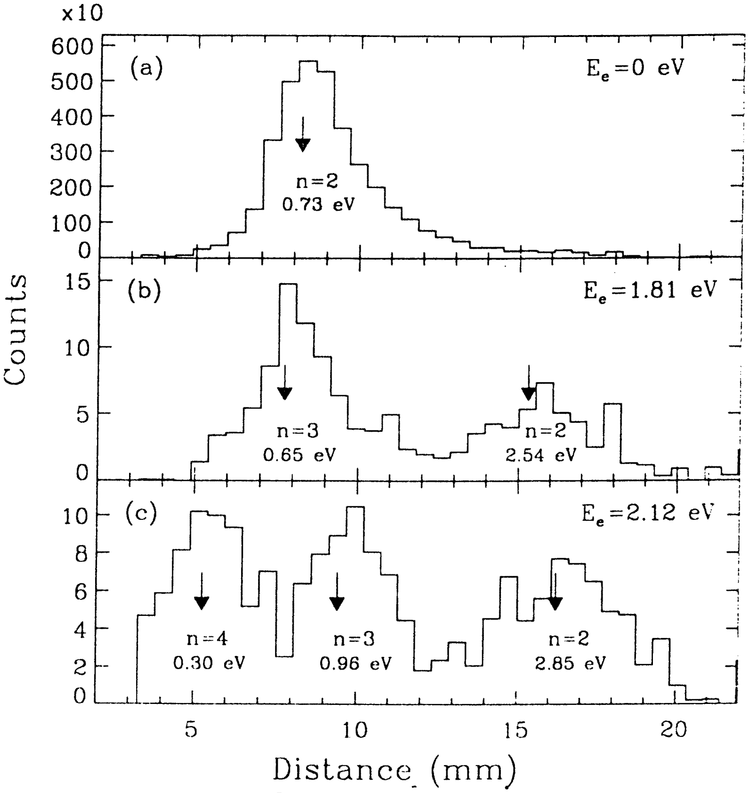

FIG. 4. Distributions of the three-dimensional distance between the DR fragments as measured for different electron energies: (a) $E_e = 0$, (b) $E_e = 1.81$ eV, and (c) $E_e = 2.12$ eV. Each peak in the spectra is marked with its corresponding final state and its kinetic energy release $E_k$.

the $n = 3$ channel is also accessible and indeed formed with relatively high branching ratio; at $E_e = 2.12$ eV (Fig. 4(c)) also the $n = 4$ channel is open and do yield a sizeable contribution. Hence, it is immediately apparent from these spectra that DR leads to substantial production of excited products as soon as the electron energy is above the threshold for their formation. For the whole series of measurements taken at $0 < E_e < 2.5$ eV, the branching ratios were obtained by integrating the surfaces of the observed peaks and normalizing the results to yield a unity sum; the results are shown in Fig. 5. The error bars are mainly due to the background subtraction and to the uncertainties in the detector efficiencies for different fragment distances. The results show that the opening of each new channel occurs very fast at its energetic threshold. However, when more and more channels open with increasing electron energy, no single asymptotic state is really predominant. The lines drawn are the results of a simple Landau-Zener model [23].

## Coulomb Explosion Imaging of $HD^+$: Measurement of Vibrational State Population

The CEI can directly measure the internuclear distance distribution of molecular ions. In this technique [24,25], a fast (MeV's) molecular ion is directed towards an ultra thin target (60 Å) where the electrons of the projectile are stripped on a time scale which is much shorter than the typical vibrational or rotational time. Thus, for a diatomic molecular ion impinging on such a foil, two highly charged ions are produced on the exit side of the foil, with an internuclear distance which is identical to the one prior to stripping. These two ions repel each other with the well known Coulomb force until they are far enough so that the initial (Coulomb) potential energy of the system has been completely transformed to kinetic energy. The velocity of each fragment is then measured using three-dimensional imaging detectors located few meters downstream (see Fig. 1). This measurement allows to extract the kinetic energy release ($E_k$) in the center of mass of the molecular ion, a value which is directly related to the initial internuclear distance $R$ of the molecular ions at the time of stripping by the foil:

$$E_k = \frac{q_1 q_2}{R} \tag{5}$$

where $q_1$ and $q_2$ are the charge states of the fragments. Such measurements are performed one molecular ion at a time, and after many events are accumulated for a storage time $t$, a distribution of kinetic energies $\tilde{P}(E_k; t)$

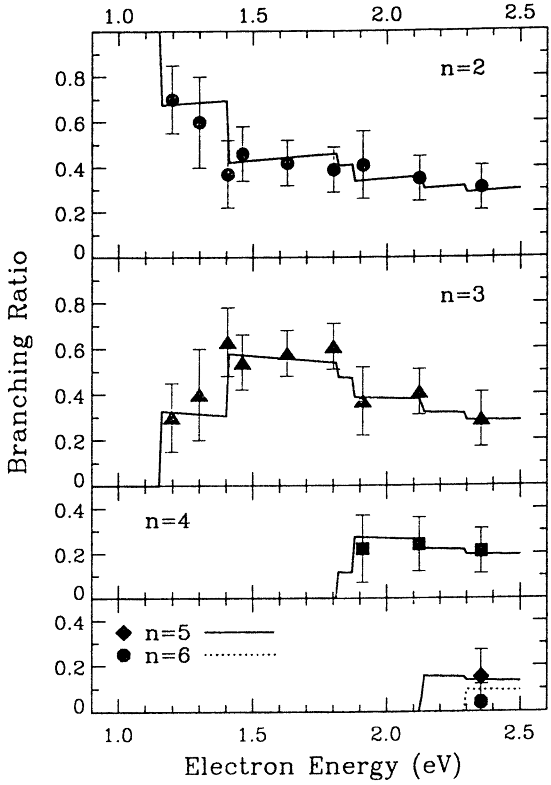

FIG. 5. Branching ratios for the DR of HD$^+$ as a function of the electron energy for the final states $n = 2$, $n = 3$, $n = 4$, and $n = 5, 6$. The symbols are the experimental results and the lines the results of the calculation. The theory for $n = 5$ and 6 is shown by full and dashed lines, respectively.

is generated. Since each events represents a "snapshot" of the internuclear distance at stripping, the kinetic energy distribution is an "image" of the internuclear distance distribution, $P(R;t)$, which by itself is directly related to the square of the nuclear vibrational wave functions $\Psi_\nu^2(R)$ of the molecular ion:

$$\tilde{P}(E_k;t)dE_k = P(R;t)dR = \sum_\nu a_\nu(t)\Psi_\nu^2(R)dR, \qquad (6)$$

where $a_\nu(t)$ is the relative population of the vibrational level $\nu$ after storing the ions for a time $t$. For most of the diatomic molecular ions, the nuclear wave functions $\Psi_\nu^2(R)$ are known, so that the distribution $\tilde{P}(E_k;t)$ can be fitted with a set of $a_\nu(t)$ as free parameters, hence making it possible to extract the vibrational state population as a function of storage time.

Fig. 6 shows the kinetic energy release distribution $\tilde{P}(E_k)$ as measured for various storage times. The vibrational cooling of the ions in the ring is clearly seen in the data, and the final distribution (at time $t > 400$ ms) matches perfectly the expected kinetic energy distribution for the ground state of $HD^+$ (see Fig. 6(D)). It is important to point out that the kinetic energy release for each state is calculated using a Monte-Carlo simulation which takes into account the small broadening due to the multiple scattering of the ions in the thin target [26]. In Figs. 6(A),(B) and (C), the different $\tilde{P}(E_k)$ contributions are shown at shorter storage times, reflecting different vibrational excitations.

Based on these distributions, both the initial population as well as the lifetime of each state can be extracted. Fig. 7 shows the time evolution for the vibrational state $\nu = 0 - 11$, and it is clearly seen that after 300 ms, the whole beam is in the vibrational ground state.

## Dissociative Recombination of Excited $HD^+$

The $HD^+$ beam was merged with the electron beam provided by the electron cooler of the TSR (see Fig. 1). The electron beam energy was tuned so that the center-of-mass energy was adjusted to $E_e = 0$. The distribution of two-dimensional distances ($D$) between the H and D fragments was measured downstream about 6 m from the center of the electron beam. For a single vibrational state, the shape of such a distribution has been calculated by Amitay *et al.* [27] and for a given kinetic energy release, the distribution rises from zero at $D = 0$, to peak at a distance $D_1$ and then decreases again

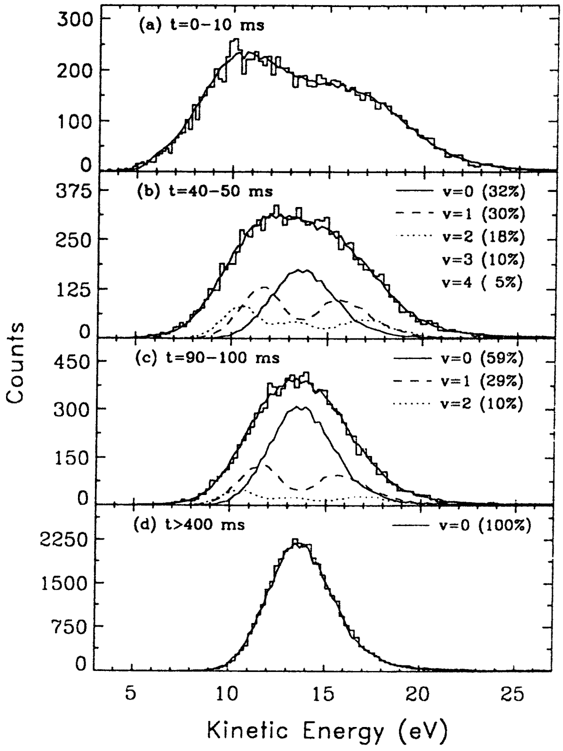

FIG. 6. Kinetic energy spectra measured for Coulomb explosion imaging of $HD^+$ for different storage time slices: (a) 0-10 ms, (b) 40-50 ms, (c) 90-100 ms, and (d) $t > 400$ ms. The thick solid lines represent the fits as described in the text. Panels (b)-(d) display also the vibrational populations (those above 5%) obtained from the fit, together with the main contributions to the spectrum (thin solid, dashed, and dotted lines)

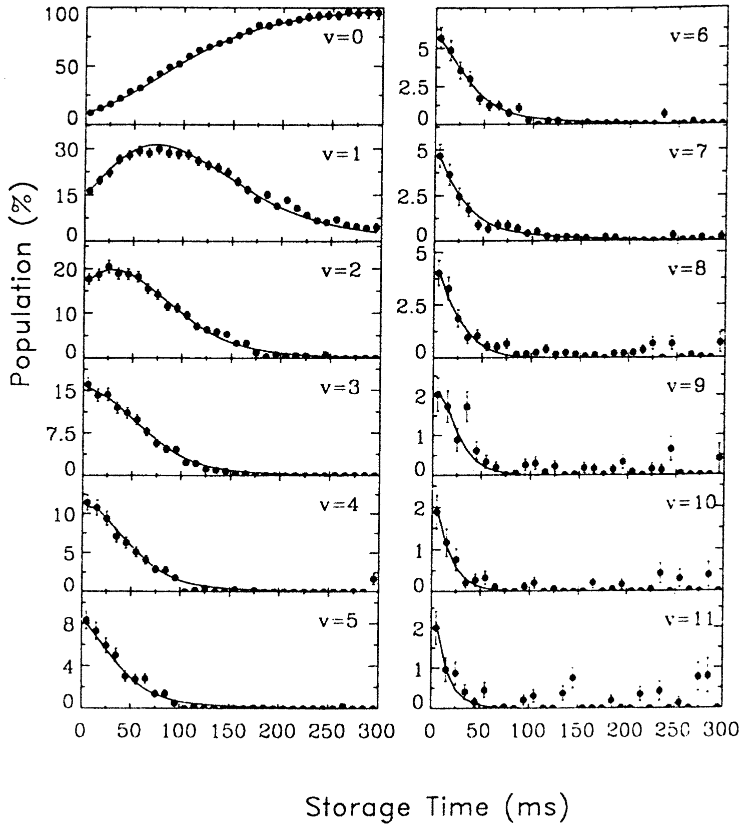

FIG. 7. Time evolution of the vibrational state population for $0 \leq \nu \leq 11$ as obtained from fitting the time-sliced CEI kinetic energy spectra. The smooth lines through the experimental points are the results of fitting the time evolution of the measured populations.

with an edge at the maximal distance $D_2$. Both $D_1$ and $D_2$ are a function of the kinetic energy release in the dissociation process [27]. Such spectra, for various storage time, are shown in Fig. 8. These distributions represent the sum of the contributions to the total DR rate. For electrons with $E_e$=0, and $HD^+$ in vibrational states $\nu = 0 - 7$, only two possible final states exist: H(1s) + D(n) (or D(1s) + H(n)) where n=2 or 3 (see Fig. 2). In such a case, it is relatively easy to extract the contributions from each vibrational state to the total DR rate coefficient. These contributions $[\nu, n]$ are shown on Fig. 8(c) and represent the initial ($\nu$) to final ($n$) state branching ratio for the DR of $HD^+$ for the various time-dependent vibrational populations.

From the contributions from the two-dimensional DR spectra, using the known population coefficients $a_\nu(t)$ as measured by the CEI technique, the relative (to $\nu = 0$) rate coefficient for each individual vibrational state can be extracted. Fig. 9 shows the final results, together with three theoretical calculations [3,28,29]. Nakashima's and Takagi's [28,29] calculations have considered only the $^1\Sigma_g^+$ dissociative state of HD (which then limits the comparison up to $\nu = 4$), while Schneider's results (presented in ref. [3]) were obtained taking into account also the higher dissociative states.

Most theoretical results are in good overall agreement with the data. In particular the prediction that the rate coefficient for high vibrational state ($\nu > 5$) is considerably higher than for lower $\nu$ is clearly confirmed. However, for two states, namely $\nu = 3$ and $\nu = 5$, the measured rate coefficients are much smaller than the theoretical values. Although the exact reasons for these differences are not clear at this point, we believe that the results demonstrates the sensitivity of the DR process to various molecular properties, even for the simplest molecular ion $HD^+$. Indeed, small variations in the position of the dissociative curve can make dramatic changes in the recombination rates for specific states [30].

## Outlook

The technique as describe above, is general. The measurement of vibrational state population using the CEI method is, in principle, valid for many diatomic molecular ions. The technique also allows to measure the DR rate coefficient of homonuclear molecular ions. These ions do not cool radiatively due to their lack of an electric dipole moment and so not even the rate coefficient for the ground vibrational state can be extracted by the generally used storage ring technique relying only on vibrational relaxation.

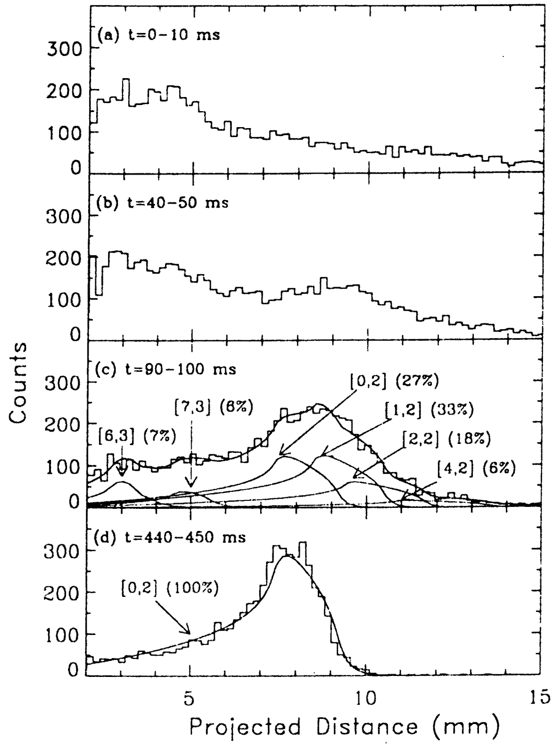

FIG. 8. Projected distance distributions as measured between the H and D fragments from the DR of vibrationally excited $HD^+$ at zero electron energy ($E_e = 0$) and different storage times: (a) 0-10 ms, (b) 40-50 ms, (c) 90-100 ms, and (d) 440-450 ms. On top of the data in panels (c) and (d), are drawn (in solid lines) the overall fits of the measured distributions. Panel (c) also shows individual contributions $[\nu, n]$ from DR starting at the vibrational level $\nu$ and ending at the final asymptote $n$ and $n' = 1$.

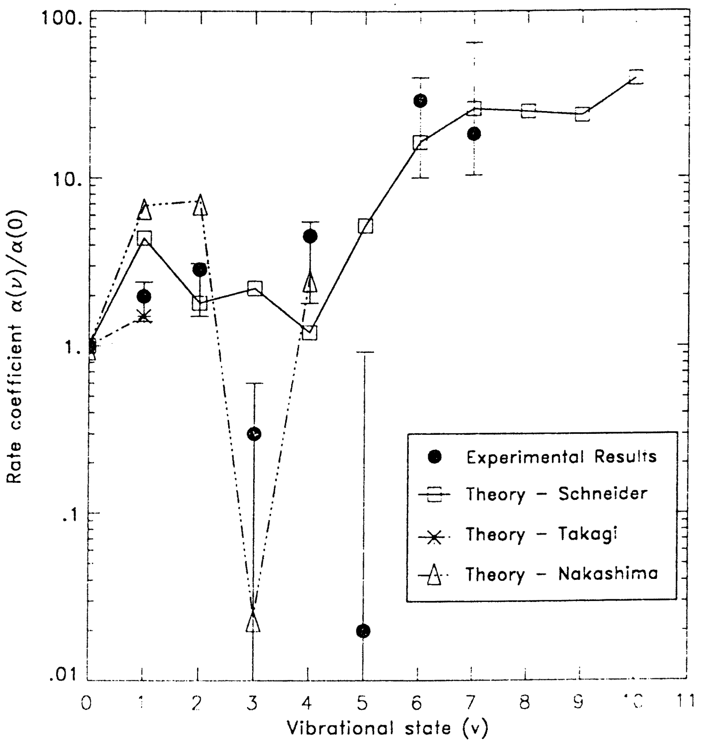

FIG. 9. Final experimental results for the relative DR rate coefficients of $HD^+$ at $E_e = 0$ as a function of the initial vibrational quantum number. Together with the experimental results, the theoretical calculations by Schneider and Suzor for $\nu = 0 - 10$ [3], by Takagi for $\nu = 0 - 1$ [28], and by Nakashima *et al.* for $\nu = 0 - 4$ [29] are also shown. Both experiment and theories are normalized to unity for $\nu = 0$. The lines through the theoretical results are drawn to illustrate the trends of the results from the various calculations.

The ability to probe the vibrational distribution of a molecular ion beam can be used to measure reaction rates for different types of processes. Among these, measurements of dissociative excitation ($AB^+ + e^- \rightarrow A + B^+ + e^-$) represent a direct extension of the method demonstrated above. Also processes where negative ions are involved, such as electron impact detachment or dissociation, can be investigated. Overall, the technique of state selected reaction rate measurement allows for an extensive comparison with theoretical calculations.

The present method is of course limited to vibrational states, as the CEI technique does not allows for a precise probing of rotational state populations (the changes in the nuclear wave function being too small, except, maybe, for very highly excited states). Another limit is the finite temperature of the ion storage ring tubes, which limit the rotational cooling to a finite population of low rotational state. However, one could conceive to reverse the effect of the storage ring: It is possible to create small amounts of molecular ions in the ground vibrational and rotational state, by using for example laser ionization technique, or even electron ionization just above threshold. Performing such processes on a supersonic beam of molecules, cold molecular ions could be created and stored in a small ion trap kept at very low temperature (few degrees Kelvin). A substantial amount of fully relaxed molecular ions could thus be accumulated, and then injected into the storage ring kept at room temperature. These ions would heat up to 300 K, in a time scale of few hundred milliseconds [31] and standard laser techniques could be used to probe the relative rotational population. This would allow the study of DR reactions (or other processes) for selected rotational states, using the storage-ring as a "heater", instead of a "cooler", as it is presently done.

## Acknowledgment

This work has been funded in part by the German Federal Minister for Education, Science, Research and Technology (BMBF) under Contract No. 06 HD 854I, by the EU/HCM program, by the German Israel Foundation (GIF) under Contract No. I-0452-200.07/95, and by the Federal Ministry of Education, Science, Research and Technology (BMBF) within the framework of the German-Israeli Project Cooperation in Future-Oriented Topics (DIP).

# REFERENCES

[1] *Atomic and Molecular Beam Methods*, edited by G. Scoles (Oxford University, New York, 1988).

[2] T. Slanger, C. E. Jasinski, G. Black, and G. E. Jadd, *Science*, **241**, 945 (1988).

[3] Z. Amitay *et al.*, Science **281**, 75 (1998).

[4] J. N. Bardsley and M. A. Biondi, *Adv. Mol. Phys.* **6**, 1 (1970).

[5] D. Kella, L. Vejby-Christensen, P. J. Johnson, H. B. Pedersen, L. H. Andersen, *Science*, **276**, 1530 (1997).

[6] S. Guberman, *Science*, **278**, 1276 (1997).

[7] J. N. Bardsley, J. Phys. B **1**, 349 (1968); **1**, 365 (1968).

[8] *Dissociative Recombination: Theory, Experiment and Applications*, Eds. J. B. A. Mitchell, and S. L. Guberman, (World Scientific, Singapore, 1989), and references therein.

[9] M. Larsson, *Ann. Rev. Phys. Chem.*, **48**, 151 (1997), and references therein.

[10] U. Hechtfischer *et al.*, Phys. Rev. Lett. **80**, 2809 (1998).

[11] D. Habs *et al.*, Nucl. Instr. and Meth. **B43**, 390 (1989).

[12] Z. Amitay *et al.*, *Phys. Rev. A*, **54**, 4032 (1996).

[13] C. Firmani, E. Ruiz, C. W. Carlson, M. Lampton, and F. Paresce, Rev. Sci. Intr, **53**, 570 (1982).

[14] S. Cheng, C. L. Cocke, V. Frohne, E. Y. Kamber, J. H. McGuire, and Y. Wang, Phys. Rev. A **47**, 3923 (1993).

[15] D. P. de Bruijn, and J. Los, Rev. Sci. Intr, **53**, 1020 (1982).

[16] C. Martin, P. Jelinsky, M. Lampton, R. F. Malina, and H. O. Anger, Rev. Sci. Intr, **52**, 1067 (1981).

[17] J. Becker, K. Beckord, U. Werner, and H. O. Lutz, Nucl. Instr. and Meth. **A337**, 409 (1994).

[18] D. Kella et al., Nucl. Instr. and Meth. **A329**, 440 (1993).

[19] A. Baer, internal report, Weizmann Institute of Science (1996)

[20] D. Zajfman *et al.*, Phys. Rev. Lett. **75**, 814 (1995).

[21] Z. Amitay *et al.*, Phys. Rev. A., accepted for publication

[22] Z. Amitay and D. Zajfman, Rev. Sci. Instrum. **68**, 1 (1997).

[23] D. Zajfman *et al.*, Phys. Rev. Lett., **79**, 1829 (1997).

[24] Z. Vager, R. Naaman, and E. P. Kanter, Science **244**, 426 (1989).

[25] D. Zajfman, Comments At. Mol. Phys. **29**, 369 (1994).

[26] D. Zajfman, T. Graber, E. P. Kanter, and Z. Vager, Phys. Rev. A **46**, 194 (1992).

[27] Z. Amitay *et al.*, Phys. Rev. A **54**, 4032 (1996).

[28] H. Takagi, in *Dissociative recombination: Theory, Experiment and Applications III*, Edited by D. Zajfman, J. B. A. Mitchell, D. Schwalm and B. R. Rowe (World Scientific, Singapore, 1996), pp. 174.

[29] K. Nakashima, H. Takagi, and H. Nakamura, J. Chem. Phys. **86**, 726 (1987).

[30] I. F. Schneider and A. Suzor-Weiner, private communication.

[31] U. Hechtischer, private communication.

# Author Index

Achler, M., 339
Afaneh, F., 339
Aguillon, F., 326
Ahmed, Musahid, 167, 238
Babikov, D., 326
Bakker, B. L. G., 56
Barat, M., 326
Barker, John R., 151
Berg, T., 56
Bersohn, Richard, 19
Bise, Ryan T., 296
Bracker, Allan S., 238
Brenot, J-C., 326
Chandler, David W., 151, 197
Chang, B.-Y., 34
Choi, Hyeon, 296
Clements, T. G., 312
Cocke, C. L., 339
Continetti, Robert E., 1, 312
Delmdahl, R., 56
Dörner, R., 339
Du, Yan, 87
Dunet, H., 326
Dylewski, Scott M., 34
Eppink, A. T. J. B., 56
Fayeton, J. A., 326
Geiser, Joseph D., 34
Gordon, Robert J., 87
Harich, S., 126
Hoetzlein, R. C., 34
Hoops, Alexandra A., 296
Houston, Paul L., 34
Jackson, William M., 103
Jacobs, D. C., 139
Jagutzki, O., 339
Kawasaki, Masahiro, 87
Kitsopoulos, Theofanis N., 230
Kohguchi, Hiroshi, 285
Lin, J. J., 126
Liu, X., 126
Lorenz, K. Thomas, 151, 197
Luong, A. K., 312
Maazouz, M., 139
Mashino, Michio, 87
Matsumi, Yutaka, 87
McBane, George C., 215
McLaren, Ian A., 103
McNesby, Kevin L., 103
Mergel, V., 339
Morris, J. R., 139
Mueller, Julie A., 34
Neumark, Daniel M., 296
Parker, D. H., 56
Peterka, Darcy S., 167, 238
Picard, Y. J., 326
Price, Roosevelt J., 103
Prior, M. H., 339
Samartzis, Peter C., 230
Schmidt-Böcking, H., 339
Sidis, V., 326
Sizun, M., 326
Smith, Derek J., 230
Spielberger, L., 339
Sugita, Akihiro, 87
Suits, Arthur G., 1, 167, 238
Vasyutinskii, Oleg S., 238
Suzuki, Toshinori, 285
Truhins, Kaspars, 87
Unny, Sujatha, 87
Wang, Li, 285
Weber, T., 339
Westley, Michael S., 197
Whitaker, Benjamin J., 68
Wilson, Ruth J., 34
Wouters, Eloy R., 238
Xu, Dadong, 103
Yang, X., 126
Yoder, Laurie M., 151
Zajfman, D., 350
Zhu, Langchi, 87

Downloaded by 89.163.34.136 on September 17, 2012 | http://pubs.acs.org
Publication Date: October 18, 2000 | doi: 10.1021/bk-2001-0770.ix001

# Subject Index

A

Abel transform
  advantages of Hankel transform, 73
  method minimizing effects of experimental noise, 155
  See also Image reconstruction
Absorption of light
  atomic photofragments, 253–257
  eliminating orientation and alignment terms by combining measurements along all Cartesian axes, 256
  expressions for 2+1 resonance enhanced multiphoton ionization (REMPI) signal for four experimental geometries, 254–255
  general relationships between linestrength factors corresponding to linearly and circularly polarized light, 255–256
  linestrength factors for linearly and circularly polarized probe light, 255
  quantum numbers designating total angular momentum of initial, excited, and final states of photofragments, 254
Acetylene, schematic energy diagram for vinyl radical and dissociation to $C_2H_2$ + H, 174, 175*f*
Aligned molecules
  intense fields, 88
  iodobenzene, 95, 98, 100
  methyl iodide, 100
  methyl iodide in two color experiment, 95, 97f
  viable mechanisms, 98, 100
  weak fields, 87–88
  See also Atomic orientation and alignment in photodissociation; Photofragment imaging studies
Alignment images
  basis functions for dissociation polarization geometries, 259f
  expression, 257
  monoenergetic photofragments, 258
Alkyl iodides, potential surface crossing, 24
Allene
  alternate mechanism for formation of $C_3H_3^+$, 116
  experiments using vacuum ultraviolet lasers, 110, 116
  mechanism for production of $C_3H_4^+$ and $C_3H_3^+$, 116
  shift in geometry from ground states of allene and allene ion, 116
  time-of-flight spectrum of $C_3H_3^+$ and $C_3H_4^+$ from photolysis at 118 nm, 114f
  translational energy distributions of $C_3H_3^+$ and $C_3H_4^+$ ions from photoionization at 118 nm, 115f
  velocity images of $C_3H_3^+$ and $C_3H_4^+$ in photoionization at 118 nm, 115f
  See also Velocity imaging using vacuum ultraviolet laser
Ammonia, Rydberg transition, 27
Ammonia, deuterated
  anisotropy parameter for dissociation, 27
  experimentally resolved and theoretically predicted values for photodissociation of $ND_3$, 28f
Angular distribution
  anisotropic for $SF_5^+$, 190, 193
  components of angular distribution

Downloaded by 89.163.34.136 on September 17, 2012 | http://pubs.acs.org
Publication Date: October 18, 2000 | doi: 10.1021/bk-2001-0770.ix002

- of electron density associated with each molecular frame state multipole, 253f
- correction factor for extracted distribution, 210
- H atom products corresponding to low rotationally excited $OH(X^2\Pi, v=0)$ products, 136f
- molecular frame angular momentum distributions, 251f
- photodissociation, 29–30
- simulated apparatus function and experimental data, 207, 210
- total H atom reaction products, 135f
- translational energy and, for Cl + ethanol reaction, 179, 181f
- translational energy and, for $SF_5^+$, 190, 192f
- See also β parameter; Ozone photodissociation

Aniline
- average recoil energy from predissociation of aromatic-Ar van der Waals clusters, 160f
- properties of aromatic-Ar van der Waals clusters, 159f

Anisotropy parameter
- active alignment of methyl iodide, 100
- alignment of molecules, 87–88
- characterization, 69
- equations for parallel and perpendicular transitions, 61
- intensity dependence for iodobenzene at 532 nm, 98, 99f
- molecular frame state multipoles in terms of, 250–251
- See also β parameter; Photofragment imaging studies

Apparatus function
- determination, 203–213
- See also Rotational state-resolved differential cross sections

Astrophysics community, microchannel plate image intensifiers, 8–9

Atom abstraction process, surfaces, 147, 148*f*

Atomic alignment, first published imaging study of, 5

Atomic orientation and alignment in photodissociation
- absorption of light by atomic photofragments, 253–257
- alignment image basis functions for dissociation polarization geometries, 259f
- anisotropy parameters representing total set of laboratory frame quantum mechanical variables, 249
- case for spherical tensors rank K=0 and component Q=0, 242–243
- case where K=1 and Q=0, ±1 expressions for photofragment orientation, 243–244
- case where K=2 and Q=0, ±1, ±2 for photofragment alignment, 245–247
- clarification of variables in 3D to 2D transformation, 257f
- coherent type dynamical functions, 242
- components of angular distribution of electron density associated with each state multipole, 253f
- describing possible dissociation mechanisms of fragment orientation by vector model, 251
- dispersion cross sections corresponding to incoherent and coherent mechanisms for photofragment orientation, 264f
- dynamical functions, 242
- eliminating orientation and alignment terms by combining

Downloaded by 89.163.34.136 on September 17, 2012 | http://pubs.acs.org
Publication Date: October 18, 2000 | doi: 10.1021/bk-2001-0770.ix002

Downloaded by 89.163.34.136 on September 17, 2012 | http://pubs.acs.org
Publication Date: October 18, 2000 | doi: 10.1021/bk-2001-0770.ix002

measurements along all three Cartesian axes, 256
experimental absorption and dispersion Doppler profiles of spin-oriented Rb photofragments, 264f
experimental geometries, 260, 262
experimental observations of angular distributions of fragment orientation, 245
expressing excitation matrix elements in terms of angular momentum polarization irreducible cross sections, 240–241
expression for molecular frame state multipoles, 249
expression for orientation or alignment image, 257
expressions for 2+1 resonance enhanced multiphoton ionization (2+1 REMPI) signal for four experimental geometries, 254–255
general expression describing intensity of absorption of probe light by photofragments, 253–254
general relationships between linestrength factors corresponding to linearly and circularly polarized light, 255–256
imaging chlorine atoms from photodissociation of $Cl_2$ at 355 nm, 266–271
imaging oxygen atoms from photodissociation of $NO_2$ at 213 nm, 271–275
imaging oxygen atoms from photodissociation of $N_2O$ at 193 nm, 275–279
investigation of v-J correlation (recoil velocity vector-angular momentum) for photofragment atomic orbital polarization, 239
ion imaging experimental procedure, 265–266
laboratory frame, 240–249
laboratory frame alignment distributions for dissociation light linearly polarized along Z axis, 248f
laboratory frame orientation distributions, 245f
linestrength factors for linearly and circularly polarized probe light, 255
molecular frame, 249–253
molecular frame model of photofragment orientation and molecular frame angular momentum distributions, 251f
molecular frame state multipoles in terms of anisotropy parameters, 250–251
monoenergetic photofragments, 258
off-diagonal state multipole corresponding to molecular frame, 251–252
orientation and alignment image basis functions, 257–262
orientation image basis functions in four different geometries with associated orientation parameters, 261f
parameters contributing to alignment components and vanishing after averaging over all recoil angles, 248–249
parameters contributing to photofragment alignment not vanishing after averaging over all recoil angles, 248
photofragment alignment studied with ion imaging, 265–279

Downloaded by 89.163.34.136 on September 17, 2012 | http://pubs.acs.org
Publication Date: October 18, 2000 | doi: 10.1021/bk-2001-0770.ix002

photofragment differential cross section for one-photon fragmentation, 241
photofragment orientation and alignment angular distributions, 240–253
photofragment orientation by circularly polarized light: photodissociation of RbI at 266 nm, 262–265
photofragment orientation with either circularly or linearly polarized dissociation light, 244–245
photofragment polarization cross sections in laboratory frame, 242
physical range of rank K=1 anisotropy parameters, 244t
potential curves of RbI, 263f
power of analysis for molecular photodissociation, 279–280
pump-probe scheme for experiment with RbI, 263
pure parallel transition, 252
pure perpendicular transition, 252
quantum numbers designating total angular momentum of initial, excited, and final states of photofragment, 254
range of multipole rank K, 241
range of rank K=2 anisotropy parameters, 247t
rank K=2 state multipole relation to incoherent parallel and perpendicular transitions, 252
relationship between anisotropy and polarization parameters, 250t
relationship between laboratory and molecular frame state multipoles, 249–250
schematic diagram of molecular beam apparatus, 265f
space-fixed reference frame for diatomic molecule, 240f
theory: two-photon ion imaging spectroscopy of polarized atomic photofragments, 240–257
transformation of expression for linestrength factors, 280–282
treating each fragment's irreducible photodissociation cross section separately, 241
vector correlations in photodissociation of molecules, 238–239
See also Photofragment alignment; Photofragment imaging studies

**B**

Back-projection approach, alternative strategy, 73–74
Basis functions, orientation and alignment image, 257–262
Benzene
  average recoil energy from predissociation of aromatic-Ar van der Waals clusters, 160f
  properties of aromatic-Ar van der Waals clusters, 159f
Biexponential fluorescence decay, first singlet excited state ($S_1$) of pyrazine, 286–287
β parameter
  alkyl iodides, 24
  t-butyl hypochlorite, 21
  definition, 19–20
  dissociation of dimethyl decacarbonyls, 23
  dissociation of $HN_3$, 27
  electronic ground, first excited and higher states for water, 22f

Downloaded by 89.163.34.136 on September 17, 2012 | http://pubs.acs.org
Publication Date: October 18, 2000 | doi: 10.1021/bk-2001-0770.ix002

- experimentally resolved and theoretically predicted values for photodissociation of $ND_3$, 28f
- femtosecond time scale, 30, 32
- generalized angular distributions, 29–30
- HCO dissociation, 26–27
- $HgI_2$ dissociation, 31f, 32
- hydrogen azide, 27
- hydrogen peroxide, 29
- hydrogen peroxide, v-J correlation, 29
- methane, 24–25
- methyl radical, 20–21
- nitrous acid spectroscopy, 21, 23
- photofragment cm translational energy distribution of H atoms and anisotropy parameter distribution β for methane, 28f
- potential surface crossing, 23–25
- release of iodine from 1-iodonaphthalene, 23–24
- slow anisotropic dissociation, 25–27
- symmetry of upper state, 20–23
- v-J correlation effects, 29–30
- water, 21, 22f

Bromine chloride, photodissociation dynamics, 3

*t*-Butyl hypochlorite, spectroscopy, 21

C

Carbon disulfide, one-color two-photon dissociation study, 4

Center-of-gravity calculation, enhancing energy resolution, 293–294

Center-of-mass (CM) frame
- projection of CM scattering distribution of ionized products, 201
- representing kinematics, 199
- source of non-uniformity in intensity and velocity, 201
- See also Rotational state-resolved differential cross sections

Center-stripe analysis, photodissociation dynamics of IBr, 4–5

Centroiding process
- benefits, 107
- See also Velocity imaging using vacuum ultraviolet lasers

Channel electron multiplier array (CEMA) plates
- schematic of ion imaging detector, 141, 142f
- See also Surface scattering

Charged coupled device (CCD) camera
- ion imaging detector, 141, 143
- See also Surface scattering

Charge transfer, scattering of state-selected $NO^+$ on GaAs(110), 149

Chemical dynamics
- advancing by technology, 1–2
- event-wise approach, 2
- origin or ion imaging technique, 103
- use of ion imaging methods, 2
- See also Imaging; Ion imaging

Chemical reaction dynamics, applications of three-dimensional imaging techniques, 9–10

Chemical reactions. *See* Velocity mapping of reaction products

Chlorine, photodissociation study by velocity map imaging, 5–6

Chlorine atoms
- alignment anisotropy parameters, 268t
- photodissociation of $Cl_2$ at 355 nm, 266–271
- physics of photofragment alignment, 269–271

Downloaded by 89.163.34.136 on September 17, 2012 | http://pubs.acs.org
Publication Date: October 18, 2000 | doi: 10.1021/bk-2001-0770.ix002

  purely adiabatic dissociation, 269–270
  See also Photofragment alignment
Chlorine molecule
  potential energy curves, 269f
  See also Chlorine atoms
Circularly polarized light
  photofragment orientation, 262–265
  See also Rubidium iodide (RbI)
$Cl + C_2H_6$ ς $HCl + C_2H_5$ reaction
  averaged 2D ion projections of HCl, 234f
  collision energy, 236
  experimental, 231, 233
  experimental apparatus, 232f
  extracting quantitative data from 2D images, 233
  factors determining uncertainty in collision energy, 236
  forward scattering, 236
  reconstructed images of 2D projections via inverse Abel transformation, 234f
  speed distributions of HCl by rotational state, 235f
  See also Velocity mapping of reaction products
Cluster predissociation. *See* Recoil energy distributions in van der Waals cluster vibrational predissociation; van der Waals (VDW) cluster predissociation
Clusters, sodium ion
  difference between cold and hot clusters situations, 337
  See also Fragmentation of sodium ion clusters by He impact
CNN radical. *See* Free radicals, photodissociation spectroscopy and dynamics
Coincidence studies
  applications to reaction dynamics, 9–10
  dissociative charge exchange and recombination, 10–11
  dissociative photodetachment dynamics, 12–13
  experimental techniques, 8–9
  fast beam experiments, 10–13
  measurements of multiple fragments, 313
  photodissociation dynamics, 12
  photoelectron-photoion and photoion-photoion experiments, 13–14
  See also Three-body dissociation dynamics of transient $O_6$ molecules
Coincident imaging spectroscopy (3D)
  applications to ion-atom collisions, 344–347
  distance of electron impact from center of electron detector versus time-of-flight of electron, 343f
  fast ion-atom collisions, 340
  final state momenta of reaction corresponding to collision velocity of 0.63 a.u., 344, 345f
  fully differential cross sections (FDCS) unveiling mechanisms of many particle transition, 339–340
  general considerations for momentum space imaging, 340–342
  ionization of atoms by femtosecond lasers, 340–341
  ionization of molecules by ion, photon, or laser impact, 341
  magnetic guiding fields for electrons, 343–344
  momentum and spatial width of target, 342
  momentum exchange pattern for projectile velocity of 6.3 a.u., 345 346f

  principles identical for ion and electron detection, 340
  projection of momentum transfer vectors of $He^{1+}$ recoil-ion, electron, and projectile in final state onto plane defined by projectile beam and scattered projectile, 346f
  projection of momentum transfer vectors of the $He^{1+}$ recoil-ion, electron, and projectile in final state onto plane, 345f
  schematic of coincident momentum space imaging spectrometer for investigating multiple ionization of molecules, 341f
  slow ion-atom collisions, 340
  three-body momentum exchange process, 344
  vacuum ultraviolet (VUV) photon-atom interaction, 340
Cold clusters, difference from hot clusters, 337
Cold target recoil ion momentum spectroscopy (COLTRIMS), collisional and photo-induced processes, 14
Collision induced fragmentation. *See* Fragmentation of sodium ion clusters by He impact
Continuum spectroscopy
  basis, 19
  methods of study, 20
  See also β parameter
Coulomb explosion imaging (CEI) technique
  CEI detector, 355–356
  kinetic energy spectra for CEI of $HD^+$ for different storage time slices, 364f
  measurement of vibrational state population, 361, 363
  molecular structure, 9
  schematic drawing of test storage ring (TSR), 354f
  three-dimensional imaging, 13
  time evolution of vibrational state population from fitting time-sliced CEI kinetic energy spectra, 365f
  See also State-to-state dissociation of molecular ions
Crossed beam reactions
  analysis of Ne + CO inelastic scattering, 223, 225
  applications of ion imaging, 215
  arrival position of ion depending on velocity and position of formation, 219
  crude estimate of differential cross section (DCS), 221–222
  density of product scattered per unit time, 217
  distribution of product ions, 218
  experimental apparatus, 198
  extracted DCS from Ne + CO experiment, 227f
  further applications, 225, 228
  general expression for observed intensity distribution, 217–219
  idealized experiment, 216
  implementing simulation, 220–221
  Imsim program, 220–221
  ions arriving at particular pixel, 218–219
  linear fitting, 222
  line profiles through data and best-fit images for Ne + CO experiment, 226f
  Newton diagram for $O(^1D) + H_2$ ς OH + H, 132f
  nonlinear fitting, 222–223
  polarization effects, 225, 228
  product imaging, 35

Downloaded by 89.163.34.136 on September 17, 2012 | http://pubs.acs.org
Publication Date: October 18, 2000 | doi: 10.1021/bk-2001-0770.ix002

Downloaded by 89.163.34.136 on September 17, 2012 | http://pubs.acs.org
Publication Date: October 18, 2000 | doi: 10.1021/bk-2001-0770.ix002

- qualitative analysis, 221–222
- real experiments: data analysis, 221–223
- real experiments: simulation, 216–221
- reducing simulation time, 221
- schematic of experimental setup for studying $O(^1D) + H_2$ ς OH + H, 131f
- signal depending on density distribution of products, 217
- simplifying approximations, 219–220
- simulated image with isotropic DCS and other parameters representing Ne + CO experiment, 224f
- study of $O(^1D) + H_2$ ς OH + H reaction, 130
- temporal overlap of molecular beams, 203
- traditional procedure, 215
- unresolved internal energy distributions, 228
- velocity mapped imaging experiment, 218–219
- See also Rotational state-resolved differential cross sections

Crossed-beam scattering, applications of imaging method, 6–7

Cross sections. *See* Rotational state resolved differential cross sections

**D**

Deconvolution, method minimizing effects of experimental noise, 155

Deuterated ammonia. *See* Ammonia, deuterated

Deuterium, multiple ionization, 9

Diatomic in molecule (DIM)
- accounting for He-cluster interaction, 327
- theory, 328
- See also Fragmentation of sodium ion clusters by He impact

Dichlorine oxide, photodissociation, 4

Differential cross sections (DCS)
- characterizing atomic and molecular many-particle reactions by fully DCS, 339–340
- demonstrating extraction of DCS from simulated experimental data, 210, 211f, 213
- idealized crossed beam experiment, 216
- photofragment DCS for one-photon fragmentation, 241
- See also Crossed beam reactions; Rotational state-resolved differential cross sections

Dimetal decacarbonyls, β value for dissociation, 23

Dinitrogen monoxide
- alignment parameters, 278t
- data images for oxygen $(^1D_2)$ from photodissociation at 193 nm, 277f, 278
- imaging oxygen atoms from photodissociation at 193 nm, 275–279
- potential curves, 276f
- product imaging technique, 37, 38f
- state multipoles for oxygen $(^1D_2)$ product, 276, 278
- strong recoil-frame orbital alignment in oxygen product, 279
- ultraviolet photodissociation, 6

Dissociation
- nonadiabatic interactions, 270
- purely adiabatic, 269–270
- See also Photodissociation; Slow anisotropic dissociation; State-to-state dissociation of molecular ions

Downloaded by 89.163.34.136 on September 17, 2012 | http://pubs.acs.org
Publication Date: October 18, 2000 | doi: 10.1021/bk-2001-0770.ix002

Dissociation mechanism. *See* Free radicals, photodissociation spectroscopy and dynamics
Dissociative charge exchange and recombination, coincidence imaging approach, 10–11
Dissociative ionization, viable mechanism for molecular alignment, 98, 100
Dissociative photodetachment of $O_6^-$. *See* Three-body dissociation dynamics of transient $O_6$ molecules
Dissociative recombination (DR)
  characterization, 11
  Coulomb explosion imaging (CEI) detector, 355–356
  DR imaging detector, 356, 358
  DR of $HD^+$ (v=0), 358–361
  DR rate coefficient for molecular ions in vibrational state, 353, 355
  excited $HD^+$, 363, 366
  $HD^+$ with low-energy electrons, 352
  ideas behind experimental technique, 353
  molecular ions $HD^+$, 351–355
  reaction of molecular ion $AB^+$, 351–352
  schematic of new multi-particle 3-D imaging detector, 357f
  sensitivity to initial vibrational state of molecular ion, 352
  three-dimensional molecular fragments imaging, 355–358
  See also State-to-state dissociation of molecular ions
Dissociative scattering, surfaces, 147, 148*f*
Doppler-selected time-of-flight method, scattering, 6–7
Doppler spectroscopy, v-J correlation, 29
Dynamical functions, transition dipole moments and fragmentation dynamics, 242

E

Electric fields
  alignment of molecules, 87–88
  See also Photofragment imaging studies
Electrons
  magnetic guiding fields, 343–344
  principles of detection, 340
  See also Coincident imaging spectroscopy (3D)
Electrostatic immersion lens, use in velocity mapping, 56
Eley–Rideal reaction mechanism, surfaces, 147, 148*f*
Energy and momentum, conservation equations, 68–69
Energy distributions, recoil. *See* Recoil energy distributions in van der Waals cluster vibrational predissociation
Energy distributions, unresolved internal, application of simulated images, 228
Energy transfer
  scattering of state-selected $NO^+$ on GaAs(110), 149
  See also Rotational state-resolved differential cross sections
Ethyl bromide
  calibrating imaging detector, 108, 110
  time-of-flight mass spectra of direct photoionization signal from seeded and neat beam, 111f
  translational energy distribution of $C_2H_5^+$ and $C_2H_4^+$ ions, 113f

Downloaded by 89.163.34.136 on September 17, 2012 | http://pubs.acs.org
Publication Date: October 18, 2000 | doi: 10.1021/bk-2001-0770.ix002

  velocity mapped images of fragments from photolysis under different beam conditions, 112f
  See also Velocity imaging using vacuum ultraviolet laser
Event counting
  image from single laser and corresponding event counted image, 59f
  image using, 60f
  method, 59–60
  See also Velocity map imaging (VELMI)
Event-wise approach
  coincidence experiments using three-dimensional imaging techniques, 9
  lines between ion imaging and, 2
$\varepsilon$-$\chi$ correlation diagram
  analysis of trajectories contributing to low $\varepsilon$ and low $\chi$ structure, 336
  assuming 1eV vibration energy for parent cluster, 336f
  assuming ionic cluster initially in rovibronic ground state, 335f
  channels $Na_5^+$ ς $Na_4^+$ + Na and $Na_4^+$ ς $Na_3^+$ + Na, 332f
  fragmentation probability as function of relative energy of fragments $\varepsilon$ and center of mass deflection angle $\chi$, 331
  See also Fragmentation of sodium ion clusters by He impact

**F**

Fast beam experiments
  application of microchannel-plate (MCP)-based imaging detectors, 10
  dissociative charge exchange and recombination, 10–11
  dissociative photodetachment dynamics, 12–13
  imaging studies of fast neutrals, 11
  photodissociation dynamics, 12
Fast beam photofragment spectroscopy. *See* Free radicals, photodissociation spectroscopy and dynamics
Femtosecond time-resolved photoelectron imaging
  advantages of photoelectron spectroscopy, 285
  angular anisotropy of photoelectron distribution, 292
  biexponential fluorescence decay of $S_1$ pyrazine, 286–287
  comparison of photoelectron spectroscopic methods, 286t
  decay of total photoelectron intensity in [1+1'] resonance enhanced multiphoton ionization (REMPI) via $S_2$ state of pyrazine and deuterated pyrazine, 292f
  enhancing energy resolution by center-of-gravity calculation, 293–294
  experimental, 287–289
  instantaneous formation of $S_1$ from $S_2$ and subsequent decay to $S_0$, 293f
  intersystem crossing yield from $S_1$ pyrazine, 293
  introducing vacuum ultraviolet (VUV) femtosecond probe laser, 294
  inverse Abel transforms of photoelectron images of [1+2'] REMPI of pyrazine via $S_1$, 290f
  [1+1'] ionization of pyrazine

Downloaded by 89.163.34.136 on September 17, 2012 | http://pubs.acs.org
Publication Date: October 18, 2000 | doi: 10.1021/bk-2001-0770.ix002

via $S_2$ state, 289
[1+2'] ionization of pyrazine via $S_1$ state, 287–288
photoelectron kinetic energy distributions in femtosecond [1+2'] REMPI of pyrazine via $S_1$, 291f
photoelectron scattering distribution in molecular frame (fixed-in-space technique), 294
photoelectron spectroscopy of wave-packet motion, 286f
possibility of relaxation in triplet manifold, 291
pump-probe experiment description, 285
pyrazine example of intermediate case in molecular radiationless transition, 286–287
real-time observation of reaction, 285
[1+2'] REMPI of pyrazine, 288f
$S_1$ state of pyrazine, 289–292
$S_2$ state of pyrazine, 292–293
schematic diagram of photoelectron imaging apparatus, 288f
snapshots of photoelectron speed and angular distributions, 290f
solid-state femtosecond laser system, 287–288
speculation of intersystem crossing mediated by $T_2(\pi,\pi*)$, 291
time dependence of total photoelectron signal in femtosecond [1+2'] REMPI of pyrazine via $S_1$, 289f
time-of-flight (TOF) method, 286
Femtosecond time scale
$\beta$ parameter, 30, 32
$HgI_2$ dissociation, 31f, 32
See also $\beta$ parameterFixed-in-space technique, providingphotoelectron scattering distribution, 294
Flyswatter
critical parameters for operating, 143
ion imaging detector, 141, 142f
See also Surface scattering
Fourier transform convolution theorem, applying for inverse transform, 71, 73
Fragmentation, scattering of state-selected $NO^+$ on GaAs(110), 149
Fragmentation of sodium ion clusters by He impact
analysis of trajectories contributing to low $\varepsilon$-$\chi$ structure, 336
apparatus based on multicoincidence detection of neutral and charged particles, 327
bulky structures involving two contributions similar to release of unique Na atom, 333
correlation between locations on vertical axis Z of two detected fragments (ZZ correlation), 330
correlation diagram showing fragmentation probability as function of relative energy of fragments $\varepsilon$ and center of mass deflection angle $\chi$ ($\varepsilon$-$\chi$ correlation), 331
diatomic in molecule (DIM) description of potential energy surfaces (PESs) accounting for He-cluster interaction, 327
difference between cold and hot clusters situations, 337
dynamical calculation, 328–329
ejection of unique Na atom, 331
electronic contribution (EM), 331–332
electronic mechanism, 330
$\varepsilon$-$\chi$ correlation diagram for channels $Na_5^+$ ς $Na_4^+$ + Na and $Na_4^+$ ς $Na_3^+$ + Na, 332f

Downloaded by 89.163.34.136 on September 17, 2012 | http://pubs.acs.org
Publication Date: October 18, 2000 | doi: 10.1021/bk-2001-0770.ix002

experimental technique, 327–328
four typical structures, 330–331
fragmentation induction by direct impulsive mechanism (IM1), 332–333
fragmentation induction by electronic transition, 331
fragmentation probabilities for various pathways, 329
He-cluster encounter inducing, 333
impulsive character of fragmentation process, 330
indirect impulsive mechanism (IM2), 332
key role of initial cluster temperature, 337–338
matrix of $\varepsilon$-$\chi$ correlation diagrams assuming a 1eV vibrational energy for parent cluster, 336f
matrix of $\varepsilon$-$\chi$ correlation diagrams for ground rovibrational state $Na_3^+$ induced fragmentation, 335f
$Na_4^+$ ς $Na_3^+$ + Na channel, 331–332
$Na_5^+$ ς $Na_4^+$ + Na channel, 331
perspective view of three lowest PESs of $Na_3^+$ in $C_{2v}$ geometry, 334f
pure character of EM mechanism in contrast to cold cluster case, 337
relative probabilities for various fragmentation pathways of $Na_n^+$ clusters, 329f
role of electron pairing in fragmentation process, 337
scheme of experiment, 328f
significant impulsive component of EM mechanisms, 334–335
studying dynamics of energy deposition, 327
theoretical calculations for $Na_3^+$, 333
theoretical results, 333–337
theoretical treatment, 328–329
ZZ correlation patterns, 330f

Free radicals, sensitivity for detection, 104
Free radicals, photodissociation spectroscopy and dynamics
  CNN radical, 303–305
  dissociation mechanism, 307–309
  dissociation mechanism involving intersystem crossing (ISC) to triplet state, 308–309
  dissociation products, 309
  energy level and correlation diagram of relevant electronic states of NCN radical along $C_{2v}$ dissociation coordinate, 308f
  examining spectroscopy of dissociative electronic state, 298
  experimental, 297–298
  fast radical beam translational spectrometer, 297f
  fragment mass distributions for HNCN and DNCN, 306f
  heats of reaction for NCN, CNN, and HNCN radicals, 300t
  HNCN radical, 305–307
  NCN, CNN, and HNCN radicals intermediates in combustion and interstellar chemistry, 296–297
  NCN radical, 298–302
  PFY spectra for CNN, 303
  PFY spectra for HNCN, 305–306
  photofragment mass distributions for CNN, 303–304
  photofragment mass distributions for HNCN, 306
  photofragment mass distributions for NCN, 300–301
  photofragment yield (PFY) spectrum of NCN, 298f, 299–300
  preparation of vibrationally and rotationally cold negative ions, 297
  translational energy distributions for CNN, 304–305

translational energy distributions for HNCN, 306, 307f
translational energy distributions for NCN, 301–302
Future prospects, imaging techniques, 14–15

H

Hankel transform
  advantages over Abel transform, 73
  Fourier transform of projected intensity, 73
  taking, of Fourier transform of projected intensity, 73
  transforming from momentum to position space of 2D image, 79–86
  See also Image reconstruction
Hartley band
  ozone photodissociation, 39
  See also Ozone photodissociation
HCO dissociation, 26–27
$HD^+$ ion. *See* State-to-state dissociation of molecular ions
Helium impact. *See* Fragmentation of sodium ion clusters by He impact
Herzberg continuum, deconvolution of $O_2$, 62, 63*f*
HNCN radical. *See* Free radicals, photodissociation spectroscopy and dynamics
Hot clusters, difference from cold clusters, 337
Hybrid techniques, future prospects, 15
Hydrogen, triatomic, charge-exchange technique for three-body breakup, 11
Hydrogen atom products
  angular distributions, 135f, 136f
  crossed molecular beam studies, 127
  detection schemes, 128
  excitation of ground state, 129–130
  H atom Rydberg "tagging" time-of-flight (TOF) technique, 128–129
  H atom Rydberg transitions from n=2 level to higher n states, 129f
  See also Rotational state resolved differential cross sections
Hydrogen azide, dissociation, 27
Hydrogen chloride rotational energy transfer process
  simulated images of experimental data, 212f, 213
  See also Rotational state-resolved differential cross sections
Hydrogen peroxide, v-J correlation effects, 29
Hyperthermal energy ions, reaction with surfaces, 139
Hypochlorous acid, photodissociation, 4

I

Image reconstruction
  Abel and Hankel transform, 69–74
  absorption probability, 69
  advantages of Hankel over Abel inversion, 73
  back-projection strategy as alternative strategy, 73–74
  C code for running programs, 79–86
  characterizing anisotropy, 69
  computing transformation from momentum to position space of 2D image using Hankel transform, 79–86
  conservation of momentum and energy equations, 68–69
  deconvolving spectroscopic data by constrained version of reblur method, 75

Downloaded by 89.163.34.136 on September 17, 2012 | http://pubs.acs.org
Publication Date: October 18, 2000 | doi: 10.1021/bk-2001-0770.ix002

Downloaded by 89.163.34.136 on September 17, 2012 | http://pubs.acs.org
Publication Date: October 18, 2000 | doi: 10.1021/bk-2001-0770.ix002

  - definition of zero-order Bessel function, 73
  - easiest way of recovering true velocity distribution, 68
  - Hankel transform of Fourier transform of projected intensity, 73
  - illustration of overlap function for typical case, 76f
  - illustration of vector correlation between polarization vector of photolysis light and recoil direction of atomic fragment for $\beta = 2, -1$, 70f
  - instrument functions and noise, 74–75
  - inverse transform by applying Fourier transform convolution theorem, 71, 73
  - measured distribution of detector, 71
  - overlap volume function, 74
  - point spread function (PSF), 75
  - quasi Wiley–McLaren arrangement, 71
  - relaxation function, 75
  - size of overlap volume fraction, 75
  - transforming ion distribution in $(r,\vartheta)$ coordinates to image in (x,y) coordinates, 72f
  - velocity distribution of photofragment ions in Cartesian coordinates, 71
- Imaging
  - orientation and alignment studies, 5–6
  - photodissociation dynamics, 3–5
  - photoelectron spectroscopy, 7
  - prospects for future, 14–15
  - scattering studies, 6–7
  - See also Atomic orientation and alignment in photodissociation; Coincidence studies
- Imaging studies, emerging area of radical photodissociation, 5
- Imsim, simulation program, 220–221
- Inelastic scattering, Ne + CO. *See* Ne + CO inelastic scattering
- Internal energy distributions, unresolved, application of simulated images, 228
- Inverse Abel transform
  - extracting quantitative data from 2D images for $Cl + C_2H_6$ ς $HCl + C_2H_5$ reaction, 233, 234f
  - recovery of three-dimensional information, 37, 38f
  - See also Ozone photodissociation; Product imaging technique
- Iodine bromide, photodissociation dynamics, 4–5
- Iodobenzene
  - photodissociation method, 89
  - single-photon photodissociation, 95
  - velocity map imaging of product iodine atoms from photodissociation, 90f, 91f, 92f
  - viable mechanisms for alignment, 98, 100
  - See also Photofragment imaging studies
- 1-Iodonaphthalene, potential surface crossing, 23–24
- Ion-atom collisions
  - applications of coincident imaging spectroscopy, 344–347
  - See also Coincident imaging spectroscopy (3D)
- Ion counting method
  - images of dinitrogen monoxide dissociation, 37, 38f
  - improvement in product imaging technique, 37
  - See also Ozone photodissociation
- Ion imaging

  aim of experiment, 68
  applications to crossed beam experiments, 215
  basic principles, 57, 58f
  comparison with velocity mapping under identical conditions, 59f
  configuration, 57, 58f
  differences in velocity selectivity and sensitivity from velocity-resolved time-of-flight technique, 158–159
  evolution of technique, 2
  image from excitation of monomer pyrazine, 155, 156f
  image of pyrazine fragments after Pyr-Xe predissociation, 155, 156f
  lines between event-wise approaches and, 2
  method, 57–58
  one-color two-photon dissociation study of $CS_2$, 4
  orientation and alignment studies, 5–6
  ozone photodissociation, 4
  photodissociation dynamics, 3–5
  resolution of technique, 153–154
  spectrometer voltages controlling time-of-flight and velocity mapping, 154
  technique for van der Waals cluster dissociation, 153–154
  use in chemical dynamics, 2
  See also Photofragment alignment; Recoil energy distributions in van der Waals cluster vibrational predissociation; Surface scattering; Velocity map imaging (VELMI)
Ionization, multiple of deuterium, 9
Ionization potentials (IPs), separating parent and product by time-of-flight mass spectrometry, 104
Ions. *See* Coincident imaging spectroscopy (3D); State-to-state dissociation of molecular ions

**K**

Kinetic energy distribution, relative calculation, 107
  See also Velocity imaging using vacuum ultraviolet lasers

**L**

Laboratory frame
  alignment distributions for dissociation light linearly polarized along Z axis, 248f
  case of spherical tensors rank, K=0 and component, Q=0, 242–243
  case where K=1 and Q=0, ±1, 243–244
  case where K=2, Q=0, ±1, ±2, 245–247
  dynamical functions, 242
  experimental observation of angular distributions of fragment orientation, 245
  orientation distributions, 245f
  parameters contributing to alignment components and vanishing after averaging over recoil angles, 248–249
  parameters contributing to photofragment alignment, 248
  photofragment differential cross section for one-photon fragmentation, 241
  photofragment orientation and alignment angular distributions, 240–249

Downloaded by 89.163.34.136 on September 17, 2012 | http://pubs.acs.org
Publication Date: October 18, 2000 | doi: 10.1021/bk-2001-0770.ix002

Downloaded by 89.163.34.136 on September 17, 2012 | http://pubs.acs.org
Publication Date: October 18, 2000 | doi: 10.1021/bk-2001-0770.ix002

- photofragment orientation by either circularly or linearly polarized dissociation light, 244–245
- physical range of rank K=1 anisotropy parameters, 244t
- range of rank K=2 anisotropy parameters, 247t
- relationship between laboratory and molecular frame state multipoles, 249–250
- space-fixed reference frame for diatomic molecule, 240f
- state multipole component relation to four possible dissociation mechanisms, 248f
- total set of laboratory frame quantum mechanical variables, 249
- See also Atomic orientation and alignment in photodissociation

Ladder climbing, viable mechanism for molecular alignment, 98

Laser, spatial profile, 206

Linear fitting, crossed beam experiments, 222

Linestrength factors, transformation of expression for, 280–282

M

Many-particle reactions
- characterizing atomic and molecular, by fully differential cross sections (DFCS), 339–340
- See also Coincident imaging spectroscopy (3D)

Mass spectrometer
- ion detectors for study of ion/surface scattering, 139–140
- See also Time-of-flight mass spectrometry

Mercury(II) iodide
- dissociation by femtosecond (fs) pulse, 32
- fs transients of different masses for parallel and perpendicular polarization of probe E vector relative to E vector dissociating $HgI_2$, 31f

Metal cluster cation-rare gas collision, application of multicoincidence techniques, 11

Methane
- calculation of ground, first triplet, and first excited singlet surfaces, 25
- photofragment cm translational energy distribution of H atoms and anisotropy parameter distribution β, 28f
- potential surface crossing, 24–25
- See also β parameter

Methanol clusters
- images of protonated monomer, dimer, trimer, tetramer, and pentamer, 119, 120f
- ion kinetic energy distributions of protonated clusters, 121f
- maximum translational energies in clusters, 119, 123
- mechanism of formation for protonated clusters, 119
- possible reactions upon absorption of vacuum ultraviolet photon, 117
- relative translational energy distributions of protonated clusters, 122f
- time-of-flight mass spectrum, 118f
- See also Velocity imaging using vacuum ultraviolet laser

Methyl iodide
- active alignment, 100
- active alignment in two color

Downloaded by 89.163.34.136 on September 17, 2012 | http://pubs.acs.org
Publication Date: October 18, 2000 | doi: 10.1021/bk-2001-0770.ix002

  experiment, 95, 97f
  first image using product imaging technique of methyl radicals, 38f
  molecular absorption, 35, 37
  photodissociation method, 89
  viable mechanisms for alignment, 98, 100
  See also Photofragment imaging studies
Methylpyrazine
  average recoil energy from predissociation of aromatic-Ar van der Waals clusters, 160f
  properties of aromatic-Ar van der Waals clusters, 159f
Microchannel-plate electron multipliers (MCPs)
  astrophysical applications, 8–9
  key development in imaging techniques, 8
Molecular absorption, methyl iodide, 35, 37
Molecular beam
  experimental apparatus, 265f
  See also Photofragment alignment
Molecular fragments imaging
  three-dimensional, 355–358
  See also State-to-state dissociation of molecular ions
Molecular frame
  components of angular distribution of electron density associated with each state multipole, 253f
  expression for molecular frame state multipoles, 249
  model of photofragment orientation and angular momentum distributions, 251f
  off-diagonal state multipoles corresponding to molecular frame Q'=+1 cyclic component, 251–252
  photofragment orientation and alignment angular distributions, 249–253
  providing photoelectron scattering distribution, 294
  pure parallel transition, 252
  pure perpendicular transition, 252
  rank K=2 relation to incoherent parallel and perpendicular transition, 252
  relationship between laboratory and molecular frame state multipoles, 249–250
  simple vector model describing possible dissociation mechanisms, 251
  state multipoles in terms of anisotropy parameters, 250–251
  See also Atomic orientation and alignment in photodissociation
Molecular frame differential cross section (MF–DCS)
  analysis method, 316–317
  dissociative photodetachment (DPD) of $O_6^-$, 319, 321
  DPD of $O_6^-$ at 532, 388, 258 nm in center-of-mass velocity space, 320f
  total energy gated MF–DCS images of $O_6$ at 388 nm, 322f
  wavelength dependence of MF–DCS spectra, 319, 321
  See also Three-body dissociation dynamics of transient $O_6$ molecules
Molecular ion $HD^+$. *See* State-to-state dissociation of molecular ions
Molecular spectroscopy, definition, 19
Molecular structure, applications of three-dimensional imaging techniques, 9–10

Momentum and energy, conservation equations, 68–69
Momentum space imaging
  general considerations, 340–342
  schematic of coincident momentum space imaging spectrometer, 341f
  See also Coincident imaging spectroscopy (3D)
Multi-channel plate (MCP) phosphor screen detector, velocity mapping apparatus, 57, 58*f*
Multiphoton photodissociation, iodobenzene, 95, 98, 100
Multiple ionization, deuterium, 9

N

$Na_n^+$ ion clusters. *See* Fragmentation of sodium ion clusters by He impact
NCN radical. *See* Free radicals, photodissociation spectroscopy and dynamics
Ne + CO inelastic scattering
  crossed beam experiment, 223, 225
  experimental image, 224f
  extracted differential cross sections (DCS), 227f
  line profiles through data and best-fit images, 226f
  simulated image with isotropic DCS and parameters representing experiment, 224f
Neutral species, transient. *See* Three-body dissociation dynamics of transient $O_6$ molecules
Newton diagram
  crossed beam $O(^1D) + H_2$ ς OH + H reaction, 132f
  inelastic scattering of HCl seeded in Ar with neat Ar molecular beam, 199, 200f
Nitrogen dioxide
  alignment parameters for oxygen, 273t
  imaging oxygen atoms from photodissociation of $NO_2$ at 213 nm, 271–275
  ion image data images from photodissociation, 272f
  photoinitiated unimolecular decomposition of jet cooled, 3–4
  recoil frame electron charge cloud distributions for oxygen atom, 275f
  schematic view showing relative orientation of transition moment in molecular and recoil frames, 274f
  time-resolved photoelectron-photoion coincidence measurements, 14
  total alignment in laboratory frame for three spin-orbit states of oxygen, 273t
Nitrogen monoxide, two-photon dissociation study using velocity map imaging, 3
Nitrous acid, symmetry of upper state, 21, 23
Non-adiabatic aspects. *See* Fragmentation of sodium ion clusters by He impact
Nonlinear fitting, crossed beam experiments, 222–223

O

$O(^1D) + H_2$ reaction. *See* Rotational state resolved differential cross sections
O6 molecules. *See* Three-body dissociation dynamics of transient $O_6$ molecules

Downloaded by 89.163.34.136 on September 17, 2012 | http://pubs.acs.org
Publication Date: October 18, 2000 | doi: 10.1021/bk-2001-0770.ix002

Downloaded by 89.163.34.136 on September 17, 2012 | http://pubs.acs.org
Publication Date: October 18, 2000 | doi: 10.1021/bk-2001-0770.ix002

Orientation image
  basis functions in four different geometries with associated orientation parameters, 261f
  experimental geometries, 260, 262
  expression, 257
  See also Atomic orientation and alignment in photodissociation
Overlap volume function
  equation, 74
  illustration for typical case, 76f
  size, 75
  See also Image reconstruction
Oxygen
  absorption spectrum and deconvolution of Herzberg continuum, 63f
  angular distributions equation, 61
  anisotropy parameter equations, 61
  central role in research, 61
  coincidence measurements of photodissociation, 9
  deconvolution of Herzberg continuum, 62
  kinetic energy distributions of $O^+$ and photoelectrons by (2+1) resonance enhanced multiphoton ionization (REMPI) of $O_2$ at 225 nm, 65f
  photodissociation using ion imaging and velocity map imaging (VELMI), 3
  potential energy diagram for electronic states, 62f
  predissociation of Schumann–Runge bands, 63–64
  resonance enhanced multiphoton ionization (REMPI)/dissociation, 64, 66
  velocity mapping of $O_2$ photophysics, 61–66
  See also Dinitrogen monoxide; Nitrogen dioxide
Ozone
  alignment of $O_2$ rotational angular momentum in dissociation, 5
  complication of dissociation, 54
  photodissociation by ion imaging, 4
  photodissociation using new ion-counting method with velocity map imaging, 4
Ozone photodissociation
  angular distribution peaking about 45° from direction of photodissociation electric vector, 44
  channels in Hartley band, 39
  detection sensitivity to various $m_j$ levels for $\beta$=1.5 and detection on $O(^1F)\ \Omega\ O(^1D)$ transition, 47f
  detection sensitivity to various $m_j$ levels for $\beta$=1.5 and detection on $O(^1P)\ \Omega\ O(^1D)$ transition, 47f
  fit to angular distribution for $O(^1D_2$, v=0)in 265 nm dissociation, 48f
  fit to angular distribution for $O(^1D_2$, v=1)in 265 nm dissociation, 48f
  fit to angular distribution for $O(^1D_2$, v=3)in 265 nm dissociation, 49f
  images for different combinations of photodissociation and ionization polarization for dissociation at 255 nm and ionization at 203 nm, 46f
  inverse Abel-transformed image of $O(^1D_2)$ (singlet product) velocity following 265-nm, 40f
  inverse Abel-transformed images of $O(^1D_2)$ velocity with various dissociation wavelengths, 39, 42f
  $m_j$ distribution for dissociation at 265 nm and vibrational distribution, 49f
  $O(^1D_2)$ inverse-Abel-transformed image following 305.7456 nm, 43f

$O(^3P_J)$ inverse-Abel-transformed images for dissociation at a variety of wavelengths, 51f
production of $O(^1D)$ at higher total kinetic energies, 44, 45f
rotational distribution of $O_2(^1\Delta_g)$ following dissociation at 305.7456 nm, 45f
singlet channel, 39, 44
translational energy distributions for $O(^3P)$ from photodissociation at various wavelengths and averaged over $O(^3P_J)$ distribution, 52f
triplet channel, 44, 50
triplet channel producing products at 226, 230, 233, 234, 240, and 266 nm, 54
vibrational distribution of $O_2(^1\Delta_g)$ (singlet product) from 265-nm, 41f
wavelength dependence of yield of $O_2(^3\Sigma_g^-, v\geq26)$, 53f
See also Product imaging technique

P

Photodissociation
coincidence measurements for oxygen, 9
deuterated ammonia, 27, 28f
differential cross section, 29–30
dinitrogen monoxide, 275–279
dynamics using ion imaging and velocity map imaging (VELMI), 3–5
HCO, 26–27
hydrogen azide, 27
hydrogen peroxide, 29
imaging Cl atoms after photodissociation of $Cl_2$ at 355 nm, 266–271
imaging oxygen atoms from $NO_2$ at 213 nm, 271–275
mercury(II) iodide, 32
multiphoton, of iodobenzene, 95, 98, 100
nitrogen dioxide, 271–275
orientation and alignment studies, 5–6
original quantum mechanical treatment, 29
rubidium iodide at 266 nm, 262–265
single-photon, of iodobenzene, 95
vector correlations, 238–239
water, 21, 22f
See also Atomic orientation and alignment in photodissociation; Ozone photodissociation; Photofragment imaging studies
Photodissociation dynamics
coincidence imaging approach, 12
continuum spectroscopy, 20
Photodissociation spectroscopy. *See* Free radicals, photodissociation spectroscopy and dynamics
Photoelectron imaging
combining with femtosecond pump-probe technique, 286
schematic of apparatus, 288f
See also Femtosecond time-resolved photoelectron imaging
Photoelectron-photofragment coincidence (PPC) spectroscopy
studying three-body dissociation dynamics of transient neutral species, 313
See also Three-body dissociation dynamics of transient $O_6$ molecules
Photoelectron-photofragment kinetic energy correlation spectra
analysis method, 316
dissociative photodetachment (DPD)

Downloaded by 89.163.34.136 on September 17, 2012 | http://pubs.acs.org
Publication Date: October 18, 2000 | doi: 10.1021/bk-2001-0770.ix002

process, 317, 319
 $O_4^-$ and $O_6^-$ at 388 nm, 318f
Photoelectron-photoion and photoion-photoion, coincidence experiments, 13–14
Photoelectron spectroscopy
 advantages, 285
 comparison of methods, 286t
 imaging, 7
 wave-packet motion, 286f
 See also Femtosecond time-resolved photoelectron imaging
Photoelectron yield. *See* Tetraoxygen ($O_4$)
Photofragment alignment
 absorption of light by atomic photofragments, 253–257
 alignment anisotropy parameters for Cl for photodissociation of $Cl_2$ at 355 nm, 268t
 alignment parameters for $O(^1D_2)$ from photodissociation of $N_2O$ at 193 nm, 278t
 alignment parameters for $O(^3P_1)$ from photodissociation of $NO_2$ at 213 nm, 273t
 anisotropy parameters describing contribution to photofragment alignment from incoherent and coherent excitation, 270–271
 atomic alignment consequence of incoherent and coherent perpendicular excitation, 271
 comparison of difference images for geometries I and II with results of simulations, 267f
 contrasting observations for $NO_2$ to coherence effects observed in diatomic molecules, 274–275
 data images for $O(^1D_2)$ from photodissociation of $N_2O$ at 193 nm, 277f, 278
 experimental procedure, 265–266
 imaging Cl atoms from photodissociation of $Cl_2$ at 355 nm, 266–271
 imaging oxygen atoms from photodissociation of $NO_2$ at 213 nm, 271–275
 imaging oxygen atoms from photodissociation of $N_2O$ at 193 nm, 275–279
 incoherent parallel excitation of parent molecule responsible for alignment , 273–274
 ion image data for $O(^3P_1)$ product, 272f
 laboratory frame, 240–249
 molecular frame, 249–253
 nonadiabatic, alignment producing, transitions for incoherent and coherent excitation, 270f
 nonadiabatic interactions, 270
 orientation and alignment angular distributions, 240–253
 physics, 269–271
 predominant incoherent, intrinsic vector correlation vanishing after averaging over recoil angles, 279
 purely adiabatic dissociation, 269–270
 recoil frame electron charge cloud distributions for $O(^3P_1)$ atom based on measured alignment parameters at indicated angles, 275f
 schematic diagram of molecular beam apparatus, 265f
 schematic potential curves for $N_2O$, 276f
 schematic potential energy curves of chlorine molecule, 269f
 schematic view of $NO_2$ showing relative orientation of transition moment in molecular and recoil frames, 274f

Downloaded by 89.163.34.136 on September 17, 2012 | http://pubs.acs.org
Publication Date: October 18, 2000 | doi: 10.1021/bk-2001-0770.ix002

Downloaded by 89.163.34.136 on September 17, 2012 | http://pubs.acs.org
Publication Date: October 18, 2000 | doi: 10.1021/bk-2001-0770.ix002

- state multipoles for O($^1D_2$) product, 276, 278
- strong recoil-frame orbital alignment in O($^1D_2$) products following photodissociation of $N_2O$ at 193 nm, 279
- total alignment in laboratory frame for three spin-orbit states of O($^3P_1$) from photodissociation of $NO_2$ at 213 nm, 273t
- See also Atomic orientation and alignment in photodissociation; Laboratory frame; Molecular frame

Photofragment imaging studies
- active alignment of methyl iodide, 100
- alignment in intense fields, 88
- alignment in weak fields, 87–88
- anisotropy parameter equation, 88
- behavior in one-color multiphoton experiments, 89, 95
- dissociative ionization, viable mechanism, 98, 100
- effective anisotropy parameter, 100
- examining various mechanisms, 98
- experimental methods, 89
- image of product I atoms by photodissociating iodobenzene with 68 mJ/cm$^2$ of 532 nm radiation, 96f
- image of product I atoms by photodissociating methyl iodide at 304.67 nm, 97f
- image of product I atoms from photodissociating iodobenzene at 266 nm, 92f
- image of product I atoms from photodissociating iodobenzene at 304.02 nm, 91f
- image of product I atoms from photodissociating iodobenzene at 304.67 nm, 90f
- intensity dependence of anisotropy parameter for iodobenzene at 532 nm, 99f
- iodine atom detection by velocity map imaging, 89
- ladder climbing, viable mechanism, 98
- multiphoton photodissociation of iodobenzene, 95, 98, 100
- potential energy of molecule, 88
- probability of absorbing photon, 87
- recoil angular distribution, 100
- relative kinetic energy of recoiling fragments of iodobenzene (304.67 and 304.02 nm), 93f
- relative kinetic energy of recoiling fragments of iodobenzene (9.2 mJ/cm$^2$ of fourth harmonic and 68 mJ/cm$^2$ of second harmonic of Nd:YAG laser), 94f
- requirements for observing active alignment, 88
- single color, one-photon photodissociation studies of iodobenzene, 89
- single-photon photodissociation of iodobenzene, 95
- unusual hourglass feature superimposed on two rings, 95, 98
- See also Atomic orientation and alignment in photodissociation

Photofragment mass distributions
- CNN radical, 303–304
- HNCN radical, 306
- NCN radical, 300–301
- See also Free radicals, photodissociation spectroscopy and dynamics

Photofragment orientation
- dispersion cross sections corresponding incoherent and coherent mechanisms, 264f

experimental absorption and dispersion Doppler profiles of spin-oriented rubidium photofragments, 264f
  photodissociation of RbI at 266 nm, 262–265
  potential curves of RbI, 263f
  See also Rubidium iodide (RbI)
Photofragment yield (PFY)
  spectra of CNN radicals, 303
  spectra of HNCN radicals, 305–306
  spectra of NCN radicals, 299–300
  See also Free radicals, photodissociation spectroscopy and dynamics
Photoionization processes, studies of energetics and dynamics, 13–14
Photon-atom interactions. *See* Coincident imaging spectroscopy (3D)
Pixellated detectors, future prospects, 14
Point spread function (PSF), equation, 75
Polarization effects, application of simulated images, 225, 228
Potential energy surfaces (PESs)
  diatomic in molecule (DIM) formalism for obtaining, 328
  See also Fragmentation of sodium ion clusters by He impact
Potential surface crossing
  alkyl iodides, 24
  iodine release from 1-iodonaphthalene, 23–24
  methane, 24–25
  See also β parameter
Product imaging technique
  application to photodissociation of ozone, 39, 44, 50
  channels for photodissociation of ozone in Hartley band, 39
  evolution, 35–39
  example of increase in resolution using ion counting technique, 38f
  experimental apparatus, 36f
  first image of methyl radicals from dissociation of methyl iodide, 38f
  images using velocity mapped imaging and ion-counting method, 38f
  inverse Abel transform recovering three-dimensional information, 37, 38f
  $N_2O$ photodissociation, 37, 38f
  problem in resolution of technique, 37
  singlet channel for ozone photodissociation, 39, 44
  "Three spheres I", 35
  triplet channel for ozone photodissociation, 44, 50
  See also Ozone photodissociation
Product translational spectroscopy, measuring product angular distribution and translational energy distributions, 127
Pump-probe experiment
  combining with photoelectron imaging, 286
  description, 285
  See also Femtosecond time-resolved photoelectron imaging
Pyrazine
  angular anisotropy of photoelectron distribution, 292
  average recoil energy from predissociation of aromatic-Ar van der Waals clusters, 160f
  decay of total photoelectron intensity in [1+1'] resonance enhanced multiphoton ionization (REMPI) via $S_1$ state of pyrazine and deuterated pyrazine, 292f

Downloaded by 89.163.34.136 on September 17, 2012 | http://pubs.acs.org
Publication Date: October 18, 2000 | doi: 10.1021/bk-2001-0770.ix002

- instantaneous formation of $S_1$ from $S_2$ and subsequent decay to $S_0$, 293f
- intersystem crossing mediated by $T_2(\pi,\pi*)$, 291, 293
- inverse Abel transforms of photoelectron images of [1+2'] REMPI via $S_1$, 290f
- ion image from excitation, 155, 156f
- ion image of fragment after Pyr-Xe cluster predissociation, 155, 156f
- [1+1'] ionization via $S_2$ state, 289
- [1+2'] ionization via $S_1$ state, 287–288
- normalized relative recoil probability distributions for predissociation of Pyr-Ar, 158f
- photoelectron kinetic energy distributions in femtosecond [1+2'] REMPI via $S_1$, 291f
- properties of aromatic-Ar van der Waals clusters, 159f
- recoil probability distributions, 157–158
- [1+2'] REMPI, 288f
- $S_1$ state, 289–292
- $S_2$ state, 292–293
- time dependence of total photoelectron signal in femtosecond [1+2'] REMPI via $S_1$, 289f
- time-of-flight profiles for pyrazine and fragment after Pyr-Ar cluster predissociation, 157f
- See also Femtosecond time-resolved photoelectron imaging; Recoil energy distributions in van der Waals cluster vibrational predissociation

Pyrimidine
- average recoil energy from predissociation of aromatic-Ar van der Waals clusters, 160f
- properties of aromatic-Ar van der Waals clusters, 159f

**Q**

Qualitative analysis, crossed beam experiments, 221–222

**R**

Radical photodissociation, emerging for imaging studies, 5

Reaction dynamics, applications of three-dimensional imaging techniques, 9–10

Reaction dynamics using velocity map imaging
- abstraction reactions of H atoms from hydrocarbons, 176
- accelerating and imaging $H^+$ ion, 170
- advantages of crossed-beam imaging, 176
- anisotropic $SF_5^+$ angular distributions, 190, 193
- Cl beam generation by photodissociation of oxalyl chloride, 177
- comparing results for Cl-$C_2H_5OH$ with Cl-$C_3H_8$, 182
- contrasting conventional ion imaging and VELMI, 171f
- crossed-beam imaging apparatus, 168, 169f
- difference images to estimate contributions from particular electronic states, 188
- energy diagram for excited states of vinyl radical with absorption of 243 nm photon, 174, 175f
- experimental, 168, 170

Downloaded by 89.163.34.136 on September 17, 2012 | http://pubs.acs.org
Publication Date: October 18, 2000 | doi: 10.1021/bk-2001-0770.ix002

Downloaded by 89.163.34.136 on September 17, 2012 | http://pubs.acs.org
Publication Date: October 18, 2000 | doi: 10.1021/bk-2001-0770.ix002

forward scattering in crossed-beam Cl-hydrocarbon systems, 182
history of interest in tetraoxygen molecules, 183
identification of novel species: $O_4$, 183, 187
image of H atoms from photodissociation of vinyl radical, 172f
images of reactively scattered hydroxyethyl radical from reaction of Cl with ethanol at two collision energies, 180f
images of $SF_5^+$ from dissociative ionization of $SF_6$, 190, 191f
imaging dissociative ionization dynamics in $SF_6$, 188, 190, 193
imaging radical dissociation dynamics, 170, 174
ionizing hydroxyalkyl radical reaction product, 177
mechanism likely involving near-collinear Cl–H–C transition state, 179, 182
modification of molecular beams apparatus for radical studies, 170
observations of tetraoxygen ($O_4$) molecules, 183, 187
photoelectron images recorded on various lines in spectra at 323.148 nm, 306.12 nm, 296.79 nm, and 294.89 nm, 185f
photoelectron yield and m/e=64 photoion yield (PIY) spectra of $O_2$ beam through DC discharge, 183, 184f
photolysis of vinyl chloride, 170
PIY spectra for $SF_6$, 189f
radicals by abstraction of H atom from ethanol by Cl atom, 177, 179
raw image of hydroxyethyl radical product of Cl + ethanol reaction, 178f
reactive scattering: Cl + $C_2H_5OH$ ς HCl + $C_2H_4OH$, 176–182
reactive scattering experiments with ethanol, 179
relevant potential curves summarizing all observations for $O_4$, 186f
schematic energy diagram for vinyl radical and dissociation to $C_2H_2$ + H, 174, 175f
sensitivity of ion imaging methods for reactive scattering, 176
sideways-backward scattering versus forward scattering events, 182
translational energy and angular distributions for $SF_5^+$ from images, 190, 192f
translational energy distribution and corresponding angular distribution for Cl + ethanol reaction, 181f
translational energy distribution for H atom from inverse Abel transformed image, 173f
translational energy distribution for inner ring from inverse Abel transformed image, 173f
van der Waals complex $O_2$–$O_2^+$ accounting for experimental results, 187
velocity map imaging (VELMI) technique, 168, 170
Reaction products. *See* Velocity mapping of reaction products
Reactive scattering, studies, 6
Reblur method, deconvolving spectroscopic data by constrained

version of, 75
Recoil angular distribution, active alignment of methyl iodide, 100
Recoil anisotropy parameter of photofragments, β
  photoinitiated unimolecular decomposition of jet cooled $NO_2$, 3–4
  See also β parameter
Recoil energy distributions in van der Waals cluster
  vibrational predissociation
  average recoil energy depending on cluster partner, 160
  average recoil energy from predissociation of pyrazine-X van der Waals clusters, 161f
  average recoil energy from predissociation of aromatic-Ar van der Waals (VDW) clusters, 160f
  calculated recoil energy distributions versus experimental data, 162, 163f
  charged deflection plates, 154–155
  classical trajectory calculations, 161–164
  cluster lifetime histograms from classical trajectory calculations, 164f
  differences in velocity selectivity and sensitivity between ion imaging and velocity-resolved time-of-flight techniques, 158–159
  ergodic collision theory, 160–161
  experimental methods, 152–155
  factors influencing resolution of ion imaging technique, 153–154
  first excited singlet ($S_1$) p-difluorobenzene-Ar and p-fluorotoluene-Ar complexes, 159
  formation of van der Waals (VDW) clusters, 153
  ion image from excitation of monomer pyrazine, 155, 156f
  ion image of pyrazine fragment after Pyr-Xe cluster predissociation, 155, 156f
  ion imaging technique, 153–154
  method minimizing effects of experimental noise, 155
  minimizing effect of perpendicular components, 155
  normalized relative recoil probability distributions for predissociation of Pyr-Ar, 158f
  properties of aromatic-Ar van der Waals clusters, 159t
  recoil probability distributions, 157–158
  recoil velocity equation, 157
  spectrometer voltages controlling time-of-flight and velocity mapping, 154
  TOF profiles for monomer pyrazine and pyrazine fragment after Pyr-Ar cluster predissociation, 157f
  translational energy histograms from classical trajectory calculations, 163f
  typical TOF profile for dissociation of Pyr-Ar, 157
  van der Waals cluster predissociation, 151–152
  VDW cluster as model of half-collision, 160–161
  velocity-resolved time-of-flight, 157–159
  velocity-resolved time-of-flight experiment, 154–155
Recoil velocity and angular distribution, photodissociation of $Cl_2O$ and HOCl, 4

Downloaded by 89.163.34.136 on September 17, 2012 | http://pubs.acs.org
Publication Date: October 18, 2000 | doi: 10.1021/bk-2001-0770.ix002

Recoil velocity of fragments
  converting 2-D image to 3-D representation, 107
  See also Velocity imaging using vacuum ultraviolet lasers
Recoil velocity vector-angular momentum (v-J) correlation effects
  beyond β parameter, 29–30
  generalized angular distributions, 29–30
  hydrogen peroxide, 29
  See also β parameter
Reconstruction, image. *See* Image reconstruction
Resonance enhanced multiphoton ionization (REMPI)
  combination with ion imaging detector, 140
  detection scheme for H atoms, 128–129
  expressions for 2+1 REMPI signal for four experimental geometries, 254–255
  imaging method, 20
  kinetic energy distributions of $O^+$ and photoelectrons by (2+1) REMPI of $O_2$ at 225 nm, 65f
  REMPI/dissociation of oxygen, 64, 66
  state selective ionization of $H^{35}Cl$ scattered products, 198–199
  See also Femtosecond time-resolved photoelectron imaging; Pyrazine; Velocity map imaging (VELMI)
Rotational energy transfer (RET), varying cross section, 197
Rotational state resolved differential cross sections
  angular dependent detection efficiencies, 134–135
  angular distribution of H atom products corresponding to low rotationally excited $OH(X^2\Pi, v=0)$ products, 136f
  angular distribution of total H atom reaction products, 135f
  angular distributions for simulated apparatus function and experimental data, 207, 210
  apparatus, 198
  apparatus function, 203–204
  correction factor for extracted distribution, 210
  course of non-uniformity in intensity and velocity, 201
  crossed beam study of $O(^1D) + H_2$ ς OH + H reaction, 130
  demonstration of DCS extraction from simulated experiment, 210, 211f, 213
  detection schemes for H atoms, 128f
  determination of apparatus function, 203–213
  excitation of ground state H atom product, 129–130
  experimental, 198–199
  experimental image intensity, 204
  experimental ion images for state-to-state j-changing collisions, 201, 202f
  experimental methods, 128–130
  extraction procedure for ideal scattering system, 207, 208f, 209f
  flowchart for scattering simulation program, 205f
  focused laser volume overlapping distribution of scattered products, 203
  H atom products from chemical reactions, 127
  H atom Rydberg "tagging" time-of-flight (TOF) technique, 128–129
  H atom Rydberg transitions from

Downloaded by 89.163.34.136 on September 17, 2012 | http://pubs.acs.org
Publication Date: October 18, 2000 | doi: 10.1021/bk-2001-0770.ix002

Downloaded by 89.163.34.136 on September 17, 2012 | http://pubs.acs.org
Publication Date: October 18, 2000 | doi: 10.1021/bk-2001-0770.ix002

  n=2 level to higher n states, 129f
  intensity of ions impinging upon detector, 204
  measuring differential cross sections (DCS), 199
  modeling of experiment, 199–203
  Newton diagram for crossed beam $O(^{1}D) + H_2$ ς $OH + H$ reaction, 132f
  Newton diagram for inelastic scattering of HCl seeded in Ar with neat Ar molecular beam, 200f
  objective of data analysis, 199
  product translational spectroscopy, 127
  projection of center-of-mass scattering distribution of ionized products, 201
  reaction of $O(^{1}D) + H_2$, 130–131
  removal of instrument dependent asymmetries, 207
  representing kinematics in center-of-mass (CM) frame, 199
  scattering simulation program, 204, 206–207
  simple schematic of experimental setup for studying crossed beam $O(^{1}D) + H_2$ ς $OH + H$ reaction, 131f
  simulated images of experimental data of HCl + Ar, 212f, 213
  spatial profile of laser, 206
  state-selective ionization of $H^{35}Cl$ scattered products by resonance enhanced multiphoton ionization (REMPI), 198–199
  temporal overlap of molecular beams, 203
  time-integrated intensity on image after scattering begins for center-of-mass collision energy, 203
  TOF spectra at three laboratory angles for H atom products using Rydberg tagging TOF technique, 133f
  total product translational energy distributions converted from TOF spectra, 134f
  using extracted angular scattering distribution as differential cross section (DCS) for new simulated image, 210
  velocity trajectory expression, 206
Rubidium iodide (RbI)
  dispersion cross sections corresponding incoherent and coherent mechanisms for photofragment orientation, 264f
  experimental absorption and dispersion Doppler profiles of spin-oriented photofragments, 264f
  photodissociation at 266 nm, 262–265
  potential curves, 263f
  pump-probe scheme, 263
Rydberg tagging
  H atom Rydberg transitions from n=2 to higher n states, 129f
  time-of-flight (TOF) detection scheme for H atoms, 128–129

S

Scattering. *See* Surface scattering
Scattering, inelastic, Ne + CO. *See* Ne + CO inelastic scattering
Scattering and recoiling imaging spectroscopy (SARIS), assigning structure of adsorbates on surfaces, 140
Schumann–Runge bands

Downloaded by 89.163.34.136 on September 17, 2012 | http://pubs.acs.org
Publication Date: October 18, 2000 | doi: 10.1021/bk-2001-0770.ix002

- predissociation after excitation of P(17) line of ν=4 manifold, 65f
- predissociation of oxygen, 63–64
- vibrational components, 63f

Simulations
- density distribution of products scattered, 217
- distribution of product ions, 218
- flowchart describing procedure generating simulated ion images, 205f
- general expression for observed intensity distribution, 217–219
- implementing crossed beam experiments, 220–221
- Imsim program, 220–221
- number of ions arriving in particular pixel, 218–219
- real crossed beam experiments, 216–221
- reducing simulation time, 221
- scattering simulation program, 204, 206–207
- simplifying approximations, 219–220
- See also Crossed beam reactions; Rotational state-resolved differential cross sections

Singlet channel. *See* Ozone photodissociation

Slow anisotropic dissociation
- β parameter, 25–27
- deuterated ammonia, 27, 28f
- HCO, 26–27
- hydrogen azide, 27
- See also β parameter

Sodium ion clusters. *See* Fragmentation of sodium ion clusters by He impact

Spectroscopy, advantages of imaging photoelectron, 7

State-to-state collisions. *See* Rotational state-resolved differential cross sections

State-to-state dissociation of molecular ions
- branching ratios for dissociative recombination (DR) of $HD^+$ as function of electron energy for final states, 362f
- Coulomb explosion imaging (CEI) detector, 355–356
- Coulomb explosion imaging of $HD^+$: measurement of vibrational state population, 361, 363
- creating small amounts of molecular ions, 369
- distributions of 3-D distance between DR fragments as measured for different electron energies, 359, 360f
- DR imaging detector, 356, 358
- DR of excited $HD^+$, 363, 366
- DR of $HD^+$, 351–355
- DR of $HD^+$ (ν=0), 358–361
- DR of $HD^+$ with low-energy electrons, 352–353
- DR rate coefficient for molecular ions in vibrational state, 353, 355
- DR reaction for molecular ion $AB^+$, 351–352
- experiments using test storage ring (TSR), 353
- extreme sensitivity of DR to initial vibrational state of molecular ion, 352
- final experimental results for relative DR rate coefficients of $HD^+$ at $E_e$=0 as function of initial vibrational quantum number, 368f
- heavy-ion storage ring technique, 352

- ideas behind experimental technique, 353
- kinetic energy distribution, image of internuclear distance distribution, 363
- kinetic energy release, 361
- kinetic energy spectra measured for CEI of $HD^+$ for different storage time slices, 364f
- limitations, 369
- measuring reaction rates for different types of processes, 369
- outlook, 366, 369
- potential energy curves for $HD^+$ and HD, 354f
- projected distance distributions as measured between H and D fragments from DR of vibrationally excited $HD^+$ at zero electron energy and different storage times, 367f
- schematic drawing of 3-D imaging detector setup, 357f
- schematic drawing of test storage ring (TSR), 354f
- storage-ring techniques measuring DR cross section for individual excited vibrational states, 352
- study of DR reactions for selected rotational states, 369
- technique for measuring vibrational-state specific reaction rates, 351
- three-dimensional fragment distance, 359
- three-dimensional molecular fragments imaging, 355–358
- time evolution of vibrational state population for $11 \geq v \geq 0$ from fitting time-sliced CEI kinetic energy spectra, 365f

Sulfur hexachloride ($SF_6$)
- anisotropic $SF_5^+$ angular distributions, 190, 193
- difference images to estimate contributions from particular electronic states, 188
- images of $SF_5^+$ from dissociative ionization of $SF_6$, 190, 191f
- imaging dissociative ionization dynamics, 188, 190, 193
- photoionization yield (PIY) spectra, 189f
- translational energy and angular distributions for $SF_5^+$ from images, 190, 192f
- See also Reaction dynamics using velocity map imaging

Surface scattering
- assembly drawing of flyswatter detector, 142f
- atom abstraction, 147
- complexity of gas/surface interactions limiting researchers, 140
- critical parameters in operating flyswatter, 143
- dissociative scattering at surfaces, 147
- Eley–Rideal reaction mechanism, 147
- experimental, 140–143
- flight times of ions through detector, 142–143
- geometrical constraints in overall analysis, 143
- image analysis, 145–146
- image analysis software, 145
- image of incident $NO^+$ ions approaching surface, 144f
- image of scattered ions after background subtraction, 146f
- image of scattered ions after filtering and thresholding, 146f
- image of scattered $NO^+$ ions at swat

Downloaded by 89.163.34.136 on September 17, 2012 | http://pubs.acs.org
Publication Date: October 18, 2000 | doi: 10.1021/bk-2001-0770.ix002

  - delay of 30 μs, 144f
- ion detectors for studying ion/surface scattering, 139–140
- ion imaging in gas-phase photodissociation, 140
- Kernel for filtering particles, 145t
- monitoring incident and scattered ions, 141
- probability density for scattered $O^-$ ($^2P$) fragments as function of final velocity and scattering angle, 149f
- reaction of hyperthermal energy ions with surfaces, 139
- scattering of state-selected $NO^+$ on GaAs(110) exhibiting energy transfer, charge transfer, and fragmentation, 149
- scattering procedure, 140–141
- schematic of ion imaging detector (flyswatter), 141f
- sequence of voltage pulses applied to flyswatter optics, 142f
- time-of-flight mass spectrum of incident $OCS^+$ ions and scattered negative ions, 148f
- velocity analysis, 147
- velocity distribution for $NO_2^-$ formed from $NO^+$ abstracting oxygen atom from O/Al(111), 148f

Symmetry of upper state
- t-butyl hypochlorite, 21
- methyl radical, 20–21
- nitrous acid, 21, 23
- water, 21, 22f
- See also β parameter

T

Tetraoxygen ($O_4$)
- history, 183
- identification by velocity map imaging, 183, 187
- photoelectron yield and m/e=64 photoion yield (PIY) spectra, 183, 184f
- summary of observations, 186f
- van der Waals complex $O_2$–$O_2^+$ accounting for experimental results, 187
- various photoelectron images, 185f
- See also Reaction dynamics using velocity map imaging

Three-body dissociation dynamics of transient $O_6$ molecules
- additional $O_2$ molecule as spectator in photochemistry of $O_6^-$, 323
- analysis by molecular-frame differential cross section (MF–DCS) spectra, 316–317
- analysis by photoelectron-photofragment energy correlation spectra (N($E_T$,eKE)), 316
- coincidence measurements of multiple fragments, 313
- experimental, 314–317
- mass electron kinetic energy (eKE), 316
- MF–DCS spectra for dissociative photodetachment (DPD) of $O_6^-$ at 532, 388, and 258 nm in center-of-mass velocity space, 320f
- molecular frame differential cross section (MF–DSC), 319, 321
- N($E_T$,eKE) spectra for $O_4^-$ and $O_6^-$ at 388 nm, 318f
- photodestruction and photodissociation cross-section measurements on $O_6^-$, 314
- photodestruction dynamics of $O_6^-$, 314
- photodestruction dynamics of $O_6^-$ at 388 nm, 321, 323

Downloaded by 89.163.34.136 on September 17, 2012 | http://pubs.acs.org
Publication Date: October 18, 2000 | doi: 10.1021/bk-2001-0770.ix002

Downloaded by 89.163.34.136 on September 17, 2012 | http://pubs.acs.org
Publication Date: October 18, 2000 | doi: 10.1021/bk-2001-0770.ix002

  - photoelectron-photofragment coincidence (PPC) spectroscopy, 313
  - photoelectron-photofragment kinetic energy correlation spectra, 317, 319
  - previous studies on small homogeneous cluster anions of $O_2$, 313–314
  - schematic of apparatus, 315f
  - stability of $O_6^-$ relative to $O_4^- + O_2$, 321
  - total energy gated MF–DCS images of $O_6$ at 388 nm, 322f
- Three-dimensional imaging techniques
  - applications to reaction dynamics, 9–10
  - experimental, 8–9
  - See also Coincidence studies
- "Three spheres I", etching illustrating product imaging technique principle, 35
- Time-of-flight mass spectrometry
  - method, 105
  - protonated methanol clusters, 117, 118f
  - separating parent and product with similar ionization potentials, 104
  - spectrum of $C_3H_3^+$ and $C_3H_4^+$ from photolysis of allene at 118 nm, 114f
  - spectrum of photoionization signal from seeded and neat ethyl bromide using 118 nm, 111f
  - TOF mass spectrum of incident $OCS^+$ ions and scattered negative ions, 148f
  - See also Velocity imaging using vacuum ultraviolet lasers
- Time-of-flight (TOF) technique
  - detection schemes for H atoms, 128f
  - H atom Rydberg "tagging", 128–129
  - three laboratory angles for H atom products from crossed beam $O(^1D) + H_2$ ς $OH + H$ reaction, 133f
- Time-resolved photoelectron imaging. *See* Femtosecond time-resolved photoelectron imaging
- Time-resolved photoelectron-photoion coincidence measurements
  - dissociation of $NO_2$ molecule, 14
  - See also Coincidence studies
- Toluene
  - average recoil energy from predissociation of aromatic-Ar van der Waals clusters, 160f
  - properties of aromatic-Ar van der Waals clusters, 159f
- Trajectory calculations, classical
  - cluster lifetime histograms, 164f
  - dynamics of pyrazine-Ar cluster dissociation, 161–164
  - translational energy histograms, 163f
  - See also Recoil energy distributions in van der Waals cluster vibrational predissociation
- Transformation, expression for linestrength factors, 280–282
- Transient neutral species. *See* Three-body dissociation dynamics of transient $O_6$ molecules
- Translational energy distributions
  - CNN radical, 304–305
  - crossed beam $O(^1D) + H_2$ ς $OH + H$ reaction, 134f
  - HNCN radical, 306, 307f
  - NCN radical, 301–302
  - See also Free radicals, photodissociation spectroscopy and dynamics
- Translational spectroscopy

- measuring product angular distribution and translational energy distributions, 127
- See also Rotational state resolved differential cross sections

Triatomic hydrogen, charge-exchange technique for three-body breakup, 11

Triplet channel. *See* Ozone photodissociation

U

Unresolved internal energy distributions, application of simulated images, 228

V

Vacuum ultraviolet laser (VUV)
- early studies of photochemistry of simple molecules, 105
- imaging dissociative ionization dynamics in $SF_6$, 188, 190, 193
- introducing VUV femtosecond probe laser, 294
- See also Sulfur hexachloride (SF6); Velocity imaging using vacuum ultraviolet laser

Vacuum ultraviolet (VUV) photon-atom interaction. *See* Coincident imaging spectroscopy (3D)

van der Waals (VDW) cluster predissociation
- cluster formation, 153
- computational investigation of cluster dissociation, 152
- insights into intramolecular and intermolecular energy flow, 151–152
- transitional modes, 151–152
- See also Recoil energy distributions in van der Waals cluster vibrational predissociation

Vector correlations
- photodissociation, 29
- photodissociation of molecules, 238–239

Velocity distribution
- measured distribution on detector, 71, 72f
- recovery, 68

Velocity imaging using vacuum ultraviolet laser
- allene ($C_3H_4$), 110, 116
- alternate mechanism for formation of $C_3H_3^+$, 116
- apparatus, 105, 106f
- benefits of centroiding process, 107
- calculated and observed maximum translational energies, 123t
- calibration time-of-flight (TOF) mass spectrum using allene, acetone, and ethyl bromide, 108, 109f
- converting 2-D image to 3-D representation of recoil velocity of selected fragment, 107
- creating VUV light at 118 nm, 108
- data acquisition method, 105, 107
- ethyl bromide for calibrating imaging detector, 108, 110
- experimental, 105–108
- images of protonated monomer, dimer, trimer, tetramer, and pentamer, 120f
- importance of systematic study of molecular photodissociation using tunable VUV lasers, 104–105
- ion kinetic energy distributions of protonated methanol clusters, 121f
- maximum translational energies in clusters, 119, 123

Downloaded by 89.163.34.136 on September 17, 2012 | http://pubs.acs.org
Publication Date: October 18, 2000 | doi: 10.1021/bk-2001-0770.ix002

mechanism for production of $C_3H_4^+$ and $C_3H_3^+$, 116
mechanism of formation for protonated clusters, 119
methanol clusters, 117, 119, 123
method for obtaining image of ion at particular m/e ratio, 108
possible reactions for absorption of VUV photon by methanol or clusters, 117
relative kinetic energy distribution calculation, 107
relative translational energy distributions of protonated methanol clusters, 122f
shift in geometry between ground states of allene and allene ion, 116
TOF spectra of direct photoionization signal from seeded and neat beam of ethyl bromide at 118 nm light, 111f
TOF spectrum of $C_3H_3^+$ and $C_3H_4^+$ from photolysis of allene at 118 nm, 114f
TOF spectrum of protonated clusters of $H^+(CH_3OH)_n$ (n=1 to 5), 118f
translational energy distribution of $C_2H_5^+$ and $C_2H_4^+$ ions, 113f
translational energy distributions of $C_3H_3^+$ and $C_3H_4^+$ ions from photoionization of allene at 118 nm, 115f
typical experiment, 108
velocity images of $C_3H_3^+$ and $C_3H_4^+$ in photoionization of allene at 118 nm, 115f
velocity images of fragments from 118 nm photolysis of ethyl bromide under different beam conditions, 112f
Velocity map imaging (VELMI)
absorption spectrum and deconvolution of Herzberg continuum, 63f
advantages, 58, 59f
advantages and disadvantages, 104
anisotropy parameter equations, 61
cold target recoil ion momentum spectroscopy (COLTRIMS), 14
comparison of velocity mapping and ion imaging under identical conditions, 59f
deconvolution of Herzberg continuum, 62
determining specific quantum states of atoms or molecules in chemical reactions, 104
event counting, 59–60
evolution of technique, 2
example of single shot image and corresponding event counted image, 59f
experimental, 57–60
images of dinitrogen monoxide dissociation, 37, 38f
image using event counting, 60f
imaging photoelectron spectroscopy, 7
ion imaging and velocity mapping methods, 57–58
ion imaging configuration, 57, 58f
kinetic energy distributions of $O^+$ and photoelectrons produced by (2+1) resonance enhanced multiphoton ionization (REMPI) of $O_2$ at 225 nm, 65f
marriage of laser and crossed molecular beam techniques, 197–198
modification of ion imaging technique, 103
new progress, 56–57
oxygen photophysics, 61–66

Downloaded by 89.163.34.136 on September 17, 2012 | http://pubs.acs.org
Publication Date: October 18, 2000 | doi: 10.1021/bk-2001-0770.ix002

Downloaded by 89.163.34.136 on September 17, 2012 | http://pubs.acs.org
Publication Date: October 18, 2000 | doi: 10.1021/bk-2001-0770.ix002

ozone photodissociation using new ion-counting method, 4
photodissociation dynamics, 3–5
photodissociation/ionization of $O_2$, 3
photodissociation of chlorine, 5–6
predissociation of $O_2$ after excitation of P(17) line of v=4 manifold, 65f
predissociation of Schumann–Runge bands, 63–64
product iodine atoms for iodobenzene photodissociation, 90f, 91f, 92f
REMPI/dissociation of $O_2$, 64, 66
schematic of apparatus, 58f
schematic potential energy diagram for electronic states of $O_2$ and $O_2^+$, 62f
sensitivity for detection of free radicals, 104
two-photon photodissociation of NO, 3
use of electrostatic immersion lens, 56
use of vacuum ultraviolet lasers, 104
See also Ion imaging; Ozone photodissociation; Photofragment imaging studies; Reaction dynamics using velocity map imaging; Rotational state-resolved differential cross sections; Velocity imaging using vacuum ultraviolet laser

Velocity mapping of reaction products
  averaged 2D ion projections of HCl, 234f
  collision energy of reaction, 236
  contrast to earlier research, 236
  experimental, 231–233
  experimental apparatus, 232f
  extracting quantitative data from 2D images, 233
  factors determining uncertainty in collision energy of reaction, 236
  forward scattering, 236
  integration of inverted images by radius for speed distributions, 233
  reaction of atomic chlorine with ethane producing hydrogen chloride and ethyl radical, 231
  reconstructed images of 2D projections via inverse Abel transformation, 234f
  speed distributions of HCl by rotational state, 235f

Velocity-resolved time-of-flight
  differences in velocity selectivity and sensitivity from ion imaging technique, 158–159
  recoil probability distributions, 157–158
  recoil velocity equation, 157
  technique for van der Waals cluster dissociation, 154–155
  typical profile for dissociation of pyrazine-Ar, 157
  See also Recoil energy distributions in van der Waals cluster vibrational predissociation

Velocity trajectory, expression, 206

Vibrational state populations
  measurement using Coulomb explosion imaging of $HD^+$, 361, 363
  See also State-to-state dissociation of molecular ions

Vinylidene, schematic energy diagram for vinyl radical and dissociation to $C_2H_2$ + H, 174, 175*f*

v-J (recoil velocity vector-angular momentum) correlation effects

  beyond β parameter, 29–30
  generalized angular distributions, 29–30
  hydrogen peroxide, 29
  See also β parameter

**W**

Water, photodissociation, 21, 22*f*
Wiley–Laren arrangement, quasi, velocity focusing, 71

**X**

X-ray diffraction experiments, macromolecular structure, 9

**Z**

ZZ correlations
  correlation between locations on vertical axis Z of two detected fragments, 330
*See also* Fragmentation of sodium ion clusters by He impact

Downloaded by 89.163.34.136 on September 17, 2012 | http://pubs.acs.org
Publication Date: October 18, 2000 | doi: 10.1021/bk-2001-0770.ix002